



Vilnius University
Lithuanian Academy of Science
Kaunas University of Technology
Center for Physical Sciences and Technology

International Conference of
Lithuanian Chemical Society

Chemistry and Chemical Technology 2015

Dedicated to Professor Vitas Daukšas
on His 80th Birth Anniversary

Programme and Proceedings
of the International Conference

Vilnius, Lithuania
January 23, 2015





Conference Organizers

Vilnius University,
Lithuanian Academy of Sciences
Kaunas University of Technology,
Center for Physical Sciences and Technology

Scientific Committee

Prof. Juozas Vidas Gražulevičius (KTU)
Prof. Eimutis Juzeliūnas (KU)
Prof. Aivaras Kareiva (VU)
Prof. Ričardas Makuška (VU)
Prof. Rimantas Ramanauskas (FTMC ChI)
Prof. Arūnas Ramanavičius (VU)
Prof. Rimantas Raudonis (VU)
Prof. Valdemaras Razumas (LMA)
Prof. Stasys Tautkus (VU)
Prof. Sigitas Tumkevičius (VU)
Prof. Eugenijus Valatka (KTU)

Organizing Committee

Prof. Sigitas Tumkevičius (VU) – **Chairman**
Dr. Jelena Dodonova (VU) – Secretary
Doc. Aušra Valiūnienė (VU)
Doc. Artūras Žalga (VU)
Olga Darčanova (VU)
Lina Mikoliūnaitė (VU)
Teresa Subatniekienė (VU)
Lukas Taujenis (VU)

ISBN 978-609-459-461-8



Organizers would like to express their warm thanks
to the sponsors of the Conference:

Patron

ThermoFisher
S C I E N T I F I C

General sponsor

BIO EK SMA

Main sponsors



 *Linea libera*



Sponsors

GRID A

 LOKMIS

 **MKDS**
innovation


eurochemicals

 **LaboChem**

LABOCHEMA is a supplier of high quality laboratory reagents, consumables, equipment and furniture. The company was found in 1997 in Vilnius, Lithuania. During last 18 years LABOCHEMA has grown from 2 employees to a leader in the Baltic region. Today more than 50 professionals are employed by LABOCHEMA group in Lithuania, Latvia and Estonia.

The vision of our company is to become the first choice for all laboratories in the Baltic states for purchasing laboratory reagents, consumables, equipment and furniture. LABOCHEMA target is to fulfil the customers needs, to supply high quality products and services and to share technical experience and research methodology, that ensures our customers success in laboratory research and quality control. Loyalty, attention to customer needs, constant progress, personnel respect and appropriate representation of product manufacturers are the core values of LABOCHEMA.

Would like to know more about us? Visit www.labochem.com

LABOCHEMA - reliable supplier for your laboratory!



Dear Participants, Colleagues and Guests!

It is our pleasure to welcome you in Vilnius at the International conference of Lithuanian Chemical Society *Chemistry and Chemical Technology 2015* (CCT2015). The conference CCT is organized every year in Vilnius or Kaunas by *Vilnius University, Kaunas University of Technology, Lithuanian Academy of Sciences and Center for Physical and Technological Sciences*. This year conference is dedicated to the famous Lithuanian chemist - *professor of Vilnius University, academician Vitas Daukšas* on the occasion of his 80th birthday anniversary. This meeting is a tribute to this outstanding person, scientist and educator.

The conference is devoted to chemists working in chemistry, biochemistry, biology, environmental sector, materials science and technology. The main aims of the conference are:

- to provide an opportunity for chemists, whose interest are pointed to fundamental and applied research, to exchange the latest concepts and information;
- to promote interactions between chemists working in different fields of chemistry in order to create links and collaborations, to encourage a cooperation between science and industry;
- to provide an opportunity for younger scientists to learn about future trends and perspectives of various fields of chemistry in a multidisciplinary environment.

We particularly appreciate the Plenary Speakers. Their enthusiastic acceptance to speak made our job effortless. We are very grateful to short oral lecturers and the large number of poster contributors, especially young investigators, for us to enjoy during the conference.

Without generous support from companies and institutions, CCT2015 would still be just a dream. For CCT2015, we most sincerely thank all who supported the conference. Your participation shows your interest to chemical sciences and this gives us the greatest satisfaction and expectations for future collaboration in various aspects.

On behalf of the organizers I would like to thank all the participants for their contribution to this conference. We wish to all participants a scientifically and socially most enjoyable conference and a pleasant stay in Vilnius.

*On Behalf of the Organizing Committee
Sigitas Tumkevičius
Conference Chair*



PROFESSOR, ACADEMICIAN VITAS DAUKŠAS ON HIS EIGHTIETH BIRTHDAY

On January 21, 2015 Professor Vitas Daukšas, one of the most eminent Lithuanian chemists, former head of the Department of Organic Chemistry of Vilnius University would have celebrated his eightieth birthday.

Professor Vitas Daukšas was born in Kaunas on January 21, 1935. In 1952 he graduated from the Vilnius 1st boys' secondary school and began chemistry studies at the Faculty of Chemistry of Moscow State M. V. Lomonosov University. After graduation from it in 1957 he continued studying chemistry at the Department of Organic Chemistry of the same university as a post-graduate student. Under the supervision of professor R. Levina he carried out a research work on the synthesis of di(*tert*-alkyl)substituted methanes and prepared a doctoral dissertation "General method of synthesis of di(*tert*-alkyl)methanes and their cyclic analogs", which he defended at Moscow D. I. Mendelejev Institute of Chemical Technology in 1961. After returning to Vilnius Vitas Daukšas was appointed Head of the recently founded (in 1959) "Laboratory of synthesis and investigation of drugs" at the Vilnius University. From 1961 Vitas Daukšas started working as a senior lecturer at the Department of Organic Chemistry of Vilnius University, at the same time being supervisor of the mentioned Laboratory. In 1965 he became a docent of the Department of Organic Chemistry and in 1969 he obtained a professorship and became one of the youngest professors in the Vilnius University at that time. In a period 1976–1991 Vitas Daukšas served as Head of the Department of Organic Chemistry and from 1997 until his retirement in 2000 he was a leading scientist at the same department.

After returning from the post-graduate studies in Moscow, Vitas Daukšas very easily and with great energy integrated into scientific activities of the Department of Organic Chemistry of Vilnius University and all the time was a very active and productive scientist. As soon as after six years of intensive work at the Vilnius University in 1967 he prepared and defended a Dr. Sci. dissertation "Derivatives of benzodioxane-1,4 (synthesis, pharmacological activity, chemical and optical properties)". In 1963-1964 V. Daukšas worked on probation at the Department of Organic Chemistry of the Faculty of Natural Sciences of Carl university (Prague, Czech Republic). In 1969/1970 he worked with the well-known professor of organic chemistry John D. Roberts at the Department of Organic Chemistry of California



Technological Institute (USA) and in 1983/1984 – at the Institute of Pharmaceutical Chemistry of the University of Frankfurt (prof. H. Oelschlager)

The major part of V. Daukšas' scientific activities was associated with the Laboratory of Synthesis and Investigation of Drugs of Vilnius University. During all the Laboratory lifetime, for almost 30 years, he was its scientific supervisor. The first synthetic work for the Laboratory was ordered by SSRS Ministry of Health. Scientists of the Laboratory had to resynthesize and study the medication *Phentolamine* which was used for treatment of peripheral circulatory system. From 1966 until 1992 this medication was produced according to the Laboratory procedures at the plant "Švyturys". Although the Laboratory from time to time received various orders to resynthesize different preparations, already at the second year of its existence Professor V. Daukšas initiated works directed towards the synthesis and search of original drugs, mainly exhibiting adrenoblocking, anti-arrhythmic, cardiogenic, anesthetic, anti-inflammatory properties. The attention was focused on the synthesis and investigation of a series of benzoxaheterocycles. Synthesis of a number of new compounds of 1,4-benzodioxane, 1,3-benzodioxolane, 1,5-benzodioxepane, 1,6-benzodioxocane and later derivatives of nitrogen heterocycle, such as benzimidazole with fragments of aminoethers, aminoalcohols, aminoketones and others in the side chain of molecules was developed and accomplished. Along with the synthesis, the reactivity, physical properties, metabolism in living organisms, pharmacokinetics of the synthesized novel compounds were investigated as well as search of relationships between chemical structure of compounds and their biological activity were performed. As a result, a method for the prediction of anti-inflammatory activity of alkylarylketones, based on spectral characteristics of these compounds has been suggested. A highly potent anesthetic, *benzodiocaine*, as well as adrenoblocking and antiarrhythmic medication, *benzodixine*, were synthesized and investigated (B. Puodžiūnaitė, L. Pikūnaitė, I. Dembinskienė). In cooperation with the Institute of Experimental and Clinical Medicine some anti-rheumatic and anti-inflammatory medications – 2,3-dihydroxybenzoic acid, its diacetate and some analogs were also resynthesized and studied. In 1973 Professor organized a research team for the synthesis of compounds, which could be applied in the agriculture as plant growth regulators (senior research fellow Dr. R. Martinkus, Dr. S. Urbonienė ir Dr. Z. Šaltytė). In cooperation with scientists of Botanical Institute of the Lithuanian Academy of Sciences, academician A. Merkys, Dr. L. Novickienė, a number of new compounds possessing the retardant properties were synthesized and tested. For example, the synthesized in the Laboratory derivatives of α -naphthylacetic acid increase the starch content in potatoes for 30 percents and their crop for 40 percent. Some other compounds of this type were found to show a stimulating effect on incrustation of lupines and could be used for increasing the content of natural nitrogen fertilizers in soil.

Under the supervision of Professor V. Daukšas, 25 doctoral dissertations were defended. V. Daukšas never refused to help or consult other doctoral students or younger colleagues from the Department of Organic Chemistry and Faculty of Medicine in preparing their dissertations in the chemistry or medicine sciences. Professor was opponent of more than 100 dissertations. Together with his doctoral students and co-workers professor V. Dauksas published about 380 scientific publications, including more than 200 scientific articles, 2 review articles, 60 USSR Inventor's Certificates, 1 patent of Lithuania Republic. Professor gave lectures in the universities of Paduja (Italy), Debrecen (Hungary), Nukus (Karakalpakija – Uzbekistan), actively participated and made more than 80 reports in scientific conferences held in USA, Japan, Sweden, Poland, Russia, Ukraine, Belarus, Azerbaijan, Georgia, Estonia, Latvia and Lithuania.

Professor for a long time was a member of the Degree-Conferring Board of Kaunas Polytechnical Institute (now Kaunas University of Technology) and of the Chemistry Faculty of Vilnius University. Professor delivered lectures on various topics of organic chemistry for



teachers at the refresher courses of the Lithuanian Institute of Teachers Training. He was a longevous member of the Editorial Board of the journal "Chemija".

For undergraduate and graduate students of the Chemistry Faculty of Vilnius University Professor V. Daukšas delivered lectures of *Organic Chemistry*, *Theoretical Principles of Organic Chemistry*, *Physical Methods of Investigation* and *Biologically Active Compounds*. He with coauthors published educational books „*Exercises and problems of organic chemistry*“ (1983), “*Structure and reactivity of organic compounds*“ (1987), and “*Explanatory dictionary of chemical terms*“ (1997); its revised edition appeared in 2003. During the preparation of the dictionary he was responsible for all terms of organic chemistry, proposed their names in accordance with IUPAC rules, specified determinations.

Vitas Daukšas' scientific competence, his scientific management and pedagogical activities were highly considered by Lithuanian scientific community. In 1985 Professor Vitas Daukšas was awarded the prestigious title of Honored Fellow of Science, in 1990 he was elected to the Lithuanian Academy of Sciences as Corresponding Member, in 2011 – as full member of Lithuanian Academy of Sciences.

Sadly, he passed away on April 26, 2013 after a long and serious illness.

Professor V. Daukšas was known as a scientist with high principles, extremely hard-working and large-minded. In a company Professor was always well-liked and had a reputation as a witty man. The brilliant memory of Professor Vitas Daukšas will remain forever in the hearts of his colleagues and students.

Sigitas Tumkevičius

Vilnius University,
Faculty of Chemistry



Programme Overview	
08:00-09:00	Registration and preparation for poster session
09:00-09:30	Conference Opening (Auditorium of Inorganic Chemistry, Hall no. 141)
	Welcome from Rimantas Vaitkus , Vice-Minister of Lithuanian Ministry of Education and Science
	Valdemaras Razumas , President of Lithuanian Academy of Sciences
	Aivaras Kareiva , Dean of the Faculty of Chemistry, Vilnius University
09:30-10:00	Sigitas Tumkevičius. To the Eightieth Birthday of Professor Vitas Daukšas
10:00-10:10	Conference information, Dr. Jelena Dodonova, Conference Secretary
10:10	Plenary Lectures (Session I) (Auditorium of Inorganic Chemistry, Hall no. 141) Chairman – Rimantas Ramanauskas, Center for Physical Sciences and Technology
10:10-10:40	Georgi Popkirov , Central Laboratory of Solar Energy and New Energy Sources, Bulgarian Academy of Sciences, Sofia, Bulgaria. Electrochemical impedance spectroscopy: dreams and reality - applications to real-world samples.
10:40-11:10	Coffee break (Auditorium of Professor Kazys Daukšas, Hall no. 223)
11:10	Plenary Lectures (Session II) (Auditorium of Inorganic Chemistry, Hall no. 141) Chairman – Aivaras Kareiva, Sigitas Tumkevičius, Vilnius University
11:10-11:40	Petras Rimantas Venskutonis , Kaunas University of Technology, Kaunas, Lithuania. Phytochemicals for functional foods and nutraceuticals.
11:40-12:10	Maris Turks , Riga Technical University, Riga, Latvia. Novel applications of sulfur dioxide in organic synthesis and analysis of organic compounds.
12:10-12:40	Saulius Juršėnas , Vilnius University, Institute of Applied Research, Vilnius, Lithuania. Tailoring the physical properties of multifunctional molecular systems.
12:40-14:30	Lunch
14:30	Short Oral Presentations (Auditorium of Inorganic Chemistry, Hall no. 141) Chairman – Juozas Vidas Gražulevičius, Kaunas University of Technology
14:30-14:45	Daumantas Matulis , Vilnius University, Institute of Biotechnology, Vilnius, Lithuania. Discovery and Characterization of Novel Selective Inhibitors of Carbonic Anhydrase IX.
14:45-15:00	Audrius Maruška , Vytautas Magnus University, Kaunas, Lithuania. Separation of anticancer fractions from willow-herb (chamerion angustifolium L.) and their molecular and biological analysis.
15:00-15:15	Jolanta Donėlienė , Kaunas University of Technology, Kaunas, Lithuania. The influence of synthetic calcium aluminosilicate hydrate with different content of aluminum on the hydration of portland cement system.
15:15-15:30	Nicola Tiso , Vytautas Magnus University, Kaunas, Lithuania. Biotechnologies for wooden railway cross-ties remediation.
15:30-15:45	Laura Baliulytė , Vilnius University, Vilnius, Lithuania. Quantum mechanical study of thermodynamics parameters of ethoxzolamide.
15:45-16:00	Rokas Gendvilas , Kaunas University of Technology, Kaunas, Lithuania. Peculiarities of α-C₂SH synthesis by conventional and microwave-assisted hydrothermal synthesis.
16:00-17:00	Poster Session and coffee (Auditorium of Professor Kazys Daukšas, Hall no. 223 and lobby)
18:00-20:00	Closing Remarks and Conference Dinner (Taurakalnis, Universiteto 3, M. Daukša yard)



TABLE OF CONTENTS

<i>PLENARY LECTURES</i>			
PL 1	G. Popkirov	Electrochemical impedance spectroscopy: dreams and reality - applications to real-world samples	19
PL 2	P.R. Venskutonis	Phytochemicals for functional foods and nutraceuticals	20
PL 3	M. Turks , J. Lugiņina, A. Stikute, D. Posevins, I. Novosjolova	Novel applications of sulfur dioxide in organic synthesis and analysis of organic compounds	21
PL 4	Saulius Jursenas	Tailoring the physical properties of multifunctional molecular systems	23

<i>ORAL PRESENTATIONS</i>			
OP 1	V. Dudutienė, J. Matulienė, A. Smirnov, D. D. Timm, A. Zubrienė, L. Baranauskienė, V. Morkūnaitė, J. Smirnovienė, V. Michailovienė, V. Juozapaitienė, A. Mickevičiūtė, J. Kazokaitė, S. Bakšytė, A. Kasiliauskaitė, J. Jachno, J. Revuckienė, M. Kišonaitė, V. Pilipuitytė, E. Ivanauskaitė, G. Milinavičiūtė, V. Smirnovas, V. Petrikaitė, V. Kairys, V. Petrauskas, P. Norvaišas, D. Lingė, P. Gibieža, E. Čapkauskaitė, A. Zakšauskas, E. Kazlauskas, E. Manakova, S. Gražulis, J. E. Ladbury, and D. Matulis	Discovery and characterization of novel selective inhibitors of carbonic anhydrase IX	25
OP 2	Audrius Maruška	Separation of anticancer fractions from willow-herb (<i>chamerion angustifolium</i> l.) and their molecular and biological analysis	26
OP 3	J. Donėlienė , A. Eisinias	The influence of synthetic calcium aluminosilicate hydrate with	28
OP 4	N. Tiso , M. Stankevičius, J. Mikašauskaitė, A. Maruška, V. Snieškienė, A. Stankevičienė, T. Makaravičius, M. Kazlauskas, V. Bartkuvienė, O. Kornjšova, O. Ragažinskienė, D. Levišauskas, E. Galli, C. Polcaro	Biotechnologies for wooden railway crossties remediation	32
OP 5	Laura Baliulytė	Quantum mechanical study of	34



		thermodynamics parameters of ethoxzolamide	
OP 6	R. Gendvilas, M. Stankevičiūtė, R. Šiaučiūnas	Peculiarities of α -C ₂ SH synthesis by conventional and microwave-assisted hydrothermal treatment	36

POSTER PRESENTATIONS

Biochemistry and Biotechnology

PP 1	T. Krivorotova, A. Cirkovas, S. Maciulyte, R. Staneviciene, S. Budriene, E. Serviene, J. Sereikaite	Nisin-pectin complex nanoparticles for food preservation	41
PP 2	L. Misevičienė, J. Šarlauskas, Ž. Anusevičius, A. Yantsevich, T. Karpenko, A. Ivanchik, A. Marozienė, J. Stankevičiūtė, A. Gilep, Y. Dichenko, S. Usanov and N. Čėnas	The study of halogen-substituted quinones as effective enzyme inactivating agents	45
PP 3	M. Talaikis, M. Mickevičius, G. Valinčius, G. Niaura	Surface enhanced raman spectroscopic study of water induced structural changes in the membrane anchoring self-assembled monolayers	49
PP 4	T. Vanagaitė, A. Valiūnienė, Ž. Margarian, L. Mikoliūnaitė, G. Valinčius	Formation of hybrid bilayer on silanized Ti/TiO ₂ electrode	53

Chemistry and Technology of Inorganic Materials

PP 5	R. Alaburdaitė, P. Bekampienė, J. Domskienė, E. Paluckienė, K. Kantminienė	Modification of bacterial cellulose by copper sulfide layers	57
PP 6	L. Alinauskas, R. Raudonis, E. Garskaite	Morphology and structure evaluation of SnO ₂ nanostructures prepared by solution-based method	61
PP 7	A. Bakutytė, R. Ivanauskas, A. Ivanauskas, I. Ancutienė	XRD studies of copper sulfide layers on glass	62
PP 8	Y. Barushka, R. Vilkauskaitė, E. Garskaite	Deposition and characterization of inorganic oxide based films for photocatalytic hydrogen generation	65
PP 9	Irma Bogdanoviciene, Akvile Ezerskyte-Miseviciene, Rainer Traksmas, Kaia Tõnsuaadu, Aivaras Kareiva	Cationic substitution effects in sol-gel derived Ca-phosphate bioceramic materials	66
PP 10	G. Braziulis, G. Prievelytė, G.	Tartaric acid-assisted sol-gel synthesis of	70



	Janulevičius, A. Žalga	various metal molybdates	
PP 11	O. Brigaitytė, R. Šlinkšienė	Raw materials influence to bulk fertilizers	71
PP 12	A. Brudzisz, A. Brzózka, G.D. Sulka	Fast and efficient method for preparation of through-hole anodic alumina membranes	75
PP 13	A. Chodosovskaja, E. Garskaite, A. Beganskiene, S. Sakirzanovas, A. Kareiva	Synthesis of aluminates from hybrid organic-inorganic precursors	76
PP 14	A. Diktanaitė, A. Žalga	Sol – gel synthesis and characterization of lithium aluminium molybdate	78
PP 15	J. Gaidukevič, J. Barkauskas, K. Petrikaitė	Graphene-based nanocomposite materials containing parathiocyanogen	79
PP 16	E. Grazenaite, J. Pinkas, P. Roupцова, Z. Losos, A. Kareiva	Synthesis and characterisation of $\text{Co}_{1-x}\text{M}_x\text{Cr}_2\text{O}_4$ as green pigments	83
PP 17	R. Ivanauskas, L. Samardokas, I. Ancutienė	Some properties of thallium selenide layers on the polyamide film surface	86
PP 18	K. Jančaitienė, R. Šlinkšienė	Production of potassium dihydrogen phosphate	88
PP 19	V. Jonauske, A. Prichodko, Z. Stankeviciute, R. Raudonis, A. Beganskiene, A. Kareiva	Sol-gel derived thin films of calcium hydroxyapatite: comparison of two coating techniques	92
PP 20	D. Juknelevicius, R. Kubilius, L. Mikoliunaite, A. Ramanavicius	A spectrophotometric study of green pyrotechnic flame properties using ammonium perchlorate, barium nitrate, shellac system	94
PP 21	S. Kareiva, Z. Stankeviciute, A. Beganskiene, A. Selskis, F. Ivanauskas, V. Klimavicius, V. Balevicius, S. Sakirzanovas, A. Kareiva	Reproducibility of sol-gel synthesis method: case of calcium hydroxyapatite	95
PP 22	E. Kiele, J. Senvaitiene, A. Griguzevičienė, R. Ramanauskas, R. Raudonis, A. Kareiva	Application of sol-gel method for the conservation of metals	98
PP 23	A. Laurikenas, J. Barkauskas, A. Kareiva	Synthesis and characterization of iron (III) acetate: precursor for metal-organic frameworks	99
PP 24	B. Macijauskienė, E. Griškoniš	Wetting of graphite felt with ethanol aqueous solutions	101
PP 25	V. Medelienė, A. Selskienė	Hierarchical nonstructural growth of copper metal matrix composite coatings with a carbon nanomaterial	103
PP 26	I. Mikalauskaitė, I. Lebedytė, M. Stalnionis, V. Karabanovas, A. Beganskiene, G. Streckytė	Synthesis of NaREF_4 : Yb 20%, Er 2% (RE=Y, Gd) and initial characterization for applications in MRI	104
PP 27	M. Misevicius, G. Kibildaite, A. Kareiva	Synthesis and characterisation of SrAl_4O_7	108
PP 28	D. Nizevičienė, N. Kybartienė	Investigation of anhydrite binder from	110

		reagent gypsum and industrial gypsum	
PP 29	O. Opuchovič, G. Kreiza, K. Kazlauskas A. Kareiva	Neodymium, terbium, praseodymium and cerium iron garnets and orthoferrites: a new class of pigments?	114
PP 30	V. Pakštas, Z. Mockus, R. Giraitis, R. Kondrotas, A. Naujokaitis, G. Stalnionis, S. Stanionytė, V. Karpavičienė, R. Juškėnas	XRD studies of homogenization and selenization of electrochemically co-deposited Cu-Zn-Sn	117
PP 31	L. Pavasaryte, B. J. Lopez, A. Kareiva	Sol-gel synthesis of europium doped Tb ₃ Al ₅ O ₁₂ , Dy ₃ Al ₅ O ₁₂ and Ho ₃ Al ₅ O ₁₂ garnets	119
PP 32	R. P. Petrauskas, S. Butkute, A. Kareiva	Formation peculiarities of Cr ³⁺ -doped Y ₃ Ga ₅ O ₁₂	123
PP 33	Jurgis Pilipavicius, Ala Chodosovskaja, Aldona Beganskiene, Aivaras Kareiva	Silver nanoplates – silica composite coatings via sol – gel route	125
PP 34	J. Raudoniene, L. Sinkevicius, R. Raudonis, E. Garskaite	Controlled synthesis of Ag ₃ PO ₄ tetrapods	129
PP 35	M. Skruodiene, M. Misevicius, A. Katelnikovas, R. Skaudzius	Luminescence properties of YAG:Tb, YAG:Cr and YAG:Tb,Cr synthesized by sol-gel method	133
PP 36	A. Smalenskaite, B. Buckus, S. Tautkus, A. Beganskiene, G. Brimas, A. Kareiva	Determination of fatty acid composition of adipose tissue by ¹ H NMR spectroscopy	137
PP 37	Z. Stankeviciute, P. Usinskas, A. Kareiva	Formation of thin films of calcium titanate and calcium hydroxyapatite on titanium substrates	140
PP 38	R. Stokienė, N. Petrašauskienė, V. Jasulaitienė, V. Janickis	X-ray photoelectron spectroscopy investigation of cobalt sulfide layers on polyamide film formed by the use of dodecathionic acid	141
PP 39	Z. Sukackienė, A. Balčiūnaitė, A. Selskis, V. Jasulaitienė, L. Tamašauskaitė-Tamašiūnaitė, E. Norkus	Investigation of sodium borohydride oxidation on CoBW/Cu modified with Au nanoparticles	144
PP 40	S. Survilienė, A. Češūnienė, R. Juškėnas, V. Jasulaitienė, A. Selskienė, P. Kalinauskas, K. Juškevičius	Electrodeposition and characterization of black chromium coatings	148
PP 41	D. Šimkūnaitė, I. Valsiūnas	Investigation of the initial stages of Cu electrodeposition onto glassy carbon electrode modified with thin layers of selenium compounds	152
PP 42	J. Vaicekauskaite, G. Lubiene, E. Garskaite	Synthesis and characterization of hydroxyapatite nanoparticles via co-precipitation and polymer matrix mediated synthesis	156

PP 43	L. Vecbiskena	Biodegradable polymer–bioceramic composite coatings	158
PP 44	S. Zadavičiūtė, K. Baltakys	The adsorption capacity of gyrolite for Mn ²⁺ ions	162
PP 45	A. Zarkov, A. Stanulis, A. Beganskiene, S. Tautkus, A. Kareiva	Synthesis of gadolinium doped ceria via sol-gel and sol-gel combustion synthesis routes	166
PP 46	N. Žmuidzinašienė, A. Šulčius, E. Griškonis	Electrodeposition of nanocrystalline Mn coatings	170
Chemistry of Organic Materials			
PP 47	K. Anusevičius, E. Slaninaite, B. Sapijanskaitė, R. Vaickelionienė, V. Mickevičius	Synthesis of new 1-(4-ethoxyphenyl) pyrrolidin-2-ones	173
PP 48	J. Bucevičius, S. Tumkevičius	Comparative study on the synthesis of (arylethynyl)pyrrolo[2,3-d] pyrimidines by stille and sonogashira coupling reactions	175
PP 49	T. Charkova, O. Eicher-Lorka, A. Matijoška, Z. Kuodis	A selective method for mono-pmb protection of glycerol	178
PP 50	A. Geštautas, B. Sapijanskaitė, V. Mickevičius	Synthesis of n-(4-methylphenyl)-N-thiazolyl-β-alanines	179
PP 51	Regina Janciene, Gema Mikulskiene, Algirdas Klimavicius	Investigation of conjugate addition of aromatic amines to 1,4-benzoquinones	181
PP 52	Lidija Kosychova, Regina Vidziunaite, Irina Bratkovskaja, Gema Mikulskiene	UV absorption and fluorescence properties of 1,5-benzodiazepine oximes	184
PP 53	J. Lugiņina, M. Turks	Nucleophilic ring opening of aziridine and azetidine derivatives in liquid sulfur dioxide	187
PP 54	K. Mickevičienė, K. Kantminienė, M. Stasevych, O. Komarovska-Porokhnyavets, V. Mickevičius, V. Novikov	Synthesis and antimicrobial activity of N-aryl-β-alanine derivatives with naphthoquinone and oxazole moieties	189
PP 55	I. Novosjolova, Ē. Bizdēna, M. Turks	Synthesis and applications of 2- and 6-alkyl/arylthiopurine derivatives	191
PP 56	I. Parašotas, V. Mickevičius	Synthesis of functionalized 3-[4-hydroxy(1,3-thiazol-2-yl)anilino]-2-methylpropanoic acids	192
PP 57	D. Posevins, M. Turks	Liquid sulfur dioxide as a reaction medium for lewis acid catalyzed ritter reactions	193
PP 58	R. Ražanas, J. Dabužinskaitė, D. Tauraitė, R. Meškys	Synthesis of acyclic and cyclic nucleosides	194
PP 59	A. Stikute, M. Turks	From allylsilanes to allylsulfoxides: application of sila-ene reaction of sulfur dioxide	196

PP 60	R. Striela, G.Urbelis, R. Mažeikaitė, L. Labanauskas	Heterogeneous catalyst for the Suzuki reaction	197
PP 61	I. Tumosienė, I. Jonuškienė, K. Kantminienė, Z. J. Beresnevičius	Antioxidative activity of azoles and their influence on rapeseed (<i>Brassica napus</i> L.) Growth <i>in vitro</i> and accumulation of metabolites	198
PP 62	A. Urbanaitė, R. Bukšnaitienė, M. Jonušis, I. Čikotienė	Synthesis of functionalized propargylic substrates and investigation of their electrophile-mediated cyclization reactions	199
PP 63	Sigita Višniakova, Indrė Urbanavičiūtė, Ilya Sychugov, Albinas Žilinskas, Kęstutis Arlauskas	Luminescent benzo- and naphthoquinolines: synthesis and investigation of photophysical properties	200
PP 64	J. Zurba, P. Kavaliauskas, V. Jakubkienė	Synthesis and antimicrobial activity of novel arylpyrimidinylureas, hydrazones and semicarbazones	203
Environmental and Analytical Chemistry			
PP 65	T. Drevinskas	Design of field portable capillary electrophoresis device with contactless impedance measuring detector	205
PP 66	R. Garjonyte, A. Balynaite, V. Melvydas, A. Malinauskas	Menadione-mediated amperometry reveals distinct modes of galactose assimilation by yeast <i>Debaryomyces hansenii</i> and <i>Pichia guilliermondii</i>	206
PP 67	A. Gefenienė, J. Čerkauskaitė, D. Kaušpėdienė, R. Ragauskas, J. Vaičiūnienė	Adsorption of cyanides from aqueous phase onto two macroporous anion exchange resins	207
PP 68	Umme Thahira Khatoon, Arunas Ramanavicius, M.K.Mohan, G.V.S.Nageswara Rao	Antimicrobial activity of Gold and Silver nanoparticles synthesized by chemical reduction method	211
PP 69	A. Lugauskas, E. Binkauskienė, I. Prosyčėvas, A. Selskienė, V. Pakštas, D. Bučinskienė, A. Ručinskienė	Effect of selected micromycetes on biointerface of steel	213
PP 70	Yu.P. Perelygin, M. Jaskuła, I.V. Rashevskaya	The precipitate-solution equilibria in the presence of excess of complexing agent	214
PP 71	Ana Šarafutdinovaa, Lidija Kosychova	Investigation lubricity of diesel with second generation oxygenates	215
PP 72	L. Taujenis, V. Olšauskaitė, A. Padarauskas	Amino acid identification by HILIC-MS/MS and enantioselective determination by chiral chromatography-MS/MS in hydrolyzed protein fertilizers samples	219
PP 73	Z. Žukauskaitė, B. Lukšienė, N. Tarasiuk, E. Maceika, S. Tautkus	Application of bio- and synthetic materials for ^{137}Cs sorption from aqueous medium	223

Physical Chemistry			
PP 74	K. Antanavičiūtė, L. Tamašauskaitė-Tamašiūnaitė, E. Norkus	Synthesis, characterization and properties of Pt-Ru-Co/Ti catalyst	226
PP 75	A. Balčiūnaitė, L. Tamašauskaitė-Tamašiūnaitė, E. Norkus	Borohydride oxidation on gold-graphene modified titania nanotubes	230
PP 76	I. Balčiūnaitė, A. Kleišmantas, E. Norkus	Influence of chemical elements on properties of rare garnets minerals	234
PP 77	O. Girčienė, L. Gudavičiūtė, A. Selskis, V. Jasulaitienė, A. Martušienė, R. Ramanauskas	Self-healing cerium conversion coatings on carbon steel	236
PP 78	E. Golovinas, L. Abariūtė, G. Valinčius, G. Niaura	Study of molecular interactions in cholesterol-phospholipid monolayer using sum frequency generation spectroscopy	240
PP 79	J. Jablonskienė, A. Matusevičiūtė, R. Kondrotas, R. Juškėnas, L. Tamašauskaitė-Tamašiūnaitė	Evaluation of Pt-Co nanocatalysts activity towards methanol oxidation in acidic medium	243
PP 80	J. Juodkazytė, B. Šebeka, I. Savickaja, A. Kadys, E. Jelmakas, T. Grinys, S. Juodkazis, T. Malinauskas	In _x Ga _{1-x} N performance as a band-gap-tunable photo-electrode for photoelectrochemical generation of hydrogen	247
PP 81	V. Kepenienė, L. Tamašauskaitė-Tamašiūnaitė, J. Vaičiūnienė, R. Kondrotas, V. Pakštas, E. Norkus,	Metal oxides supported platinum nanoparticles as electrocatalysts for ethanol oxidation	248
PP 82	V. Kepenienė, M. Vagner, A. Balčiūnaitė, A. Matusevičiūtė, L. Tamašauskaitė-Tamašiūnaitė, E. Norkus	Microwave-assisted synthesis of platinum supported cerium oxide-graphene for methanol oxidation	252
PP 83	E. Kurowska-Tabor, K. Gawlak, G.D. Sulka, M. Jaskuła	The effect of electrolyte bath composition on the Zn content in AgZn nanowires grown inside AAO templates	256
PP 84	Svetlana Malickaja, Mindaugas Macernis and Juozas Sulskus, Leonas Valkunas	Study of artificial light harvesting antennae by quantum chemical methods	257
PP 85	I. Matulaitienė, E. Pociūtė, Z. Kuodis, O. Eicher-Lorka, G. Niaura	SERS study of 4-imidazolemethanol interaction with copper electrode	258
PP 86	A. Matusevičiūtė, A. Balčiūnaitė, R. Kondrotas, L. Tamašauskaitė-Tamašiūnaitė, E. Norkus	Microwave-assisted synthesis of graphene supported silver and platinum-silver nanoparticles for formaldehyde oxidation	261
PP 87	S. Ostachavičiūtė, E. Valatka	Influence of Co-P layer on the structure and electrochemical properties of Se-WO ₃ thin	265

		films	
PP 88	A. Pawlik, M. Jarosz, G. D. Sulka	Effect of the modification of nanoporous titanium dioxide layers on drug delivery profiles	269
PP 89	Karolina Syrek, Joanna Kapusta-Kołodziej, Magdalena Jarosz, Grzegorz D. Sulka	Effect of hydrodynamic conditions on growth of anodic titanium dioxide (ATO) layers	270
PP 90	R. Stagniūnaitė, V. Kepenienė, E. Norkus, L. Tamašauskaitė-Tamašiūnaitė	Graphene and niobium(V) oxide/graphene supported platinum-cobalt catalysts as cathode material for fuel cells	271
PP 91	L. Staišiūnas, R. Kondrotas, A. Grigučevičienė, K. Leinartas, P. Miečinskas, E. Juzeliūnas	Thin film Mg-Nb alloys: structure and corrosion in chloride medium	275
PP 92	M. Špandyreva, I. Ignatjev, Z. Kuodis, O. Eicher-Lorka, G. Niaura	Structure of phenyl-terminated self-assembled monolayers with amide group revealed by sers	277
PP 93	A. Zabelaitė, A. Balčiūnaitė, S. Lichušina, D. Šimkūnaitė, L. Tamašauskaitė-Tamašiūnaitė, E. Norkus	Investigation of hydrazine oxidation on ZnCo modified with gold nanoparticles	281
PP 94	E. Wierzbicka, G. D. Sulka	Nanogold electrodes fabrication and their application for sensing of adrenaline	284
Polymer Chemistry and Technology			
PP 95	I. Berulis, S. Žalėnkienė, L. Pečiulytė, V. Krylova	Preparation and investigation of Se thin layers on home made polyimide films composite	286
PP 96	M. Bistrickas, D. Gudeika, J.V. Grazulevicius	Synthesis and properties of 1,3,6,8-carbazole-based compound linked via ethynyl-containing linkages	289
PP 97	M. Bistrickas, D. Gudeika, L. Peciulyte, J.V. Grazulevicius	Synthesis and properties of 1,3,6,8-substituted carbazole derivatives	292
PP 98	A. Garbaras, Eivydas Andriukonis, V. Remeikis, L. Mikoliunaite, A. Popov, A. Ramanavicius	Application of stable isotope ratio mass spectrometry for the stoichiometry determination in the biocomposite	295
PP 99	J. Jonikaitė-Švėgždienė, V. Merkytė, T. Krivorotova, R. Makuška	Synthesis of anionic molecular brushes by „RAFT grafting from“ approach	296
PP 100	S. Kašėtaitė, J. Ostrauskaitė, V. Gražulevičienė	Glycerol-based polymeric composites reinforced with production wastes	299
PP 101	G. Krucaite, D. Tavgeniene, D. Sipaviciute, B. Stulpinaite	Electroactive polymers containing electronically isolated naphthyl-substituted carbazole rings	301
PP 102	R. Laurinavičiūtė, L. Pečiulytė, D. Volyniuk, J.V.	Derivatives of indole with reactive functional groups as electroactive materials	304



	Gražulevičius		
PP 103	E. Lekniute-Kyzike, J. Bendoraitiene	Enzymatic degradation of starch and its cationic derivatives	308
PP 104	S. Mačiulytė, T. Kochanė, S. Budrienė	Preparation of poly(urethane-urea) microcapsules using poly(vinyl alcohol) as the polyol	311
PP 105	A. Popov, L. Mikoliunaite, A. Ramanavicius, A. Ramanaviciene	Synthesis and investigation of gold nanoparticles-polypyrrole and glucose oxidase-polypyrrole nanocomposites	315
PP 106	A. Radzevič, R. Celiešiūtė, T. Rakickas, Š. Vaitekoniš, R. Pauliukaitė	Stabilization of conducting polymers composed from natural monomers on electrode surface	316
PP 107	R. Rutkaitė, M. Babelytė, P.P. Danilovas, V. Navikaitė	Diphilic properties of propylene oxide and octenyl succinic anhydride modified starches and their coatings	317
PP 108	S. Saitarly, Yu. Pushkarev, V. Plavan	Study of influence of oligobutadienes' molecular parameters on their rheological properties	321
PP 109	A. Sankauskaitė, P. Bekampienė, I. Prosyčėvas, V. Urbelis, S. Varnaitė-Žuravliova, D. M. Tumėnienė, S. Stygienė	The influence of microporous pu film on the antimicrobial properties of silver nanoparticles treated textile	325
PP 110	R. Simanaityte, D. Gabrielaitis, A. Kausaite-Minkstimiene	Environmentally friendly chemical synthesis of polypyrrole particles	328
PP 111	Deimante Simanaviciute, Ramūnas Vinciušas, Rima Klimaviciute	Adsorption of methyl orange on cationic cross-linked starches with tertiary amino groups	332
PP 112	A. Sliptsov, B. Savchenko, N. Sova, V. Paharenko	Study of polyolefin grafting reactions	335
PP 113	I. Sliptsova, B. Savchenko, N. Sova, V. Paharenko	Chemical recycling of polyester waste	339
PP 114	J. Širvaitytė, P. Bekampienė, J. Domskienė, I. Jonuškienė, V. Valeika	<i>In situ</i> modification of bacterial cellulose by adding essential oil during fermentation	343
PP 115	E. Valančienė, L. Miknius, N. Pedišius	The influence of zeolite catalyst on polypropylene waste thermal decomposition kinetics and thermodynamics	347
PP 116	V. Zilinskaite, M. Bistrickas, D. Gudeika, J.V. Gražulevičius	Synthesis and properties of monomer and polymer based on indandione moiety	350



Chemistry and Chemical Technology 2015

Vilnius University, Faculty of Chemistry,
Naugarduko 24, Vilnius, Lithuania
January 23, 2015

Plenary lectures





**ELECTROCHEMICAL IMPEDANCE SPECTROSCOPY:
DREAMS AND REALITY - APPLICATIONS TO REAL-WORLD SAMPLES**

G. Popkirov

*Central Laboratory for Solar Energy and New Energy Sources
Bulgarian Academy of Sciences, 72, Tzarigradsko Chossee, 1784 Sofia, Bulgaria
E-mail: gp.tf.uni-kiel.de*

Electrochemical impedance spectroscopy (EIS) is a powerful tool for non-destructive study of electrochemical systems, which can yield information for the structure of the electrode/electrolyte interface, as well as for the mechanisms and kinetics of electrochemical reactions. This lecture will be concerned with the two techniques of impedance spectroscopy measurements, i) based on data acquisition in the frequency domain, the so called frequency response analysis (FRA-EIS); and ii) the time domain technique (FFT-EIS) using multi-sine perturbation and fast Fourier transform (FFT) algorithm to obtain at once the impedance spectra in a wide frequency range. In a short historical background these two EIS measurement methods will be presented and briefly compared. As with any experimental technique, well defined measurement conditions, accurate measurement and meaningful analysis of obtained data are required. The specific limitations of the accuracy set by the measurement devices e.g. the potentiostat/galvanostat will be pointed out. The importance of the measurement conditions, the electrochemical cell arrangement and the specific role of the reference electrode will be emphasized. Unfortunately, one of the most “disturbing” factors in the ambitious attempt to obtain valid and accurate impedance data appears to be the electrochemical process itself.

Impedance can be correctly defined as a transfer function that correlates the response of a sample to a perturbation, only if the conditions of linearity, stability, time invariance of the sample's parameters and the causality of the response with respect to the perturbation, are all obeyed, at least during the time of measurement. EIS is widely used in investigations of corrosion, batteries, fuel cells, electroplating, pure and modified metal and semiconductor electrodes, bio-materials etc. All these objects of investigation have in common non-linearity of the current-voltage relationship, high degree of non-stationarity and even show non-casual behaviour of their response to external perturbation. Thus, although EIS is now a well established standard measurement technique in electrochemistry much has to be done to establish proper methods for the validation of the obtained data. The main question, namely how to fit, interpret and analyse the impedance spectra should be only posed if the validity of the data is proven. Methods for post-measurement validation and even some attempts for correction of impedance data, obtained upon conditions of non-stationarity (for instance – with superimposed relaxation) will be presented and discussed. An easy to apply validation method based on comparison of the frequency content of the perturbation and response signals will be demonstrated. The information needed, i.e. the spectra of the perturbation and response signals, is an intermediate result obtained during calculation of the impedance spectra in a FFT-EIS measurement. By displaying these spectra on the computer screen, one can easily decide if the performed measurement will yield valid or invalid impedance spectra. The appearance of new (not present in the perturbation signal spectrum) harmonic frequencies becomes an indicator that measured data are distorted. The experimenter can even (with some experience) recognize the reason of measurement failure, e.g. current relaxation, noise, violation of linearity, oscillation, etc.

The lecture will focus on the difficulties of the EIS measurement of real electrochemical cells and the importance of the proper choice of measurement technique and conditions.



PHYTOCHEMICALS FOR FUNCTIONAL FOODS AND NUTRACEUTICALS

P.R. Venskutonis

Kaunas University of Technology, Radvilėnų pl. 19, LT-50254, Kaunas, Lithuania

E-mail: rimas.venskutonis@ktu.lt

Plant kingdom is an important source of bioactive compounds having a potential to affect various human diseases. Generally, chemical compounds naturally occurring in plants are called phytochemicals (*phyto* means "plant" in Greek). In history, various plant species served for discovery of natural drugs, which afterwards had been synthesized and nowadays are used worldwide. Another important stimulus, which remarkably encouraged search and studies of phytochemicals, was development of new concepts of functional foods and nutraceuticals (the latter term is a combination of words 'nutrition' and 'pharmaceuticals'). A food is defined as a functional food if it has clearly been documented that it has one or more properties beneficial to human health by improving the state of health and/or reducing health risks in addition to its nutritional value, while plant origin bioactive phytochemicals are the main ingredients which may provide the above-mentioned properties to food.

Although hundreds of different species, particularly medicinal, aromatic and spicy plants, have been used in folk medicine and foods since ancient times, the activities of many species still rely on empirical knowledge, which has not been supported by the scientific data obtained by modern analysis techniques. So far as underutilized medicinal and other plants may contain valuable bioactive constituents, comprehensive characterisation of such species remains an interesting task, both from the scientific and practical application points of view.

Among phytochemicals natural antioxidants remain in the focus of numerous research teams all over the world. Therefore, the scope of information in this area is extremely large, diverse and rather difficult for systematic reviewing and assessment. For instance, keyword combination 'natural antioxidant' in the Thomson Reuters WEB of Science database gave 15486 hits, including 1432 review articles (time of access 17/12/2014). The interest in natural antioxidants is determined by the universality of their action in various redox systems and consequently broad spectra of possible applications: such phytochemicals are considered as ingredients for functional foods, nutraceuticals, cosmetics, medicines and other uses. For instance, the interest in natural antioxidants to be used for the stabilisation of lipid containing foods remarkably increased because of emerging information about possible toxicity of synthetic antioxidants as well as consumer preferences towards natural food additives.

Hundreds of botanical species were studied resulting in discovery of thousands of chemical structures with antioxidative capacity, which are used by the plants for different biological tasks, e.g. as a photoprotective defence systems in plant cells. Consequently, every plant species, subspecies, variety and genotype may be an object for the assessment of antioxidant potential and the presence of radical scavenging, antioxidative and other bioactive phytochemicals. On the other hand, the main biochemical synthesis pathways are common for many species; therefore, the main antioxidant structures elucidated in botanicals are similar to many of them. These structures include simple phenolic compounds, phenolic acids, flavonoids, coumarins, sesquiterpene lactones, terpenoids and their derivatives as well as other classes of phytochemicals. Considering many possibilities of substitutions and intermolecular binding (esterification, glycosidation) as well as improvements in spectral analysis methods the number of identified natural antioxidants is rapidly increasing. Therefore this area will remain as an exciting research topic in the future, particularly for phytochemists and food scientists.

NOVEL APPLICATIONS OF SULFUR DIOXIDE IN ORGANIC SYNTHESIS AND ANALYSIS OF ORGANIC COMPOUNDS

M. Turks, J. Lugiņina, A. Stikute, D. Posevins, I. Novosjolova

Faculty of Material Science and Applied Chemistry, Riga Technical University,

3 P. Valdena Str., Riga, LV-1007, Latvia

E-mail: maris_turks@ktf.rtu.lv

At ambient conditions sulfur dioxide is a colorless, non-combustible gas. It should be noted that SO₂ reveals a rather long liquid range: it boils at -10 °C and freezes at -75.5 °C. Most importantly, SO₂ condenses easily by compression due to its high critical temperature (157.35 °C, 7.88 MPa). Thus, its phase diagram predicts only ~10 atm pressure at 60 °C in a closed reactor [1]. It should be noted that the phase diagram of SO₂ is very similar to that NH₃ which is used as well-accepted liquid phase (b.p. of NH₃ = -33 °C) in distinct synthetic procedures. Sulfur dioxide has a high dipole moment (1.61 D). Therefore it readily can dissolve both organic and inorganic salts. The solubility row for alkali metal halides in liquid sulfur dioxide is as follows: MI > MBr > MCl > MF. On the other hand, SO₂ has been reported as reaction medium for processes involving carbenium ions [2].

This has prompted us to search for organic reactions that would profit from their running in liquid SO₂ as a reaction medium. We have discovered that carbamate-protected aziridines and azetidines undergo efficient ring-opening reactions in liquid SO₂ with I and II group metal halides, including NaCl and KBr (Scheme 1). The advantage of this approach is based on the fact that carbamate groups (Cbz, Boc) can be easier removed if required than their well-described sulfonamide counterparts.



Scheme 1.

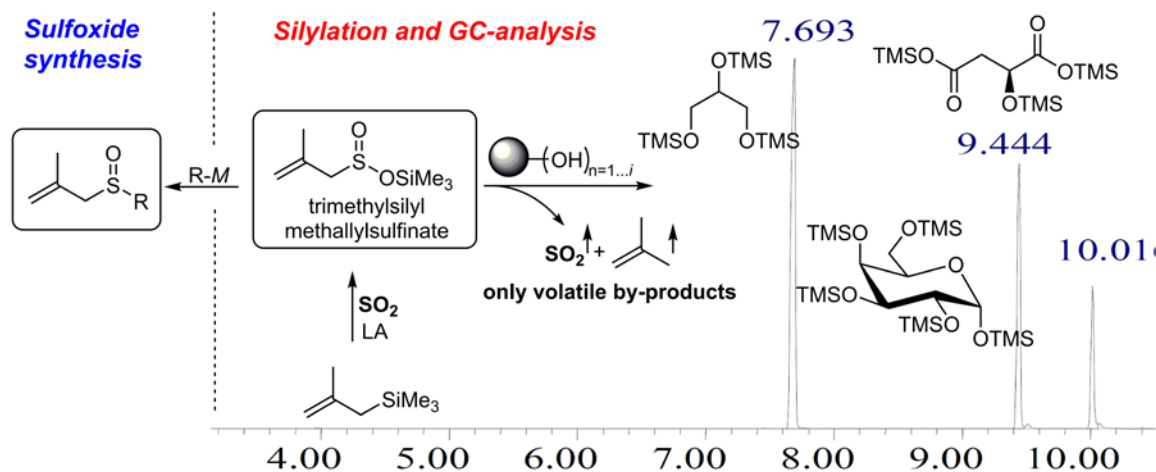
We have also found application of liquid SO₂ as an interesting solvent for the Ritter reactions (Scheme 2) [3]. The screening of suitable Lewis acid catalysts and scope and limitations of amidation reaction under these conditions will be discussed.



Scheme 2.

In recent years many applications of SO₂ and its crystalline surrogates in organic synthesis have been reported [4]. In 2002, Vogel *et al.* described synthesis of trimethylsilyl 2-methylprop-2-ene-1-sulfinate in a Lewis acid catalyzed sila-ene reaction between

methallylsilane and sulfur dioxide [5]. It was found that this reagent easily transfers the silyl group to alcohols [6]. Here we report the use of Vogel's silyl sulfinate in qualitative and quantitative gas chromatographic analysis of organic substances, as well as in organic synthesis (Scheme 3). In our hands the aforementioned reagent has been successfully applied



Scheme 3.

in the user-friendly silylation procedure of alcohols, polyols, carboxylic and hydroxycarboxylic acids and mixtures of different polyhydroxy compounds (e.g.: glycerol, resorcinol, tartaric acid, malic acid, D-ribose, D-mannose and D-glucose) and their subsequent gas chromatographic analysis [7]. A typical experimental procedure involves simple mixing of the aforementioned reagent with the selected analyte in MeCN or THF directly before injection in a gas chromatograph. The elaborated analysis conditions are suitable for both qualitative and quantitative analysis. In the latter case both the internal standard method and application of calibration curve gave good results. The main advantage of this silylation process is the generation of volatile byproducts: sulfur dioxide and isobutene.

Additionally, the reactions of silyl sulfonates with organometallic reagents providing a direct entry in sulfoxide synthesis will be discussed. This opens a novel approach for allylsulfoxide synthesis from allylsilanes *via* the *sila-ene* reaction of the latter with SO_2 followed by addition of Grignard reagents.

Acknowledgments: This work was supported by the Latvian Council of Science Grant 12.0291. J.L., D.P. and A.S. thank the Latvian Academy of Sciences and JSC "Olainfarm" for scholarships. I.N. thanks the European Social Fund within the project «Support for the implementation of doctoral studies at Riga Technical University» for a scholarship.

References

1. L. Hasenberg, R. Bender. In Corrosion Handbook; Ed. R. Bender, Wiley, Frankfurt, 2008, p. 6.
2. G. A. Olah, D. J. Donovan, J. Am. Chem. Soc., **100** (1978) 5163-5169.
3. J. M. Bakke, B. Knudsen, Acta Chem. Scand., **48** (1994), 234-239.
4. a) J. Lugiņina, Synlett, **25** (2014) 2962-2963; b) A. S. Deeming, E. J. Emmett, C. S. Richards-Taylor, M. C. Willis, Synthesis, **46** (2014) 2701-2710; c) P. Vogel, M. Turks, L. Bouchez, D. Marković, A. Varela-Álvarez, J. Á. Sordo, Acc. Chem. Res. **40** (2007) 931-942; d) P. Vogel, D. Markovic, M. Turks, In Stereoselective synthesis of drugs and natural products; Eds. V. Andrushko, N. Andrushko, Wiley-Blackwell, 2013, pp.623-666.
5. a) L.C. Bouchez, P. Vogel, Synthesis, (2002), 225-231; b) L. C. Bouchez, S. Reddy Dubbaka, M. Turks, P. Vogel, J. Org. Chem., **69** (2004), 6413-6418.
6. X. Huang, C. Craita, L. Awad, P. Vogel, Chem. Commun., (2005) 1297-1299.
7. I. Novosjolova, M. Turks, Phosphorus Sulfur Silicon Rel. Elem., (2015) in press.



TAILORING THE PHYSICAL PROPERTIES OF MULTIFUNCTIONAL MOLECULAR SYSTEMS

Saulius Jursenas

Institute of Applied Research, Vilnius University, Lithuania

E-mail: saulius.jursenas@ff.vu.lt

Search for the new materials with advanced properties is one of the major tasks of the rapidly developing field of organic optoelectronics. Currently much attention is being focused on the multifunctional compounds, i.e. molecules composed of several fragments carrying different functionalities. Multifunctional materials are expected not only to increase the device performance but also to simplify their architectures and fabrication procedures.

On the other hand, multifunctionality unavoidably involves an increase in complexity of molecular properties giving rise to new collective effects, such as intramolecular charge transfer, intramolecular twisting and isomerization, formation of complexes etc. In a solid state, molecular complexity results in different packing morphology, and thus, in various intermolecular interactions, which considerably affect excitation localization, energy transfer and emission properties. Hence, further development of the multifunctional molecular compounds for device applications requires thorough analysis and optimization of the emerged collective properties.

Here we review our recent work on tailoring the physical properties of various multifunctional molecular systems targeted for organic electronics devices. We show fine-tuning of electronic states of anthracene by substituting at the 2-, 9-, 10- positions leading to an excellent emissive and charge transport properties of the molecules for OLED applications. We present optimization of singly bonded carbazole and fluorine triade laser emitters emphasizing on importance of the linking position and alkyl spacers. We demonstrate optimization of charge transport properties and tuning of exciton diffusion length in starshape triphenylamine systems which is important for solar cell applications. Further we discuss tailoring of photophysical properties of intramolecular charge-transfer systems based on naphthalimide compounds by introduction of polar substituents, variation of intramolecular twisting angle and changing polarity of the surrounding. Finally, highly selective metal ion detection system based on fluorescence enhancement in naphthalimide derivatives is presented.



Chemistry and Chemical Technology 2015

Vilnius University, Faculty of Chemistry,
Naugarduko 24, Vilnius, Lithuania
January 23, 2015

Oral presentations



Discovery and Characterization of Novel Selective Inhibitors of Carbonic Anhydrase IX

V. Dudutienė¹, J. Matulienė¹, A. Smirnov¹, D. D. Timm¹, A. Zubrienė¹, L. Baranauskienė¹, V. Morkūnaitė¹, J. Smirnovienė¹, V. Michailovienė¹, V. Juozapaitienė¹, A. Mickevičiūtė¹, J. Kazokaitė¹, S. Bakšytė¹, A. Kasiliauskaitė¹, J. Jachno¹, J. Revuckienė¹, M. Kišonaitė¹, V. Pilipuitytė¹, E. Ivanauskaitė¹, G. Milinavičiūtė¹, V. Smirnovas¹, V. Petrikaitė^{1,4}, V. Kairys², V. Petrauskas¹, P. Norvaišas¹, D. Lingė¹, P. Gibieža¹, E. Čapkauskaitė¹, A. Zakšauskas¹, E. Kazlauskas¹, E. Manakova³, S. Gražulis³, J. E. Ladbury⁵, and D. Matulis¹

¹ Department of Biothermodynamics and Drug Design, Institute of Biotechnology,

² Department of Bioinformatics, Institute of Biotechnology,

³ Department of Protein–DNA Interactions, Institute of Biotechnology,

Vilnius University, V. A. Graičiūno 8, Vilnius, Lithuania,

⁴ Department of Drug Chemistry, Faculty of Pharmacy, Lithuanian University of Health Sciences, A. Mickevičiaus 9, Kaunas, Lithuania,

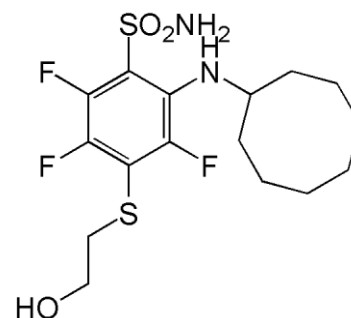
⁵ Department of Biochemistry and Molecular Biology, University of Texas MD Anderson Cancer Center, 1515 Holcombe Boulevard, Houston, Texas, United States

E-mail: daumantas.matulis@bti.vu.lt

Human carbonic anhydrase IX (CA IX) is highly expressed in tumor tissues and its selective inhibition provides potential target for treatment against numerous cancers. Development of potent, highly selective inhibitors against this target remains an unmet need in anti-cancer therapeutics. A series of fluorinated benzenesulfonamides with substituents on the benzene ring were designed and synthesized. Several of these exhibited a highly potent and selective inhibition profile against CA IX. Three fluorine atoms significantly increased the affinity by withdrawing electrons and lowering the pK_a of the benzene sulfonamide group.

The bulky ortho substituents such as cyclooctyl or even cyclododecyl groups fit to the hydrophobic pocket in the active site of CA IX but not CA II, as shown by the compound cocrystal

	CA IX	CA I
FTSA K_d	1.1 nM	50,000 nM
ITC K_d	15 nM	>10,000 nM
SF K_i	<5.0 nM	46,000 nM



structure with the chimeric CA IX. The strongest inhibitor of recombinant human CA IX catalytic domain produced in human cells achieved the affinity of 50 pM. However, the high affinity diminished the selectivity. The most selective compound for CA IX exhibited 10 nM affinity. The compound which showed the best balance between affinity and selectivity properties bound with 1 nM affinity. The inhibitors described in this work provide the basis for novel anticancer therapeutics targeting CA IX [1].

References

1. Dudutiene, V. *et.al.* *J. Med. Chem.* **2014**, *57*, 9435.

**SEPARATION OF ANTICANCER FRACTIONS FROM WILLOW-HERB
(*CHAMERION ANGUSTIFOLIUM* L.) AND THEIR MOLECULAR AND
BIOLOGICAL ANALYSIS**

A. Maruška¹, T. Drevinskas¹, V. Kaškonienė¹, O. Ragažinskienė², V. Briedis³, R. Ugenskienė⁴

¹Faculty of Natural Sciences, Vytautas Magnus University, Vileikos str. 8, LT-44404 Kaunas, Lithuania

²Kaunas Botanical Garden of Vytautas Magnus University, Sector of Medicinal Plants, Ž. E. Žilibero str. 6, LT- 46324 Kaunas, Lithuania

³Faculty of Pharmacy, Lithuanian University of Health Sciences, Mickevičiaus str. 9, LT-44307 Kaunas, Lithuania

⁴Institute of Oncology, Lithuanian University of Health Sciences, Eivenių g. 2, LT-50009 Kaunas, Lithuania

E-mail: a.maruska@gmf.vdu.lt

Chamerion angustifolium (L.) Holub (family *Oenotheraceae*, other name *Epilobium angustifolium*), is an extensive genus with approximately 170 species worldwide, 28 in Europe. Recent studies show that many of *Epilobium* spp. accumulate biologically active compounds with high therapeutic importance [1]. High ratio of ellagitannins, mainly oenothetin B, together with myricetin, quercetin, kaempferol and their various glycosides are found in *Epilobium* species [1]. The main pharmacological activity of *C. angustifolium* L. is attributed to oenothetin B [2-4]. Literature data shows that oenothetin B compose 225.8 mg/g, while other flavonoids 13.4 mg/g of *C. angustifolium* (L.) [5].

The aim of this study was to optimize the fractionation of *C. angustifolium* L. water extract and separate the fraction of oenothetin B from other minor compounds. The fractionation using different ratios of solvents (pure water and water:ethanol) and solid phase extraction was performed. The HPLC analysis with antiradical (DPPH) reaction detection was applied in order to evaluate the quality of fractionation.

The HPLC analysis showed that the use of different ratios of solvents and time combinations did not allow to separate fraction of oenothetin B from other minor compounds (*Figure 1*).

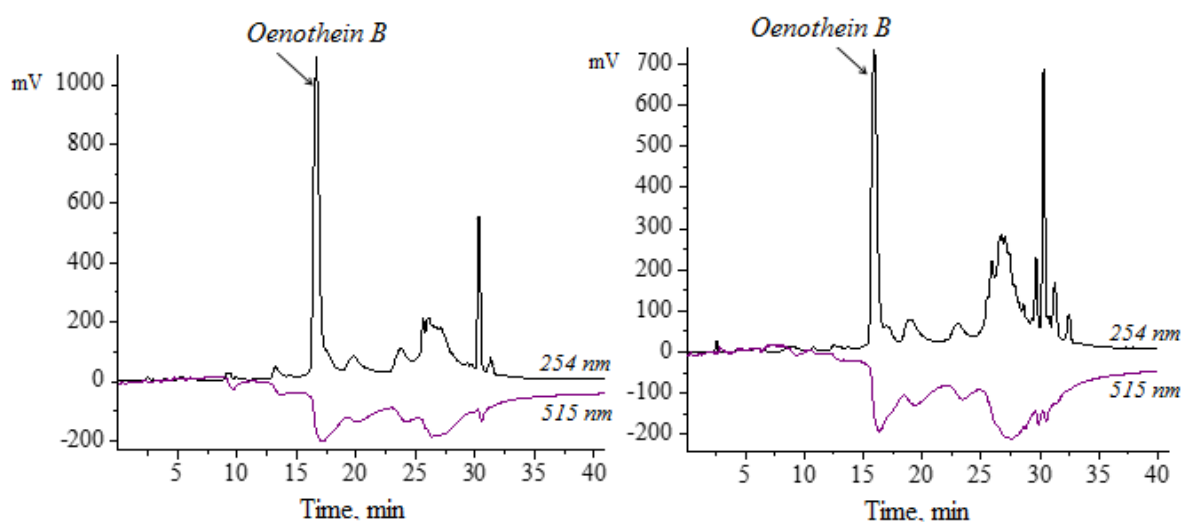


Figure 1. The comparison of HPLC-DPPH chromatograms of *C. angustifolium* L. extracts: at the left – extract obtained after extraction with water (ratio 1:2.5); at the right – the residues of water extract, additionally extracted with 70% (v/v) ethanol.

Solid phase extraction was more perspective for the separation of oenothain B. This analysis allowed to separate almost 90% of oenothain B (Figure 2).

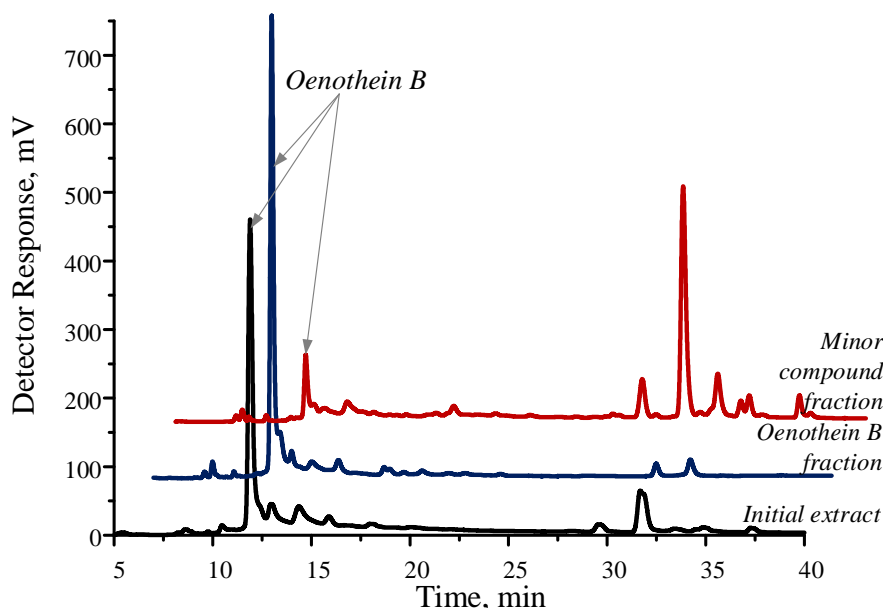


Figure 2. The comparison of HPLC chromatograms of *C. angustifolium* L. extract and fractions obtained using solid phase extraction.

The quantitative analysis of separated compounds and identification of other phenolic compounds were out of the scope of this study. The fraction of other flavonoids of *Epilobium* species consists of myricetin, quercetin, kaempferol and their various glycosides [6-7]. Phenolic acids, like ferulic, gallic, protocatechuic, cinnamic, caffeic, gentisic and chlorogenic, were also identified in the extract of *C. angustifolium* L. [8].

The anticancer activity of *C. angustifolium* L. extract and its fractions, obtained by solid phase extraction, was evaluated against breast cancer cells (MDA-MB-231, MCF7, and MDA-MB-468) and results will be presented during the conference.

References

1. B.H. Tóth, B. Blazics, A. Kéry, *J. Pharmaceut. Biomed.*, **2009**, *49*, 26.
2. A.G. Ramstead, I.A. Schepetkin, M.T. Quinn, M.A. Jutila. *PloS one*, **2012**, *7(11)*, e50546.
3. I.A. Schepetkin, L.N. Kirpotina, L. Jakiw, A.I. Khlebnikov, C.L. Blaskovich, M.A. Jutila, M.T. Quinn, *J. Immunol.*, **2009**, *183*, 6754.
4. S. Vogl, P. Picker, J. Mihaly-Bison, N. Fakhrudin, A.G. Atanasov, E.H. Heiss, C. Wawrosch, G. Reznicek, V.M. Dirsch, J. Saukel, B. Kopp, *J. Ethnopharmacol.*, **2013**, *149*, 750.
5. A.K. Kiss, A. Bazylo, A. Filipek, S. Granica, E. Jaszewska, U. Kiarszys, A. Kośmider, J. Piwowarski, *Phytomedicine*, **2011**, *18*, 557.
6. B. Ducrey, J.L. Wolfender, A. Marston, K. Hostettmann, *Phytochem.*, **1995**, *38*, 129.
7. A. Maruška, O. Ragažinskienė, O. Vyšniauskas, V. Kaškonienė, V. Bartkuvienė, O. Kornyšova, V. Briedis, K. Ramanauskienė, *Adv. Med. Sci.*, **2014**, *59*, 136.
8. A. Hiermann, B. Radl, *J. Chromatogr. A*, **1998**, *803*, 311.

Acknowledgements

The study was financially supported by the Research Council of Lithuania (grant No. MIP 084/2012).

THE INFLUENCE OF SYNTHETIC CALCIUM ALUMINOSILICATE HYDRATE WITH DIFFERENT CONTENT OF ALUMINUM ON THE HYDRATATION OF PORTLAND CEMENT SYSTEM

J. Donėlienė¹, A. Eišinas²

KTU Department of Silicate Technology, Radvilėnų pl. 19, 44249, Kaunas, Lithuania

E-mail: jolanta.doneliene@ktu.lt

Abstract

The influence of synthetic CASH additive on the hydration of Portland cement was determined. It was estimated that, after 8 hours of isothermal curing at 130 °C temperature, when the molar ratio of A/(S+A) was equal to 0.1, calcium aluminosilicate hydrates are dominating in the synthesis products. Moreover, only the traces of calcium silicate hydrate are observed. Meanwhile, in the mixtures with a higher amount of Al₂O₃ (A/(S+A) = 0.15), almost all Al₂O₃ participate in the formation of CASH: the dehydration of CASH and the quantity of absorbed heat is 2 times larger than in the samples with a lower A/(S+A) molar ratio. It should be noted that the CASH additive accelerates the early stage of hydration of OPC and the induction period is effectively eliminated. It was found that the mentioned compound accelerated the second and third exothermic reactions and the amount of cumulative heat is greater in OPC and CASH mixtures, and increases with the decreasing Al/(Al+Si) molar ratio in CASH samples.

Introduction

Concrete is one of the widely used materials all over the world. Ordinary Portland cement (OPC) is used as the primary binder to produce the concrete. The demand of concrete is increasing day by day for the need of development of infrastructure facilities. However, it is well known that the production of OPC not only consumes significant amount of natural resources and energy but also releases substantial quantity of carbon dioxide to the atmosphere [1]. Geopolymers which are based on aluminosilicate ores presents a viable alternative for replacing OPC.

Most of calcium silicate hydrates (CSH) and calcium aluminosilicate hydrates (CASH) and related phases are relevant to cement industry and have potential as geothermal well sealants as well as autoclaved construction materials [2]. CASH is a mineral of silicates, having the general formula Ca₃Al₂(SiO₄)_{3-x}(OH)_{4x} (0 < x < 3) and includes a group of minerals where the [SiO₄]⁴⁻ tetrahedra are partially or completely replaced by OH⁻. The Al-containing hydrogarnet includes hydrogrossular (Ca₃Al₂(SiO₄)_y(OH)_{4(3-y)}; 0 < y < 3) with the end member katoite (Ca₃Al₂(OH)₁₂ or C₃AH₆ in cement notation) [3; 4]. The CASH system is highly complex and is comprised of crystalline to amorphous phases with variable composition that builds up a wide family of phases, which are interesting for the variety of their structural arrangements, the peculiarity of the transformation processes in which they are involved and the relationships with compounds which form during the hydration of the OPC [2].

The main objective of the present work was to examine the influence of synthetic CASH additive on the hydration of Portland cement.

Materials and methods

In this study the following reagents for CASH synthesis were used as starting materials: fine-grained SiO₂·nH₂O (“Reaktiv”, Russia, ignition losses 7 %, specific surface area S_a=1047.4 m²/kg), calcium oxide (“Stanchem”, Poland, CaO was burned at 500 °C for 2 h, specific surface area S_a=960.6 m²/kg; purity, 99 %) and aluminum oxide (“Sigma-Aldrich”, Germany, Al₂O₃ was burned at 475 °C for 4 h, specific surface area S_a=261.9 m²/kg)

Samples of ordinary Portland cement were prepared in a laboratory grinding mill by grinding cement clinker (JSC “Akmenes cementas”, Lithuania) with a 4.5 % additive of gypsum (“Sigma-Aldrich”, Germany) up to S_a=450 m²/kg. The chemical analysis and phase composition of clinker are shown in Table 1.

Table 1. Chemical and mineralogical composition of clinker.

Oxides	SiO ₂	Al ₂ O ₃	Fe ₂ O ₃	CaO	MgO	Na ₂ O	K ₂ O	SO ₃ ²⁻	Ignition of losses	Insoluble particles
Amount, %	19.72	5.41	4.21	62.76	3.41	0.16	1.08	2.08	0.93	0.24
Minerals	3CaO·SiO ₂		2CaO·SiO ₂		3CaO·Al ₂ O ₃		4CaO·Al ₂ O ₃ ·Fe ₂ O ₃			
Amount, %	63.19		8.89		7.21		12.81			

CASH was synthesized under hydrothermal conditions for 8 hours at 130 °C temperature from a stoichiometric compositions (C/S = 0.55) of calcium oxide and SiO₂·nH₂O mixture and A/(S+A) = 0.1 or 0.15 (A – Al₂O₃). Dry primary mixture was mixed with water in the vessels of stainless steel (water/solid ratio of the suspension W/S = 10.0). The hydrothermal synthesis has been carried out in unstirred suspensions in 25 ml volume PTFE cells, which were placed in „Parr instruments“ (Germany) autoclave, under saturated steam pressure. The product was filtered off, dried at 50 ± 5 °C, and put through a sieve with an 80-µm mesh.

The X-ray powder diffraction (XRD) data were collected with a D8 Advance (Bruker AXS). Simultaneous thermal analysis (STA: differential scanning calorimetry — DSC and thermogravimetry — TG) (Netzsch instrument STA 409 PC Luxx) was also employed for measuring the thermal stability and phase transformation of samples at a heating rate of 15 °C/min, the temperature ranged from 30 °C up to 1000 °C under air atmosphere. Isothermal calorimetry - an eight channel (TAM Air III) isothermal calorimeter was used to investigate the heat evolution rate of OPC and OPC blended with 10% by weight of CASH. Glass ampoules (20 ml) each containing 3 g dry cementitious material were placed in the calorimeter and the injection units for each ampoule filled with amounts of water equivalent to a W/(OPC+additive) ratio of 0.5. After a steady temperature of 25 °C had been reached, the water was injected into the ampoules and mixed inside the calorimeter with the dry material for 20 s (frequency 2–3 s⁻¹).

Results and discussion

It was determined that, after 8 hours of isothermal curing at 130 °C temperature, when the molar ratio of A/(S+A) was equal to 0.1, calcium aluminosilicate hydrates (*d*-spacing–0.513, 0.444, 0.336, 0.204, 0.174 nm) are dominating in the synthesis products and only the traces of the semi-crystalline C-S-H(I)-type calcium silicate hydrate (*d*-spacing–0.304, 0.279, 0.182 nm) are observed in XRD patterns (Fig. 1, a, curve 1). It should be noted that, in the mixtures with a higher amount of Al₂O₃ (A/(S+A) = 0.15), almost all Al₂O₃ participate in the formation of CASH, because the intensities of diffraction maximums characteristic to the latter compounds are markedly increased (Fig. 1, a, curve 2). While, a decrease in the intensities of diffraction peaks typical to semi-crystalline C-S-H(I) are noticed. Moreover, regardless of the enhanced reactivity of raw materials, the synthesis products are still carbonized due to the obtained CaCO₃ in the system. The previous results were confirmed by STA analysis data. On DSC curve, an endothermic effect at ~ 300 °C can be attributed to the dehydration of CASH and the quantity of absorbed heat is 2 times larger (260.5 J/g) in the mixtures with A/(S+A) molar ratio of 0.15 than in the samples with a lower A/(S+A) molar ratio (113.8 J/g) (Fig. 1, b).

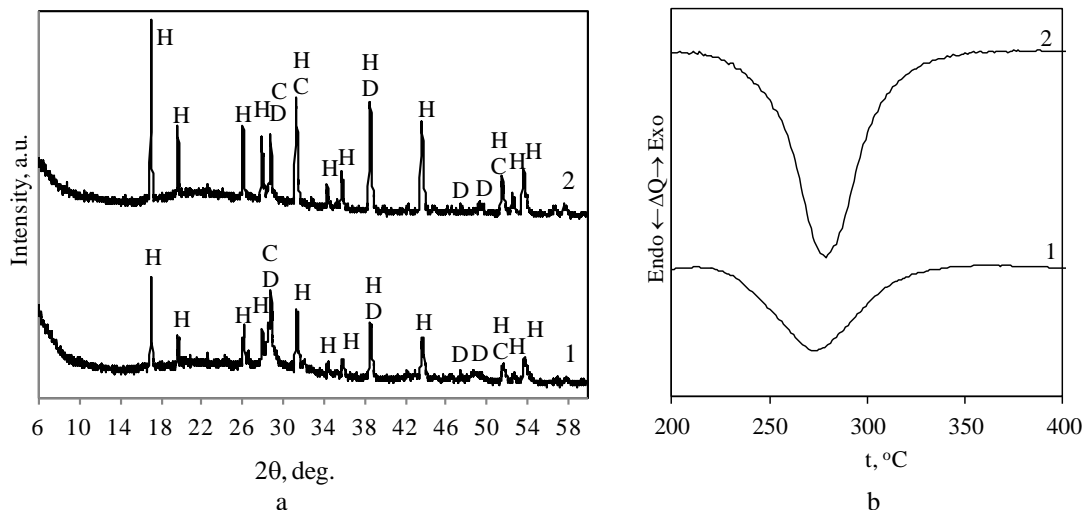


Fig. 1. X-ray diffraction pattern (a), DSC curves (b) of synthesis products after 8 h isothermal treatment at 130 °C when the molar ratio of $\text{Al}_2\text{O}_3/(\text{SiO}_2+\text{Al}_2\text{O}_3)$ was equal to: 1 – 0.1, 2 – 0.15. Indexes: C – C-S-H(I), H – calcium aluminosilicate hydrate, D – CaCO_3 .

In the next stage of experiment, the rate of heat evolution was calculated on the basis of a unit weight of ordinary Portland cement (OPC). Thus, the rates can be compared with each other, and the contribution from the amount of CASH can be separated. The rate of heat evolution (W/g_{OPC}) and the cumulative heat of hydration (J/g_{OPC}) data of the binary blended pastes are presented in Figs. 2, 3 and 4.

In the initial reaction, there is a rapid evolution of the heat culminating in a peak within the first 1–2 min. This was ascribed to the effects of the heat of wetting of the cement and hydration of free lime. In the first few minutes of hydration, there was a rapid release of Ca^{2+} , OH^- , $\text{H}_2\text{SiO}_4^{4-}$, SO_4^{2-} , and alkali ions from the cement compounds. It should be emphasized that hydration at this stage is accelerated by CASH because the first peak of all samples with this additive produces an increase of the maximum heat evolution rate relative to OPC, but this effect decreases as the molar ratio of $\text{Al}/(\text{Al}+\text{Si})$ decreases (Fig. 2). Presumably, the CSH accelerates the early stage of hydration of OPC and its individual compounds because of the adsorption reaction with both alkaline and calcium ions.

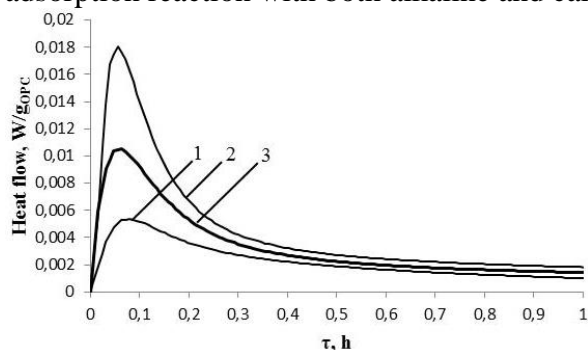


Fig. 2. The heat evolution rate of OPC samples during the early stage of hydration. Amount of additive, wt. %: 1 – 0; 2 – 10 ($\text{Al}/(\text{Al}+\text{Si})=0.1$); 3 – 10 ($\text{Al}/(\text{Al}+\text{Si})=0.15$).

It was determined that in the samples with additive the induction period is effectively shortened: in pure OPC paste, hydration takes about 3.0 h, meanwhile, with an additive – only 1.3 h, when the molar ratio of $\text{A}/(\text{S}+\text{A}) = 0.1$; and about 1.5 h, when the molar ratio of $\text{A}/(\text{S}+\text{A}) = 0.1$ (Fig. 3, a).

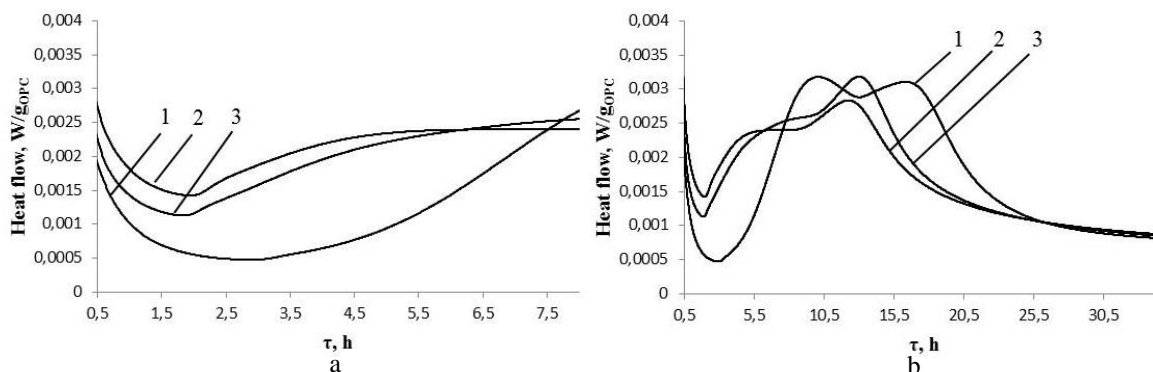


Fig. 3. Heat evolution rate of OPC samples for the following amounts of additive, wt. %: 1 – 0; 2 – 10 (Al/(Al+Si)=0.1); 3 – 10 (Al/(Al+Si)=0.15).

It was estimated that this additive accelerated the second and thirdly exothermic reactions of OPC hydration and its individual compounds (Fig. 3, b).

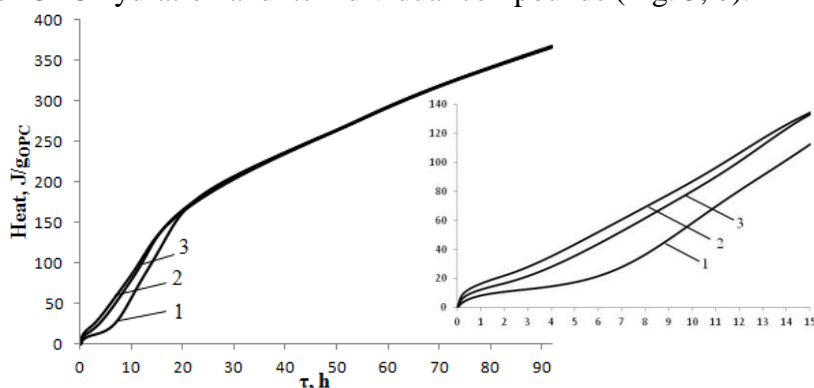


Fig. 4. Cumulative heat of OPC samples when the amount of additive was as follows, wt. %: 1 – 0; 2 – 10 (Al/(Al+Si)=0.1); 3 – 10 (Al/(Al+Si)=0.15).

At later stages of hydration, CASH behaves as the usual pozzolanic additive during the OPC hydration, because the amount of cumulative heat is greater in OPC and CASH mixtures, and increases with the decreasing Al/(Al+Si) molar ratio in CASH samples (Fig. 4).

Conclusions

- It was determined that, after 8 hours of isothermal curing at 130 °C temperature, when the molar ratio of A/(S+A) was equal to 0.1, calcium aluminosilicate hydrates are dominating in the synthesis products and only the traces of calcium silicate hydrate are observed. Meanwhile, in the mixtures with a higher amount of Al₂O₃ (A/(S+A) = 0.15), almost all Al₂O₃ participate in the formation of CASH. The dehydration of CASH and the quantity of absorbed heat is 2 times larger in the mixtures with A/(S+A) molar ratio of 0.15.
- The additive of CASH accelerates the early stage of hydration of OPC and induction period is effectively eliminated.
- It was found that the additive accelerated the second and thirdly exothermic reactions and the amount of cumulative heat is greater in OPC and CASH mixtures, and increases with the decreasing Al/(Al+Si) molar ratio in CASH samples.

Acknowledgments. This work was partly supported by a grant (No. MIP – 025/2014) from the Research Council of Lithuania.

References

1. P. R. Vora, U. V. Dave, *Procedia Eng.*, **2013**, *51*, 210–219.
2. C. A. Rios, C. D. Williams, M. A. Fullen, *Appl. Clay Sci.*, **2009**, *43*, 228–237.
3. K. Byrappa et al., *J Mater Sci*, **2006**, *41*, 1395–1398.
4. B.Z. Dilnesa et al., *Cem. Concr. Res.*, **2014**, *59*, 96–111.



BIOTECHNOLOGIES FOR WOODEN RAILWAY CROSSTIES REMEDIATION

**N. Tiso¹, M. Stankevičius¹, J. Mikašauskaitė¹, A. Maruška¹, V. Snieškienė²,
A. Stankevičienė², T. Makaravičius¹, M. Kazlauskas¹, V. Bartkuvienė¹, O. Kornyšova¹,
O. Ragažinskienė², D. Levišauskas³, E. Galli⁴, C. Polcaro⁴**

¹*Department of biochemistry and biotechnologies, Vytautas Magnus University, Vileikos st. 8,
LT-44404, Kaunas, Lithuania*

²*Kaunas Botanical Garden, Vytautas Magnus University, Z. E. Zilibero st. 6, Kaunas LT-
46324 Kaunas, Lithuania*

³*Process Control Department, Kaunas University of Technology Studentų st. 50, LT-51368
Kaunas, Lithuania*

⁴*National Research Council (CNR), Institute of Agroenvironmental and Forestal Biology
(IBAF) & Institute of Chemical Methodologies (IMC), Area della Ricerca di Roma, Via
Salaria Km 29,300, 00015, Monterotondo (Roma), Italy
E-mail: tiso.nicola@gmail.com*

Creosote is a complex mixture of polycyclic aromatic hydrocarbons (PAHs), phenols and heterocyclic compounds. It has been widely used for more than a century as a wood preservative as insecticide and fungicide for products such as poles, fences and railway crossties to enhance their life expectancy against biological decay.

Nowadays Polycyclic Aromatic Hydrocarbons (PAHs) and related pollutants, such as coal tar and creosote, represent a major environmental concern as it has been pointed out by several American and European laws and regulations, such as Directive on Waste (2001/90/EC and 76/769/EC)⁽¹⁾⁽²⁾. Several PAHs contained in creosote have been identified to be hazardous for human health due to teratogenicity, carcinogenicity and mutagenicity.

Common waste disposal options such as burning and land filling the expended creosote-treated wood waste are inappropriate nowadays due to health, economical and environmental reasons.

Mycoremediation for decontamination is one of effective alternative waste disposal options⁽³⁾⁽⁴⁾.

The aim of this research is to determine the resistance of selected basidiomycetes and ascomycetes to PAHs and related pollutants and to evaluate their effectiveness in the bioremediation PAHs, coal tar and creosote, with a particular focus onto the possibility to use white-rot fungi for the bioremediation of creosote in expended wood sleepers.

Fungal species which have demonstrated higher resistance to different pollutant concentrations have been further investigated to determine their ability to produce ligninolytic enzymes, such as laccase (E.C. 1.10.3.2), manganese dependent peroxidase (E.C. 1.11.1.13), lignin peroxidase (E.C. 1.11.1.13), in order to assess their bioremediation potential.

Furthermore paired interaction assays were used to investigate the possibility of enhancing the remediation process effectiveness by applying a consortium of fungi. Composition of coal tar and creosote in railway wood sleepers samples was determined by using analytical methods such as GC-FID, GC-MS, HPLC, UPLC while enzymatic activity was estimated by qualitative enzymatic assay in vitro and UV-visible spectroscopy.

The screening of PAHs composition of samples collected from different locations in Lithuania has been made and samples were classified according to various parameters including decay level, age and chemical composition of the impregnation of the sleeper. The composition of chemicals varies between intact and rotten sleepers. Few sleeper samples differ from others with strong coal tar odour and dark colour. Analysis resulted in the total amount of PAH in the extracts of these samples exceeding 1000 ppm per millilitre.



About 30 strains of fungi were collected and screened from various matrices and different habitats in Lithuania. The 9 more perspective strains have been subsequently identified by taxonomical observation and DNA analysis and more deeply investigated.

Five different species of fungi (*Pleurotus ostreatus* SMR 684, *Pleurotus eryngii* VMU001, *Bjerkandera adusta* VMU004, *Irpex lacteus* VMU003 and *Schizophyllum commune* VMU002) shown to possess high resistance to different coal tar and single 3-,4-ringed PAHs concentrations and capability to produce peroxidases.

36 different fungal consortia have been investigated and in some cases a positive effect on enzymatic production was observed.

Sequential application of mycoremediation and phytoremediation is currently under investigation.

Acknowledgement: This project is financed by EUSFA, grant No VP1-3.1-ŠMM-10-V-02-010 (BIOREM).

References

1. Commission of the European Communities **2001**. "COMMISSION DIRECTIVE 2001/90/EC". =<http://eur-lex.europa.eu/>.
2. Commission of the European Communities **2007**. "COMMISSION DIRECTIVE 76/769/EEC". =<http://eur-lex.europa.eu/>.
3. E. Galli , E. Brancaleoni, F. Di Mario, E. Donati, M. Frattoni, C.M. Polcaro, P. Rapanà. *Chemosphere* **72**, **2008**, 1069–1072.
4. C.M. Polcaro, E. Brancaleoni, E. Donati, M. Frattoni, E. Galli, L. Migliore, P. Rapanà. *Bull. Environ. Contam. Toxicol.* **81** **2008** 180-184.

QUANTUM MECHANICAL STUDY OF THERMODYNAMICS PARAMETERS OF ETHOXZOLAMIDE

L.Baliulytė^{1,2}, J.Tamulienė²

¹*Vilnius University, Faculty of Natural Sciences, M.K. Ciurlionio st. 21/27, LT-03101 Vilnius, Lithuania, E-mail: Laura.Baliulyte@gf.stud.vu.lt*

²*Vilnius University, Institute of Theoretical Physics and Astronomy, A. Gostauto 12, LT-01108 Vilnius, Lithuania*

Nowadays, carbonic anhydrases are targets for pharmaceutical research although the main drawback of available compounds is insufficient selectivity towards particular carbonic anhydrases ribozymes. Major class of the human carbonic anhydrases (hCA), that catalyze the reversible hydration of carbon dioxide, possesses a primary sulfonamide group. Moreover, carbonic anhydrases play significant role in multiple pathological processes, especially tumor progression [1].

Determination of the intrinsic binding constant, Gibbs free energy, enthalpy, entropy and heat capacity of binding requires significant effort and a number of measurements at various pHs and temperatures. L.Baranauskiene and D.Matulis show the reaction linked to ethoxzolamide binding to h-carbonic anhydrase and state, that protonation contributions must be dissected from binding reactions in order to obtain the intrinsic binding value. The processes are related with the binding of ethoxzolamide to hCA XIII: deprotonation of the inhibitor sulfonamide group and protonation of the zinc-bound hydroxide to make water molecule and consecutive binding of the two active species [2]. We research only deprotonation of the inhibitor sulfonamide group.

The structure of ethoxzolamide molecule (Fig.1) and their fragments deprotonated were studied by the Becke's three-parameter hybrid functional, applying the non-local correlation provided by Lee, Yang, and Parr (B3LYP) [3] a representative standard DFT method with the cc-pVTZ basis [4] in ethanol. Ethanol pH varies in the range of 7-7.2. This pH value corresponds to the experimental conditions [2]. We calculate intrinsic Gibbs free energy and intrinsic enthalpy of the deprotonation of the sulfonamide group. The deprotonation reaction is mentioned as reaction necessary to link ethoxzolamide binding to h-carbonic anhydrase. The bond lengths and orders of the neutral and ionized ethoxzolamide molecule estimate by us to find H atoms that could be deprotonated. In Fig. 1 is marked H atoms, which could dissociate from the molecule to form ions. In our notation, Ions I, II, and- III could be produced when H21, H8 and H15 atoms respectively dissociate (Fig 1). The enthalpy and Gibbs free energy of the ethoxzolamide Ions I, II and III are listed in Table 1.

Table 1. Calculated enthalpy and Gibbs free energy of the ethoxzolamide Ions I, II and III

	Ion I	Ion II	Ion III
Enthalpy, kJ/mol	-58.08	114.28	-62.21
Gibbs free energy, kJ/mol	-92.94	79.63	-94.54

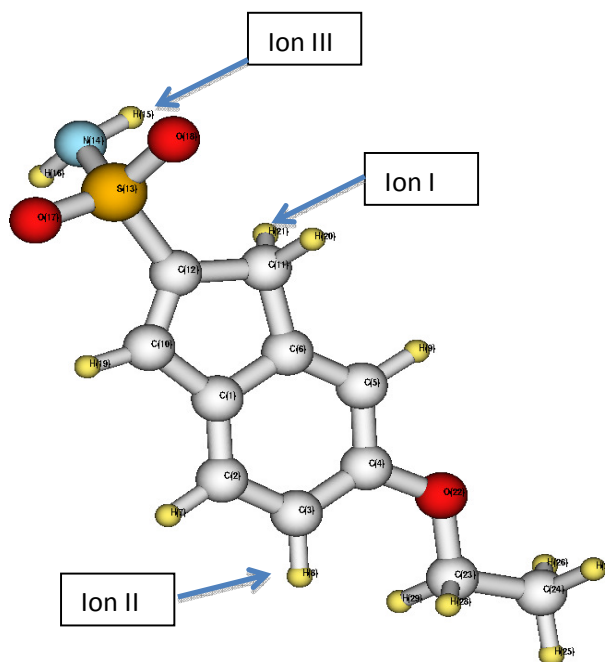


Fig. 1. View of the ethoxzalamide molecule

According to our results (Table 1) the enthalpies of the process investigated vary in the range of -62.35kJ/mol to 114.28kJ/mol at ethanol, whereas experimentally measured enthalpies -29.5kJ/mol , while that taking into account the number of linked protons is equal to 26.8kJ/mol [2]. Ion I and III production reaction are exothermic ($\Delta H < 0$)- heat is let out of the system into the surroundings, whereas Ion II production reaction is endothermic ($\Delta H > 0$)- heat is let into the system from the surroundings. Gibbs free energies calculated (Table 1) vary in the range of -94.72kJ/mol to 79.63kJ/mol . According to our calculations, Ion I and Ion III production reaction is energetically favorable, forward reaction proceeds spontaneously because the change in Gibbs energy is negative. However, Ion II production reaction is energetically unfavorable, the reverse reaction proceeds spontaneously, because the change in Gibbs energy is positive. Referring to these results, we may state, that production of the ion II is not realized. It is clearly to see that calculated and measured values of enthalpies are not coincided. We simulated ethoxzalamide deprotonation in ethanol, whereas in L.Baranauskiene and D.Matulis paper pH is only mentioned, but experimental medium is not described. We predict that in this reaction, not only medium pH is important, but also medium molecular structure and their chemical properties; i.e.- thermochemical reaction parameters in the same pH medium are different for a possible ethoxzalamide interaction with molecules insolution. Additional research is necessary to confirm the above prediction.

Acknowledgment

The authors are thankful for the high performance computing resources provided by the Information Technology Open Access Center of Vilnius University.

References

1. CT Supuran. *Curr Top Med Chem.* 9 (2007):825-833.
2. L. Baranauskiene, D. Matulis. *BMC biophysics.* 5 (2012).
3. AD Becke. *J. Chem. Phys.* 98 (1993) 5648.
4. RAKendall, TH Dunning, RJ Harrison. *J. Chem. Phys.* 96 (1992):6796.

PECULIARITIES OF α -C₂SH SYNTHESIS BY CONVENTIONAL AND MICROWAVE-ASSISTED HYDROTHERMAL TREATMENT

R. Gendvilas, M. Stankevičiūtė, R. Šiaučiūnas

Department of Silicate Technology, Kaunas University of Technology,

Radvilėnų pl. 19, LT-50254 Kaunas, Lithuania

e-mail: rokas.gendvilas@ktu.lt

Abstract

A new interest in the synthesis of α -C₂SH raised due to the recently created hydraulic cementitious material, as this calcium silicate hydrate is used as a main precursor in the production. In this work, conventional and microwave-assisted hydrothermal treatment methods were compared for the first time while applying them for the synthesis of α -C₂SH. It was determined that α -C₂SH can be obtained from limestone and quartz mixture by applying regular hydrothermal synthesis at 200 °C for 2 h (suspension mixing speed is 50 rpm) while adding 5 % Na₂O additive. Additionally, the possibility of using a microwave-assisted hydrothermal treatment for the synthesis was tested.

Keywords: α -C₂SH, XRD, Microwave-assisted hydrothermal treatment.

Introduction

Recently, synthesis, properties and structure of a dibasic calcium silicate hydrate α -C₂SH – a mostly common compound formed during a hardening of autoclaved calcium silicate products, have obtained a new interest, because on its basis a new hydraulic cementitious materials family has been created [1]. Some decades early, many studies have been conducted regarding the synthesis of α -C₂SH [2, 3]. According to several sources, α -C₂SH forms quite easily under hydrothermal conditions from CaO and silicic acid in the temperature range 150–200 °C [4, 5]. Its formation is very slow when using quartz as SiO₂ component [6]. However, the reactivity of quartz can be improved by adding Na₂O to the CaO-SiO₂ mixture [7]. α -C₂SH can also be obtained as a product of the hydration of cement minerals (Ca₂SiO₄, Ca₃SiO₅) and ordinary Portland cement (OPC) slurries at 130 – 220 °C in saturated water steam atmosphere [8].

Lately, microwave-assisted hydrothermal treatment was presented as a very efficient way of synthesis in various fields, including its possible application in the production of cements [9]. In addition, data can be found comparing conventional hydrothermal and modern microwave methods for the synthesis [10, 11]. Authors emphasize, that microwave treatment is more advantageous due to its shorter time and finer particles of the products.

In this work, conventional and microwave-assisted hydrothermal treatment methods are compared for the first time while applying them for the synthesis of α -C₂SH. Presumably, successful employment of a modern microwave-assisted hydrothermal synthesis method would significantly lower both time and energy consumption required for the preparation of this compound as a precursor for the new generation binder material production.

Materials and methods

In this work the following materials were used: quartz sand (“Anyksciu kvarcas”, Lithuania, S_a = 369 m²/kg, SiO₂ = 99.5 %), limestone (“Naujasis kalcitas”, Lithuania, S_a = 434 m²/kg, CaO = 50.88 %) and NaOH (“Reachem Slovakia”, Slovakia, NaOH = 99 %). Limestone was burnt at 1000 °C for 2 h (CaO_{free} = 87 %).

The molar ratio of the initial mixture, consisting of burnt limestone and quartz sand, CaO/SiO₂ was equal to 2. NaOH solution (5 % of Na₂O from the mass of dry materials was

dosed in the form of NaOH solution) was added into the mixture to maintain the liquid/solid ratio of 10.0.

The conventional hydrothermal synthesis of α -C₂SH was carried out in stirred (50 rpm) suspensions in stainless steel autoclave (Parr Instrument) at 200 °C for 4, 8, and 12 h. Isothermal temperature was reached after 2.5 h. Microwave-assisted hydrothermal synthesis was carried out in stirred suspensions placed in glass beakers, which were placed in microwave reactor (Anton Parr Microwave 300). Synthesis was carried out at 175 and 200 °C for 2 and 4 h, liquid/solid ratio was equal to 10.0. Isothermal temperature was reached in 5 min in order to fasten the process.

Products of the synthesis were filtered, rinsed with acetone and dried in an air conditioned chamber at 100±1 °C. Samples for the analysis were sieved through 80 mm mesh.

X-ray fluorescence analysis (XRF) was performed using S4 Explorer (Bruker AXS).

The X-ray powder diffraction analysis (XRD) analysis of the samples was performed on the D8 Advance diffractometer (Bruker AXS).

The specific surface area of the raw materials was determined by the Blaine's method with air permeability apparatus Model 7201 (Toni Technik Baustoffprüfssysteme GmbH).

Scanning electron microscopy analysis (SEM) was performed using Zeiss EVO MA-15 (Carl Zeiss NTS GmbH).

Results and discussion

Chemical composition of limestone was determined using XRF analysis (Fig. 1). The dominant oxide in the material was proved to be CaO. According to the XRD results, most of it was bound in the form of calcite (d – 0.385; 0.303; 0.283; 0.250; 0.228; 0.209; 0.193; 0.191; 0.187 nm) (Fig. 2, curve 1). Additional compounds identified in the XRD curve were dolomite (d – 0.371; 0.290; 0.220; 0.202 nm) and quartz (d – 0.425; 0.334; 0.228 nm). In order to achieve higher reactivity of limestone, it was calcinated at 1000 °C for 2 h. The results of burnt limestone XRD analysis confirmed that most of the calcite turned to more reactive calcium oxide (d – 0.278; 0.240; 0.170; 0.145; 0.139 nm) (Fig. 2, curve 2).

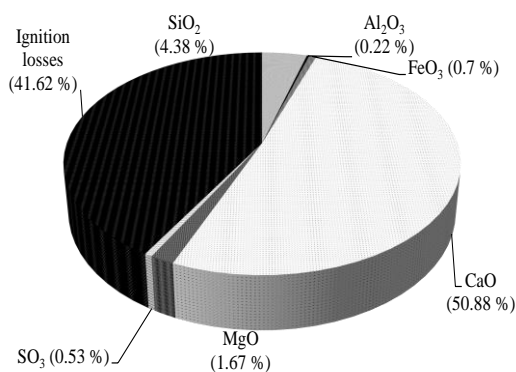


Fig. 1 The results of limestone XRF analysis

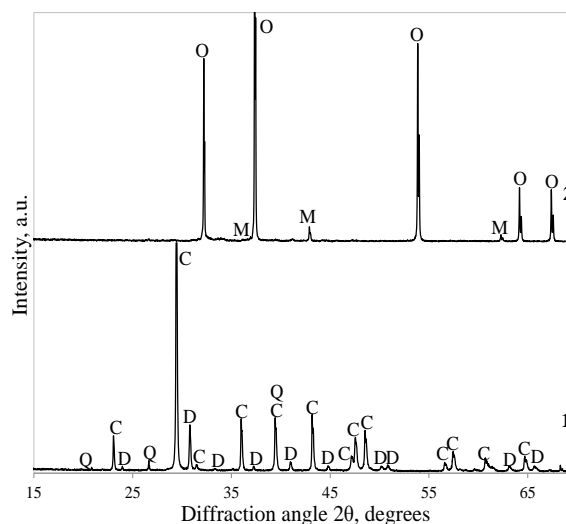


Fig. 2 The XRD patterns of raw (1) and burnt (2) limestone. Indexes: C – calcite, D – dolomite, Q – quartz, O – calcium oxide, M – magnesium oxide

Mixture of thermally treated limestone and quartz (with an addition of 5 % Na₂O) was hydrothermally treated at 200 °C in mixed suspensions when using conventional heating for the synthesis. The results of XRD analysis confirmed the formation of α -C₂SH (d – 0.532;

0.422; 0.354; 0.327; 0.313 nm) already after 4 h of the synthesis (Fig. 3, curve 1). In addition, the formation of this dibasic calcium silicate hydrate was confirmed using SEM analysis, as rectangular plates attributed to it were witnessed in the images (Fig. 4). Peaks of unreacted portlandite ($d = 0.490; 0.311; 0.263; 0.193; 0.180$ nm), quartz and newly formed 1.13 nm tobermorite ($d = 1.126; 0.551; 0.353; 0.353; 0.309; 0.298$ nm) were also identified in the curve. Latter calcium silicate hydrate exhibits a radically lower CaO/SiO₂ ratio (formula can be written as follows: Ca₅(OH)₂Si₆O₁₆·4H₂O). In this case, the added Na⁺ ions accelerated the solubility rate of quartz by eroding the surface of particles and increasing the concentration of SiO₄⁴⁻ ions in the reaction media. On the other hand, data can be found that increment in pH values of the solution drastically reduces the reactivity of Ca(OH)₂ [12]. Therefore, the formation of 1.13 nm tobermorite traces during the synthesis can be explained by the influence of the Na₂O additive: the additive increased the solubility of quartz, but reduced the activity of Ca(OH)₂, therefore the compound of much lower CaO/SiO₂ ratio was formed.

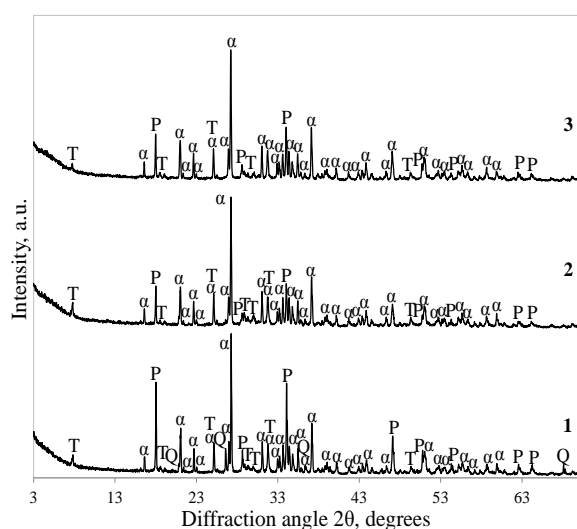


Fig. 3 XRD patterns of the products after 4 (1), 8 (2) and 12 h (3) hydrothermal synthesis at 200 °C (50 rpm)

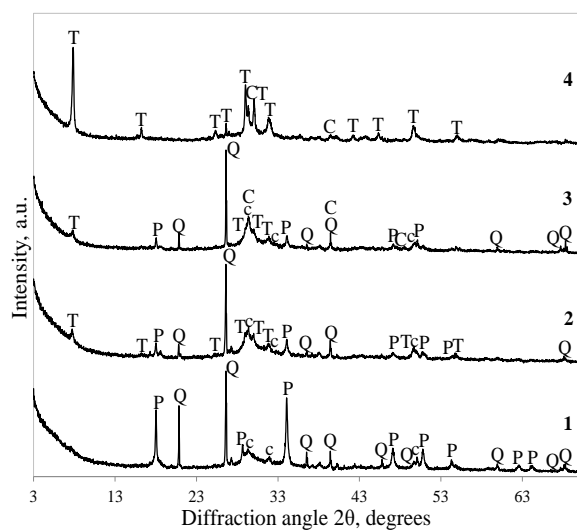
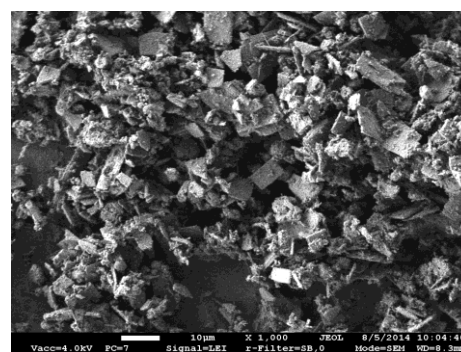
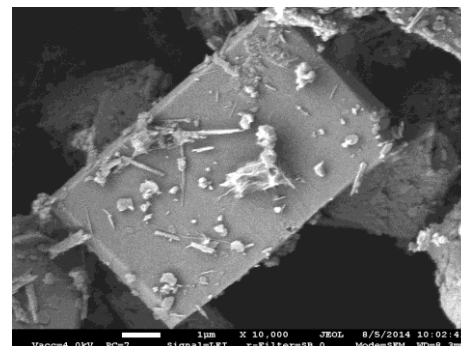


Fig. 5 XRD patterns of the products after 2 (1), 4 h (2) microwave synthesis at 175 °C, 2 (3) and 4 h (4) at 200 °C



a



b

Fig. 4 SEM images of the products of hydrothermal synthesis at 200 °C (50 rpm) after 4 h when the magnification is ×1000 (a) and ×10000 (b).

Extending the duration of the hydrothermal synthesis to 8 h resulted in a slight decrease of the α -C₂SH peaks intensity (Fig. 3, curve 2). In addition, no peaks attributed to quartz were witnessed in the curve and the intensity of portlandite peaks decreased vividly, suggesting the further reaction between these two components. Presumably, it resulted in the formation of 1.13 nm tobermorite, because slight increment in its peaks in the XRD curve was witnessed. Increment in the duration of the hydrothermal synthesis to 12 h had no substantial effect on the formation of the compounds (Fig. 3, curve 3).

In order to test the possibility of applying modern microwave-assisted hydrothermal synthesis for the obtaining α -C₂SH, the same mixture was treated in microwave-powered reactor. According to the literature, hydrothermal reactions should be faster using microwave heating, therefore 175 °C temperature was chosen for the initial test. Additionally, the duration of reaching the isothermal temperature was reduced to 5 min. The XRD results of the 2 h synthesis product revealed, that unreacted Ca(OH)₂ and quartz are the dominant phases (Fig. 5, curve 1). The only newly formed compound was nearly amorphous C-S-H (I) type calcium silicate hydrate (d – 0.304; 0.279; 0.182 nm). Increasing the duration of the synthesis to 4 h resulted in the formation of 1.13 nm tobermorite (Fig. 5, curve 2). Presumably, applying more rapid heating resulted in a major decrease of the Ca(OH)₂ solubility, therefore the initial CaO/SiO₂ ratio was lowered. This hypothesis is in a good agreement with the literature data: the solubility of Ca(OH)₂ is only 0.12 g/kg H₂O at 200 °C [13]. Due to the much faster heating rate when applying microwave-assisted hydrothermal treatment, this temperature was reached within 5 min instead of 2.5 h, therefore the transition of Ca²⁺ ions to the solution was greatly reduced changing the CaO/SiO₂ ratio of the reactive media.

Conclusions

- α -C₂SH can be obtained from limestone and quartz mixture by applying conventional hydrothermal synthesis at 200 °C for 2 h (suspension mixing speed is 50 rpm) while adding 5 % Na₂O additive. However, it co-exists with unreacted starting materials and 1.13 nm tobermorite. α -C₂SH becomes the dominant compound in the products after 8 h of the synthesis.
- α -C₂SH was not obtained by using microwave-assisted hydrothermal synthesis. Increased heating speed and Na₂O additive influenced the CaO/SiO₂ ratio of the reactive media greatly; therefore the dominant compound formed during the synthesis was a calcium silicate hydrate of much lower CaO/SiO₂ ratio – 1.13 nm tobermorite.

References

1. T. Link, F. Bellman, H. M. Ludwig, M. Ben Haha, *Cem. Concr. Res.*, **2015**, 67, 131.
2. H. G. Midgley, S. K. Chopra, *Mag. Concr. Res.*, **1960**, 34, 19.
3. J. M. Butt, L. N. Raskovic, D. M. Heiker, A. A. Maier, O. I. Goratschewa, *Silikattechnik*, **1961**, 12, 281 (in German).
4. H. Ishida, S. Yamazaki, K. Sasaki, Y. Okada, and T. Mitsuda, *J. Am. Ceram. Soc.*, **1993**, 76, 1707.
5. K. Garbev, B. Gasharova, G. Beuchle, S. Kreis, P. Stemmermann, *J. Am. Ceram. Soc.*, **2008**, 91, 263.
6. T. Yano, K. Urabe, H. Ikawa, T. Teraushi, N. Ishizawa, S. Udagawa, *Acta Cryst.*, **1993**, 49, 155.
7. A. Rozycka, L. Kotwica, J. Malolepszy, *Mat. Lett.*, **2014**, 120, 166.
8. K. Yanagisawa, X. Hu, A. Onda, K. Kajiyoshi, *Cem. Concr. Res.*, **2006**, 36, 810.
9. A. Buttress, A. Jones, S. Kingman, *Cem. Concr. Res.*, **2015**, 68, 112.
10. O. A. Dudarko, C. Gunathilake, V. V. Sliesarenko, Y. L. Zub, M. Jaroniec, *Coll. Surf. A: Physicochem. Eng. Aspects*, **2014**, 459, 4.
11. X. Yan, E. Michael, S. Komarneni, J. R. Brownson, Z. F. Yan, *Ceram. Int.*, **2013**, 39, 4757.
12. E. J. Reardon, R. Fagan, *App. Geochem.*, **2000**, 15, 327.
13. H. Gundlach, *Dampfgehartete Baustoffe*, Bauverlag GmbH, Wiesbaden, **1973**, 365 (In German).



Chemistry and Chemical Technology 2015

Vilnius University, Faculty of Chemistry,
Naugarduko 24, Vilnius, Lithuania
January 23, 2015

Poster presentations

Biochemistry and Biotechnology



NISIN-PECTIN COMPLEX NANOPARTICLES FOR FOOD PRESERVATION

T. Krivorotova¹, A. Cirkovas¹, S. Maciulyte², R. Staneviciene³, S. Budriene², E. Serviene³, J. Sereikaite¹

¹Vilnius Gediminas Technical University, Sauletekio al. 11, LT-10223 Vilnius, Lithuania

²Vilnius University, Naugarduko 24, LT-03225 Vilnius, Lithuania

³Nature Research Centre, Akademijos 2, LT-08412 Vilnius, Lithuania

E-mail: jolanta.sereikaite@vgtu.lt

Introduction

Nisin is a small cationic peptide composed of 34 amino acid residues (3.5 kDa). It is produced by *Lactococcus lactis* subsp. *lactis* and belongs to the class I of bacteriocins named lantibiotics. *L. lactis* is a food grade lactic acid bacterium and is generally recognized as safe (GRAS). As a consequence, nisin as a product of *L. lactis* was approved by the US Food and Drug Administration for food applications. Nisin was also recognized as a food additive in EU and was assigned the number E234 [1, 2]. Nisin exhibit a wide spectrum antimicrobial activity against Gram-positive bacteria and is suitable for food preservation [1]. It is largely used in dairy industry against clostridia spoilage in processed hard and semi-hard cheese, cheese spreads and dairy desserts. However, reduced antimicrobial activity of nisin in some food products was observed. This is thought to be due to interference with food components such as lipids or due to enzymatic degradation of peptide [3-5].

This study is aimed at developing of nisin-pectin nanoparticles in order to protect nisin from the interaction with food components and to ensure the stability of antimicrobial peptide during food processing and storage period.

Materials and Methods

For the preparation of nisin-pectin nanoparticles, nisin (NisinZTM P) was purchased from Handary S.A. (Brussels, Belgium). Both high methoxyl pectin (HMP, M_w 30000-100000, degree of esterification 60%) and low methoxyl pectin (LMP, M_w not determined, degree of esterification $\leq 26\%$) from citrus peel were purchased from Fluka and Sigma, respectively. All materials were used without additional purification. The stock solutions of pectin as well of nisin were prepared by dissolving 500 mg or 1000 mg of each one in 500 mL of deionized water. Prior to use, the solutions were filtered through 0.2 μ m pore size filters, and a desired pH value in the range of 4.0 to 7.0 was adjusted with 0.1 M NaOH. For the formation of nanoparticles, a volume of nisin solution in the range of 5 to 30 mL at the concentration of 1 mg/mL (or 20 mL and 25 mL at the concentration of 2 mg/mL) was added dropwise to the pectin solution under constant stirring at room temperature. Prior to the addition of nisin, pectin solution was diluted with water to obtain final 50 mL of nisin-pectin mixture at the pectin concentration of 0.4 mg/mL and the nisin concentration in the range of 0.1 to 1 mg/mL, and the value of solution pH was adjusted additionally.

For the determination of nisin loading efficiency, 0.5 mL of nanoparticle solution was centrifuged at 5000xg at room temperature for 30 min using ultra-filtration tubes (Roti[®]-Spin MINI-10, M.W. cutoff of 10 kDa). The content of free nisin in the supernatant (in outer tube) was determined by capillary zone electrophoresis (CZE) method using 7100 Capillary Electrophoresis unit (Agilent Technologies). CZE was performed at 20 °C using PVA-coated silica capillary (50 μ m ID, 64.5 cm total length, 56 cm effective length). Run buffer was 25 mM sodium acetate, pH 4.0. The sample was introduced into the capillary by hydrodynamic injection for 4 s at 50 mbar. The separation was carried out at 30 kV with positive polarity at the inlet. Peptide was detected at 200 nm. The percentage of residual free nisin was calculated comparing peak areas of supernatant samples and blank samples containing all components

except pectin. The efficiency of nisin loading (LE) was calculated using Eq.: $LE (\%) = (\text{Total nisin} - \text{free nisin}) / \text{Total nisin}$.

The hydrodynamic radius of nanoparticles was determined using Zetasizer NanoZS (Malvern Instruments) equipped with a 4 mV HeNe laser at a wavelength of 633 nm. Measurements of the intensity of the scattered light were performed at 25 °C and at the angle of 173°. The size distributions were obtained from the correlation functions, and the data were analyzed using Malvern Zetasizer software 7.03. The zeta-potential of nanoparticles was measured using above mentioned equipment. The electrophoretic mobility was converted to the zeta potential according to the Smoluchowski equation.

For the estimation of bacteria sensitivity to nisin-pectin nanoparticles, the bacteria *Bacillus subtilis*, *Escherichia coli*, *Klebsiella sp.* and *Arthrobacter sp.* were grown overnight at 37 °C and 30 °C, respectively. Gram-positive bacteria *Bacillus subtilis* and *Arthrobacter sp.* were collected (2×10^6 cells/sample) by centrifugation at 3000xg for 5 minutes. The identical amount of collected Gram-negative bacteria *Escherichia coli* and *Klebsiella sp.* cells was additionally treated with the permeabilization solution containing 0.8 M sorbitol, 4 mM DTT, 0.5 M EDTA and 10 mM Tris-HCl, pH 7.5 for 30 min at 37 °C. Then, bacterial cells were mixed with one milliliter of nisin-pectin nanoparticle solution. Samples were incubated at room temperature (20 °C) for 24 h with gentle agitation. Serial dilutions were performed in 0.9% NaCl and 5 µL of each solution were drop-seeded onto LB-agar plates with following incubation overnight at 37 °C for *Bacillus subtilis*, *Escherichia coli*, *Klebsiella sp.* and 30 °C for *Arthrobacter sp.* bacteria. After incubation, colonies were counted as CFU (colony forming units), and the mean value of CFU/mL was calculated. For agar-diffusion assay, 5 µL nisin-pectin nanoparticles of different concentrations were spotted on the LB agar plates seeded with Gram-positive *Bacillus subtilis* or *Arthrobacter sp.* (2×10^7 cells/plate) that were incubated at 37 °C or 30 °C, respectively, for 24 h, and growth inhibition zones were analyzed.

Results and Discussion

Nisin-pectin nanoparticles were prepared by ionic complexation method [6]. The data of nisin loading efficiency using pectin with different degree of esterification at various values of pH are presented in Table 1. In the case of both HMP and LMP, the highest nisin loading efficiency was found at pH 7.0. Moreover, HMP was able to bind higher amount of nisin than LMP. It follows that not only electrostatic, but also hydrophobic interactions are important for the formation of nisin-pectin nanoparticles. As seen from Fig. 1, the average size of nisin-loaded HMP particles is lower as compared with HMP. Moreover, at pH 4.0 the additional peak of intensity in the range of 20 - 40 nm is observed (Fig. 1B). The increase of nisin concentration slightly influenced the hydrodynamic radius of nisin-loaded HMP nanoparticles (Fig. 2A).

Table 1. Nisin loading efficiency of biopolymer nanoparticles created by ionic complexation at the pectin concentration of 0.4 mg/mL.

Content of nisin, mg/mL	LE ^{HMP} , %				LE ^{LMP} , %			
	pH				pH			
	4.0	5.0	6.0	7.0	4.0	5.0	6.0	7.0
0.1	100	100	100	100	100	100	100	100
0.2	100	100	100	100	100	100	100	100
0.4	96	100	100	100	100	100	100	100
0.5	-	-	-	-	-	98	100	100
0.6	88	100	100	100	-	-	-	-
0.8	88	90	100	100	69	80	94	95
1.0	83	84	95	100	64	79	87	94

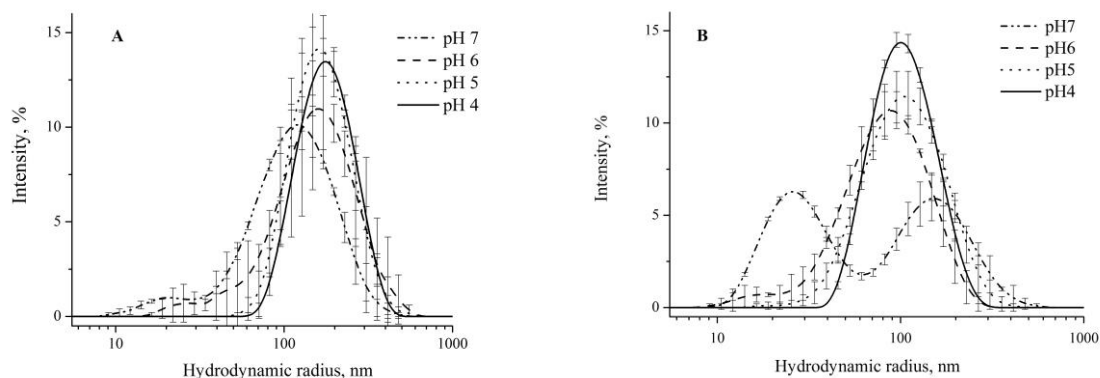


Fig. 1. Size distributions of HMP (A) and nisin-loaded HMP nanoparticles (B) at different pH values. Final concentrations of HMP and nisin in the solution were equal to 0.4 mg/mL.

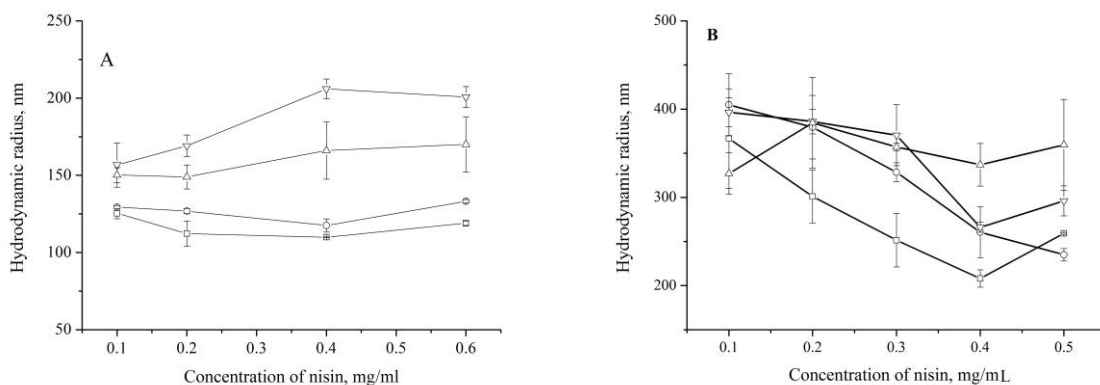


Fig. 2. Size of nisin-loaded HMP (A) and nisin-loaded LMP (B) nanoparticles prepared at different pH values as a function of nisin concentration; -□-, pH 4; -○-, pH 5; -∇- pH 6; -Δ-, pH 7. Final concentrations of HMP and LMP in the solution were equal to 0.4 mg/mL.

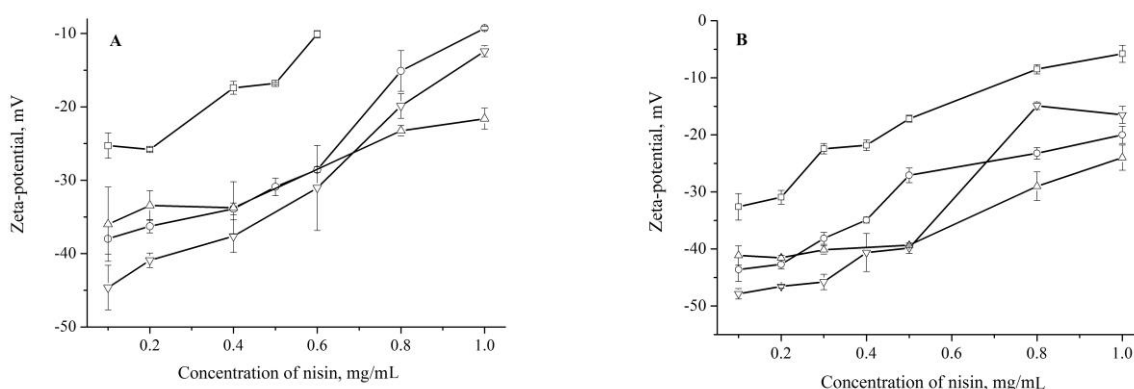


Fig. 3. Zeta-potential of nisin-loaded HMP (A) and nisin-loaded LMP (B) nanoparticles prepared at different pH values as a function of nisin concentration; -□-, pH 4; -○-, pH 5; -∇- pH 6; -Δ-, pH 7. Final concentrations of HMP and LMP in the solution were equal to 0.4 mg/mL.

In the case of LMP, the decrease of nanoparticle size is observed with increasing nisin concentration (Fig. 2B). The zeta-potentials continuously increased with increasing nisin concentration. It indicates nisin-loaded HMP or LMP nanoparticle formation (Fig. 3).

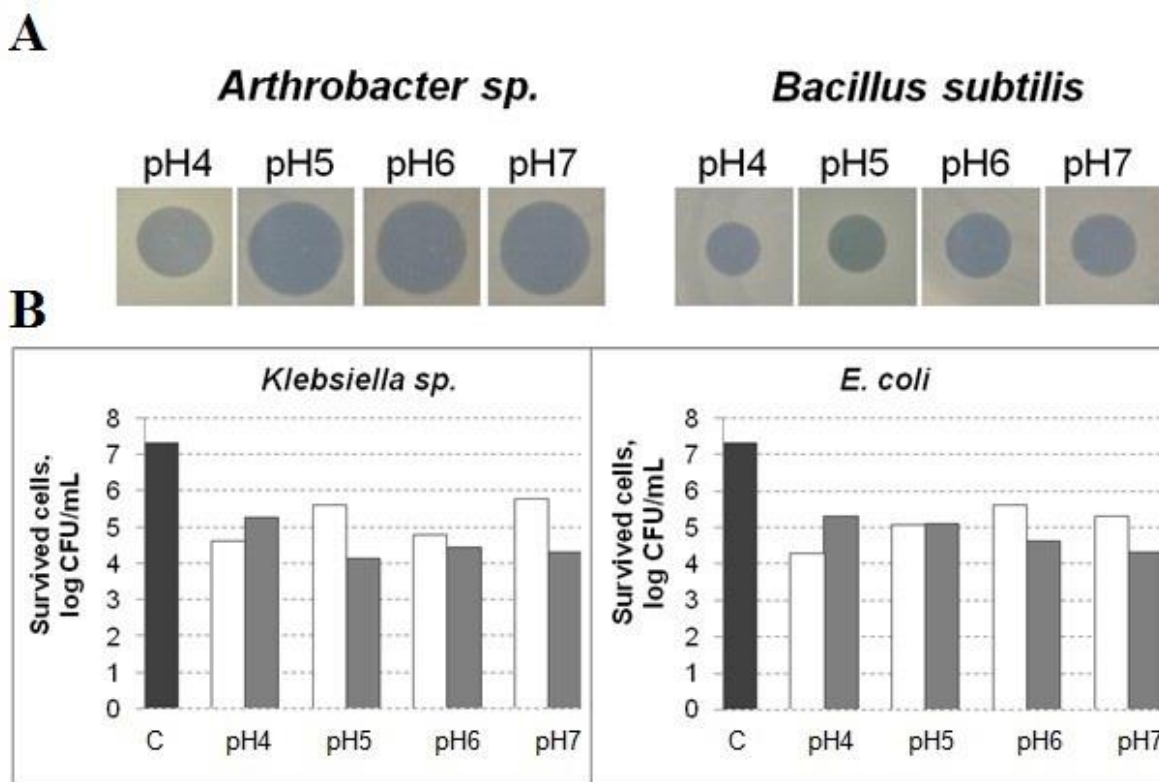


Fig. 4. Analysis of bacteria sensitivity to nisin-loaded HMP nanoparticles. Gram-positive bacteria were tested by applying agar-diffusion assay and measuring growth inhibition zones (A). Gram-negative bacteria that survived the overnight treatment with nisin-loaded HMP nanoparticles were analyzed by counting viable cells (CFU) (B). Dark grey column represents control experiment, white and light grey columns represent the experiments with nanoparticles prepared using 0.2 mg/mL and 0.4 mg/mL of nisin, respectively, and 0.4 mg/mL of HMP.

Nisin loaded HMP nanoparticles were biologically active and completely inhibited the growth of both Gram-positive microorganisms tested in the experiment (Fig. 4A). Moreover, antibacterial effect against *Arthrobacter sp.* was approximately two-fold higher compared to *Bacillus subtilis* as lysis zones were twice larger in diameter. Antibacterial activity of nisin-loaded HMP nanoparticles against permeabilized Gram-negative bacteria *Escherichia coli* and *Klebsiella sp* was lower comparing to the action against Gram-positive bacteria (Fig. 4B). The number of cells that survived the overnight treatment with nisin-loaded HMP nanoparticles decreased from 100 to 1000 fold as compared with untreated control cells.

Acknowledgement

This study was funded by the Research Council of Lithuania, Grant No. SVE-03/2014.

References

1. E.M. Balciunas, F.A.C. Martinez, S.D. Todorov, B.D. Gombossy de Melo Franco, A. Converti, R. Pinheiro de Souza Oliveira, *Food Control*, **32** (2013) 134-142.
2. A.D. Paiva, E. Breukink, In *Antimicrobial Peptides and Innate Immunity*; Eds. P.S. Hiemstra, S.A.J. Zaat, Springer, Basel, 2013, p.53.
3. E. Chollet, I. Sebti, A. Martial-Gros, P. Degraeve, *Food Control*, **19** (2008) 982-989.
4. I.M. Aasen, S. Markussen, T. Moretro, T. Katla, L. Axelsson, K. Naterstad, *Int. J. Food Microbiol.*, **87** (2003) 35-43.
5. M. Bhatti, A. Veermachaneni, L.A. Shelef, *Int. J. Food Microbiol.*, **97** (2004) 215-219.
6. M. Chopra, P. Kaur, M. Bernela, R. Thakur, *Food Control*, **37** (2014) 158-164.

THE STUDY OF HALOGEN-SUBSTITUTED QUINONES AS EFFECTIVE ENZYME INACTIVATING AGENTS

**L. Misevičienė^{*1}, J. Šarlauskas^{*1}, Ž. Anusevičius¹, A. Yantsevich², T. Karpenko², A. Ivanchik²,
A. Marozienė¹, J. Stankevičiūtė¹, A. Gilep², Y. Dichenko², S. Usanov² and N. Čėnas¹**

¹ Vilnius University Institute of Biochemistry, Vilnius, Lithuania

² Institute of Bioorganic Chemistry NASB, Minsk, Belarus

* E-mail: lina.misevičienė@bchi.vu.lt

* E-mail: jonas.sarlauskas@gmail.com

Two-electron (hydride)-transferring flavoenzyme NAD(P)H-quinone oxidoreductase 1 (DT-diaphorase, NQO1; EC 1.6.99.2) is an antioxidant/detoxifying enzyme, recently recognized as one of the most important contributors to chemo-resistance in some human cancers such as cholangiocarcinoma (CCA) which is highly resistant to most of the classical chemotherapeutic treatments ([] and references therein). However, the mechanisms of NQO1 contribution to chemotherapy are still almost unknown.

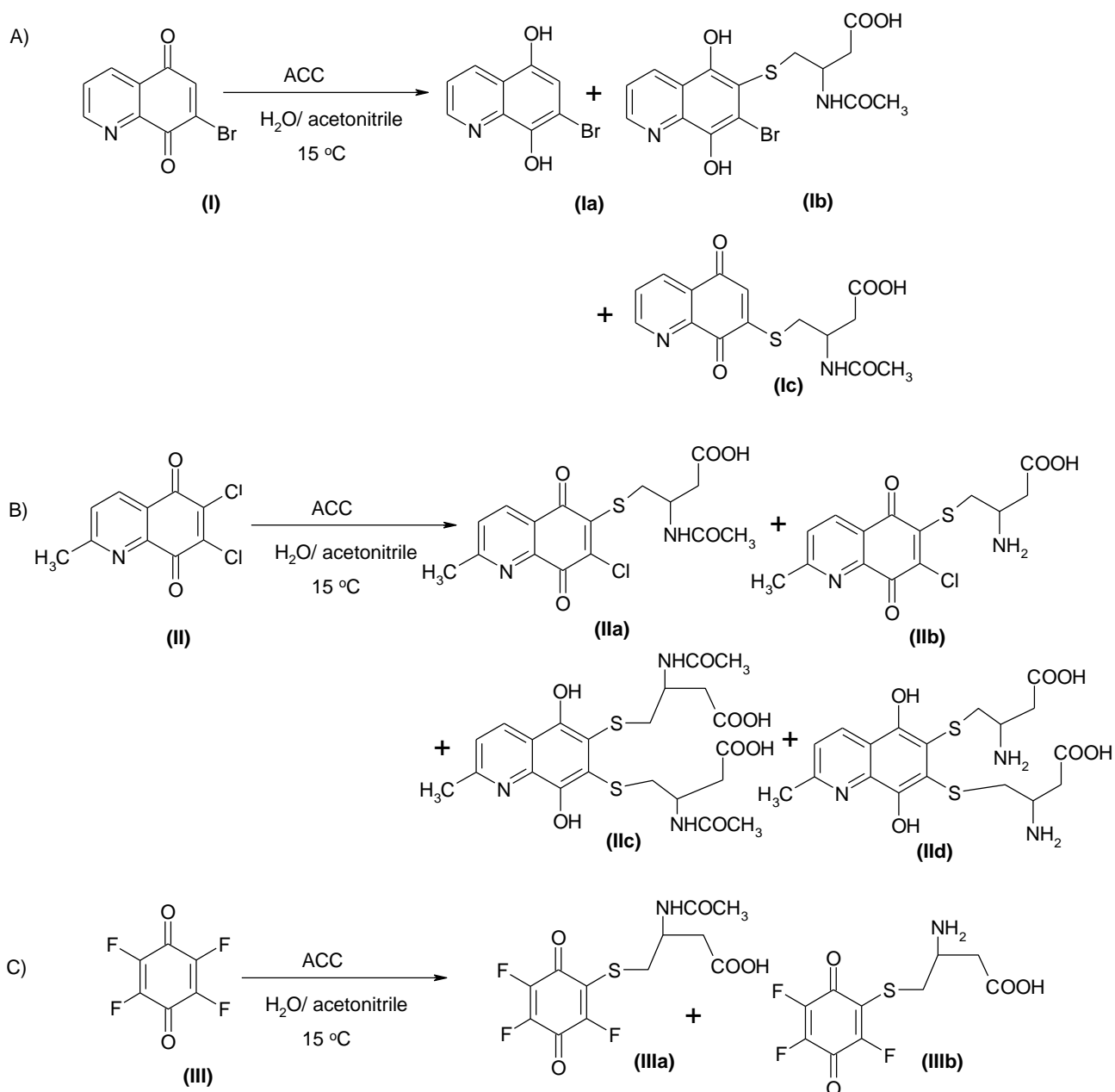
As it has been found in the one of the newest publications [1], by knocking down NQO1, cancer cells become more susceptible to chemotherapeutic agents.

Our laboratory has a long time experience and multidisciplinary approach in the studies of mechanisms of NQO1-catalyzed bioreduction and/or bioactivation of some redox-active xenobiotics, medicinal drugs or pollution agents like quinones, nitroaromatic and heterocyclic N-oxide compounds. Thus, in continuation of our work, we represent here some preliminary results on the study of 5 halogenated quinones such as 7-bromoquinolin-5,8-dione (**I**, 7-Br-QQ); 2-methylquinolin-5,8-dione (**II**, 2-Me-Cl₂QQ); 2,3,5,6-tetrafluoro-1,4-benzoquinone (**III**, F₄BQ); 2,3,5,6-tetrachloro-1,4-benzoquinone (**IV**, Cl₄BQ) and 2,3,5,6-tetrabromo-1,4-benzoquinone (**V**, Br₄BQ) as inactivating agents of NQO1.

All halogenated quinones have been synthesized by known classical methods, using halogenation and oxidation reactions as described in [2]; it is important to note, that the yields of heterocyclic quinones (**I**, 7-Br-QQ and **II**, 2-Me-Cl₂QQ) have been found to be almost 10 times less as compared to those of model 1,4-benzoquinone (**III-V**) derivatives.

Aiming to understand the mechanism of covalent adduct formation of halogenated quinones, at first stage of this study, some model reactions has been performed employing thiol reagent N-acetylcystein (ACC) as nucleophile. The main reaction products of these reactions have been identified *in situ* by means of fast LC-MS system. The major reaction products, being identified in positive mode, are shown in **Scheme 1**.

Scheme 1: The formation of adducts of halogenated quinones as identified by means of LC-MS system: **(I)** 7-Br QQ ; **(II)** 2-Me-Cl₂QQ and F₄BQ **(III)**:



As it can be seen from Scheme 1, there are two kind of products formed, one is normal nucleophilic displacement product, and another is Michael adduct. The same but slower reactions are going and products are formed during the interaction of N-acetylcysteine with Cl₄BQ (**IV**) and Br₄BQ (**V**) (*data not shown*).

Next, we have examined the interaction of NQO1 with halogenated quinones. As it has been previously defined [3], Cl₄BQ acts as an irreversible inhibitor rather than a substrate of this enzyme. In this work, NQO1 inactivation reaction products were analyzed by means of MALDI-TOF analyses. The fast analytical system BRUKER MicroFlex MALDI-TOF (matrix-absorption laser desorption instrument time-of-flight) were used for this task. Briefly, the reaction mixture, containing 0.5 ml K-phosphate buffer, 35 μ L halogenated quinone solution in acetonitrile („stock“ prepared by dissolution of 2 mg quinone in 2 mL of CH₃CN) and 15 μ L of NQO1 solution (from „stock“ with NQO1 concentration of 106 μ M) was incubated for 4 hours; then NQO1 was

denaturated by 70% ethanol, centrifugated and washed 2 times with 70% ethanol, and finally diluted in 20 μL of 70% formic acid solution. 1 μL has been taken from this solution and used for the analysis on MALDI-TOF matrix, containing synaptic acid. The samples obtained by these procedures have been analysed (**Fig.1**).

Figure 1. MALDI-TOF mass spectrum of (a) purified NQO1 (control, i.e., without pre-incubation with halogenated quinone) and (b) NQO1 pre-incubated with 7-BrQQ (**I**).

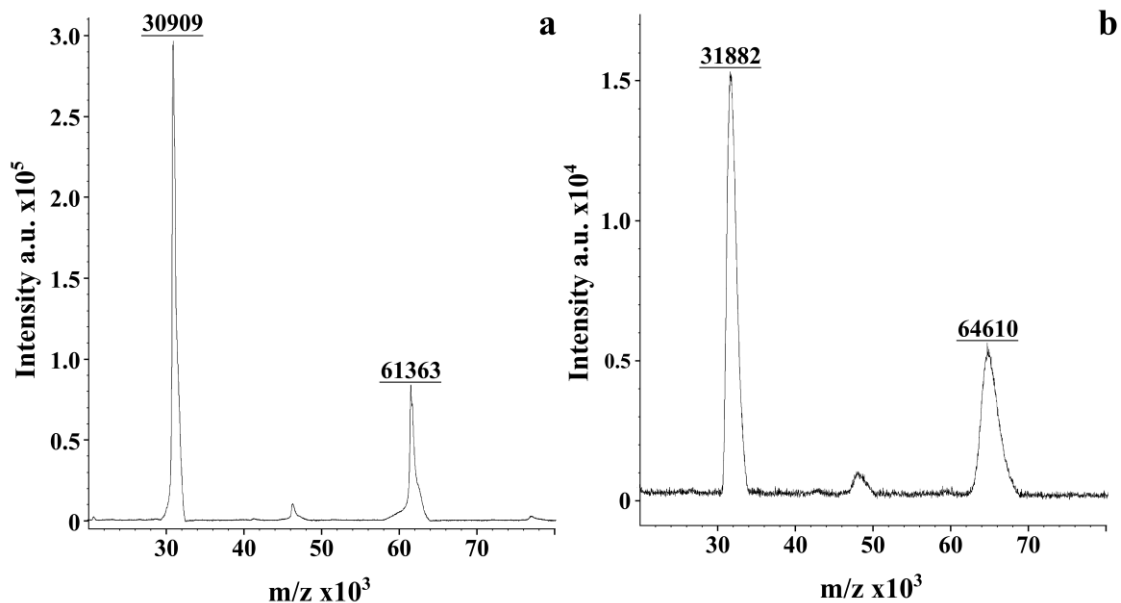


Figure 2. NQO1 pre-incubated with 2-Me-Cl₂QQ (**II**) (left) and F₄BQ (**III**) (right):

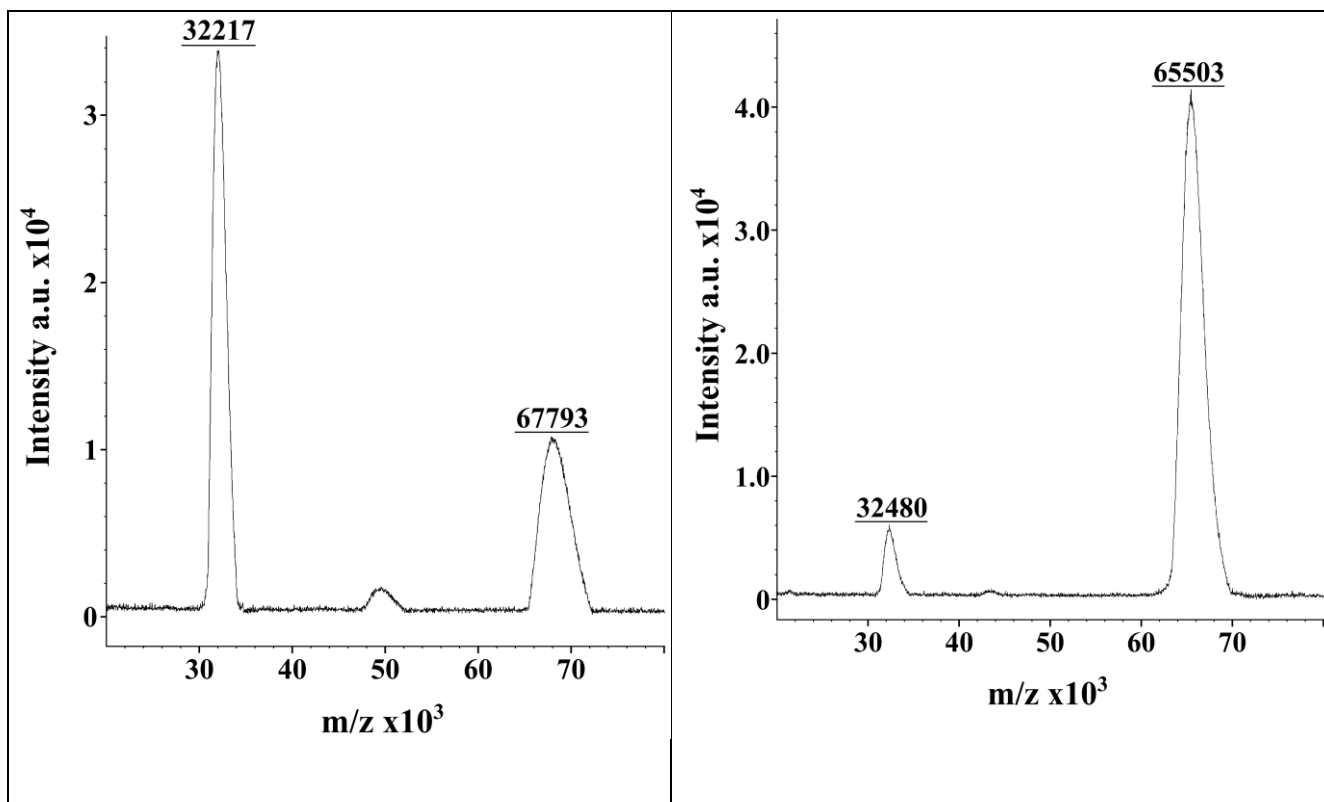
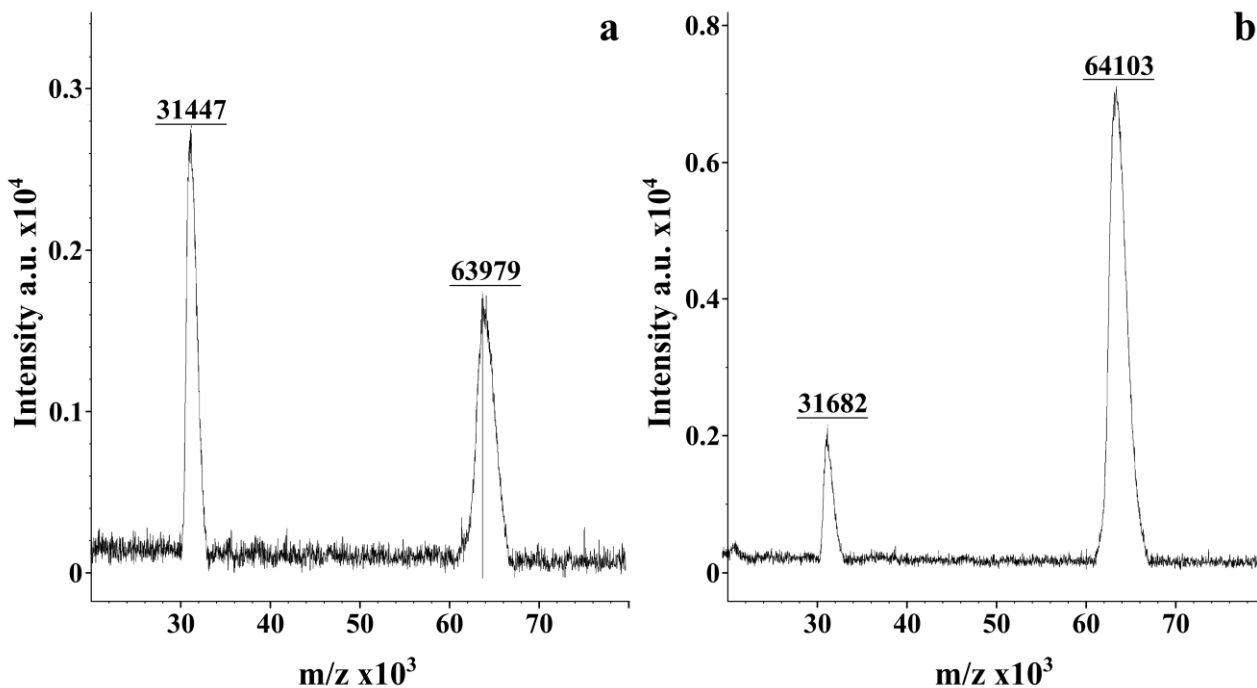


Figure 3. NQO1 pre-incubated with (III, F₄BQ)



The obtained data show that NQO1 undergoes covalent modification by halogenated quinone compounds. The pre-incubation of NQO1 with halogenated quinones was found to inactivate quinone reductase activity of NQO1. More thorough studies are required to identify the actual residues involved in the covalent modification of the enzyme by halogenated quinones.

This study was funded by the Scientific Council of Lithuania under the Grant "New Generation N-Heterocyclic Quinones: Rational Synthesis and Elucidation of Anticancer Activity", No. MIP-032/2014.

References:

1. Grundmann, Ch., Chinone II in *Houben-Weyl Methoden der organischen Chemie* (Stuttgart), Vol. 7, Part 3B, p. 16, 629 (1979).
2. Zeekpudsa, P. et al.: Suppression of NAD(P)H-quinone oxidoreductase 1 enhanced the susceptibility of cholangiocarcinoma cells to chemotherapeutic agents. *J. Exp. & Clin. Cancer Res.*, 2014, V.33:11-13.
3. Osman, A.; Boeren, S. Studies of the DT-diaphorase-catalyzed reaction employing quinones as substrates: evidence for a covalent modification of DT-diaphorase by tetrachloro-p-benzoquinone. *Chem.-Biol. Interact.*, 2004, 147, 99-108.

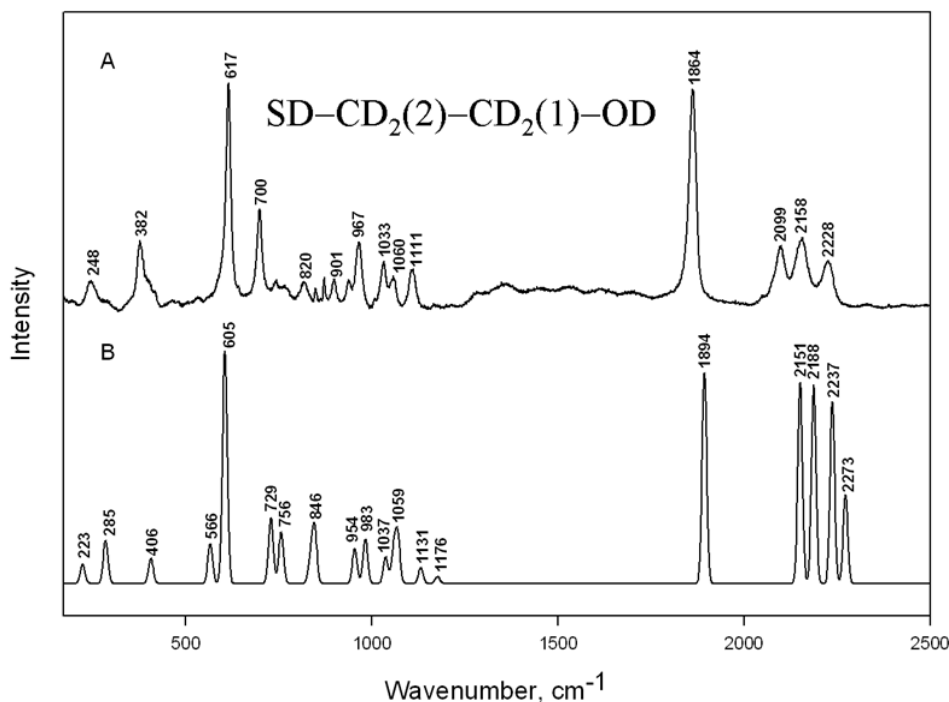


Fig. 2. Comparison of deuterium labeled β -mercaptoethanol (β Med) Raman spectrum (A) and calculated spectrum of β Med (B). Calculations were performed at B3LYP/6-311++g(2d,p) level for *gauche* conformer. Excitation wavelength is 785 nm.

The intense band at 1864 cm^{-1} in the experimental spectrum belongs to S–D stretching vibration. The corresponding band in calculated spectrum is observed at 1894 cm^{-1} . Calculations allow discriminating the high frequency vibrational modes to vibrations of C1D_2 and C2D_2 groups. Thus, observed bands at 2099 , 2158 , and 2228 cm^{-1} belong to $\nu_s(\text{C1D}_2)$, $\nu_s(\text{C2D}_2)$, and $\nu_{as}(\text{C1D}_2)$ stretching modes, respectively. Deformation mode $\delta(\text{CCO})$ is visible at 382 cm^{-1} and 406 cm^{-1} in the experimental and calculated spectra, respectively. The bands at 1033 , 1060 , and 1111 cm^{-1} (Fig. 2A) are associated with $\delta(\text{COD})+\delta(\text{CSD})$, $\delta(\text{COD})$, and $\delta(\text{C1D}_2)$ vibrational modes, respectively.

Incubation in water of tether monolayer prepared from ethanolic solution containing β Med (70%) and WC14(30%) results in subtle changes in the SERS spectrum of β Med (Fig. 3). Clear bands near 594 and 678 cm^{-1} belong to C–S stretching vibrations of *gauche* and *trans* conformers of adsorbed β Med. Comparing with liquid β Med spectrum (Fig. 2A), the frequencies of the $\nu(\text{C–S})_G$ and $\nu(\text{C–S})_T$ decrease by $22\text{--}23\text{ cm}^{-1}$ indicating formation of covalent bond between the S and Au atoms [3–5]. Strong interaction with Au surface induces shift of C–S mode to lower wavenumbers because of adsorption induced withdrawal of electron density from the C–S bond and the metal mass effect [3,4]. Employment of deuterated β -mercaptoethanol provides possibility for discrimination of C–S stretching modes of adsorbed β Med and WC14. Thus, low intensity feature near 712 cm^{-1} evidence presence of chemisorbed WC14 molecules in *trans* conformation of Au–S–CH₂–CH₂ moiety. The relative intensity of 1100-cm^{-1} band increases in the surface spectrum comparing with the liquid β Med spectrum. Based on quantum chemical analysis this band is assigned to predominant $\delta(\text{C1D}_2)$ vibration containing some contribution from $\nu(\text{C–C})$ stretching mode. The low intensity peak at higher frequency side (near 1130 cm^{-1}) is associated with in-phase C–C stretching vibration of hydrocarbon chains of adsorbed WC14 in all-*trans* conformation

[3.4]. The band near 893 cm^{-1} may also contain some contribution from the CH_2 rocking mode of WC14.

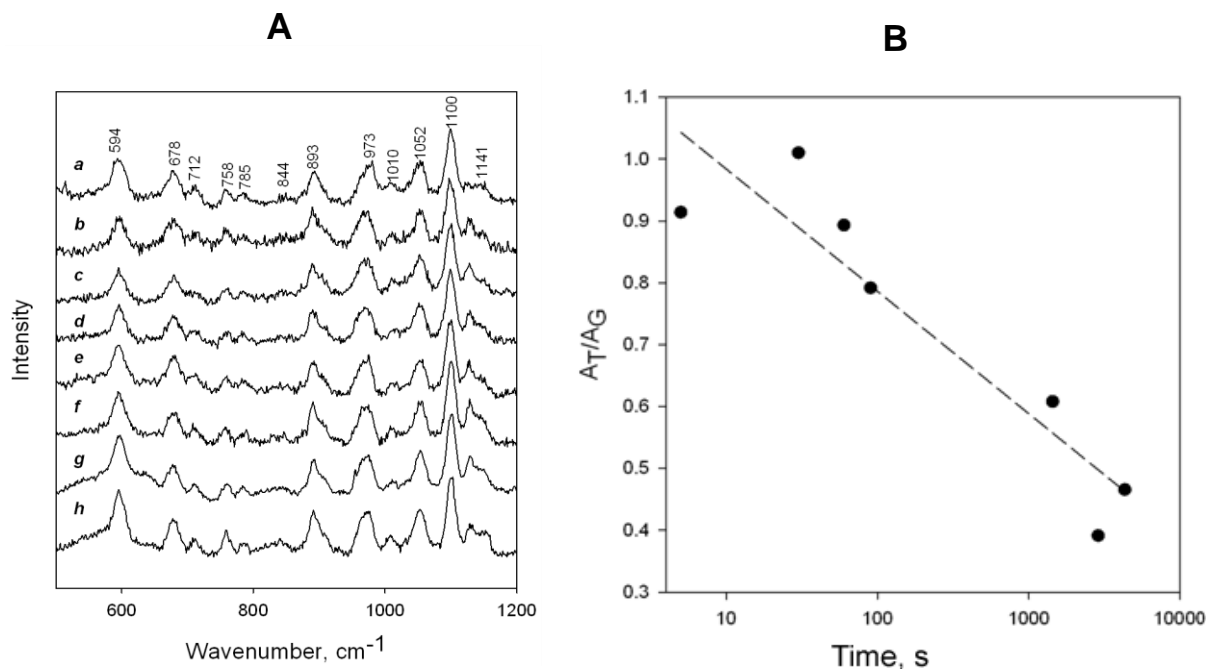


Fig. 3. (A) SERS spectra of tether layer self-assembled on Au surface from ethanolic solution containing βMED (70%) and WC14 (30%) of (a) dry electrode, and incubated in water for (b) 5 min, (c) 30 min, (d) 60 min, (e) 120 min, (f) 24 h, (g) 48 h, and (h) 72 h. Spectra are normalized according to the intensity of 1100 cm^{-1} band $\delta(\text{C1D}_2)$. Excitation wavelength is 785 nm. (B) Dependence of the ratio of integrated intensities of $\nu(\text{C-S})_{\text{T}}$ (A_{T}) and $\nu(\text{C-S})_{\text{G}}$ (A_{G}) bands of adsorbed βMED on the incubation time in water.

To evaluate quantitatively water-induced effect on the relative population of *trans* and *gauche* conformers for adsorbed βMED , we have fitted the experimental spectra with Gaussian-Lorentzian form components and calculated the areas of corresponding C-S modes in SERS spectra (A_{T} and A_{G}). Near linear decrease in $A_{\text{T}}/A_{\text{G}}$ ratio with increasing of incubation time was observed (Fig. 3B). Thus, incubation in water enlarges the population of *gauche* conformers of adsorbed βMED . The reasons might be associated with increase in interaction of hydroxyl group of βMED with metal surface and/or clustering of adsorbed WC14. Because *gauche* conformers require more surface space, clustering of WC14 might stimulate such isomerization process.

Figure 4 compares SERS spectra of tether monolayer prepared from ethanolic solution containing βMED (30%) and WC14 (70%) observed after incubation of different time in water. Because adsorption solution contained higher concentration of WC14 compound, increase in the relative intensity of WC14 bands is clearly visible in the SERS spectra. The $\nu(\text{C-C})_{\text{T}}$ band of WC14 alkyl chains in all-*trans* conformation near $1128\text{--}1130\text{ cm}^{-1}$ becomes clearly visible and after incubation in water for 72 h comparable with the intense band from βMED near $1098\text{--}1100\text{ cm}^{-1}$ (Fig. 4h). In addition, the relative intensity of band near 892 cm^{-1} associated with rocking vibration of CH_2 groups increases. It should be noted that the low intensity feature near $1012\text{--}1010\text{ cm}^{-1}$ is associated with vibrational mode of WC14 compound. This assignment was confirmed by spectroscopic analysis of pure WC14 (100%) monolayer. Such band might be associated with symmetric stretching vibration of C-O-C fragment.

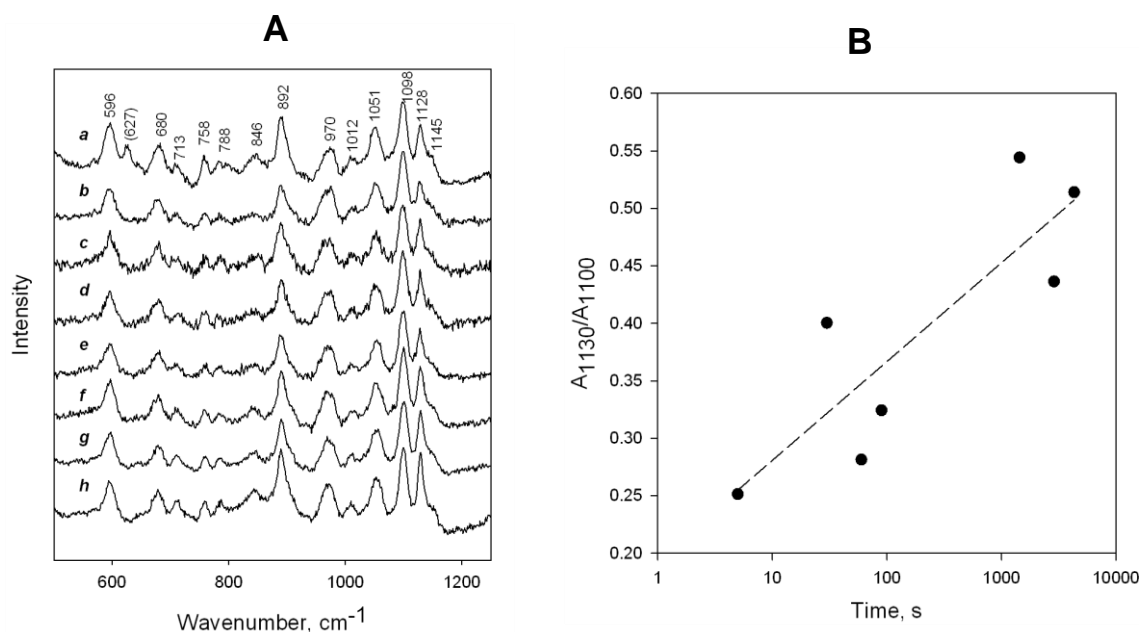


Fig. 4. (A) SERS spectra of tether layer self-assembled on Au surface from ethanolic solution containing β MED (30%) and WC14 (70%) of (a) dry electrode, and incubated in water for (b) 5 min, (c) 30 min, (d) 60 min, (e) 120 min, (f) 24 h, (g) 48 h, and (h) 72 h. Spectra are normalized according to the intensity of 1098 cm^{-1} band $\delta(\text{C1D}_2)$. Excitation wavelength is 785 nm. (B) Dependence of the ratio of integrated intensities of $\nu(\text{C-C})_{\text{T}}$ (A_{1130}) of WC14 and $\delta(\text{C1D}_2)$ (A_{1100}) of β MED on the incubation time in water.

Quantitative analysis of the relative integrated intensity of 1130 cm^{-1} band due to $\nu(\text{C-C})_{\text{T}}$ stretching vibration of alkyl chains of WC14 revealed near linear increase tendency with increasing incubation time in water (Fig. 4B). Such observation suggests water-induced formation of clusters of adsorbed WC14 molecules leading to stabilization of all-*trans* conformation of alkyl chains. This interpretation is in harmony with observed increase in population of *gauche* conformers of β MED after incubation of the sample in water.

In conclusion we have employed SERS technique to probe the water induced structural changes in the tether monolayer self-assembled from WC14 and β -mercaptoethanol. Deuterated β -mercaptoethanol (β MED) was used to discriminate vibrational modes of adsorbed compounds. Water-induced increase in population of adsorbed *gauche* conformers of β MED as well as increase in number of *trans* conformers in WC14 alkyl chains was detected suggesting formation of clusters of WC14 at interface.

Acknowledgment

This work was funded by the European Social Fund under National Integrated Programme Biotechnology & Biopharmacy, grant VP1-3.1-SMM-08-K01-005 (BIOTEFA).

References

1. R.L.C. Naumann, C. Nowak, W. Knoll, *Soft Matter*, 7 (2011) 9535–9548.
2. D. J. McGillivray, G. Valincius, D.J. Vanderah, W. Febo-Ayala, J. Woodward, F. Heinrich, J.J. Kasianowicz, M. Lösche, *Biointerfaces*, 2 (2007) 21–33.
3. M.A. Bryant, J.E. Pemberton, *J. Am. Chem. Soc.*, 113 (1991) 3629–3637.
4. M.A. Bryant, J.E. Pemberton, *J. Am. Chem. Soc.*, 113 (1991) 8284–8293.
5. I. Matulaitienė, Z. Kuodis, O. Eicher-Lorka, G. Niaura, *J. Electroanal. Chem.*, 700 (2013) 77–85.

FORMATION OF HYBRID BILAYER ON SILANIZED Ti/TiO₂ ELECTRODE**T. Vanagaitė¹, A. Valiūnienė¹, Ž. Margarian¹, L. Mikoliūnaitė¹, G. Valinčius²**¹*Department of Physical Chemistry, Faculty of Chemistry, Vilnius University, Naugarduko 24, Vilnius LT-03225, Lithuania*²*Department of Bioelectrochemistry and Biospectroscopy, Institute of Biochemistry, Vilnius University, Mokslininku 12, LT-08662, Lithuania***Abstract**

Phospholipid bilayer membranes are vital constructs of living organisms as they form boundaries between the intracellular cytoplasm and the extracellular environment, as well as organelles, in cells. In this work we report on our attempts to assemble artificial phospholipid bilayer model membranes on Ti/TiO₂ surface. To provide hydrophobic cushion for phospholipids the surface of Ti/TiO₂ was initially functionalized with trichloro(octadecyl)silane (OTS). Increased hydrophobicity of the solid support allowed vesicle fusion and the formation of a hybrid 1,2-dioleoyl-sn-glycero-3-phosphocholine (DOPC) bilayer, as probed by the electrochemical impedance spectroscopy (EIS). Vesicles on a Ti/TiO₂ electrode prepared by magnetron sputtering was manufactured and investigated. Contact angle (CA), atomic force microscopy (AFM) and the EIS were used to detect and follow all stages of formation the hybrid bilayer.

Introduction

The lipid bilayer structures such as membranes are flat sheets that form a continuous barrier around all cells. Accordingly, cell membranes are vital constructs in cell biology because these membranes separate the interior of all cells from the outside environment. The processes in cells, i.e. transport through cell membranes, molecular recognition, membrane permeation, signalling, etc. are very complicated and hard to explain. The development of models for biological membranes is required to explain the mechanical properties of membranes and such processes as adsorption of proteins and ion transport through membranes; also to discuss biosensors, biocatalysts, medicine, etc. It is important to note that the membrane model should be formed on a solid surface of biocompatibility characteristics - biological inertness (should not denature proteins) and chemical inertness to body fluids. Titanium and its alloys have been used extensively in biomedical devices and components, because of its chemical stability, mechanical resistance, absence of toxicity and what is the most important – biocompatibility. Titanium has these characteristics because of oxide layer on its surface in which TiO₂ is the most stable oxide film [1-3]. In this work hydrophobic monolayer using OTS was formed on Ti/TiO₂ electrode, and hybrid bilayer of phospholipids using DOPC vesicles was manufactured. The main purpose of present study was to manufacture OTS monolayer and DOPC bilayer, also to investigate obtained hybrid bilayer by using the methods of contact angle (CA), atomic force microscopy (AFM) and electrochemical impedance spectroscopy (EIS).

Experimental

For all substrates silicon (100) wafers were initially coated with titanium by magnetron sputtering PVD75 (Kurt J. Lesker Company, USA) vacuum deposition system. The formation of the OTS self-assembled monolayer was carried out using 5% OTS/n-heptane (puriss, p.a.)

solution. The Ti/TiO₂ slides were immersed into the solution for 60 min at 50° – 60°C temperature. The substrates were then removed from the OTS solution and dried under a stream of N₂. Vesicles were prepared by solubilizing phospholipid in the working buffer at the total lipid concentration of 2 mM.

CV and EIS measurements were performed using μ Autolab type III system with an ordinary three-electrode cell. Contact angles of the investigated surfaces were measured by using Theta Lite optical tensiometer dropping a 10 μ L drop of water. Veeco (USA) measuring system “Catalyst” was used to analyse the surface of investigated electrodes. AFM images were collected and viewed using atomic force microscope software “Gwyddion 2.10”.

Results and discussion

Ti/TiO₂ electrode prepared by magnetron sputtering was investigated by measuring the contact angle of electrode before and after silanization with OTS. The values of CA observed before silanization were $49.9^{\circ} \pm 8.5^{\circ}$. After the silanization, they increased to $99.1^{\circ} \pm 5.4^{\circ}$. Fusion of the DOPC vesicles on OTS monolayer sharply decreased CA values to 30° indicating the formation of the hybrid bilayer structure with the hydrophilic phosphocholine groups in DOPC facing the exterior.

The EIS data (Fig. 1) shows that the complex capacitance of bare Ti/TiO₂ interface is $6.61 \pm 1.1 \mu\text{Fcm}^{-2}$. It sharply decreases to $0.89 \pm 0.2 \mu\text{Fcm}^{-2}$ after the electrode was silanized. Fusion of the DOPC vesicles triggers further decrease of the capacitance to $0.53 \pm 0.1 \mu\text{Fcm}^{-2}$. This result reflects that formation of the phospholipid layer on OTS monolayer occurs.

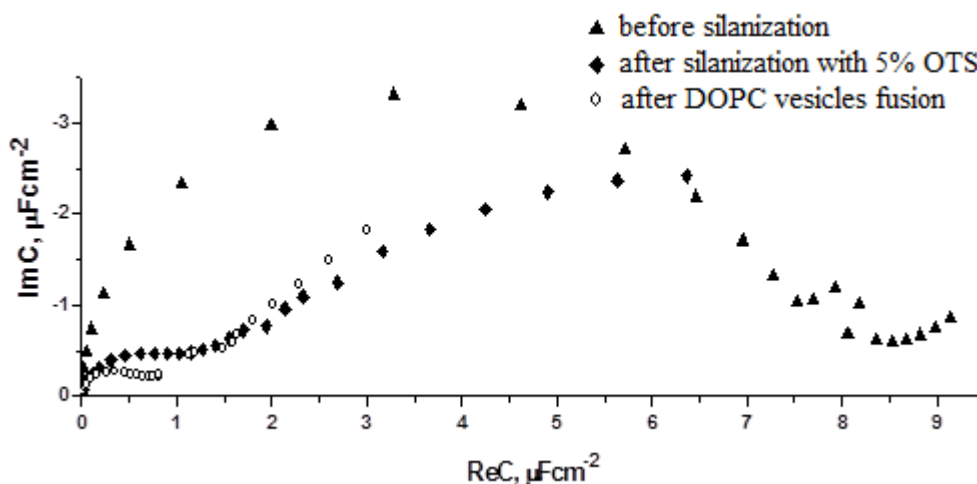


Fig. 1. Electrochemical impedance spectra of Ti/TiO₂ electrode when bilayer of DOPC was formed.

AFM data (Fig.2) indicates that the surface of silanized Ti/TiO₂ electrode is covered by spherical particles with a mean diameter of about 40-50 nm and height of about 3 nm. AFM images of the silanized electrode surface after DOPC vesicle fusion (Fig.2c) show the presence about 1 μ m diameter features, which interacted differently with the AFM cantilever probe, compared to the phospholipid-free surface.

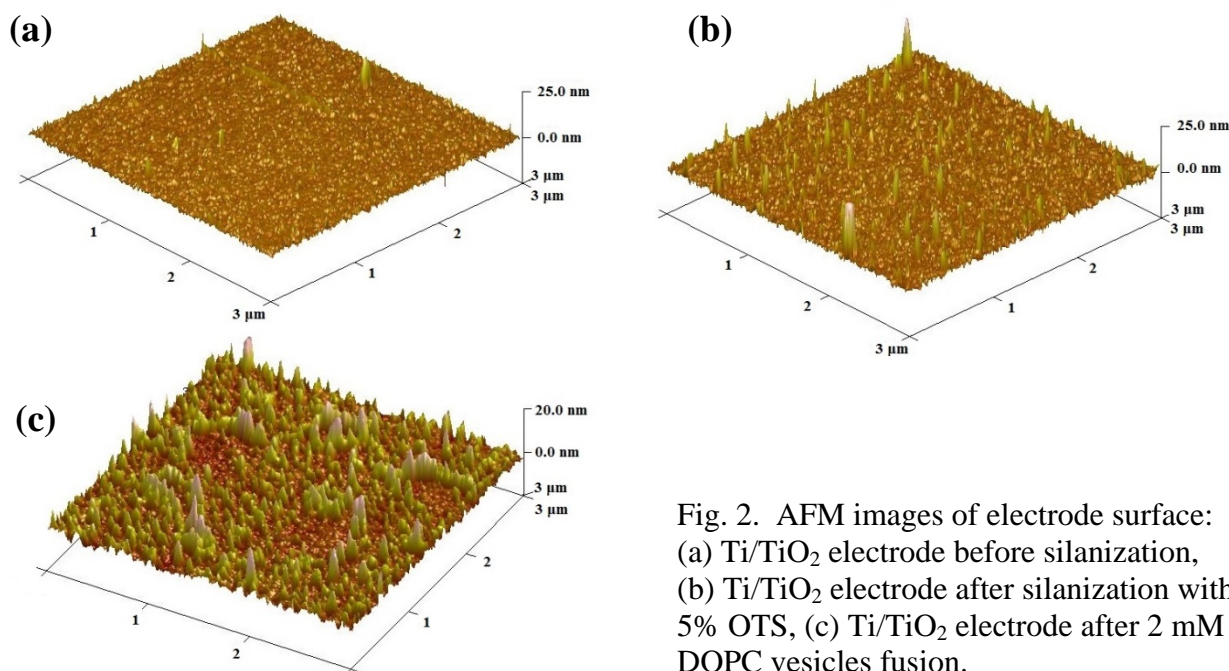


Fig. 2. AFM images of electrode surface: (a) Ti/TiO₂ electrode before silanization, (b) Ti/TiO₂ electrode after silanization with 5% OTS, (c) Ti/TiO₂ electrode after 2 mM DOPC vesicles fusion.

Conclusions

By using the method of EIS it was determined that complex capacitance decreased from 6.61 ± 1.1 to $0.89 \pm 0.2 \mu\text{Fcm}^{-2}$ after the Ti/TiO₂ electrode was silanized with 5% OTS. These results in parallel with the CA data demonstrate that the compact hydrophobic layer is formed on the electrode surface. After applying 2 mM DOPC vesicle solution to the OTS monolayer complex capacitance decreased to $0.53 \pm 0.1 \mu\text{Fcm}^{-2}$ indicating the formation of the additional phospholipid layer on OTS, which presumably occurs through the vesicle fusion. The EIS results correlate with results obtained in AFM experiments, which showed that the surface of silanized Ti/TiO₂ electrode is covered by spherical particles with a diameter of about 40-50 nm and height of about 3 nm. The derivatives about 1 μm in diameter were obtained on the silanized electrode after the bilayer of DOPC was formed. Summarizing obtained data it can be concluded that hybrid phospholipid bilayer can be formed on metal oxide electrodes, using hydrophobic OTS monolayer to incorporate phospholipid membrane.

Acknowledgement

This work was supported by the European Structural Funds, project No.VP1-3.1-ŠMM-10-V-02-024 (MiniFOB). T.Vanagaitė acknowledges access to the magnetron sputtering equipment at the Biocatalysis Open Access Center (Institute of Biochemistry, Vilnius University).

REFERENCES

1. Xuanyong Liu, Paul K. Chu, Chuanxian Ding. *Materials Science and Engineering R* 47 (2004) 49-121.
2. Madhav Prasad Neupane, Il Song Park, Sook Jeong Lee, Kyoung A Kim, Min Ho Lee, Tae Sung Bae. *Int. J. Electrochem. Sci.*, 4 (2009) 197-207.
3. Fan Zhang, F. J. Xu, E. T. Kang, and K. G. Neoh. *Ind. Eng. Chem. Res.* 2006, 45, 3067 – 3073.



Chemistry and Chemical Technology 2015

Vilnius University, Faculty of Chemistry,
Naugarduko 24, Vilnius, Lithuania
January 23, 2015

Poster presentations

Chemistry and Technology of Inorganic Materials



MODIFICATION OF BACTERIAL CELLULOSE BY COPPER SULFIDE LAYERS

R. Alaburdaitė¹, P. Bekampienė², J. Domskienė², E. Paluckienė¹, K. Kantminienė¹*1 KTU, Radvilenu pl. 19, Kaunas, LT-50270, Lithuania**2 Textile Institute, Demokrato g. 53, Kaunas, LT-48485, Lithuania**E-mail: rasa.alaburdaite@ktu.lt*

Modified polymers can be used instead of metal conductors; some of which sometimes are susceptible to corrosion. Polymers with thin layers of *d*-metal sulfides are used for galvanic metallization, and as radio wave absorbers, and polaroids of the infrared spectrum. They are also used as active sorbents for selective gas sensors operating at room temperature or approximate to it; as well as in the production of solar cells [1-4]. Copper sulfides distinguish themselves by the variety of stoichiometry and valuable physical properties. One of the most important physical properties of Cu_xS that determines the wide usage of these compounds is electrical conductivity. Depending on the stoichiometric composition, the copper sulfides can be used as insulators, semiconductors, electrical conductors, and some of them as superconductors [5].

In recent years, sorption-diffusion method for modification of various polymers by semiconductive and electrically conductive layers of Cu_xS has been studied [6-7]. To the best of our knowledge, there is no data about formation of copper sulfide layers on bacterial cellulose (BC) in the scientific literature.

BC is preferred over the plant cellulose as it can be obtained in higher purity and exhibits a higher degree of polymerization and crystallinity index. Cellulose and cellulose derivatives have drawn growing attention as abundant and renewable eco-friendly materials. Cellulose-based composites are promising for use as components of flexible polymer displays [8, 9]; biocompatible and biodegradable flexible OLEDs etc. [10, 11].

The aim of this work was to determine a method for the formation of the electrically conductive layers of copper sulfides on the surface of bacterial cellulose film.

Keywords: bacterial cellulose; copper sulfide; XRD.

Experimental

For evaluation of the interactions between BC and Cu_xS microscope investigation and XRD analysis were performed.

Distilled water, chemically and analytically pure reagents were used to prepare solutions.

BC preparation. The BC was produced using Kombucha strains primary referred to the gram-negative bacteria species *Gluconacetobacter xylinus* (formerly *Acetobacter xylinum*). Black tea (2 g) was added to 1 L of water and the mixture was allowed to boil for 5 min. The obtained tea solution was cooled to room temperature and tea leaves were removed by filtration. Afterwards, 10 g of sucrose and 100 mL of 6% yeast extract were added. The prepared solution was incubated with Kombucha strain and fermentation was carried out at standard room conditions ($26 \pm 1^\circ\text{C}$ temperature and $65 \pm 5\%$ relative air humidity) for 7 days in static cultivation conditions. The received membrane was washed with water, dried on horizontal surface and subjected to analysis.

The microscope investigation was performed with an *Olympus CX 31* microscope (Philippines).

The XRD analysis was performed on the D8 Advance diffractometer (Bruker AXS, Germany) operating at the tube voltage of 40 kV and tube current of 40 mA. The X-ray beam was filtered with Ni 0.02 mm filter to select the $\text{CuK}\alpha$ wavelength. Diffraction patterns were recorded in a Bragg-Brentano geometry using a fast counting detector Bruker LynxEye based on silicon strip technology. The specimens were scanned over the range of $2\theta = 3\text{--}70^\circ$ at a scanning speed of 6° min^{-1} using a coupled two theta/theta scan type.

Solutions pH was measured using a pH-meter WTW330, with combinative glass and Ag/AgCl electrode and temperature meter WTW SenTix 41 (Germany).

Results

Cu_xS layers on native BC were formed using several different solutions using sorption-diffusion or bath deposition methods. At first, sorption-diffusion method [6] was applied. A BC film was saturated by sulfur in 0.4 mol/l thiourea solution with 0.01 mol/l hydroquinone of different pH values: 0 and 9. Sulfurization process was carried out from 20 to 70°C using a different treatment time from 60 min to 24 h. Sulfurized BC was rinsed with distilled water and was treated with an aqueous 0.4 mol/l CuSO_4 with 0.1 mol/l hydroquinone at 80°C for 10-90 min. BC samples were rinsed and dried at room temperature. It should be noted, that in acidic medium the sulfurized samples with Cu_xS became hard, with a lot of white spots, and the ones prepared in the base solution were fragile. Color of the samples varied from light brown to black. Unfortunately, a uniform sulfide layer did not form, and, thus, no surface testing was possible.

In the absence of the desired result of one cycle, the number of cycles was increased from 1 to 5. However, no positive result was obtained, and the conclusion was drawn that the sorption-diffusion method failed.

In the further experiments, the formation of Cu_xS layers on BC was attempted using chemical bath deposition [7] method at 20 and 70°C using solution with different pH values (2.6 and 10.9). After treatment, BC samples were rinsed with distilled water and dried at room temperature.

Samples modified in 0.13 mol/l $\text{Na}_2\text{S}_2\text{O}_3$ and 0.13 mol/l CuSO_4 solutions with $\text{NH}_3 \cdot \text{H}_2\text{O}$ additive were gray-green, but uneven. On the samples treated in the solution with EDTA additive (pH 2.6), black layers formed and visually they seemed continuous.

When concentration of the solutions was increased to 0.2 mol/l, the obtained copper sulfide layers were intact and the samples were gray (pH 10.9) (Fig. 1b) and black (pH 2.6) (Fig. 1c).

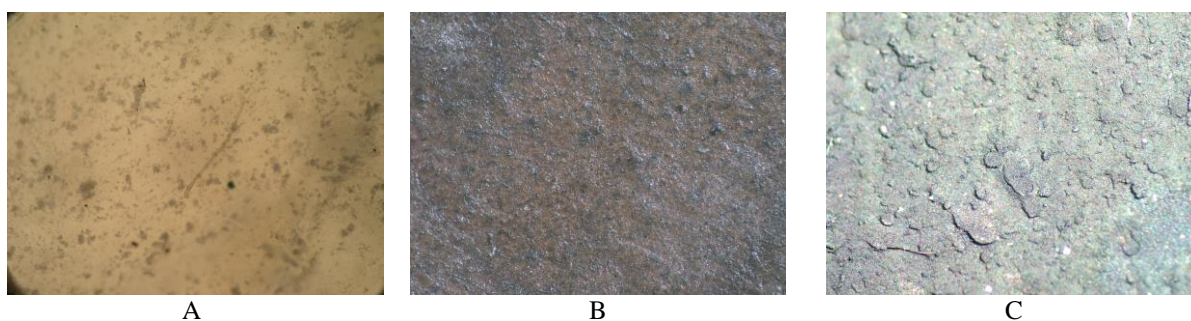


Fig. 1. BC films ($\times 400$ times): **A** – native BC film; **B** – BC film modified with Cu_xS layers in alkaline solution (pH 10.9); **C** – BC film modified with Cu_xS layers in acidic solution (pH 2.6)

X-ray diffraction analysis showed a crystalline structure of the virgin BC film [12]. Three peaks were observed at $2\theta = 14.42^\circ$ ($d = 0.609 \text{ nm}$), 16.8° ($d = 0.526 \text{ nm}$), and 22.66° ($d = 0.391 \text{ nm}$).

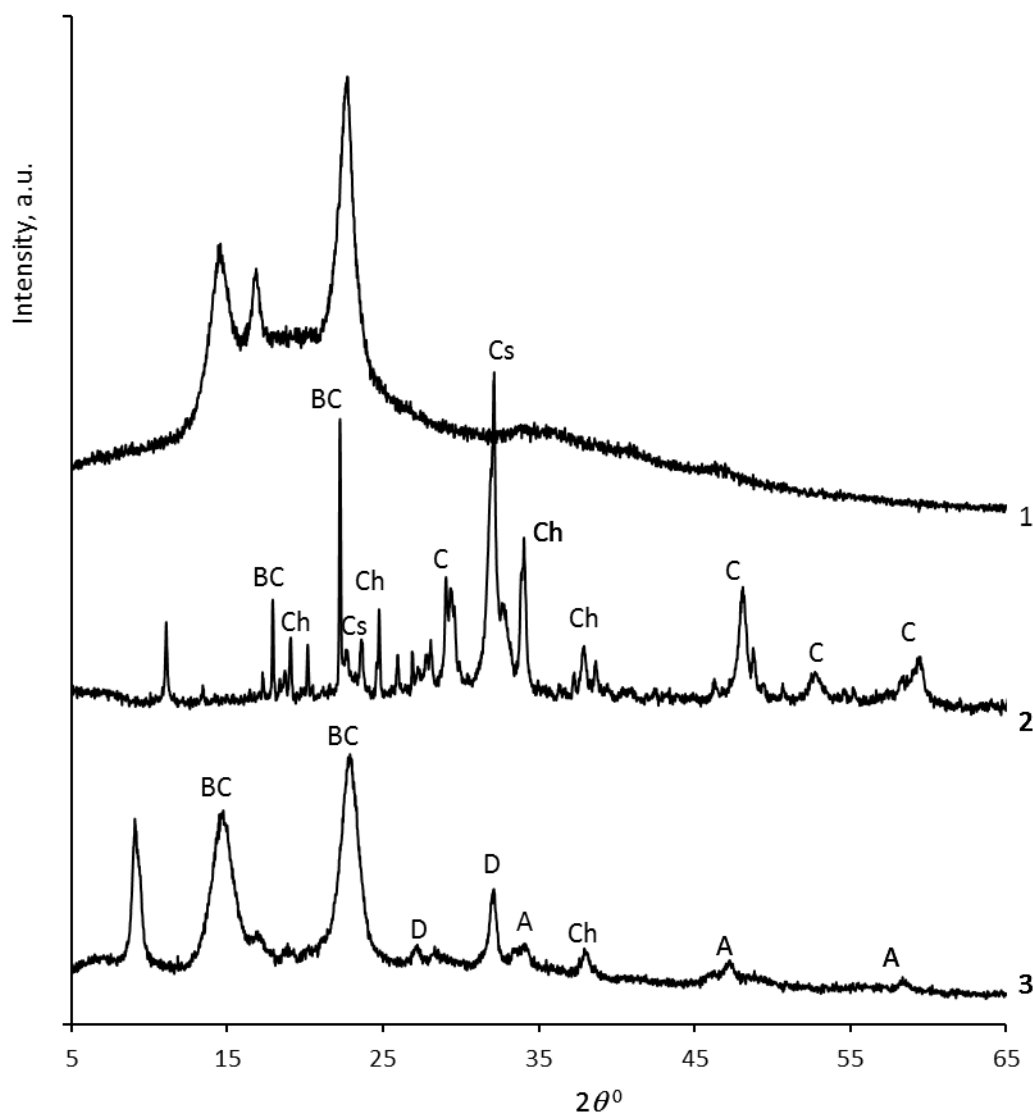


Fig. 2. X-ray diffraction patterns of the native BC (1), BC film with Cu_xS layers formed in acidic solution (pH 10.9) (2), and the ones obtained in alkaline solution (pH 2.6) (3) at 70 C. C – covellite, Ch – chalcocite, Cs – copper sulfide, D – djurleite, A – anilite

The X-ray diffraction analysis of the modified BC films prepared using 0.2 M of copper sulphate, sodium thiosulfate and EDTA acidic solution showed the following copper sulfide phases: chalcocite, Cu_2S [2-1272] ($d = 0.306, 0.272, 0.263,$ and 0.233 nm) and [12-227], ($d = 0.466, 0.439, 0.360, 0.319, 0.238,$ and 0.186 nm), copper sulfide, $\text{Cu}_{1.96}\text{S}$ [12-205] ($d = 0.390, 0.376, 0.303, 0.279, 0.196,$ and 0.168 nm), and covellite, CuS [78-877] ($d = 0.326, 0.189, 0.158,$ and 0.140 nm), [6-464] ($d = 0.173$ nm) and [78-2122] ($d = 0.155$ nm). Other expressed peaks seen at $2\theta 22,24^\circ$ ($d = 0.399$ nm) and $17,9^\circ$ ($d = 0.495$ nm) belong to BC.

The spectra of BC modified in alkaline solution with NH_3 showed copper sulfide phases as follows: djurleite, $\text{Cu}_{31}\text{S}_{16}$ [42-564] ($d = 0.604, 0.328,$ and 0.315 nm), anilite, Cu_7S_4 [72-617] ($d = 0.192, 0.158$ nm), [33-489] ($d = 0.262$ nm), and chalcocite, Cu_2S [12-227] ($d = 0.262,$ nm). The peaks seen at $2\theta 22,82^\circ$ ($d = 0.389$ nm) and $14,66^\circ$ ($d = 0.603$ nm) belong to BC.

Conclusions

X-ray diffraction analysis of the modified BC films in acidic solution has shown that the copper sulfide phases – chalcocite, copper sulfide, and covellite, CuS – form and the ones formed on BC films in alkaline solution are djurleite, anilite, and chalcocite.

References

1. V. Popescu, H. I. Nascu, *J. Optoelectron. Adv. Mat.*, 2006, 8, 1874.
2. A. Galdikas, A. Mironas, V. Strazdiene, A. Šetkus, I. Ancutiene, V. Janickis, *Sens Actuators B*, 2000, 67, 76.
3. A.A. Sagade, R. Sharma, *Sens. Actuators B*, 2008, 133, 135.
4. G. Alvarez, J.J. Flores, J.O. Aguilar, O. Gómez-Daza, C.A. Estrada, M.T.S. Nair, P.K. Nair, *Sol Energy*, 2005, 78, 113.
5. Y.T. Nien, I.G. Chen, *J Alloys and Compounds*, 2009, 471, 553.
6. R. Alaburdaitė, S. Grevys, E. Paluckienė, *Mat Sci*, 2011, 17, 399.
7. V. Krylova, M. Andrulevičius, *Int J Photoenergy*, 2009, <http://dx.doi.org/10.1155/2009/304308>.
8. I. Shah, R.M. Brown Jr., *Appl Microbiol Biotechnol*, 2005, 66, 352.
9. C. Legnani, C. Vilani, V.L. Calil, H. Barud, W.G. Quirino, C.A. Achete, S.J.L. Ribeiro, M. Cremona, *Thin Solid Films*, 2008, 517, 1016.
10. A.N. Aleshin, A.S. Berestennikov, P.S. Krylov, I.P. Shcherbakov, V.N. Petrov, I.N. Trapeznikova, R.I. Mamalimov, A.K. Khripunov, A.A. Tkachenko, *Synthetic Metals*, 2015, 199, 147.
11. Z. Shi, S. Zang, F. Jiang, L. Huang, D. Lu, Y. Ma, G. Yang, *RSC Adv*, 2012, 2, 1040.
12. K.C. Cheng, J.M. Catchmark, A. Demirci, *J Biol Eng.*, 2009, 3: 12. doi: 10.1186/1754-1611-3-12.

MORPHOLOGY AND STRUCTURE EVALUATION OF SnO₂ NANOSTRUCTURES PREPARED BY SOLUTION-BASED METHOD

L. Alinauskas, R. Raudonis, E. Garskaite

Department of Applied Chemistry, Faculty of Chemistry, Vilnius University, Naugarduko 24, Vilnius LT-03225, Lithuania

E-mail: laurynas.alinauskas@chf.vu.lt

Tin (IV) oxide (SnO₂) is a n-type semiconductor used as a solid-state gas sensor material [1]. It is known that response to gas strongly depend on SnO₂ morphology, microstructure and particle size. A possibility to produce these materials as nanorods and nanotubes can increase their surface area as well as surface to volume ratio and subsequently alter gas sensing properties.

In this work we report the synthesis of nanocrystalline SnO₂ 1D structures prepared by solution-based and hard templating method [2]. Morphology, crystallinity and crystal structure of prepared SnO₂ nanostructures were evaluated using scanning electron microscopy (SEM), transmission electron microscopy (TEM) and X-ray diffraction (XRD) techniques. Results show that SnO₂ 1D structures annealed at 650 °C were homogeneous and single phase with particle sizes around 10-15 nm (Fig. 1).

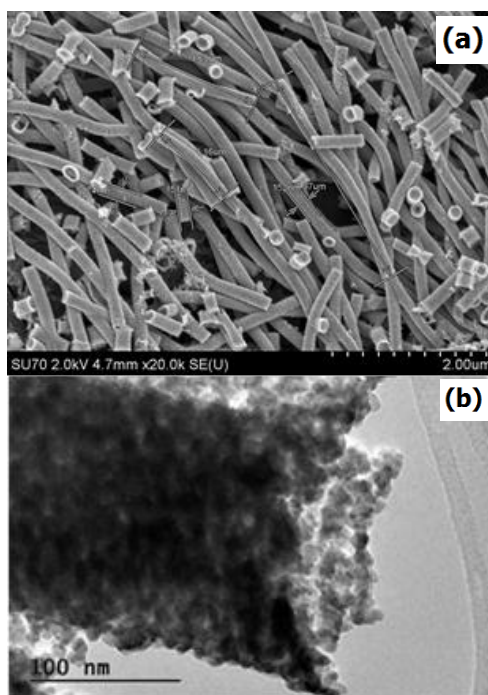


Fig. 1. FE-SEM (a) and HR-TEM (b) micrographs of SnO₂ nanostructures annealed at 650 °C for 5 h.

Acknowledgement

This work was partly supported by COST MP1202 “Rational design of hybrid organic-inorganic interfaces: the next step towards advanced functional materials” project. ICL is acknowledged for HR-TEM analysis.

References

1. M. Batzill and U. Diebold. *Prog. Surf. Sci.*, 79 (2-4) (2005) 47-154.
2. U. Lafont, et al., *J. Nanosci. Nanotech.*, 10 (7) (2010) 4273-4278.

XRD STUDIES OF COPPER SULFIDE LAYERS ON GLASS**A. Bakutytė, R. Ivanauskas, A. Ivanauskas, I. Ancutiėnė***Department of Physical and Inorganic Chemistry, Kaunas University of Technology**Radvilėnu str. 19, LT-50254 Kaunas, Lithuania**E-mail: ingrida.ancutiene@ktu.lt*

Metal sulfide films possess useful electrical and optical properties and can be found in many technical applications. Copper sulfide thin films are one of the potentially useful metal chalcogenides with significant variation in properties depending on the stoichiometry (Cu_xS , $1 \leq x \leq 2$). Copper sulfide is a semiconductor material, that optical and electrical properties varying significantly as a function of its composition. At room temperature, five stable phases of Cu_xS are known to exist in the bulk form: CuS (covellite), $\text{Cu}_{1.75}\text{S}$ (anilite), $\text{Cu}_{1.8}\text{S}$ (digenite), $\text{Cu}_{1.95}\text{S}$ (djurleite), Cu_2S (chalcocite) [1, 2]. The different phases of Cu_xS exhibit considerable variations of properties, therefore they can be used in different potential applications, such as solar control coatings, solar cells, photothermal conversion of solar energy, electroconductive coatings, microwave shielding coatings, etc. [1, 3].

In this study copper sulfide layers on glass have been formed by the use of molten elemental sulfur as the precursor of sulfur. For the characterization of the obtained layers X-ray diffraction (XRD) method was used.

Cu_xS layers were formed on microscopic glass slides of dimension 25 mm \times 25 mm. Slides were thoroughly cleaned with cleaning liquid soap and ultra-sonic cleaning was carried out by dipping the glass slide into acetone at 40 °C for 10 min, then rinsed with distilled water and dried. For the formation of copper sulfide layers the glass slide was dipped in molten sulfur at 150 °C for 10 s and then sulfurized sample was treated with a copper (II/I) salt solution at 40 or 60 °C for 1–20 min. 0.4 M Cu(II/I) salt solution was made from crystalline $\text{CuSO}_4 \times 5\text{H}_2\text{O}$ and a reducing agent, hydroquinone, as described in [4]. The XRD studies on a DRON-6 diffractometer operating with Cu K_α radiation (Ni filter) at 30 kV and 20 mA were performed. X-ray diffractograms of samples were treated using the programs Search Match, ConvX, Xfit and Microsoft Excel.

The phase composition of the formed layer was established by comparing its X-ray diffraction patterns with those of known minerals [5–7]. The chemical composition and crystal structure of the majority of Cu_xS minerals such as chalcocite, djurleite, digenite, anilite, yarrowite, covellite were investigated [8]. The crystal structure of Cu_xS depends on the chemical composition and conditions of synthesis.

On keeping glass samples with sulfur layer for a different period in the copper salt solution at 40 °C, Cu_xS layers of different composition were obtained. The X-ray diffraction patterns of the layers showed that peaks of various copper sulfide phases exist in the layer rather than only of one (Fig. 1). Analysis of the diffraction patterns of samples also showed some peaks of unreacted elemental sulfur S (1-478), S_{10} (77-227) and synthetic sulfur (24-733). When the period of treatment with the Cu(II/I) salt solution was 1 min (curve 1), the phases of djurleite (42-564, 34-660), anilite (72-617, 33-489), covellite (78-880) and digenite (47-1748) are observed. This XRD pattern shows numerous peaks of djurleite $\text{Cu}_{31}\text{S}_{16}$ phase (42-564) at $2\theta=18,65$; 22,26; 22,89; 24,68; 25,66; 31,06; 34,74; 35,75°. The peak of djurleite at $2\theta=22,89^\circ$ predominates in the X-ray diffraction pattern. The peaks of anilite Cu_7S_4 (72-617) at $2\theta=15,96$; 51,90; 52,89° are observed too. When the period of treatment was 5 min (curve 2), the same phases of sulfur and copper sulfides are detected. The XRD pattern shows numerous peaks of synthetic sulfur at $2\theta=28,72$; 37,79; 47,75; 53,92°. The peaks of djurleite and covellite CuS at $2\theta=27,61^\circ$ dominate in this X-ray diffraction pattern.

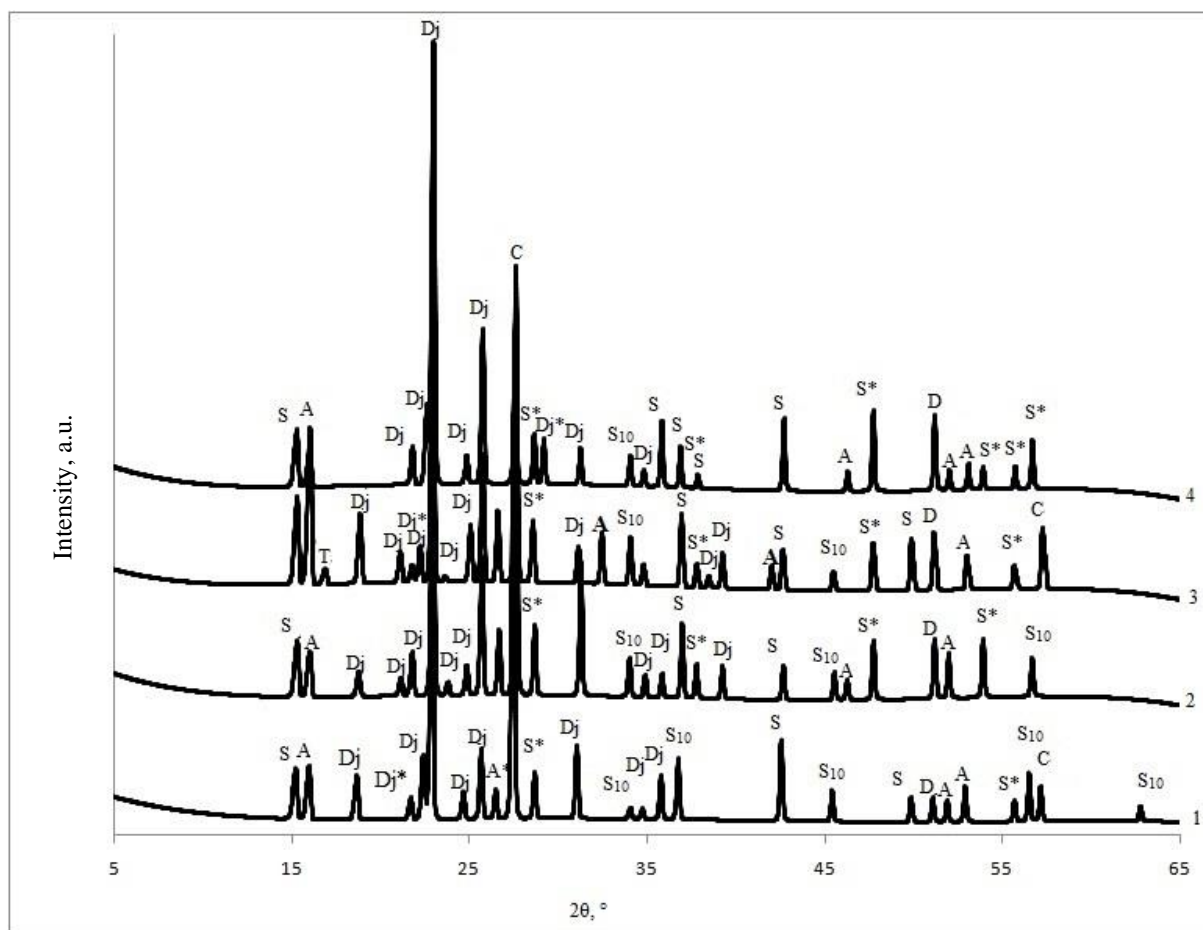


Fig.1. X-ray diffraction patterns of obtained layer (peak of sulfur (1-478)–S, sulfur syn (24-733)–S*, sulfur S₁₀ (77-227)–S₁₀, djurleite Cu₃₁S₁₆ (42-564)–Dj, djurleite syn Cu₃₁S₁₆ (34-660)–Dj*, digenite Cu₉S₅ (47-1748)–D, anilite Cu₇S₄ (72-617)–A, anilite syn Cu₇S₄ (33-489)–A*, talnakhite Cu₃₄S₃₂ (71-2438)–T, covellite CuS (78-880)–C). Treatment time of glass sample with sulfur layer in the Cu(II/I) salt solution at 40°C, min: 1 – 1, 2 – 5, 3 – 10, 4 – 20.

When the treatment time was prolonged until 10 min (curve 3), a negligible peak of talnakhite Cu₃₄S₃₂ (71-2438) at $2\theta=16,88^\circ$ is noticeable. After 20 min of treatment time with copper salt solution (curve 4) the djurleite phase remains as dominating phase in copper sulfide layer. Hence, the phase composition of copper sulphide layer depends on the treatment time of glass sample with sulfur layer in the Cu(II/I) salt solution. The dominated phase in the composition of sulfide layer is djurleite Cu₃₁S₁₆. When the period of keeping in the copper salt solution is prolonged, more copper sulfides form and the intensity of copper sulfide peaks increases.

On keeping glass samples with sulfur layer in the copper salt solution at 60 °C for 1 or 5 min (Fig. 2), some peaks of unreacted elemental sulfur S (1-478), S₁₀ (77-227) and synthetic sulfur (24-733) also are detected. Analysis of the X-ray diffraction patterns showed that djurleite, anilite and covellite prevail in the composition of obtained layer. When the period of treatment was 1 min (curve 1), the numerous peaks of djurleite Cu₃₁S₁₆ (42-564) at $2\theta=18,81; 21,14; 22,97; 23,65; 25,69; 31,21^\circ$ and anilite Cu₇S₄ (72-617) at $2\theta=16,02; 26,59; 32,47; 42,01; 51,16; 52,96^\circ$ phases are observed. Only one peak of talnakhite Cu₃₄S₃₂ (71-2438) at $2\theta=16,92^\circ$ and one peak of covellite CuS (78-880) at $2\theta=27,58^\circ$ in this X-ray diffraction pattern are detected. When the treatment time was prolonged until 5 min (curve 2), the numerous peaks of djurleite Cu₃₁S₁₆ and anilite Cu₇S₄ phases are observed too. The dominated phase in the composition of sulfide layer is djurleite Cu₃₁S₁₆ at $2\theta=22,93^\circ$.

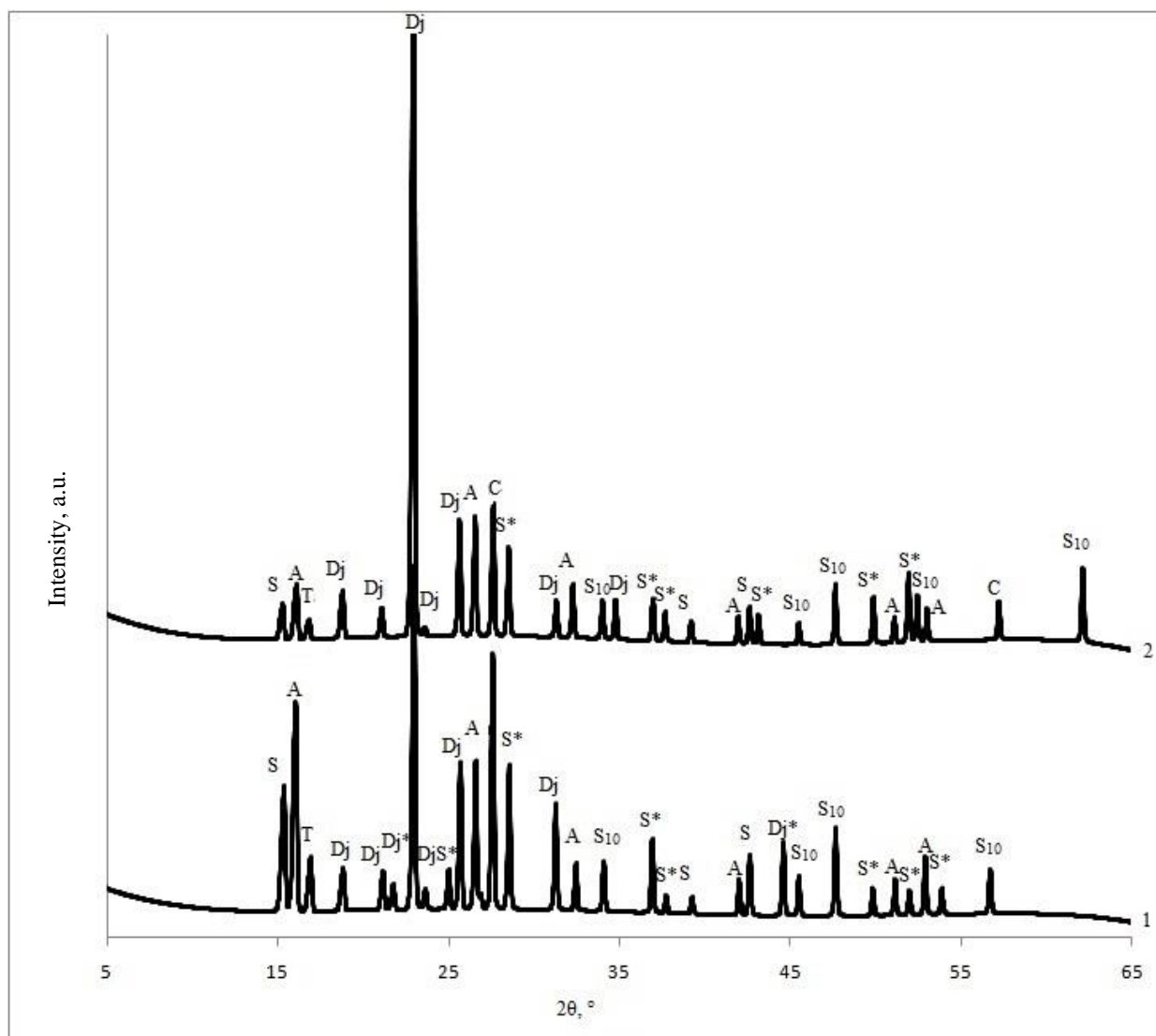


Fig.2. X-ray diffraction patterns of obtained layer (peak of sulfur (1-478)–S, sulfur syn (24-733)–S*, sulfur S₁₀ (77-227)–S₁₀, djurleite Cu₃₁S₁₆ (42-564)–Dj, djurleite syn Cu₃₁S₁₆ (34-660)–Dj*, digenite Cu₉S₅ (47-1748)–D, anilite Cu₇S₄ (72-617)–A, talnakhite Cu₃₄S₃₂ (71-2438)–T, covellite CuS (78-880)–C). Treatment time of glass sample with sulfur layer in the Cu(II/I) salt solution at 60°C, min: 1 – 1, 2 – 5.

In conclusion, by X-ray diffraction studies of obtained layers we detected five copper sulfide phases (djurleite, digenite, anilite, talnakhite and covellite) and three phases of unreacted sulfur. The phase composition of copper sulfide layer on glass depends on the treatment time in the copper(II/I) salt solution. The peak of djurleite Cu₃₁S₁₆ predominates in the X-ray diffraction patterns.

References

1. P. Vas-Umnuay, C. Chang, *ECS Journal of Solid State Science and Technology*, **2013**, 2, P120.
2. K. D. Yuan, J. J. Wu, M. L. Liu, L. L. Zhang, F. F. Xu, L. D. Chen, F. Q. Huang, *Appl. Phys. Lett.*, **2008**, 93, 132106.
3. M. D. Xin, K. W. Li, and H. Wang, *Appl. Surf. Sci.*, **2009**, 256, 1436.
4. I. Ancutiene, V. Janickis, S. Grevys, *Chemistry*, **1997**, 2, 3.
5. A. Žebrauskas, A. Mikalauskiene and V. Latvys, *Chemistry*, **1992**, 3, 131.
6. T. Yamamoto, T. Kamigaki, E. Kubota, *Kobunshi Ranbunsku. Soc. Polym. Sci.*, **1987**, 44, 327.
7. R. Nomura, K. Konyao, H. Matsuda, *Ind. Eng. Chem. Res.*, **1988**, 28, 887.
8. R. Goble, *Canad. Mineral.*, **1985**, 23, 61.

DEPOSITION AND CHARACTERIZATION OF INORGANIC OXIDE BASED FILMS FOR PHOTOCATALYTIC HYDROGEN GENERATION

Y. Barushka¹, R. Vilkauskaite², E. Garskaite¹

¹ *Department of Applied Chemistry, Faculty of Chemistry, Vilnius University, Naugarduko 24, Vilnius LT-03225, Lithuania*

² *Department of Chemistry and Bioengineering, Faculty of Fundamental Sciences, Vilnius Gediminas Technical University, Sauletekio al. 11, Vilnius LT-10223, Lithuania.*

E-mail: yauhen.barushka@chf.vu.lt

Copper (I) oxide (Cu_2O) is a p-type oxide with direct bandgap of 2 eV. In recent years it has been explored as a photocatalyst for solar-driven water splitting and hydrogen generation [1].

In this work we present the deposition of homogeneous Cu_2O films through a low-temperature, solution based process. Indium tin oxide (ITO) and fluoride tin oxide (FTO) coated glass plates were used as substrates. Morphological and structural features of deposited films and crystals were evaluated using scanning electron microscopy (SEM) (Fig. 1) and X-ray diffraction (XRD) analysis. The effects of solution composition and processing conditions on the material morphology are also discussed and presented.

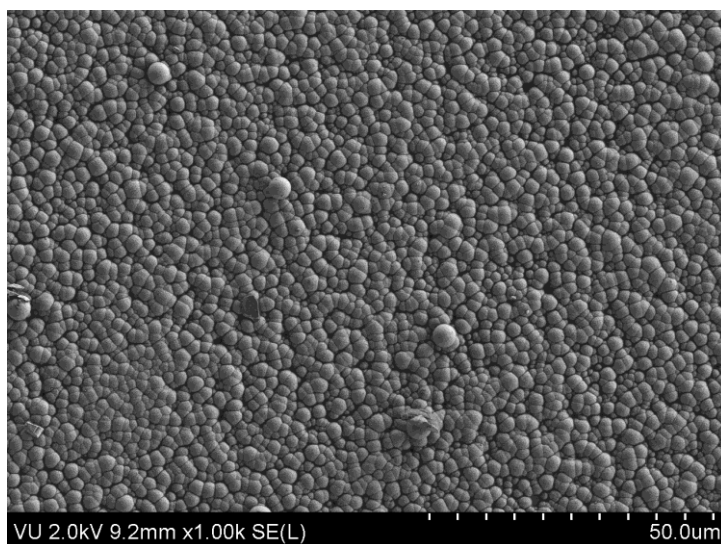


Fig. 1 FE-SEM micrograph of Cu_2O film.

References

1. A. Paracchino, et al., *Nat. Mater.* 10 (6) (2011) 456-461.

CATIONIC SUBSTITUTION EFFECTS IN SOL-GEL DERIVED Ca-PHOSPHATE BIOCERAMIC MATERIALS

Irma Bogdanoviciene ¹, Akvile Ezerskyte-Miseviciene ², Rainer Traksmaa ³, Kaia Tõnsuaadu ¹, Aivaras Kareiva ²

¹ *Laboratory of Inorganic Materials, Tallinn University of Technology, Ehitajate tee 5, 19086 Tallinn, Estonia*

² *Department of Inorganic Chemistry, Vilnius University, Naugarduko 24, LT-03225 Vilnius, Lithuania*

³ *Centre for Materials Research, Tallinn University of Technology, Ehitajate tee 5, 19086 Tallinn, Estonia*

Abstract. Aqueous sol-gel chemistry route based on ammonium–hydrogen phosphate as the phosphorus precursor, calcium acetate monohydrate as source of calcium ions, and EDTA as complexing agent have been used to prepare Zn²⁺, Mg²⁺ or Sr²⁺ substituted calcium orthophosphates ceramic. The phase transformations, composition, and structural changes in the polycrystalline samples were studied by Fourier transform infrared (FTIR) spectroscopy, X-ray powder diffraction analysis (XRD), and scanning electron microscopy (SEM). It was shown that introduced cations in the systems have significant impact on the orthophosphate ceramics formation process and on the morphology and phase composition of the samples.

Introduction

Calcium orthophosphates are of special significance for humans because they represent the inorganic part of bones and teeth tissues. Therefore, due to chemical similarity to biological calcified tissues the majority of artificially prepared calcium orthophosphates possess remarkable biocompatibility and bioactivity. Biphasic, triphasic and multiphasic calcium orthophosphates have been considered as biomaterials for reconstruction of bone defects, dental and orthopedic applications [1]. In recent years, calcium phosphates, especially hydroxyapatite (CHAp) and tricalcium phosphate (TCP), have attracted significant interest in simultaneous use as bone substitute and drug delivery vehicle, adding a new dimension to their application [2]. Most natural bio-apatites, as well as other components of the composite of orthophosphates, are non-stoichiometric because of the presence of minor constituents as cations (Mg²⁺, Zn²⁺, Na⁺, Sr²⁺ etc.). The traces of metal ions introduced into structure of phosphates change their physical, chemical and biological properties [3, 4]. In this study, new Zn²⁺, Mg²⁺ or Sr²⁺ mono-substituted calcium phosphate based bioceramic materials were prepared and investigated. The impact of zinc, magnesium and strontium on the formation of calcium orthophosphate ceramics was determined.

Experimental

For the preparation of zinc, magnesium and strontium substituted calcium phosphate based ceramic materials a sol-gel synthesis route was used. In the sol-gel process, calcium acetate monohydrate, Ca(CH₃COO)₂·H₂O, and ammonium dihydrogen phosphate, NH₄H₂PO₄, were selected as Ca and P sources, respectively. The zinc and magnesium nitrates and strontium acetate were used as sources for Zn, Mg and Sr, respectively. Ethylene diamine tetraacetic acid (EDTA) was used as complexing agent in the sol-gel processing. Four different Ca-M-P-O gel samples, where M = 0.5%, were prepared with the molar ratio of

Ca:M/P = 1.67, and heated up to 900, 1000 and 1100 °C for 24 h in air. The samples are indicated as Ca-PO, Ca:Zn-PO, Ca:Mg-PO, and Ca:Sr-PO. The phase composition and morphology of the samples were examined by FTIR, XRD and SEM analysis methods.

Results and discussion

The XRD patterns of Ca-PO, Ca:Zn-PO, Ca:Mg-PO, and Ca:Sr-PO samples heated at 900, 1000 and 1100 °C are presented in Fig. 1.

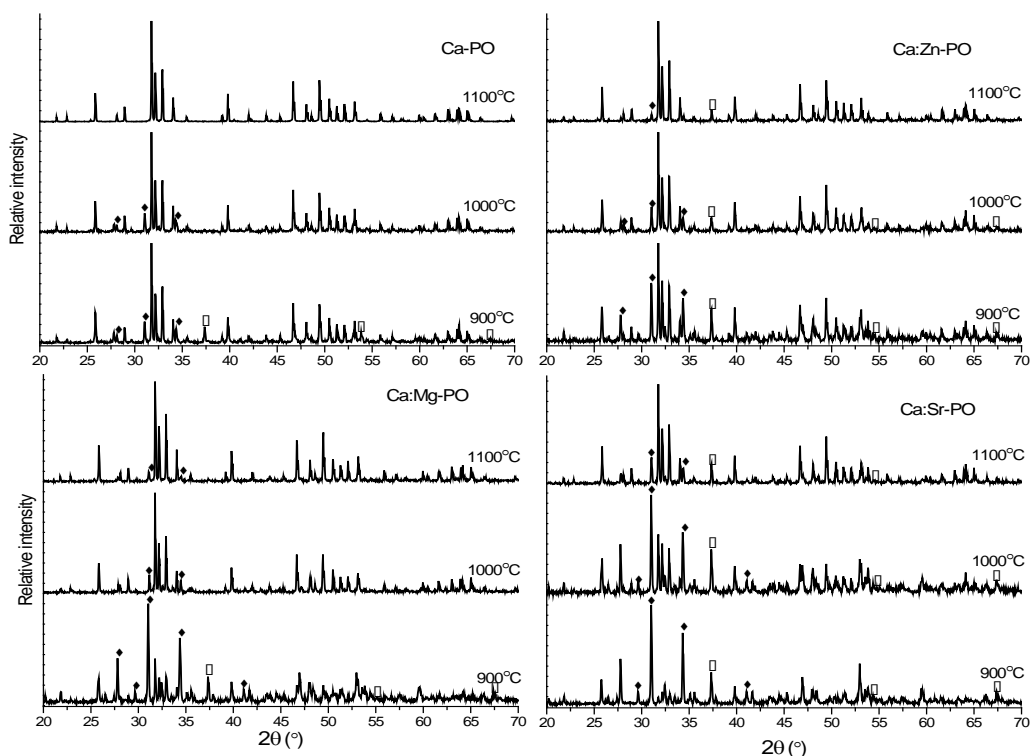


Fig. 1. XRD patterns of the ceramic products obtained after calcination of Ca-PO, Ca:Zn-PO, Ca:Mg-PO and Ca:Sr-PO gels at 900, 1000 and 1100 °C. Impurity phases are marked: ◆ - β - $\text{Ca}_3(\text{PO}_4)_2$ (PDF [70-2065]), ● - CaO (PDF [82-1690])

As seen, the products obtained at 900 °C have slightly different phase composition. The XRD patterns of Ca-PO, Ca:Zn-PO and Ca:Mg-PO samples show the formation of CHAp and TCP as main crystalline phases. However, in the case of Sr-substituted sample almost single-phase β - $\text{Ca}_3(\text{PO}_4)_2$ was obtained. Besides, a small amount of CaO is also formed in all samples. After annealing at 1000 °C, the XRD patterns of all samples show the formation of CHAp as dominant phase and minor amount of TCP. The XRD patterns of Zn- and Sr-substituted samples contained peaks attributable to the CaO phase. After annealing at 1100 °C the single calcium hydroxyapatite phase has formed in Ca-PO sample. In the all substituted samples very small amount of TCP and CaO still remains, Fig. 2 shows the FTIR spectra of Ca-PO, Ca:Zn-PO, Ca:Mg-PO and Ca:Sr-PO gel samples heated at 1100 °C.

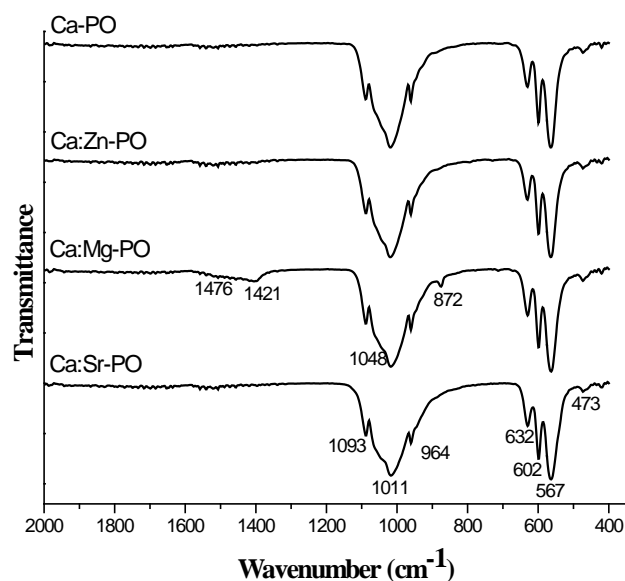


Fig. 2. FTIR spectra of the ceramic products obtained after calcination of Ca-PO, Ca:Zn-PO, Ca:Mg-PO and Ca:Sr-PO gels at 1100 °C.

FTIR spectra of the synthesized samples are very similar. The FTIR spectra of all samples show P–O v4 vibration bands at $\sim 602\text{ cm}^{-1}$ and $\sim 567\text{ cm}^{-1}$, P–O v3 at $\sim 1011\text{ cm}^{-1}$, and have peaks at $\sim 632\text{ cm}^{-1}$ which possibly correspond to the O–H vibration of OH groups in hydroxyapatite. C–O v2 bands at $\sim 872\text{ cm}^{-1}$, and v3 $\sim 1420\text{ cm}^{-1}$ showed the formation of B type carbonated apatite in the Ca:Mg-PO sample [5-7].

SEM pictures of obtained samples are given in Fig. 3.

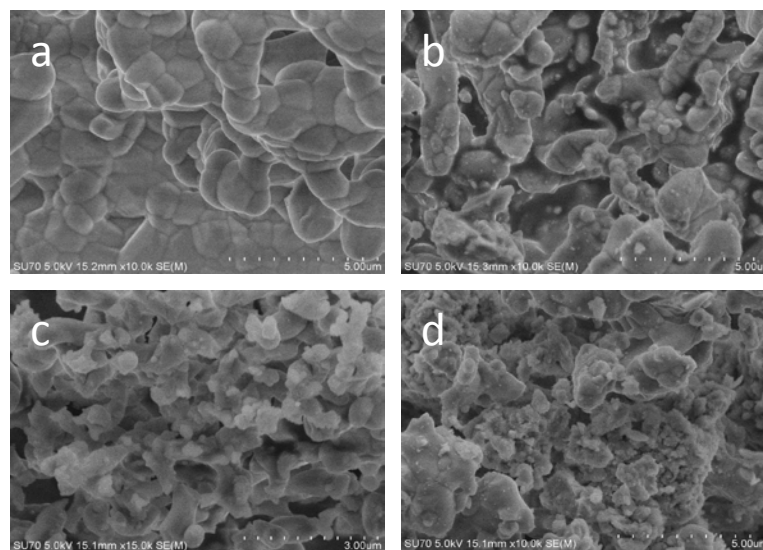


Fig. 3. SEM micrographs of the ceramic products obtained after calcinations of Ca-PO (a), Ca:Zn-PO (b), Ca:Mg-PO (c) and Ca:Sr-PO (d) at 1000 °C.

Products from the Ca-PO gels are composed of agglomerated spherical crystallites from 500 nm to 1 μm in size. The SEM micrograph of Ca:Zn-PO sample shows the formation of similar particles, however, the elongated particles about 3 μm in size have also formed. The Ca:Mg-PO sample is composed of particles having very different size and shape. The elongated particles of 1 μm in length and 300 nm in width as well as small crystallites



about 200-500 nm in size have formed in this case. The Ca:Sr-PO solids are composed of very similar particles ~ 300 nm in size. In conclusion, the nature of substituent has strong effect on the morphology of phosphate bioceramics.

Conclusions

The present study demonstrates that the phase composition and morphology of sol-gel derived Ca-phosphate bioceramic materials is highly dependent on the temperature and nature of substituents (Zn, Mg and Sr).

References

- [1] S.V. Dorozhkin, Biphasic, triphasic and multiphasic calcium orthophosphates. *Acta Biomater.*, 8 (2012) 963–977.
- [2] S. Bose, S. Tarafder, Calcium phosphate ceramic systems in growth factor and drug delivery for bone tissue engineering: A review. *Acta Biomater.*, 8 (2012) 1401–1421.
- [3] J. C. Elliott, “Structure and Chemistry of the Apatites and Other Calcium Orthophosphates”. Elsevier, Amsterdam-London-New York-Tokyo, 1994.
- [4] Le Geros RZ. Calcium Phosphate-Based Osteoinductive Materials. *Chem Rev.* 2008;108:4742–53.
- [5] Berzina-Cimdina L, Borodajenko N. Research of calcium phosphates using Fourier transform infrared spectroscopy. *Infrared spectroscopy–materials science. Materials Science, Engineering and Technology: 2012*
- [6] Chen J, Wang Y, Chen X, Ren L, Lai Ch, He W. Qiqing Zhang. A simple sol-gel technique for synthesis of nanostructured hydroxyapatite, tricalcium phosphate and biphasic powders. *Materials Lett.* 2011;65:1923–6
- [7] Antonakos A, Liarokapis E, Leventouri Th. Micro-Raman and FTIR studies of synthetic and natural apatites. *Biomaterials.* 2007;28:3043–54.



TARTARIC ACID-ASSISTED SOL-GEL SYNTHESIS OF VARIOUS METAL MOLYBDATES

G. Braziulis¹, G. Prievelytė¹, G. Janulevičius¹, A. Žalga¹

*1 Department of Applied Chemistry, Faculty of Chemistry, Vilnius University, Naugarduko 24, LT-03225 Vilnius, Lithuania
E-mail: gedasv2@gmail.com*

Metal molybdates of the general formula $AMoO_4$ ($A = Mg, Ca, Sr, Ba, Cd, Zn, Pb, \text{etc.}$) have been studied extensively for decades, owing to their technological importance in a variety of applications such as phosphors, scintillation materials, microwave devices, catalysts, or optoelectronic devices [1].

Many different preparation techniques are successfully used for the synthesis of different inorganic ceramic materials. Among these different synthesis routes, the solution-based synthetic methods play a crucial role in the design and production of fine ceramics and have been successful in overcoming many of the limitations of the traditional solid-state, high-temperature methods. The use of solution chemistry can eliminate major problems, such as long diffusion paths, impurities, and agglomeration, and result in products with improved homogeneity. In the past few decades, many researchers have carried out the studies on the formation of metal complexes with organic ligands. Furthermore, the metal complexes with organic ligands have been used for the preparation of ceramics and metal oxide thin films by sol-gel process, using metal nitrates, chlorides, and acetates as starting materials. Besides, metal salts are very useful, inexpensive, and very easy to handle in comparison to metal alkoxides, and hence they are good alternatives for the conversion to oxides by thermal decomposition. They can be dissolved in many kinds of organic solvents in which metal complexes are formed. From this point of view, the wet synthesis route called an aqueous sol-gel method, is really attractive and compared to other techniques, as it has the advantages of a good control of the starting materials and of the processing parameters, a high purity of the raw materials, and the low temperature of the process [2].

The preparation and characterization of the $M'-Mo-O$ nitrate-tartrate ($M' = Ca, Sr \text{ and } Ba$) gels, which were produced by the simple tartaric acid-assisted aqueous sol-gel method and calcined at various temperatures are reported. The surface morphology of all samples annealed at 600 and 700 °C by scanning electron microscopy (SEM) was investigated in detail. The homogeneous spherical grains of $SrMoO_4$ with an average diameter of about 500 nm have formed when the synthesis at 700 °C was carried out. In the case of $BaMoO_4$ the agglomeration of close-packed spherical crystals with well-defined edges in size up to 20 μm that are surrounded by irregular crystals of size less than 5 μm was observed. Meanwhile, in the case of $CaMoO_4$ the growing of homogeneous spherical grains with an average diameter of about 200–300 nm was noticed.

References

1. G. Braziulis, G. Janulevičius, R. Stankeviciute, A. Zalga, *J. Therm. Anal. Calorim.*, **2014** 118, 613.
2. A. Zalga, Z. Moravec, J. Pinkas, A. Kareiva, *J. Therm. Anal. Calorim.*, **2011** 105, 3.

RAW MATERIALS INFLUENCE TO BULK FERTILIZERS

O. Brigaitytė¹, R. Šlinkšienė²*1 UAB "BALTKALIS", Jasinskio str. 10, Vilnius, Lithuania**2 Department of Physical and Inorganic Chemistry, KTU, Radvilenu str. 19, Kaunas, Lithuania**E-mail: odeta.brigaityte@gmail.com*

For all plants during growth and development it is very important to get optimal nutrient content, so it is extremely important to choose the well – balanced fertilizers. Frequency of fertilization and appropriate nutrient content depends on species and varieties of cultivated plant. Potassium is one of the major plant nutrients, which regulates and improves the process of plant nutrition, increases resistance to disease, reduces the accumulation of nitrates, promotes photosynthesis, organic matter and sugar synthesis and metabolic processes in plants [1].

In Mineral fertilizers manufacturing industry main source of potassium – the composition of various natural potassium salts deposits. Potassium is found in many minerals, especially silicates, as well as chlorides, nitrates, sulphates and others. Sometimes potash ores include useful impurities: bromine, iodine, copper, zinc and others [2]. Recently, in order to make best use of all chemicals, other by-products and waste from human activities, people are in search for possibility of recycling. This often results in the production of fertilizers containing nutrients required by plants without harmful impurities [3, 4].

Fertilizer granulation method mainly depends on the selection of the fertilizer components in physical – chemical properties and the physical form in which the materials are granulated, and can be dry material granulating action with water or steam; pulp granulation; melt granulation; compact granulation. One of the main determinants of the granulation process is agglomeration. Agglomeration – a process in which individual fine material particles bound into a solid pellet [5–7]. Stages of the process are shown in Figure 1.



Fig. 1. Dry matter agglomeration spray fluid [7]

Agglomeration preferably takes place using plastic material or when a strong adhesion force is acting. Plasticity and adhesion forces are strengthened by accessories. Technologically, the easiest way is to pour acid into water.

This work was carried out to determine the influence of phosphoric acid supplement for NPK fertilizer production and for their properties and by reference to some of the granulation process parameters (size of granules in a granulated mixture and moisture content).

Materials and methods

For production of NPK10–20–20+S +Mg granular compound fertilizer were used the following technical salts: $(\text{NH}_4)_2\text{SO}_4$, $(\text{NH}_4)_2\text{HPO}_4$, $\text{NH}_4\text{H}_2\text{PO}_4$, a by-product from production of magnesium from a carnallite, this is a technical potassium chloride with calcium and magnesium additives, which come from the company "AVISMA" (Russia) and the so called "electrolyte potassium" (KE) and sand. For irrigation of the mixture to be granulated was used water acidified with phosphoric acid.

NPK fertilizers were granulated in a laboratory drum granulator - dryer BGD based on the design and operation of industrial granulator's data [9]. Assessing geometric parameters of a laboratory drum granulator with a purpose to obtain a granular product there were produced 200 g of a required composition and fineness (0, 10, 20, 30 and 40 % raw particles with a diameter of 1–2 mm) of raw materials. The raw materials mixture before pelleting was irrigated with water acidified with phosphoric acid of dry mas. Granulated fertilizers were dried, fractionated and determined their chemical a physical properties. For process pellet strength assessment and comparison, for measure of the granules strength was used the apparatus CPG – 9M, with a measuring range from 0.1 to 10 MPa. Set crushing strength of 20 beads and according to interval rating by calculating the arithmetic average [9]. Moisture content was determined by a humidity analyser HG53, which is based on the thermogravimetric principle [10].

Results and Discussion

In previous work [11] has been trying to use a “potassium electrolyte” as a source of potassium in compound fertilizers, but the agglomeration process was quite difficult and product results were not as good as you can expect to achieve. In order to improve the quality of the fertilizer on account of agglomeration has been used water acidified with phosphoric acid. Small amount of acid should not adversely affect the pH of the fertilizer, but has a positive influence on the adhesion of particles of raw materials, increase the adhesion strength effect, i.e. improves the agglomeration process [12].

In order to determine the phosphoric acid additive in irrigated water and particulate materials in the mixture affects the amount of the granulation process and the granular properties were evaluated using (25 samples), granulating the same brand (NPK 10–20–20+S+Mg) as a potassium fertilizer, and as a raw material using an electrolyte of potassium.

For granulation were prepared raw mixtures with varying fineness, i.e. using different materials mixed particles with a diameter less than 1 mm (100, 90, 80, 70 and 60 %) and particles having a diameter of 1–2 mm (0, 10, 20, 30 and 40 %). For irrigation of the mixture were used the following amounts 15; 17.5; 18.5; 19.5 and 20 ml (or 7; 8.1; 8.5; 8.8 and 9.1 % on the dry weight of the mixture) of preheated to 70 °C acidified water. The produced fertilizer were dried at 70 °C for about 12 hours and then were analysed for physical and chemical properties (moisture content evaporated of the pellets during drying of the granulated product, static strength of the pallets, pH of 10 % solution). The data obtained are shown in Table 1.

From the data in Table 1 we see that moisture content evaporated during drying of the granulated fertilizers is not directly proportional to the amount of water used for irrigation and the quantity varies in the range of 0.68 % to 2.8 %. When analysing dependence of pH of 10 % of the fertilizer solution on the amount of water used for irrigation and on fraction composition of raw materials we can see that in all cases values of pH of 10 % solutions of the brand of NPK 10–20–20 are close to neutral and range of about 6.2. One of the key properties of granular NPK fertilizers is their granulometric composition, which is characterized by the fine fraction (recycle product consisting of <2 mm size pellets), commercial fraction (pellet diameter of 2–5 mm) and the coarse fraction (pellet diameter 5 mm) parts.

As is apparent from Table 1 granulometric data, depending on the quantity of the acidified water used for irrigation of the raw materials mixture, change also quantities of fine, market and coarse fractions. At 100% of the particles having a diameter <1 mm maximum (~89.55 %) of fines and minimum (2.93 %) of the coarse fraction is obtained when content of water used for irrigation of the raw materials is 7.0 % of the dry weight of the mixture. In this

case, due to the lack of moisture there is no agglomeration and does not form pellets. Gradually increasing quantity of acidified irrigation water up to 9.1 %, agglomeration process is better, so the fine fraction is reduced to 4.15 %, while large – an increase to 64.1 %.

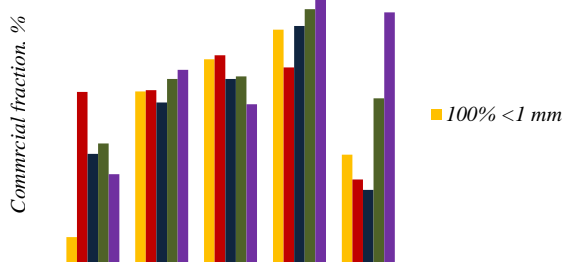
Table 1. Granulation conditions and properties of the granulated NPK 10–20–20+S+Mg fertilizers

Sam- ple	Quantity of H ₂ O+H ₃ PO ₄ for irrigation, %	Fraction composition of raw materials, %		Granulometric composition, %				Moisture in product, %	10% solution pH
		< 1 mm	1–2 mm	<2 mm	2–3 mm	3–5 mm	>5 mm		
1	7	100	-	89,55	4,57	2,95	2,93	0,91	6,19
2	8.1	100	-	47,30	44,00	6,35	1,40	0,82	6,22
3	8.5	100	-	32,85	41,35	18,45	7,35	1,05	6,22
4	8.8	100	-	15,40	38,50	30,00	16,10	1,20	6,17
5	9.1	100	-	4,15	8,20	23,55	64,10	1,16	6,20
6	7	90	10	37,40	30,00	20,20	12,40	1,05	6,17
7	8.1	90	10	40,50	35,40	15,30	8,80	1,03	6,24
8	8.5	90	10	22,25	36,35	24,60	16,80	1,13	6,19
9	8.8	90	10	3,50	16,80	40,60	39,10	1,15	6,15
10	9.1	90	10	1,56	7,56	16,90	73,98	1,16	6,21
11	7	80	20	58,60	17,80	14,20	9,40	0,68	6,27
12	8.1	80	20	44,50	30,15	16,95	8,40	0,96	6,25
13	8.5	80	20	31,60	31,20	22,80	14,40	1,29	6,29
14	8.8	80	20	8,30	34,30	35,30	22,10	2,76	6,27
15	9.1	80	20	0,75	10,60	10,80	77,85	2,80	6,23
16	7	70	30	60,36	24,30	10,74	4,60	0,98	6,29
17	8.1	70	30	35,50	32,60	21,40	10,50	1,19	6,28
18	8.5	70	30	30,45	32,45	22,30	14,80	2,55	6,26
19	8.8	70	30	10,30	36,80	37,70	15,20	2,51	6,31
20	9.1	70	30	1,10	9,00	39,30	50,60	2,18	6,29
21	7	60	40	71,20	17,50	8,53	2,77	0,88	6,23
22	8.1	60	40	35,60	35,40	21,30	7,70	1,48	6,24
23	8.5	60	40	41,40	28,25	18,30	12,05	1,47	6,31
24	8.8	60	40	7,20	37,30	40,50	15,00	2,39	6,28
25	9.1	60	40	6,00	3,00	42,60	20,40	2,24	6,31

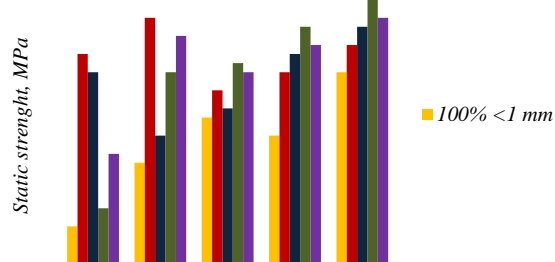
When the raw material consists of 90 % of the particles having, diameter of <1 mm and 10 % 1–2 mm in diameter, the result changes analogous to the case where the raw material mixture composed of 100 % <1 mm in diameter. Raw material mixture using 80 % <1 mm and 20 % of 1 mm particles, maximum (44.5 to 58.6 %) of fine fraction and minimum (8.4–9.4 %) of the coarse fraction is obtained when water content for irrigation is from 7.0 to 8.1 % of dry weight of the mixture. An analogous relationship established where the 1–2 mm diameter particles of the raw material mixture were increased to 30 or 40 %.

The Figure 2 shows that using 10 % content of particle <1 mm of raw materials mainly commercial fraction (~68.5 %) was obtained with 8.8 % acidified water. Increasing the amount of water acidified to 9.1 %, quantity of commercial product is very significantly reduced.

Commercial fraction pellets static strength dependence from fraction composition of raw materials and moisture content of raw materials, using acidified water are shown (Fig. 3). In Figure 3 shows that the commercial fraction pellet static strength is more dependent on acidified water content and less – on fraction composition of the raw materials.



Water amount in raw



Water in raw material

Fig. 2. Dependence of quantity of Fertilizer commercial fraction (2–5 mm) on fraction composition of the raw materials mixture and on amount of acidified water

Fig. 3. Commercial fraction (2–5 mm) chips static strength dependence of raw materials and the size distribution of acidified water content

In order to produce high quality 10–20–20+Mg+S brand of NPK fertilizers, which are sufficiently marketable fraction using the KE and the acidified water requires less moisture than granulation using KCl [11] and tap water, i.e. instead of 10.1 % water content, 8.5 % is sufficient. Analysis of the theoretical results give an opportunity to the traditional granulated NPK fertilizer production technology to be adapted to a case where as potassium source can be used a by-product from production of magnesium from a carnallite („potassium electrolyte“). Considering the fact that the „potassium electrolyte“ is technical, with the accessories (H_2O ; $MgCl_2$; $CaCl_2$) salt, characterized by the absorbency and dust levels, typical technological scheme should be amended so that it would be appropriate fertilizers, using KE additive and phosphoric acid to produce.

Summary

It can be said that 10–20–20+Mg+S brand of NPK fertilizer, using such raw material, and a potassium source of raw materials – KE, for irrigation using 8.5–8.8 % acidified water to form sufficient marketable fraction (50–80 %) and generated enough static strength of granules (4.4 to 5.6 MPa).

References

1. R. Paleckiene, A.M. Sviklas. *Fertilizer Agrochemicals*. **2012**. 152.
2. BC Guide to the Mineral Fertilizers. A basic handbook on fertilizers and Their use <http://www.scribd.com/doc/76525057/17991-ABC-Guide-to-Mineral-Fertilizer>
3. P.J. Legg. *International Journal of Environment and Resource (IJER)*. **2013**. 2(3). 59-66.
4. *Solid waste and emergency response. Waste-Derived fertilizers*. The United States Environmental Protection Agency. 1997th
5. <http://www.pharmainfo.net/reviews/pharmaceutical-micropellets-overview>
6. O. Miserque *Handbook of solid fertilizer blending: code of good practice for quality*. European fertilizer blenders Association. **2005**.
7. <http://sternmaid.de/en/agglomeration/>
8. R. Siauciunas, K. Baltakys, A. Baltušnikas. *Instrumental analysis of silicate materials*. Kaunas. **2007**. 244.
9. REPORT CEN. *Fertilizers- Crushing strength determination on fertilizer grains*. CR BS 1233: 2006th
10. R. Paleckiene, A.M. Sviklas, R. Slinksienė, V. Štreimikis. *Polish Journal of Environmental Studies*. **2012**. 21(4). 993-999.
11. R. Šlinksienė, O. Brigaitytė. *Chemical technology*. **2013**. 2(64). 63-71.
12. <http://nptel.ac.in/courses/103107086/module5/lecture2/lecture2.pdf>.



FAST AND EFFICIENT METHOD FOR PREPARATION OF THROUGH-HOLE ANODIC ALUMINA MEMBRANES

A. Brudzisz, A. Brzózka, G.D. Sulka

Department of Physical Chemistry & Electrochemistry, Faculty of Chemistry, Jagiellonian University in Krakow, Ingardena 3, Krakow 30060, Poland

E-mail: anna.brudzisz@uj.edu.pl

The worldwide trend of device miniaturization has become an important reason for the development of inexpensive and efficient methods for synthesis of novel, nanostructured materials. In last few decades, porous anodic alumina membranes (PAMs) were widely investigated and frequently used as templates for the synthesis of functional 1D and 2D materials. A detachment of the porous alumina film from the Al substrate and removal of the barrier layer covering the pore bottoms are crucial steps in a preparation of the through-hole PAMs [1]. In typically used chemical methods, the remaining Al substrate is dissolved in a CuCl_2 or HgCl_2 solution and the barrier layer is removed by a wet chemical etching in phosphoric acid. As obtained PAM's are brittle, contaminated with heavy metal ions, pores are widen and the method is time-consuming. In 2002 Lira and Paterson presented a new electrochemical method for the PAM detachment from the Al substrate [2]. By applying a short voltage pulse, the membrane is detached and pore are opened.

Herein, we report a modified voltage detachment method that uses a mixture of HClO_4 and ethanol (1:1 vol.). In our research we applied different pulses for the detachment of porous alumina formed under selected experimental conditions. We also present a consistent mechanism of voltage pulse detachment.. The proposed method is better controllable, faster and more environmentally friendly as compared to the typically used chemical etching. As-obtained PAMs were successfully used for electrodeposition of metallic nanostructures.

References

1. W. Chen, J.-S. Wu, J.-H. Yuan, X.-H. Xia, X.-H. Lin, *J. Electroanal. Chem.*, **600** (2007) 257–264
2. H. L. Lira, R. Paterson, *J. Membr. Sci.*, **206** (2002) 375–387

SYNTHESIS OF ALUMINATES FROM HYBRID ORGANIC-INORGANIC PRECURSORS

A. Chodosovskaja^{1,*}, **E. Garskaite**², **A. Beganskiene**¹, **S. Sakirzanovas**², **A. Kareiva**¹

¹ Department of Inorganic Chemistry, Faculty of Chemistry, Vilnius University, Naugarduko 24, Vilnius LT-03225, Lithuania

² Department of Applied Chemistry, Faculty of Chemistry, Vilnius University, Naugarduko 24, Vilnius LT-03225, Lithuania

*E-mail: alachodosovskaja@gmail.com

Yttrium aluminium garnet ($\text{Y}_3\text{Al}_5\text{O}_{12}$, YAG) has the garnet structure, excellent chemical stability, high temperature creep resistance and good optical properties [1-3]. Neodymium doped yttrium aluminium garnet (Nd:YAG) is one of the most important laser materials. Crystals are available from different commercial suppliers with dopant concentration up to 2.5at% [4]. Differently doped an un-doped YAG nanopowders were synthesized by means of microwave assisted citrate gel process at a reduced calcinations temperature, by co-precipitation, by chelate-polymerization and many other methods. The obtained results using these new methodologies were compared with those conventional heat treatments [9-14]. When garnet phase is doped with samarium, cerium or europium, secondary phases like perovskite (YAlO_3 , YAP) and hexagonal (YAlO_3 , YAH) have been observed.

Over the last few decades, the sol-gel techniques have been used to prepare a variety of mixed-metal oxides, nanomaterials and nanoscale architectures, nanoporous oxides, organic-inorganic hybrids [15-21]. It has been demonstrated that the sol-gel process offers considerable advantages such as better mixing of the starting materials and excellent chemical homogeneity in the final product. Moreover, the molecular level mixing and the tendency of partially hydrolyzed species to form extended networks facilitate the structure evolution thereby lowering the crystallization temperature. Recently for the preparation of different garnets and other mixed-metal oxides we elaborated an aqueous glycolate sol-gel processing route [22, 23].

Several lanthanide aluminium garnets (i.e., $\text{Ce}_3\text{Al}_5\text{O}_{12}$, $\text{Pr}_3\text{Al}_5\text{O}_{12}$, $\text{Nd}_3\text{Al}_5\text{O}_{12}$, $\text{Sm}_3\text{Al}_5\text{O}_{12}$) has not been synthesized so far, to the best our knowledge. Rare earth aluminium garnets ($\text{RE}_3\text{Al}_5\text{O}_{12}$) were reported to be thermodynamically stable with $\text{RE} = \text{Gd} - \text{Lu}$. Garnet structures with larger rare earth ions (Sm, Eu) are metastable, in favour of the competing perovskite type. Besides, the garnet phase does not exist for the lighter rare earth elements. Garnets with $\text{RE} = \text{Sm}$ and Eu were reported only as side phases from autoclave reactions in 1,4-butanediol at temperatures around 300 °C. Thus, $\text{Sm}_3\text{Al}_5\text{O}_{12}$ garnet phase is not synthesized and characterized so far. However, theoretically some substitution of Y^{3+} by Sm^{3+} at dodecahedral sites in YAG structure could be possible since the values of ionic radii of these elements differ marginally. Therefore, the main aim of this study was for the first time to investigate samarium substitution effects in $\text{Y}_{3-x}\text{Sm}_x\text{Al}_5\text{O}_{12}$ garnet structure compound synthesized using an aqueous sol-gel processing route.

Yttrium aluminium garnet powders substituted by samarium $\text{Y}_{3-x}\text{Sm}_x\text{Al}_5\text{O}_{12}$, ($x = 0.1, 0.15, 0.25, 0.5, 0.75, 1.0, 1.5, 2.0, 2.5$ and 3.0) were prepared by simple an aqueous sol-gel method. In the aqueous sol-gel process, the following materials were used: Y_2O_3 (99.99%, Aldrich), Sm_2O_3 (99.99%, Aldrich), $\text{Al}(\text{NO}_3)_3 \cdot 9\text{H}_2\text{O}$ (99.99%, Aldrich), acetic acid (99.5%, Chempur, Poland) and ethane-1,2-diol (99%, Merck). Y and Sm acetates were prepared by dissolving the corresponding oxides in $2 \cdot 10^{-1}$ M acetic acid (100 ml). Clear solutions were obtained after stirring at 60-65 °C for 10 h in beakers covered with a watch-glass. Then, aqueous solution of aluminium nitrate nonahydrate (25 ml) was added to the yttrium acetate solution. The mixture

was stirred at 65 °C for 40 min and solution of samarium acetate was added. The resulting mixture was stirred at 65 °C for 1 h, followed by drop-wise addition of ethane-1,2-diol (2 ml) upon vigorous stirring. The resulting sols were stirred at the same temperature for another 1 h and then concentrated by slow solvent evaporation at 65 °C until they turned into transparent gels. The gels were dried in an oven at 110 °C for 24 h. The resulting gel powders were ground in an agate mortar and heated in air at 800 °C for 5 h by slow temperature elevation (~3-4 °C min⁻¹). After grinding in an agate mortar, the powders were further sintered in air at 1000 °C for 10 h.

X-ray diffraction analysis (XRD) was performed on a Bruker AXE D8 Focus diffractometer with a LynxEye detector using Cu K_α radiation. Infrared spectra of samples in KBr pellets were recorded with a Bruker Equinox 55/S/NIR FTIR spectrometer (resolution 1 cm⁻¹). The particle size and morphology of the resultant Y_{3-x}Sm_xAl₅O₁₂, (x = 0.1, 0.25, 0.35, 0.5, 0.6, 0.7, 0.8, 1.5, 2.0, 2.5, and 3.0) garnet powders were examined using FE-SEM Zeiss Ultra 55 field Mission scanning electron microscope with In-Lens detector.

In this work Y³⁺ substitution by Sm³⁺ in yttrium aluminium garnet (Y_{3-x}Sm_xAl₅O₁₂) synthesized by an aqueous sol-gel process has been investigated. It was concluded from the XRD data that full substitution of yttrium by samarium is possible only at low concentrations of Sm. However, with high substitution SmAlO₃ phase was the main phase in the mixture with YAG. The obtained XRD results of synthesized Y_{3-x}Sm_xAl₅O₁₂ compounds were fully supported by IR results. It was determined that the range of IR spectra in the wavenumber region of ~900-500 cm⁻¹ could be successfully used to distinguish the garnet and perovskite crystalline phases. Moreover, the SEM measurements showed that the morphological features of sol-gel derived Y_{3-x}Sm_xAl₅O₁₂ samples also depends on phase purity of ceramic materials.

A. Chodosovskaja is thankful for postdoctoral fellowship which is funded by European Union Structural Funds project "Postdoctoral Fellowship Implementation in Lithuania" (SF-PD-2012-12-31-0397). Authors thank Dr. N. Dubnikova for helpful discussions.

References:

- [1] X. Li, Q. Li, J. Wang, S. Yang and H. Liu, *Opt. Mater.* 29 (2007) 528.
- [2] J. Geusic, H. M. Marcos and L. G. Van Uitert, *Appl. Phys. Lett.* 4 (1964) 182.
- [3] T. A. Parhasarathy, T. Mah and K. Keller, *Ceram. Eng. Sci. Proc.* 12 (1991) 1767.
- [4] T. Yokoyama, *Bull. Ceram. Soc. Jpn.* 23 (1988) 461.
- [5] J. Lu, M. Prabhu and J. Song, *Appl. Phys. Lett.* B71 (2000) 469.
- [6] D. Klimm, S. Ganschw, A. Pajaczkowska and L. Lipinska, *J. Alloys Compd.* 436 (2007) 204.
- [7] R. V. Bakradze, G. N. Kuznecova, S. A. Baryshev, T. N. Selivanova and V. Z. Byckov, *Inorg. Mater.* 4 (1968) 395.
- [8] ACerS-NIST, Phase equilibria diagrams, CD-ROM database (Ver. 3.0.1).
- [9] M. L. Saladino, G. Nasillo, D. C. Martino and E. Caponetti, *J. All. Comp.* 491 (2010) 737.
- [10] T.-M. Chen, S. C. Chen and C.-J. Yu, *J. Solid State Chem.* 144 (1999) 437.
- [11] J. Marchal, T. Hinklin, R. Beranwal, T. Johns and R. M. Laine, *Chem. Mater.* 16 (2004) 822.
- [12] E. Caponetti, M. L. Saladino, F. Serra and S. Enzo, *J. Mater. Sci.* 42 (2007) 4418.
- [13] R. Singh, R. K. Khardekar, A. Kumar and D. K. Kohli, *Mater. Lett.* 61 (2007) 921.
- [14] E. Caponetti, S. Enzo, B. Lasio and M. L. Saladino, *Opt. Mater.* 29 (2007) 1240.
- [15] J. Livage, M. Henry and C. Sanchez, *Progr. Solid State Chem.* 18 (1988) 259.
- [16] C. J. Brinker and G. W. Scherrer, *Sol-gel science: the physics and chemistry of sol-gel processing*, Academic Press, New York, 1990.
- [17] B. L. Cushing, V. L. Kolesnichenko and C. J. O'Connor, *Chem. Rev.* 104 (2004) 3893.
- [18] J. D Mackenzie and E. P. Bescher, *Acc. Chem. Res.* 40 (2007) 810.
- [19] F. Qiu, X. Pu, J. Li, X. Liu, Y. Pan and J. Guo, *Ceram. Inter.* 31 (2005) 663.
- [20] J. Schafer, W. Sigmund, S. Roy and F. Aldinger, *J. Mater. Res.* 12 (1997) 2518.
- [21] C. Yu, D. Cai, K. Yang, J. C. Yu, Y. Zhou and C. Fan, *J. Phys. Chem. Solids* 71 (2010) 1337.
- [22] A. Katelnikovas, J. Barkauskas, F. Ivanauskas, A. Beganskiene and A. Kareiva, *J. Sol-Gel Sci. Techn.* 41 (2007) 193.
- [23] S. Cizauskaite, V. Reichlova, G. Nenartaviciene, A. Beganskiene, J. Pinkas, A. Kareiva, *Mater. Chem. Phys.* 102 (2007) 105.



SOL – GEL SYNTHESIS AND CHARACTERIZATION OF LITHIUM ALUMINIUM MOLYBDATE

A. Diktanaitė, A. Žalga

*Department of Applied Chemistry, Faculty of Chemistry, Vilnius University, Naugarduko 24,
LT-03225 Vilnius, Lithuania*

E-mail: austeja.diktanaite@gmail.com

Ionic motion in solid oxides plays an essential role in many technological applications including electrolytes in solid state ionic devices such as fuel cells and sensors. In most ionic conductors, the mobile ions are mono- or divalent, such as Na^+ , Li^+ , Ag^+ , F^- , and O^{2-} . However, trivalent ions are generally expected to be poor conducting species and trivalent ionic conductors are thus rare [1].

$\text{LiAl}(\text{MoO}_4)_2$ is a member of the crystal family of layered double molybdates and tungstates with the general formula $\text{M}^{\text{I}}\text{M}^{\text{III}}(\text{M}^{\text{VI}}\text{O}_4)_2$, where M^{I} = alkali metal, M^{III} = Al, In, Cr, Bi, Fe, RE (rare earths), and M^{VI} = Mo or W, exhibit interesting structural and physicochemical properties, and are used as acousto-optic filters, second-harmonic generators and laser crystals. They exhibit ferroelectric, ferroelastic or even ferromagnetic properties and have been extensively studied for the last 50 years [2].

In this study, we report the synthesis of the Li–Al–Mo–O tartrate gel precursor with the initial composition for $\text{LiAlMo}_2\text{O}_8$ ceramic prepared by simple, inexpensive, and environmentally benign aqueous sol–gel method [3, 4]. Its crystal structure and surface morphology of the as-prepared oxides has been investigated. The crystallization processes of the Li–Al–Mo–O tartrate gel precursor were characterized by X-ray diffraction (XRD) and thermogravimetry-differential thermal analysis (TG-DTA). Scanning electron microscopy (SEM) was also used to characterize the shape and size distribution of the final ceramic.

References

1. N. Kim, J. F. Stebbins, *Chem. Mater.*, **2009** 21, 309.
2. M. Maczka, S. Kojima, J. Hanuza, *J. Raman Spectrosc.*, **1999** 30, 339.
3. G. Braziulis, G. Janulevicius, R. Stankeviciute, A. Zalga, *J. Therm. Anal. Calorim.*, **2014** 118, 613.
4. A. Zalga, Z. Moravec, J. Pinkas, A. Kareiva, *J. Therm. Anal. Calorim.*, **2011** 105, 3.

GRAPHENE-BASED NANOCOMPOSITE MATERIALS CONTAINING PARATHIOCYANOGEN

J. Gaidukevič¹, J. Barkauskas¹, K. Petrikaitė¹

1 Vilnius University, Faculty of Chemistry, Naugarduko str. 24, LT – 03225, Vilnius, Lithuania

E-mail: justina.daksevic@chf.stud.vu.lt

Introduction

Graphene oxide (GO) is a product of graphite oxidation, containing hydroxyl and epoxy groups bonded to sp^3 hybridized carbon on the basal plane, in addition to carbonyl and carboxyl groups located at the edges of sp^2 hybridized carbon. Functional groups are responsible for the hydrophilic properties and dispersibility of GO in water or other polar organic solvents [1]. GO dispersions are used to produce GO films. GO films are among the most commonly used precursors to produce graphene coatings. Graphene is a single layer of carbon atoms bound through sp^2 bonds forming a hexagonal two-dimensional crystal lattice. It has a very high electron mobility at room temperature, reaching values of up to $200,000 \text{ cm}^2 \text{ V}^{-1} \text{ s}^{-1}$. This form of carbon is the strongest material ever known, theoretically perfect graphene sheet is about 100 times stronger than steel. Graphene has high thermal conductivity up to $5000 \text{ W m}^{-1} \text{ K}^{-1}$, extremely high theoretical specific surface area $2630 \text{ m}^2/\text{g}$ and is not permeable to gas [2]. However, pure graphene sheets are limited for many applications despite their excellent characteristics. One possible route to improving these properties would be to use graphene in composite materials. Graphene can be readily doped with heteroatoms (e.g., nitrogen, boron, sulfur) or modified with organic molecules, polymers, or inorganic components. More recently, graphene-based nanocomposite materials have been demonstrated as potential metal-free catalysts or supporting materials for non-precious metal catalysts for oxygen reduction reaction (ORR) which is the key process in fuel cells [3].

The aim of this work was to prepare and investigate graphene-based nanocomposite materials containing parathiocyanogen $(\text{SCN})_n$. This polymer was synthesized by different methods and products were compared with each other. Although parathiocyanogen has been known for a long time, its solid state structure continues to be uncertain and controversial. $(\text{SCN})_n$ can be prepared in a single step by chemical oxidation of thiocyanate (SCN^-) anion using $\text{S}_2\text{O}_8^{2-}$, Cl_2 or Br_2 as the oxidizing agents, or by electrochemical oxidation [4]. Alternatively, parathiocyanogen can be produced via spontaneous polymerisation of $(\text{SCN})_2$, which occurs above 3°C [5]. The application of $(\text{SCN})_n$ as a semiconductor solar cell electrode material, photocatalyst and also as a lithium-ion battery electrode material has been studied [6].

Experimental

In the laboratory $(\text{SCN})_n$ was synthesized by solid-solid reaction between peroxydisulphate and thiocyanate [4]. The solvent-free, solid–solid reaction is carried out by grinding (from 10 to 90 minutes) a mixture of KSCN and $(\text{NH}_4)_2\text{S}_2\text{O}_8$ in a mole ratio (2:1) in an agate mortar with a pestle at room temperature. Therefore, to purify the $(\text{SCN})_n$ the crude product was washed with water until the washings are free from thiocyanate, peroxydisulphate and sulphate, respectively. A similar procedure for the preparation of $(\text{SCN})_n$ from GO by KSCN was carried out. Simultaneously, $(\text{SCN})_n$ was prepared by the oxidation of ammonium thiocyanate using ammonium peroxydisulfate in an aqueous solution [6]. A similar procedure for the preparation of $(\text{SCN})_n$ from GO by NH_4SCN was carried out. Also $(\text{SCN})_n$ was obtained by thermal polymerization of thiocyanogen by synthesis protocol reported by F. Cataldo [5]. GO was synthesized from the natural graphite by synthesis protocol reported by Yan et al. In a typical experiment, graphite powder was treated with

conc. H_2SO_4 , $\text{K}_2\text{S}_2\text{O}_8$ and P_2O_5 [7]. Then this pre-oxidized graphite was subjected to oxidation by Hummers method [8].

Characterization

XRD studies were performed using a MiniFlex II (Rigaku) diffractometer with $\text{Cu K}\alpha$ ($\text{K}\alpha_1 = 1.54056\text{\AA}$) radiation. XRD of the powder samples was recorded for 2θ values from 5° to 55° . The characterization was done at 30 kV and 15 mA with a step size of 0.010° and a dwell time of 1.0 s. The molecular weight of $(\text{SCN})_n$ was determined by the gel permeation chromatography of an Viscotek GPCmax Chromatography system, using TSKgel GMHHR-M column. Tetrahydrofuran was used as the mobile phase at 30°C with a 0.5 mL/min flow rate. Electrochemical measurements of modified GO with KSCN were performed using an electrochemical system "PARSTAT 2273" with a conventional three-electrode system composed of an auxiliary platinum plate electrode, a reference Ag/AgCl (KCl , 3 M) electrode, and a working graphite rod coated with graphene-based nanocomposite material (O 3 mm) electrodes. The electrochemical experiments were conducted in O_2 and N_2 saturated 0.5 M H_2SO_4 (or 0.1 M KOH) electrolyte for the oxygen reduction reaction. The potential range is cyclically scanned between -0.6 and $+0.82$ V at a scan rate of 50 mVs^{-1} (of 20 mVs^{-1} in alkali condition) at the room temperature after purging O_2 or N_2 gas for 5 min and 20 min respectively.

Results and discussions

X-Ray diffraction measurements have been usually used to characterize the phases present in any reactant mixture and provide a means of identification of products, solid reactants and intermediates. XRD patterns of initial reactants and $(\text{SCN})_n$ obtained by different methods are presented in Fig. 1. and Fig. 2.

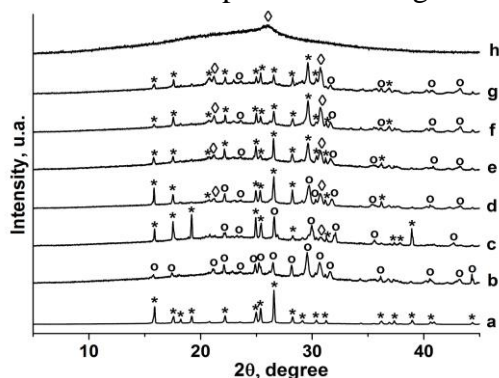


Fig. 1. X-ray powder diffraction pattern of $(\text{SCN})_n$ obtained via solid-solid reaction. (a) – $(\text{NH}_4)_2\text{S}_2\text{O}_8$, (b) – KSCN , (c, d, e, f, g) – reactants KSCN and $(\text{NH}_4)_2\text{S}_2\text{O}_8$ mixture for various durations of time, (h) – $(\text{SCN})_n$ free from thiocyanate peroxydisulphate and sulphate.

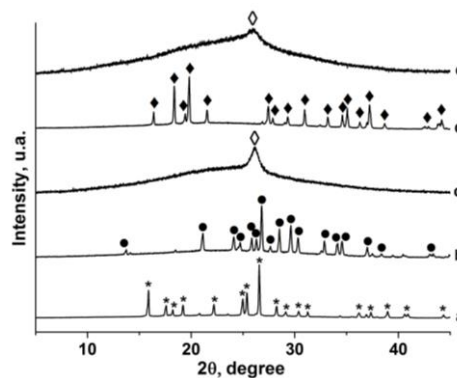


Fig. 2. X-ray powder diffraction pattern of $(\text{SCN})_n$ obtained in solutions. (a) – $(\text{NH}_4)_2\text{S}_2\text{O}_8$, (b) – NH_4SCN , (c) – $(\text{SCN})_n$ obtained by the oxidation of thiocyanate using peroxydisulfate in an aqueous solution, (d) – $\text{Pb}(\text{SCN})_2$, (e) – $(\text{SCN})_n$ obtained from thiocyanate prepared from Br_2 .

The XRD patterns of initial reactants (Fig. 1 (a, b) and Fig. 2 (a, b, d) are compared using data from JCPDS database. In Fig. 1 we see that at the start of the reactions the pattern (Fig. 1 (c, d, e, f, g)) is a combination of KSCN and $(\text{NH}_4)_2\text{S}_2\text{O}_8$. After some time, a new set of reflections appear, corresponding to the product $(\text{SCN})_n$. On completion of the reaction the only set of reflections remaining is that of the product (Fig. 1 (h)). The transformation of KSCN , NH_4SCN or $\text{Pb}(\text{SCN})_2$ to $(\text{SCN})_n$ can be accompanied with a change in the crystalline system [4]. The XRD pattern of $(\text{SCN})_n$ obtained from different crystalline reactants (Fig. 1 (h) and Fig. 2 (c, e) and by different routes are very similar and are characterized by unique reflection at about $2\theta = 26.12^\circ$.

The molecular weight of $(\text{SCN})_n$ was determined by size exclusion chromatography (SEC). This method was employed to find the mean number average molecular weight (M_n),

mean weight average molecular weight (M_w) and polydispersity index of $(SCN)_n$. An elugram of SEC for the $(SCN)_n$ is shown in Fig. 3.

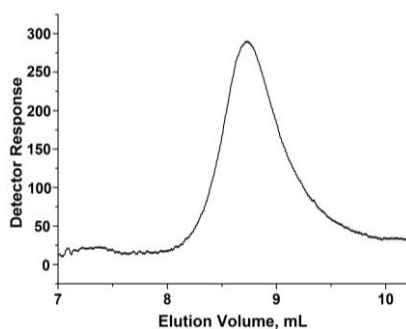


Fig. 3. SEC chromatogram of $(SCN)_n$.

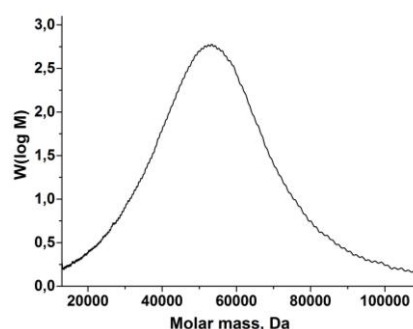


Fig. 4. A distribution of molecular weight of $(SCN)_n$ along with the rankings of the various average molecular weight.

The main fraction of the $(SCN)_n$ is eluted between 8 and 10 mL with a maximum at 8.73 mL. This maximum is attributed to high amounts of long chain polythiocyanogen. The elugram of $(SCN)_n$ was converted to a distribution of molecular weights along with the rankings of the various average molecular weights in Fig. 4. The elugram of $(SCN)_n$ shows that the polymer distribution ranges from approximately 20000 Da to 90000 Da, with a maximum peak intensity at 53198 Da, coincident with polythiocyanogen fractions. The molecular masses of $(SCN)_n$ computed by the SEC software were $M_n = 53759$ and $M_w = 56384$ with a polydispersity index $M_w/M_n = 1.049$. The results of the chromatogram demonstrate that the polythiocyanogen is monodisperse and polymer nature, containing narrow unimodal peak.

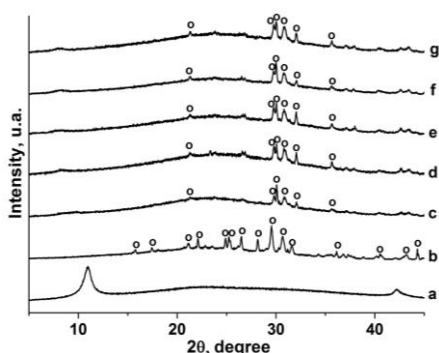


Fig. 5. X-ray powder diffraction pattern of product obtained via solid-solid reaction. (a) – GO, (b) – KSCN, (c, d, e, f, g) – reactants KSCN and GO mixture for various durations of time.

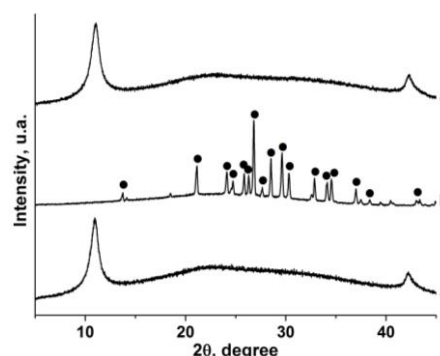


Fig. 6. X-ray powder diffraction pattern of product obtained in an aqueous solution. (a) – GO, (b) – NH_4SCN , c – product obtained by mixing GO with NH_4SCN in an aqueous solution at room temperature.

To prepare graphene-based nanocomposite materials containing parathiocyanogen, the solvent-free, solid–solid reaction is carried out by grinding for different amounts of time a mixture of KSCN and GO in an agate mortar with a pestle at room temperature. The XRD patterns of obtained products are shown in Fig. 5 (c, d, e, f, g). For comparison, the XRD pattern of GO is also presented (Fig. 5 (a)). The fresh GO powders showed a characteristic peak at $2\theta = 10.97^\circ$, corresponding to a d-spacing of 0.806 nm. After the grinding for 10 min GO with KSCN (Fig. 5 (c)), the characteristic peak of GO at $2\theta = 10.4^\circ$ disappeared while six peaks at 21.3° , 29.8° , 30.0° , 30.8° , 32.0° and 35.7° , which were attribute to the (111), (210), (120), (112), (211) and (022) lattice planes of KSCN (JCPDS, no.00-009-0388), respectively appeared, suggesting the successful reduction of GO powders to graphene by KSCN. When the grinding time increases up to 90 min, the peaks, characteristic of KSCN phase, clearly

decreased in intensity. The Fig. 6 shows the result of reaction between GO and NH_4SCN in aqueous solution at room temperature. In Fig.6 (c) we see that under these conditions the reaction of GO with NH_4SCN do not occur.

The electrocatalytic behavior of GO/KSCN nanocomposite material by oxygen reduction reaction (ORR) in 0.5 M H_2SO_4 (or 0.1 M KOH) solution was evaluated using a three-electrode system. The cyclic voltammograms at a GO/KSCN nanocomposite modified graphite rod electrode in N_2 and O_2 saturated 0.5 M H_2SO_4 (or 0.1 M KOH) solution were presented in Fig. 7 and Fig. 8 respectively. Apparently, ORR peak for GO/KSCN nanocomposite material is observed at + 0.46 V in O_2 saturated 0.5 M H_2SO_4 solution (Fig 7 (b)), whereas the value of reduction current peaks in N_2 saturated solution decreased about 10.5 time (Fig. 7 (a)). ORR peak for GO/KSCN nanocomposite material in 0.1 M KOH (Fig. 8) is absent.

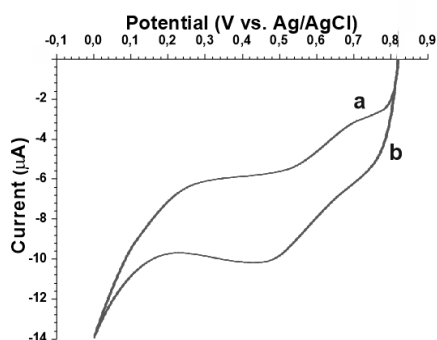


Fig. 7. Typical cyclic voltammograms at a scan rate of 50 mV s^{-1} in O_2 (b) and N_2 (a) saturated 0.5M H_2SO_4 solution.

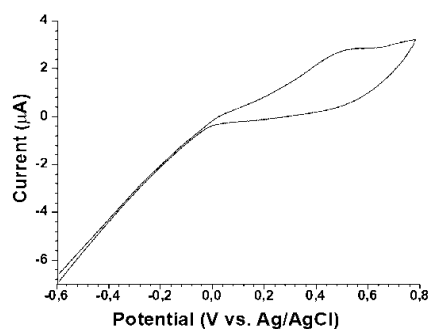


Fig. 8. Typical cyclic voltammograms at a scan rate of 20 mV s^{-1} in O_2 saturated 0.1M KOH solution.

Conclusions

$(\text{SCN})_n$ was synthesized by solid-solid reaction between SCN^- and $\text{S}_2\text{O}_8^{2-}$, by the oxidation of SCN^- in an aqueous solution and by the thermal polymerization of SCN^- . The XRD pattern of $(\text{SCN})_n$ obtained by different routes are very similar and are characterized by unique reflection at about $2\theta = 26.12^\circ$. The molecular weight of $(\text{SCN})_n$ computed by the SEC software were $M_n = 53759$ and $M_w = 56384$ with a polydispersity index $M_w/M_n = 1.049$. In the laboratory GO was obtained by Hummers method. Afterward the GO particles were modified with KSCN by the solvent-free, solid–solid reaction, and with NH_4SCN in aqueous solution at room temperature. At the room temperature KSCN reduce GO powders to graphene, whereas the reaction of NH_4SCN with GO powders do not occur. Electrochemical measurements show that ORR peak for GO/KSCN nanocomposite material is observed at +0.46 V in O_2 saturated 0.5 M H_2SO_4 solution, whereas the value of reduction current peaks in N_2 saturated solution decreased about 10.5 time. ORR peak for GO/KSCN nanocomposite material in 0.1 M KOH is absent.

Acknowledgements. This work was funded by the European Social Fund under National Integrated Programme Biotechnology and Biopharmacy, grant VP1-3.1-SMM- 08-K01-005.

References

1. M. Hakimi, P. Alimard, *World Applied Programming*, **2012**, 2, 377-388.
2. V. Singh, D. Joung, Lei Zhai, S. Das, S. I. Khondaker, *Progress in Materials Science*, **2011**, 56, 1178-1271.
3. N. Mahmood, C. Zhang, H. Yin, Y. Hou, *J. Mater. Chem. A*, **2014**, 2, 15.
4. S.A. Kahani, M. Sabeti, *J. Inorg. Organomet. Polym.*, **2011**, 21, 458-464.
5. F. Cataldo, *J. Inorg. Organomet. Polym.*, **1997**, 7, 35-50.
6. S. A. Kahani, M. Sabeti, M. T. Yosefi, *Phosphorus, Sulfur, and Silicon*, **2013**, 188, 1584-1590.
7. X. Yan, J. Chen, J. Yang, Q. Xue, P. Miele, *Applied Materials&Interfaces*, **2010**, 9, 2521-2529.
8. W. S. Hummers, R. E. Offeman, *J. Am. Chem. Soc.*, **1958**, 80, 1339.

SYNTHESIS AND CHARACTERISATION OF $\text{Co}_{1-x}\text{M}_x\text{Cr}_2\text{O}_4$ AS GREEN PIGMENTS**E. Grazenaite¹, J. Pinkas^{2,3}, P. Roupova^{4,5}, Z. Losos², A. Kareiva¹**

¹ Department of Inorganic Chemistry, Vilnius University Naugarduko 24, LT-03225 Vilnius, Lithuania

² Faculty of Science, Masaryk University, Kamenice 753/5, Bohunice, 619 00 Brno, Czech Republic

³ Central European Institute of Technology (CEITEC), Masaryk University, Koliste 13a 602 00 Brno, Czech Republic

⁴ Institute of Physics of Materials, Academy of Science, Zizkova 22, 616 62 Brno, Czech Republic

⁵ Department of Structural and Phase Analysis, Brno University of Technology, Technicka 2896/2, 616 69 Brno, Czech Republic

E-mail: egle.grazenaite@chf.stud.vu.lt

Cobalt chromium oxide CoCr_2O_4 having spinel crystal structure is a bluish green colour compound, which could be used as a pigment, magnetic material and catalyst. Cobalt chromite is a normal type spinel, where the tetrahedral sites are occupied by the Co^{2+} cations, which gives for the pigment a blue colour, and the octahedral sites by the Cr^{3+} cations, which gives a green colour [1, 2]. Due to a high thermal stability, high mechanical resistance and the easy incorporation of chromophore ions into the spinel lattice, spinel-type compounds recently have attracted interests for using them as ceramic pigments. Latter characteristic enables different types of doping, which produces variety of colours [2–4]. In this work, $\text{Co}_{(1-x)}\text{M}_x\text{Cr}_2\text{O}_4$ samples ($\text{M} = \text{Cu}^{2+}, \text{Zn}^{2+}, \text{Ni}^{2+}$; $x = 0.0; 0.25; 0.5; 0.75; 1.0$) were prepared by a sol-gel method [5].

In the sol-gel synthesis, $\text{Co}(\text{NO}_3)_2 \cdot 6\text{H}_2\text{O}$, $\text{Cr}(\text{NO}_3)_3 \cdot 9\text{H}_2\text{O}$, $\text{Cu}(\text{CH}_3\text{COO})_2 \cdot \text{H}_2\text{O}$, $\text{Ni}(\text{NO}_3)_2 \cdot 6\text{H}_2\text{O}$ and $\text{Zn}(\text{CH}_3\text{COO})_2 \cdot 2\text{H}_2\text{O}$ were used as starting materials. The stoichiometric amounts of salts were dissolved in water and appropriate solutions were mixed together for 20 min. Secondly, 1,2-ethanediol as a complexing agent was added and stirring was proceeded for 1 h at 50 °C. The solvent was evaporated at 60–65 °C. The obtained gel samples were dried at 105 °C temperature for 20 h, triturated in an agate mortar and calcined at 700 °C for 3 h. The powders were ground repeatedly and annealed at 1000 °C temperature for 10 h. Obtained powders were thoroughly ground in the agate mortar and used for characterization.

X-ray diffraction (XRD) analysis was performed on Rigaku SmartLab diffractometer using $\text{CuK}\alpha_1$ radiation ($\lambda = 1.540593 \text{ \AA}$). Fourier transform infrared (FTIR) spectra of the samples were recorded by a Bruker Tensor 27 equipment on absorbance mode with a resolution 4 cm^{-1} for each spectrum, which consisted of 32 scans. For all measurements the KBr pellet technique was applied. Raman spectra were measured using Horiba Scientific LabRam HR Evolution spectrometer with the Olympus microscope (objective magnification 50) in the spectral range of 80–1000 cm^{-1} at 532 nm.

Fig. 1 shows XRD patterns of $\text{Co}_{(1-x)}\text{M}_x\text{Cr}_2\text{O}_4$ ($\text{M} = \text{Cu}^{2+}, \text{Zn}^{2+}, \text{Ni}^{2+}$) spinels, when substitution ratio is equal 1.0. It is evident that cubic phases of ZnCr_2O_4 (PDF [00-022-1107]) and NiCr_2O_4 (PDF [00-075-1728]), and tetragonal structure of copper chromite CuCr_2O_4 (PDF [00-034-0424]) have formed. The sharp diffraction peaks of the XRD patterns presume that obtained products are well-crystalline materials.

The FTIR spectra of $\text{Co}_{1-x}\text{Cu}_x\text{Cr}_2\text{O}_4$ ($x = 0.25; 0.5; 0.75$ and 1.0) samples presented in Fig. 2 show typical spectra of normal spinel structure, which is characterized in the region of 700–400 cm^{-1} . In this region the spectra present two absorption bands corresponding to the stretching vibration of metal-oxygen bond [6].

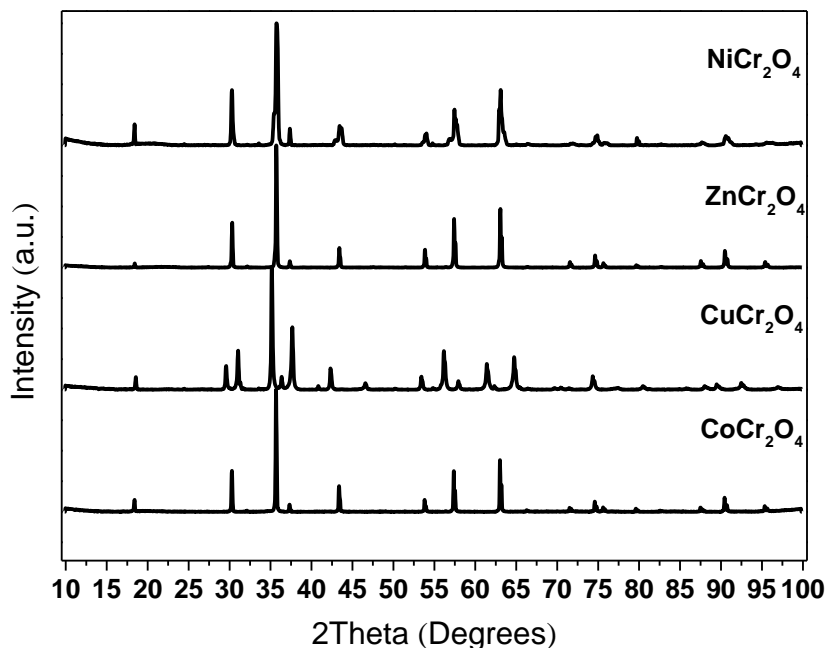


Fig. 1. XRD patterns of non-substituted and full substituted ($x = 1.0$) by Cu^{2+} , Zn^{2+} and Ni^{2+} cobalt chromite spinels.

For all spectra, the band between $600\text{--}700\text{ cm}^{-1}$ corresponds to the stretching band of Cr–O in the octahedral system and the broad band around 500 cm^{-1} is assigned to the stretching bond of metal (Co and Cu)–O in the tetrahedral system [6]. Unfortunately, we were not able to identify additional bands at about 550 and 563 cm^{-1} for the powders with $x = 0.75$ and 1.0 , respectively. All other spectra of Zn and Ni-doped powders were similar with no additional bands, confirming the spinel structure.

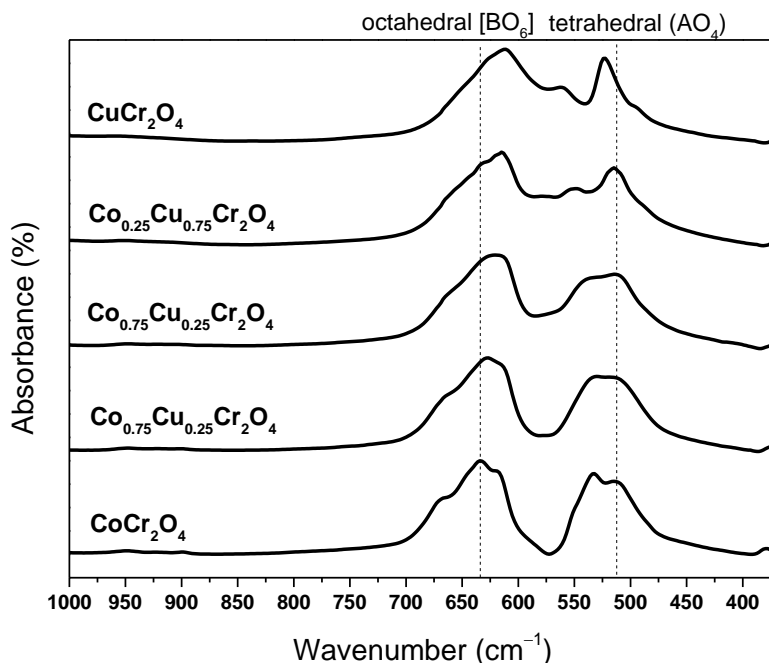


Fig. 2. FTIR spectra of $\text{Co}_{1-x}\text{Cu}_x\text{Cr}_2\text{O}_4$ ($x = 0.25; 0.5; 0.75$ and 1.0) samples.

The Raman spectra of $\text{Co}_{1-x}\text{Cu}_x\text{Cr}_2\text{O}_4$ ($x = 0.25; 0.5; 0.75$ and 1.0) powders are represented in Fig. 3.

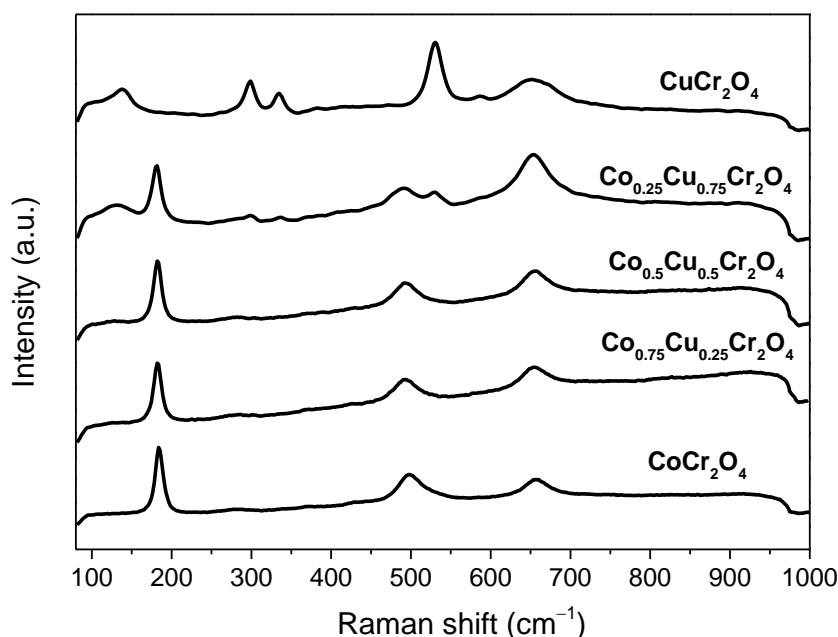


Fig. 3. Raman spectra of $\text{Co}_{1-x}\text{Cu}_x\text{Cr}_2\text{O}_4$ ($x = 0.25; 0.5; 0.75$ and 1) samples.

According to literature [7], the typical Raman spectra of the pure cubic spinel consist of five fundamental bands ($A_{1g} + E_g + 3F_{2g}$). In our case, only characteristic sharp band at about 180 cm^{-1} and broad bands at about 490 and 650 cm^{-1} ($x = 0.25; 0.5$ and 0.75) are well resolved and could be attributed to $F_{2g}(3)$, E_g and A_{1g} modes, respectively. However, additional bands at $298, 335$ and 530 cm^{-1} are observed for the samples with the substitution ratios of 0.75 and 1.0 . Unfortunately, we were not able to explain the appearance of these bands as well.

Conclusions

Cobalt chromite based spinel $\text{Co}_{(1-x)}\text{M}_x\text{Cr}_2\text{O}_4$ samples ($M = \text{Cu}^{2+}, \text{Zn}^{2+}, \text{Ni}^{2+}$; $x = 0.0; 0.25; 0.5; 0.75; 1.0$) were successfully synthesized by sol-gel method. The XRD results confirmed that all samples were spinels of cubic structure, except CuCr_2O_4 spinel was tetragonal, as it was expected. However, XRD data revealed that all powders have small amount of impurity phases. FTIR and Raman spectroscopic analyses proved the results of spinel structure with additional phases.

References

1. H.R. Hedayati, A.A. Sabbagh Alvani, H. Sameie et al., *Dyes Pigments*, **2015**, *113*, 588.
2. L.K.C. de Souza, J.R. Zamian, G.N. da Rocha Filho et al., *Dyes Pigments*, **2009**, *81*, 187.
3. S. Mestre, M.D. Palacios and P. Agut, *J. Eur. Ceram. Soc.*, **2012**, *32*, 1995.
4. S.A. Eliziario, J.M. de Andrade, S.J.G. Lima et al., *Mater. Chem. Phys.*, **2011**, *129*, 619.
5. D. Jasaitis, A. Beganskiene, J. Senvaitiene et al., *Chemija*, **2011**, *22*, 125.
6. S.A. Hosseini, M.C. Alvarez-Galvan, J.L.G. Fierro et al., *Ceram. Int.*, **2013**, *39*, 9253.
7. D. Zakutna, A. Repko, I. Matulkova et al., *J. Nanoparticle Res.*, **2014**, *16*, 2251.

SOME PROPERTIES OF THALLIUM SELENIDE LAYERS ON THE POLYAMIDE FILM SURFACE

R. Ivanauskas, L. Samardokas, I. Ancutienė

Department of Physical and Inorganic Chemistry, Kaunas University of Technology,

Radvilenu str 19, LT-50254 Kaunas, Lithuania

E-mail: remigijus.ivanauskas@ktu.lt

The modification of polymers by formation on their surface of thin layers of inorganic compounds, namely, chalcogenides, with important physical properties leads to obtaining of composites with different properties. During the last decade binary chalcogens of IIIA group metals because of their unique physical properties are intensively studied both by physicists and chemists in global scale [1, 2]. The thallium selenides can be used for the production the photoconductors [3] and photocells [4], which are sensitive to the infrared radiation and suitable to applications in modern microelectronics [5]. The interest in thallium selenide layers was previously focused mostly on their possible use to production of photocells [6] and photoconductors [7]. Use of thallium compounds has almost been eliminated in recent years due to their toxicity. Indium is twenty times more expensive than thallium. Consequently, thallium may still become attractive as group IIIA element due to its price. Therefore, semiconductors of IIIA group based on thallium are possible alternative to those where In or Ga are routinely used.

The layers of thallium selenides are commonly produced by vacuum evaporation [8] or by the deposition method from solutions [9].

In present work the thin layers of selenide thallium on polyamide films were formed by sorption-diffusion method via heterogeneous chemical reactions in two stages. In the first stage, polymer was seleniumized in a $0.05 \text{ mol} \cdot \text{dm}^{-3}$ concentration solution of potassium selenotrithionate, ($\text{K}_2\text{SeS}_2\text{O}_6$), in HCl ($c=0.1 \text{ mol} \cdot \text{dm}^{-3}$) at $60 \text{ }^\circ\text{C}$ up to 1.5 h. In the second stage, seleniumized films of PA 6 10 min were treated with an aqueous solution of thallium sulfate at 70 or $80 \text{ }^\circ\text{C}$.

The purpose of the present work was to characterize thallium selenide layers formed on polyamide films.

The concentration of thallium in thallium selenide layers formed on PA 6 films surface were determined using the method of atomic absorption spectrophotometry (AAS). Atomic Force Microscopy (AFM) was performed to investigate morphological changes, resulting in PA film surface after thallium selenide layers deposition. AFM allows for a quantitative description of surfaces in terms of their feature average and maximum height, as well as RMS roughness. $12 \text{ } \mu\text{m} \times 12 \text{ } \mu\text{m}$ 3D AFM topography images of thallium selenide layer on PA film and unreacted PA sample are shown in Figure 1 with the corresponding measured topographical parameters tabulated in Table 1. It can be seen that the surface characteristics of the PA film changes, when on the surface of the polymer the layer of thallium selenide was formed. Isolated aggregates on the surface PA films treated with solution of Tl_2SO_4 at $70 \text{ }^\circ\text{C}$ are observed (Fig 1b). They are distinguished by their size ($0.5\text{--}1.8 \text{ } \mu\text{m}$) and shape on the background of the layer. When the temperature of solution of Tl_2SO_4 was raised up to 80°C the amount of clusters and agglomerates on the surface of polymer film increases considerably. Clearly distinct larger clusters on the surface no longer can be seen (Fig. 1c). The particles of a similar size ($\sim 0.5 \text{ } \mu\text{m}$) with sharp peaks (height $\sim 120 \text{ nm}$) are dominated on the surface. The layer of thallium selenide becomes more homogeneous. This is confirmed by the data of Table 1. It can be seen that raising the temperature of the Tl_2SO_4 solution in the second stage of formation the layer of thallium selenide on PA film surface promotes of this layer maximum height (A) and average height (Z_{mean}) decrease. Accordingly, these

parameters of the surface of unreacted PA sample and PA samples with thallium selenide layer change A $67.4 \rightarrow 393.6 \rightarrow 185.2$ nm and Z_{mean} , $-27.76 \rightarrow 109.48 \rightarrow 68.64$ nm. Increase in thallium concentration from 15.15 to 20.82 $\mu\text{mol} \cdot \text{g}^{-1}$ with the increasing temperature of Tl_2SO_4 solution from 70 to 80°C, as well as decreasing difference between A and Z_{mean} values, in addition to the decreasing root-mean-square roughness, R_q , ($4.59 \rightarrow 27.8 \rightarrow 23.4$ nm), shows that thallium selenide materials formed at higher temperature contain similar height and size surface features thus being more homogenous and compact. That is also confirmed by the average roughness, R_a , ($3.45 \rightarrow 15.4 \rightarrow 18.4$) and skewness, R_{sk} , ($0.82 \rightarrow 3.00 \rightarrow 0.51$) measurements obtained.

In summary, the raising of the temperature of Tl_2SO_4 solution allows to form on the polymer the layer of thallium selenide with low structural disorder surface.

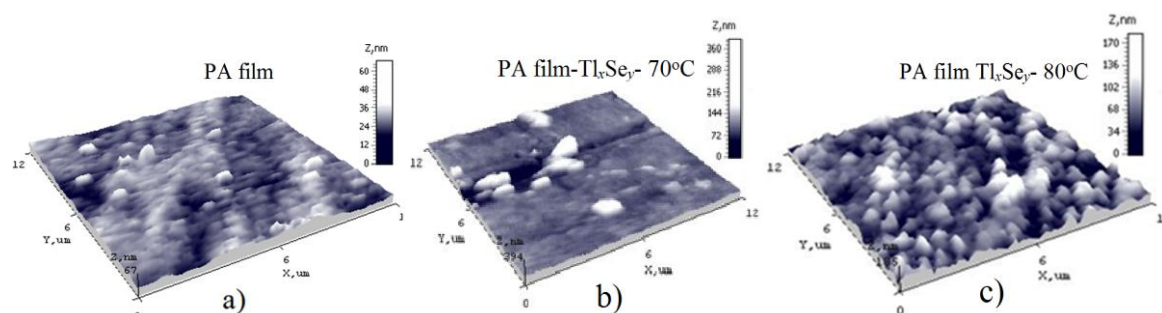


Fig. 1. X-ray diffraction 3D-AFM topographical images of PA film without and with thallium selenide layers.

Table 1. The data of roughness surface of PA 6 film and without and with thallium selenide layers.

Sample	Maximum Height A , nm	Average Height Z_{mean} , nm	Average Roughness, R_a , nm	Root-Mean-Square Roughness R_q , nm	Skewness R_{sk} , nm
PA film	67.4	27.76	3.45	4.59	0.82
PAfilm- Tl_3Se_7 -70°C	393.6	109.48	15.4	27.8	3.00
PA-film- Tl_3Se_7 -80°C	185.2	68.64	18.4	23.4	0.51

Acknowledgements. This work was partly supported by project "Promotion of Student Scientific Activities" (VP1-3.1-ŠMM-01-V-02-003) from the Research Council of Lithuania. This project is funded by the Republic of Lithuania and European Social Fund under the 2007–2013 Human Resources Development Operational Programme's priority 3.

References

1. A. Author, B. Author, *J. Am. Chem. Soc.*, **2010**, *01*, 20. N.B. Singh, G. Kanner, M. Marable, A. Berghmans, D. Knuteson, D. Kahler, et al., *Emerg. Mater. Res.*, **2012**, *01*, 185.
2. R. Sreekumar, T.H. Sajeesh, T. Abe, Y. Kashiwaba, C. Sudha Kartha, K.P. Vijayakumar, *Phys.Stat. Sol.*, **2013**, *250*, 95.
3. S. Hussein, A. Nagat, N. Mohamed, *Cryst. Res. Technol.*, **1989**, *24* (7), 685.
4. P.Nayar, W. Hamilton, *Appl. Optics*, **1977**, *16* (11), 2942.
5. A. Panich, M. Shao, C. Teske, W. Bensch, *Phys. Rev. B*, **2006**, *74*, 233305.
6. R.N. Bhattacharya, P. Pramanik, *Bull. Mater. Sci.*, **1981**, *3*, 403.
7. D. Suteu, D. Bilba, F. Dan, *J. Appl. Polym. Sc.*, **2007**, *105*, 1833.
8. M. Mangalam, K Rao Nagaraja, N. Ranganajan, M. Siddiqi, C. Suryanarayana, *J. Phys. Soc. Jpn.*, **1969**, *8*, 1258.
9. G. Shaw, I. Parkin, *Main Group Met. Chem.*, **2001**, *24* (4), 195.



PRODUCTION OF POTASSIUM DIHYDROGEN PHOSPHATE

K. Jančaitienė, R. Šlinkšienė

Department of Physical and Inorganic Chemistry, KTU

Radvilėnų pl. 19, LT-3028 Kaunas, Lithuania

E-mail address: kristina.jancaitiene@ktu.lt

The aim of this work is to analyze the possibilities of producing potassium dihydrophosphate from aqueous solutions of KCl and $\text{NH}_4\text{H}_2\text{PO}_4$, by conversion method, when the molar ratio is equal as 0.8:0.2, the temperature 60 °C.

Introduction

Potassium is an essential plant nutrient and is required in large amounts for proper growth and reproduction of plants. Potassium is considered second only to nitrogen, when it comes to nutrients needed by plants, and is commonly considered as the “quality nutrient.” It affects the plant shape, size, color, taste and other measurements attributed to healthy produce. Plants absorb potassium in its ionic form, K^+ .

Potassium has many different roles in plants: in photosynthesis, potassium regulates the opening and closing of stomata, and therefore regulates CO_2 uptake; potassium triggers activation of enzymes and is essential for production of Adenosine Triphosphate (ATP), ATP is an important energy source for many chemical processes taking place in plant issues; potassium plays a major role in the regulation of water in plants (osmo-regulation), both uptake of water through plant roots and its loss through the stomata are affected by potassium; known to improve drought resistance; protein and starch synthesis in plants require potassium as well, potassium is essential at almost every step of the protein synthesis, in starch synthesis, the enzyme responsible for the process is activated by potassium; activation of enzymes – potassium has an important role in the activation of many growth related enzymes in plants [1]. KCl is often a component of different compound fertilizers or mixes of fertilizers. It is suitable for fertilization of most plants, in particular cereal corn. On the other hand, a high concentration of chlorine (47.7 %) does not allow its use for fertilization of sensitive plants: grapes, hops, tobacco, most vegetables and especially flowers. Potassium fertilizers without chlorine are used for these plants: potassium sulfate, more rarely – potassium nitrate, and even more rare – potassium phosphates. Usage of potassium phosphates, in particular concentrated potassium and phosphorus fertilizers, is restricted by the high price of the product. Therefore it is mostly used for fertilization of greenhouse plants, as more expensive fertilizers do not make such a large part of their prime cost.

Potassium dihydrophosphate (KH_2PO_4) is crystalline material, with 34.60 % amount of potassium, recalculated into K_2O , and with 52.15 % of phosphorus, recalculated into P_2O_5 . Under normal conditions, KH_2PO_4 is stable and a nonflammable material. It can be used not only as a component of mineral fertilizer or compound fertilizers [2], but also in the food industry as an additive (emulsifier, humectant, sequestrant, stabilizer, thickener) [3]. As a crystal, potassium dihydrophosphate is noted for its non – linear optical properties in a laser fusion system [4].

Experimental

The chemically pure substances of KCl and $\text{NH}_4\text{H}_2\text{PO}_4$ were used in this work. Conversion reaction between potassium chloride and ammonium dihydrophosphate was analyzed by the determination of balance between liquid and solid phases in izomolar series solutions. Aqueous solutions of these salts were prepared by dissolving basic materials – KCl and $\text{NH}_4\text{H}_2\text{PO}_4$ – in the following molar ratio: 1:0, 0.8:0.2, 0.6:0.4, 0.5:0.5, 0.4:0.6, 0.2:0.8, 0:1. Total amount of moles is equal to 5.5 mol.

The chemical composition of liquid and crystallized solid phases were analyzed by chemical analysis methods: concentration of ammonium nitrogen (NH_4^+) – by the Kjeldahl method [5]; concentration of phosphorus (P_2O_5) – by photocolourimetric method [5]; concentration of potassium (K_2O) – by marginal solutions method [6], by use of flame photometer PFP – 7; concentration of chlorine (Cl^-) – by potentiometric method, with use of silver nitrate [7].

All samples were characterized by X – ray powder diffraction (XRD), analysis infra-red molecular absorption spectroscopy (IR) [8] and scanning electron microscopy (SEM) [9].

Results and discussion

The balance of KCl and $\text{NH}_4\text{H}_2\text{PO}_4$ solid and liquid phases were analyzed under isothermal conditions at 60°C temperature. Phases were separated from each other by filtering through a Buchner filter and analyzed by chemical and instrumental analysis methods. Chemical composition of solid and liquid phases, determined by chemical methods, is presented in the Table 1.

As shown in the Table 1 the results of the balance composition of both phases is different.

Table 1. The chemical composition of liquid and solid phases, obtained during conversion at 60°C temperature

t, °C	KCl, mol.r.	$\text{NH}_4\text{H}_2\text{PO}_4$, mol.r.	Solid phase, %				Liquid phase, %			
			N	P	K	Cl	N	P	K	Cl
60	1.0	0	0	0	50.20	61.50	0	0	13.21	13.70
	0.8	0.2	0.85	21.66	32.27	1.87	1.39	1.11	12.41	13.71
	0.6	0.4	1.89	21.99	31.07	1.47	2.43	2.14	3.06	3.71
	0.5	0.5	3.90	22.03	28.75	0.63	2.69	2.86	2.73	7.75
	0.4	0.6	6.61	24.18	15.07	1.45	2.80	3.95	2.39	2.38
	0.2	0.8	10.21	28.61	12.24	1.31	3.19	5.31	1.36	1.85
	0	1.0	12.07	26.72	0	0	3.36	7.39	0	0

Content nitrogen in the solid phase varies from 0.85 to up 10.21 %, as well as phosphorus from 21.66 to up 28.61 %, potassium from 12.24 to up 32.27 %. Liquid phase composition varies as follows: nitrogen – 1.39 to 3.19 %; phosphorus – from 1.11 to 5.31 %, and potassium – from 1.36 to 12.41 %. The results shows that the largest concentrations of potassium at solid phase was obtained, when molar ratio of potassium chloride and ammonium dihydrogen phosphate was equal as 0.8:0.2.

On the basis of the data acquired by X-ray analysis (Fig. 1), it is safe to claim that, when molar ratio between potassium chloride and ammonium dihydrogen phosphate is 0.8:0.2, the composition of solid phase closest to that of potassium dihydrogen phosphate obtained at 60°C (Fig. 1, (a) curve). The below X-ray pictures show most of the peaks that are characteristic to potassium dihydrogen phosphate.

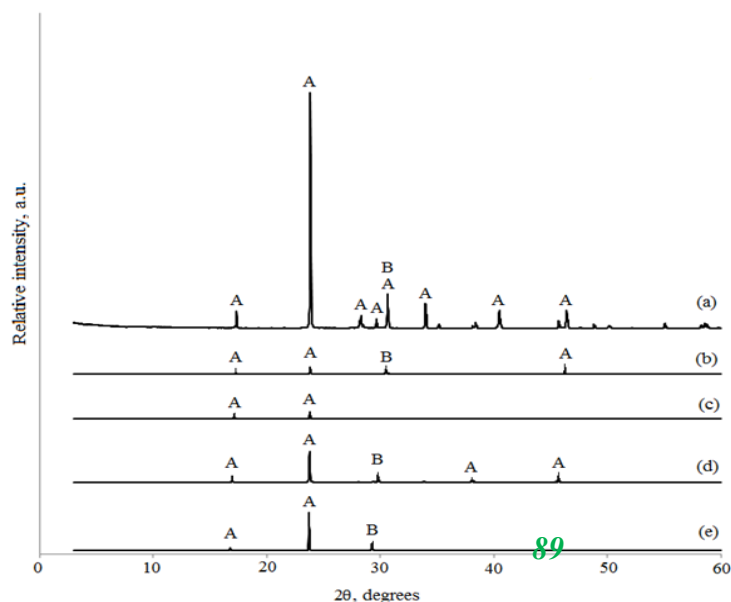


Fig. 1. The XRD analysis curves of the solid phase obtained during conversion, performed at 60°C temperature, when the molar ratio of KCl and $\text{NH}_4\text{H}_2\text{PO}_4$ is following: (a) – 0.8:0.2; (b) – 0.6:0.4; (c) – 0.5:0.5; (d) – 0.4:0.6; (e) – 0.2:0.8; A – KH_2PO_4 , B – KCl

IR spectra (Fig. 2) have been written in order to analyse the obtained solid phases in more detail. IR spectroscopic curves (Fig. 2, (a) – (e)) shows valence vibrations that correspond to NH_4^+ , $-\text{OH}$ and PO_4^{3-} functional groups.

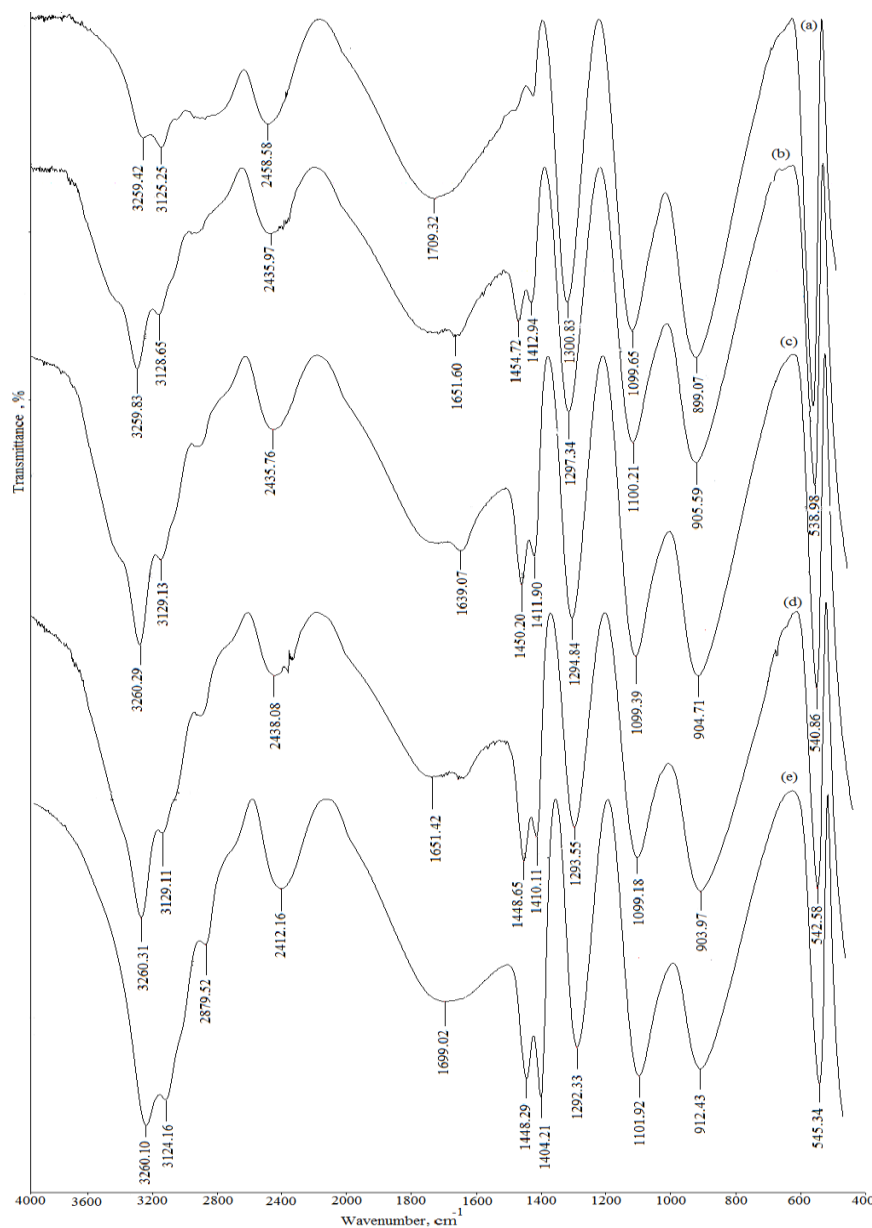


Fig. 2. IR spectrums of the solid phase obtained during conversion, performed at 60 °C temperature, when the molar ratio of KCl and $\text{NH}_4\text{H}_2\text{PO}_4$ is following: (a) - 0.8:0.2; (b) - 0.6:0.4; (c) - 0.5:0.5; (d) - 0.4:0.6; (e) - 0.2:0.8

Continuing the experiment, SEM pictures of the solid phase have been made (Fig. 3, a, b).

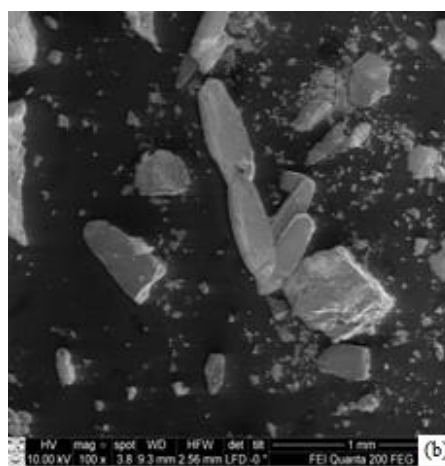
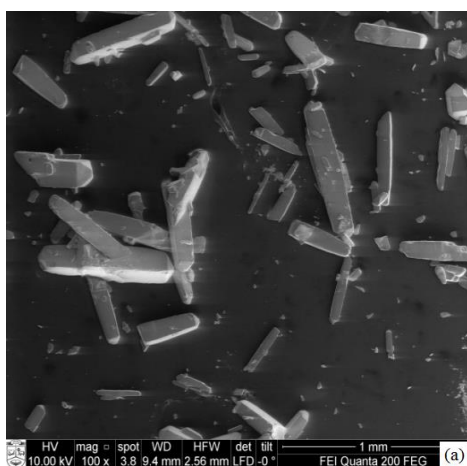


Fig. 3. Scanning electron micrographs of the pure KH_2PO_4 (a) particles and the product (b) particles, when the molar ratio of KCl and $\text{NH}_4\text{H}_2\text{PO}_4$ is equal as 0.8:0.2 performed at 60 °C temperature

The solid phase obtained during the conversion reaction between potassium chloride and ammonium dihydrogen phosphate at 60°C temperature (Fig. 3, b), is very similar to pure potassium dihydrogen phosphate (Fig. 3, a) by its surface and shape.

In order to get the most accurate results of the composition of the investigated materials, using the SEM method, their element schemes have been drawn (Fig. 4).

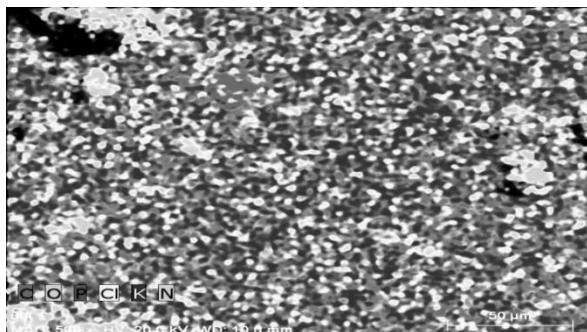


Fig. 4. SEM analysis (elements schemes) of the solid phase, when the molar ratio of KCl and $\text{NH}_4\text{H}_2\text{PO}_4$ is equal as 0.8:0.2 and performed at 60 °C temperature

The presented images show that the largest part in the composition of the analysed material consists of potassium, phosphorus and oxygen, and the presence of chlorine and ammonium is very low.

In some time, crystals of various shapes have developed in the leftover aqueous solutions after separation of the solid phase after the conversion reaction between KCl and $\text{NH}_4\text{H}_2\text{PO}_4$ (Fig. 5). As can be seen from this picture, crystals has a tetragonal structure.

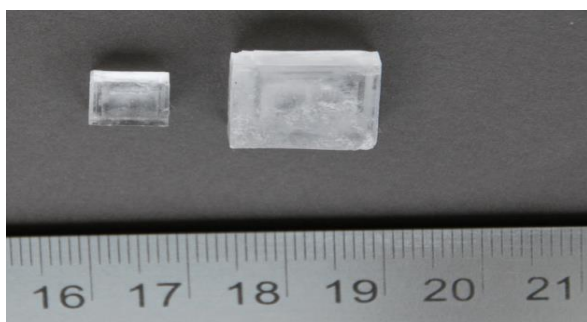


Fig. 5. Photograph of grown crystals, when the molar ratio of KCl and $\text{NH}_4\text{H}_2\text{PO}_4$ is equal as 0.8:0.2 and performed at 60 °C temperature

Conclusions

It was determined that in the solid phase, when the molar ratio of potassium chloride and ammonium dihydrophosphate is equal as 0.8:0.2, a solid phase is obtain, with the composition (K – 32.27 %, P – 21.66 %) and performed at 60 °C temperature is according to composition of pure potassium dihydrophosphate (K – 28.67 %, P – 22.79 %). The XRD data, IR and SEM analysis confirmed the results of chemical analysis.

References

1. Acces to the internet: <http://www.smart-fertilizer.com/articles/potassium-in-plants>.
2. R. Paleckienė, A. M. Sviklas, *Agrochemicals of the fertilizers*, Kaunas, **2012**, 152.
3. CODEXalimentarius [<http://www.codexalimentarius.net/gsaonline/additives/details>].
4. Jegatheesan, J. Murugan, B. Neelakantaprasad, G. Rajarajan, *International Journal of Computer Applications*, **2012**.
5. *The Fertilizers (Sampling and Analysis) regulations // Agriculture. Statutory Instruments*, London , **1991**.
6. D. Mickevičius, *Methods of chemical analysis (First part)*, Vilnius, **1998**, 408.
7. D. Mickevičius, *Methods of electrochemical analysis*, Vilnius, **1977**.
8. R. Šiaučiūnas, K. Baltakys, A. Baltušnikas, *Instrumental analysis of the silicate materials*, Kaunas, **2007**, 245.
9. Scanning Electron Miceroscope. Acces to the internet: <http://www.purdue.edu/rem/rs/sem.htm>.

**SOL-GEL DERIVED THIN FILMS OF CALCIUM HYDROXYAPATITE:
COMPARISON OF TWO COATING TECHNIQUES****V. Jonauskė^{1,*}, A. Prichodko¹, Z. Stankeviciute², R. Raudonis², A. Beganskiene¹, A. Kareiva¹**¹ *Department of Inorganic Chemistry, Faculty of Chemistry, Vilnius University, Naugarduko str. 24, Vilnius LT-03225, Lithuania*² *Department of Applied Chemistry, Faculty of Chemistry, Vilnius University, Naugarduko str. 24, Vilnius LT-03225, Lithuania***E-mail: vilma.jonauske@chf.stud.vu.lt*

Calcium hydroxyapatite ($\text{Ca}_{10}(\text{PO}_4)_6(\text{OH})_2$, CHAp) is the main inorganic component of natural human hard tissues. Artificial or synthetic CHAp is known as bioactive material. Consequently, CHAp supports the growth of natural tissues, being resistant to the side effects from immune system [1]. Due to the chemical similarity between synthetic CHAp and natural bone, synthetic CHAp exhibits strong affinity to host hard tissues and has excellent biocompatibility and osteoconductivity [2, 3]. Due to these properties CHAp is widely used in medical field such as orthopedic devices, dental replacements, tissue engineering, antimicrobial coating applications [4, 5]. However, the mechanical weakness of the CHAp limits its practical applications to those requiring little or no load bearing parts. For this reason, CHAp-coated metallic implants have the potential to be used for load-bearing implant applications in dentistry and orthopedics [6, 7]. Due to its low cost, strong mechanical properties and good formability the most widely used material for these medical and dental applications is 316L stainless steel [8, 9]. The performance of metals and their alloys with bioactive CHAp coating gave promising results [10].

Several synthesis methods for the preparation of calcium hydroxyapatite films on different substrates are suggested: plasma spray technique, pulsed laser deposition, electrophoretic deposition, hot pressing, magnetron sputtering, biomimetic process, polymeric route, micro-arc oxidation, sol-gel processing. Sol-gel processing route for thin films have some benefits over other methods such as simplicity, synthesis at low temperatures, effectiveness, suitability for complex-shaped implants and cost efficiency [11, 12]. Our activity in this work was focused on the synthesis of CHAp coatings on 316L stainless steel substrate using sol-gel processing route. The next aim was a comparison of suitability of two different coating techniques, such as dip-coating and spin-coating.

Calcium acetate monohydrate and phosphoric acid were used as precursors for the preparation of CHAp coatings. As was already mentioned, dip-coating and spin-coating techniques were employed to produce CHAp coatings by sol-gel method. CHAp thin films were obtained by coating the substrates 1, 5, 15 and 30 times. Stainless steel rectangles were dip-coated in the gel solution, with immersing and a withdrawal rates of 85 mm/min and 40 mm/min, respectively. For spin-coating, approximately 0.5 ml of coating solution was placed on top of the round substrate using syringe and then spin coated at 2000 RPM for 60 s in air. Both rectangle and circle substrates were annealed up to 30 times following the same procedures accordingly. The samples of CHAp precursor gels on the substrates were heated in an oven at 850 °C for 5 h. For the characterization of obtained samples, the coatings were analysed using X-ray diffraction (XRD) analysis, scanning electron microscopy (SEM), Fourier transform infrared spectroscopy (FTIR), atomic force microscopy (AFM) and the contact angle measurements. The results of analyses of calcium hydroxyapatite thin films on stainless steel substrate are evaluated and discussed. The obtained results have showed that both dip-coating and spin-coating techniques are suitable for the preparation of CHAp thin films on stainless steel substrate. It was demonstrated, that the formation of calcium hydroxyapatite depends on

dipping (or spinning) time and annealing duration. After the first immersing, withdrawal and annealing procedures the formation of amorphous phases took place. More intensive diffraction peaks attributable to CHAp phase were observed in the XRD patterns of specimens obtained after 15 dip-coating or spin-coating procedures. With further increasing immersing, withdrawal and annealing to 30 times, the only peaks of calcium hydroxyapatite and calcium phosphate phases could be detected.

The financial support to A.P. from the Research Council of Lithuania under project "Postdoctoral Fellowship Implementation in Lithuania" (No. 004/102) is acknowledged.

References:

1. L.Q. Tri, D.H.C. Chua, *Applied Surface Science*, **2009**, 256, 76–80.
2. I. Bogdanoviciene et al., *Materials Research Bulletin*, **2006**, 41, 1754–1762.
3. D.-M. Liu et al., *Biomaterials*, **2001**, 22, 1721–1730.
4. H.H. Beheri et al., *Materials and Design*, **2013**, 44, 461–468.
5. M. Sygnatowicz, A. Tiwari, *Materials Science and Engineering*, **2009**, 29, 1071–1076.
6. D.-M. Liu et al., *Biomaterials*, **2002**, 23, 691–698.
7. B.-D. Hahn et al., *Thin Solid Films*, **2011**, 519, 8085–8090.
8. T. Fu et al., *Vacuum*, **2012**, 86, 1402–1407.
9. I. Gurappa, *Surface and Coatings Technology*, **2002**, 161, 70–78.
10. H. Khandelwal et al., *Applied Surface Science*, **2013**, 265, 30–35.
11. C. J. Tredwin et al., *Dentalmaterials*, **2013**, 29, 166–173.
12. T. Kokubo et al., *Biomaterials*, **2003**, 24, 2161–2175.

A SPECTROPHOTOMETRIC STUDY OF GREEN PYROTECHNIC FLAME PROPERTIES USING AMMONIUM PERCHLORATE, BARIUM NITRATE, SHELLAC SYSTEM

D. Juknelevicius¹, R. Kubilius², L. Mikoliunaite¹, A. Ramanavicius¹

1) Vilnius university faculty of chemistry, Naugarduko 24, LT-03225, Vilnius

2) Pyrotechnics R&D department, Blikas Ltd., Motorų 6, LT-02190, Vilnius

E-mail: dominykas24@gmail.com

Barium compounds have been used for green colored flame production in pyrotechnics and military [1-4]. At high temperatures (2000 K) barium can undergo reactions in flame to form BaO, BaOH, BaCl, that produce certain emissions in UV-VIS range [3, 5]. Depending on the pyrotechnic composition and the ratio of the constituents, flames of different nature can be obtained. Usually the ratio is adjusted to obtain best colored flame quality, maximum light output or a desired burning rate.

In this experiment green flame's spectrophotometric measurements were performed. The three-component pyrotechnic system of barium nitrate, ammonium perchlorate and shellac resin was analyzed and compared. The ratio of oxidizers varied in the experiment in order to analyze flame kinetics i.e. to see how it influences the formation of certain emitters.

The experimental setup and methodic was similar as in previous experiments [6]. The pyrotechnic compositions for colored flame production were prepared by mixing dry, finely ground ingredients. The ratios of the components were selected in a way to maintain oxygen balance equal to zero. Pellets of compositions were pressed with a hydraulic press and afterwards a fuse was pasted on the top of the pellet for ignition. The finished test units were dried and burned in a spectrophotometric measurement stand. Flame's emission spectra and burn rates of the compressed compositions were registered by measuring radiant flux at a certain wavelength λ in time. The spectrometer OceanOptics USB4000 was used to acquire spectral data in UV-VIS range. The emission spectra were analyzed and color points and excitation purity in CIE 1931 chromaticity diagram were calculated (Figure 1).

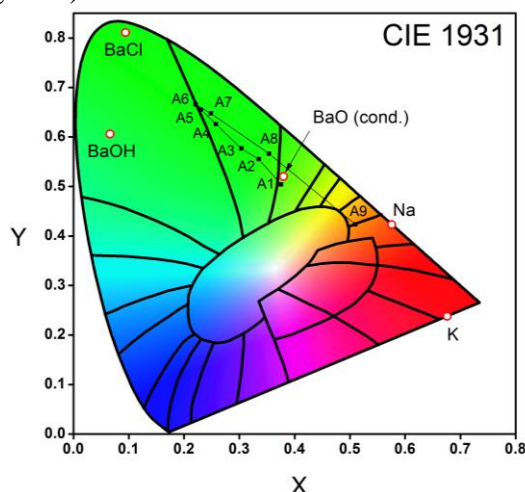


Figure 1. The distribution of experimental color points in CIE 1931 chromaticity diagram.

References

1. J.D. Moretti, S.M. Harbol, D.E. Riegner, N. Carlucci, J.J. Sabatini, J.C. Poret, J. Energ. Mater. 2014, **32**, 293.
2. G. Steinhäuser, T.M. Klapötke, Angew. Chem. Int. Ed. 2008, **47**, 3330.
3. K.L. Kosanke, B.J. Kosanke, J.Pyro. Inc., Whitewater 2004, p. 1.
4. W. Meyerriecks, K.L. Kosanke, J. Pyro. Inc. 2003, **18**, 1.
5. B.E. Douda, Report AD A951815, U.S. Naval ammunition depot, Crane, Indiana 1964.
6. D. Juknelevicius, L. Mikoliunaite, S. Sakirzanovas, R. Kubilius, A. Ramanavicius, Z. Anorg. Allg. Chem. 2014, **640**, 2560.

REPRODUCIBILITY OF SOL-GEL SYNTHESIS METHOD: CASE OF CALCIUM HYDROXYAPATITE

S. Kareiva^{1,*}, **Z. Stankeviciute**¹, **A. Beganskiene**², **A. Selskis**³, **F. Ivanauskas**⁴, **V. Klimavicius**⁵, **V. Balevicius**⁵, **S. Sakirzanovas**¹, **A. Kareiva**²

¹ *Department of Applied Chemistry, Faculty of Chemistry, Vilnius University, Naugarduko 24, Vilnius LT-03225, Lithuania*

² *Department of Inorganic Chemistry, Faculty of Chemistry, Vilnius University, Naugarduko 24, Vilnius LT-03225, Lithuania*

³ *Institute of Chemistry, Center for Physical Sciences and Technology, A. Gostauto 9, LT-01108 Vilnius, Lithuania*

⁴ *Department of Computer Science, Vilnius University, Naugarduko 24, LT-03225, Vilnius, Lithuania*

⁵ *Department of General Physics and Spectroscopy, Vilnius University, Sauletekio 9-3, LT-10222 Vilnius, Lithuania*

**E-mail: simonas@5grupe.lt*

Calcium hydroxyapatite ($\text{Ca}_{10}(\text{PO}_4)_6(\text{OH})_2$, CaHA) due to the chemical similarity with natural bone exhibits strong affinity to host hard tissues and has excellent biocompatibility and osteoconductivity [1-6]. Due to these properties CaHA is widely used in medical field such as orthopedic devices, dental replacements, tissue engineering, antimicrobial coating applications [7-15]. The human bone structure very much depends on the bone type, location of bone in the human skeleton, on human age, gender, race and other factors. Especially the morphological features of bone microstructure are different for young healthy and osteoporotic specimens (Fig. 1).

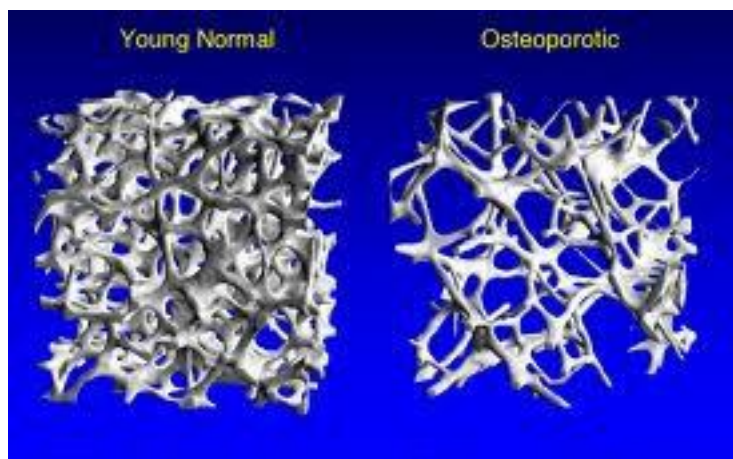


Fig. 1. The microstructure of healthy and osteoporotic human bones.

Therefore, for the practical applications the CaHA should be prepared with different porosity and with particles having different shape, size and particle size distribution. Several synthesis methods for the preparation of calcium hydroxyapatite are suggested: co-precipitation, spray pyrolysis technique, microwave radiation, solid state reaction, biomimetic process, polymeric route, and sol-gel processing. Sol-gel processing route for thin films have some benefits over other methods such as simplicity, synthesis at low temperatures, effectiveness, and cost

efficiency. It must be emphasized, that the scientists have synthesized a variety of different structures of calcium hydroxyapatite (Fig. 2).

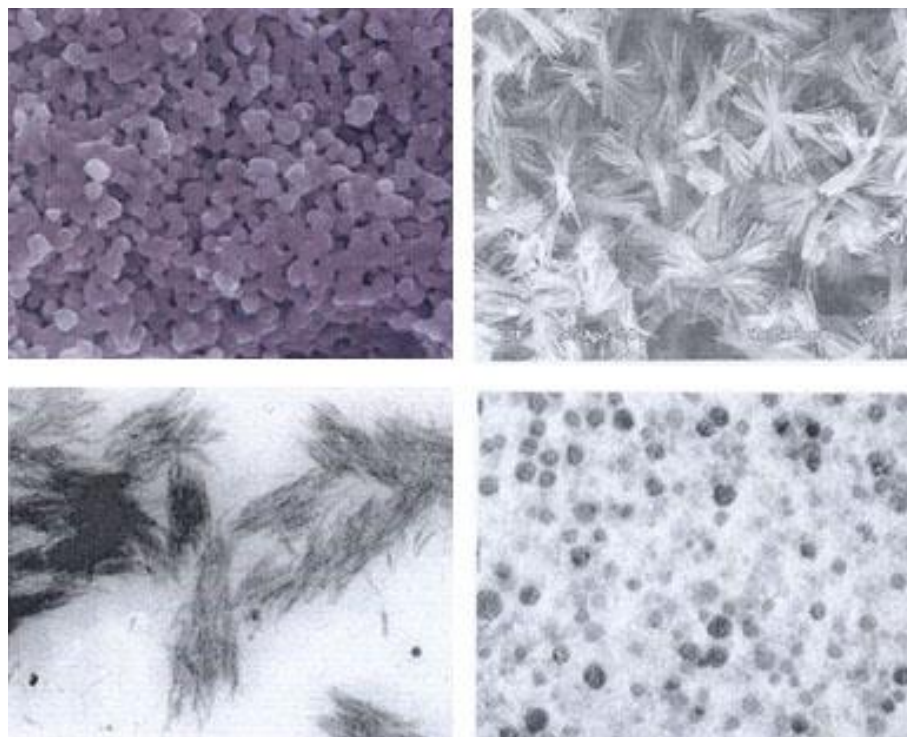


Fig. 2. SEM micrographs of synthetic CaHA samples.

However, the pure reproducibility of the results still remains a problem for the synthetic chemists. In this work, calcium hydroxyapatite was synthesized using modified sol-gel methods in order to investigate the repeatability of results. Five different complexing agents were selected to be used in the sol-gel processing experiments: EDTA ($C_{10}N_2H_{16}O_8$), DCTA ($C_{14}H_{22}N_2O_8 \cdot H_2O$), tartaric acid ($C_4H_6O_6$), ethylene glycol ($C_2H_6O_2$) and glycerol ($C_3H_8O_3$).

For the preparation of $Ca_{10}(PO_4)_6(OH)_2$ calcium acetate monohydrate, $Ca(CH_3COO)_2 \cdot H_2O$, and phosphoric acid, H_3PO_4 , were selected as Ca and P sources, respectively, in Ca/P mole ratio 1.67. Firstly, calcium acetate monohydrate was dissolved in distilled water under continuous stirring at 65 °C. After stirring at 60-65 °C for 1 h, the appropriate amount of H_3PO_4 was added to the above solution. Finally, complexing agent dissolved in 50 ml of distilled water was added. The obtained solution was stirred in a beaker covered with watch glass for 10 h at the same temperature. After evaporation of solvent the transparent white gels were obtained. The gels were dried in an oven for 10 h at 110 °C. The obtained powders were grinded in agate mortar and heated at 800 °C for 5 h, and repeatedly 2 times at 1000 °C for 5 h.

The synthesis products were characterized by infrared (IR) spectroscopy, X-ray powder diffraction (XRD) analysis, and scanning electron microscopy (SEM). NMR measurements were carried out on spectrometer operating at resonance frequencies of 400 and 162 MHz for 1H and ^{31}P , respectively, at 298 K.

All five complexing agents exhibited good properties in terms of compatibility with reaction. XRD analysis showed that calcium hydroxyapatite has formed as predominating phase independent on the nature of complexing agent. However, the purest phase was obtained from the sol-gel synthesis in which either ethylene glycol or glycerol were used. The investigation of repeatability of results has shown that sol-gel synthesis of calcium hydroxyapatite is sensitive to synthesis conditions. Again, best



repeatability of phase purity and morphological features of sol-gel derived calcium hydroxyapatite was obtained when ethylene glycol or glycerine were used as complexing agents.

References:

1. D.-M. Liu et al., *Biomaterials*, **2001**, 22, 1721-1730.
2. I. Bogdanoviciene et al., *Materials Research Bulletin*, **2006**, 41, 1754-1762.
3. P. Malmberg and H. Nygren, *Proteomics*, **2008**, 8, 3755-3762.
4. P. Habibovic et al., *Journal of Orthopedic Research*, **2008**, 26, 1363-1370.
5. I. M. Pelin et al., *Materials Science and Engineering C*, **2009**, 29, 2188-2194.
6. L. Chen et al., *Nanotechnology*, **2011**, 22, 105708.
7. H.H. Beheri et al., *Materials and Design*, **2013**, 44, 461-468.
8. E. Rodriguez-Carmona, A. Villaverde. *Trends in Microbiology*, **2010**, 18, 423-430.
9. G. X. Tong et al., *Nanoscale*, **2014**, 6, 778-787.
10. I. Bogdanoviciene et al., *Key Engineering Materials*, **2014**, 617, 229-232.
11. E. Garskaite et al., *Crystal Engineering Communications*, **2014**, 16, 3950-3959.
12. S. V. Dorozhkin. *Journal of Materials Science: Materials in Medicine*, **2013**, 24, 1335-1363.
13. S. V. Dorozhkin. *Materials*, **2013**, 6, 3840-3942.
14. J. F. Wang et al., *International Journal of Molecular Science*, **2014**, 15, 10150-10168.
15. A. Kuttor et al., *Frontier Materials Science*, **2014**, 8, 46-52.



APPLICATION OF SOL-GEL METHOD FOR THE CONSERVATION OF METALS

E. Kiele^{1,*}, J. Senvaitiene^{1,2}, A. Grigucevičienė³, R. Ramanauskas³, R. Raudonis¹, A. Kareiva⁴

1 Department of Applied Chemistry, Faculty of Chemistry, Vilnius University, Naugarduko 24, LT-03225 Vilnius, Lithuania

2 Pranas Gudynas Centre for Restoration, Lithuanian Art Museum, Rudninku 8, LT-01135 Vilnius, Lithuania

3 Center for Physical Sciences and Technology, Institute of Chemistry, A. Goštauto 9, LT-01108 Vilnius, Lithuania

4 Department of Inorganic Chemistry, Faculty of Chemistry, Vilnius University, Naugarduko 24, LT-03225 Vilnius, Lithuania

Corrosion inhibitors, polymer and synthetic wax coatings are used for the conservation of historical metals and metal alloys. However, these methods do not provide successful preservation of metal objects for a longer time. Therefore, new methods for the conservation of metals' have been established. Investigations are essentially focused on the developing of better quality, faster, long-term, anticorrosion preservation methods that could be applied in conservation and restoration of metals.

The sol-gel method is one of the most prospective and newest techniques that have been widely applied for conservation of glass, mosaics and other cultural heritage objects. Various different coatings can be formed by using sol-gel method: hydrophobic, anticorrosion, protective and other. Sol-gel protective coatings have shown great chemical stability, oxidation control and enhanced corrosion resistance for metal substrates. Moreover, the sol-gel method is an environmentally friendly technique for the protection of surface and had showed the potential for the replacement of toxic pretreatments and coatings which have traditionally been used for increasing corrosion resistance of metals.

In the present study, a novel sol-gel processing route for the preparation of methyl-modified silica coatings on the surface of metals and metal alloys have been developed. The aim of the study was to inquire into the best properties containing coating that could be used for the conservation and preservation of metal objects in order to protect them from adverse influence of environment.

The mixture of silica sol (3% SiO₂) and hexamethyldisilozane (HMDS) was used for the preparation of methyl-modified silica sols which were applied for the surface treatment of metals. Coatings of methyl-modified silica sols were deposited on copper, brass, bronze and steel specimens. For the comparison, the polymeric coatings (Paraloid B 67, Cosmolloid H 80, Antik Patina) were also deposited on steel substrates. All specimens were photochemically aged and investigated.

The surface morphology features of uncoated and coated, unaged and aged specimens were investigated by atomic force microscopy (AFM), scanning electron microscopy and energy dispersion spectroscopic analysis (SEM-EDX). The hydrophobicity was evaluated by contact angle measurements. The surfaces of thin films were also characterized using Fourier transform infrared spectroscopy (FTIR) and electrochemical measurements.

SYNTHESIS AND CHARACTERIZATION OF IRON (III) ACETATE: PRECURSOR FOR METAL-ORGANIC FRAMEWORKS

A. Laurikenas, J. Barkauskas, A. Kareiva.

*Department of Inorganic Chemistry, Vilnius University, Naugarduko 24, LT-03225
Vilnius, Lithuania*

E-mail: andrius.lauriken@gmail.com

Iron (III) acetate is the coordination compound more commonly known as basic iron acetate. With the formula $[\text{Fe}_3\text{O}(\text{OAc})_6(\text{H}_2\text{O})_3]\text{OAc}$, (OAc is CH_3CO_2^-) it is a salt, composed of the cation $[\text{Fe}_3(\mu^3\text{O})(\text{OAc})_6(\text{H}_2\text{O})_3]^+$ and acetate anion [1]. Reduction of the cation affords the neutral mixed-valence derivative that contains one ferrous and two ferric centers. Former investigations revealed that iron (III) acetate is trinuclear [1, 2]. The Fe centres are equivalent, each being octahedral, being bound to six oxygen ligands, including a triply bridging oxide at the center of the equilateral triangle [3, 4]. The aim of this study was to prepare and characterize iron (III) acetate as a precursor for MOFs.

For the preparation of iron (III) acetate acetic acid/hydrogen peroxide type synthesis was chosen focusing on its simplicity [1,4]. 11,2 g of iron powders were placed in a beaker and 12 ml of 50 % acetic acid was added. Reaction mixture was heated to 75 °C and mixed till all of metallic iron fully reacted with acetic acid and mixture colour turned green. Next, 6 ml of 30 % hydrogen peroxide were added to fully oxidize Fe^{2+} ions to Fe^{3+} . The obtained mixture was filtered and solvent evaporated. Crude iron (III) acetate crystals were recrystallized from ethanol. 2,95 g of dark red crystals were obtained, yield 81 %.

The SEM micrographs of obtained crystals are shown in Fig. 1.

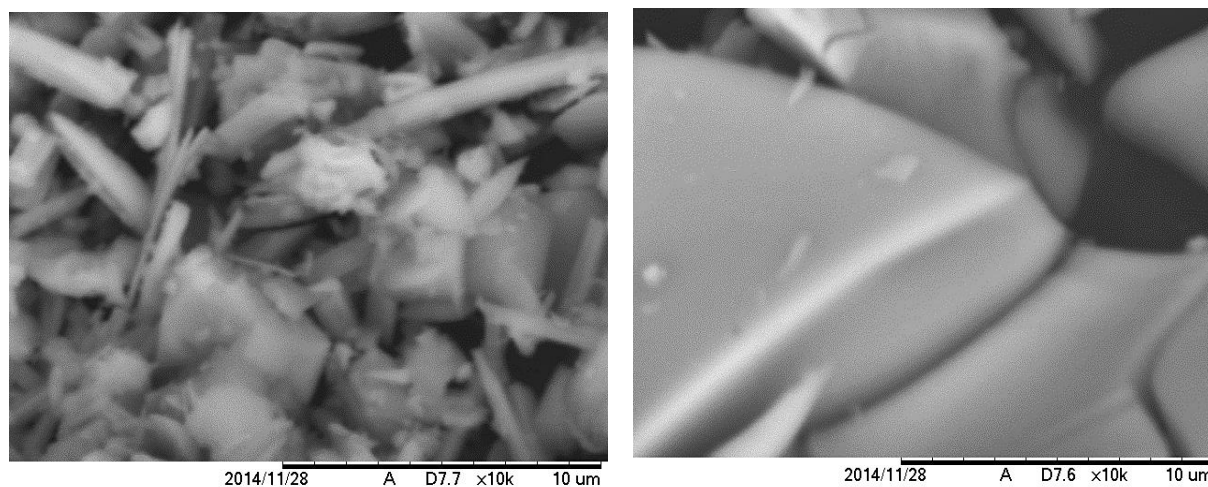


Fig. 1. SEM micrographs of crude (*left*) and recrystallized (*right*) iron (III) acetate. Magnification 10k x.

As seen, crude iron (III) acetate sample is composed of irregular form rods 50-80 μm in size. However, recrystallized sample shows different surface microstructure. Apparently, sharp-edged crystallites about 85-100 μm in size have formed during recrystallization process. Energy-dispersive X-ray spectroscopy (EDX) was used for the determination of elemental composition of synthesized sample (Table 1).

Table 1. Elemental analysis data for $\text{C}_{14}\text{H}_{27}\text{O}_{18}\text{Fe}_3$ determined from EDX.

Calculated %	C, 25.83; O 44.25; H 4.18; Fe 25.74
Found %	C, 27.04; O 43.81; H 2.01; Fe 27.14

The results from Table 1 show a good agreement between determined and calculated data. X-ray diffraction analysis results (see Fig. 2) let us to conclude that synthesized iron (III) acetate is partially amorphous.

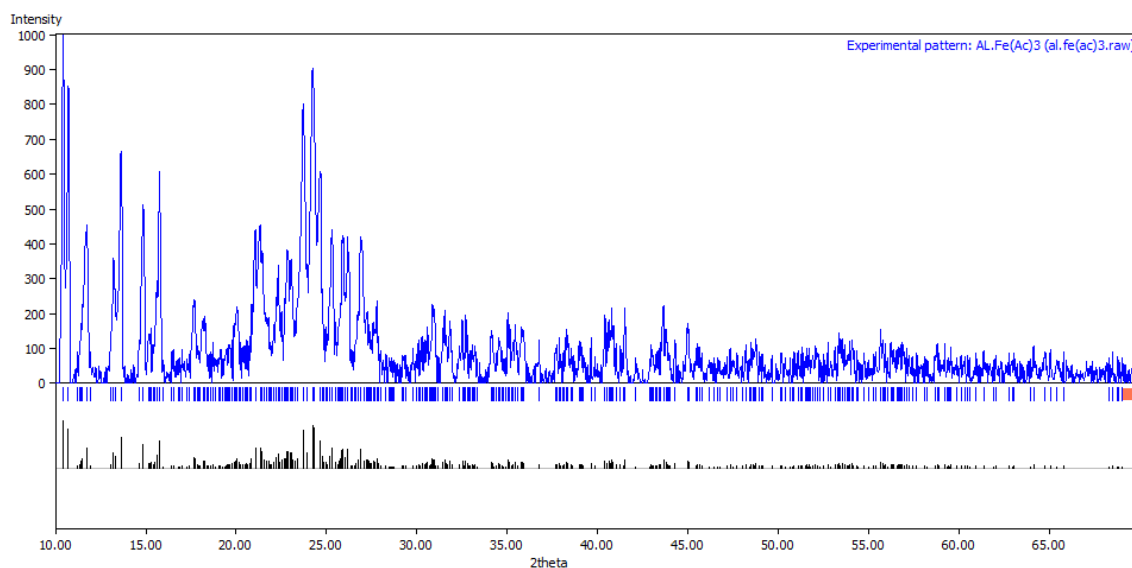


Fig 2. XRD pattern of iron (III) acetate.

References

1. K. I. Turte, S. G. Shova, V. M. Meriacre, M. Gdaniec, Y. A. Simonov. Synthesis and structure of trinuclear iron acetate. *Journal of Structural Chemistry*, 2002, Vol. 43, pp. 108-117,
2. B. N. Figgis, G. B. Robertson. Crystal-molecular structure and magnetic properties of $\text{Cr}_3(\text{CH}_3\text{COO})_6\text{OCl}\cdot 5\text{H}_2\text{O}$. *Nature*, 1965, Vol. 205, pp. 694-695.
3. J. Burgess, M. V. Twigg. Iron: Inorganic & Coordination Chemistry" *Encyclopedia of Inorganic Chemistry*, Ed. R. Bruce King, 2011.
4. R. C. Paul, R. C. Narula, S. K. Vasisht. Iron(III) acetates. *Transition Metal Chemistry*, 1978, Vol. 3, pp. 35-38.

WETTING OF GRAPHITE FELT WITH ETHANOL AQUEOUS SOLUTIONS

B. Macijauskienė, E. Griškonis

*Department of Physical and Inorganic Chemistry, Kaunas University of Technology,
Radvilėnų pl. 19, LT-50254 Kaunas, Lithuania
E-mail: brigita.macijauskiene@ktu.edu*

The carbon and carbon-based materials are widely investigated substances and find application in various areas of material science and technologies [1]. Graphite is one of the allotropic forms of carbon, which is characterized by strong anisotropy and good electrical conductivity. Both the natural and synthetic graphite, as well as some graphitized substances (e.g. polymers), beside good electrical conductivity, have low density, high thermal and chemical stability. Graphite felt (GF) is artificial material, often derived after carbonization and graphitization of polyacrylonitrile fiber felt [2]. Both the bare and modified GF are widely used in electrochemistry [3] and for development of new design microbial, direct methanol and regenerative fuel cells [4-7]. A wide range of methods are used for modification of GF to improve its chemical and electrochemical properties, but in most cases so-called wet-processes in aqueous solutions are employed. However, limitation of these processes is poor wettability of hydrophobic surface of GF fibers. The boiling in strong alkaline solutions and pretreatment in oxidizing inorganic acid solutions are applied for increasing of GF hydrophilicity [7, 8]. The surface of GF filaments becomes more hydrophilic after electrochemical oxidation in sulfuric acid solution as well [6]. Considerably quicker wetting of GF filaments can be achieved by using low surface tension liquids which are well miscible with water (eg. ethanol) and therefore later could be leached out from the GF matrix [9].

The aim of this investigation was to determine the minimum concentration of ethanol in the aqueous solution, which ensures fast enough and efficient wetting of filaments in the whole volume of GF matrix. GF samples of 20 mm length and 10 mm width were cut out from GF sheet of 4 mm thickness (Wale Apparatus, USA) and used throughout all experiments. Aqueous solutions of different concentrations of ethanol were prepared by mixing calculated volumes of double-distilled water (specific conductivity less than $0.5 \mu\text{S}\cdot\text{cm}^{-1}$) and ethanol $\text{C}_2\text{H}_5\text{OH}$ rectificate (96 %, v/v). Wettability of GF filaments was evaluated by measuring contact angle between outside surface of dry GF samples and approximately $4 \mu\text{l}$ volume droplets of distilled H_2O and aqueous solutions of different $\text{C}_2\text{H}_5\text{OH}$ concentrations at room temperature ($20\pm 1^\circ\text{C}$).

As seen in photographs (Fig 1.), surface of dry GF is highly hydrophobic and therefore droplets of H_2O did not penetrate in air-filled matrix of GF filaments for a long time (up to 24 hours and more). Contact angle between extremely rough surface of GF sample and droplets of distilled H_2O was approximately 130° and it is related with a very low surface energy of porous network of GF filaments.

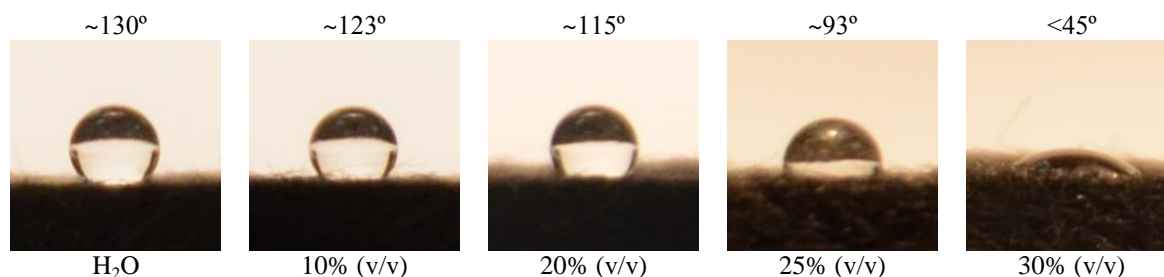


Fig. 1. Typical views of droplets of distilled H_2O and aqueous $\text{C}_2\text{H}_5\text{OH}$ solutions of different concentrations on the surface of dry GF sample at room temperature. Values of contact angle and concentration of $\text{C}_2\text{H}_5\text{OH}$ aqueous solutions are presented above and below the pictures, respectively.

Aqueous solutions containing up to 20 % (v/v) of C_2H_5OH also showed poor wettability of GF filaments. Contact angles between surface of GF sample and droplets of 10 % and 20 % (v/v) C_2H_5OH aqueous solutions were 123° and 115° , respectively. Satisfactory wettability of GF filaments was observed when concentration of C_2H_5OH in aqueous solution reached 25 % (v/v). In this case contact angle decreased to approximately 93° , and the droplet of 25 % (v/v) C_2H_5OH aqueous solution remained on the surface of GF sample only up to one minute before complete penetration into GF. Extremely good and quick wettability of GF filaments was shown by 30 % (v/v) C_2H_5OH aqueous solution. The droplets of this solution remained on the surface of GF sample for a very short time (up to few seconds) and the observed value of contact angle did not exceed 45° . GF samples impregnated with 25 % and 30 % (v/v) C_2H_5OH aqueous solutions and rinsed with distilled water subsequently demonstrated good wettability, if were not dried (Fig. 2). This phenomenon is most probably related to the fact that C_2H_5OH aqueous solutions of 25 % (v/v) and greater concentrations have almost twice lower surface tension than pure water [10]. Decreasing of surface tension of higher concentration C_2H_5OH aqueous solution led to decreasing of interfacial forces on the liquid-solid phases, i.e. C_2H_5OH solution-GF filaments, interface and easily filling of GF matrix with wetting liquid. Most probably, C_2H_5OH molecules, adsorbed on the surface of GF filaments, increase surface energy significantly and therefore GF filaments become more hydrophilic. It could be concluded that fast and easy hydrophilization of bare GF before further wet modification processes (e.g. electroless or electrodeposition of metals etc.) could be performed by using C_2H_5OH aqueous solution of at least (sufficient) 25 % (v/v) concentration.



Fig. 2. Typical views demonstrating different wettability of dry GF sample (left) and GF sample previously impregnated with 25 % (v/v) C_2H_5OH aqueous solution and rinsed with water (right). Both beakers filled with distilled H_2O .

References

1. T.D. Burchell, Carbon Materials for Advanced Technologies. Pergamon, New York, 1999.
2. M.S.A. Rahaman, A.F. Ismail, A. Mustafa, **92(8)** (2007) 1421-1432.
3. D. Golub, Y. Oren, Journal of Applied Electrochemistry, **20** (1990) 877-879.
4. Y. Zhang, J. Sun, Y. Hu, S. Li, Q. Xu, International Journal of Hydrogen Energy, **37** (2012) 16935-16942.
5. A. Bauer, E.L. Gyenge, C.W. Oloman, Journal of Power Sources, **167** (2007) 281-287.
6. J. Xi, W. Zhang, Z. Li, H. Zhou, L. Liu, Z. Wu, X. Qiu, Int. J. Electrochem. Sci., **8** (2013) 4700-4711.
7. H. Zhou, H. Zhang, P. Zhao, B. Yi, Electrochimica Acta, **51(28)** (2006) 6304-6312.
8. B. Sun, M.S. Kazacos, Electrochimica Acta, **37(13)** (1992) 2459-2465.
9. B.L. Ouay, Th. Coradin, Ch. Laberty-Robert, J. Mater. Chem. B, **1** (2013) 606-609.
10. G. Vasquez, E. Alvarez, J.M. Navaza, Journal of Chemical and Engineering Data, **40(3)** (1995) 611-614.

HIERARCHICAL NONSTRUCTURAL GROWTH OF COPPER METAL MATRIX COMPOSITE COATINGS WITH A CARBON NANOMATERIAL

V. Medelienė, A. Selskienė

Institute of Chemistry of Center for Physical Sciences and Technology, A. Goštauto 9, LT-01108 Vilnius, Lithuania

viktorija.medeliene@gmail.com

Creation of novel functional composite materials based on the nanocarbon is one of the directions of modern nanotechnology [1,2]. Advanced materials with a high innovation potential in many cases can be created through microstructural design in order to achieve desirable properties and performance. Nowadays, efforts are focused on the investigation of hierarchical architectures in comparison with the conventional multistage surface structure for further enhancement of the electrochemical and functional performance of materials. Hierarchical architectures of structure have attracted considerable interest of researchers in recent years, compared to a multistage structure due to their high surface-to-volume ratio, high organic pollutant adsorption, and excellent incident light scattering within the structures [3].

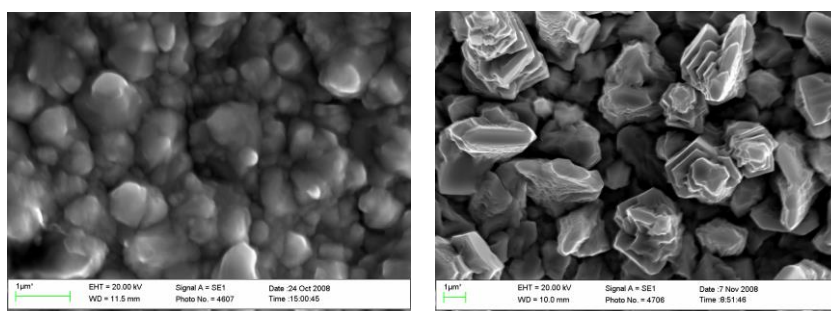


Fig. 1. SEM image of copper (a) and copper metal matrix composite Cu-CNM (b) coatings.

It has been determined that the composite electrodeposited in an acidic copper electrolyte composite with a crossbred carbon based CNM nanomaterial stimulated formation of nanostructured coatings with a smoother relief as compared with that of a pure copper coating and had lower R_a parameters of the standard surface roughness: 69.3 ± 42 nm for the copper metal matrix composite Cu-CNM, while R_a of a pure copper coating is 253.7 ± 39 nm. The topographical study of the investigated composites has shown that the copper matrix has a fractal cauliflower-like structure, which is a specific feature of nanostructured coatings. The research has proved that a novel cauliflower-like nanostructure is distinguished for its hierarchical nonstructural formation and possesses a high surface area as compared to that of the multistage structure of a pure copper coating (Fig. 1). This is an advantage leading to carbon-based copper metal matrix composite Cu-CNM fabrication.

Keywords: copper, carbon nanomaterial, nanocomposite, multistage structure, hierarchical structure

References

- [1] Qing Li, Nasir Mahmood, Jinghan Zhu *et al.*, *Nano Today*, 9 (5) (2014) 668.
- [2] V. Medelienė, V. Stankevič, *2011 Jahrbuch Oberflächentechnik* 67 (2011) 38.
- [3] S. Bernard, P. Miele, *Materials Today*, 17 (9) (2014) 443.

Acknowledgments. The authors wish to express their gratitude to prof. J. Barkauskas and dr. A. Rukšėnas for the synthesis of the CNM (Vilnius University, Department of Chemistry, Vilnius, Lithuania)

SYNTHESIS OF NaREF₄: Yb 20%, Er 2% (RE=Y, Gd) AND INITIAL CHARACTERIZATION FOR APPLICATIONS IN MRI

I. Mikalauskaitė¹, I. Lebedytė¹, M. Stalnionis², V. Karabanovas², A. Beganskienė¹, G. Streckytė²

¹Faculty of Chemistry, Vilnius University, Naugarduko st. 24, LT-03225, Vilnius, Lithuania

²National Cancer Institute, P. Baublio g 3b., LT-08406, Vilnius, Lithuania

E-mail: ieva.mikalauskaite@stud.chf.vu.lt

Upconversion is an optical process based on sequential absorption of more than one photons because of relatively long lifetime and favorable energy levels of rare earth ions. Due to very low toxicity, strong NIR-to-visible upconversion fluorescence [1] and high resistance to photobleaching [2], UCNPs are an alternative to organic dyes or quantum dots in biomedicine for cancer diagnostics and therapy. Compared to fluorescence imaging, magnetic resonance imaging (MRI) has better penetration ability in tissues [3], therefore Gd based materials could be a promising alternative for multimodal imaging.

NaYF₄ phonon energy is ~360 cm⁻¹ which explains why NaYF₄ is a suitable host lattice for efficient upconversion process involving different rare earth ions (mainly Er³⁺ and Tm³⁺)[4]. Various rare-earth metal ions provide different luminescence intensity at different emission bands. UCNPs properties depend on synthesis method (modified co-precipitation, reversed micelle, hydrothermal, thermal decomposition method) mostly due to particle size, shape and differences in overall luminescence efficiency. One of the most common methods is thermal decomposition, however, due to hydrophobic surface of obtained nanoparticles, further surface modification in order to be used in biological systems is inevitable.

From X-ray diffraction (XRD) analysis pure cubic NaYF₄:Yb 20%, Er 2% phase is obtained at 300 °C. Comparing to reference pattern of undoped NaYF₄ (PDF (ICDD) 00-077-2042), a slight shift towards smaller 2θ values can be indicated since larger Y³⁺ ions have been partially replaced by Yb³⁺, Er³⁺. By varying conditions of a typical thermal decomposition synthesis procedure different phase of NaYF₄ is obtained, indicating that less symmetrical hexagonal phase tends to form at 330 °C in 1 hour.

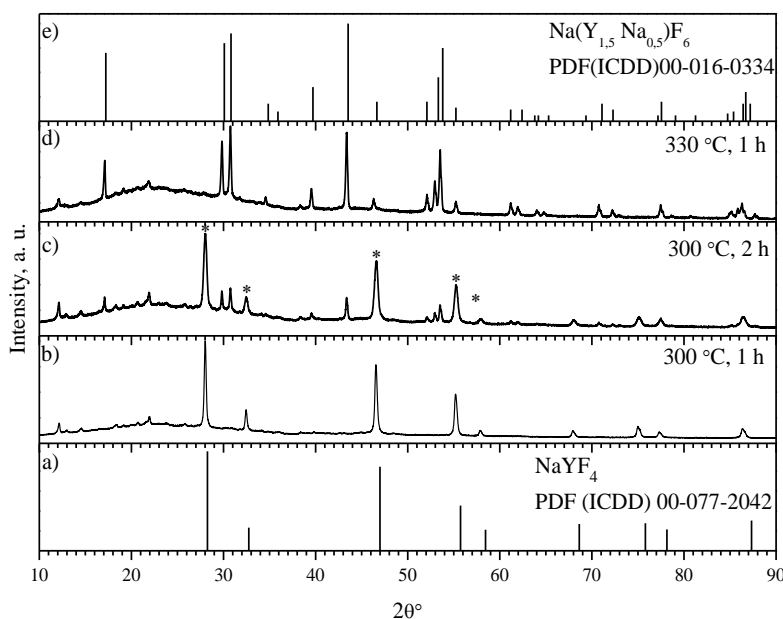


Figure 1. XRD patterns of NaYF₄ synthesized at different temperatures (b, d) and different duration (b, c).

Impurities (marked as asterisks) are indicated as cubic NaYF₄ phase

In order to obtain multimodal imaging agents, Y^{3+} ions in fluoride matrix were replaced with Gd^{3+} ions, leaving the same amounts of doping ions (Yb 20%, Er 2%). XRD analysis (Fig. 2) confirms that both cubic and hexagonal phase nanoparticles were formed at the same reaction conditions.

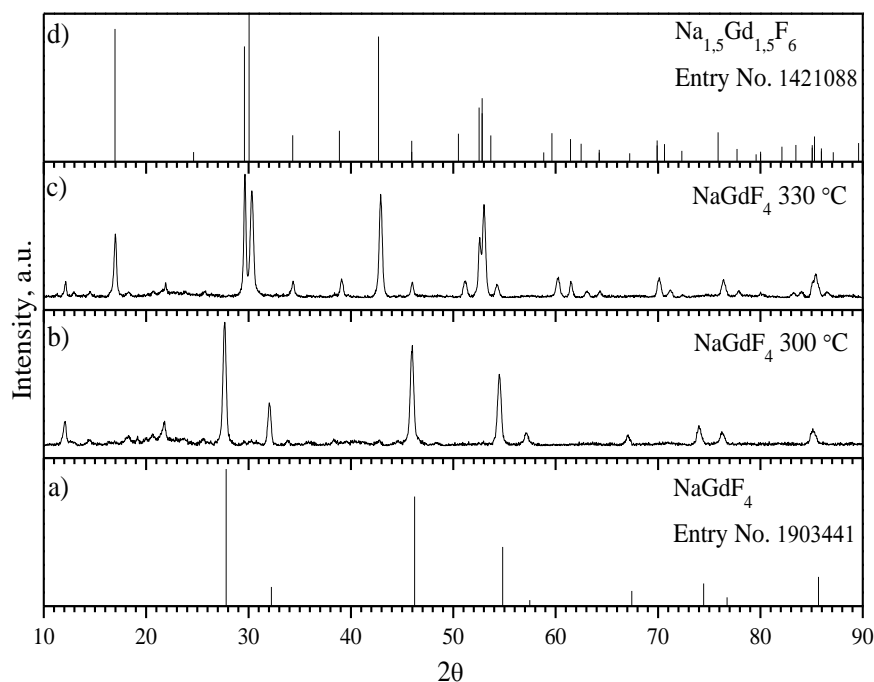


Figure 2. XRD patterns of $NaGdF_4$ synthesized at different temperatures (b, c). $NaGdF_4$ cubic (a) and hexagonal (d) phase reference patterns

Upconversion luminescence spectra of synthesized $NaREF_4:Yb\ 20\%,\ Er\ 2\%$ were measured under 980 nm laser diode excitation. Despite of different host material no significant emission band shifts can be seen in figure 3. The emission bands can be assigned to transitions of Er^{3+} ions: green emission at 522 nm corresponding to ${}^2H_{11/2} \rightarrow {}^4I_{15/2}$ transition and at 540 nm corresponding to ${}^4S_{3/2} \rightarrow {}^4I_{15/2}$ transition as well as red emission at 653 nm corresponding to ${}^4F_{9/2} \rightarrow {}^4I_{15/2}$ transition. Moreover, blue emission band at 409 nm corresponding to ${}^2H_{9/2} \rightarrow {}^4I_{15/2}$ transition is noticeable in hexagonal phase (Fig. 3, blue line).

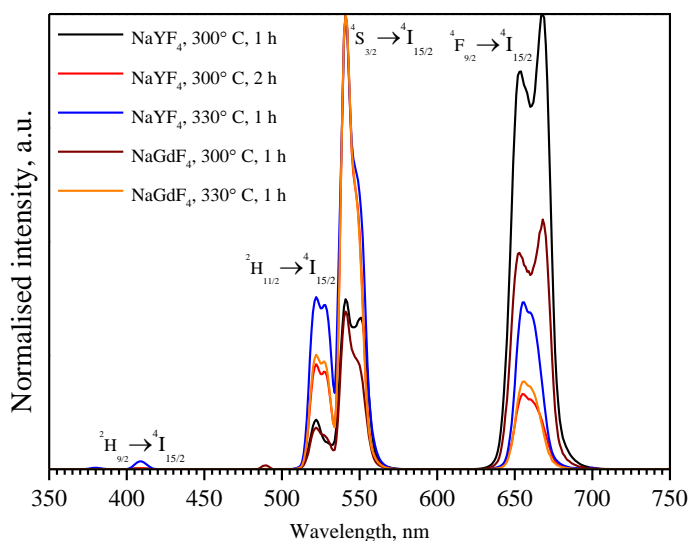


Figure 3. Upconversion luminescence spectra of $NaREF_4:Yb\ 20\%,\ Er\ 2\%$ particles (RE=Y, Gd)

However, for full application in biology or medicine, it is necessary to modify the hydrophobic surface of the UCNPs. One of the main drawbacks when dispersing nanoparticles in aqueous media is reduced upconversion luminescence intensity due to quenching effect of water. Upconversion luminescence measurement was performed after surface modification with nonionic triblock copolymer Pluronic F-127.

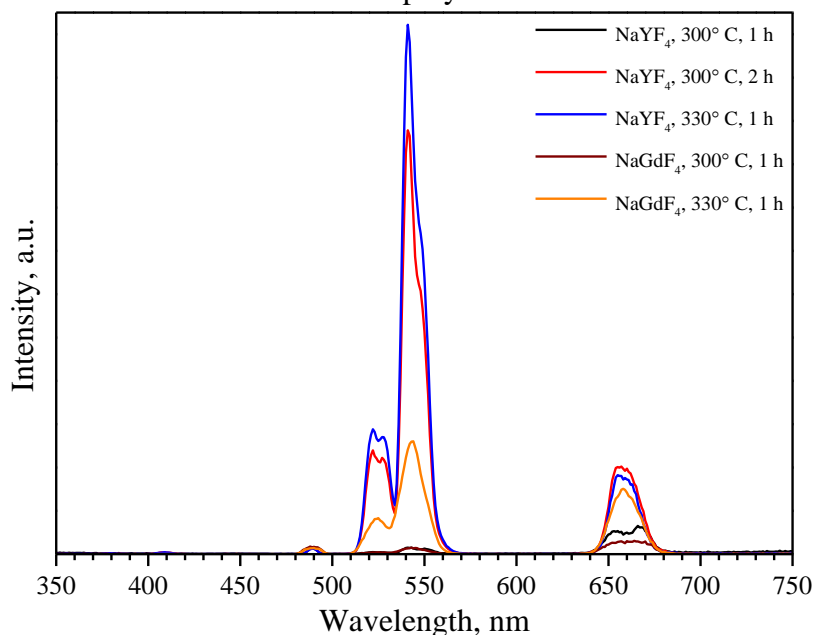


Figure 4. Upconversion luminescence spectra of NaREF₄: Yb 20%, Er 2% particles (RE=Y, Gd) after surface modification with Pluronic F127

From figure 4 it can be seen, that emission peaks assigned to Er³⁺ ion transitions from excited energy levels to ground level ⁴I_{15/2} remains unaffected, whereas a decrease in emission intensity by several orders of magnitude is apparent. However, this drawback will not outweigh the benefits of UCNP as multimodal fluorophores.

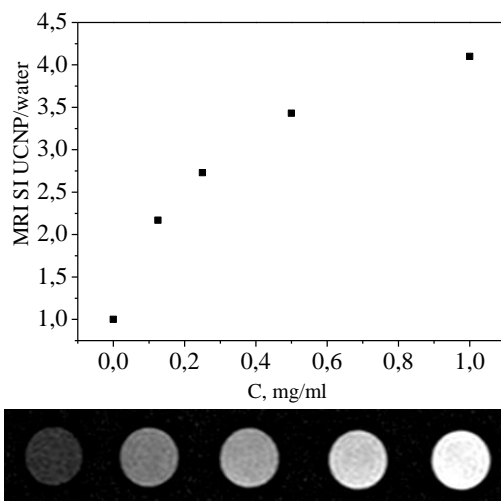


Figure 5. Signal intensity of aqueous suspensions of UCNP versus the concentration of NaGdF₄: Yb 20%, Er 2% in solution. The insert on the graph shows transversal slices of T1-weighted MR in vitro images of different concentrations of UCNP dissolved in water



A Pluronic F127 solution with certain amount of UCNP was placed in a series of 2 mL plastic Eppendorf test tubes varying the concentration of UCNP for imaging. The tubes containing the UCNP solutions were arrayed in order of concentrations, and water was placed as a control. From the measurements it can be seen, that such UCNP's can enhance the MRI signal intensity up to 4-fold compared with water (Figure 5).

Therefore, in order to prepare multimodal NaGdF₄: Yb 20%, Er 2% imaging agents, only a simple surface modification procedure is required with no additional treatment during the modification procedure. Further evaluation of hydrophilic UCNPs impact on the viability of cells needs to be carried out.

References

1. R. A. Jalil, Y. Zhang. *Biomaterials* **2008**, *29*, 4122-4128.
2. M. Wang, G. Abbineni, A. Clevenger, C. B. Mao, S. K. Xu. *Nanomed-Nanotechnol* **2011**, *7*, 710-729.
3. X. Wu, M. Wu, J. L. X. J. Zhao. *Nanomed-Nanotechnol* **2014**, *10*, 297-312.
4. J. F. Suyver, J. Grimm, M. K. van Veen, D. Biner, K. W. Kramer, H. U. Gudel. *J Lumin* **2006**, *117*, 1-12.

SYNTHESIS AND CHARACTERISATION OF SrAl₄O₇**M. Misevicius, G. Kibildaite, A. Kareiva***Department of Inorganic Chemistry, Vilnius University, Naugarduko st. 24, LT-03225
Vilnius, Lithuania**E-mail: martynas.misevicius@chf.vu.lt***Introduction**

In SrO-Al₂O₃ system, there are four stable double oxides, namely Sr₃Al₂O₆, SrAl₂O₄, SrAl₄O₇ and SrAl₁₂O₁₉, and other strontium aluminates phases, such as Sr₄Al₂O₇, Sr₄Al₁₄O₂₅, Sr₁₂Al₁₄O₃₃ and Sr₁₀Al₆O₁₉, as described in the literature [1]. The most publications on strontium aluminates phases are related with the strong green emission (~530 nm) of Eu²⁺ in stoichiometric SrAl₂O₄ with monoclinic trydimite structure [2, 3]. It was reported that SrAl₂O₄:Eu²⁺, Dy³⁺, B³⁺ has greatly enhanced phosphorescence properties compared not only with SrAl₂O₄:Eu²⁺, but also with ZnS:Cu⁺, Co²⁺. In addition to higher chemical stability, the intensity and the duration of the phosphorescence of SrAl₂O₄:Eu²⁺, Dy³⁺, B³⁺ make it possible to observe a continuous light emission for 10 h, hence greatly renewing interests in the phosphorescence phenomenon [4].

Strontium aluminate SrAl₄O₇ structure is monoclinic with space group C2/c (No. 15) and having cell parameters $a = 13.04$, $b = 9.01$, $c = 5.55$ and $\beta = 106.502^\circ$ [5]. It also has high-pressure form called β -SrAl₄O₇ [6]. Compared to other strontium aluminates (SrAl₂O₄, Sr₃Al₂O₆, SrAl₁₂O₁₉ and Sr₄Al₁₄O₂₅), it less described in scientific literature. Capron and Douy suggested the synthesis of SrAl₄O₇ from a spray-dried amorphous precursor, and specified its stability domains [7]. The results showed that kinetics of formation of this phase is very low, consequently the crystallization of SrAl₄O₇ is sensitive to the heating rate [7].

Experimental

SrAl₄O₇ samples were prepared by conventional solid state reaction. Al₂O₃, SrCO₃ and H₃BO₃ were used as starting materials. The stoichiometric amounts of raw materials were thoroughly ground in an agate mortar and then sintered in a furnace using different temperatures and times. The end products were also ground in an agate mortar and used for the characterization.

Powder X-ray diffraction (XRD) analysis has been carried out employing Rigaku MiniFlex II diffractometer. Scanning electron microscopy (SEM) has been performed using Hitachi SU-70 microscope.

Results and Discussion

In order to examine role of boric acid on phase formation, a series of strontium aluminates with different amount of additional H₃BO₃ were prepared. XRD analysis revealed (Fig. 1) that sample prepared without addition of boric acid constituted of SrAl₂O₄ phase, while addition of 2.5% by weight of H₃BO₃ resulted in domination of SrAl₄O₇ phase with trace amounts of SrAl₂O₄. Samples prepared with additional 5% of boric acid resulted in monophasic compounds. Further increasing amount of fluxing agent in the samples resulted in formation of additional phase of strontium aluminium borate SrAl₂B₂O₇. Influence of different annealing time and temperature on the formation of SrAl₄O₇ phase was also investigated in this study. We found that 5 h at 950 °C is sufficient in order to obtain single phase SrAl₄O₇ samples. Shorter annealing times resulted in mixture of SrAl₄O₇ and SrAl₂O₄ phases. The phase composition of the synthesized samples, however, was almost the same with increasing annealing time.

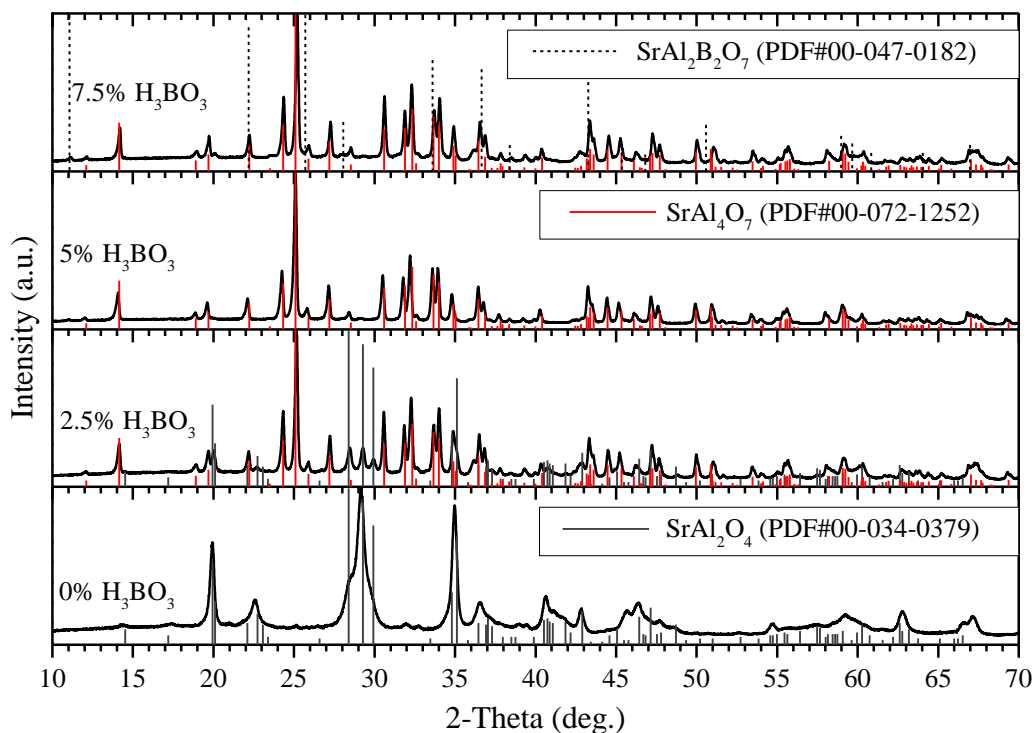


Fig. 1. XRD patterns of SrAl_4O_7 samples prepared using different amount of boric acid in the processing.

Conclusions

It was demonstrated that single phase SrAl_4O_7 samples could be synthesized by solid state reaction synthesis by annealing starting materials for 5 h at 950 °C. However, the fluxing agent (boric acid; 5% by weight) should be added to the mixture of starting compounds. Otherwise, the obtained products contained mixtures of other strontium aluminate phases.

References

1. A. Douy, M. Capron. *Journal of the European Ceramic Society* 2003, 12, 2075-2081.
2. K. Van den Eeckhout, P.F. Smet, D. Poelman. *Materials* 2010, 4, 2536-2566.
3. M. Avdeev, S. Yakovlev, A.A. Yaremchenko, V.V. Kharton. *Journal of Solid State Chemistry* 2007, 12, 3535-3544.
4. F. Clabau, X. Rocquefelte, S. Jobic, P. Deniard, M.H. Whangbo, A. Garcia, T. Le Mercier. *Chemistry of Materials* 2005, 15, 3904-3912.
5. A.J. Lindop, D.W. Goodwin. *Acta Crystallographica Section B Structural Crystallography and Crystal Chemistry* 1972, 8, 2625-2626.
6. K.-I. Machida, G.-Y. Adachi, J. Shiokawa, M. Shimada, M. Koizumi. *Acta Crystallographica Section B: Structural Crystallography and Crystal Chemistry* 1982, 3, 889-891.
7. M.L. Capron, A. Douy. *Journal of the American Ceramic Society* 2002, 12, 3036-3040.

INVESTIGATION OF ANHYDRITE BINDER FROM REAGENT GYPSUM AND INDUSTRIAL GYPSUM

D. Nizevičienė¹, N. Kybartienė²

*Kaunas University of Technology, Faculty of Electrical and Electronics Engineering¹,
Studentu 48, Faculty of Chemical Technology², Radvilenu pl. 19, Kaunas, Lithuania*

E-mail: dalia.nizeviciene@ktu.lt, nora.kybartiene@ktu.lt

1. Introduction

Anhydrite binding material is largely applied in the construction industry. It can be produced from natural anhydrite or industrial waste (e.g. phosphogypsum, nitrogypsum, fluorgypsum, flue gas desulfurization gypsum (FGD gypsum) and others [1-3].

A large underground layers of natural anhydrite are in Lithuania, but they are located at the depth of 150-300 m. There are technical difficulties in extensive mining at such depth. A possible alternative of anhydrite is making anhydrite binder from industrial gypsum by heating the materials at 600–1000 °C temperature with activators of the process.

Lithuanian JSC “Lifosa” produces 2 mln. tons of industrial waste-phosphogypsum per year. Phosphogypsum differs in chemical properties depending on raw material and technology used [4]. It is difficult to apply results by other researchers obtained with another materials in another conditions. There is not sufficient knowledge about the exact influence of the dehydration temperature and additives on the physical and mechanical properties of anhydrite binder produced from phosphogypsum. The aim of work is to compare a possible alternatives of the formation of anhydrite binder when reagent gypsum or phosphogypsum are used.

2. Materials and methods

Reagent gypsum $\text{CaSO}_4 \cdot 2\text{H}_2\text{O}$ (Lach-Ner, Czech Republic, purity - 99%). The specific surface area S_{spec} of gypsum is 640 m^2/kg . The pH is 8.3.

Phosphogypsum (JSC “Lifosa”, Kirovsk apatite). The pH is 4.8. Phosphogypsum was ground and neutralized by lime till pH 11.5 and then used in experiments. The specific surface area S_{spec} of phosphogypsum is 400 m^2/kg . The chemical composition is given in Table 1.

Table 1. Chemical composition of phosphogypsum

Constituents, wt.%								
CaO	SO ₃	R ₂ O ₃	R ₂ O	P ₂ O _{5t}	P ₂ O _{5 w.s.}	F	others	Ign. Loss
31.90	46.00	1.02	0.35	0.60	0.10	0.14	0.14	19.75

Glass is used as additive. It is household waste – the fragments of green bottle glass, the grain size is less than 0.2 mm. The specific surface area of ground glass is 460 m^2/kg . The pH is 10.3. The chemical composition is given in Table 2.

Table 2. Chemical composition of glass

Constituents, wt.%							
CaO	SO ₃	R ₂ O ₃	SiO ₂	MgO	Cr ₂ O ₃	Na ₂ O	K ₂ O
7.50	0.20	2.14	71.07	4.12	0.20	13.69	1.08

Cupola dust is used as additive. It is industrial waste of rock wool production, the particle size is less than 0.2 mm. The specific surface area of cupola dust is 2400 m^2/kg . The pH is 9.2. The chemical composition is given in Table 3.

Table 3. Chemical composition of cupola dust

Constituents, wt.%						
CaO	R ₂ O ₃	SiO ₂	Cr ₂ O ₃	Na ₂ O	K ₂ O	Ign. Loss
3.52	18.28	39.82	12.68	7.20	5.47	13.3

The chemical composition of materials was determined by classical methods of chemical analysis according to the standards LST EN 196-2, GOST 20851.2-75.

The pH was measured by pH-meter 673 M, when the ratio of water and solid material is 10.

The specific surface area S_{spec} was determined by the Blaine's method according to the standard LST EN 196-6.

The scanning electron microscopy (SEM) was carried out with FEI QUANTA 200F.

The physical-mechanical properties were determined according to the standard LST EN 196-3. The only exception was that 2x2x2 cm size samples were formed up. The samples were hardened in 90 % relative humidity environment and compressed by press ELE Automat.

The material was burnt at the temperature of 800 or 900 °C for 30 minutes in the muffle furnace.

3. Results

Anhydrite binder produced from reagent gypsum or neutralized phosphogypsum hydrated, bound and hardened very slowly (Table 1). The specimens of the anhydrite binder that was produced at the temperature of 800 °C had no strength characteristics after 7 days.

Table 4. The properties of anhydrite binder

Material from	Temp. of heating, °C	S_{spec} , m ² /kg	W/A	Setting time, h/min		Compressive strength after hardening, MPa		
				Initial	Final	3 days	7 days	28 days
Reagent gypsum	800	500	0.50	45	60	-	-	8.0
	900	200	0.43	24	62	-	3.1	9.2
Phosphogypsum	800	600	0.34	8/30	9/30	-	-	9.5
	900	600	0.29	5/45	8/20	-	5.2	15.7

The properties of anhydrite binder at the different temperatures can be explained by the differences of crystals structure. The crystals of anhydrite produced by heating gypsum or phosphogypsum at 800°C temperature keep a shape of irregular prism typical to gypsum. Their surface is crannied (Fig. 3). It can be assumed that the evaporation of the crystallization water forms the micro cracks in the crystal structure.

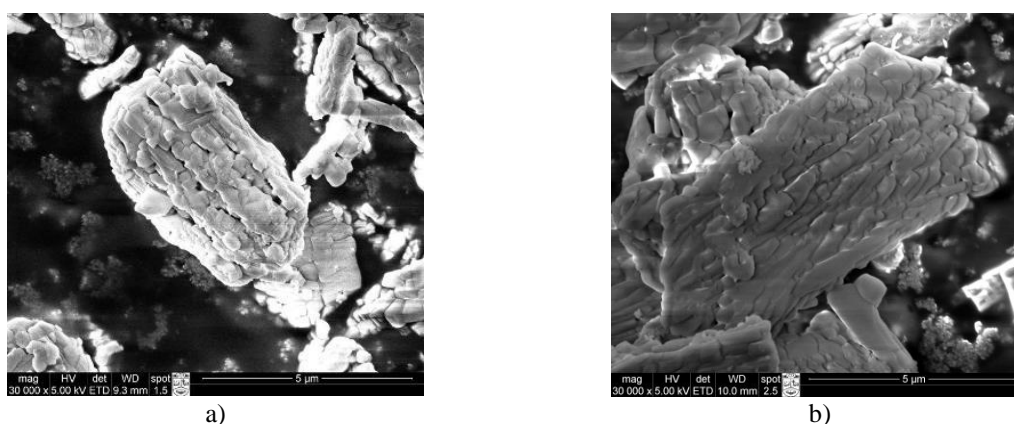


Fig. 3. SEM of anhydrite produced from reagent gypsum (a) and from phosphogypsum (b) at 800 °C temperature

The crystals of the anhydrite binder calcined at 900 °C temperature were smooth and melted without micro cracks (Fig. 4). Such structure of crystals requires less amount of water for obtaining the formation mixture of normal consistence (Table 4). It has an influence to the compressive strength of the samples.

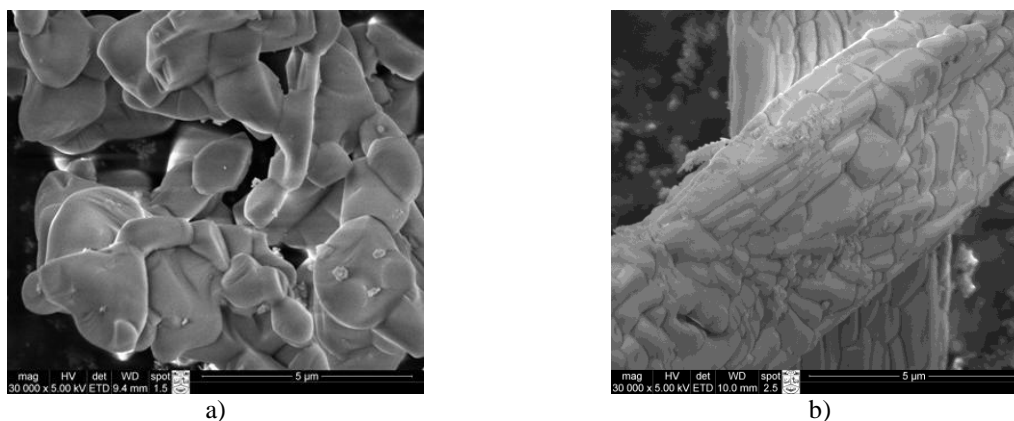


Fig. 4. SEM of anhydrite produced from reagent gypsum (a) and from phosphogypsum (b) at 900 °C temperature

Anhydrite binder produced from reagent gypsum or neutralized phosphogypsum bound and hardened very slowly thus glass and cupola dust were used to activate the process. The physical and mechanical properties of anhydrite binder produced from gypsum with 5% of additives at temperature of 800 and 900 °C are presented in Table 5.

Table 5. The properties of anhydrite binder with additives

Mixture	Temp. of heating, °C	S_{spec} , m ³ /kg	W/A	Setting time, h/min		Compressive strength after hardening, MPa		
				Initial	Final	3 days	7 days	28 days
Reagent gypsum/glass	800	600	0.37	2/00	4/00	4.5	6.8	10.7
	900	600	0.31	1/30	2/15	8.7	12.7	16.4
Reagent gypsum/cupola dust	800	600	0.34	2/05	4/25	3.2	5.4	8.2
	900	600	0.36	1/30	2/40	6.1	8.6	12.4
Phosphogypsum/ /glass	800	600	0.34	0/35	1/00	10.1	12.5	15.2
	900	600	0.29	0/15	0/35	11.7	16.1	18.8
Phosphogypsum/ /cupola dust	800	600	0.34	2/05	2/30	7.4	9.0	10.9
	900	600	0.29	0/40	0/55	8.0	9.5	16.2

The results show that both additives accelerates binding of anhydrite binder and increases the early compressive strength of specimens. This effect is more evident when anhydrite binder produced at 900 °C temperature than in case of 800 °C temperature. This effect was observed for all materials and all additives.

The initial setting time of the anhydrite binder produced from the reagent gypsum or phosphogypsum with additives was 0.25-2 hours meanwhile the initial setting time of the anhydrite binder produced from the reagent gypsum or phosphogypsum without additives was longer (from 6 hours till 2 days). The compressive strength of specimens of the anhydrite binder that was produced from the reagent gypsum or phosphogypsum with additives was higher compared to the specimens of anhydrite binder without additives.

The anhydrite binder with 5 % glass exhibited the best physical and mechanical properties among all the investigated anhydrite binders. The additives used during the calcinations differ by an alkalinity. The glass has the higher alkalinity (pH is 10.3) in comparison with the cupola dust (pH is 9.2).

It is possible to assume, that anhydrite binder produced from the phosphogypsum with additives and burnt at 800 and 900 °C temperature bound and hardened faster than anhydrite binder produced from the reagent gypsum because during the calcination of the phosphogypsum neutralized by lime the CaO occurs in the system, as also alkaline compounds of Na⁺, K⁺ present in the composition of the additives and phosphogypsum also, act as the activators for binding the anhydrite. The activators used in practice for binding



anhydrite material form complex saline that enhance the hardening and improve the strength properties of the material [5, 6].

4. Conclusions

Anhydrite binder produced from reagent gypsum or neutralized phosphogypsum without additives calcined at 800 or 900 °C temperature hydrated, bound and hardened very slowly.

Anhydrite binder produced from the phosphogypsum with additives and burnt at 800 and 900 °C temperature bound and hardened faster than anhydrite binder produced from the reagent gypsum.

References

1. D. Gazdic, *Adv. Mat. Res.*, **2014**, 897, 53.
2. J. Cesniene, *Ceram-Silik*, **2007**, 51, 3, 153.
3. V. Leskeviciene, D. Nizeviciene, *Ceram-Silik*, **2010**, 54, 2, 152.
4. P. Becker, *Phosphates and phosphoric acid: raw materials, technology, and economics of the wet process*, Marcel Decker, Inc., New York, **1989**.
5. N. B. Singh, *J. Am. Ceram. Soc.*, **2005**, 88, 1, 196.
6. S. Marinkivic, A. Kostic-Pulek, S. Popov, J. Djinovic, P. Trifunovic, *J. Min. Met.*, **2004**, 40B, 1, 89.

NEODYMIUM, TERBIUM, PRASEODYMIUM AND CERIUM IRON GARNETS AND ORTHOFERRITES: A NEW CLASS OF PIGMENTS?

O. Opuchovič¹, G. Kreiza², K. Kazlauskas² A. Kareiva¹

¹*Department of Inorganic Chemistry, Vilnius University, Naugarduko 24, LT-03225, Vilnius, Lithuania*

²*Institute of Applied Research, Vilnius University, Sauletekio 9-III, LT-10222 Vilnius, Lithuania*

E-mail: olga.opuchovic@chf.vu.lt

Investigation of pigment phase composition, surface morphology and crystal structure is important for identification of old pigments as well as for the preparation and modification of new ones. Despite the fact, that there are a lot of colour materials of inorganic origin, pigment producers are still interested in pigments that present intense tonalities and which are in agreement with the technological and environmental requirements. Among synthetic inorganic ceramic pigments, in fact, there is a restricted choice for red/pink and orange colours [1]. New non-toxic ceramic pigments with high temperature stability requires searching for new host structures and new synthesis methods involving less toxic materials [2]. Nowadays in developing stable new pigments lanthanide oxides are used instead of toxic elements, such as cadmium, cobalt, lead and chromium [3-6]. Among new lanthanide containing pigments there are LaFeO₃ [7], LnFeO₃ (where Ln = Gd, La, Yb, Tm, Lu) [8], HoFeO₃ [9], ErFeO₃, NdFeO₃ and SmFeO₃ [10].

In this study, inorganic lanthanide-iron-based oxide pigments (Ln₃Fe₅O₁₂ and LnFeO₃; Ln = Ce, Pr, Nd, Tb) were synthesized by aqueous sol-gel method. The phase composition of prepared pigments was investigated by X-ray diffraction (XRD) analysis and morphological features were revealed using scanning electron microscopy (SEM).

X-ray diffraction analysis results demonstrated that most of prepared iron-based lanthanide mixed-metal oxides are not single phase compounds (Table 1). In the pigmentary field, however, it is not always necessary to obtain single-phase system, but the conditions of the synthesis have to be appropriate for the industrial occupancy [11].

Table 1. Phase composition of prepared pigments.

Sample name	Expected composition	Identified phases in pigments
P1	NdFeO ₃	NdFeO ₃ and Fe ₂ O ₃
P2	Nd ₃ Fe ₅ O ₁₂	3NdFeO ₃ and Fe ₂ O ₃
P3	TbFeO ₃	TbFeO ₃ and Tb ₃ Fe ₅ O ₁₂
P4	Tb ₃ Fe ₅ O ₁₂	Tb ₃ Fe ₅ O ₁₂
P5	PrFeO ₃	PrFeO ₃
P6	Pr ₃ Fe ₅ O ₁₂	3PrFeO ₃ and Fe ₂ O ₃
P7	CeFeO ₃	CeO ₂ and Fe ₂ O ₃
P8	Ce ₃ Fe ₅ O ₁₂	CeO ₂ and Fe ₂ O ₃

Synthesized pigments were used for the preparation of ceramic glazes. The colour of the pigments in powdered form and glazes was evaluated according to the Commission Internationale de l'Eclairage (CIE) through $L^*a^*b^*$ coordinates [12]. In this system, L^* is the colour lightness ($L^* = 0$ for black and $L^* = 100$ for white), a^* is the green (-)/red (+) axis, and b^* is the blue (-)/yellow (+) axis. Table 2 shows CIE L^* , a^* , b^* parameters of pigment

samples and prepared glazes. Obviously, pigments P1 and P5, i. e. the Nd-Fe-O and Pr-Fe-O samples heated at 1000 °C, have the highest values of a^* and b^* parameters. Both pigments reveal perovskite type structure. On contrary, lowest value of parameter a^* has pigment P4 (3Tb-5Fe-O, heated at 1000 °C), which is single phase terbium iron garnet. Despite the fact, that pigments have evident difference in parameter a^* , glazes, prepared with these pigments show only slight difference in the same coordinate. Glazes, containing cerium in its composition showed not homogeneous surface morphology, because of pale yellow areas on it. This is evident from glaze parameter b^* , which is increased. Moreover, these glazes have the lowest value of parameter a^* .

Table 2. L^* , a^* and b^* parameters of pigments and glazes.

Sample	Pigment			Glaze		
	L^*	a^*	b^*	L^*	a^*	b^*
P1	50.12	15.56	12.37	38.35	7.94	6.03
P2	47.57	12.39	9.09	38.8	8.24	4.59
P3	50.9	10.4	11.76	40.9	11.54	8.94
P4	50.92	6.71	11.38	39.89	11.82	8.6
P5	50.85	15.66	14.58	39.77	10.85	9.19
P6	47.14	10.17	6.78	38.92	12.48	11.28
P7	45.9	10.95	3.56	58.35	4.22	17.47
P8	45.32	10.53	2.98	53.37	5.2	15.99

Best quality glaze was obtained with single phase $Tb_3Fe_5O_{12}$ garnet structure pigment. The surface of this glaze is uniform and reveals red shade. The worst quality glazes were obtained with the pigments containing cerium in their composition, as separate parts of surface of glazes are covered with pale yellow colour areas.

For more detailed characterization of surface of different quality glazes, SEM micrographs are obtained and presented in Fig. 1.

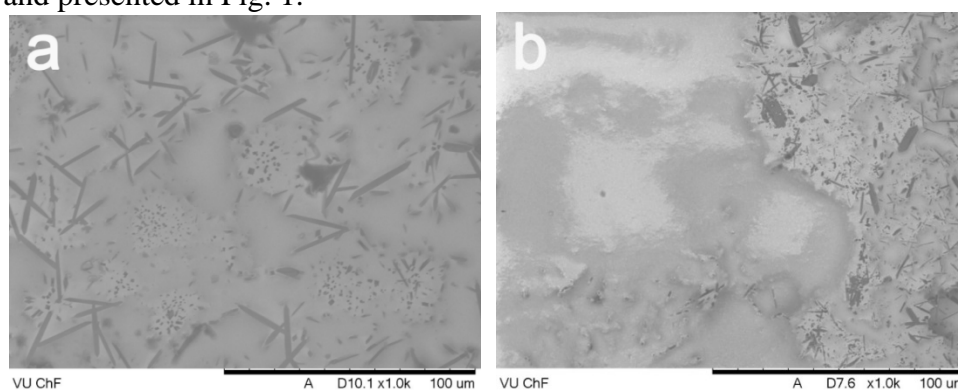


Fig. 1. SEM micrographs of glazes prepared with $Tb_3Fe_5O_{12}$ (a) and CeO_2 and Fe_2O_3 (b) pigments.

The SEM micrograph of glaze P4 shows that small needle-like particles are evenly distributed over whole surface of glaze. However, the huge part of the surface of glaze obtained with cerium pigment is covered by cloudy aggregates.

References



1. M. Hosseini-Zori, E. Taheri-Nassaj, A.R. Mirhabibi, *Ceram. Int.*, **2008**, *34*, 491.
2. Y. Marinova, J.M. Hohemberger, E. Cordoncillo, P. Escribano, J.B. Carda, *J. Eur. Ceram. Soc.*, **2003**, *23*, 213.
3. S.F. Santos, M.C. de Andrade, J.A. Sampaio, A.B. da Luz, T. Ogasawara, *Dyes Pigments*, **2007**, *75*, 574.
4. L. Sandhya Kumari, P. Prabhakar Rao, M. Lakshmipathy Reddy, *J. Alloy. Compd.*, **2008**, *461*, 509.
5. R.C. Olegário, E.C. Ferreira de Souza, J.F. Marcelino Borges, J.B. Marimon da Cunha, A.V. Chaves de Andrade, S.R. Masetto Antunes, A.C. Antunes, *Dyes Pigments*, **2013**, *97*, 113.
6. V. James, P. Prabhakar Rao, S. Sameera, S. Divya, *Ceram. Int.*, **2014**, *40*, 2229.
7. J.D. Cunha, D.M.A. Melo, A.E. Martinelli, M.A.F. Melo, I. Maia, S.D. Cunha, *Dyes Pigments*, **2005**, *65*, 11.
8. Ž. Dohnalová, P. Šulcová, M. Trojan, *J. Therm. Anal. Calorim.*, **2008**, *91*, 559.
9. P.C. Piña, R. Buentello, H. Arriola, E.N. Nava, *Hyperfine Interact.*, **2008**, *185*, 173.
10. C. Piña, H. Arriola, N. Nava, *J. Phys. Conf. Ser.*, **2010**, *217*, 012036.
11. Ž. Dohnalová, M. Vontorčíková, P. Šulcová, *J. Therm. Anal. Calorim.*, **2013**, *113*, 1223.
12. I.C.O. Illumination, Recommendations on Uniform Color Spaces, Color-difference Equations, Psychometric Color Terms, CIE, 1978.

**XRD STUDIES OF HOMOGENIZATION AND SELENIZATION OF
ELECTROCHEMICALLY CO-DEPOSITED Cu-Zn-Sn**
**V. Pakštas¹, Z. Mockus¹, R. Giraitis¹, R. Kondrotas¹, A. Naujokaitis¹, G. Stalnionis¹, S.
Stanionytė¹, V. Karpavičienė¹, R. Juškėnas¹**

*1 Center for Physical Sciences and Technology, Institute of Chemistry, A. Goštauto 9, LT-01108 Vilnius, Lithuania
E-mail: vidas@chi.lt*

Chalcopyrite type compound $\text{Cu}_2\text{ZnSnSe}_4$ (CZTSe) is a direct band gap semiconductor with a high absorption coefficient $\alpha > 10^4 \text{ cm}^{-1}$ which makes it an ideal absorber for the thin film solar cells. Various routes used for a fabrication of CZTSe thin films could be grouped into physical and chemical. Electrochemical deposition among chemical approaches for preparation of CZT precursor layer is the most frequently implemented. The electrochemical deposition of the CZT can be conducted in two ways: i) deposition of stacked layers i.e. deposition of Cu, Zn and Sn layers from corresponding electrolyte solutions; ii) co-deposition of Cu-Zn-Sn alloy from just one electrolyte solution. Despite deposition route used next steps are: i) homogenization of the electrodeposited CZT precursor layer i.e. annealing at temperatures of up to 400 °C in Ar or N_2 atmosphere; ii) selenization of the CZT precursor at temperatures of 400 – 560 °C to form CZTSe absorber layer. Different intermetallic compounds (IMC) and selenides form during these heat treatments. Studies carried out by different researchers yielded sometimes contradictory results [1, 2]. That could be related with different deposition approaches used as well as with particular heat treatment and XRD characterization techniques.

The current work presents the XRD studies of electrochemically co-deposited CZT layers on Mo/glass substrate after preliminary annealing at temperatures in the range 200 – 350 °C under inert gas atmosphere and after selenization in Ar gas + Se vapour. The CZT layers of about 600 nm in thickness were deposited in stirred citrate solution containing CuSO_4 , ZnSO_4 and SnSO_4 under potentiostatic conditions. The phase composition was examined using x-ray diffractometer SmartLab (Rigaku) equipped with a rotating Cu anode x-ray tube. Different XRD techniques were used to get reliable results: i) Bragg-Brentano geometry with graphite monochromator on the diffracted beam; ii) grazing incidence XRD; iii) powder XRD with CALSA monochromator for measurement in Cu $K_{\alpha 1}$ radiation ($\lambda=0.15406 \text{ nm}$); iv) high temperature XRD in-situ measurements. Sample surface and cross-section images were examined in scanning electron microscope (SEM) Helios Nanolab 650. The cross-sections were made by focused ion beam (FIB) and chemical composition determined by EDX in the same SEM.

Typical as-deposited CZT layer contained about 45.0 at.% of Cu, 29.0 at.% of Zn and 26.0 at.% of Sn according to the EDX analysis. The XRD analysis showed the CZT layers were comprised of 3 to 4 metallic phases: $\gamma\text{-Cu}_5\text{Zn}_8$, $\eta\text{-Cu}_{6.26}\text{Sn}_5$, pure Sn and sometimes traces of $\varepsilon\text{-Cu}_3\text{Sn}$ were detected. Examination of CZT layer by SEM revealed that layer was composed of small aggregates comprised of nanometric size crystallites and was rather porous.

The homogenization of CZT layers was achieved by heating at temperatures in the range 200 – 350 °C under Ar or He atmosphere. Figure 1 shows XRD pattern of CZT layer annealed at temperature of 230 °C. The pattern evidences that the precursor layer still contained the same three phases as the as-deposited CZT. However, sharper XRD peaks pointed to an increased crystallinity. Figure 1 depicts also diffractogram of CZT layer annealed at 300 °C. In the latter case the Sn phase was not present and XRD peaks the IMC phases were shifted towards lower diffraction angles indicating formation of tin solid solution in both of the phases. This phenomenon was not observed by other researchers. The current XRD studies also proved that the hexagonal $\eta\text{-Cu}_{6.26}\text{Sn}_5$ phase forms in the CZT precursor on the contrary to other

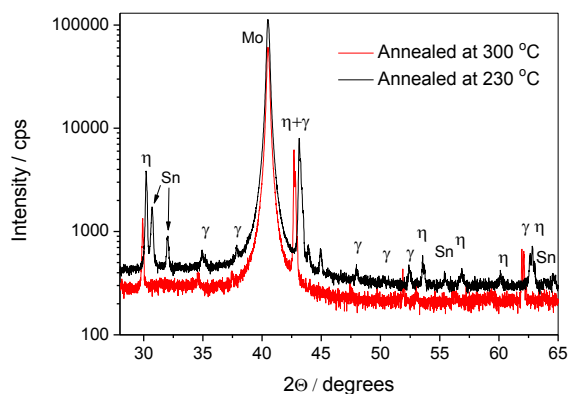


Figure 1. The XRD patterns of CZT layers annealed at temperatures of 230 °C and 300 °C.

researchers, which claimed the monoclinic Cu_6Sn_5 was formed in the electrodeposited CZT. SEM cross-section images showed that the CZT layer annealed at temperature of 300 °C was composed of micrometer size grains. Further increase in the annealing temperature did not cause significant changes neither in the phase composition nor in the morphology.

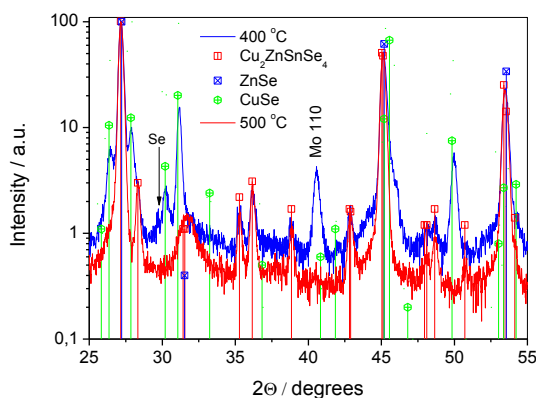


Figure 2. The XRD patterns of CZT layers annealed at temperatures of 400 °C (a) and 500 °C (b).

The CZT selenization process was studied in temperature range 400 – 560 °C. The XRD pattern presented in Figure 2 shows that formation of CZTSe phase started already at temperature of 400 °C though ZnSe and CuSe phases also were present. Further increase in selenization temperature resulted in decrease in quantity of the two latter phases and in growing up of CZTSe crystallinity. The diffractogram of CZT selenized at temperature of 500 °C (Figure 2) proved that already at this temperature pure $\text{Cu}_2\text{ZnSnSe}_4$ was formed. Further increase in temperature resulted only in better crystallinity and increase in quantity of MoSe_2 . The current studies revealed that the CZT heat treatment at temperatures > 250 °C leads to formation of only two IMC: tin solid solutions in cubic $\gamma\text{-Cu}_5\text{Zn}_8$ phase and in hexagonal phase $\eta\text{-Cu}_{6.26}\text{Sn}_5$. The $\text{Cu}_2\text{ZnSnSe}_4$ compound started already to form at temperature of about 400 °C, however the pure CZTSe phase could only be formed at temperatures > 500 °C.

References

1. R.A. Wibowo, W.H. Jung, M.H. Al-Faruqi, I. Amal, K.H. Kim, *Mater. Chem. Phys.*, **124** (2010) 1006 – 1010.
2. X. He, H. Shen, W. Wang, J. Pi, Y. Hao, X. Shi, *Appl. Surf. Sci.*, **282** (2013) 765 – 769.

Sol-Gel Synthesis of Europium Doped $Tb_3Al_5O_{12}$, $Dy_3Al_5O_{12}$ and $Ho_3Al_5O_{12}$ Garnets

L. Pavasaryte^{1*}, **B. J. Lopez**², **A. Kareiva**¹

¹ Department of Inorganic Chemistry, Vilnius University, Naugarduko 24, LT-03225 Vilnius, Lithuania

² Departament de Química Inorgànica i Orgànica, Universitat Jaume I, E-12071 Castelló de la Plana, Spain

E-mail: lina.pavasaryte@gmail.com

1. INTRODUCTION

The yttrium aluminium garnet ($Y_3Al_5O_{12}$, YAG) doped with a transition metal or lanthanide ions is an important solid-state laser material widely used in luminescence systems, window materials for a variety of light sources, and for fiber-optic telecommunication systems. The YAG oxides are also widely applied as phosphors in cathode-ray tubes (projection TV sets), field emission, vacuum fluorescent, and electroluminescent displays and as scintillators in X-ray and positron emission tomographs [1, 2]. Many different synthesis methods of synthetic garnets are described in the literature. The solid-state reaction route is a widely used method for the preparation of powders from a mixture of the solid starting materials. Various wet-chemical methods, which include combustion, co-precipitation, hydrothermal, spray pyrolysis, sol-gel and microemulsion methods have been developed and successfully used for low-temperature production of phase-pure garnet powders and related systems. Recently we have demonstrated that monophasic yttrium aluminium garnet powders and related garnet structure compounds with homogeneously distributed lanthanide elements within the garnet matrix can be successfully synthesized by the simple aqueous sol-gel process. The evaluated synthetic technique to garnet structure compounds using acetate-nitrate-glycolate intermediate illustrates the simplicity and superior potential of the proposed method [3, 4]. The molecular level mixing and the tendency of partially hydrolyzed species to form extended networks facilitate the structure evolution thereby lowering the crystallization temperature. The reactivity of such precursors makes the preparation of particular phases possible at ambient and gentle conditions [5].

Several lanthanide aluminium garnets (i.e., $Tb_3Al_5O_{12}$, $Dy_3Al_5O_{12}$ and $Ho_3Al_5O_{12}$) have not been yet synthesized with various doping level of europium, to the best our knowledge. Therefore, the main aim of this study was to prepare $Tb_3Al_5O_{12}:Eu^{3+}$, $Dy_3Al_5O_{12}:Eu^{3+}$ and $Ho_3Al_5O_{12}:Eu^{3+}$ using sol-gel technique

2. EXPERIMENTAL

The lanthanide aluminium garnet samples were synthesized by an aqueous sol-gel method. In the aqueous sol-gel process, the following materials were used: Ho_2O_3 (99.9 %), Tb_4O_7 (99.9 %), Dy_2O_3 (99.99%) and Eu_2O_3 (99.99%). Ho, Dy and Tb oxides were dissolved in nitric acid (about 10 ml) with small amount of water. Clear solutions were obtained after stirring at 60-65 °C in beakers covered with a watch-glass till dissolved. When oxides dissolved, mixture washed with water till neutral pH. Then aluminium nitrate nonahydrate and appropriate amount of europium oxide dissolved in small amount of nitric acid were added to above solutions and diluted till 100 ml. The resulting mixtures were stirred at 65 °C for 1 h, followed by dropwise addition of ethane-1,2-diol ($HOCH_2CH_2OH$) upon vigorous stirring. The resulting sols were mixed at the same temperature for another 1 h and then

concentrated by slow solvent evaporation at 65 °C until they turned into transparent gels. The gels were dried in an oven at 100 °C for 24 h. The resulting gel powders were ground in an agate mortar and heated in air at 800 °C for 4 h by slow temperature elevation (5 °C min⁻¹). After grinding in an agate mortar, the powders were further sintered in air at 1000 °C temperature for 10 h.

The synthesized samples were characterized by X-ray powder diffraction (XRD) analysis, Fourier transform infrared (FTIR) spectroscopy and scanning electron microscopy (SEM). The XRD studies were performed on D8 Bruker AXS powder diffractometer using CuK α 1 radiation. The diffraction patterns were recorded at the standard rate of 1.5 2 θ / min. The FTIR spectra were recorded with a Perkin-Elmer FT-IR Spectrum 1000 spectrometer. The scanning electron microscope DSN 962 was used to study the surface morphology and microstructure of the obtained ceramic samples.

3. RESULTS AND DISCUSSION

3.1 XRD characterization of LnAG:Eu powders

The phase purity and compositional changes of the Tb₃Al₅O₁₂ (TAG), Dy₃Al₅O₁₂ (DAG) and Ho₃Al₅O₁₂ (HAG) doped with different amount of Eu ions were controlled by X-ray diffraction analysis (see Figs. 1-3, respectively).

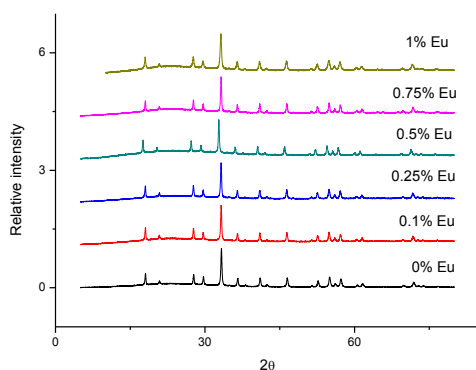


Figure 1. XRD patterns of the Tb-Al-O:Eu gels annealed at 1000 °C.

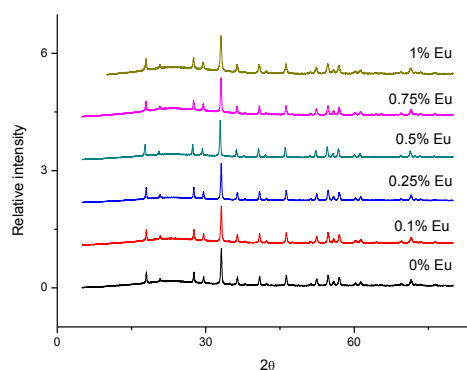


Figure 2. XRD patterns of the Dy-Al-O:Eu gels annealed at 1000 °C.

The XRD results presented in Fig. 1 revealed that ceramics obtained at 1000 °C consists of one Tb₃Al₅O₁₂ crystalline phase. The obtained XRD patterns are in a good agreement with the reference data for TAG (PDF [04-006-4054]). Fig. 2 shows that only one Dy₃Al₅O₁₂ phase (PDF [04-006-4053]) was obtained after calcination of Dy-Al-O:Eu precursors at 1000 °C. In the case of the Ho-Al-O system, the analogous results were obtained (Fig. 3). Evidently, the obtained

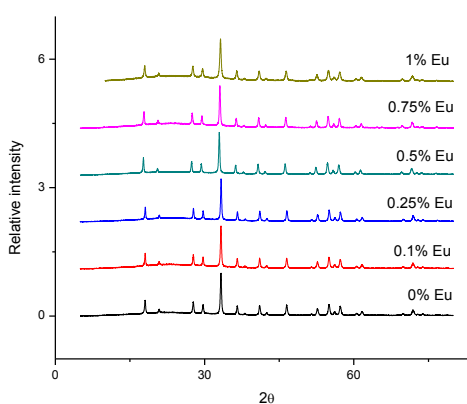


Figure 3. XRD patterns of the Ho-Al-O:Eu gels annealed at 1000 °C.

XRD patterns are in a good agreement with the reference data for $\text{Ho}_3\text{Al}_5\text{O}_{12}$ (PDF [04-001-9715]).

3.2 Infrared spectroscopy

FTIR spectroscopy was used as additional tool for the structural characterization of the ceramic materials obtained by the aqueous sol-gel method. The FTIR spectra of ceramic materials obtained after the calcinations of the Ho-Al-O:Eu gels at 1000 °C for 10 h are shown in Fig. 4.

The FTIR spectra of synthesized ceramics show several quite intense broad bands at 675 cm^{-1} , 720 cm^{-1} and 775 cm^{-1} , which are typical metal-oxygen (M-O) absorptions for the garnet-type compounds [47-49]. The FTIR spectra of Tb-Al-O and Dy-Al-O garnets doped with europium were very similar to the presented in Fig. 4. The most important feature is that intensive bands are determined in the region of $900\text{--}450\text{ cm}^{-1}$, which may be also attributed to the stretching modes of the isolated $[\text{AlO}_4]$ tetrahedral and $[\text{AlO}_6]$ octahedra in the garnet structure, i.e. these bands correspond to the formation of crystalline TAG:Eu, DAG:Eu and HAG:Eu. Thus, the observed M–O vibrations which in view of the earlier reports are characteristic of RE–O and Al–O stretching frequencies let us to conclude, that the FTIR results are consistent with crystallization process observed by XRD measurements. Consequently, the FTIR results absolutely support the conclusions made on grounds of the XRD measurement and prove that there is no left organic matter in the sol-gel derived garnet structure compounds [6-8].

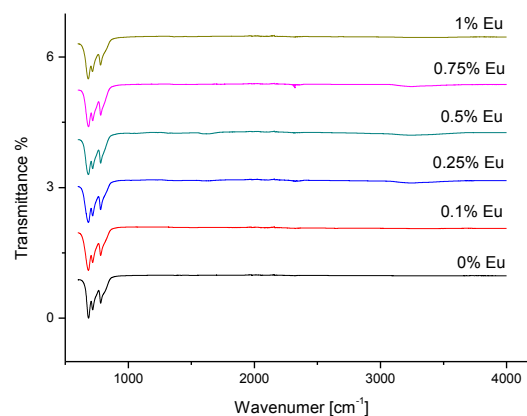


Figure 4. FTIR spectra of the $\text{Ho}_3\text{Al}_5\text{O}_{12}$:Eu garnets

3.3 Scanning electron microscopy

The textural properties of the calcined TAG:Eu, DAG:Eu and HAG:Eu powders were investigated by SEM, from which the grain size and typical morphologies were obtained. Scanning electron micrographs of the TAG:0.5%Eu, DAG:0.5%Eu and HAG:0.5%Eu samples calcined at 1000 °C are shown in Fig. 5.

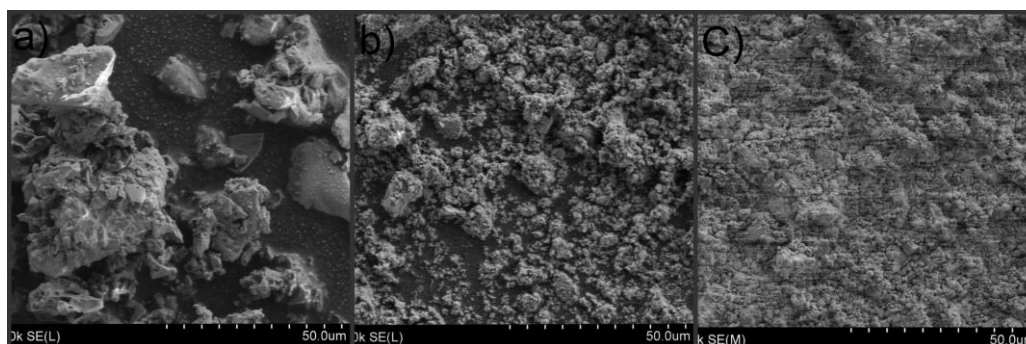


Figure 5. SEM micrographs of TAG:Eu (a), DAG (b), HAG (c) doped with 0.5% of Eu^{3+} .

Individual particles seem to be submicro-sized plate-like crystals and they partially fused to form hard agglomerates. The SEM micrograph presented in Fig. 5 shows the formation of very homogeneous mixed-metal oxides, and the formation of a continuous network of crystallites is evident. However, pores and voids can also be seen, which result probably from the escaping gases during calcination. The DAG:Eu and HAG:Eu garnet particles are a little differently shaped comparing with TAG:Eu garnet. Apparently, the particles were formed with more pronounced agglomeration, indicating good connectivity between the grains.

4. Conclusions

The sinterability and microstructural evolution of synthesized lanthanide aluminium garnets by an aqueous sol-gel process were investigated in the present study. In this work aqueous sol-gel process was used to prepare $Tb_3Al_5O_{12}$, $Dy_3Al_5O_{12}$ and $Ho_3Al_5O_{12}$ doped with different amount of europium. It was concluded from the XRD data that monophasic $Tb_3Al_5O_{12}:Eu$, $Dy_3Al_5O_{12}:Eu$ and $Ho_3Al_5O_{12}:Eu$ garnets can be easily synthesized at 1000 °C using the proposed sol-gel chemistry approach. Europium inside garnet structure slightly shifted the reflection peaks in the XRD patterns. The biggest shift was observed in the XRD pattern of the samples with 0.5% of Eu. The XRD results were supported by FTIR and SEM. Thus, the developed synthesis route offers unique opportunities for the synthesis of optical materials, since it is suited for the production of thin/thick films, monoliths and fibbers. The luminescent properties of these Eu^{3+} -doped garnets are under investigation.

REFERENCES

1. H. J. Yang, L. Yuan, G. S. Zhu, A. B. Yu, and H. R. Xu, *Mater. Lett.* **63**, 2271 (2009).
2. H. K. Yang, and J. H. Jeong, *J. Phys. Chem. C* **114**, 226 (2010).
3. R. Skaudzius, A. Katelnikovas, D. Enseling, A. Kareiva, and T. Juestel, *J. Lumin.* **147**, 290 (2014).
4. A. Zabiliute, S. Butkute, A. Zukauskas, P. Vitta, and A. Kareiva, *Appl. Optics*, **53**, 907 (2014).
5. B. L. Cushing, V. L. Kolesnichenko, and C. J. O'Connor, *Chem. Rev.* **104**, 3893 (2004).
6. Xia Li, Hong Liu, Jiyang Wang, Hongmei Cui, Feng Han, *J. Am. Ceram. Soc.*, 87 [12] 2288-2290 (2004).
7. Lin Xing, Luming Peng, Min Gu, Guodong Tang, *J Alloys Comp.* 491 (2010) 599-604.
8. Nathalie Pralad, Genevieve Chadeyron, Audrey Potdevin, Jerome Deschamps, Rachid Mahiou, *J. Eur. Ceram. Soc.* 33 (2013) 1935-1945.

FORMATION PECULIARITIES OF Cr³⁺-DOPED Y₃Ga₅O₁₂**R. P. Petrauskas, S. Butkute, A. Kareiva**

*Department of Inorganic Chemistry, Faculty of Chemistry, Vilnius University, Naugarduko
24, LT-03225 Vilnius, Lithuania
E-mail: skirmante.butkute@chf.vu.lt*

Thousands of articles are published about garnet structure materials, and interest on this crystal structure compounds is not decreasing till now. For instance, this current calendar year more than one thousand articles touching garnet theme are published. Even fifty of them described different synthesis methods in order to obtain huge varicosity in composition of included elements, different doping concentrations, physical states, particle size and etc. All these studies lead to better physical properties, like: thermal resistivity, magnetism and, of course, luminescence. Despite potential industrial applications of the garnets, scientific interest on them for last fifty years focused mainly as light source [1]. It is known that some plants productivity could be increased by growing them in special lighting composition: the red (620–680 nm), far-red (700–760 nm) and blue (400–500 nm) [2]. From these three light regions is still missing far-red efficient and stable source for plant cultivation, as it is InGaN direct-emission blue and AlGaInP - red LEDs [3]. In our study, composition of elements in garnet is chosen as possible light-emitting diode (LED) for far-red luminescence used for plant cultivation in greenhouses. The results of synthesis and characterization of Y₃Ga₅O₁₂ (YGG) doped with 8 mol% of Cr³⁺ as a continuation of our previous work [4] are presented herein.

In this work YGG doped with 8 mol% of Cr³⁺ (YGG8Cr) samples were synthesized via sol-gel combustion method. Y₂O₃, Ga₂O₃ and Cr(NO₃)₃·10.9H₂O were used as starting materials and tris(hydroxymethyl)aminomethane (TRIS) as complexing agent and fuel for self-initiating combustion process. Metal oxides were dissolved in concentrated HNO₃. TG analysis was employed for estimation of the amount of water crystallization in Cr(NO₃)₃·xH₂O. Aqueous solutions of Y³⁺, Ga³⁺ and Cr³⁺ with desired molar ratio were mixed together and the necessary amount of TRIS was added. The formation of gel takes around 1 h at 60–75 °C with constant mixing in a covered beaker. TRIS initiates a spontaneous self-combustion process when the gel is completely dried. The obtained very crumbly ash-like powders were heated at 800 °C for 5 h for complete residues of organic matter. The resulting powders were split in to two parts, from one part pellets were pressed, another – used as powders to evaluate the difference in the growth of polycrystalline garnets. Pellets and powders were heated for 10 h at 1000, 1100, 1200, 1300 and 1400 °C with heating rate of 3 °C/min. FTIR, TG, XRD, SEM and EDX methods were used to characterize the obtained materials.

Figure 1 presents XRD patterns of powders (P) and pellets (T) heated at 1100 and 1400 °C. It is clearly seen that all measured patterns fit perfectly with reference pattern of Y₃Ga₅O₁₂. It can be seen that diffraction peaks are much broader of samples obtained in powder form. Besides, the peaks from pellets are much sharper when synthesis was performed at higher calcination temperatures.

The morphological features of YGG8Cr powders and pellets annealed at different temperatures are presented in SEM micrographs (Fig. 2.). From the SEM images it can be seen that crystallite size depends very much on the processing conditions. Fig. 2 (A) nicely presents that garnet sample is composed of porous and agglomerated structure with irregular shaped particles. Very good connectivity between grains could be observed for the pelletized sample (Fig. 2(B)). Moreover, the particle size of YGG8Cr samples obviously increases by increasing calcination temperature from 1100 to 1400 °C. And this increase is pronounced for both processing routes.

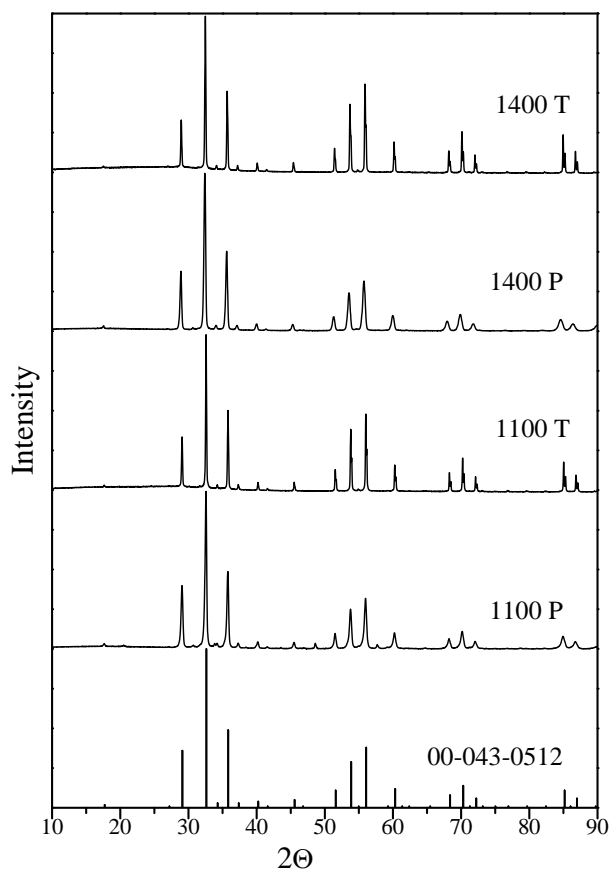


Fig. 1. XRD patterns of YGG8Cr powders (P) and pellets (T) sintered at 1100 and 1400 °C.

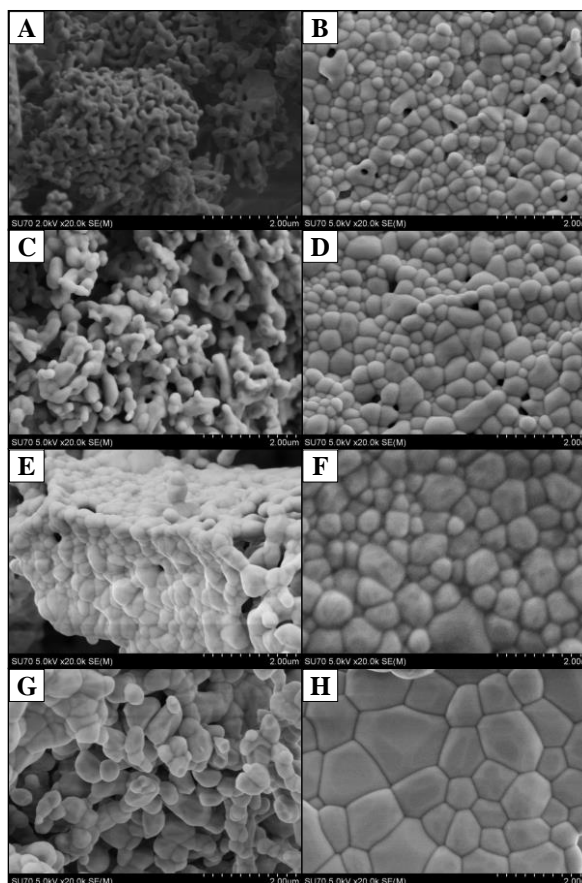


Fig. 2. SEM images of YGG8Cr powders (a), (c), (e), (g) and pellets (b), (d), (f) (h) sintered at different temperatures: (a), (b) 1100 °C; (c), (d) 1200 °C; (e), (f) 1300 °C; (g), (h) 1400 °C.

Acknowledgments

Funding from the European Community's social foundation under Grant Agreement No VP1-3.1-ŠMM-08-K-01-004/KS-120000-1756 is acknowledged.

References

1. E. Anticfidancev, J. Holsa, J.C. Krupa, M. Lemaitreblaise, P. Porcher, *J Phys-Condens Mat*, 4 (1992) 8321-8330.
2. R.J. Bula, R.C. Morrow, T.W. Tibbitts, D.J. Barta, R.W. Ignatius, T.S. Martin, *Hortscience*, 26 (1991) 203-205.
3. G. Tamulaitis, P. Duchovskis, Z. Bliznikas, K. Breive, R. Ulinskaite, A. Brazaityte, A. Novickovas, A. Zukauskas, *J Phys D Appl Phys*, 38 (2005) 3182-3187.
4. A. Zabiliute, S. Butkute, A. Zukauskas, P. Vitta, A. Kareiva, *Appl Optics*, 53 (2014) 907-914.

SILVER NANOPATES – SILICA COMPOSITE COATINGS VIA SOL – GEL ROUTE

Jurgis Pilipavicius¹, Ala Chodosovskaja¹, Aldona Beganskiene, Aivaras Kareiva¹

1 Vilnius University, Faculty of Chemistry, Department of Inorganic Chemistry

E-mail: jurgis.pilipavicius@chf.vu.lt

1. Introduction

Noble metal nanoparticles have been investigated and applied in many research areas including chemical catalysis [1], biochemistry [2], optics [3], and electronics [4]. Recent years, scientists are focused in anisotropic Silver and Gold nanoparticles properties and their application in various fields [5]. Silver nanoprisms (NPRs) are one of the most interesting nanoparticle type, because of wide tuneability and high intensity of surface plasmon resonance (SPR) band [6]. Manipulating particle thickness and edge length, it is possible to obtain SPR peak position in 400 – 1300 nm range, when conventional spherical exceeds only 600 nm [7]. These properties opens the gateway for application in near infrared working technologies, like telecommunications [7] or surface enhanced Raman spectroscopy (SERS) [8].

Our investigation is focused on synthesis of Silver nanoprism composite materials. One of the approach is silica/Ag NPRs coatings. Our approach is make silica-silver nanoprism coatings by self-assembly of particles on functionalized silica surface. *Xue, C., et al. [9]* already made an investigation on this topic, but still lacking information about how different surface affects Ag NPRs self-assembly.

In this work we investigated influence of differently prepared silica surface to assembly of silver NPRs. Therefore we synthesized a Silver NPRs with average edge lengths of 94 ± 15 nm, made silica coatings by sol-gel technique, functionalized surfaces using different silanes by silanization, and deposited NPRs on silica coating surface. Particles were deposited on differently functionalized colloidal silica coating surface. Produced composite coatings were evaluated by scanning electron microscopy (SEM).

2. Experimental

Chemicals. Tetraethyl orthosilicate (TEOS, 98%), (3-Aminopropyl)triethoxysilane (APTES, 99%), N-[3-(Trimethoxysilyl)propyl]ethylenediamine (AEAPTMS, 98%), (3-Mercaptopropyl)trimethoxysilane (MPTMS 99%), Silver nitrate (AgNO_3 , 99%), Poly(sodium 4-styrenesulfonate) (PSSS, 1000000 Mw), Sodium Borohydride (NaBH_4 , 99%), L-Ascorbic Acid ($\text{C}_6\text{H}_8\text{O}_6$, 99%) were purchased from Sigma-Aldrich and used without further purification. Absolute ethanol (99.9 %) prepared by refluxing with preheated CaO , and after distilled.

Synthesis of silver NPRs. Silver NPRs were made by seed-mediated method which include two steps – producing silver nanoseeds and nanoprism growing.

Making silver seeds. In this experiment, silver seed are obtained by mixing aqueous trisodium citrate (20 mL, 25 mM), PSSS (1 ml, 0.5 g/L), freshly prepared NaBH_4 (1.2 mL, 10 mM) solutions, followed by addition of aqueous AgNO_3 (20 mL, 0.5 mM). Addition rate of AgNO_3 was 2 mL/min. The rate was maintained using syringe pump.

Growing of NPRs. Silver NPRs are produced by mixing 35 ml distilled water, aqueous ascorbic acid (0.525 mL, 10 mM) solution, 0.560 mL of prepared silver seeds solution, followed by addition of aqueous AgNO_3 (21 mL, 0.5 mM) at a rate of 1 mL/min. Obtained Silver seeds and NPRs solutions characterized by UV-VIS spectroscopy (Perkin Elmer Lambda 35), Scanning Electron Microscopy (SEM, Hitachi FE-SEM SU-70).

Synthesis of colloidal silica and coating procedure. Colloidal silica sols in ethanol were made by base catalyzed TEOS hydrolysis and condensation. For this purpose TEOS, Ammonia, Water, and Ethanol were mixed with molar ratio 1:0.2:2.3:38 respectively. Sols were left at room temperature for 10 days. Particle size was determined by Dynamic Light Scattering (DLS, Malvern Instruments Zetasizer Nano ZS) method.

For coating process microscope soda-lime glass slides were used as substrate. Substrates were cleaned by immersing them in piranha solution (volume ratio 1:4 of H₂O₂ and H₂SO₄ respectively) for 15 min. After that substrates were washed with deionized water few times, and dried by leaving in desiccator for 24 h at room temperature. Coatings were made by Dip-Coating technique (KSV Dip Coater D). For all samples were used constant 40 mm/min withdrawal speed. Coated samples were ready for the next step – surface silanization.

Surface modification and deposition of Silver NPRs. Thermal silanization. Coatings and uncoated substrates were functionalized by three alkoxysilanes – APTES, AEAPTMS and MPTMS. For all of them the same silanization method were used. First of all, three different 3% alkoxysilane solutions in toluene were prepared. Then substrates were immersed in solution and refluxed for 12 hours under argon atmosphere. After modification, substrates were washed several times with pure toluene and acetone.

For deposition of Silver NPRs, functionalized substrates were immersed into further prepared Silver NPRs colloidal solution and kept for 7 days. The composite coatings were gently washed with distilled water and left to dry in room temperature.

3. Results and discussions

Synthesis of Silver NPRs. For silver nanoprism synthesis was selected the seed-mediated method, which was firstly suggested by Aherne, D., et al. [6]. Synthesized particles by this method are sufficiently monodisperse, and it is faster and easier to obtain comparing to photoconversion method [10].

By this thermal method silver NPRs were synthesized in high yield, with edge length about 94 ±15 nm. Average particle sizes were calculated from SEM micrographs (fig 1.) As can be seen from fig. 1, obtained particles are plate-like structure and almost all have trigonal or hexagonal shape, but varies in size.

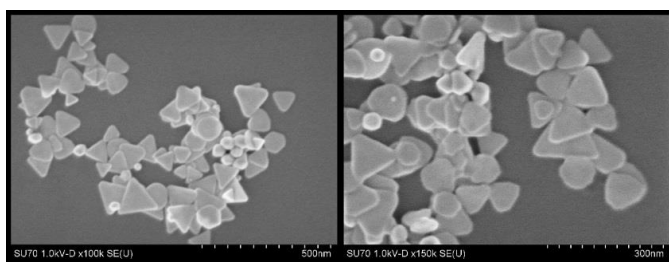


Figure 1. SEM images of synthesized Ag NPRs particles

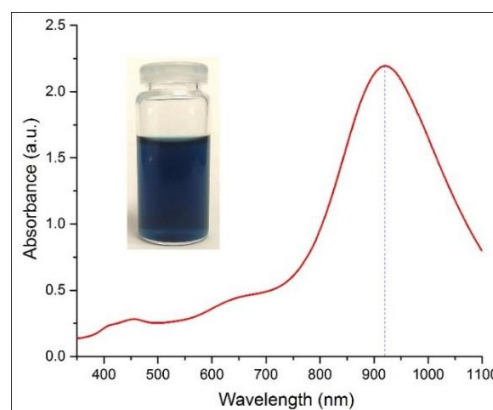


Figure 2. Absorption spectra of synthesized Ag NPRs solution

Obtained colloidal Silver NPRs solution are relatively stable and no significant changes were observed in few months. Single SPR band (fig. 2) shows high intensity absorption at 921 nm, which gives a blue color of NPRs colloidal solution. Red shifted SPR peak indicates presence of high aspect ratio anisotropic particles like triangular NPRs or nanohexagons in solution. Also observable SPR peak is slightly broadened, but it is common for all plasmonic particles which has absorption in near infrared [5].

Synthesis of colloidal silica, fabrication of coatings and surface silanization. As mentioned in experimental section, in this research base catalyzed silica sol were used. During this reaction, usually forms silica spheres which diameter can be varied form nanometer to submicrometer scale. Exact size of the spheres is controlled by initial ratio of starting materials [11]. Accordingly, 3% (w/w) monodisperse colloidal silica in ethanol, with 30 ± 11 nm average sphere diameter were made by selecting appropriate ratio of standing materials [12]. After sol synthesis, coatings were formed using dip-coating method and samples were kept for next step – surface functionalization.

In this work we selected thermal silanization method. By this technique, ideally, only one layer of silane is formed on coating surface. Coated substrates functionalized by – APTES, AEAPTMS and MPDMS. This surface modification method is straightforward and well-studied, however silanized surface must be characterized to make sure, that surface functionalization were succeeded. In our case, to make sure that silanization process was successful, water contact angles (CA) and surface free energy (SFE) measurements were made (table 1).

Table 1. Measured water contact angle and SFE values of silanized coatings

Sample name	Modifying silane	Contact angle, deg.	Dispersive free energy, mN/m	Surface Polar energy, mN/m	Surface free energy, mN/m	Total Surface free energy, mN/m
JV025	None	40.20	36.80	24.27		61.07 \pm 4,45
JV026	APTES	69.75	31.16	9.82		40.98 \pm 5,09
JV027	AEAPTMS	66.75	25.94	13.55		39.48 \pm 4,60
JV028	MPTMS	54.84	37.55	14.94		52.49 \pm 5,31

For SFE measurements we selected Harmonic Mean (Wu) method which gives more accurate results when surface have high SFE values. In order to calculate surface free energy, in contact angle measurements we used four solvents – diiodomethane, water, glycerol and ethylene Glycol.

As can be seen form table 1, all silanized coatings have higher CA and smaller total SFE values, comparing with non-silanized coating. As result of high amount of polar hydroxyl groups on surface, highest wetting capabilities has non-functionalized silica films. MPTMS modified coatings has slightly better wetting properties and higher surface free energy comparing with APTES and AEAPTMS functionalized coatings.

Silver NPRs self-assembly on silanized surfaces. In this section we investigated silver NPRs self-assembly on differently silanized silica coatings. We tried to find out which silanized surface is more suitable for assembly of NPRs. Thus, as mentioned in experimental section, in order to obtain self-assembled silver NPRs layer, functionalized coatings were vertically immersed in plastic vials with containing silver NPRs solution and kept for 1 week at room temperature. After this procedure, samples were ready for UV-Vis measurements.

Coatings were investigated by SEM. SEM images of differently silanized-Ag NPRs self-assembled coatings are presented in figure 3.

Most even arrangement of Ag NPRs are visible on APTES functionalized coating – particles are arranged mostly as monolayer and noticeable aggregation is minimal. The image of AEAPTMS functionalized surface confirm aggregation of particles and uniform monolayer no longer forms. Consequently, this layer of Ag NPRs looks grayish and no SPR is observable in UV-Vis spectra. Only separate, wide spread particles are observed on MPTMS functionalized coating. The UV-Vis spectra data show weak absorbance of unmodified coating and no Ag NPRs are observed on SEM image.

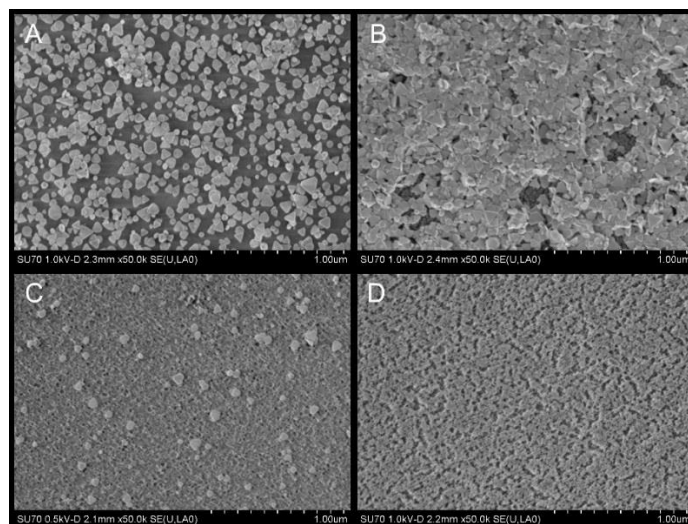


Figure 3. SEM images of Ag-silica composite coatings: silanized by APTES (A), AEAPTMS (B), MPTMS (C) and non-silanized (D)

4. Conclusions

This research showed that most homogeneous silica-Ag NPRs coatings are obtained when surfaces were silanized with APTES. However, AEAPTMS silanized coatings tend to aggregation of silver NPRs layer, while MPTMS functionalized coatings have low affinity to Ag NPRs. Nevertheless, we successfully made functionalized silica coatings by sol-gel method and formed Ag NPRs layer on them via self-assembly process. This type of coatings can be applied for further research in SERS, or used for making multilayer coatings to obtain Ag NPR- silica embedded matrixes. On the other hand, the influence of other surface parameters to Ag NPRs self-assembly, like surface roughness, silanization method and etc., should be further investigated.

Acknowledgment

Postdoctoral fellowship of A.C. is being funded by European Union Structural Funds project "Postdoctoral Fellowship Implementation in Lithuania" within the framework of the Measure for Enhancing Mobility of Scholars and Other Researchers and the Promotion of Student Research (No. SF-PD-2012-12-31-0397) of the Program of Human Resources Development Action Plan.

References

1. Signori, A.M., K.D. Santos, R. Eising, B.L. Albuquerque, F.C. Giacomelli, and J.B. Domingos, *Langmuir*, **2010** 17772-17779
2. Abalde-Cela, S., P. Aldeanueva-Potel, C. Mateo-Mateo, L. Rodriguez-Lorenzo, R.A. Alvarez-Puebla, and L.M. Liz-Marzan, *J R Soc Interface*, **2010** S435-S450
3. Chen, X., J. Tao, G. Zou, W. Su, Q.J. Zhang, and P. Wang, *Chemphyschem*, **2010** 3599-3603
4. Matsui, I., *J Chem Eng Jpn*, **2005** 535-546
5. Xiao, J. and L. Qi, *Nanoscale*, **2011** 1383-1396
6. Aherne, D., D.M. Ledwith, M. Gara, and J.M. Kelly, *Adv Funct Mater*, **2008** 2005-2016
7. Bastys, V., I. Pastoriza-Santos, B. Rodríguez-González, R. Vaisnoras, and L.M. Liz-Marzán, *Adv Funct Mater*, **2006** 766-773
8. Yi, Z., X. Xu, X. Wu, C. Chen, X. Li, B. Luo, J. Luo, X. Jiang, W. Wu, Y. Yi, and Y. Tang, *Appl. Phys. A*, **2013** 335-342
9. Xue, C., X. Chen, S.J. Hurst, and C.A. Mirkin, *Adv. Mater.*, **2007** 4071-4074
10. Xue, C. and C.A. Mirkin, *Angew Chem Int Edit*, **2007** 2036-2038
11. Boonstra, A.H. and T.N.M. Bernards, *J. Non-Cryst. Solids*, **1989** 249-259
12. Pilipavicius, J., I. Kazadojev, A. Beganskiene, A. Melninkaitis, V. Sirutkaitis, and A. Kareiva, *Mater Sci-Medzg*, **2008** 283-287

CONTROLLED SYNTHESIS OF Ag_3PO_4 TETRAPODS**J. Raudoniene¹, L. Sinkevicius², R. Raudonis¹, E. Garskaite¹**¹*Department of Applied Chemistry, Faculty of Chemistry, Vilnius University, Naugarduko 24, Vilnius LT-03225, Lithuania*²*Department of Physical Chemistry, Faculty of Chemistry, Vilnius University, Naugarduko 24, Vilnius LT-03225, Lithuania
E-mail: edita.garskaite@chf.vu.lt***Introduction**

Silver orthophosphate (Ag_3PO_4) is a photocatalyst that can harness visible light to oxidize water with the quantum yields of up to 90% [1]. Recently, it has been demonstrated that shape and morphology of Ag_3PO_4 crystals strongly influence its photocatalytic performance [2]. Therefore, the control over synthesis process to achieve the formation of crystals with desirable shape is an important pursuit.

Solution-based synthesis is one of the most common routes proposed to prepare Ag_3PO_4 crystals. Shape of crystals can be tailored according to solution composition and processing conditions. For example, Wang *et al.* demonstrated the preparation of tetrapod-shaped Ag_3PO_4 crystals under presence of urea [3]. Dong *et al.* showed the synthesis of various crystals when mixed solvent of dimethylformamide and water was used conjointly with different external conditions and reaction times [4]. Bi *et al.* reported synthesis of single crystalline Ag_3PO_4 sub-microcubes produced by reacting the $[\text{Ag}(\text{NH}_3)_2]^+$ complex with Na_2HPO_4 at room temperature [5]. Martin *et al.* proposed synthesis of microsized Ag_3PO_4 tetrahedrons when AgNO_3 -ethanol mixture was added drop-wise to the H_3PO_4 -ethanol solution [6]. In all cases the understanding and controlling chemistry processes during solution-based synthesis are key in growing various nanostructured materials with advanced functionalities.

Here we report the preparation of Ag_3PO_4 tetrapods via solution-based synthesis method. The effects of solution composition and processing conditions on material morphology were explored. Scanning electron microscopy, transmission electron microscopy and X-ray diffraction analysis were used to characterize material morphological and structural properties.

Keywords: Silver phosphate, photocatalyst, water splitting.

Experimental*Synthesis of Ag_3PO_4 crystals*

Ammonium hydrogen phosphate ($(\text{NH}_4)_2\text{HPO}_4$, 98.0% min, ACS, Alfa Aesar), ammonium dihydrogenphosphate ($(\text{NH}_4)\text{H}_2\text{PO}_4$ $\geq 99.99\%$ trace metals basis, Sigma-Aldrich) and silver nitrate (AgNO_3 , ACS reagent, $\geq 99.0\%$, Sigma-Aldrich) were used as precursors for preparation of Ag_3PO_4 crystals of different shapes. Ag_3PO_4 tetrapod crystals were synthesized via precipitation method at room temperature mixing aqueous solutions of $\text{NH}_4\text{H}_2\text{PO}_4$ and AgNO_3 . Obtained yellow crystals were mixed with magnetic stirrer for 5 min. After decantation crystals were three times prewashed with distilled water and then left for 48 h in the dark to dry. Spherical particles were produced in the same procedure only $\text{NH}_4\text{H}_2\text{PO}_4$ solution replacing with $(\text{NH}_4)_2\text{HPO}_4$ solution.

Characterization

Morphology of prepared crystals was evaluated using field emission scanning electron microscopy (FE-SEM, SU70, Hitachi). The phase composition and crystal structure of the Ag_3PO_4 crystals were studied by X-ray diffraction (XRD, Rigaku, MiniFlex II). TEM characterization was performed at 200 kV using field emission transmission electron microscopy (JEM 2100F, JOEL).

Results and discussion

Selected SEM micrographs of Ag_3PO_4 crystals with specific morphology (tetrapod, spherical, cube and mixed-shape) are presented in Fig. 1. Tetrapod shaped crystals of 12 μm in diameter were produced when $\text{NH}_4\text{H}_2\text{PO}_4$ was used as a precursor, while spherical particles of 100-400 nm were obtained when $(\text{NH}_4)_2\text{HPO}_4$ was introduced into solution (Fig. 1 (a) and (b)).

A series of experiment were carried out where concentration of $\text{NH}_4\text{H}_2\text{PO}_4$ was alternated. SEM analysis showed that morphology of produced Ag_3PO_4 crystals was changing from tetrapod to cube shape with intermediate stages where mixed-shape crystals were obtained (Fig. (a), (c) and (d)).

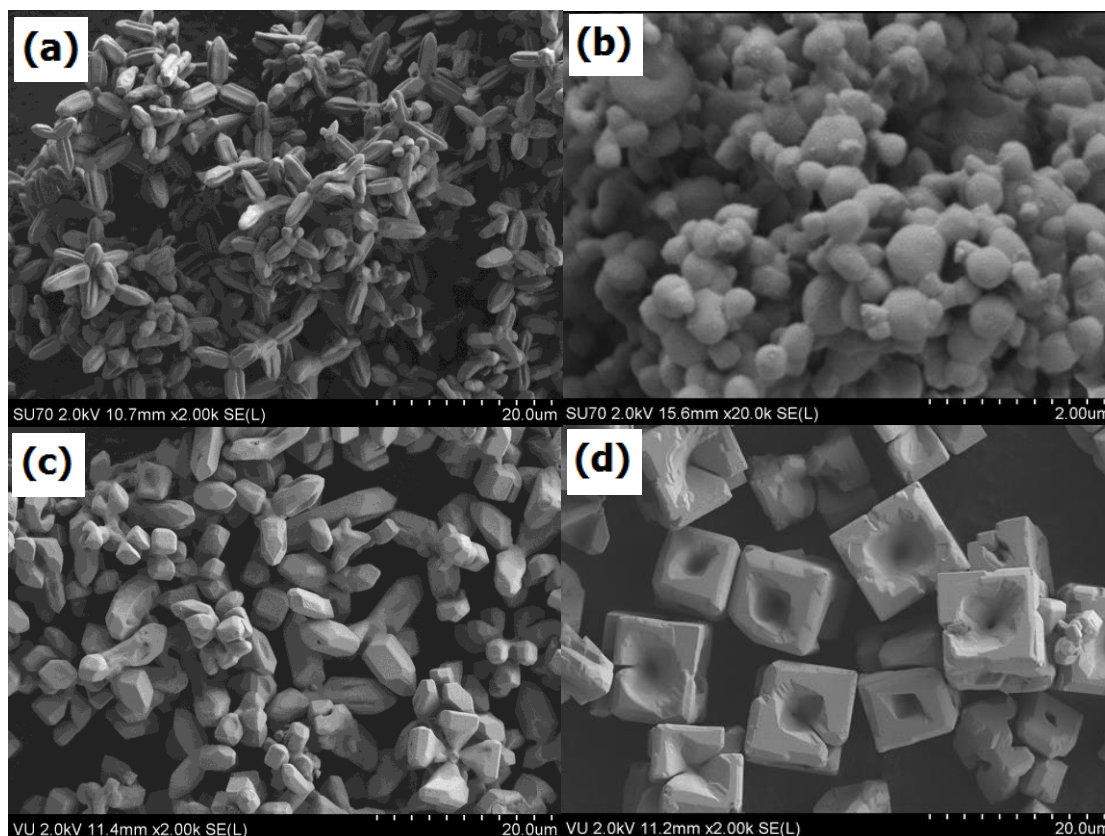


Fig. 1 FE-SEM micrographs of Ag_3PO_4 crystals produced under different conditions: (a) $\text{NH}_4\text{H}_2\text{PO}_4$ and (b) $(\text{NH}_4)_2\text{HPO}_4$ were used as precursors, (c) and (d) varying $\text{NH}_4\text{H}_2\text{PO}_4$ concentration.

Furthermore, experiments were carried out when stirring time and speed were altered. Obtained results show that crystal shape is not affected by these processing conditions.

A typical XRD pattern of Ag_3PO_4 tetrapod crystals is presented in Fig. 2. All Bragg reflections in presented pattern were indexed and assigned to the cubic Ag_3PO_4 phase (JCPDS No. 06-0505). All other samples exhibited similar diffraction patterns.

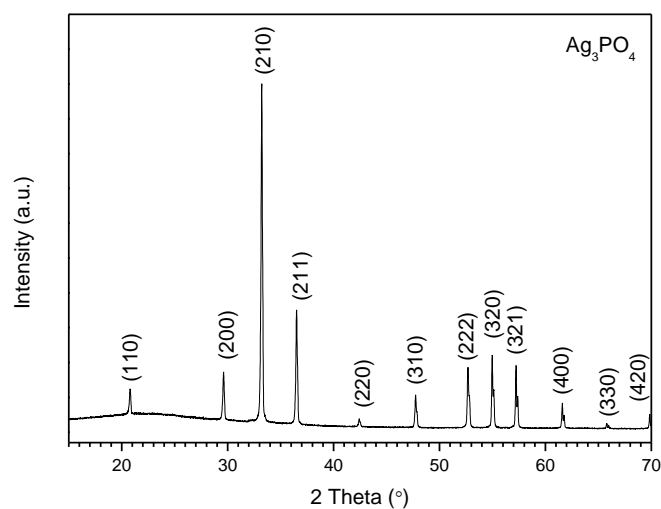


Fig. 2 XRD diffraction pattern of Ag_3PO_4 crystals.

Representative FE-TEM images of Ag_3PO_4 crystals are presented in Fig. 3. However, to perform HR-TEM analysis of crystals was not possible due to decomposition of sample under illumination with electron beam of 200 kV (Fig. 3 (b)).

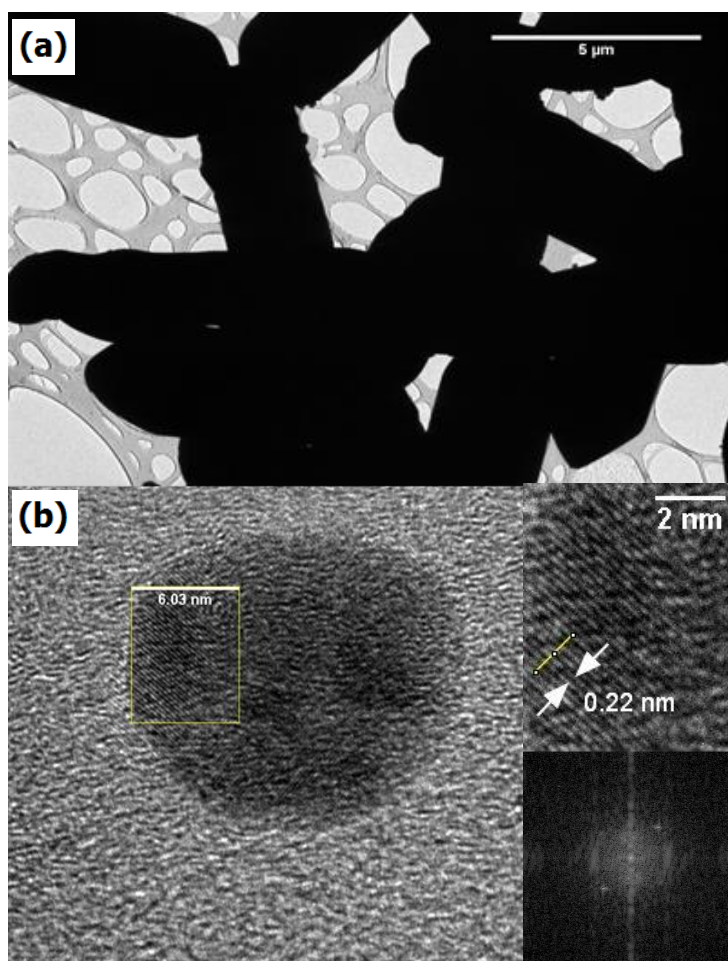


Fig. 3 FE-TEM images: (a) Ag_3PO_4 crystals, (b) HR-TEM of Ag nanoparticles produced after degradation of Ag_3PO_4 crystals under 200 kV (insets: (top) the interplanar spacing between the atoms and (bottom) FFT pattern).



The interplanar spacing (d value) of Ag particle was measured as 0.22 nm, which is in agreement with the reported value of the (111) crystallographic plane of cubic Ag (JCPDS No. 04-0783).

Conclusions

Simple and efficient solution based approach to produce Ag_3PO_4 crystals of various controlled shape has been demonstrated. Results showed that Ag_3PO_4 crystals with different morphology could be obtained by varying precursors and their concentration in solvent of water.

Acknowledgement

This work was partly supported by STSM COST MP1202 “Rational design of hybrid organic-inorganic interfaces: the next step towards advanced functional materials” project. ICL is acknowledged for HR-TEM analysis.

References

1. Z. Yi. et al., *Nat. Mater.* 9 (7) (2010) 559-564.
2. Y. Bi et al., *J. Am. Chem. Soc.* 133 (17) (2011) 6490-6492.
3. J. Wang et al., *CrystEngComm.* 15 (1) (2013) 39-42.
4. P. Dong et al., *J. Mat. Chem. A* 1 (15) (2013) 4651-4656.
5. Y. Bi et al., *Chem. Comm.* 48 (31) (2012) 3748-3750.
6. D. J. Martin et al., *Energ. Environ. Sci.* 6 (11) (2013) 3380-3386.



LUMINESCENCE PROPERTIES OF YAG:Tb, YAG:Cr AND YAG:Tb,Cr SYNTHESIZED BY SOL-GEL METHOD

M. Skruodiene¹, M. Misevicius², A. Katelnikovas¹, R. Skaudzius²

1 Department of Analytical and Environmental Chemistry, Vilnius University, Naugarduko 24, LT-03225 Vilnius, Lithuania

2 Department of Inorganic Chemistry, Vilnius University, Naugarduko 24, LT-03225 Vilnius, Lithuania

E-mail: monika.skruodiene@chf.vu.lt

Since 1928, it became possible to determinate synthetic and natural compounds which have garnet structure [1]. The yttrium aluminum garnet ($\text{Y}_3\text{Al}_5\text{O}_{12}$, YAG) was one of the first synthetic garnet which has a huge interest in studies for different kind of applications till nowadays [2]. Sol-gel method is a synthesis route successfully applied to obtain garnets. Y_2O_3 and $\text{Al}(\text{NO}_3)_3 \cdot 9\text{H}_2\text{O}$ are used as starting materials, HNO_3 as catalyst agent, citric acid as complexing agent to synthesize YAG. This method has a lot of advantages among other synthesis routes such as high reactivity, good homogeneity and probability to get phase pure garnets at low temperature range [3].

The YAG has a cubic garnet structure, stable crystal lattice, therefore doped YAG by rare earths elements and/or transition metal ions is widely used in optical technologies, luminescent and fiber-optic telecommunication systems [4]. It is also very important in laser ceramics and solid-state phosphor systems. Moreover, YAG doped with transition metal ions is used as saturable absorbers in passive Q-switch crystals for lasing technique. YAG:Cr is long-life phosphors used in liquid crystal light valve projection displays. Cr^{3+} doped garnets exhibit emission in red and far-red regions. It is known that there are three main processes in successful growth of plants, which require light in red, far-red and blue spectral ranges. That means YAG:Cr takes part in potential use in phosphor-converted light-emitting diodes that meet photomorphogenetic needs of plants. Meanwhile, YAG:Tb is not sensitive to temperature changes and it is suitable for contrast-enhanced display application in high ambient illumination conditions [2] [5-7] [8]. Eu^{3+} , Tb^{3+} and Ce^{3+} ions are able to emit visible radiation in red, green and blue colour spectra. They can incorporate into one site (D_{2h} symmetry) of the YAG lattice. It decreases the energy transfers between dopants occurring in multi-site hosts and causing non-radiative transitions and decrease of the luminescence efficiency. YAG doped with these dopants has improved chemical and physical properties (temperature characteristics, resistance to brightness saturation and matrices resistance to high intensity electron beams). YAG:Tb has potential and can be used as phosphor materials such as cathode-ray and projection television tubes, X-ray phosphors and scintillators [9-11]. Luminescence efficiency of the phosphor depends on synthesis and preparation method and the size of garnet's particles. The smaller particles – the greater efficiency [12].

In the present work, YAG, YAG:Cr, YAG:Cr,Tb and YAG:Tb phosphors were synthesized by citric sol-gel method. Yttrium oxide (Y_2O_3 , Aldrich, 99.99 %), aluminum nitrate ($\text{Al}(\text{NO}_3)_3 \cdot 9\text{H}_2\text{O}$, Roth, $\geq 98\%$), chromium nitrate ($\text{Cr}(\text{NO}_3)_3 \cdot 9\text{H}_2\text{O}$, Aldrich, 99%), terbium oxide (Tb_4O_7 , Alfa Aesar 99,99%) were used as starting materials. Citric acid ($\text{C}_6\text{H}_8\text{O}_7 \cdot \text{H}_2\text{O}$, Penta, 99.5%) was used as complexing agent. Starting materials were weight to yield compositions with formulas: $\text{Y}_3\text{Al}_5\text{O}_{12}$, $\text{Y}_{2.61}\text{Tb}_{0.15}\text{Al}_5\text{O}_{12}$, $\text{Y}_{2.61}\text{Cr}_{0.24}\text{Tb}_{0.15}\text{Al}_5\text{O}_{12}$, $\text{Y}_{2.76}\text{Cr}_{0.24}\text{Al}_5\text{O}_{12}$. Insoluble in water starting oxides were dissolved in hot diluted nitric acid. The excess of nitric acid was evaporated and the formed nitrates were washed 3 times with distilled water. Then the starting compounds (nitrates) were added the transparent solution and the obtained solution was stirred for additional 30 minutes at 70-80 °C. Finally, the complexing agent at a molar ratio of 1:2 to all metal ions was added into the clear solution.

The formed sol was stirred for 1 h at the same temperature. The final solution was placed into the drying oven at 140 °C. After the concentrating sol by slow evaporation of solvent it turned into transparent gel. The gels were dried in the oven overnight at the same condition. The resulted yellowish/greenish brown products were ground to fine powders, which were firstly annealed at 1000 for 2 h in covered crucibles in air to remove the organic components and residual nitrates. Subsequently, obtained powders were annealed at different temperatures (1000, 1200, 1400 and 1600 °C) for 4 h in air.

The XRD data were collected at 10°–70° 2θ range (step width of 0.01°, scan speed 10°C/min) for phase identification at ambient temperature using Ni-filtered Cu Kα₁ radiation on Rigaku MiniFlex II diffractometer. Scanning electron microscopy (SEM) images were taken for the morphology characterization with Hitachi SU-70. Luminescence spectra were recorded on an Edinburgh Instruments FLS980 spectrometer equipped with a 450 W We arc lamp, a cooled (-20 °C) single-photon counting photomultiplier (Hamamatsu R928) and a lens optics for powders samples. The photoluminescence emission spectra were corrected by a correction file obtained from a tungsten incandescent lamp certificated by the National Physics Laboratory (UK). For recording emission and excitation spectra emission and excitation slits were set to 0.3 and 2.0 nm, respectively. The step size was 0.5 nm and integration time 0.2 s.

The powder XRD patterns of YAG powders annealed at different temperatures in air and XRD patterns of doped and co-doped YAG annealed at 1600 °C are presented in Fig. 1.

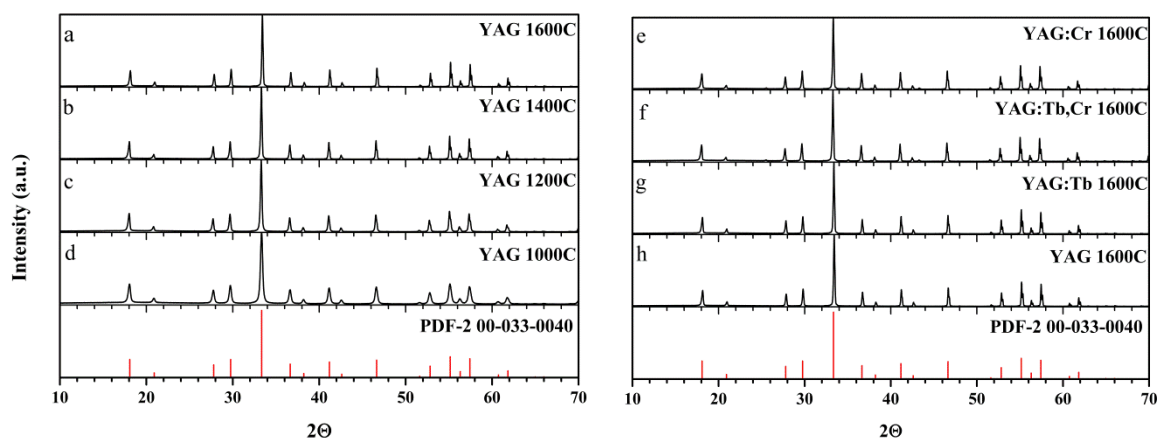


Fig.1. XRD patterns of YAG annealed at different temperatures (1000 °C – 1600 °C (a–d)) and doped and co-doped YAG annealed at 1600 °C YAG:8%Cr (e), YAG:5%Tb8%Cr (f), YAG:5%Tb (g) and YAG(h).

Each peak matches well the reference patterns of YAG (PDF2 [00-033-0040]) [13]. It is obvious, that 1000 °C temperature is high enough to yield the single phase cubic garnet structure. Nevertheless, in literature it is reported that the garnet phase starts to form even at 800 °C [5]. The XRD pattern peaks of samples annealed at 1000 °C are rather broad. Raising the sintering temperature from 1000 °C to 1600 °C resulted in much narrower peaks indicating that the size of particles is increased. The same pattern was observed for terbium, chromium or terbium and chromium doped samples. The XRD patterns also show that doping by rare earth and/or transition metal ions does not affect the phase formation. The ions were successfully introduced into the garnet lattice, since each peak of patterns matches well with the reference data of YAG.

The morphology features of YAG, doped YAG and co-doped YAG annealed at different temperatures were inspected by taking SEM images (Fig.2). It is clear that doping does not affect the morphology of samples (Fig. 2. (a–d)). All samples possess well-shaped irregular sphere-like morphology. During the annealing process the partly melted nanosheets become cross-linked causing highly agglomerated particles. In addition, it is obvious that the increase of the sintering temperature from 1000 °C to 1600 °C results the growth of particle, what goes

hand to hand with the peak narrowing in the XRD patterns at elevated temperatures. (Fig.2. (e-h)).

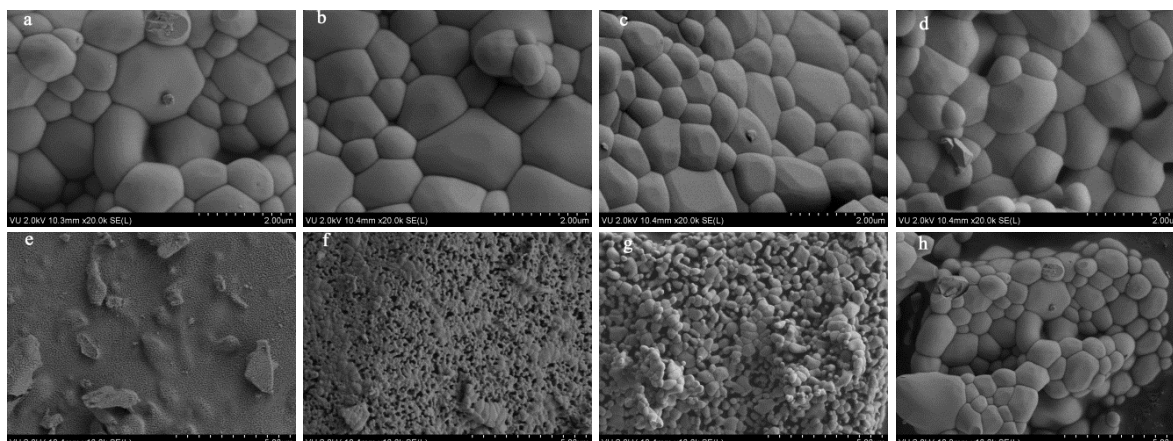


Fig.2. SEM images of YAG annealed at 1600 °C (a), YAG:5% Tb annealed at 1600 °C (b), YAG:5% Tb, 8% Cr annealed at 1600 °C (c), YAG:8% Cr annealed at 1600 °C (d), YAG annealed at 1000 °C (e), YAG annealed at 1200 °C (f), YAG annealed at 1400 °C (g), YAG annealed at 1600 °C (h).

Finally, the presence of pores are clearly visible, which could be formed due the escaping gasses during the burning of organic components and residual nitrates.

The luminescence spectra of YAG: 5% Tb, YAG: 8% Cr and YAG: 5%Tb, 8%Cr are shown in Fig.3.

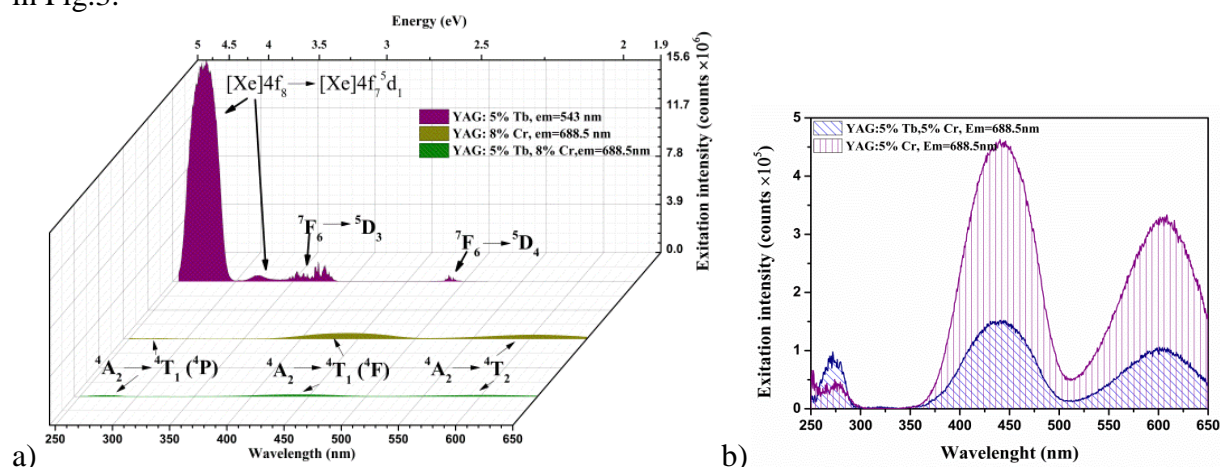


Fig.3. Excitation spectra of doped and co-doped YAG annealed at 1600°C, recorded for the strongest emission line at 688.5 and 543 nm, respectively.

The bands with the maximum at 267 nm and 317 nm are attributed to the low and high spin transitions $[Xe] 4f_8 \rightarrow [Xe] 4f_7 5d_1$ of Tb^{3+} , respectively, while the peaks at 350-390 nm correspond to the $7F_6 \rightarrow 5D_3$ transitions (Fig.3a.). Evidence for the presence of $7F_6 \rightarrow 5D_4$ transitions is also observed at 480-500 nm. All these terbium transitions are quenched in terbium-chromium co-doped YAG. Meanwhile, the $4A_2 \rightarrow 4T_2$, $4A_2 \rightarrow 4T_1(4F)$ and $4A_2 \rightarrow 4T_2(4P)$ transitions of Cr^{3+} dominate in the excitation spectra of YAG: 8% Cr and YAG: 5%Tb, 8%Cr (Fig.3b.). Emission spectra excited by 273 nm or 600 nm wavelength light of YAG: 5% Tb, YAG: 8% Cr and YAG: 5% Tb, 8% Cr phosphors are shown in Fig. 4. The emission spectrum of terbium doped YAG exhibits peaks corresponds to $5D_4 \rightarrow 7F_6$ (at 480-510 nm, blue region), $5D_4 \rightarrow 7F_5$ (at 535-565 nm, green region), $5D_4 \rightarrow 7F_4$ and $5D_4 \rightarrow 7F_3$ (at 580-610 nm and 610-635 nm, red region) transitions. The most intensive peak is at 543 nm. This yields a green-yellowish emission spectrum.

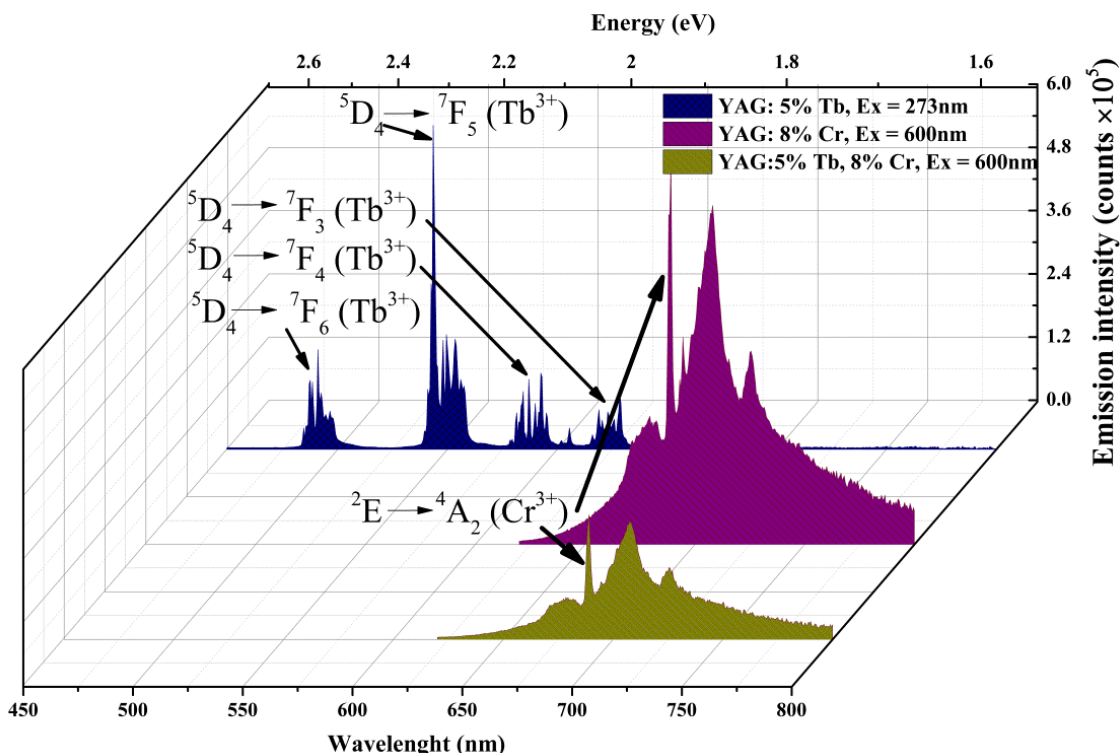


Fig.4. Emission spectra of YAG: 5% Tb, YAG: 8% Cr and YAG: 5%Tb, 8%Cr annealed at 1600°C.

YAG: 8%Cr, YAG: 5%Tb, 8%Cr phosphors has a wide band in red (620–680 nm) and far-red (700–800 nm) region. The maximum of emission at 689 nm is contributed the the ${}^2E \rightarrow {}^4A_2$ transition of Cr^{3+} ions in YAG: 8%Cr and YAG: 5%Tb: 8% Cr. The introducing of terbium ions in YAG:Cr $^{3+}$ resulted the decrease of the intensity of Cr^{3+} if the samples are excited by 600 nm wavelength.

The effect of the terbium and chromium concentrations in YAG is under investigation.

References

1. F. Euler, J. A. Bruce, *Acta Cryst.*, **1965**, *19*, 971-978
2. P. Gluchowski, R. Pazik, D. Hreniak, W. Strek, *J Lumin* **2009**, *129*, 548-553.
3. Z. H. Sun, D. R. Yuan, H. Q. Li, X. L. Duan, H. Q. Sun, Z. M. Wang, X. C. Wei, H. Y. Xu, C. N. Luan, X. Dong, M. Lv, *J Alloy Compd* **2004**, *379*, L1-L3.
4. K. Guo, M. L. Huang, H. H. Chen, X. X. Yang, J. T. Zhao, *J Non-Cryst Solids* **2012**, *358*, 88-92.
5. A. Leleckaite, A. Kareiva, *Opt Mater* **2004**, *26*, 123-128.
6. A. Kareiva, *Mater Sci-Medzg* **2011**, *17*, 428-437.
7. E. De la Rosa, L. A. Diaz-Torres, P. Salas, A. Arredondo, J. A. Montoya, C. Angeles, R. A. Rodriguez, *Opt Mater* **2005**, *27*, 1793-1799.
8. A. Zabiliute, S. Butkute, A. Zukauskas, P. Vitta, A. Kareiva, *Appl Optics* **2014**, *53*, 907-914.
9. D. Hreniak, W. Strek, P. Mazur, R. Pazik, M. Zabkowska-Waclawek, *Opt Mater* **2004**, *26*, 117-121.
10. Y. Hakuta, T. Haganuma, K. Sue, T. Adschiri, K. Arai, *Mater Res Bull* **2003**, *38*, 1257-1265.
11. Kinsman, K. M., Mckittrick, J., *J Am Ceram Soc* **1994**, *77*, 2866-2872.
12. P. F. S. Pereira, M. G. Matos, L. R. Avila, E. C. O. Nassor, A. Cestari, K. J. Ciuffi, P. S. Calefi, E. J. Nassar, *J Lumin* **2010**, *130*, 488-493.
13. *Natl. Bur. Stand. (U.S.) Monogr.* **25** *19*, 11, **1982**.

DETERMINATION OF FATTY ACID COMPOSITION OF ADIPOSE TISSUE BY ^1H NMR SPECTROSCOPY

A. Smalenskaite¹, B. Buckus², S. Tautkus³, A. Beganskiene¹, G. Brimas², A. Kareiva¹

¹Department of Inorganic Chemistry, Vilnius University, Vilnius, Lithuania

²Clinic of Gastroenterology, Nephrourology and Surgery, Vilnius University, Vilnius, Lithuania

³Department of Environmental and Analytical Chemistry, Vilnius University, Vilnius, Lithuania

E-mail: aurelija.smalenskaite@gmail.com

Introduction

Medical studies revealed that adipose tissue not only stores energy reserves of fat in the form of a protective function, but also is involved in the metabolism and biochemical processes. Obesity has been clearly associated with numerous pathophysiologic processes and comorbidities, such as metabolic syndrome, type 2 diabetes mellitus and cardiovascular disease which is the most common cause of death in the western world. Central obesity been shown to be more associated with metabolic syndrome and there is evidence of excellent results in treatment with the control of obesity. In this work the samples were taken from volunteer obese patients and analysed using ^1H NMR spectroscopy. This method provides a possible alternative to conventional chromatographic methods for determining the composition of fats. ^1H NMR gives information about fat chemical and structural composition, as well as microstructure in human patients. Parameters such as mean unsaturation, mean poly-unsaturation, and mean chain length can provide useful information about diet, fat distribution and metabolism.

Experimental

Adipose tissue samples were homogenised according to Kaminskas [1]. The lipids were extracted by 20 ml of chloroform/methanol (2:1, v/v) using a modified Folch procedure [2]. ^1H NMR spectra were recorded on a Bruker Ascend 400 spectrometer operating at 9.4 Tesla, corresponding to the resonance frequency of 400 MHz for the ^1H nucleus, equipped with a direct detection four nuclei probe head and field gradients on z axis. Samples were analyzed in 5 mm NMR tubes. The ^1H NMR samples were prepared by dissolving 0.5 mL fat in 2 mL CDCl_3 . The chemical shifts are reported in ppm, using the TMS as internal standard. Typical parameters for ^1H NMR spectra were: 45° pulse, 20 ppm spectral window, 16 scans. The average acquisition time was approximately 1.5 min.

Results and discussions

^1H NMR spectra of different fat samples have the similar qualitative view. The differences between them are reflected on the integral values of the characteristic peaks which in a specific spectral region can be assigned to certain structural elements and one can determine the amount of different acyl groups in fat. Fig. 1 represents the ^1H NMR spectrum of fat. The chemical shifts and peak assignments are shown in Table 1 [3, 4]. The fatty acid composition of adipose tissue from different volunteers was determined by using statistical method. Based on the integral values of the ^1H NMR spectra the composition of adipose tissue was estimated on two classes of fatty acids: unsaturated and saturated. For the chemometric equations the following notation were adopted [5]: n , s represents the molar ratio of unsaturated and saturated acids; x represents the number of double bonds from the polyunsaturated fatty acids; I_1 , I_2 , I_3 , etc. represents the integral values of the signals; k is a coefficient which correlates the signal integral with the number of protons that signal is due to [6, 7]. The molar ratio of unsaturated fatty acids: $n = (I_4)/(4 \cdot k)$. The molar ratio of saturated fatty acids: $s = 1 - n$. The number of double bonds obtained: $x = I_9/2 \cdot k \cdot n$; $k = 3 \cdot I_7/4$.

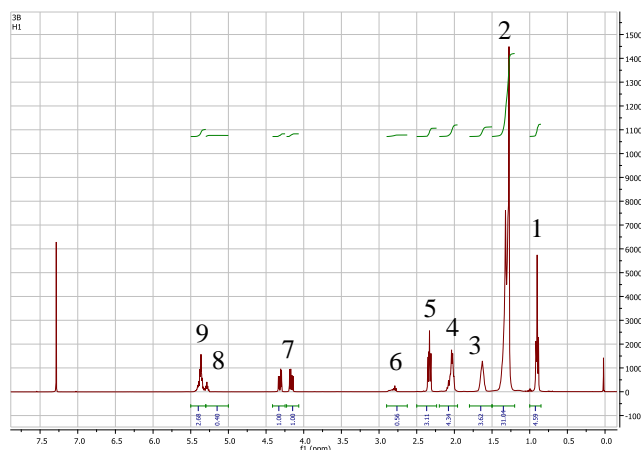


Fig. 1. ^1H NMR spectrum of fat.

Table 1. Chemical shifts and peak assignment of ^1H NMR spectra.

Signal	δ (ppm)	Proton
1.	0.95	$-\text{CH}_3$ methyl
2.	1.2	$-(\text{CH}_2)_n$ - all fatty acids
3.	1.6	$-\text{OCO}-\text{CH}_2-\text{CH}_2-$ β -methylene
4.	2.02	$-\text{CH}_2-\text{CH}=\text{CH}-$ allylic
5.	2.2	$-\text{CH}_2-\text{COOH}$ acyl
6.	2.76	$-\text{CH}=\text{CH}-\text{CH}_2-\text{CH}=\text{CH}$ bis-allylic
7.	4.16–4.36	$-\text{CH}_2-\text{OCOR}$ glycerol (α position)
8.	5.36	$-\text{CH}-\text{OCOR}$ glycerol (β position)
9.	5.4	$-\text{CH}=\text{CH}-$ vinyl

Based on chemometric equations, the composition of fat samples from 5 different patients from different layers (A – subcutaneous, B – preperitoneal and C – central) was calculated in terms of mono-unsaturated, poly-unsaturated and saturated fatty acids. The results are presented in Table 2 and Fig. 2.

Table 2. Fatty acids composition determined from ^1H NMR.

Sample	x, % mol	n, %	s, %
3A	1.214612	73	27
3B	1.240741	72	28
3C	1.217778	75	25
4A	1.167442	72	28
4B	1.194313	70	30
4C	1.185355	73	27
5A	1.260274	73	27
5B	1.275229	73	27
5C	1.25	76	24
6A	1.12782	67	34
6B	1.106796	69	31
6C	1.186207	73	28
7A	1.183099	71	29
7B	1,215596	73	27
7C	1,193833	76	24

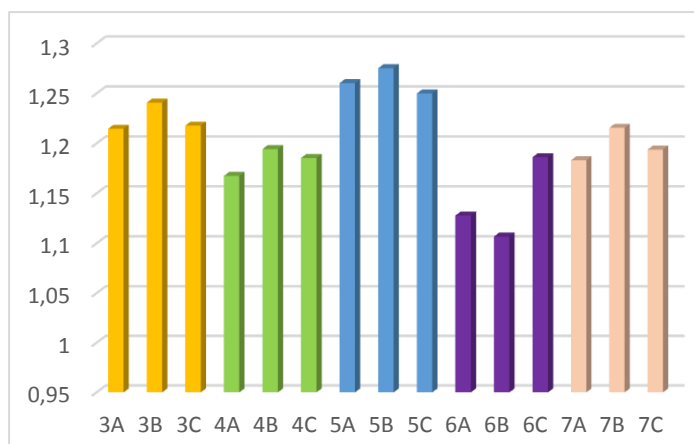


Fig. 2. Polyunsaturated fatty acids composition in different patient's layers.

According to the [8], we can make an assumption that patients with metabolic disorder have lower level of polyunsaturated and high level of monounsaturated fatty acids in the adipose tissue. Patients (3, 4 and 7) have similar fatty layers, but patients 5 and 6, possibly, have a different pathology.

Conclusions

The fat samples were extracted according to the *Folch* method from different adipose tissue and analyzed by ^1H NMR spectroscopy. This method in comparison with gas chromatography is faster, does not require any additional sample preparation and can be applied directly for the analysis of triglycerides. The determination of the amount of unsaturated fat acids may provide important information about the metabolic status and could be helpful in the identification of subjects of metabolical interest.

References

1. A. Kaminskas, Biomedicinos mokslai, medicina, 2009.
2. J. Folch, M. Lees, G. Stanley, Journal of Biological Chemistry 1957, 226.
3. G. Knothe, J. A. Kenar, European Journal Science and Technology, 2004, 106.
4. D. Mickevičius, Cheminės analizės metodai 1 dalis. Spektroinė analizė. 1998.
5. A. Bratu, M. Michalache, A. Hanganu, N. A. Chira, M. C. Todasca, S. Rosca, U.P.B. Sci. Bull, 2013, 75.
6. N. C. Chira, M. C. Todasca, A. Nicolescu, A. Rosu, M. Nicolae, S. I. Rosca, Revista de chimie, 2011, 62.
7. N. C. Chira, M. C. Todasca, A. Nicolescu, G. Paunescu, S. Rosca, UPB Scientific Bulletin, 2009.
8. A. Kaminskas, A. Abraitiene, V. Urbanavicius, Z. Kucinskiene, Laboratorine medicina, 2007, 9.



FORMATION OF THIN FILMS OF CALCIUM TITANATE AND CALCIUM HYDROXYAPATITE ON TITANIUM SUBSTRATES

Z. Stankeviciute¹, P. Usinskas¹, A. Kareiva²

¹*Department of Applied Chemistry, Vilnius University, Naugarduko 24, LT-03225 Vilnius, Lithuania;*

²*Department of Inorganic Chemistry, Vilnius University, Naugarduko 24, LT-03225 Vilnius, Lithuania;*

E-mail: zivile.stankeviciute@chf.vu.lt

Titanium and Ti-based alloys have become popular materials as biomedical and dental materials because of its excellent degree of biocompatibility and high mechanical performance. Calcium hydroxyapatite (HAp) is widely used as biomaterial for dental and medical applications. HAp-coated titanium implants have excellent biocompatibility [1, 2]. Adherence of HAp films formed on titanium substrate is weak, because of the lack of chemical interaction between HAp and titanium. Calcium titanate is reported as a good substrate for apatite growth with the potential to enhance osseointegration and osteoconduction and can be an intermediate layer on titanium substrate, which provide excellent adherence to both titanium substrate and HAp [3, 4].

Sol-gel techniques for a long time have been used for the fabrication of glasses, ceramics, films and powders. This method generates materials with controlled chemical composition and low levels of impurities. The nature and concentration of precursors, the nature of the solvent, the use of modifying agents, pH, the synthesis temperature, influence the microstructure and thus the properties of the resulting material [5].

In this study, thin CaTiO₃ layer on Ti substrate and HAp films on CaTiO₃ layer were prepared. The obtained synthesis products were characterized by X-ray diffraction (XRD) analysis, scanning electron microscopy (SEM), infrared (IR) spectroscopy and contact angle measurements. Ti substrates were prepared by mechanically polishing commercial pure Ti plates and then ultrasonically washed in acetone, ethanol and distilled water. The intermediate calcium titanate thin films were prepared on titanium substrate by spin- or dip-coating technique from Ca-O sols using analytical grade calcium acetate monohydrate and EDTA deprotonated with triethanolamine as complexing agent and aqueous solution of 3 % polyvinyl alcohol. For the formation of calcium hydroxyapatite thin films on the obtained CaTiO₃ layer Ca-P-O sol with phosphoric acid was used in a Ca/P ratio 1.67. Spin and dip-coated 5 layers of thin films on titanium substrate were calcined subsequently at 850 °C for 5 h with heating rate of 1 °C/min.

The phase composition, microstructure and properties of calcium titanate and hydroxyapatite thin films on titanium substrates are evaluated and discussed.

References

1. M. Aminzare, A. Eskandari, M.H. Baroonian, A. Berenov, Z.R. Hesabi, M. Taheri, S.K. Sadrezaad, *Ceram. Int.* **39** (2013) 2197–2206.
2. A. Carrado, N. Viart. *Solid State Sci.* **12** (2010) 1047–1050.
3. M. Inoue, A.P. Rodriguez, T. Takagi, N. Katase, M. Kubota, N. Nagai, H. Nagatsuka. *J. Biomater. Appl.* **24** (2010) 657–672.
4. A.V. Stanishevsky, S. Holliday. *Surf. Coat. Technol.* **202** (2007) 1236–1241.
5. T. Kokubo. *Bioceramics and their clinical applications*. Woodhead Publishing, Abington, 2008, p. 785.

X-RAY PHOTOELECTRON SPECTROSCOPY INVESTIGATION OF COBALT SULFIDE LAYERS ON POLYAMIDE FILM FORMED BY THE USE OF DODECATHIONIC ACID

R. Stokienė¹, N. Petrašauskienė¹, V. Jasulaitienė², V. Janickis¹

1 Department of Inorganic Chemistry, Kaunas University of Technology, Radvilėnų 19, LT-50254 Kaunas, Lithuania

*2 Institute of chemistry of center for physical sciences and technology, A. Goštauto 9, LT-01108 Vilnius, Lithuania
E-mail: ruta.stokiene@ktu.lt*

Sulfides of various transition metals show interesting electrical and optical properties such as semiconductivity, luminescence, and photoconductivity [1-2]. Cobalt sulfide exists in various crystalline phases such as CoS, Co₃S₄, CoS₂, Co_{1-x}S, Co₄S₃, Co₂S₃ and Co₉S₈ [3]. They are found to have potential applications as solar energy absorbers [4], in ultra high density magnetic recording devices [5], anodes for Li-ion batteries [6] and catalyst for hydrodesulphurization and dehydroaromatization [7]. Additionally, the cobalt sulfide finds novel applications in selective coatings and solar cells, optical filters, temperature sensors, optical wave guides and IR detectors [8].

Cobalt sulfide thin films were prepared using various techniques such as the electrodeposition technique [4], the chemical bath deposition [9] or modified chemical bath deposition method [10].

In our studies the layers of cobalt sulfide on polyamide 6 (PA) were obtained by a sorption–diffusion method. The method consists of 2 stages. In the first stage – sulfurization of the polymer – PA films are treated with the solution of dodecathionic acid, H₂S₁₂O₆, the molecules of which contain chains of divalent sulfur atoms, ⁻O₃S–S_{n-2}–SO₃⁻. In the second stage, the sulfurized polymer is treated with a solution of Co(II) salts and thin layers of cobalt sulfides forms on the surface of polymer. The aim of present work was to study the composition of Co_xS_y layers on PA, using X-ray photoelectron spectroscopy (XPS).

A PA 6 film (PA-6, 500 μm thick, density 1.13 g/cm⁻³) produced in Germany was used. Prior the experiments, pieces of the film 15×70 mm in size had been boiled in distilled water for 2 h to remove the remainder of the monomer. Then they were dried with filter paper and kept in a desiccator over CaCl₂ for 24 h.

PA films were sulfurized in a thermostatic vessel up to 6 h at a temperature of 30 °C using a continually stirred 0.002 mol·dm⁻³ solution of H₂S₁₂O₆, prepared by the method given in [11]. For the formation of Co_xS_y films the samples of sulfurized PA were treated with cobalt(II) ammonia complex solution at 78 °C, which was prepared by mixing 340 volume parts of 0.16 M CoSO₄·7H₂O solution with 100 volume parts of 25 % NH₃ solution. The reductor – hydroxylamine sulfate ((NH₂OH)₂·H₂SO₄ – 0.12 M) was added to obtain more stable solution [12]. After treatment with the solution Co(II) salts, PA samples were rinsed with distilled water, dried over anhydrous CaCl₂ and used in further experiments.

The composition of the cobalt sulfide coatings was studied by X-ray photoelectron spectroscopy. XPS data for surfaces of Co_xS thin films were obtained on the upgraded vakuum generator (VG) ESCALAB MKII spectrometer fitted with a new XR3 twin anode. The non- monochromatised MgK_α X-ray source was operated at hv = 1253.6 eV with 300 W power (20mA/15kV) and the pressure in the analysis chamber was lower than 5·10⁻⁷ Pa during spectral acquisition. The spectra were acquired with electron analyser pass energy of 20eV for narrow scans and resolution of 0.05 eV. The binding energies employed for calibration were 83.96eV for Au4f_{7/2} of metallic gold and 932.6eV for Cu2p_{3/2} of Cu metal. The spectra calibration, processing and fitting routines were done using Thermo Scientific

Advantage software (5.918). All spectra were recorded at a 90° take-off angle and referenced to the C1s component set at a binding energy of 284.6 eV. The “smart background” was used for background subtraction which iteratively adjusts the background. Standard Scofield factors were used for calculation of the elemental composition. Ar⁺ ion etching was performed in the preparation chamber using 2 keV Ar⁺ ions bombardment with a beam current density of 20 μA cm⁻² for a period of 1 min., where the pressure was maintained at 6×10⁻⁵ Torr. The recorded spectra were compared with the reference spectra [13, 14].

The coatings surfaces and the coatings etched by Ar⁺ ions in deeper layers (~ 4 nm) were studied and their composition was determined. From the obtained data, i.e. the atomic percentages of elements, binding energies and individual elements of Co2p_{3/2}, S2p and O1s spectra, it was possible to predict the compounds of the layers (Table 1).

In the surface of PA samples, modified by cobalt sulfides, the presence of various cobalt, sulfur and oxygen compounds (CoS, Co₉S₈, CoS₂, Co(OH)₂) was determined.

Table 1. XPS data of the layers containing Co_xS_y formed on PA surface. PA was sulfurized at the temperature of 30 °C in H₂S₁₂O₆ solution and then treated with Co(II) solution

Sample No.	Etching conditions	Element	Content, at %	Binding energy, eV	Possible composition of layer
1	PA sulfurized for 2.0 h				
	Surface	Co	7.65	782.37	Co(OH) ₂
		S	23.31	169.75	CoSO ₄
		O	30.45	532.50	Co(OH) ₂
	Etching for 60 s (-20μA)	Co	23.05	779.78	CoS, CoS ₂ , Co(OH) ₂ , Co ₉ S ₈
		S	25.34	162.37	Co ₉ S ₈ , CoS, CoS ₂
		O	25.48	531.05	Co(OH) ₂
2	PA sulfurized for 4.0 h				
	Surface	Co	6.65	782.64	Co(OH) ₂
		S	19.84	169.78	CoSO ₄
		O	34.65	532.58	Co(OH) ₂
	Etching for 60 s (-20μA)	Co	19.50	779.98	CoS, CoS ₂ , Co ₉ S ₈
		S	21.26	162.51	Co ₉ S ₈ , CoS
		O	26.03	531.11	Co(OH) ₂

In the XPS study of the cobalt sulfide coating, we paid attention to the distribution of Co, O, and S elements over the surface and throughout the depth of the coating. The processes of PA film sulfurization and cobalt sulfide containing layer formation take place in a natural environment; therefore, it is impossible to prevent its influence. Semi hydrophilic polymer PA, under the action of environment, absorbs on its surface oxygen, moisture and other compounds. Our results show that the surface of the coatings contains up to ~35 at.% oxygen (binding energy *E_b* value of O1s ~532.5 eV) and ~ 26 at.% oxygen was found in deeper layers of the coating (binding energy *E_b* value of O1s ~531.1 eV).

The Co2p_{3/2} spectrum, shown in Fig. 1a, contains a main peak located at a binding energy value of 779.9 eV and a shake-up feature at higher binding energy. These peaks can be assigned to Co²⁺ of CoS phase as supported by the literature [15]. Further, the Co2p_{3/2} spectrum can be de-convoluted into couple of more constituent components corresponding to the following chemical states as Co(OH)₂.

Fig. 1b shows that the binding energy value of S2p is around 162.5 eV, indicating that most of the S species exist as S²⁻ (CoS phase). This compound was detected after the 4 nm thick was etched with Ar⁺ ions. The most intense peak is seen at a binding energy 169.75 eV, which can be assigned to sulfur S⁶⁺ bond to oxygen (CoSO₄). This compound was detected only on the surface of the coatings.

The measured binding energies E_b of O1s (532.5 eV) electrons (Fig. 1c) suggest that oxygen occurs in the form of $\text{Co}(\text{OH})_2$. These compounds were detected not only on the surface, but also in deeper layers of the coating. $\text{Co}(\text{OH})_2$ may be formed while washing coatings with water. In the same O1s region (at 531.35 eV) is peak of PA 6 binding energy [13].

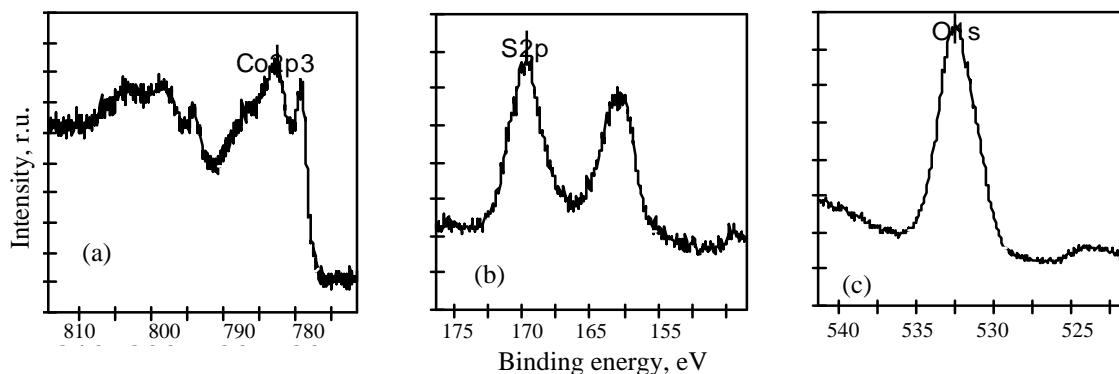


Fig. 1. XPS $\text{Co}2p_{3/2}$, $\text{S}2p$ and $\text{O}1s$ spectra of Co_xS_y layers on PA surface obtained during PA treatment for 2 h at the temperature of 30°C in $\text{H}_2\text{S}_{12}\text{O}_6$ solution and then treated with $\text{Co}(\text{II})$ solution.

Thus the results of XPS study confirmed the formation of cobalt sulfide containing layers on the surface of PA: on the layer's surface and in the etched surface various cobalt sulfide and cobalt hydroxide ($\text{Co}(\text{OH})_2$) are present. From the data of analysis it follows that the composition of the layers formed in different conditions is rather similar.

References

1. N. Razik, *J. Mater. Sci. Lett.*, **1987**, 6, 1443
2. T. Suzuki, T. Yagi, S.I. Akimoto, *J. Appl. Phys.*, **1983**, 54, 748.
3. A. Wold, K. Dwight, *Solid State Chemistry*. Chapman and Hall Inc, New York, **1993**.
4. G.B. Smith, A. Ignatiev, G. Zajac, *J. Appl. Phys.*, **1980**, 51, 4186.
5. T.M. Whitney, J.S. Jiang, P. Searson, C. Chien, Fabrication and magnetic properties of arrays of metallic nanowires, *Science*, **1993**, 261, 1316.
6. G.H. Yue, P.X. Yan, X.Y. Fan, M.X. Wang, D.M. Qu, Z.G. Wu, C. Li, D. Yan, *Electrochem. Solid-State Lett.*, **2007**, 10(3), D29.
7. Y.G. Feng, T. He, N. Alonso-Vante, *Chem. Mater.* **2008**, 20, 26.
8. S. Aripnammal, T.Srinivasan, *Res. J. Recent. Sci.*, **2013**, 2(1),102.
9. P.K. Basu, P. Pramanik, *J. Mater. Sci. Lett.* **1986**, 5, 1216.
10. Z. Yu, J. Du, S. Guo, J. Zhang, Y. Matsumoto, *Thin Solid Films*, **2002**, 415 (1-2), 173.
11. J. Janickis, J. Valančiūnas, V. Zelionkaitė, V. Janickis, S. Grevys, *Trans. Lithuanian Acad. Sci.*, **1975**, B 3(88), 83.
12. N. Švickus, *Formation and modification of cobalt sulfide coatings*. Doctoral dissertation, Vilnius, **2001**.
13. <http://xpssimplified.com/>.
14. C.D. Wagner, W.M. Riggs, L.E. Davis, J.F. Moulder, G.E. Muilenber, *Handbook of X-Ray Photoelectron Spectroscopy*. Physical Electronics Division, Perkin-Elmer, Minnesota, **1979**.
15. S. R. Ray, B. Sarma a, A. L. Jurovitzki, M. Misra, *Chemical Engineering Journal*, **2015**, 260, 671.



INVESTIGATION OF SODIUM BOROHYDRIDE OXIDATION ON CoBW/Cu MODIFIED WITH Au NANOPARTICLES

Z. Sukackienė, A. Balčiūnaitė, A. Selskis, V. Jasulaitienė, L. Tamašauskaitė-Tamašiūnaitė, E. Norkus

Institute of Chemistry, Center for Physical Sciences and Technology

A. Goštauto 9, LT-01108 Vilnius, Lithuania

E-mail: zita@icp.lt

Introduction

Recently, as traditional energy resources are getting low, a search for alternatives is getting more and more active. Renewable energy sources are being used more and more often. Fuel cells are considered as an alternative energy source, which allow direct conversion of chemical energy to electric energy. On type of the fuel cell, the direct borohydride fuel cell (DBFC), has recently been investigated as a potential candidate for portable and mobile applications due to its high energy density and ease with which borohydride can be stored and transported [1-4]. The direct borohydride fuel cell is based on borohydride oxidation and oxygen electrochemical reduction. The main attention is paid to the search of new nanostructured substances, which will be able to increase the efficiency of fuel cells as well as to use simple and cheap catalysts formation technologies.

In this study we present a simple way for preparation of the gold-cobalt-boron-tungsten catalysts with low Au loadings deposited on the copper surface via the galvanic displacement technique [5] which involves electroless copper deposition followed by a spontaneous Au displacement from the 1 mM HAuCl_4 solution. The morphology and composition of the prepared catalysts were characterized using Field - Emission Scanning Electron Microscopy (FESEM), Energy Dispersive X-ray Spectroscopy (EDAX) and of X-ray Photoelectron Spectroscopy (XPS). The electrochemical behavior of the fabricated Au/CoBW/Cu catalysts was examined towards the oxidation of BH_4^- ions in an alkaline medium by means of cyclic voltammetry (CV).

Experimental

Electroless deposition of CoBW was performed on the copper surface deposited with a prior activation step with Pd(II) ion. Prior to electroless deposition of CoBW, Cu substrates (1 cm x 1 cm) were pre-treated with 50-100 % calcium magnesium oxide, known as "Vienna Lime" (Kremer Pigmente GmbH&Co. KG), and rinsed with deionized water. Then the Cu substrates were placed into the electroless cobalt deposition solution, the main composition of which was as follows (mol l^{-1}): CoSO_4 - 0.1, $\text{NH}_2\text{CH}_2\text{COOH}$ - 0.2 (glycine), $\text{C}_4\text{H}_8\text{ONH}_2\text{BH}_3$ (morpholine borane) - 0.2, Na_2WO_4 - 0.003, $\text{C}_6\text{H}_8\text{O}_7$ - 0.0175 (citric acid). The bath operated at pH 7 and 60 °C. Solutions pH was adjusted with 20 % NaOH. The thickness of the CoBW coatings was ca. 1 μm .

Au nanoparticles were deposited on the CoBW/Cu coatings by immersion of CoBW in a 1 mM HAuCl_4 solution at pH 1.8 and 25°C for 0.5, 1, 5 and 15 min. The surface-to-volume ratio was 2 $\text{dm}^2 \text{l}^{-1}$. Then, the fabricated catalysts were used for borohydride electro-oxidation measurements without any further treatment.

The electrocatalytic activity of the prepared catalysts was examined towards borohydride oxidation by cyclic voltammetry. Experiments were made with a Metrohm Autolab potentiostat (PGSTAT100) using Electrochemical Software (Nova 1.6.013). A conventional three-electrode electrochemical cell was used for electrochemical measurements. The as-prepared CoBW/Cu and Au/CoBW/Cu catalysts with a geometric area of 2 cm^2 were employed as working electrodes, an Ag/AgCl electrode was used as reference

and a Pt sheet was used as a counter electrode. The presented current densities are normalized with respect to the Au loadings for each catalyst.

The morphology and composition of the fabricated catalysts were characterized using a SEM/FIB workstation Helios Nanolab 650 with an energy dispersive X-ray (EDX) spectrometer INCA Energy 350 X-Max 20. The Au metal loading was estimated from EDX data using ThinFilmID software.

The composition of obtained coatings was investigated by means of X-ray Photoelectron Spectroscopy using vacuum generator ESCALAB MKII spectrometer using X-radiation of Al $K\alpha$ (1486.6 eV, pass energy of 20 eV). To obtain depth profiles, the samples were etched in the preparation chamber by ionized argon at a vacuum of $5 \cdot 10^{-4}$ Pa. XPS analyses are given for films at a depth of 20 and 40 nm.

The Au metal loading was estimated from ICP-OES measurements. The ICP optical emission spectra were recorded using an ICP optical emission spectrometer Optima 7000DV (Perkin Elmer).

Results and discussions

The CoBW coatings were deposited on the copper electrode by the autocatalytic reduction of Co (II) ions applying morpholine borane as a reducing agent.

FESEM images of as-prepared CoBW/Cu (a) and Au/CoBW/Cu (b-e) catalysts are presented in Fig 1. According to the FESEM data, CoBW coating, deposited on the copper surface consists of cobalt layer with crystallites in size from 110 to 760 nm (Fig. 1a). Immersion of CoBW/Cu in the gold-containing solution for 0.5, 1, 5 and 15 min, results in deposition of the Au crystallites in size of 7-40 (Fig. 1b), 15-50 (Fig. 1c, d) and 30-85 nm (Fig. 1e), respectively, on the CoBW/Cu surface.

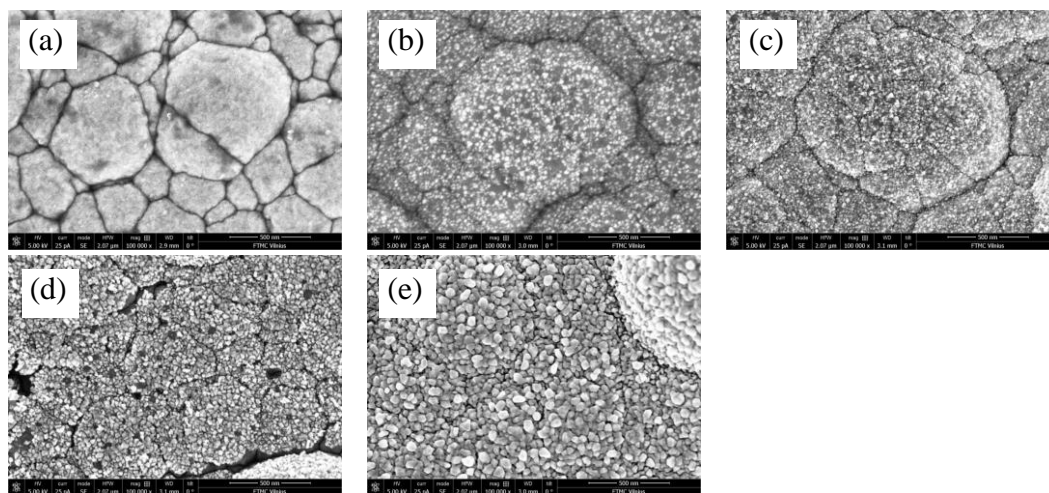


Fig. 1. FESEM images of as-prepared CoBW/Cu (a) and Au/CoBW/Cu (b-e) catalysts. The Au/CoBW/Cu catalysts were prepared by immersion of CoBW/Cu electrodes into 1 mM HAuCl_4 (pH 1.8) at 25 °C, respectively, for 0.5 min (b), 1 min (c), 5 min (d) and 15 min (e).

The XPS spectral analysis of the CoBW coatings obtained showed the following composition at a depth of 20 nm: ca. 59.76 at. % of Co, 6 at. % of W and 4 at. % of B and at a depth of 40 nm: 66.81 at. % of Co, 8.5 at. % of W and 4 at. % of B. Au nanoparticles were deposited on the CoBW/Cu electrode by galvanic displacement of gold from a HAuCl_4 solution.

It has been determined that the Au loadings were 5.8, 7.6, 23.2 and 53.3 $\mu\text{g cm}^{-2}$ in the as-prepared Au/CoBW/Cu catalysts after immersion of the CoBW/Cu electrodes into 1 mM HAuCl_4 (pH 1.8) at 25 °C for 0.5, 1, 5 and 15 min, respectively.

The oxidation of BH_4^- ions on differently formed catalysts was investigated by cyclic voltammetry. Figure 2 presents the borohydride oxidation current densities normalized by the Au loadings for each catalyst (5th cycles) recorded on the Au/CoBW/Cu catalysts with different Au loadings in the range from 5.8 to 53.3 $\mu\text{g cm}^{-2}$ in a 0.05 mol l^{-1} NaBH_4 + 1 mol l^{-1} NaOH solution at a potential scan rate of 10 mV s^{-1} .

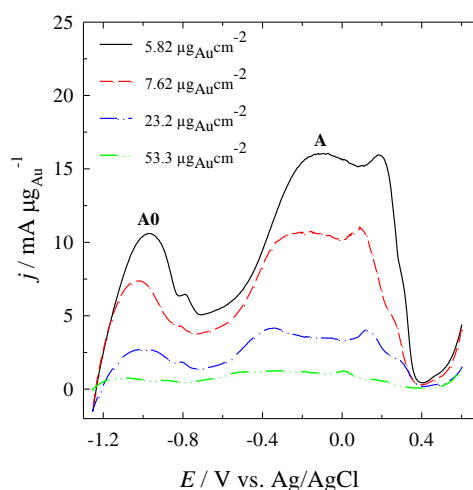


Fig. 2. Stabilized positive-potential going scans (5th) of the Au/CoBCu/Cu catalysts recorded in a 0.05 M NaBH_4 + 1 M NaOH solution at a potential scan rate of 10 mV s^{-1} , 25 °C. The Au/CoBW/Cu catalysts were prepared by immersion of the CoBW/Cu electrodes in 1mM HAuCl_4 (pH 1.8) for 0.5 min (solid line), 1 min (dashed line), 5 min (dash-dotted line), 15 min (dash-dot-dotted line).

As evident from Fig. 2, two anodic peaks **A0** and **A** are seen in the CVs plots. The first peak **A0** is related with the oxidation of hydrogen generated by sodium borohydride hydrolysis. The second peak **A** is related with direct borohydride oxidation. As seen from the data Fig. 2, current densities of anodic peaks **A0** and **A**, recorded on the Au/CoBW/Cu catalysts with different Au loadings from 5.8 to 53.3 $\mu\text{g cm}^{-2}$, decreases with increasing of Au loadings. Figure 3 presents bar plots of borohydride oxidation current densities normalized by the Au loadings for each catalyst, obtained at a potential peaks **A0** (a) and **A** (b).

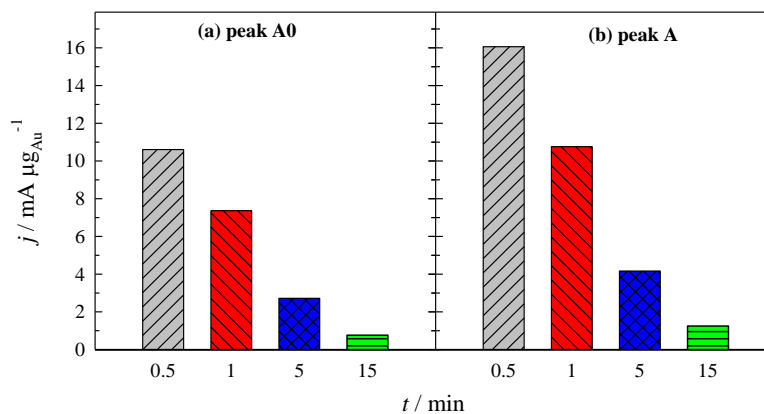


Fig. 3. Bar plots of Au-metal mass activity for borohydride oxidation obtained from Au/CoBCu/Cu catalysts at a potential of peak **A0** (a) and **A** (b) derived from Fig. 2. The Au/CoBW/Cu catalysts were prepared by immersion of CoBW/Cu electrodes in 1mM HAuCl_4 (pH 1.8) for 0.5 min, 1 min, 5 min, 15 min.

As seen from the data in Fig. 3, the highest mass activity ($\text{mA } \mu\text{g}_{\text{Au}}^{-1}$) for the both oxidation peaks **A0** at and **A** has the Au/CoBW/Cu catalyst with the Au loading of $5.8 \mu\text{g cm}^{-2}$ and with deposited Au nanoparticles in size from 7 to 40 nm. Current densities of both anodic peaks **A0** and **A** are ca. 1.4-3.9-14.0 and 1.5-3.9-13.0, respectively, times higher at Au/CoBW/Cu with the Au loading of $5.8 \mu\text{g cm}^{-2}$ as compared to those at Au/CoBW/Cu with the Au loadings of 7.6, 23.2 and $53.3 \mu\text{g cm}^{-2}$, respectively (Fig. 3).

Conclusions

A series of the Au/CoBW/Cu catalysts with low Au loadings were prepared by a simple way which involves electroless CoBW deposition followed by a spontaneous Au displacement from the gold-containing solution. It has been shown that the highest mass activity towards the electro-oxidation of borohydride exhibits the Au/CoBW/Cu catalyst with the Au loading of $5.8 \mu\text{g cm}^{-2}$ and with deposited Au nanoparticles in size from 7 - 40 nm.

References

1. C. Celik, San F.G. Boyaci and H.I. Sarac, *J. Power Sources*, **185**, 197 (2008).
2. C. Celik, San F.G. Boyaci and H.I. Sarac, *J. Power Sources*, **195**, 599 (2010).
3. C.P. de Leon, F.C. Walsh, D. Pletcher, D.J. Browning and J.B. Lakeman, *J. Power Sources*, **155**, 172 (2006).
4. S.C. Amendola, P. Onnerud, M.T. Kelly, P.J. Petillo, S.L. Sharp-Goldman and M. Binder, *J. Power Sources*, **84**, 130 (1999).
5. Z. Sukackienė, A. Balčiūnaitė, L. Tamašauskaitė-Tamašiūnaitė, V. Pakštas, A. Selskis, E. Norkus, *ECS Transactions*, **59(1)**, 295 (2014).

ELECTRODEPOSITION AND CHARACTERIZATION OF BLACK CHROMIUM COATINGS

S.Survilienė, A.Češūnienė, R.Juškešas, V. Jasulaitienė, A.Selskienė, P.Kalinauskas, K.Juškevičius,

Center for Physical Science and Technology, A.Gostauto 9, 01108 Vilnius, Lithuania

E-mail: sveta@ktl.mii.lt

Abstract

Black chromium coatings were electrodeposited on steel, Cu and Ni surfaces from a Cr(III) bath containing ZnO as a second main component. The phase structure of black chromium may be characterized as a zinc solid solution in chromium or a chromium solid solution in zinc depending on the chromium/zinc ratio in the deposit. The metallic phase was found to be nearly absent in the deposits. The near-surface layer is rich in hydroxides, whereas, oxides of both metals become dominant close to the substrate/coating interface. The electrodeposited black chromium possesses good optical properties for the absorption of solar energy.

Introduction

Black coatings are widely used in solar collectors due to their high absorptance. Black deposits containing chromium are used under the name “black chromium” in solar collector manufacture. The earlier sources [1-2] suppose that the black chromium film is composed of metallic and oxide phases and metal is incorporated into the oxide film as fine separate grains forming light absorption centers, owing to which the deposits may appear black. In other works [3, 4] no evidence for metallic chromium was found. It was shown [5] that the substrate influences the structure, morphology, chemical composition and selective characteristics of black chromium. According to the published data [6], the Cr/ α -Cr₂O₃ coatings deposited on Cu or stainless steel substrates are good candidates for solar absorbers. Recently the emphasis has moved towards using trivalent chromium baths for electrodeposition of solar selective black coatings [7]. The use of Ni²⁺, Co²⁺ or Fe²⁺ ions as a second main component made it possible to improve the efficiency of Cr(III) bath [8]. However, the information on the use of zinc as a second main component in a trivalent black chromium bath is lacking. Taking into account that zinc is an anodic metal as compared to nickel, iron or other cathodic metals, it was expected that co-deposition of zinc with chromium will improve the protection of the substrate.

The aim of this research was to obtain solar selective black chromium using a trivalent chromium bath containing zinc as a second main component and to study the properties of the deposits in order to optimize the bath composition and plating parameters.

Experimental

Black chromium coatings were electrodeposited on steel, Cu and Ni undercoat (10 μ m) using Pt anodes. Before electrodeposition the substrates were mechanically polished with further electropolishing. A current density of 40 A·dm⁻² and a temperature of 20 °C were selected as a compromise between efficiency and deposit quality. The electrodeposition rate of black chromium was determined gravimetrically. The coatings were examined using the SEM, EDS, XRD and XPS methods. A spectrophotometer Secord 250 plus was used to determine the reflection of black chromium. The corrosion resistance of the coatings was tested using a salt-spray chamber.

Results and discussion

A black coating of good appearance without grey or rainbow tones and without burning on the sample edges may be deposited from the electrolyte containing $\text{CrCl}_3 \cdot 6\text{H}_2\text{O}$ (250 g l^{-1}), $\text{NH}_2\text{CH}_2\text{COOH}$ (18.75 g l^{-1}), H_3BO_3 (30 g l^{-1}), NaCl (60 g l^{-1}), NaNO_3 (3.0 g l^{-1}), ZnO (5.0 g l^{-1}) [9]. To elucidate the relationship between the composition and structure of black chromium, XRD tests were performed for samples with different amounts of main components (chromium and zinc). The results are presented in Fig.1.

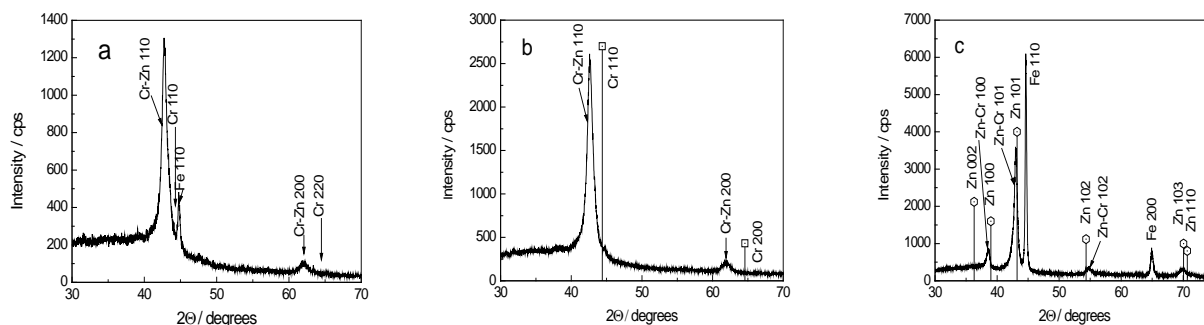


Fig.1 XRD patterns for black chromium of different composition: Cr/Zn = 1.8 (a), Cr/Zn = 1 (b), Cr/Zn = 0.7 (c).

Positions of two broad peaks on pattern (a) do not match those of pure chromium and the lattice parameter $a = 0.2997 \pm 0.0003 \text{ nm}$ may be assigned to the CrZn phase peculiar to a solid solution. Positions of the peaks on pattern (b) and the lattice parameter $a = 0.2995 \pm 0.0003 \text{ nm}$ are also associated with the zinc solid solution in chromium. Pattern (c) shows peaks which assigned to the hexagonal structure peculiar to zinc with the values of lattice parameters ($a = 0.2690 \pm 0.0003 \text{ nm}$, $c = 0.4825 \pm 0.0003 \text{ nm}$) close to those of pure zinc. It is suggested that this is a chromium solid solution in zinc.

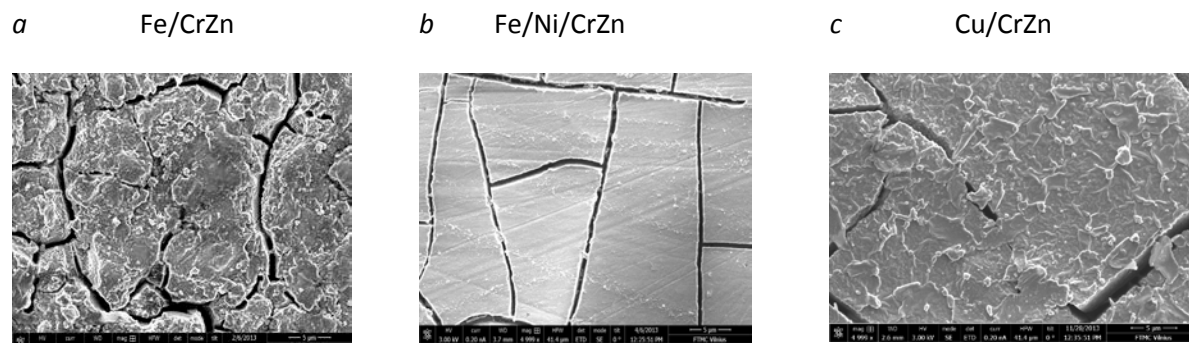


Fig.2 Surface morphology of black chromium deposited on steel (a), Ni undercoat (b) and Cu (c).

Fig. 2 shows that samples obtained on steel plated with nickel prior to black chromium have finer grained and less rough structures compared to those of black chromium deposited just on the steel (a) or Cu (c) substrates. It is evident, that the initial roughness of steel surface is transformed into a less rough one after bright nickel deposition on steel.

The results of corrosion tests indicated that ZnO made it possible to improve the corrosion resistance of black chromium, especially using the substrate plated with Ni.

Analysis of XPS spectra has shown that the top layers of black chromium coatings are composed of various Cr(III) and Zn(II) components and organic substances, whereas, metallic Cr is almost absent. The ratios Cr/Cr(III) and Cr/Cr(III)+Zn(II) were found to be 10/27 and 2/28 for black chromium without and with zinc, respectively (Table 1).

Table 1. BE of 2p and 1s electrons in the deconvoluted spectra recorded before and after sputtering of top layers of black chromium with no zinc (sample “a”) and with zinc (sample “b”).

Depth nm	Sample “a”			Sample “b”			
	Cr2p3 eV	O1s eV	C1s eV	Cr2p3 eV	O1s eV	Zn2p3 eV	C1s eV
0	574.2±0,1 577.3±0,1 579.2±0,1	531.0±0,1 532.8±0,1 534.4±0,1	285.4±0,1 286.7±0,1 289.4±0,1	577.3±0,1 579.0±0,1	532.8±0,1 534.2±0,1 535.4±0,1	1022.6±0,1 1023.2±0,1	286.0±0,1 287.6±0,1 289.9±0,1
6	574.5±0,1 576.7±0,1 578.7±0,1	530.4±0,1 531.9±0,1 533.9±0,1	284.7±0,1 286.0±0,1 288.8±0,1	575.8±0,1 577.3±0,1 578.2±0,1	530.4±0,1 532.3±0,1 533.9±0,1	1021.6±0,1 1023.0±0,1	283.4±0,1 284.8±0,1 286.3±0,1
15	574.4±0,1 576.3±0,1 578.0±0,1	530.6±0,1 532.1±0,1	284.3±0,1 285.4±0,1 287.6±0,1	575.7±0,1 577.0±0,1 578.5±0,1	529.9±0,1 531.5±0,1 533.3±0,1	1021.7±0,1 1023.5±0,1	283.1±0,1 284.6±0,1 286.1±0,1 288.7±0,1
45	574.3±0,1 576.0±0,1 577.7±0,1	530.6±0,1 532.0±0,1 533.7±0,1	282.7±0,1 284.5±0,1 286.2±0,1	574.3±0,1 576.0±0,1 577.2±0,1 578.8±0,1	530.3±0,1 531.7±0,1 533.6±0,1	1021.9±0,1 1023.3±0,1	282.9±0,1 284.3±0,1 285.6±0,1 287.5±0,1
120	574.1±0,1 575.9±0,1 577.6±0,1	530.6±0,1 531.8±0,1	282.5±0,1 284.5±0,1 286.6±0,1	574.1±0,1 576.0±0,1 577.5±0,1 579.4±0,1	530.3±0,1 531.7±0,1 533.2±0,1	1021.9±0,1 1023.3±0,1	283.1±0,1 284.7±0,1 286.7±0,1

The peak at BE = 574.1-574.5 eV, which is characteristic of metallic Cr⁰ [10], exists in all depth levels of sample “a”, whereas, in sample “b” it emerges only after sputtering of the top layers (about 45 nm). The other peak (BE=575.0-576.6 eV), which suggests the presence of Cr₂O₃, CrO_x, emerges after sputtering top thin layer of about 6 nm in both “a” and “b” samples. The presence of hydrated oxides and hydroxides (BE=577.5±0.4 eV) in both samples may be related to the alkalinity of the near cathode layer owing to the increasing hydrogen evolution during electrolysis. The peaks at BE ~580 eV are attributable to the metal-organic compounds which dominate on the surface. As for Zn2p3 spectra it is not easy to characterize the individual components, because BE of metallic Zn⁰ (BE = 1021.6 eV) coincides very closely with that of Zn(II) in ZnO (BE = 1021.2-1022.0). The peak at BE = 1022.7 is attributed to Zn(OH)₂. Analysis of these results shows that owing to the presence of ZnO in the Cr(III) bath, the percentage of metallic chromium is substantially reduced in black chromium which is quite important for good solar selective characteristics of the coating.

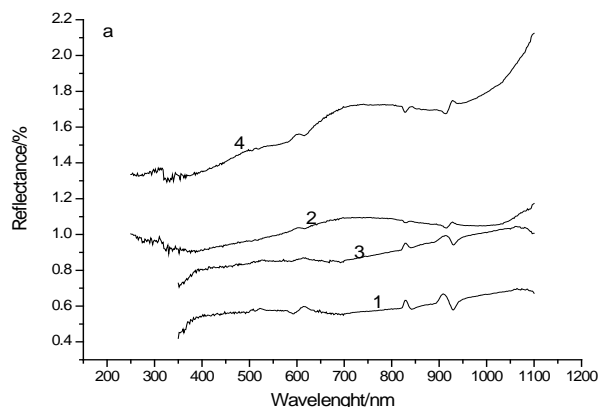


Fig.3 Spectral reflectance of black chromium deposited on steel (1), steel/Ni (2), Cu (3), Cu/Ni (4) substrates.

The spectra in Fig. 3 encompass a wavelength range of 350 to 1100 nm, which is compatible with the range of solar radiation spectrum. The role of substrate-surface finish evaluated through the reflectance of black chromium testifies that the spectral reflectance depends on the substrate as follows: steel < steel/Ni < Cu < Cu/Ni. Although difference between the absorption coefficient of sample with Ni undercoat and sample without Ni undercoat was found to be insignificant, the use of Ni undercoat is desired because of improvement in corrosion resistance.

Conclusions

Black chromium deposited from Cr(III) bath containing ZnO exhibits a high solar absorptance. The phase structure of black chromium may be characterized as the zinc solid solution in chromium or the chromium solid solution in zinc depending on the chromium/zinc ratio in the deposit. The metallic phase is nearly absent in black chromium deposited from a Cr(III)+ZnO bath. The near-surface layer of the black coating is rich in hydroxides, whereas, the oxides of both metals predominated in depth towards the substrate/coating interface. The results confirm some of earlier observations and provide new information on the composition and properties of black chromium.

References

1. S.R. Rajagopalan, K.S.Indira. *J. Inst. Metals* **93**(4) (1964) 129.
2. S.R. Rajagopalan, K.S. Indira, K.S.G. Doss. *J. Electroanal. Chem.* **10** (1965) 465-472.
3. C.Anandan, V.K. William Grips, K.S. Rajam, V.Jayaram, Parthasarathi Bera: *Appl. Surf. Sci.* **191** (2002) 254-260.
4. K.D. Lee: *J. Korean Phys. Soc.*, **51** (2007) 135-144.
5. J. Quintana, P.J. Sebastian: *Sol. Energy Mater. Sol. Cells*, **33** (1994) 465-474.
6. S. Khamlich, O. Nemraoui, n. Mongwaketsi, R. McCrindle, N. Cingo, M. Maaza: *Physica* **B 407** (2012) 1509-1512.
7. M.R. Bayati, M.H. Shariat, K. Janghorban: *Renewable Energy* **30** (2005) 2163-2178.
8. H.Gutwein, E.Erben, A.Muhlratzer, B.Cornils, B.Tihanyi, W.Dewin. US Patent No. 4473447, 25 September 1984.
9. S.Survilienė*, A.Češūnienė, R.Juškenas, A.Selskienė, D.Bučinskienė, P.Kalinauskas, K.Juškevičius, I. Jurevičiūtė: "The use of trivalent chromium bath to obtain a solar selective black chromium coating", *Applied Surface Science*, **305** (2014) 492-497.
10. Alexander V. Naumkin, Anna Kraut-Vass, Stephen W. Gaarenstroom, and Cedric J. Powell, NIST Standard Reference Database 20, Version 4.1 (Web Version) .

INVESTIGATION OF THE INITIAL STAGES OF Cu ELECTRODEPOSITION ONTO GLASSY CARBON ELECTRODE MODIFIED WITH THIN LAYERS OF SELENIUM COMPOUNDS

D. Šimkūnaitė*, I. Valsiūnas

Center for Physical Science and Technology, Goštauto 9, Lt-01108, Vilnius, Lithuania
nemezius@ktl.mii.lt

Modification of the GC electrode with selenium compounds was performed by means of the electrochemical deposition method. Structural and morphological characterization of the modified GC electrode was carried out by scanning electron microscopy (SEM) and X-ray photoelectron spectroscopy (XPS). The initial stages of Cu electrodeposition onto the GC electrode modified with thin layers of selenium compounds were investigated by the means of cyclic voltammetry and chronoamperometry. Surface analysis has revealed the presence of Cu₂Se in the modifying layer. The analysis of electrochemical data indicates an instantaneous 2D nucleation and growth of Cu nuclei in accordance with the model developed by Bewick et al. for the early stages of metal electrocrystallization onto a foreign substrate.

Keywords: copper, initial stages, electrodeposition, glassy carbon electrode modified with copper selenium compounds

Introduction

Copper selenide system has received considerable attention concerning copper selenide layers as highly promising semiconductor compounds for a wide range of possible applications in solar or photovoltaic cells, Shottky-diodes, gas sensors, superionic conductors or thermoelectric converters, etc.. Moreover, copper selenide layers are known to serve as an intermediate or precursor for the synthesis of the ternary compound semiconductor CuInSe₂ (CIS) that is used in high efficient photovoltaic elements.

Copper selenide is characterized by many phases and structural forms. Usually it exists in stoichiometric Cu₂Se, Cu₃Se₂, CuSe forms as well as non-stoichiometric, Cu_{2-x}Se. The formation of these compositions is totally depended on the method of the preparation applied. A variety of techniques have been proposed for synthesis of thin selenide films, including hot injection, vacuum evaporation, mechanical alloying, sol gel method, chemical bath deposition and etc. However, electrodeposition has been the most convenient one, since it is least costly, effective, simple and readily adoptable, provides mild conditions for film growth and allows controlling the growth rate of the former. The main disadvantage of this method is contamination of the target material with impurities like free Se or Cu.

Generally, a simple two-step approach for the synthesis of semiconductor thin films is applied. It concerns the initial electrochemical modification of the substrate (e.g., Au) with the chalcogen (e.g., Se⁰), followed by its subsequent electroreduction in a chalcogen-free electrolyte dosed with a suitable amount of the metal ion (e.g., Cu²⁺) [1]. A separate solution for each reactant has also been employed for the deposition of copper selenide by so-called electrochemical atomic layer epitaxy (EC ALE) technique [2]. The former is based on the alternating electrodeposition of atomic layers of two elements at underpotentials to form a binary compound using a cycle. The cycle is repeated to achieve the desired thickness of the deposit. Ideally it is supposed, that the 2-D growth mode should promote the epitaxial deposition.

Provided that chemical composition of the layer crucially affects the optoelectronic properties of the parent semiconductor a possibility to control this parameter becomes of essential significance. Therefore the investigation of the initial stages (nucleation and growth) of electrodeposition is of primary importance as it plays a decisive role in the film structure and properties [3]. To our knowledge, there have been no reports about the early stages of Cu

electrocrystallisation onto a glassy carbon (GC) electrode modified with copper selenide species, for now.

This study is focused on the preparation of the modified GC electrode with thin layers of selenium compounds by electrochemical deposition method as well as on the investigation of the early stages of Cu nucleation and growth onto so-prepared GC electrode in the sulphuric acid medium. Surface analysis techniques (XPS and SEM/EDX) and electrochemical measurements (cyclic voltammetry, chronoamperometry) were employed.

Results and discussion

Modification of the bare GC surface was performed by the electrochemical deposition method. The preparation of the modifying layer was carried out in a 0.5 M H_2SO_4 + 0.01 M CuSO_4 + 0.05 mM H_2SeO_3 solution. The deposition potential $E_{\text{dep}} = +0.28$ V vs. SHE at temperature $t = 20^\circ$ C was applied. The consumed current charge density calculated from the integration of the current transients was $Q = 2.5$ mC cm^{-2} .

Figure 1 provides structural and morphological information of the GC electrode surface modified with copper selenide species. Spherical-sized particles develop and vary to tens of nm in size forming a large network along with the significantly smaller ones in the background. XPS data clearly confirm the presence of copper and selenium species onto GC surface. Determined binding energy values at 932.7 eV for Cu $2p_{3/2}$ and at 54.6 eV for Se $3d_{5/2}$ point to the availability of Cu_2Se in the modifying layer (Fig. 1 b, c). Moreover, these data are supported by the Augers electron spectra for Cu (Cu L_2VV) since the determined value of kinetic energy is 917.9 eV. They are also in line with the data received by the EDX data analysis, where the relation of concentrations (at.%) of separate Cu and Se elements in the modifying layer was determined to be 69:31.

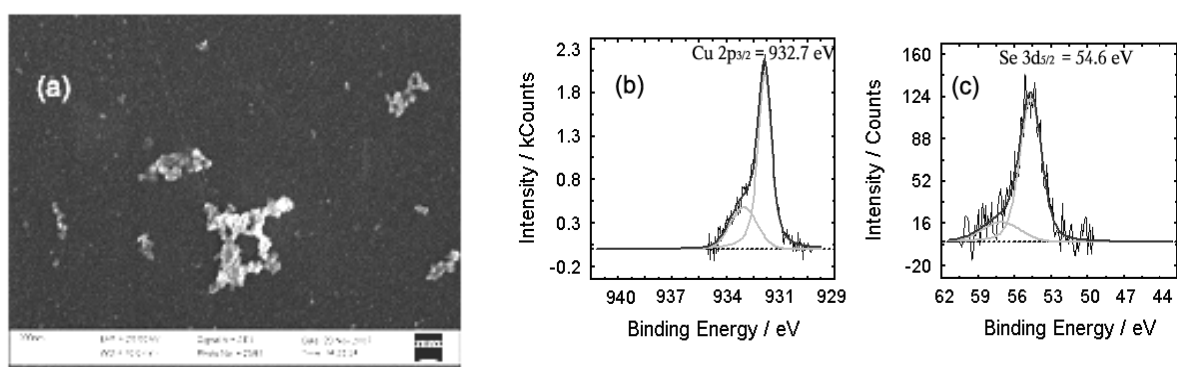


Fig. 1. (a) SEM image and (b, c) representative XP spectra for binding energies of Cu $2p_{3/2}$ (b) and Se $3d_{5/2}$ (c) of the GC electrode modified with Cu-Se species obtained by electrochemical deposition at $E_{\text{dep}} = +0.28$ V vs. SHE.

The electrochemical behaviour of the modified GC electrode was investigated towards Cu reduction by the means of cyclic voltammetry and chronopotentiometry. Figure 2 presents representative cyclic voltammograms for both unmodified and modified GC electrodes with selenide species recorded in 0.5 M H_2SO_4 + 0.01 M CuSO_4 solution at a sweep rate of 10 mV s^{-1} . General shapes of cyclic voltammograms reveal that the modification of the GC electrode results in the notably increased cathodic current followed by the development of two cathodic peaks in different potential domains. One peak is traditionally located in the overpotential region at E c.a. +0.18 V (Fig. 2a), while the other one is determined in the potential region at E c.a. +0.35 V where Cu underpotential deposition is usually observed onto a foreign metal substrate (Fig. 2b inset). It should be noted that no Cu adlayers onto the bare GC surface have

been found in the UPD region [4]. According to the Cu-Se phase diagram the former current peak at more positive potential (E c.a. +0.35 V) can be related to the formation of non-stoichiometric compound Cu_{2-x}Se or stoichiometric Cu_2Se one [5,6].

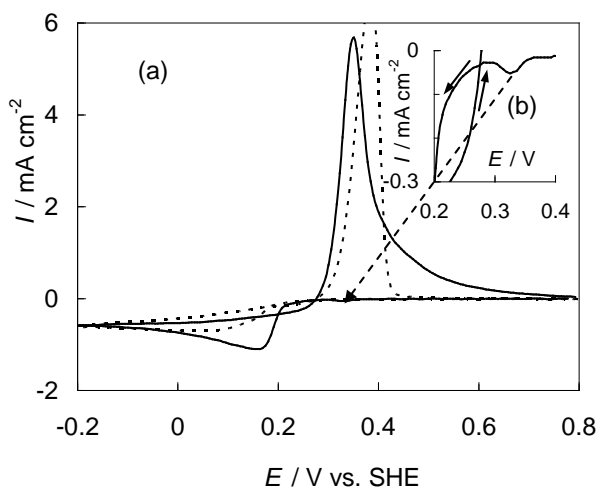


Fig. 2. (a) Cyclic voltammograms for the unmodified GC (dashed line) and GC modified with Cu-Se species (solid line) in 0.5 M H_2SO_4 + 0.01 M CuSO_4 solution at a sweep rate of 10 mV s^{-1} . (b) The inset shows cyclic voltammograms in the expanded scale.

Chronoamperometric investigations of Cu nucleation and growth on so-modified GC electrode in the more positive potential region were performed. A set of potential steps that started from $E_{\text{start}} = +0.80 \text{ V}$ to E_{dep} between +0.34 and +0.27 V for the modified GC electrode with thin layers of selenium compounds was applied and is presented in Fig. 3a. As potential is moved progressively towards lower values the increase in current maximum and decrease in time maximum is observed. Such behaviour of transients suggests the existence of the nucleation and growth processes for all the potentials applied. Any typical transients for nucleation and growth of a new phase for Cu on unmodified GC surface were detected in the potential region under study.

The mechanism of nucleation and growth of new phase onto foreign substrate was determined by analysis of current transients as a function of potential from the chronoamperometric measurements presented in Fig. 3a. A comparison of theoretically calculated and experimentally obtained current transients via the non-linear fitting method in Fig. 3b shows that the deposition of Cu onto the modified GC electrode with thin layers of selenides in the potential region from +0.34 to +0.30 V quite well fits the instantaneous 2D nucleation and growth model developed by Bewick et al. [7]. At more negative potentials starting from +0.29 V the deviation from instantaneous growth mode is observed and points to the contribution of different aspects of Cu deposition processes.

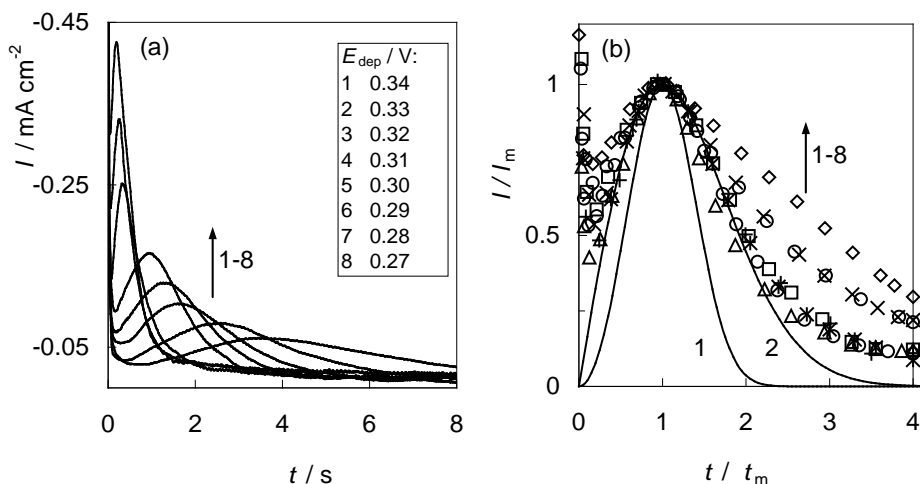


Fig. 3 (a) Potentiostatic current transients for the Cu electrodeposition onto the GC electrode modified with Cu-Se species obtained by potential steps from $E_{\text{start}} = +0.80$ V to different deposition potentials E_{dep} in 0.5 M H_2SO_4 + 0.01 M CuSO_4 solution, (b) Nondimensional plots of potentiostatic transients in Fig. 3a. Lines: theoretical instantaneous (1) and progressive (2) 2D nucleation and growth according to the Bewick model.

Conclusions

The electrochemical deposition method was used to obtain the modified GC electrode with thin layers of copper selenides. Surface analysis techniques revealed the presence of Cu_2Se in the modifying layer. The early stages of Cu electrodeposition on so-modified GC electrode in a 0.5 M H_2SO_4 + 0.01 M CuSO_4 solution were studied by means of cyclic voltammetry and chronoamperometry. The analysis of the results shows that current density significantly increases in the case when the GC electrode is modified with thin selenide layers. The nucleation and growth of Cu on so-modified GC electrode in potential region applied quite well fits the instantaneous 2D nucleation and growth model developed by Bewick et al.

Acknowledgement

Authors appreciate Dr. V. Jasulaitiene and Dr. A. Sielskis input in providing necessary XPS and SEM data for structural surface analysis.

References

- [1] W. Lee, N. Myung, K. Rajeshwar, C.W. Lee, *J Electrochem. Science and Technology*, **2013**, 4, 140.
- [2] M. Bouroushian, *Electrochemistry of Metal Chalcogenides*, Springer-Verlag Berlin Heidelberg 2010.
- [3] E. Budevski, G. Staikov, W. J. Lorenz, in: *Electrochemical Phase Formation and Growth*, VCH, Weinheim, New York, Basel, Cambridge, Tokyo, 1996.
- [4] A.I. Danilov, E.B. Molodkina, Y.M. Polukarov, *Rus. J. Electrochem.*, **2002**, 38, 732.
- [5] K.K. Mishra, K. Rajeshwar, *J. Electroanal. Chem.*, **1989**, 271, 279.
- [6] P. Carbonelle, L. Lamberts, *Electrochim. Acta*, **1992**, 37, 1321.
- [7] A. Bewick, M. Fleischmann, H.R. Thirsk, *Faraday Soc.* **1962**, 58, 2200.

SYNTHESIS AND CHARACTERIZATION OF HYDROXYAPATITE NANOPARTICLES VIA CO-PRECIPITATION AND POLYMER MATRIX MEDIATED SYNTHESIS

J. Vaicekauskaite¹, G. Lubiene², E. Garskaite²

¹Department of Chemistry and Bioengineering, Faculty of Fundamental Sciences, Vilnius Gediminas Technical University, Sauletekio al. 11, Vilnius LT-10223, Lithuania

²Department of Applied Chemistry, Faculty of Chemistry, Vilnius University, Naugarduko 24, Vilnius LT-03225, Lithuania

E-mail: edita.garskaite@chf.vu.lt

Hydroxyapatite ($\text{Ca}_{10}(\text{PO}_4)_6(\text{OH})_2$, HAp) is bioactive and biocompatible material widely used for dental, maxillofacial or orthopaedic applications [1]. However, its specific applications strongly depend on the particle size, phase purity and morphology of prepared material.

A synthesis method and solution parameters (pH, zeta potential, concentration and synthesis temperature) play an important role in determining properties of HAp and subsequently its bio-applications.

In this work we present a polymer matrix mediated synthesis of HAp via co-precipitation method. Prepared gels containing HAp nanoparticles were dried and calcined at 400-800 °C. An effect of the polymer (polyethylene glycol (PEG) and polyvinyl-alcohol (PVA)) on nucleation and growth of HAp particles and crystallinity of prepared material has been investigated. Sintering temperature, morphology, crystallinity and phase composition of the HAp nanopowders were studied by thermogravimetry (TG), scanning electron microscopy (SEM), Fourier transform infrared (FTIR) spectroscopy and X-ray diffraction (XRD) techniques.

Thermogravimetric analysis curves (TG/DTA) of HAp-PEG gel (Fig. 1) show that major mass loss occurs and residual organics decompose below 600 °C, while changes in the actual material might be initiated around 800 °C.

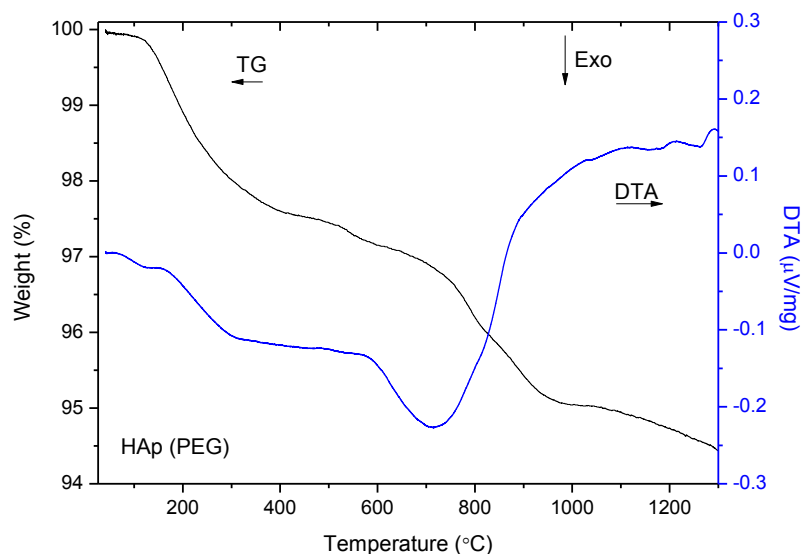


Fig. 1. TG/DTA curves of HAp-PEG gel.

The Bragg reflections in the XRD pattern (Fig. 2) of the HAp-PEG sample annealed at 600 °C were assigned to the polycrystalline HAp phase which is consistent with literature (JCPDS No. 86-0740) (data not presented).

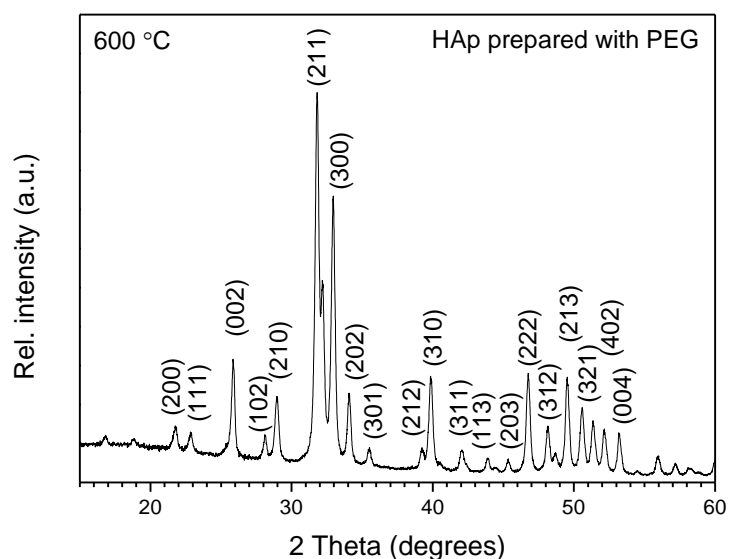


Fig. 2 XRD diffraction patterns of HAp-PEG sample annealed at 600 °C.

No impurity phases were observed. The crystallite sizes of the powders were estimated by the line broadening of the (002), (202), (222), (203) and (004) reflection using the Scherrer equation. HAp was nano-crystalline, with crystallite sizes ranging from 26 to 40 nm. The crystallinity and carbonate content in the prepared samples were estimated performing a peak deconvolution.

References

1. K. Fox, *et al.*, Chem. Phys. Chem., 13 (10) (2012) 2495-2506.

BIODEGRADABLE POLYMER–BIOCERAMIC COMPOSITE COATINGS

L. Vecbiskena

Riga Technical University, 3/7 Paula Valdena St., LV 1048, Riga, Latvia

E-mail: linda.vecbiskena@rtu.lv

Introduction

Nowadays, biomedical coating research focuses on understanding the interaction between the implant surface and biological system and the exploitation of this knowledge to design improved interfaces [1,2]. The incorporation of inorganic nanofillers – hydroxyapatite (HA) and β -tricalcium phosphate (β -TCP) – in resorbable organic polymers has been shown to accelerate *in situ* the specific interaction with bone cell surface receptors and thus can properly direct cell proliferation and differentiation [3–5]. This study takes on the challenge, with attention to physicochemical and biological characteristics, to tune a chitosan matrix by exploiting electrochemical surface modification technology. The effect of nanostructured HA and β -TCP particles on the bioactivity and cell response behavior were investigated.

Materials and methods

Amorphous precursors of HA and β -TCP were obtained through wet-chemical precipitation from aqueous supersaturated solutions, as described in previous work [6]. An ammonium phosphate solution ($[\text{H}_2\text{PO}_4^-] = 0.25 \text{ M}$ (for HA synthesis) or $[\text{HPO}_4^{2-}] = 0.24 \text{ M}$ (for β -TCP synthesis) and calcium nitrate solution ($[\text{Ca}^{2+}] = 0.30 \text{ M}$) containing 30 ml ammonium hydroxide solution (26% NH_3 basis) were rapidly mixed (synthesis pH was around 10). The resulting precipitate was immediately filtered, rinsed with water, treated with ethanol and subsequently oven-dried. The dried powders were heated at 850 °C for 60 min and then cooled in air to room temperature.

Electrolytic cathodic deposition was performed in chitosan–acetic acid solution ($[\text{CH}] = 1 \text{ g/L}$) containing nanostructured calcium phosphate particles (i. $[\text{HA}] = 0.4 \text{ g/L}$, ii. $[\beta\text{-TCP}] = 0.3 \text{ g/L}$, and iii. HA/ β -TCP = 70/30 wt%, the particle size distribution was in the range of 200 nm to approx. 2 μm). Coatings were obtained by electrochemical deposition onto titanium specimens (c.p. grade 2 Ti, 10 mm diameter, 0.5 mm thickness) [7] in galvanostatic mode ($J = 30 \text{ mA cm}^{-2}$, Source-Meter 2425, Keithley Instruments).

Coatings were characterized via X-ray diffraction (XRD) and scanning electron microscopy (SEM), immersed in simulated body fluid (SBF) and tested *in vitro* with osteosarcoma cell line (Saos-2).

Results and discussion

Chitosan–nanostructured calcium phosphate coatings were obtained with a regular surface morphology respecting the chitosan pores between 50 and 200 μm and a homogeneous distribution of inorganic phase within the chitosan matrix (Figure 1a).

The bond strength between bone and bioactive material is determined by the formation rate of an apatite structure [8]. The surface reactions occurred within the first 24H to 72H after immersion in SBF, the white nuclei were observed on the surface (Figure 1b, 1c). As demonstrates Figure 2, after 28 days of immersion, the apatite structure gradually grew all

over the surface. Compared with pure chitosan (Figure 2a), the biocomposite with nanostructured calcium phosphates formed apatite more readily during the immersion process, which suggests that the biocomposite possessed better mineralization (Figure 2b–2d).

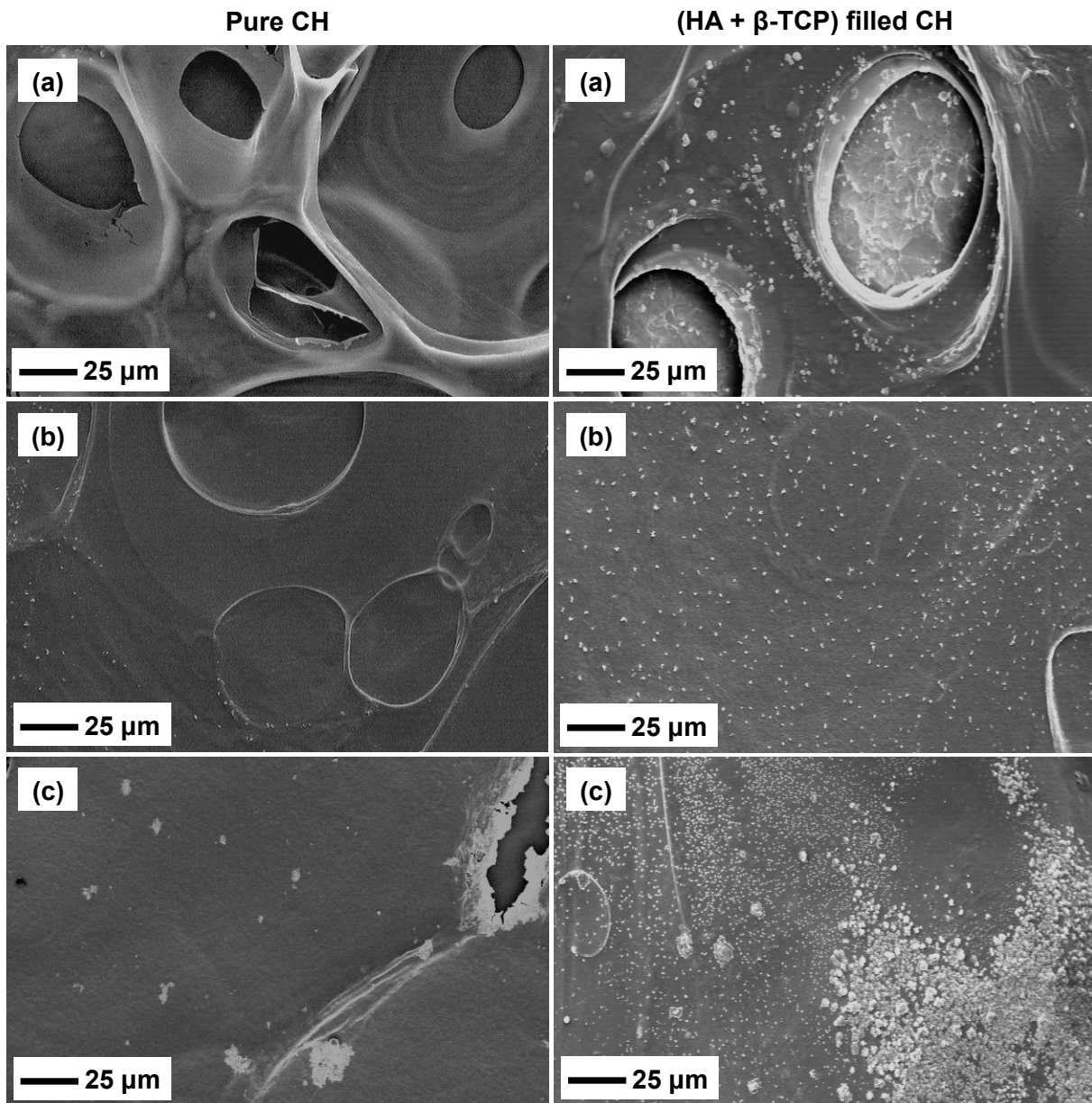


Figure 1. SEM images of surface morphology: (a) deposited coating; (b) 24H and (c) 72H of immersion in SBF.

The coatings were evaluated *in vitro* using an osteosarcoma cell line Saos-2 in order to consider the further applications. As shown in Figure 3, cells were spread all over the chitosan–nanostructured calcium phosphate coatings presenting a round shape and completely spread morphology, adhering to the surface. Their viability increased up to 14 days of culture and no significant differences have been detected compared to control (Ti). After 7 days, the cells were connected to each other forming a continuous cell layer on the surface.

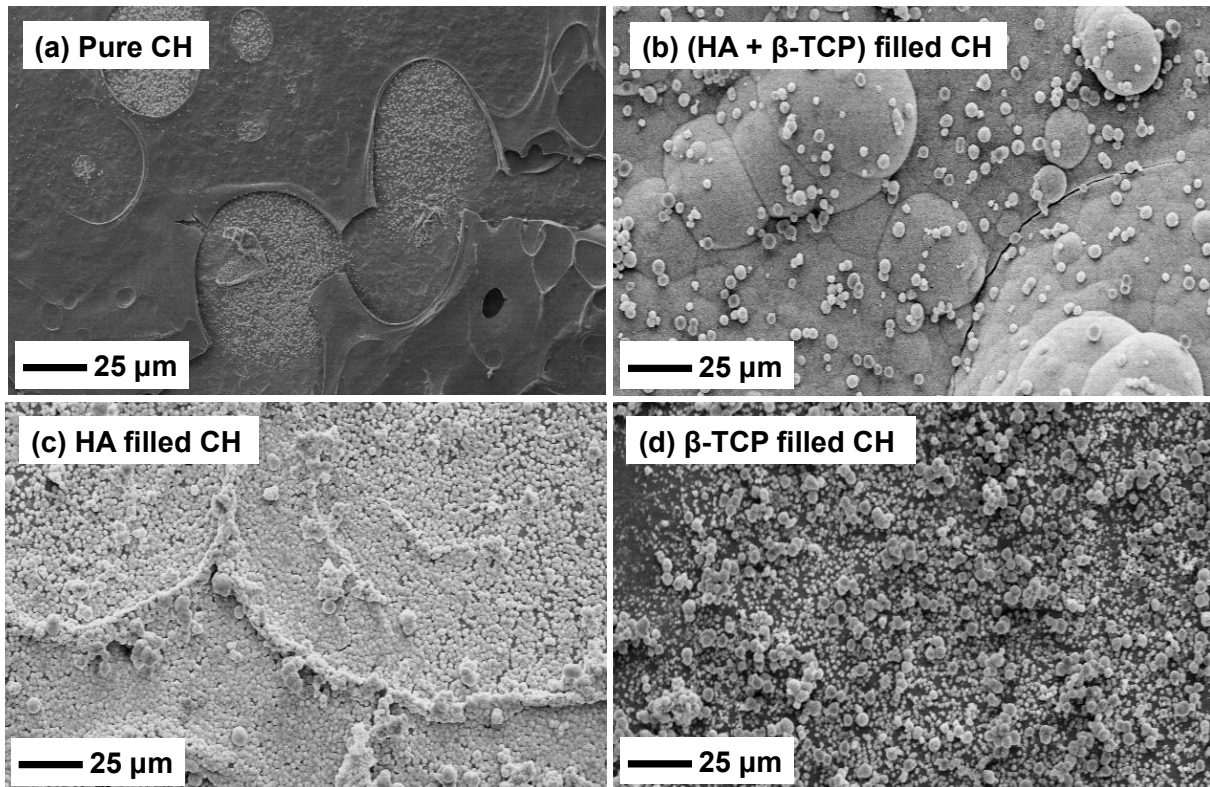


Figure 2. SEM images of surface morphology: (a), (b), (c) and (d) after 28 days of immersion in SBF.

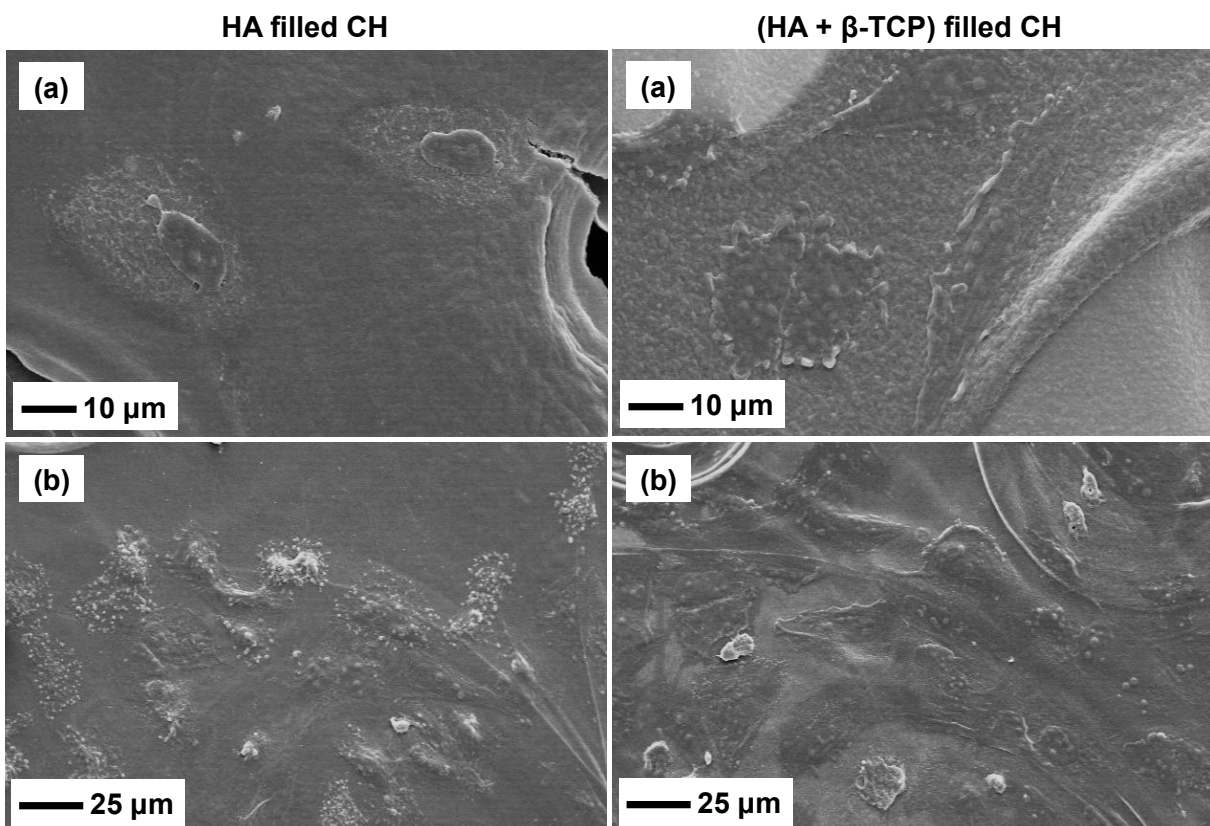


Figure 3. SEM images of Saos-2 cell attachment on biocomposite coatings after culture: (a) 24H and (b) 7 days.



Conclusion

Different chitosan–nanostructured calcium phosphate coatings were successfully obtained via electrolytic cathodic deposition and characterized, by evaluating their physicochemical and biological properties. The tuning of HA and/or β -TCP resulted in an increase of the coating bioactivity and its ability to improve osteoblast-like cell attachment and spreading.

Acknowledgements

This work was done during the author's stay at the Department of Chemistry, Materials and Chemical Engineering 'G. Natta', Politecnico di Milano, supported by the Italian Government Bursaries for Foreign and I.R.E. Students, Italian Government Study Grants (Academic Year 2013/2014). LV is grateful to Lina Altomare, Luigi De Nardo and Roberto Chiesa for helpful discussions and suggestions throughout the study, and Monica Moscatelli, Department of Chemistry, Materials and Chemical Engineering 'G. Natta', Politecnico di Milano, for the SEM micrographs.

References

1. S.B. Goodman, Z. Yao, M. Keeney, F. Yang, *Biomaterials*, **2013**, *34*, 3174.
2. R.A. Surmenev, M.A. Surmeneva, A.A. Ivanova, *Acta Biomater.*, **2014**, *10*, 557.
3. S.V. Dorozhkin, *J. Mater. Sci.*, **2009**, *44*, 2343.
4. W.W. Thein-Han, R.D.K. Misra, *Acta Biomater.*, **2009**, *5*, 1182.
5. Y.H. Kang, H.C. Kim, *et al.*, *Tissue Eng. Regen. Med.*, **2011**, *8(1)*, 23.
6. L. Vecbiskena, L. De Nardo, R. Chiesa. *Key Eng. Mater.*, **2014**, *604*, 212.
7. L. Altomare, L. Draghi, R. Chiesa, L. De Nardo, *Mater. Lett.*, **2012**, *78*, 18.
8. D.C. Greenspan, *Tandläkartidningen Årg*, **1999**, *91(8)*, 3336.



THE ADSORPTION CAPACITY OF GYROLITE FOR Mn^{2+} IONS

S. Zadavičiūtė¹, K. Baltakys¹

1 Department of Silicate Technology, Kaunas University of Technology, Radvilenu 19, LT-50254 Kaunas, Lithuania

E-mail: zadaviciute.skirma@gmail.com

Introduction

Many technological developments occurred in the last years, but the most adverse aspect of global industrialization is the negative environmental impact. Large concentrations of toxic pollutants appear frequently in drinking water and wastewater posing an important environmental issue. The problem of removing pollutants from water is an important process and is becoming more important with the increasing of industrial activities [1-3]. A large number of industries discharge metal-containing effluents into water resources without adequate treatment. Contamination of the environment by manganese is currently an area of concern. Although, manganese is an essential micronutrient, however over and above concentration becomes toxic and causes poisonous effects such as memory impairment, disorientation, hallucinations speech disturbance, compulsive behavior and acute anxiety [4-5]. The main sources of this element are ferromanganese and steel production, mining industry, electrical, radio engineering and electronics manufacturing, chemical industry, ore-concentration factories and flotation of various non-ferrous metals [6-7]. In the last few decades adsorption has become a well-established technique to remove pollutants [8]. In previous studies [9-10], it was showed that gyrolite acts as adsorbent for the purification of water with heavy metals ions. The aim of this work was to investigate adsorption capacity of gyrolite for manganese ions.

Materials and methods

Fine-grained $SiO_2 \cdot nH_2O$ („Stanchem“, ignition losses, 7.84 %; specific surface area $S_a = 1804 \text{ m}^2/\text{kg}$ by Blaine) and CaO (calcium hydroxide was burned $950 \text{ }^\circ\text{C}$ for 0.5 hours; $S_a = 1234 \text{ m}^2/\text{kg}$; purity 98.83) was used as starting materials. Hydrothermal synthesis of gyrolite has been carried out in autoclave under the saturated steam pressure at $200 \text{ }^\circ\text{C}$; the duration of isothermal curing was 48 hours, the molar ratio of primary mixture was $CaO/SiO_2 = 0.66$. These synthesis conditions were chosen according to previously published data [11]. The products of the synthesis have been filtered, rinsed with ethyl alcohol to prevent carbonization of materials, dried at the temperature of $50 \pm 5 \text{ }^\circ\text{C}$ and sieved through a sieve with a mesh width of $50 \text{ }\mu\text{m}$

Adsorption experiments were carried out at $25 \text{ }^\circ\text{C}$ temperature in the thermostatic absorber Grant SUB14 by stirring 1 g of gyrolite in 100 ml of $Mn(NO_3)_2 \cdot yH_2O$ solutions containing $0.25 \text{ g Mn}^{2+}/\text{dm}^3$ for 60 min. The concentrations of heavy metal ions were determined using a Perkin-Elmer Analyst 4000 spectrometer. The value of pH was taken by Hanna instrument (Hi 9321, microprocessor pH meter). The same methodology was applied for the simultaneous adsorption with a mixture of Ni^{2+} , Mn^{2+} , Fe^{3+} , Co^{2+} , Cu^{2+} , Zn^{2+} ions solutions, which concentration was equal to $0.25 \text{ g} \cdot \text{Me}/\text{dm}^3$.

In order to determined kinetic parameters of adsorption reactions, a kinetic models (*pseudo-second order and pseudo-first order*) have been developed and fitted for the adsorption process of the Mn^{2+} ions into gyrolite [12-14].

Results and discussion

It was determined that after 30 s of adsorption, when the initial concentration of Mn^{2+} ions was equal to 0.25 g/dm^3 , about 75% ($18.64\text{ mg Mn}^{2+}/\text{g}$) of manganese ions were intercalated in to the structure of gyrolite (Fig. 1, a). It was found that the adsorption rate slightly increases by prolonging the experiment duration due to exchange in the quantity of incorporated Mn^{2+} ions. After 10 min, the equilibrium ($21.49\text{ mg Mn}^{2+}/\text{g}$) is attained and the removal of mentioned ions is complete (Fig. 1, b).

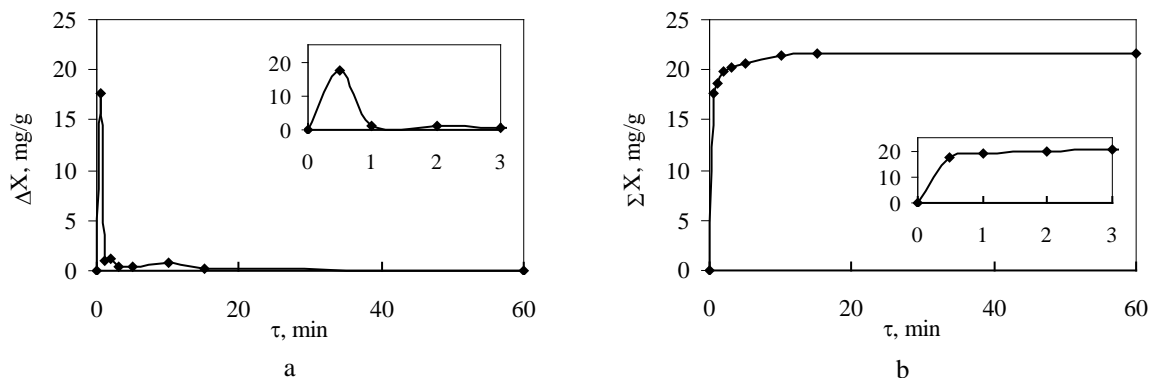


Fig. 1. Differential (a) and integral (b) kinetic curves of Mn^{2+} ions adsorption by gyrolite

It should be noted that during the intrusion of Mn^{2+} ions into the gyrolite structure, calcium ions are released from the crystal lattice of the adsorbent into solution. Most of the Ca^{2+} ions were released in the first minutes, and their amount slightly varies when the process of adsorption is prolonged (Fig. 2). It was determined that the largest amount of Ca^{2+} ions ($12.11\text{ mg Ca}^{2+}/\text{g}$) was released into solution after 30 s, when the pH value was equal to 7.23 (Fig. 2, a). It was estimated that the concentration of Ca^{2+} ions increases slightly with the increase of adsorption duration (Fig. 2, b). It should be underlined that pH value change is attributed to the degree of release of Ca^{2+} ions from the structure of the gyrolite solid in solution during the reaction. Therefore, it is no coincidence that the pH value of solution varied from 5.82 to 7.74 only at the beginning of reaction.

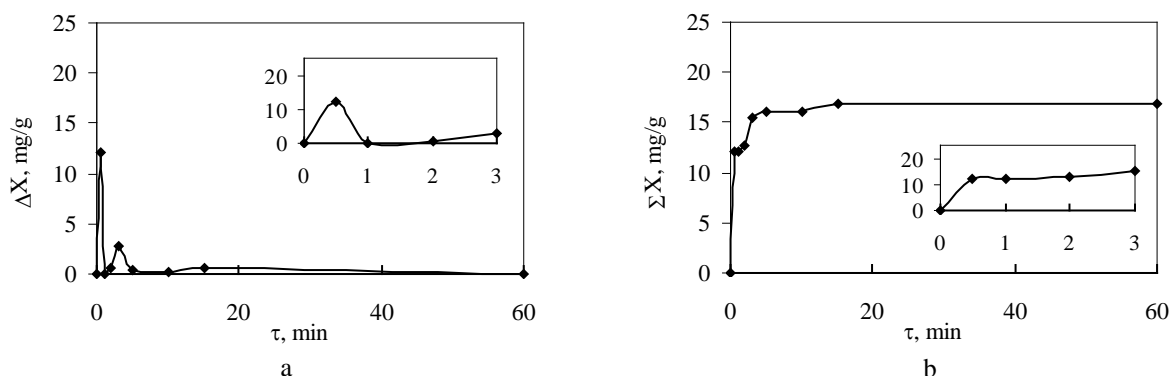


Fig. 2. Differential (a) and integral (b) kinetic curves of Ca^{2+} ions concentration variation in acidic solution

In order to evaluate Mn^{2+} ions capacity of gyrolite with multiple adsorbates, which usually dominate in waste waters, the experiments of simultaneous adsorption were performed in a mixture of Co^{2+} , Ni^{2+} , Zn^{2+} , Mn^{2+} , Cu^{2+} , Fe^{3+} ions solutions ($0.25\text{ g}\cdot\text{Me}/\text{dm}^3$).

Table 1. Variation of adsorbed Mn^{2+} ions during adsorption

	Duration of adsorption, min							
Adsorbed Mn^{2+} ions	0.5	1	2	3	5	10	15	60

$\Delta X, \text{mg/g}$	24.11	0.11	0.11	0.16	0.32	0.10	0.02	0.03
$\Sigma X, \text{mg/g}$	24.11	24.22	24.32	24.49	24.81	24.91	24.92	24.95

It was determined that adsorption type have an effect on the total amount of adsorbed manganese ions in solution. It should be noted that, after the same duration (0.5 min), almost all Mn^{2+} ions (>96%) entered the structure of adsorbent (Table 1.). It should be noted that during simultaneous adsorption, the ion exchange reactions proceeds differently than with single ions.

It should be noted that gyrolite acts as a chemisorbent but not like usual adsorbent. In order to confirm this fact, after adsorption process gyrolite substituted with Mn^{2+} ions was dried up and immersed in distilled water. It was proved that Mn^{2+} ions did not appear in the solution after 60 minutes at 25 °C. Thus, the latter process is irreversible.

Thus, our research allows us to state that the adsorption reactions are specific to the chemisorption process. In order to determine adsorption kinetic parameters, kinetics models have been developed and fitted for the reactions of the Mn^{2+} ions by gyrolite. By using a pseudo-first order kinetic rate equation in a linear form ($\log(q_e - q_t) = \log q_e - \frac{k_1}{2.303}t$), the amount of adsorbed ions ($q_{e(\text{exp})}$) and the first order constants k_1 (min^{-1}) were determined experimentally from the slope and intercept plot of $\log(q_{e(\text{exp})} - q_t)$ vs. t.

Table 2. The kinetic parameters of the pseudo first and pseudo second order kinetic models

Adsorbates	Ions	R^2	$q_{e(\text{exp})}, \text{mg}\cdot\text{g}^{-1}$	$q_{e(\text{cal})}, \text{mg}\cdot\text{g}^{-1}$	$k, \text{g}\cdot\text{mg}^{-1}\cdot\text{min}^{-1}$
Single	Pseudo first-order kinetic models				
	Mn^{2+}	0.89	21.67	5.63	-
	Pseudo second-order kinetic models				
	Mn^{2+}	0.99	21.67	21.88	0.23
multiple	Pseudo first-order kinetic models				
	Mn^{2+}	0.69	24.95	1.87	-
	Pseudo second-order kinetic models				
	Mn^{2+}	1	24.95	25.00	1

R^2 : correlation coefficient; $q_{e(\text{exp})}$: the equilibrium adsorption capacity, $\text{mg}\cdot\text{g}^{-1}$, calculated from experimental data (Fig. 1, Table 1); $q_{e(\text{cal})}$: the equilibrium adsorption capacity, $\text{mg}\cdot\text{g}^{-1}$, calculated by using equations (3) and (4) of kinetic models.

It was observed that the pseudo-first order model did not fit well, because the calculated $q_{e(\text{cal})}$ values disagreed with the experimental $q_{e(\text{exp})}$ values, and the values of the correlation coefficient (R^2) were low single ions (0.89) and simultaneous adsorption (0.69) (Table 2).

Using the pseudo-second order kinetics equation ($\frac{t}{q_t} = \frac{1}{kq_e^2} + \frac{1}{q_e}t$), the amount of adsorbed

ions ($q_{e(\text{exp})}$) and the second order constants k_2 ($\text{g}\cdot\text{mg}^{-1}\cdot\text{min}^{-1}$) were determined experimentally from the slope and intercept of plot t/q_t vs. t. The values of the calculated $q_{e(\text{cal})}$ and experimental $q_{e(\text{exp})}$ are represented in Table 2. An agreement between $q_{e(\text{exp})}$ experimental and $q_{e(\text{cal})}$ calculated values for the pseudo-second order model was observed. It was found that the manganese ions simultaneous adsorption rate ($k_2 = 1 \text{ g}\cdot\text{mg}^{-1}\cdot\text{min}^{-1}$) 4 times is higher than the Mn^{2+} ion ($k_2 = 0.23 \text{ g}\cdot\text{mg}^{-1}\cdot\text{min}^{-1}$) (Table 2). These data agree with experimental results: Mn^{2+} ions simultaneous adsorption reactions (Table 1) proceed more rapid than single ions (Fig. 1).

Conclusions

The adsorption capacity of gyrolite and intrusion of Mn^{2+} ions in its structure depends on reaction time and adsorption type. It was determined that the incorporation of simultaneous adsorption of Mn^{2+} ions occurs more intensive than single manganese ions because after 60 min only 86 % of them (21.49 mg Mn^{2+} /g) are intercalated into the structure of gyrolite, whereas simultaneous adsorption – over 99 % (24.95 mg Mn^{2+} /g).

It was found that the adsorption reactions are not reversible processes and follow a pseudo-second order model. It was found that the simultaneous adsorption rate ($k_2 = 1 \text{ g}\cdot\text{mg}^{-1}\cdot\text{min}^{-1}$) is higher than the single ion adsorption ($k_2 = 0.23 \text{ g}\cdot\text{mg}^{-1}\cdot\text{min}^{-1}$).

References

1. J. Febriantoa, A. N. Kosasiha, J. Sunarsob, Y. H. Jua, N. Indraswatib, S. Ismadjia, *J. Hazard. Mater.*, **2009**, 162.
2. D. Park, Y. Yun, J.H. Jo, J.M. Park, *Ind. Eng. Chem. Res.* **2006**, 45. (pp. 5059–5065)
3. B. V. Bruggen, C. Vandecasteele, *Environ. Pollut.*, **2003**, 03, 122.
4. H.G. Seiler, A. Sigle, *Hand book on toxicity of inorganic com-pounds*. Marcel-Dekker, New York, **1998**.
5. D. Savovaa, N. Petrova, M. F. Yardimb, E. Ekincib, T. Budinovaa, M. Razvigorovaa, V. Minkovaa, *Carbon.*, **2003**, 10, 41.
6. S. K. Agarwal, *Heavy metal pollution*. Aph Publishing Corporation, New Delhi, **2009**.
7. N. Boudiaa, R. Halleyc, G. Kennedyd, J. Lamberte, L. Gareaua, J. Zayeda, *Sci. Total. Environ.*, **2006**, 1(31), 366.
8. Cheung, C. W., Porter, J. F., McKay, G., *Water. Res.*, **2001**, 03, 35.
9. A. Bankauskaitė, K. Baltakys, *Mater. Sci. Poland.*, **2009**, 03, 27.
10. K. Baltakys, A. Eisinas, I. Barauskas, E. Prichockiene, E. Zaleckas, *J. Sci. Ind. Res. India.*, **2012**, 71.
11. S. Merlino, *Mineral. Mag.*, **1988**, 52.
12. S. Lagergren, *Zur theoric der sogenannten adsorption gelöster stoffe*. Kungliga Svenska, Vetenskapsakademiens, **1898**.
13. Y. S. Ho, D.A.J. Wase, C.F. Forster, *Trans IChemE Part B*, **1994**, 17.
14. Y. S. Ho, D.A.J. Wase, C.F. Forster, *Water. Res.*, **1995**, 29.



SYNTHESIS OF GADOLINIUM DOPED CERIA VIA SOL-GEL AND SOL-GEL COMBUSTION SYNTHESIS ROUTES

A. Zarkov¹, A. Stanulis², A. Beganskiene², S. Tautkus¹, A. Kareiva²

¹*Department of Analytical and Environmental Chemistry, Vilnius University, Naugarduko 24, LT-03225 Vilnius, Lithuania*

²*Department of Inorganic Chemistry, Vilnius University, Naugarduko 24, LT-03225 Vilnius, Lithuania*

E-mail: aleksej.zarkov@chf.vu.lt

Introduction

Solid oxide fuel cells (SOFC) are among the most promising devices to generate energy in an efficient and environmentally friendly way. One of the most important characteristic of SOFC is operating temperature, which is traditionally 1000 °C for SOFC using conventional yttria-stabilized zirconia (YSZ) electrolytes. Such a high temperature is required for achieving a proper ionic conductivity of electrolyte, however, it leads to the difficulties with sealing and interconnects. In order to reduce SOFC operating temperature alternative electrolyte are developed. The reduction in operating temperature leads to higher chemical stability of SOFCs and allows using comparatively inexpensive materials [1]. Gadolinium doped ceria (GDC) is one of the most attractive material for the use as an electrolyte in intermediate temperature SOFC due to its high ionic conductivity in the temperature range from 500 to 700 °C [2].

In the present work GDC powders with different gadolinium content (10, 15 and 20 mol%) were prepared by sol-gel and sol-gel combustion synthesis routes using glycerol as a complexing agent and fuel. The results on the influence of synthesis conditions on the powder characteristics are presented herein.

Experimental

For the preparation of GDC powders by sol-gel combustion (SGC) synthesis route cerium(III) nitrate hexahydrate ($\text{Ce}(\text{NO}_3)_3 \cdot 6\text{H}_2\text{O}$, Alfa Aesar, 99.99%) and gadolinium(III) nitrate hydrate ($\text{Gd}(\text{NO}_3)_3 \cdot x\text{H}_2\text{O}$, Alfa Aesar, 99.9%) were used as starting materials. The appropriate amounts of metal nitrates were dissolved in deionized water in a tall beaker followed by the addition of glycerol as a complexing agent and fuel for self-burning reaction. The amount of fuel was estimated according to the principle of propellant chemistry [3]. In our work the stoichiometric fuel to oxidant ratio was chosen and calculated glycerol to metal nitrates ratio was 1.07:1.0. The resulting solution was evaporated while continuous stirring at 100 °C. After the sol transformed into transparent gel the temperature of the hot plate was increased to 250 °C and spontaneous ignition process took place yielding a pale-yellow ash. Final ashes were collected and annealed in a muffle furnace at different temperatures up to 800 °C in air atmosphere.

For the synthesis of GDC powders by sol-gel (SG) technique the appropriate amounts of cerium(III) acetate hydrate ($\text{Ce}(\text{CH}_3\text{COO})_3 \cdot x\text{H}_2\text{O}$, Sigma-Aldrich, 99.9%) and gadolinium(III) acetate hydrate ($\text{Gd}(\text{CH}_3\text{COO})_3 \cdot x\text{H}_2\text{O}$, Alfa Aesar, 99.9%) were dissolved in deionized water. Glycerol as complexing agent was then added to the above solution in the same ratio as in the case of sol-gel combustion synthesis route. The obtained solution was mixed for 1 h at 60 °C and then concentrated by evaporation of solvent at 100 °C until it turned into a viscous gel. The resulted gel was dried in the oven overnight and finally annealed in a furnace under the same conditions as for sol-gel combustion synthesis route.

Thermogravimetric analysis of starting compounds $\text{Gd}(\text{NO}_3)_3 \cdot x\text{H}_2\text{O}$, $\text{Ce}(\text{CH}_3\text{COO})_3 \cdot x\text{H}_2\text{O}$ and $\text{Gd}(\text{CH}_3\text{COO})_3 \cdot x\text{H}_2\text{O}$ was performed prior synthesis in order to determine the exact content of water crystallization.

X-ray diffraction (XRD) analysis data were collected in the range of $10^\circ \leq 2\theta \leq 80^\circ$ using Ni-filtered Cu K_α radiation on Rigaku MiniFlex II diffractometer working in Bragg-Brentano ($\theta/2\theta$) geometry. The step width and integration time was 0.02° and 1 s, respectively. The morphology of the final powders was characterized by scanning electron microscopy performed with a Hitachi SU-70 field-emission scanning electron microscope (FE-SEM). The thermal decomposition of the precursors was analysed through thermogravimetric analysis using Perkin Elmer STA 6000 Simultaneous Thermal Analyzer. Specific surface area of calcined powders was measured using a surface area analyzer Micrometrics TriStar II 3020 based on BET principle and nitrogen adsorption.

Results and discussion

The phase crystallinity and purity of all samples were characterized by means of XRD analysis. The powder XRD patterns of 20GDC sample obtained by SGC process and annealed at different temperatures are given in Fig. 1.

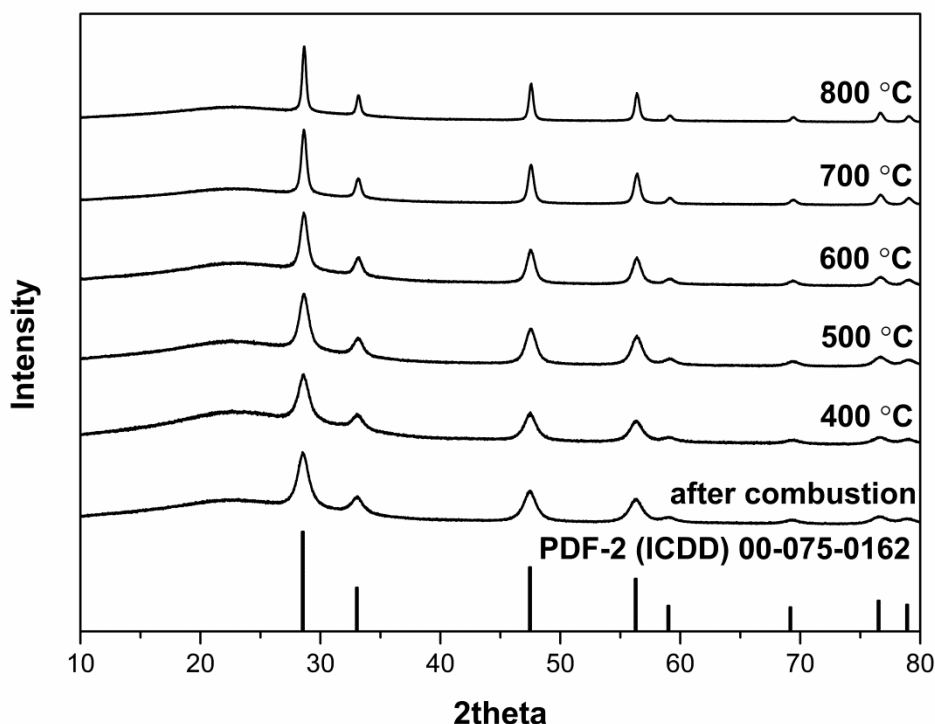


Fig. 1. XRD patterns of 20GDC prepared by SGC synthesis route and annealed at different temperatures for 5 h.

It is clearly seen that crystalline phase is already formed after combustion process. The diffraction peaks of synthesized powders are very broad indicating nano-crystalline nature of the powders. The peak broadening, however, decreased with increasing annealing temperature. No X-ray reflections arising from byproducts such as Ce_2O_3 are observed. Fig. 2 shows the XRD patterns of 20GDC powders prepared by SG synthesis route and annealed at different temperatures. The crystalline compound forms already after annealing sample at 400°C . Again, the degree of crystallinity increases with increasing annealing temperature. All the diffraction peaks match very well the standard XRD data of

$Gd_{0.2}Ce_{0.8}O_{1.9}$ (ICDD 00-075-0162). High background intensity in the small angle region observed for both synthesis routes is due to amorphous sample holder.

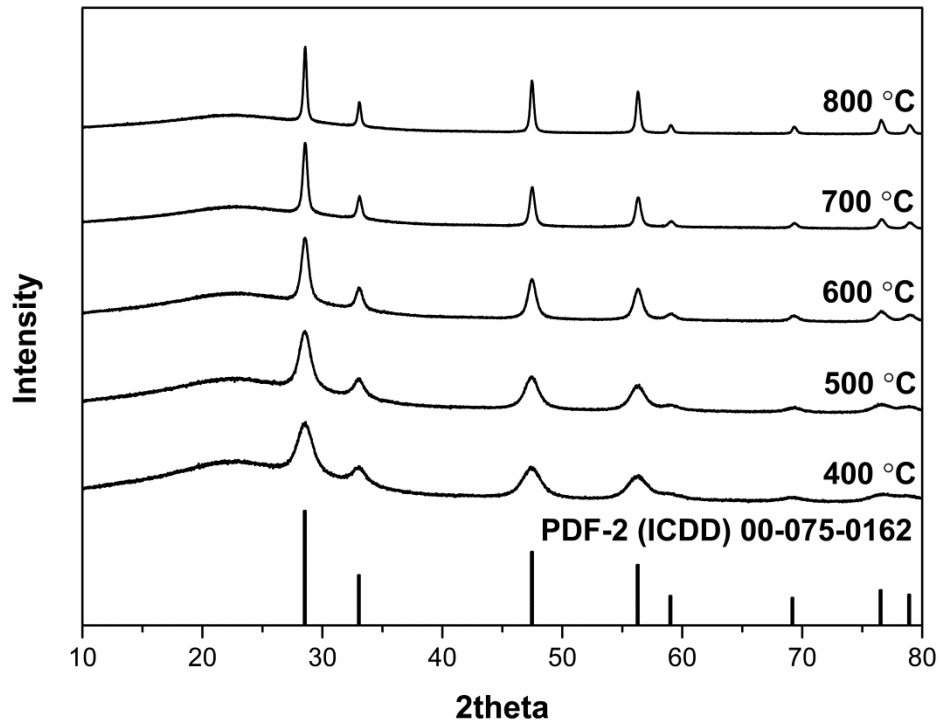


Fig. 2. XRD patterns of 20GDC prepared by SG synthesis route and annealed at different temperatures for 5 h.

The morphology of synthesized GDC powder samples were examined using scanning electron microscopy (Fig. 3).

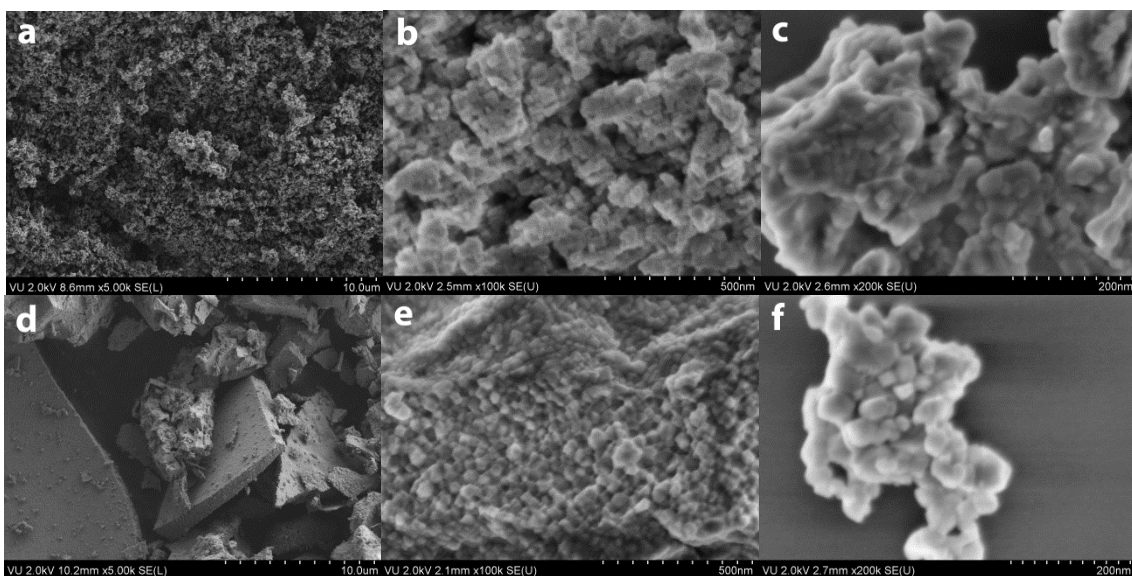


Fig. 3 SEM micrographs of 20GDC powders synthesized at 800 °C by SGC (a, b, c) and SG (d, e, f) methods.

The SEM micrographs of 20GDC specimen synthesized at 800 °C by SGC method are shown in Fig. 3 (a, b, c). It can be seen that uniform particles are formed (Fig. 3a). However, a closer

look (Fig. 3b, c) revealed that these particles consist of smaller (~20-50 nm) undefined shape crystallites necked to each other. At the same time, 20GDC powders prepared by SG method exhibit different morphological features (Fig. 3d). After calcination at 800 °C the plate-like monoliths having different size and covered by smaller particles were obtained. The crystallite size is slightly smaller comparing to SGC method and lies in the range of approximately 20-40 nm (Fig. 3e, f). The variation in stoichiometry of the final compounds did not result in any significant morphological changes for both synthesis routes. Specific surface area for the same 20GDC samples was found 19.0 and 12.9 m²/g (synthesized by SGC and SG methods, respectively).

Conclusions

GDC powders with different gadolinium content (10, 15 and 20 mol%) were prepared by sol-gel and sol-gel combustion synthesis routes. The results of XRD analysis showed that synthesized powders were single-phase compounds and possessed the expected crystal structure. The morphology of powders was determined to be strongly dependent on the processing route. However, the crystallite size was rather similar for all synthesis products. Specific surface area of 20GDC powders synthesized by SGC was found significantly higher in comparison with SG synthesis route.

References

- [1] R. Fuentes, R. Baker, *International Journal of Hydrogen Energy*, 33 (2008) 3480-3484.
- [2] B.C.H. Steele, *Solid State Ionics*, 129 (2000) 95-110.
- [3] S.R. Jain, K.C. Adiga, V.R. Pai Verneker, *Combustion and Flame*, 40 (1981) 71-79.

ELECTRODEPOSITION OF NANOCRYSTALLINE Mn COATINGS

N. Žmuidzinašienė, A. Šulčius, E. Griškoniš*Department of Physical and Inorganic Chemistry, Kaunas University of Technology,**Radvilėnų pl. 19, LT-50254 Kaunas, Lithuania**E-mail: nerita.galvanauskaite@ktu.lt*

The manganese is the most electronegative metal ($E^{\circ}_{\text{Mn}^{2+}/\text{Mn}} = -1.18$ V vs. SHE), which can be electrodeposited from aqueous solution. Electrodeposits of Mn are potentially useful as sacrificial coatings for protecting ferrous substrates against corrosion [1]. A number of compounds of sulphur [2], selenium [3, 4], and tellurium [5, 6] as additives in manganese electrodeposition baths allow to obtain Mn coatings of good quality and with the moderate or high current efficiency.

In this experiment the manganese sulphate and ammonium sulphate bath (MASB) of the following composition was used: 0.95 M $(\text{NH}_4)_2\text{SO}_4$ and 0.62 M MnSO_4 , pH ~ 2.3 . Mn coatings were obtained at room temperature ($20 \pm 1^\circ\text{C}$) from MASB with optimal 2.2 mM concentration of sodium tellurate $\text{Na}_2\text{TeO}_4 \cdot 2\text{H}_2\text{O}$ as additive [7]. No agitation of MASB was applied during all electrodeposition processes. Mild carbon steel (St-3, Russia) plates (20x20 mm) were used as a substrate for the electrodeposition of Mn coatings. Pb-1 % Ag alloy plates coated with a MnO_2 film were used as insoluble anodes. A constant charge of 7200 coulombs was used in all electrodeposition experiments and cathodic current density varied in the range from 2 to 30 $\text{A} \cdot \text{dm}^{-2}$. The structure of electrodeposits was investigated by X-ray diffraction (XRD) analysis using Bruker D8 Advance diffractometer. The phases of Mn coatings were identified from XRD patterns by using Bruker AXS software EVA and PDF-2 database. The calculation of crystallite size was performed in a conventional way according to the Scherrer's formula after the measurements of the full widths at the half maxima of the peaks in the XRD patterns by means of computer software XFIT. The morphology of electrodeposits was investigated by atomic force microscopy (AFM) with microscope NT 206 (Belarus) by scanning a surface area of $12 \times 12 \mu\text{m}$ of Mn coatings in the contact mode. Additionally, observation of the surface of Mn electrodeposits was performed using FEI Qanta 200 FEG scanning electron microscope (SEM).

XRD analysis has shown that Mn coatings, obtained in the range of cathodic current density from 2 to 15 $\text{A} \cdot \text{dm}^{-2}$, consist of a mixture of brittle α -Mn (body centred cubic) and plastic β -Mn (cubic) phases. The structural changes of Mn coatings have been observed when higher cathodic current densities were used during electrodeposition process. In the coating obtained at current densities 20 and 30 $\text{A} \cdot \text{dm}^{-2}$, the α -Mn phase predominates. Broadening of the XRD peaks indicates that structure of these electrodeposits is clearly nanocrystalline. The average crystallite size of Mn coatings, obtained at cathode current densities from 2 to 10 $\text{A} \cdot \text{dm}^{-2}$, calculated according to the Scherrer's formula, decreases approximately from 75 to 20 nm (Fig. 1). The average crystallite size of Mn coatings, electrodeposited at higher current densities (10–30 $\text{A} \cdot \text{dm}^{-2}$), varies slightly and is in the range from 20 to 25 nm. The similar dependence, i.e. decreasing of the surface roughness and average height values of Mn coatings with the increase of current densities until 20 $\text{A} \cdot \text{dm}^{-2}$ (including), has also been observed (Table 1). The smooth changes of skewness from positive to negative values had suggested that with increasing of cathodic current densities predomination of the bumps on the surface of Mn coatings changed to the more flat surface, where morphological valleys prevail. Visual and SEM observations (Fig. 2) led to the conclusion, that semi-glossy Mn coatings of best quality were obtained from MASB with 2.2 mM concentration of Na_2TeO_4 additive at cathodic current density of 15 $\text{A} \cdot \text{dm}^{-2}$.

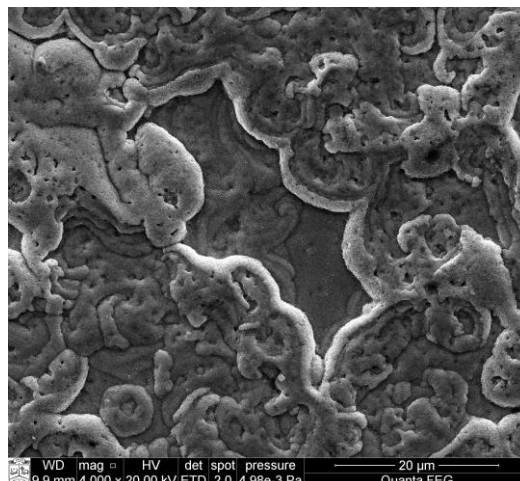
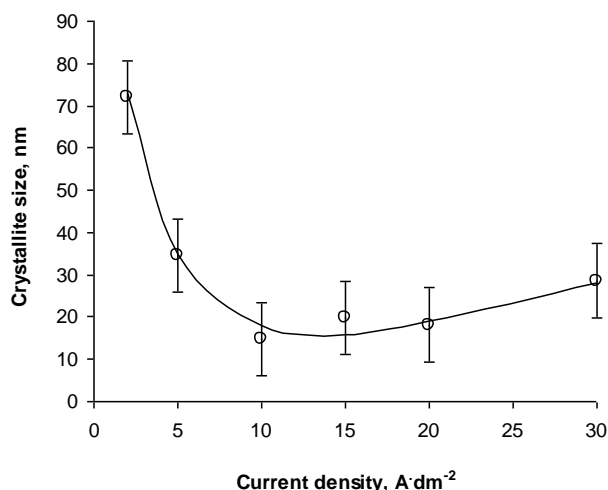


Fig. 1. Influence of current density on mean crystallites sizes of Mn coatings obtained from MASB with 2.2 mM Na₂TeO₄ additive at room temperature. Calculation was performed from characteristic XRD peaks at $2\theta \sim 43^\circ$ and $\sim 45^\circ$

Fig. 2. SEM image of Mn coating obtained from MASB with 2.2 mM Na₂TeO₄ additive at room temperature and at cathodic current density 15 A·dm⁻²

Table 1. Roughness, average height and skewness values measured by AFM for Mn coatings, obtained from MASB with 2.2 mM Na₂TeO₄ additive at room temperature

Parameter	Current density, A·dm ⁻²			
	2	10	20	30
Root mean square roughness R _q , nm	229.08	92.85	76.51	164.00
Average roughness R _a , nm	185.10	71.15	60.98	131.48
Average height Z _{mean} , nm	809.42	346.91	288.42	1239.86
Skewness, R _{sk}	0.24	0.01	-0.18	-0.52

References

1. W. Zhang, C.Y. Cheng, Hydrometallurgy, **89** (2007) 37–159.
2. P. Diaz-Arista, G. Trejo, Surf. Coat. Technol., **201** (2006) 3359–3367.
3. W. Li, Sh. Zhang, Appl. Surf. Sci., **257** (2011) 3275–3280.
4. X. Fan, S. Xi, D. Sun, Z. Liu, Du. Jun, C. Tao, Hydrometallurgy, **127-128** (2012) 24–29.
5. R.K. Sharma, A.C. Rastogi, G. Singh, Mater. Chem. Phys., **84** (2004) 46–51.
6. R.K. Sharma, G. Singh, Y.G. Shula, H. Kima, Phys. B, **390** (2007) 314–319.
7. N. Galvanauskaitė, A.Sulcius, E.Griskonis, P. Diaz-Arista, Trans IMF, **89** (2011) 325–332.



Vilnius University, Faculty of Chemistry,
Naugarduko 24, Vilnius, Lithuania
January 23, 2015

Poster presentations

Chemistry of Organic Materials



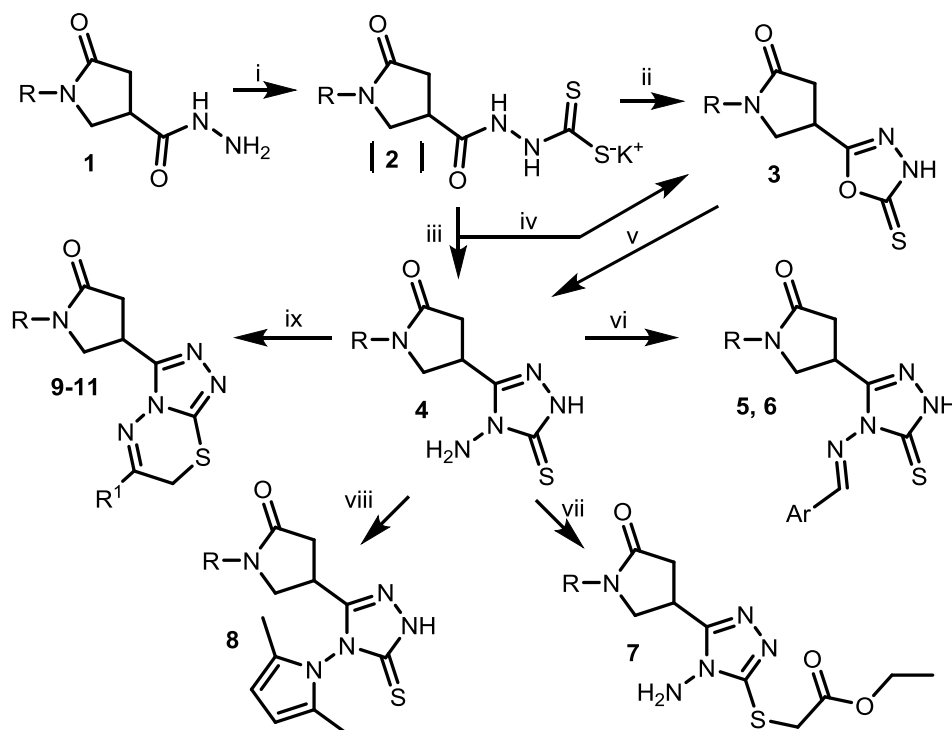
SYNTHESIS OF NEW 1-(4-METHOXYPHENYL)PYRROLIDIN-2-ONES

K. Anusevičius, E. Slaninaitė, B. Sapijanskaitė,
R. Vaickelionienė, V. Mickevičius

Kaunas University of Technology, Radvilėnų pl. 19, 50254 Kaunas, Lithuania

E-mail: Vytautas.Mickevicius@ktu.lt

The 1,3,4-oxadiazole [1, 2] and 1,2,4-triazole [3–5] compounds have attracted particular attention due to the wide range of their biological properties. One of the ways to obtain oxadiazole and triazole heterosystems is their synthesis from dithiocarbazates. For the synthesis of oxadiazole and triazole derivatives, hydrazide **1** was heated with carbon disulfide in 2-propanol in the presence of potassium hydroxide. Upon refluxing, the formed potassium dithiocarbazate **2** was dissolved in water, and the reaction mixture acidified with diluted hydrochloric acid to pH 1 gave 1-(4-methoxyphenyl)-4-(4,5-dihydro-5-thioxo-1,3,4-oxadiazol-2-yl)pyrrolidin-2-one (**3**). The formation of the oxadiazolethione ring in compound **3** has been proven by the signals at 163.9 ppm (O-C=N) and 177.9 ppm (C=S) in ^{13}C NMR spectrum and by the broad singlet at 14.78 ppm (NH) in ^1H NMR spectrum. A characteristic absorption band of the NH group of compound **3** was observed at 3056 cm^{-1} in the IR spectrum. The absorption bands at 1658 cm^{-1} and 1248 cm^{-1} have been ascribed to the C=O group of the pyrrolidinone ring and the C=S group of the oxadiazole cycle, respectively. Aminotriazole **4** was obtained by heating potassium dithiocarbazate **2** with hydrazine hydrate or heating the corresponding 1,3,4-oxadiazole **3** with hydrazine hydrate in water. The resonances at 155.9 ppm (N-C=N) and at 171.1 ppm (C=S) in ^{13}C NMR spectrum as well as the ones at 5.56 ppm (NH_2) and 13.61 ppm (NH/SH) in ^1H NMR spectrum revealed the formation of the 5-membered triazole **4**.



R = 4- $\text{CH}_3\text{OC}_6\text{H}_4$; Ar = C_6H_5 ; 4- $\text{CH}_3\text{C}_6\text{H}_4$; R₁ = **9**) C_6H_5 ; **10**) 4- ClC_6H_4 ; **11**) 4- $\text{NO}_2\text{C}_6\text{H}_4$

Reagents and conditions: i: KOH, CS_2 , MeOH, Δ , 24 h; ii: 10 % HCl, pH 1;

iii: $\text{N}_2\text{H}_4 \cdot \text{H}_2\text{O}$, Δ , 8 h, CH_3COOH , pH 7; iv: 10 % HCl, pH 1; v: $\text{N}_2\text{H}_4 \cdot \text{H}_2\text{O}$, H_2O , Δ , 24 h;

vi: ArCHO 2-PrOH, HCl, Δ , 8 h; vii: Ethyl chloroacetate, triethylamine, 2-PrOH, Δ , 7 h;

viii: 2,5-Hexanedione, HCl, EtOH, Δ , 7 h; ix: α -Haloketone, triethylamine, MeOH, Δ , 4 h

The condensation of aminotriazole **4** with aromatic aldehydes was carried out providing the corresponding Schiff bases **5**, **6**. Treatment of the 4-(4-amino-5-thioxo-4,5-dihydro-1*H*-1,2,4-triazol-3-yl)-1-(4-methoxyphenyl)-pyrrolidin-2-one (**4**) with 1.2 equivalents of ethyl chloroacetate in the presence of triethylamine resulted in the formation of the only *S*-alkylated product **7**. During reaction of 4-amino-1,2,4-triazole **4** with 2,5-hexanedione, performed in the refluxing 2-propanol in the presence of a catalytic amount of hydrochloric acid, the *N*-substituted pyrrole derivative **8** was synthesized. The formation of a 2,5-dimethylpyrrole ring, included into the **8** composition, has been proven by the singlets at 1.98 ppm (CH₃), 5.95 ppm (=CH), and 14.27 ppm (NH) in ¹H NMR spectrum. In the final stage of this work, the 4-(6-(4-substituted phenyl)-7*H*-[1,2,4]triazolo[3,4-*b*][1,3,4]thiadiazin-3-yl)-1-(4-methoxyphenyl)pyrrolidin-2-ones **9–11** were synthesized from aminotriazole **4** and the corresponding α -haloketones in methanol in the presence of triethylamine.

References

1. J. Cook, I. Shulman, J. J. Bielak, U. S. Pat. 6984602 B2 (2006).
2. X. Qian, R. Zhang, J. Chem. Technol. Biotechnol., **67** (1996) 124-130.
3. V. Mickevičius, V. Intaitė, A. Voskienė, K. Kantminienė, M. Stasevych, O. Komarovska-Porokhnyavets, V. Novikov, Heterocycles, **81**(3) (2010) 649-658.
4. B. S. Holla, B. Veerendra, M. K. Shivananda, B. Poojary, Eur. J. Med. Chem., **38** (2003) 759-767.
5. J. M. Kane, M. W. Dudley, S. M. Sorensen, F. P. Miller, J. Med. Chem., **31** (1988) 1253-1258.

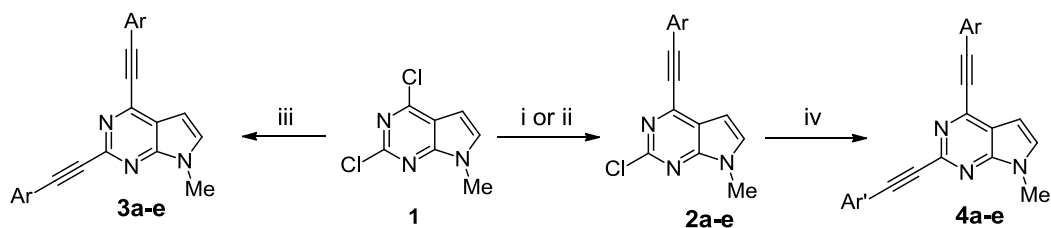
**COMPARATIVE STUDY ON THE SYNTHESIS OF
(ARYLETHYNYL)PYRROLO[2,3-*d*]PYRIMIDINES BY STILLE AND
SONOGASHIRA COUPLING REACTIONS**

J. Bucevičius, S. Tumkevičius

Vilnius University, Faculty of Chemistry, Department of Organic Chemistry, Naugarduko 24,
LT-03225 Vilnius, Lithuania
E-mail: Jonas.Bucevicius@chf.vu.lt

Over recent years, organic molecules with a π -conjugated backbone have received much attention in both academic and industry due to their applications in a wide range of electronic and optoelectronic devices [1-3]. Pyrimidine ring containing heterocycles owing to their aromaticity, significant π -deficiency and ability of nitrogen atoms to take part in the chelation processes, are desired structural units to be incorporated in more complex organic structures targeted for numerous applications [4-6]. Recently, we have shown that pyrrolo[2,3-*d*]pyrimidines bearing π -conjugated aromatic assemblies in positions 2 and 4 exhibit strong UV-blue fluorescence and are promising candidates as fluorescent functional materials [7-9]. However in this biaryl system aromatic and heteroaromatic rings are slightly turned out of plane. This can worsen some characteristics of functional materials. In order to achieve elongation of π -conjugation along the scaffold and to obtain molecules with more planar geometry we have chosen ethynyl group as a linker between aromatic parts of the molecule. Continuing our work aimed on the search of efficient photoactive materials we present herein the results on the synthesis of pyrrolo[2,3-*d*]pyrimidines bearing arylethynyl groups by Sonogashira and Stille reactions.

Scheme 1.



- i) Ar-C \equiv CH, 2 mol% Pd(PPh₃)₂Cl₂, 1 mol% CuI, Et₃N, 60 °C;
- ii) 1.2 equiv. Ar-C \equiv C-SnBu₃, 1 mol% Pd(PPh₃)₂Cl₂, 4 mol% AsPh₃, toluene, 2-6 h, 80 °C;
- iii) 2.6 equiv. Ar-C \equiv C-SnBu₃, 5 mol% Pd(PPh₃)₂Cl₂, 20 mol% AsPh₃, toluene, 48-72 h, reflux;
- iv) 1.5 equiv. Ar'-C \equiv C-SnBu₃, 5 mol% Pd(PPh₃)₂Cl₂, 20 mol% AsPh₃, toluene, 48-72 h, reflux;

Easily accessible 2,4-dichloro-7-methylpyrrolo[2,3-*d*] (**1**) was chosen as starting material. For the synthesis of the target alkynylpyrrolopyrimidines Sonogashira coupling of 2,4-dichloropyrrolo[2,3-*d*]pyrimidine (**1**) has been attempted. After brief optimisation we have found reaction conditions (Scheme 1) leading to the formation of 2-chloro-4-(arylethynyl)pyrrolopyrimidines **2a-e** in reasonable yields. Lower yields were obtained with arylethyne bearing strong electron-donating groups (Table 1, entries 3,4). Comparative synthesis of 2-chloro-4-(arylethynyl)pyrrolopyrimidines by Stille cross-coupling reaction of **1** with (arylethynyl)tributylstannanes was investigated. After optimization of the reaction conditions we have found that 2,4-dichloropyrrolopyrimidine **1** reacted with

(arylethynyl)tributylstannanes in toluene at 80 °C in the presence of Pd(PPh₃)₂Cl₂/AsPh₃ as a catalyst system to give 4-(arylethynyl)-2-chloropyrrolo[2,3-*d*]pyrimidines (**2a-e**) in good yields (Table 1). Stille reaction provided compounds **2a-e** in higher yields than the Sonogashira coupling.

Table 1. Preparation of 4-(arylethynyl)-2-chloropyrrolo[2,3-*d*]pyrimidines (**2a-e**) by Sonogashira and Stille reactions.

Entry	Compound	Ar	Yield, %	
			Sonogashira	Stille
1	2a	Ph	68	88
2	2b	3-MeC ₆ H ₄	73	84
3	2c	4-MeOC ₆ H ₄	46	71
4	2d	4-Me ₂ NC ₆ H ₄	24	64
5	2e	4-FC ₆ H ₄	58	70

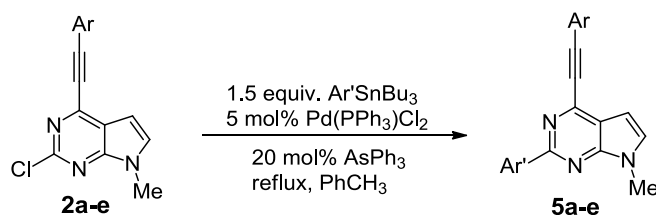
Any attempts to obtain 2,4-(diarylethynyl)pyrrolo-pyrimidines **3** or **4** by the second Sonogashira coupling at the position 2 of pyrrolopyrimidine **2** failed. In order to obtain desired 2,4-di(arylethynyl)pyrrolo[2,3-*d*]pyrimidines (**3a-d**) double Stille coupling of compound **1** was performed with increased amount of catalyst (5 mol% Pd(PPh₃)₂Cl₂/20 mol% AsPh₃) at reflux temperature of toluene and by using 2.6 equivalents of (arylethynyl)tributylstannanes. Similarly, treatment of 4-(arylethynyl)-2-chloropyrrolo[2,3-*d*]pyrimidines (**2**) with the selected (arylethynyl)tributylstannanes under the same reaction conditions afforded compounds **4a-g** in 68-82% yields (Table 2, entries 5-11).

Table 2. Preparation of 2,4-di(arylethynyl)pyrrolo[2,3-*d*]pyrimidines (**3a-d**, **4a-f**).

Entry	Compound	Ar	Ar'	Yield, %
1	3a	Ph	-	71
2	3b	3-MeC ₆ H ₄	-	69
3	3c	4-MeOC ₆ H ₄	-	56
4	3d	4-FC ₆ H ₄	-	61
5	4a	Ph	4-MeOC ₆ H ₄	69
6	4b	Ph	4-FC ₆ H ₄	80
7	4c	3-MeC ₆ H ₄	Ph	68
8	4d	4-FC ₆ H ₄	Ph	82
9	4e	4-FC ₆ H ₄	4-MeOC ₆ H ₄	79
10	4f	4-MeOC ₆ H ₄	4-FC ₆ H ₄	73
11	4g	4-MeOC ₆ H ₄	Ph	81

Suzuki-Miyaura coupling reaction was examined with compounds **2**. However, the 2-chlorine group in compounds **2a-e** appeared to be inert in the Suzuki coupling with arylboronic acids. For example, in the Suzuki reaction of **2a** with phenylboronic acid different catalysts Pd(OAc)₂, Pd(PPh₃)₂Cl₂, Pd(dppf)₂Cl₂, ligands (PPh₃, 2-biPhCy₂P), bases (Na₂CO₃, Cs₂CO₃, K₃PO₄) and solvents (THF, toluene, 1,4-dioxane) were employed, however, no formation of the desired 2-phenyl derivative **5a** in reasonable yield was observed.

Scheme 2.



For this reason, on the example of compounds **2a,b,e** Stille coupling with (aryl)tributylstannanes has been carried out (Scheme 2). In contrast to the unsuccessful synthesis of compounds **5** by the Suzuki coupling, the Stille reaction afforded the corresponding 2-aryl-4-(arylethynyl)pyrrolo[2,3-*d*]pyrimidines **5a-g** in high 76-88% yields (Table 3).

Table 3. Preparation of 2-aryl-4-(arylethynyl)pyrrolo[2,3-*d*]pyrimidines (**5a-g**).

Entry	Compound	Ar	Ar'	Yield, %
1	5a	Ph	Ph	82
2	5b	Ph	4-FC ₆ H ₄	76
3	5c	Ph	4-CF ₃ C ₆ H ₄	86
4	5d	3-MeC ₆ H ₄	Ph	81
5	5e	3-MeC ₆ H ₄	4-FC ₆ H ₄	88
6	5f	3-MeC ₆ H ₄	4-CF ₃ C ₆ H ₄	85
7	5g	4-FC ₆ H ₄	4-CF ₃ C ₆ H ₄	86
1	5a	Ph	Ph	82

Structure of the synthesized compounds was confirmed by ¹H, ¹³C, ¹⁹F NMR, IR and HRMS data. The Sonogashira and Stille coupling of 2,4-dichloro-7-methylpyrrolo[2,3-*d*]pyrimidines first occurs at the position 4 of the pyrrolopyrimidine. Evidence of such a regioselectivity is supported by a single crystal X-ray structure of compound **5g** and by NOESY spectra of compounds **2** in which cross-peaks of low intensity showing interaction between *ortho*-protons of 4-(phenylethynyl) group and 5-H of the pyrrolopyrimidine ring are observed.

In summary, an efficient synthesis of alkynylpyrrolo[2,3-*d*]pyrimidines by the palladium catalyzed cross-coupling reaction of 2,4-dichloro-7-methylpyrrolo[2,3-*d*]pyrimidine with (arylethynyl)tributylstannanes has been developed. The protocol tolerates many functional groups and allows to generate a wide library of novel pyrrolo[2,3-*d*]pyrimidine derivatives including those with different arylethynyl groups in positions 2 and 4 of the heterocycle.

Acknowledgement

The research was funded by a grant (No. MIP-027/2013) from the Research Council of Lithuania. The authors express their gratitude to Dr. G. Bagdziunas (Kaunas University of Technology) for the X-ray structure analysis.

References

1. M. T Bernius, M. Inbasekaran, J. O'Brien, W. S. Wu, *Adv. Mater.* **2000**, *12*, 1737.
2. G. Hughes, M. R. Bryce, *J. Mater. Chem.* **2005**, *15*, 94.
3. Y. Tao, Q. Wang, C. Yang, Q. Wang, Z. Zhang, T. Zou, J. Qin, D. A. Ma, *Angew. Chem. Int. Ed.* **2008**, *47*, 8104.
4. S.J. Su, C. Cai, J. Kido, *Chem. Mater.* **2011**, *23*, 274.
5. C. Hadad, S. Achelle, I. Lopez-Solera, J.C. Garcia-Martinez, J. Rodriguez-Lopez, *Dyes. Pigm.* **2013**, *97*, 230.
6. J. Weng, Q. Mei, Q. Ling, Q. Fan, W. Huang, *Tetrahedron* **2012**, *68*, 3129.
7. S. Tumkevicius, J. Dodonova, K. Kazlauskas, V. Masevicius, L. Skardziute, S. Jursenas, *Tetrahedron Lett.* **2010**, *51*, 3902.
8. J. Dodonova, L. Skardziute, K. Kazlauskas, S. Jursenas, S. Tumkevicius, *Tetrahedron* **2012**, *68*, 329.
9. L. Skardziute, K. Kazlauskas, J. Dodonova, J. Bucevicius, S. Tumkevicius, S. Jursenas, *Tetrahedron*, **2013**, *69*, 9566.

A SELECTIVE METHOD FOR MONO-PMB PROTECTION OF GLYCEROL

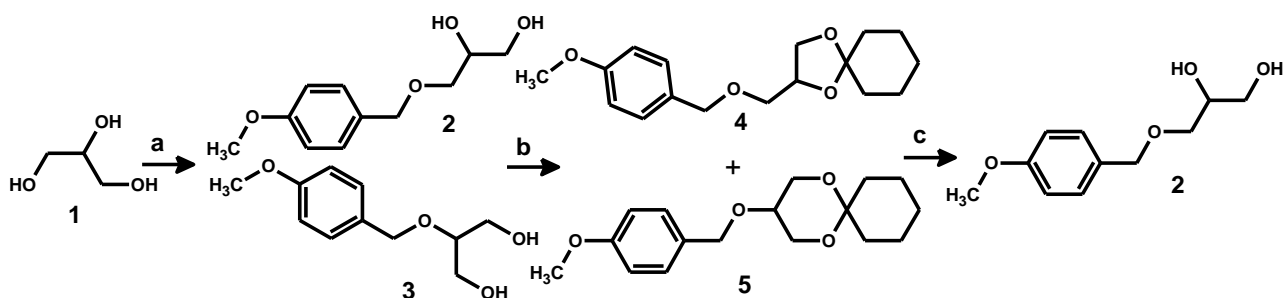
T. Charkova, O. Eicher-Lorka, A. Matijoška, Z. Kuodis

Center for Physical Sciences and Technology, A. Goštauto St. 9, LT-01108 Vilnius, Lithuania

E-mail: lorka@ktl.mii.lt

In our ongoing project of developing novel syntheses of different molecular systems based on tailoring the reactive properties of surfaces, we synthesized glycerol-based lipids for the farther tethered bilayer lipid membrane (tBLM) design and research [1, 2]. In the synthesis of long glycerol-based lipids we choosed hydroxyl group protection with *p*-anisyl alcohol (PMBOH). The PMB group has an advantage over the so popular benzyl group due to its ease of deprotection under mild conditions in the presence of other functional groups. The most commonly employed methods for PMB protection of alcohols involve usage of *p*-methoxybenzyl chloride (PMBCl) or *p*-methoxybenzyl bromide (PMBBr), however both reagents are prone to decomposition [3, 4].

We suggest mono-protection of glycerol hydroxyl group with commercially available, stable, easy to handle PMBOH in the presence of acidic resins amberlyst-15 (A-15) and amberlit-200c (A-200). Firstly, glycerol was protected with PMBOH under several conditions: in dioxane and glycerol mixture (under MW), in dioxane (85-100 °C), in glycerol (70-90 °C), in benzene (reflux), in dichloromethane (reflux) using 10-30 % A-15 and 20-60% A-200. Gas Chromatograph-Mass Spectrometer analysis (GC-MS) allowed to identify two main mono-protected glycerols (compounds 2 and 3 in scheme) and three additional products (diPMB ether, triPMB glycerols). The best result was get with 20 % A-15 (yield 66%) in dichloromethane (DCM). The ratio of two mono-PMB glycerols was 9,4:1. Next, it was decided to do two simple reactions for farther separation of main isomers without column chromatography, using only extraction methods. Mono-protected glycerols were tried to couple with acetone, cyclopentanone and cyclohexanone in order to get two possible cyclic isomers with different solubility. The best selectivity was achieved (only product 4 was formed) in reaction with cyclohexanone and CuSO₄ in DCM at room temperature (yield 88%). Next, dioxolane fragment was decomposed with 2M HCl in methanol and CaCl₂ at 0 – +5 °C, yielding (94 %) corresponding monoglycerol 2. Other tested conditions (1M and 5M HCl in methanol, -5 – +25 °C, Na₂S₂O₅, Na₂SO₄, Na₂SO₃, CuSO₄ usage) of this reaction were less successful.



Scheme. Glycerol protection and PMB protected monoglycerols separation method. (a: PMBOH, 20 % A-15, DCM, reflux, yield 66%; b: cyclohexanone, 40 % A-15, 2 ekv. CuSO₄, DCM, r.t., yield 88%; c: 2M HCl in methanol, 2 ekv. CaCl₂, 0 – +5 °C, yield 94%).

References

1. M. Eeman, M. Deleu, *Biotechnol. Agron. Soc. Environ.* **14** (2010) 719-736.
2. J. A. Jackman, W. Knoll, N.-J. Cho, *Materials* **5** (2012) 2637-2657.
3. P. J. Kociński, *Protecting Groups*. Stuttgart, New York, 2004.
4. S. P. Chavan, K. R. Harale, *Tetrahedron Lett.* **53** (2012) 4683–4686.

SYNTHESIS OF *N*-(4-METHYLPHENYL)-*N*-THIAZOLYL- β -ALANINES

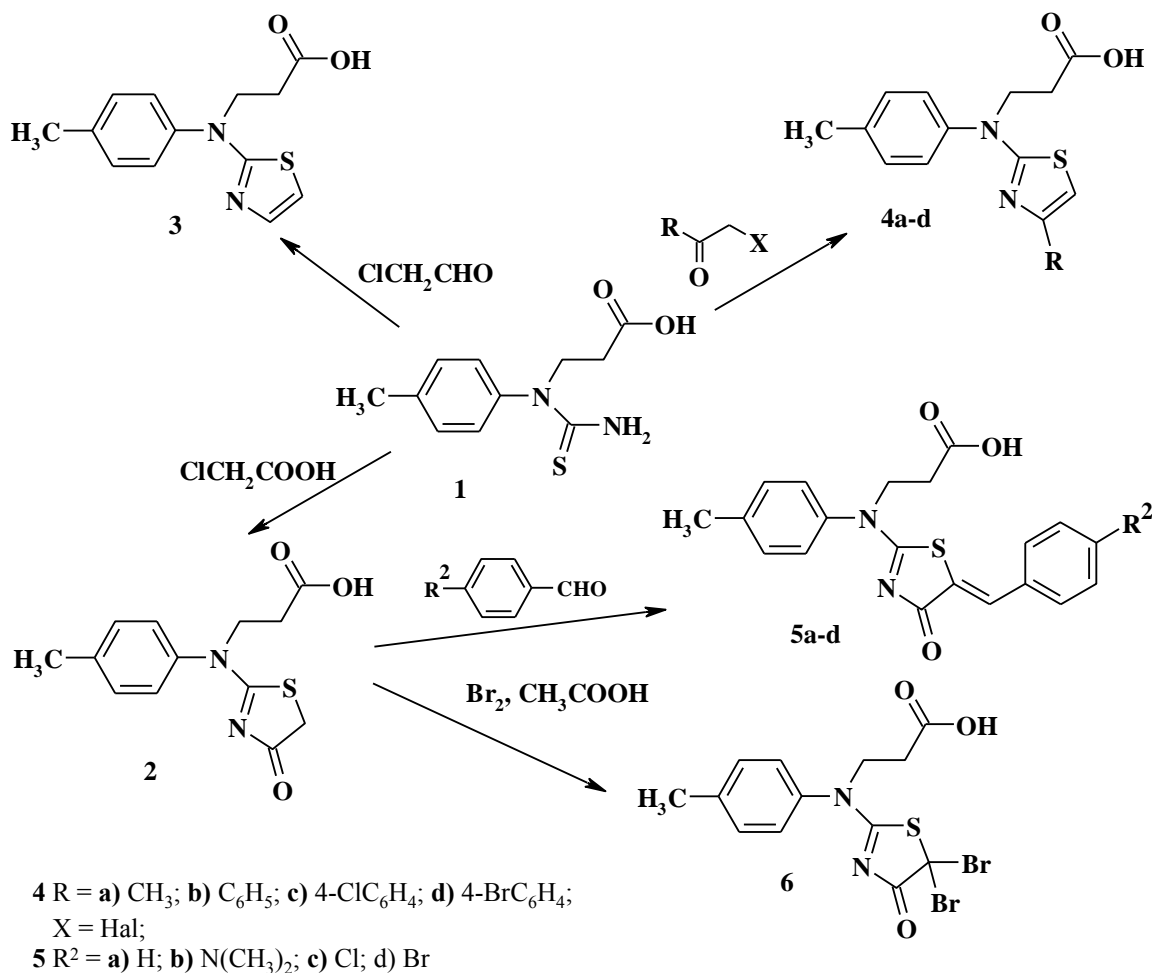
A. Geštautas, B. Sapijanskaitė, V. Mickevičius

Kaunas University of Technology, Radvilėnų pl. 19, 50254 Kaunas, Lithuania

E-mail: Birutė Sapijanskaite@ktu.lt

Thiazoles and their derivatives are found to be associated with various biological activities such as antibacterial [1-3], fungicidal [4], antitumor [5], antihypertensive [6], anti-pseudomonal infection [7]. In this work, *N*-(4-methylphenyl)-*N*-thiocarbamoyl- β -alanine (**1**) was used as a precursor in the synthesis of aminothiazole derivatives according to the Hantzsch reaction.

The reaction of *N*-(4-methylphenyl)-*N*-thiocarbamoyl- β -alanine (**1**) with monochloroacetic acid in water in the presence of sodium carbonate gave *N*-(4-methylphenyl)-*N*-(4oxo-4,5-dihydro-1,3-thiazol-2-yl)- β -alanine (**2**). 3-[(4-Methylphenyl)(1,3-thiazol-2-yl)amino]propanoic acid (**3**) was obtained from *N*-(4-methylphenyl)-*N*-thiocarbamoyl- β -alanine (**1**) and chloroacetaldehyde in acetone.



The target product **3** was isolated from the reaction mixture by adding 10 % sodium acetate solution. The doublets at 6.69 ppm and 7.17 ppm in the ^1H NMR spectrum for compound **3** were ascribed to the protons of thiazole ring.

The substituted thiazoles **4a-d** were synthesized from thioureido acid **1** and various haloketones in acetone at reflux. In all reactions, sodium acetate was used for the transformation of aminothiazolium halide into the base. The reactions of compound **2** with various aromatic aldehydes in water in the presence of sodium carbonate and glycine provided compounds **5a-d**, which were isolated from the reaction mixtures by acidifying them with acetic acid.

Bromination of compound **2** was performed in acetic acid at 60 °C for 4 h and resulted in formation of 3-[(5,5-dibromo-4oxo-4,5-dihydro-1,3-thiazol-2-yl)(4-methylphenyl)amino]-propanoic acid (**6**).

The structures of synthesized compounds have been confirmed by the elemental analysis, ¹H, ¹³C NMR, and IR spectroscopy.

References

1. K. Liaras, A. Geronikaki, J. Glamoclija, A. Ciric, M. Sokovic, *Bioorg. Med.Chem.*, **19(24)** (2011) 7349-7356.
2. K. Anusevičius, I. Jonuškienė, V. Mickevičius, *Monatsh. Chem.*, **144(12)** (2013) 1883-1891.
3. V. Mickevičius, A. Voskienė, I. Jonuškienė, et. al., *Molecules*, **(18)** (2013) 15000-15018.
4. E. Chimenti, B. Bizzarri, A. Bolasco, *Eur. J. Med. Chem.*, **46(1)** (2011) 378-382.
5. B. Jiang, X. H. Gu, *Bioorg. Med. Chem.*, **8(2)** (2000) 363-371.
6. David J. Carini, Ruth R. Wexler, US Pat. 4632930 A, 1986.
7. K. Tsuji, H. Ishikawa, *Bioorg. Med. Chem. Lett.*, **4(13)** (1994) 1601-1606.

INVESTIGATION OF CONJUGATE ADDITION OF AROMATIC AMINES TO 1,4-BENZOQUINONES

Regina Janciene, Gema Mikulskiene*, Algirdas Klimavicius

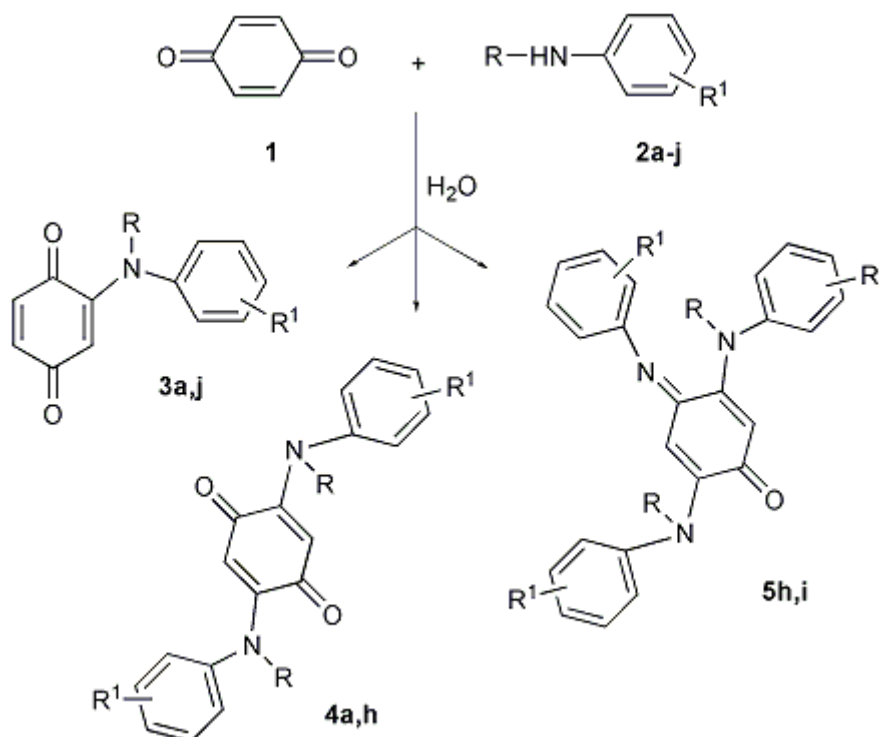
Vilnius University Institute of Biochemistry, Mokslininku 12, LT-08662 Vilnius, Lithuania

E-mail: gema.mikulskiene@bchi.vu.lt

Currently 2-aryl-amino-1,4-benzoquinones are widely studied in our institute as redox mediators applicable for some oxidoreductases [1]. The aim of our work was to synthesize a series of 2-substituted 1,4-benzoquinone derivatives bearing arylamino group with various substituents in *o*-, *m*- and *p*-positions of aromatic ring, to study in detail structure and properties of obtained products using NMR spectroscopy.

For this purpose, a conjugate addition of aromatic amines: *N*-methylaniline, *o*-, *m*- and *p*-nitro-, methoxy- and fluorosubstituted anilines to 1,4-benzoquinone was investigated. 2-Arylaminoquinones are readily formed in the reaction of 1,4-benzoquinone with amines at 50–70 °C in aqueous solutions [2]. This work reports that by-products are not formed in this reaction. However, previous publications describe a facile formation of 2,5-disubstituted derivatives by treatment of 1,4-benzoquinone with amines [3]. With the aim to avoid the formation of such derivatives the reactions (Scheme 1) were carried out at low temperatures in dilute solutions [4].

Scheme 1



	a	b	c	d	e	f	g	h	i	j
R	Me	H	H	H	H	H	H	H	H	H
R ¹	H	2-NO ₂	3-NO ₂	4-NO ₂	2-OMe	3-OMe	4-OMe	2-F	3-F	4-F

The first attempt to synthesize 2-substituted quinone derivatives **3e-g** by treatment of 1,4-benzoquinone (**1**) with methoxyanilines **2e-g** at the described conditions [2] was unsuccessful, due to very impure products obtained and the purification of latter was not achieved. Consequently the influence of reaction time, temperature, dilution and the ratio of reagents on the yield and purity of products was investigated to optimize the synthesis conditions of target 2-arylamino-1,4-benzoquinones. The results of investigation are presented in Table 1.

Table 1. Optimal conditions of the synthesis of 2-arylamino-1,4-benzoquinones **3a-j**

Compounds	Reaction time, h	Reaction temp., °C	Ratio of reagents quinone/amine, mol/mol	Dilution quinone/H ₂ O, mmol/ml	Yield (from amine), %
3a	1/4	5	2/1	20/200	43
3b	2/3	60	2/1	20/200	31
3c	1/3	60	1/1	20/40	61
3d	20	30	3/1	30/350	40
3e	1/4	5	2/1	20/200	54
3f	1/6	0	4/1	40/300	43
3g	1/4	5	2/1	20/200	48
3h	1/4	0	2/1	20/300	43
3i	1/3	60	4/1	40/300	44
3j	1/4	5	2/1	20/200	37

The yield of compounds **3a-j** was moderate because the reaction was stopped at the start of crystallization. When the reaction was processed till the end of crystallization, the reaction products were obtained in a very good yield, but impure.

Since some derivatives of nitro- and methoxyaniline and 1,4-benzoquinone were described previously [5], we focused on the synthesis of *o*, *m*, *p*-fluoroaniline derivatives. It was established that the reaction of *o*-fluoroaniline with quinone even at 0 °C temperature gave the mixture of three products – mono- (**3h**), di- (**4h**) and tri- (**5h**) substituted quinone derivatives with the yield of 43, 18 and 15 %, respectively. *p*-Fluoroaniline **2j** under the same reaction conditions did not give di- and tri-substituted products, while *m*-fluoro derivative **3i** was formed only by heating at 60 °C. Chromatographic purification of crude product afforded 44 % of mono-substituted derivative **3i** and 17 % of compound **5i**.

The structure of all newly synthesized 1,4-benzoquinone derivatives was identified by ¹H, ¹³C, DEPT (¹³C), ¹H/¹³C 2D (HETCOR and HMBC) NMR spectra [6]. Compound **3j** was used for the determination of increments of 2-substituted 1,4-quinone moiety for aromatic ring carbon atoms ($C_i = 12.43$ ppm, $C_o = -5.43$ ppm, $C_m = 1.12$ ppm, $C_p = -1.83$ ppm), which were successfully employed for structure elucidation of relative compounds. The study compounds **h-j** possess fluorine atom at *o*-, *m*-, or *p*-position of the aromatic ring. Due to the specific magnetic properties of fluorine atom, a spin-spin coupling (up to 4 bonds) multiplets were observed in ¹H and ¹³C NMR spectra. The splitting, arising from the fluorine, complicate the analysis of the aromatic region of the NMR spectra. The multiplets of the aromatic resonances in the ¹H NMR spectra overlap and are insufficiently informative, whereas in case of ¹³C NMR spectra the multiplets are well resolved. In fluorine substituted aromatic ring C_i atom resonated as doublet with $^1J_{CF} \sim 247$ Hz, $C_o - ^2J_{CCF} \sim 21$ Hz, $C_m - ^3J_{CCCF} \sim 10$ Hz, $C_p - ^4J_{CCCCF} \sim 2.5$ Hz in ¹³C NMR spectra of current study. The differences between pairs of $^2J_{CCF}$ and $^3J_{CCCF}$ values observed in the same aromatic ring can be rationalized in terms of the substituent effects. Taking into account investigated compounds **5h** and **5i** bearing three *o*- *m*-fluorine substituted aromatic rings respectively the three sets of chemical shifts corresponding aromatic ring carbons and *J* values were observed in ¹³C NMR spectra. The formation of compounds **5h** and **5i** was proved by the presence of resonances at



about 155 ppm (C=N) and 180 ppm (C=O) in ^{13}C NMR spectra and by the three signals in ^{19}F NMR resonance spectra each integrated to one fluorine atom. Two signals of fluorine are broadened and one - sharp due to different interconnection between quinone and aromatic moieties.

The analysis of molecular modeling data showed existence of extended π -system in all study compounds.

Resonances

1. J. Razumiene, E. Voitechovich, R. Janciene, A. Palaima, Int. Conf. "BOS 2014", 6-9 July, Vilnius, Lithuania, **2014**, 124.
2. J. S. Yadav, B. V. S. Reddy, T. Swamy, K. S. Shankar, *Monatsh. Chem.*, **2008**, 139, 1317.
3. N. Makarova, A. Y. Berlin, *Zh. Obshch. Khimii*, **1967**, 37, 637.
4. S. Ioffe, N. A. Filipova, Z. Y. Khavin, *Zh. Obshch. Khimii*, **1954**, 24, 702.
5. N. Grinev, V. I. Shvedov, E. K. Panisheva, N. S. Bogdanova, I. S. Nikolajeva, G. N. Pershin, *Xim.-Farm. Zh.*, **1971**, 5, 3.
6. S. A. Richards, J. C. Hollerton, *Essential Practical NMR for Organic Chemistry*. Wiley & Sons, New York, **2011**.

UV ABSORPTION AND FLUORESCENCE PROPERTIES OF
1,5-BENZODIAZEPINE OXIMES

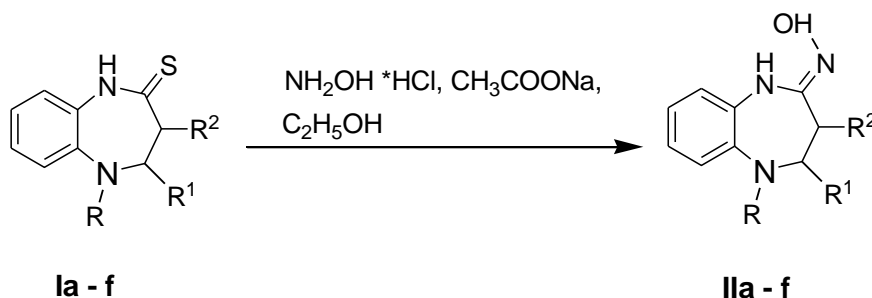
Lidija Kosychova^{a,b,*}, Regina Vidziunaite^a, Irina Bratkovskaja^a, Gema Mikulskiene^a

^a Vilnius University Institute of Biochemistry, Mokslininku 12, LT-08662 Vilnius, Lithuania

^b Klaipeda University, H.Manto 84, LT-91001 Klaipeda, Lithuania

E-mail: lidija.kosychova@bchi.vu.lt

A literature survey revealed oxime derivatives belonging to an important compounds in organic synthesis. It is known that oximes may be used as intermediates for the preparation of amides by Beckmann rearrangement and for conversion of no carbonyl compounds to the carbonyl derivatives [1]. The 1,4- ir 1,5-benzodiazepine oximes are precursors of tricyclic benzodiazepine derivatives. The investigation of spectral properties of these compounds is very important for determination of the chemical reactivity and kinetic parameters of conversion. In our previous investigation [2] was shown, that determination of spectral properties of novel 5,6-dihydro-4*H*-tetrazolo-[1,5-*a*][1,5]benzodiazepine derivatives allows to apply the new compounds in practice. The 1,3,4,5-tetrahydro-2*H*-1,5-benzodiazepine oximes **IIa-f** were obtained by refluxing of 1,5-benzodiazepinethiones **Ia-f**, sodium acetate and hydroxylamine hydrochloride in anhydrous ethanol (scheme 1). Compounds were characterized by the methods of ¹H, ¹³C NMR, IR and elemental analysis [3].



Compounds	R ¹	R ²	R ³
Ia IIa	CH ₃	H	H
Ib IIb	CH ₃	CH ₃	H
Ic IIc	CH ₃	H	CH ₃
Id IId	C(O)NHC ₆ H ₅	H	H
Ie IIe	C(O)NHC ₆ H ₅	CH ₃	H
If IIf	C(O)NHC ₆ H ₅	H	CH ₃

The aim of this work was to examine the UV absorption and fluorescence spectral properties of 1,5-benzodiazepine oximes applying spectrophotometric and fluorescence methods. The UV-visible spectra of 1,5-benzodiazepine-4- oximes were recorded in the region 220-400 nm. Obtained absorption spectra of compounds are presented in Figure 1.

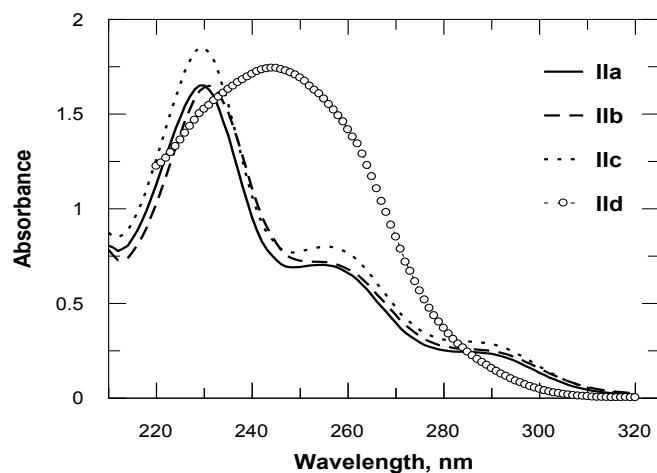


Fig.1. The absorption spectra of compounds **IIa-c** and **IIId**

Absorption spectra of compounds (**IIa-c**) containing electron donor groups are comparable and showed three bands in the 220-240, 245-265 and 280 -300 nm region. Absorption maximums at 230, 290 nm and shoulders in the region 250 -270 nm were observed for compounds **IIa-c**, and insignificantly influenced by solution pH. Significant differences of absorption spectra for compounds **IIa-c** were noticed in the 240-270 nm regions. The only a shoulder was observed at the acidic pH (2.5-5.0), but clear absorption maxima at 255 nm was observed at pH 5.5-8.0. Broad absorbance signal in the 230-260 nm region with maxima at 245 nm was observed for compound **IIId** containing electron acceptor group.

Fluorescence properties of the study compounds **IIa-c** were also investigated. Very weak fluorescence was observed for compounds containing electron acceptor groups **IIId-f**, whereas compounds containing electron donor groups **IIa-c** show good fluorescence.

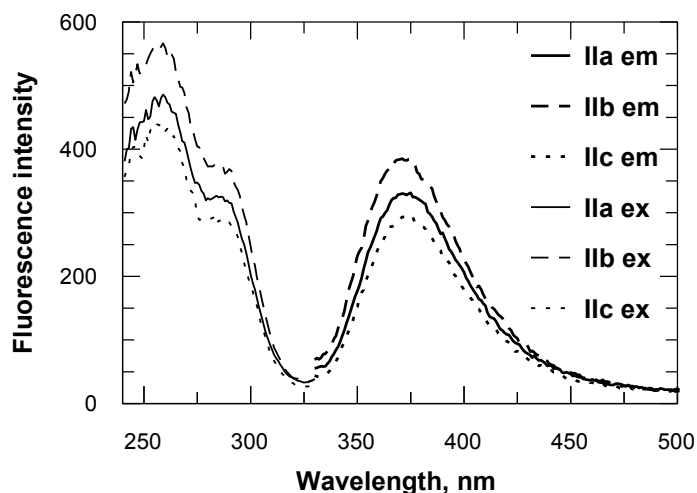


Fig.2. Excitation and emission spectra of compounds **IIa-c**

Excitation spectra of investigated compounds **IIa-c** were observed in the region 240-330 nm, using $\lambda_{em} = 380$ nm (Fig.2). The excitation wavelength ($\lambda_{ex} = 290$ nm) was used for fluorescence excitation, because compounds **IIa-c** show lower absorption at this wavelength. The emission spectra of compounds containing electron-donor groups (presented in Fig. 2) were observed in the region 330-500 nm and show comparable patterns.

The fluorescence excitation and emission spectra so as absorption spectra of **IIa-c** were measured at different solution pH. Variation of pH slightly influenced on the compounds **IIa-c** absorption and emission spectra, but strongly influenced fluorescence intensity. Compounds fluorescence intensity decreased with solution pH decreasing. Using spectrophotometric and spectrofluorimetric data of compounds **IIa-c** pK_a values were determined and are presented in Table 1.

Table 1. pK_a values of compounds **IIa-c**.

Compound	pK _a from absorption spectra	pK _a from fluorescence spectra
IIa	4.1 ± 0.1	4.20 ± 0.05
IIb	4.4 ± 0.2	4.40 ± 0.03
IIc	4.1 ± 0.2	4.26 ± 0.03

The pK_a values determined by spectrophotometric and spectrofluorimetric methods are similar.

References

1. L. Saikia, S. Das, A. J. Thakur, *Synth. Commun.*, **2011**, *41* (1), 1071.
2. L. Kosychova, R. Vidziunaite, G. Mikulskiene, I. Bratkovskaja, R. Janciene, *ARKIVOC*, in press, (status - accepted 2014-05-21).
3. L. Kosychova, Z. Stumbrevičiūtė. L. Plečkaitienė, Z. Staniulyte, B. D. Puodžiūnaitė, *Chemija (Vilnius)*, **2006**, *17* (1), 21.

NUCLEOPHILIC RING OPENING OF AZIRIDINE AND AZETIDINE DERIVATIVES IN LIQUID SULFUR DIOXIDE

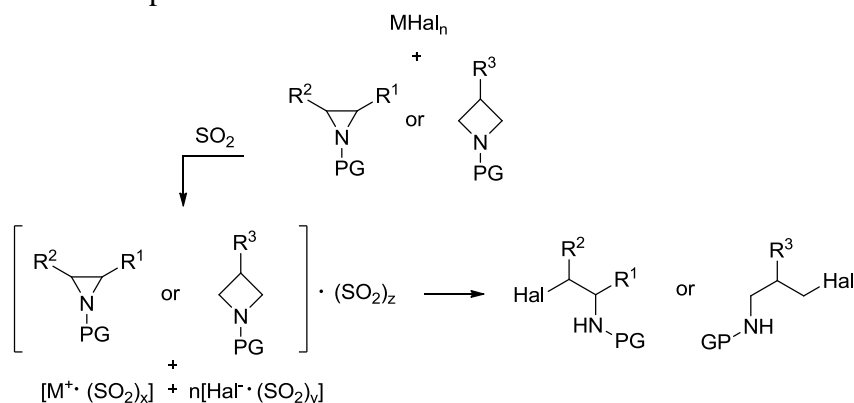
J. Luginina, M. Turks

*Faculty of Material Science and Applied Chemistry, Riga Technical University, Paula
Valdena Str. 3, Riga, LV-1007, Latvia
maris_turks@ktf.rtu.lv*

Aziridine and azetidine moieties are important small ring *N*-heterocycles in organic synthesis due to their biological and pharmacological properties and synthetic potential as a building blocks [1]. Modifications of these aza-heterocycles can lead to the formation of various classes of compounds, such as heterocycles [2], alkaloids [3] and non-natural amino acids [4]. The reactivity of aziridines and azetidines strongly depends on variation of ring substituents, activation of nitrogen atom and ring strain. Due to the latter, the most common transformations of these heterocycles are the nucleophilic ring-opening reactions (NRORs). NRORs have been exhaustively described in excellent reviews [5].

Halogen nucleophiles can be introduced under acidic conditions (e.g.: with HCl) [6]. Another source of halogen nucleophiles are metal halides. However, there are only a few precedents of ring opening using halides MX_n [7].

Here we present a new synthetic process of aziridine and azetidine NRORs with metal halides and other nucleophiles in liquid sulfur dioxide. The use of sulfur dioxide in organic synthesis has recently seen a renaissance [8]. Reactions were carried out in three temperature modes. The efficiency of each aziridine or azetidine ring opening reaction was monitored in several solvents in parallel experiments: $SO_{2(liq.)}$, DMSO, MeCN, TFE. We have used I and II group metal halides as a nucleophile source.



The obtained results showed that the aza-heterocycles NRORs in liquid sulfur dioxide occurs noticeably faster and cleaner than in other solvents.

In summary, we have discovered an effective synthetic approach for aziridine and azetidine ring opening with metal halides in liquid sulfur dioxide. The results on the scope and limitations of this method using variously substituted aziridines and azetidines and various nucleophiles will be discussed.



References

1. a) A. Padwa, A. D. Woolhhouse, *In Comprehensive Heterocyclic Chemistry*; Ed. W. Lwowski, Pergamon: Oxford, **1984**, Vol.7, pp 47-93. b) D. Tanner, *Angew. Chem., Int. Ed. Engl.*, **1994**, 33, 559. c) A. Dureault, I. Tranchepain, J. C. Depezay, *J. Org. Chem.*, **1989**, 54, 5324. d) M. K. Ghorai, A. Kumar, D. P. Tiwar, *J. Org. Chem.*, **2010**, 75, 137.
2. D. Tanner, H. M. He, *Tetrahedron* **1992**, 48, 6079.
3. T. Hudlicky, H. Luna, J. D. Price, F. Rulin, *J. Org. Chem.*, **1990**, 55, 4683.
4. W. McCoull, F. A. Davis, *Synthesis* **2000**, 1347.
5. J. Legters, L. Thijs, B. Zwanenburg, *Recl. Trav. Chim. Pays-Bas* **1992**, 11, 16.
6. a) G. Righi, C. Potini, P. Bovicelli, *Tetrahedron Lett.*, **2002**, 43, 5867. b) G. Righi, T. Franchini, C. Bonini, *Tetrahedron Lett.*, **1998**, 39, 2385.
7. a) S. Florio, R. Luisi, *Chem. Rev.*, **2010**, 110, 5128. b) P. Lu, *Tetrahedron* **2010**, 66, 2549. c) X. E. Hu, *Tetrahedron* **2004**, 60, 2701.
8. a) J. Luginina, *Synlett* **2014**, 25, 2962. b) A. S. Deeming, E. J. Emmett, C. S. Richards-Taylor, M. C. Willis, *Synthesis* **2014**, 46, 2701.

SYNTHESIS AND ANTIMICROBIAL ACTIVITY OF *N*-ARYL- β -ALANINE DERIVATIVES WITH NAPHTHOQUINONE AND OXAZOLE MOIETIES

K. Mickevičienė¹, K. Kantminienė¹, M. Stasevyč², O. Komarovska-Porokhnyavets², V. Mickevičius¹, V. Novikov²

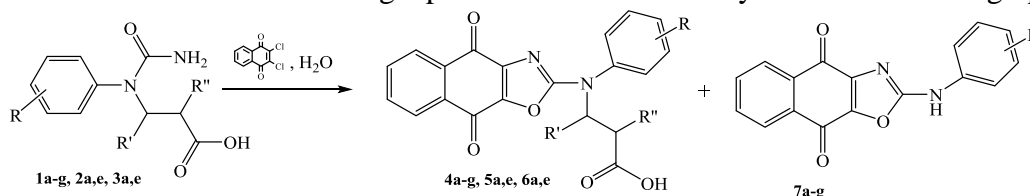
¹ Kaunas University of Technology, Radvilėnų rd. 19, LT-50254, Kaunas, Lithuania

E-mail: kristina.mickeviciene@ktu.lt

² Lviv Politechnic National University, Bandera str. 12, 79013, Lviv-13, Ukraine

Amino acids, their derivatives, and products of their cyclization are important in the synthesis of biologically active compounds. *N*-Substituted β -alanines have been widely studied for many different applications because of their biological activity such as growth stimulators of agricultural crops [1, 2] and their antimalarial activity [3]. Natural and synthetic quinones also exhibit a variety of biological activities such as cytotoxic, antiviral, anti-inflammatory, antimalarial, antibacterial, antifungal, and antiproliferative [4, 5].

In this work, we report the synthesis of new potentially biologically active *N*-aryl- β -alanine derivatives. Compounds **4a-g**, **5a,e**, **6a,e** and **7a-g** were obtained by stirring the mixture of corresponding compound **1a-g**, **2a,e**, **3a,e** and 2,3-dichloro-1,4-naphthoquinone in water under reflux for 14 h. The target products were isolated by column chromatography.



R = a) 4-H, b) 4-Br, c) 3-Cl, d) 4-Cl, e) CH₃, f) 4-OC₂H₅, g) 2,4-(CH₃)₂; 1, 4 R' = R'' = H, 2, 5 R' = CH₃, R'' = H, 3, 6 R' = H, R'' = CH₃

The synthesized compounds **4a-g**, **5a,e**, **6a,e**, **7a,e** were evaluated for their antibacterial and antifungal activity against *Escherichia coli* B-906, *Staphylococcus aureus* 209-P, *Mycobacterium luteum* B-917, *Candida tenuis* VKM Y-70 and *Aspergillus niger* VKM F-1119 strains by diffusion [6] and serial dilution methods (determination of minimum inhibitory concentration MIC) [7]. Their activity was compared to that of the known antibacterial agent vancomycin and the antifungal agent nystatin.

Compound **4a** had better antibacterial activity against *S. aureus* in comparison with vancomycin and showed inhibition diameter 18.7 mm (at 0.1 % concentration). Some other compounds (**4b**, **4c**, **4e**, **6a** and **6e**) showed significant activity against *S. aureus*. Compounds **4d**, **4e**, **4f** and **6e** were moderately active against *M. luteum*.

The evaluation of antifungal activity (diffusion method) had revealed that compounds **4a**, **4b**, **4c**, **4d**, **4e**, **4f** showed a moderate fungicidal effect against *C. tenuis* at a 0.5% concentration (the inhibition zone diameters were 12.0-16.0 mm), whereas compound **7a** showed better fungicidal effect at 0.5% and at 0.1% concentrations than antifungal drug nystatin (inhibition diameters were 22.7 and 21.0 mm). The test-culture *A. niger* appeared to be moderate sensitive to compounds **4a** and **7a** (d = 17.0 mm), **4e** (d = 12.0 mm), **6a** (d = 14.7 mm) at a 0.5% concentration.

Acknowledgements: Postdoctoral fellowship is being funded by European Union Structural Funds project 'Postdoctoral Fellowship Implementation in Lithuania'.

References

1. V. Mickevičius, A. Voskienė, I. Jonuškienė, R. Kolosej, et.al. *Molecules*, **2013**, 18(12), 15000.
2. I. Jonuškienė, S. Kuusienė, V. Mickevičius, *Chem. Technol.*, **2008**, 49, 53.
3. M. Sathe, D. Thavaselvam, A.K. Srivastava, M.P. Kaushik, *Molecules*, **2008**, 13, 432.
4. S. B. Ferreira, F.D. da Silva, et.al. *Arch. Pharmazie*, **2010**, 343, 81.



5. V.K. Tandon, H.K. Maurya, et.al. *Eur. J. Med. Chem.*, **2009**, *44*, 1086.
6. National Committee for Clinical Laboratory Standard, Performance Standards for Antimicrobial Disk Susceptibility Tests; Approved Standard - Eleventh Edition, document M02-A11. National Committee for Clinical Laboratory Standart, Wayne, 2012.
7. National Committee for Clinical Laboratory Standard, Reference method for broth dilution antifungal susceptibility testing of conidium forming filamentous fungi: approved standard – second edition, document M38-A2. National Committee for Clinical Laboratory Standart, Wayne, 2008.

SYNTHESIS AND APPLICATIONS OF 2- AND 6-ALKYL/ARYLTHIOPURINE DERIVATIVES

I. Novosjolova, Ē. Bizdēna, M. Turks

Faculty of Material Science and Applied Chemistry, Riga Technical University,
Paula Valdena Str. 3, Riga, LV-1007, Latvia
E-mail: maris_turks@ktf.rtu.lv

Synthesis of novel triazolylpurine nucleosides is constantly developing field because of the wide spectrum of their biological activity [1]. In 2013, the synthesis of 2,6-bis-triazolylpurine nucleosides and their applications in the nucleophilic heteroaromatic substitution reactions were described [2].

Here we report the use of 2,6-bis-triazolylpurine nucleoside **1** and 2,6-diazidopurine nucleoside **3** in the nucleophilic aromatic substitution reactions with different arylthiols. When the S_NAr reactions between bistriazole **1** and different arylthiols were made, C(6)-substituted products **2a-c** were obtained. While nucleophilic substitution reactions between diazide **3** and different arylthiols gave the mixture of possible products **4** and **5** which were subsequently subjected to 1,3-dipolar cycloaddition reaction and two differently substituted products **6** and **7** were obtained. For example, when 4-*t*-BuC₆H₄SH, K₂CO₃ and DMF were used in the S_NAr reaction followed by click reaction between intermediates **4** and **5** and phenylacetylene, products **6** and **7** were obtained in 19 and 33% yield, respectively. Interestingly, when *tert*-butylhydroquinone was added to the nucleophilic reaction between diazide **3** and 4-*t*-BuC₆H₄SH, subsequent click reaction gave products **6** and **7** in 2 and 61% yield. The comparison of chemical reactivity between bistriazole **1** and diazide **3** and different arylthiols is underway in our laboratory.

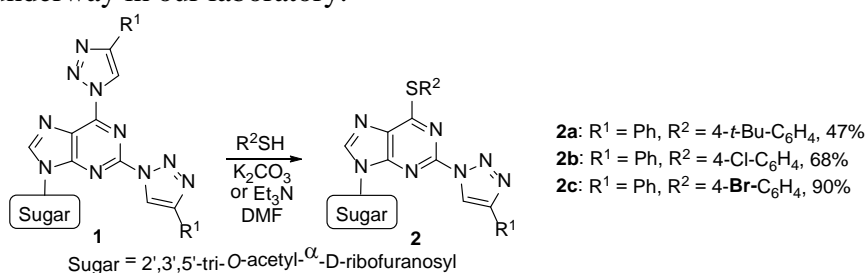


Fig. 1. Synthesis scheme of nucleosides **2**

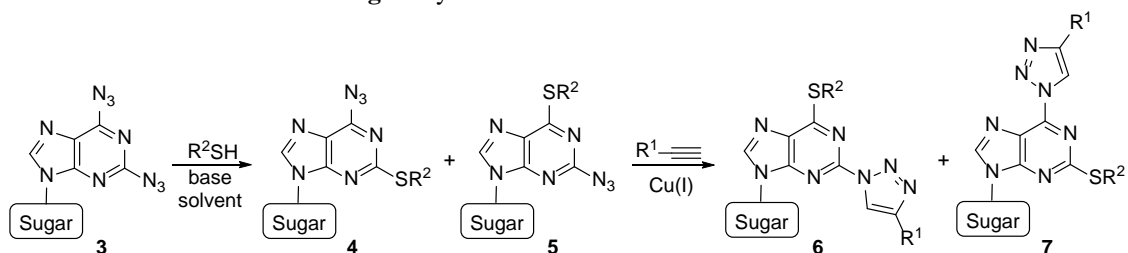


Fig. 2. Synthesis scheme of derivatives **6** and **7**

I.N. thanks the European Social Fund within the project «Support for the implementation of doctoral studies at Riga Technical University» for a scholarship.

References

1. a) L. Cosyn; K. K. Palaniappan; S.-K. Kim; H. T. Duong; Z.-G. Gao; K.A. Jacobson; S. Van Calenbergh, *J. Med. Chem.*, **2006**, 49, 7373; b) M. K. Lakshman; A. Kumar; R. Balachandran; B. W. Day; G. Andrei; R. Snoeck; J. Balzarini, *J. Org. Chem.*, **2012**, 77, 5870.
2. a) A. Kovaļovs; I. Novosjolova; Ē. Bizdēna; I. Bižāne; L. Skardziute; K. Kazlauskas; S. Jursenas; M. Turks, *Tetrahedron Lett.*, **2013**, 54, 850; b) I. Novosjolova; Ē. Bizdēna; M. Turks, *Tetrahedron Lett.*, **2013**, 54, 6557.

SYNTHESIS OF FUNCTIONALIZED 3-[4-HYDROXY(1,3-THIAZOL-2-YL)ANILINO]-2-METHYLPROPANOIC ACIDS

I. Parašotas, V. Mickevičius

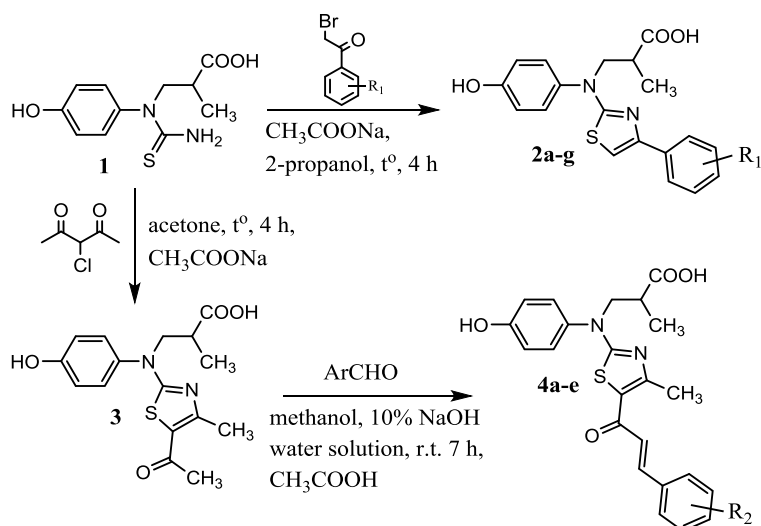
Kaunas University of Technology, Radvilėnų pl. 19, 50254, Kaunas, Lithuania

E-mail: irmantas.parasotas@yahoo.com

β -Amino acids and their fragments are found in biologically active compounds such as peptides, depsipeptides, lactones, alkaloids; also they show interesting pharmacological effects [1, 2] in a free form. β -Lactame antibiotics penicillins, cephalosporins comprise the largest therapeutic class of antibiotics.

The aim of this work was to synthesize new potentially biologically active compounds containing *N*-substituted β -amino acids and thiazole moieties.

The starting compound *N*-(4-hydroxyphenyl)-*N*-thiocarbamoyl- α -methyl- β -alanine (**1**) was prepared by the published procedure [3]. Compounds **2a-g** was synthesized from thioureido acid **1** and corresponding α -halocarbonylic compounds. Reactions was performed



R₁ = a) H, b) 4-fluoro, c) 4-nitro, d) 4-chloro, e) 4-ciano, f) 4-bromo, g) 3,4-dichloro

R₂ = a) 4-chloro, b) 4-fluoro, c) 4-bromo, d) 3-chloro, e) 3,4-dichloro

in 2-propanol at reflux for 4 h. Compound **3** was obtained by interaction of compound **1** and 3-chloro-2,4-pentanedione in acetone. Using well known aldol condensation (Claisen-Schmidt condensation) reaction chalcones **4a-e** were synthesized from compound **3** by the published procedure [4]. The C _{α} -C _{β} double bond in the enone moiety of chalcones can potentially adopt either a *Z* or an *E* configuration. The ¹H NMR spectrum of each compounds exhibited CH=CH protons around 7.19–7.59 ppm, with *J*>15, would suggest that the compounds were produced with an (*E*) configuration [4].

References

1. J. Patočka, *Mil. Med. Sci. Lett.*, **80**, 2 (2011).
2. E. Juaristi, V. A. Soloshonok, *Enantioselective Synthesis of β -amino Acids (E)*, 2nd edn., Wiley-VCH, Hoboken, NJ (2005).
3. K. Anusevicius, R. Vaickelioniene, V. Mickevičius. *Chem.Heterocycl. Compd.*, **48(7)**, 1105 (2012).
4. K. Liaras, A. Geronikaki, J. Glamoclija, A. Ciric, M. Sokovic, *Bioorg. Med. Chem.*, **19(10)**, 3136 (2011).

LIQUID SULFUR DIOXIDE AS A REACTION MEDIUM FOR LEWIS ACID CATALYZED RITTER REACTIONS

D. Posevins, M. Turks

*Faculty of Material Science and Applied Chemistry, Riga Technical University,
Paula Valdena Str. 3, Riga, LV-1007, Latvia
E-mail: maris_turks@ktf.rtu.lv*

The Ritter reaction is a one-pot process, that involves reaction between nitriles and *in-situ* generated carbocation to give amides [1]. The reaction typically requires at least stoichiometric amounts of corrosive Brønsted acid (most often sulfuric acid) in a strongly ionizing solvent, thus limiting its substrate scope to compounds with functionalities, that can endure such conditions [2]. Over the past two decades a lot of attention was devoted to development of catalytic variations of Ritter reaction [3]. Some Brønsted and Lewis acids proved to be efficient catalysts [3]. Unfortunately, there are often some limitations including relatively high catalyst loading, prolonged reaction times or limited substrate scope.

Sulfur dioxide is well known to be a readily available and handy building block for synthetic preparations [4]. Moreover, it can be easily liquified at -10 °C to give a colorless mobile liquid (SO_{2(liq.)}), that has its own unique properties. One of such useful properties is its ability to facilitate the formation of carbenium ions [5]. Taking this into consideration we were encouraged to explore the possible applications of SO_{2(liq.)} in synthetic transformation that involves formation of these active species, such as Ritter reaction. To the best of our knowledge there is only one example of Ritter reaction performed in SO_{2(liq.)}, that includes the use of BF₃-SO₂ complex as a catalyst [6].

We report here our studies on Ritter reactions in SO_{2(liq.)}. Application of different Lewis and Brønsted acidic catalysts in SO_{2(liq.)} was examined. The scope and limitations of substrate, reagent and catalyst use for Ritter reactions in liquid sulfur dioxide will be discussed.

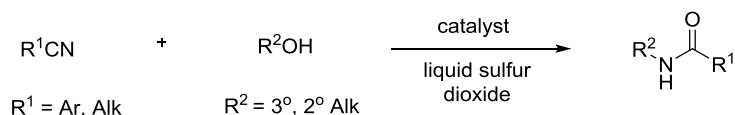


Fig. 1. Ritter reactions in liquid sulfur dioxide

References

1. Krimen, L. I.; Cota, D. J., *Org. React.*, **1969**, *17*, 213.
2. Ritter, J. J.; Minieri, P. P. *J. Am. Chem. Soc.* **1948**, *70*, 4045.
3. Guérinot, A.; Reymond, S.; Cossy, J. *Eur. J. Org. Chem.* **2012**, 19.
4. (a) Luginina, J. *Synlett*, **2014**, *25*, 2962.; (b) Deeming, A.; Emmett, E.; Richards-Taylor, C.; Willis, M. *Synthesis*, **2014**, *46*, 2701.
5. Feigel, M.; Kessler, H.; Leibfritz, D.; Walter, A. *J. Am. Chem. Soc.* **1979**, *101*, 1943.
6. Bakke, J. M.; Knudsen, B. *Acta Chem. Scand.* **1994**, *48*, 234.

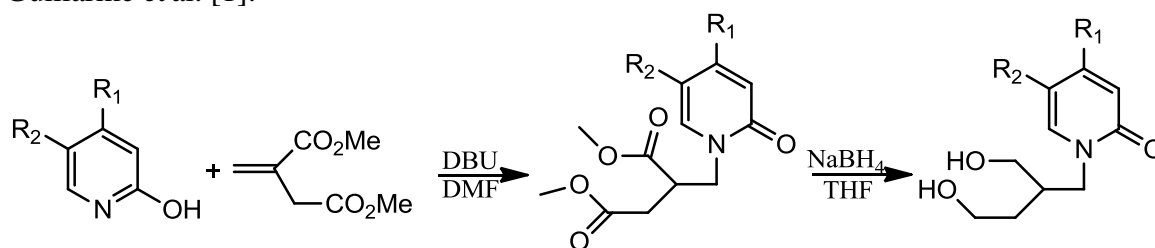
SYNTHESIS OF ACYCLIC AND CYCLIC NUCLEOSIDES

R. Ražanas, J. Dabužinskaitė, D. Tauraitė, R. Meškys

Department of Molecular Microbiology and Biotechnology, Institute of Biochemistry, Vilnius University, Mokslininkų 12 Vilnius, LT-08662, Lithuania
E-mail: daiva.tauraitė@bchi.vu.lt

Nucleoside analogues act as antitumor and antiviral agents via inhibition of the enzymes - DNA and RNA polymerases, thymidylate synthetase, adenosine deaminase, adenosine kinase etc. Interest in acyclic nucleosides started only in 1970 when acyclovir was reported as a potent anti-viral agent. In addition, novel modified nucleosides could be promising building blocks for aptamer synthesis. The purpose of this work is to synthesize various cyclic and acyclic nucleoside analogues, which could be used in the biochemical research as enzymes inhibitors.

Several acyclic nucleosides were synthesized by Michael addition of different heterocyclic bases (hydroxypyridine nucleobase), using synthetic method proposed by Guillaume et al. [1].

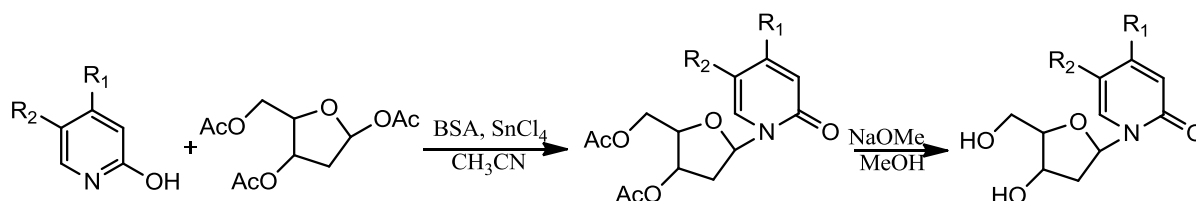


R₁ = H; OH; Cl; Br R₂ = H; COOH

Scheme 1

For the synthesis of acyclic nucleosides, the dimethyl itaconate was used as an Michael acceptor (Scheme 1). Synthesized diesters were purified by reverse phase chromatography or silica gel column chromatography in a moderate yield. Reduction of diester adducts with NaBH₄ afforded acyclic nucleosides in a moderate to high yield.

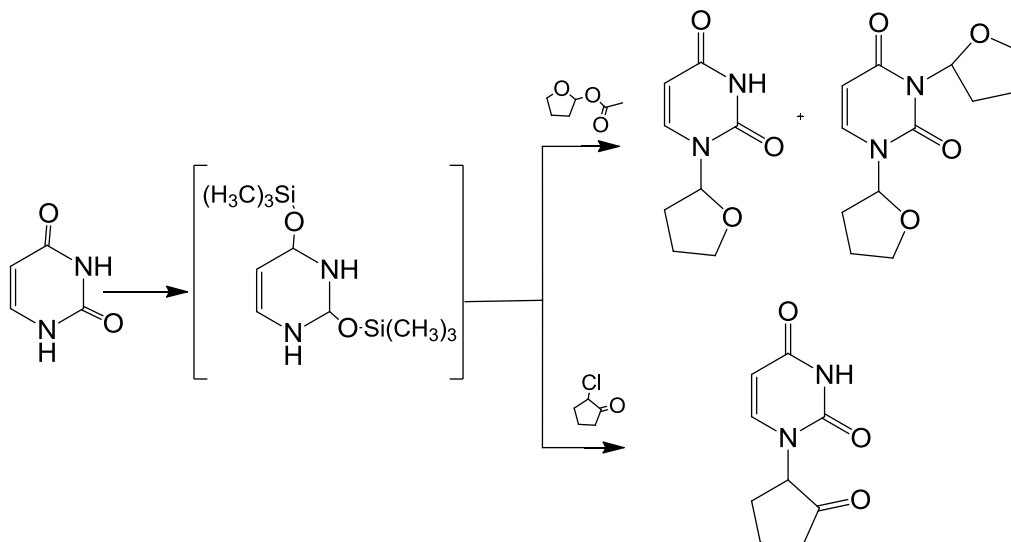
The same heterocyclic hydroxypyridine bases were used for the synthesis of cyclic nucleosides. The synthesis of modified 2-deoxyribonucleosides is shown in the Scheme 2.



R₁ = H; OH; Cl; Br R₂ = H; COOH

Scheme 2

Hydroxypyridine nucleobases were glycosylated with 1,3,5-tri-*O*-acetyl-2'-deoxyribose catalysed by tin (IV) tetrachloride [2] to form protected nucleosides. The protected nucleosides were further purified by reversed phase chromatography or silica gel column chromatography. Compounds were isolated in high yields. The deprotection step and reversed phase chromatography purification afforded the modified nucleosides in moderate yields.



Scheme 3

The synthesis of *N*-substituted uracil analogues is shown in the Scheme 3. Uracil was silylated with *N,O*-bis(trimethylsilyl)acetamide in the presence of acetonitrile. This moisture-sensitive intermediate was alkylated with an excess of 2-acetoxytetrahydrofuran, prepared by modification of 2,3-dihydrofuran and *p*-toluensulfonic acid in the acetic acid, in the presence of tin (IV) chloride to give a mixture of mono- and di- *N*-alkylated uracils [3]. 1-(2'-Oxocyclopentyl)-uracil was synthesized by the reaction of silylated uracil with 1-chloro-2-oxopentyl in the presence of tin (IV) chloride [4]. The *N*-substituted uracil derivatives were isolated in a moderate yield after silica gel column chromatography purification.

The structure and the purity of synthesized cyclic and acyclic nucleosides were proved by NMR spectroscopy and HPLC-MS analysis methods. All synthesized modified nucleosides will be tested as inhibitors of DNA and RNA polymerases.

Acknowledgement

The work was supported by European Social Fund (ESF) under the Human Resources Development Action Programme, the Global Grant measure, project No. VP1-3.1-ŠMM-07-K-03-015.

References

1. S. Guillarme, S. Legoupy, A.M. Aubertin, C. Olicard, N. Bourgoignon, F. Huet, *Tetrahedron*, **2003**, 59, 2177.
2. H.A. Knoblauch, C.E. Muller, L. Jarlebark, G. Lawoko, T. Kottke, M.A. Wikstrom, E. Heilbronn, *Eur. J. Med. Chem.*, **1999**, 34, 809.
3. N.P. Dolman, J.C.A. More, A. Alt, J.L. Knauss, H.M. Troop, D. Bleakman, G.L. Collingridge, D.E. Jane, *J. Med. Chem.*, **2006**, 49, 2579
4. M. Mori, H. Hatta, S. Nishimoto, *J. Org. Chem.*, **2000**, 65, 4641

FROM ALLYLSILANES TO ALLYLSULFOXIDES: APPLICATION OF SILA-ENE REACTION OF SULFUR DIOXIDE

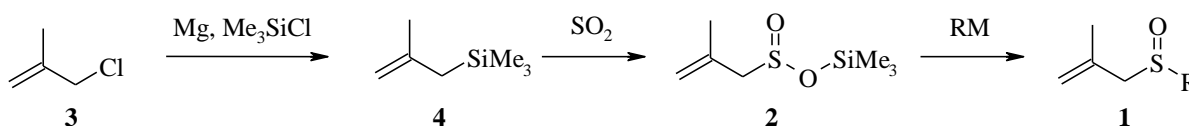
A. Stikute, M. Turks

*Faculty of Material Science and Applied Chemistry, Riga Technical University, Paula
Valdena Str. 3/7, LV-1007, Riga, Latvia
E-mail: maris_turks@ktf.rtu.lv*

Sulfoxides exhibit a wide range of biological properties, e.g. anticancer, antihepatitis, and antibacterial activity [1], and are used as medication [2]. Chiral sulfoxides are used as chiral auxiliaries in transition metal catalysed reactions, including Diels-Alder cycloaddition, 1,4-addition and in C-H bond activation [3].

The most common approach for synthesis of sulfoxides is oxidation of sulfides [4]. Also nucleophile addition to electrophilic sulfonamides and sulfinates [5] is used.

Herein we report a synthetic method towards variously substituted methallylsulfoxides **1**. General approach includes organometallic addition to trimethylsilyl methallylsulfinate **2** (Scheme 1). Intermediate **2** was prepared by Barbier reaction conditions from methallylchloride **3** and consequent sila-ene reaction between intermediate **4** and sulfur dioxide.



Scheme 1. Synthetic route to sulfoxides **1**

In order to optimize the reaction conditions for transformation **2** → **1** we investigated different reaction conditions. The optimal results arising from variation of solvent, temperature, organometallic reagent and Lewis acid additive will be discussed.

References

1. (a) K. Suwanborirux, K. Charupant, S. Amnuoyopol, S. Pummangura, A. Kubo, N. Saito, *J. Nat. Prod.*, **2002**, 65, 935. (b) L. Johansen, O. Christopher, C. Mawhinney, C. Chappell, A. Brown, M. Frank, M. Foley, R. Altmeyer, Y. Chen, *US Pat. 2010/9970*, **2010**.
2. M. J. Kendall, *Aliment. Pharmacol. Ther.*, **2003**, 17, 1.
3. (a) E. M. Stang, M. C. White, *J. Am. Chem. Soc.*, **2011**, 133, 14892. (b) J. Chen, J. Chen, F. Lang, X. Zhang, L. Cun, J. Zhu, J. Deng, J. Liao, *J. Am. Chem. Soc.*, **2010**, 132, 4552. (c) C. Jiang, D. J. Covell, A. F. Stephan, M. S. Plummer, M. C. White, *Org. Lett.*, **2012**, 14, 1386.
4. C. J. Carrasco, F. Montilla, E. Alvarez, C. Mealli, G. Manca, A. Galindo, *Dalton Trans.*, **2014**, 43, 13711.
5. Z. Han, D. Krishnamurthy, P. Grover, Q. K. Fang, X. Su, H. S. Wilkinson, Z.-H. Lu, D. Magiera, C. H. Senanayake, *Tetrahedron*, **2005**, 61, 6386.

HETEROGENEOUS CATALYST FOR THE SUZUKI REACTION

R. Striela, G. Urbelis, R. Mažeikaitė, L. Labanauskas*State research institute Center for Physical Sciences and Technology, Akademijos 7, LT-08412 Vilnius, e-mail: romualdas.striela@gmail.com*

For Suzuki reactions, soluble complex palladium catalysts are normally employed alongside bases; these are rarely recoverable without elaborate and wasteful procedures that are commercially unacceptable. In recent years there has been an increasing interest in developing greener processes. In this context, heterogeneous catalysis is emerging as an alternative to homogeneous processes so that catalysts can be recovered after the reaction and re-used several times to achieve very high turnover numbers [1-3].

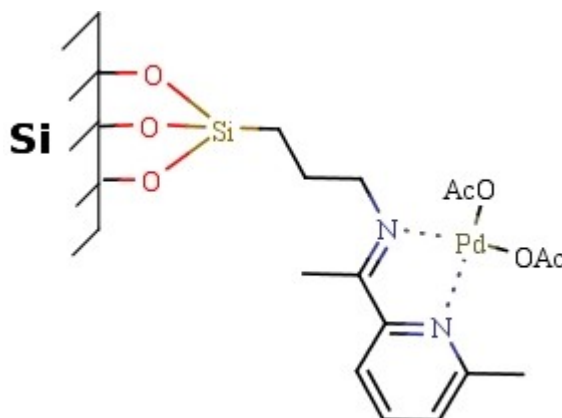


Figure 1. Silica supported palladium catalyst

In this work we present a synthesis of heterogeneous catalyst prepared by the anchoring of palladium on the surface of modified silica (Figure 1) and its application for the Suzuki cross-coupling reaction between arylbromides and aryl- or alkylboronic acids.

References

1. J. K. Shorrock, J. H. Clark, K. Wilson and J. Chisem, *Org. Proc. Res. Dev.*, **5**, 249, **2001**.
2. K. Okubo, M. Shirai and C. Yokoyama, *Tetrahedron Lett.*, **43**, 7115, **2002**.
3. S. Paul, J. H. Clark, *Green Chemistry*, **5**, 635–638, **2003**.

ANTIOXIDATIVE ACTIVITY OF AZOLES AND THEIR INFLUENCE ON RAPESEED (*BRASSICA NAPUS* L.) GROWTH *IN VITRO* AND ACCUMULATION OF METABOLITES

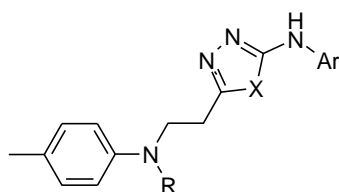
I. Tumosienė, I. Jonuškienė, K. Kantminienė, Z. J. Beresnevičius

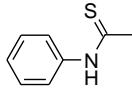
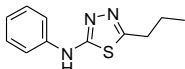
Kaunas University of Technology, Radvilėnų pl. 19, LT-50254 Kaunas, Lithuania

E-mail: ingrida.tumosiene@ktu.lt

Antioxidants are widely studied for their capacity to protect organisms and cells from damage induced by oxidative stress. Cancer, emphysema, cirrhosis, atherosclerosis, and arthritis have all been correlated with oxidative damage [1]. Rapeseed phenolic compounds are potent antioxidants in various environments. Flavonoids in plants have demonstrated elevated capacity for scavenging free radicals associated with various diseases [2].

Azole derivatives **1–5** were screened for their antioxidative activity and their influence on rapeseed (*Brassica napus* L.) growth *in vitro*, DPPH inhibition, and changes in metabolite amount was investigated. Compounds **1–5** were synthesized from *N*-(4-methylphenyl)- β -alanine hydrazide as described in [3].



Compound no	R	X	Ar
1	H	S	C ₆ H ₅
2	H	S	4-CH ₃ C ₆ H ₄
3	H	O	3,5-(CH ₃) ₂ H ₆ H ₃
4		S	C ₆ H ₅
5		S	C ₆ H ₅

Antioxidative activity of the tested compounds was measured by DPPH using the widely used method [4]. As the obtained results indicate, *N*-(4-methylphenyl)-5-{2-[(4-methylphenyl)amino]ethyl}-1,3,4-thiadiazole-2-amine (**2**) scavenged as much as 90% of free DPPH radicals, showing the best antioxidant activity. Antioxidant activity of the extracts of the plants, grown on MS medium in the presence of 1 mg l⁻¹ of 1,3,4-thiadiazole-2-amine **2**, against DPPH was also the highest, 87.3%.

In the initial *in vitro* tests, solutions of **1–5** at different levels of concentrations (0.5–5 mg l⁻¹) were used to wet filter paper and rapeseed “Terra H” seeds were germinated on it. Compound **4** had the best effect on growth of the seedlings and roots and this effect did not depend on concentration.

The investigation of the influence of diazoles **1–5** on organogenesis of rapeseed by means of *in vitro* methods used in biotechnology followed by the determination *in vivo* of the amount of proteins, flavanoids, phenolic compounds and tanines has revealed that, compound **2** stimulated the accumulation of proteins (5.6 times more than the control) and flavonoids (2.1 times more than the control) the most.

References

1. Y. Ünver, S. Meydanal, K. Sancak, D. Ünlüer, R. Ustabas, E. Dügdü, Turk. J. Chem., **35** (2011) 265–277.
2. O. M. Andersen, K. R. Markham, In Flavonoids: Chemistry, biochemistry and applications; Ed. O. M. Andersen, K. R. Markham, CRC press, Taylor & Francis Group, Boca Raton, Florida, USA, 2006, p. 1197.
3. I. Tumosienė, I. Jonuškienė, K. Kantminienė, Z. J. Beresnevičius, Monatsh. Chem., **143** (2012) 1441–1450.
4. L. N. Madhu, K. N. Suchetha, B. K. Sarojini. DIT, **3** (2011) 297–300.

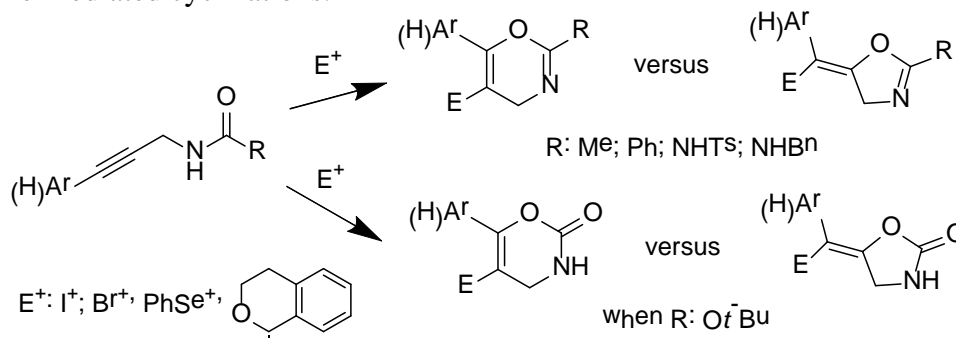
SYNTHESIS OF FUNCTIONALIZED PROPARGYLIC SUBSTRATES AND INVESTIGATION OF THEIR ELECTROPHILE-MEDIATED CYCLIZATION REACTIONS

A. Urbanaitė, R. Bukšnaitienė, M. Jonušis, I. Čikotienė

Department of Organic Chemistry Faculty of Chemistry, Vilnius University, Naugarduko 24,
LT-03225, Vilnius, Lithuania

E-mail: aurelija.urbanaite@chf.stud.vu.lt

Cyclizations of propargylamine derivatives give a wide variety of 1,3-oxazine, oxazoline, oxazole, oxazinone or oxazolidinone rings bearing compounds, which attract attention due to their biological properties [1] and utilization as the intermediates in organic synthesis [2]. Transition metal salts or strong bases catalyzed cyclizations of propargylic substrates are typical for the synthesis of compounds containing 1,3-oxazine, oxazoline, oxazole, oxazinone or oxazolidinone ring systems [3]. Whereas there are only few publications of electrophilic cyclizations of propargylic substrates in the literature [4]. Keeping in mind that electrophilic cyclizations are efficient processes for the synthesis of functionalized cyclic compounds, we synthesized various propargylic amides, carbamates and ureas and investigated their electrophile-mediated cyclizations.



In this work, we tested the reactivity of propargylic amides, carbamates and ureas with some electrophilic reagents under catalyst-free conditions. The scope, limitations and mechanistic aspects for the synthesis of functionalized oxazine, oxazoline, oxazinone and oxazolidinone derivatives will be discussed.

References

- a) B. P. Mathew, A. Kumar, S. Sharma, R. K. Shukla, M. Nath, *Eur. J. Med. Chem.*, 45 (2010) 1502; b) K. P. Madauss, E. L. Stewart, S. P. Williams, *Med. Res. Rev.*, 27 (2007) 374; c) T. J. Sindhu, A. R. Bhat, K. Krishnakumar, S. D. Arikatt, G. Vincent, M. Chandran, *IJPSR*, 4 (2013) 134; d) A. L. Wolfe, K. K. Duncan, N. K. Parelkar, S. J. Weir, G. A. Vielhauer, D. L. Boger, *J. Med. Chem.*, 55 (2012) 5878; e) N. Chinkov, A. Warm, E. M. Carreira, *Angew. Chem. Int. Ed.*, 50 (2011) 2957.
- a) H. Richter, R. Frohlich, C. G. Daniliuc, O. G. Mancheno, *Angew. Chem. Int. Ed.*, 51 (2012) 8656; b) S. Sato, M. Shibuya, N. Kanoh, Y. Iwabuchi, *Chem. Commun.*, (2009), 6264.
- a) B. M. Nilsson, U. Hacksell, *J. Heterocycl. Chem.*, 26 (1989) 269; b) A. Arcadi, S. Cacchi, L. Cascia, G. Fabrizi, F. Marinelli, *Org. Lett.*, 3 (2001) 2501; c) C. Jin, J. P. Burgess, J. A. Kepler, C. E. Cook, *Org. Lett.*, 9 (2007) 1887; d) M. Harmata, C. Huang, *Synlett*, (2008) 1399; e) A. S. K. Hashmi, J. P. Weyrauch, W. Frey, J. W. Bats, *Org. Lett.*, 6 (2004) 4391; f) A. Oppedisano, C. Prandi, P. Ventruello, A. Deagostino, G. Goti, D. Scarpi, E. G. Occhiato, *J. Org. Chem.*, 78 (2013) 11007; g) R. R. Machin, J. Adrio, J. C. Carretero, *J. Org. Chem.*, 71 (2006) 5023; h) O. P. Pereshivko, V. A. Peshkov, A. Peshkov, J. Jacobs, L. Van Meervelt, E. V. Van der Eycken, *Org. Biomol. Chem.*, 12 (2014) 1741; i) M. J. Campbell, F. D. Toste, *Chem. Sci.*, 2 (2011) 1369.
- a) A. Monleon, G. Blay, L. R. Domingo, M. C. Munoz, J. R. Pedro, *Chem. Eur. J.*, 19 (2013) 14852; b) C. Madaan, S. Saraf, G. Priyadarshani, P. Purushotham Reddy, S. K. Guchhait, A. C. Kunwar, B. Sridhar, *Synlett*, 23 (2012) 1955; c) Y. Hu, R. Yi, C. Wang, X. Xin, F. Wu, B. Wan, *J. Org. Chem.*, 79 (2014) 3052.

LUMINESCENT BENZO- AND NAPHTHOQUINOLINES: SYNTHESIS AND INVESTIGATION OF PHOTOPHYSICAL PROPERTIES

Sigita Višniakova¹, Indrė Urbanavičiūtė², Ilya Sychugov³, Albinas Žilinskas¹, Kęstutis Arlauskas²

¹ Vilnius University, Department of Organic Chemistry, Naugarduko g. 24, Vilnius LT-Lithuania

² Vilnius University, Department of Solid State Electronics, Saulėtekio al. 9, bld. III, Vilnius LT-10222, Lithuania

³ KTH Royal Institute of Technology, Material Physics Department, Electrum 229, Kista-Stockholm Sweden

E-mail: albinas.zilinskas@chf.vu.lt

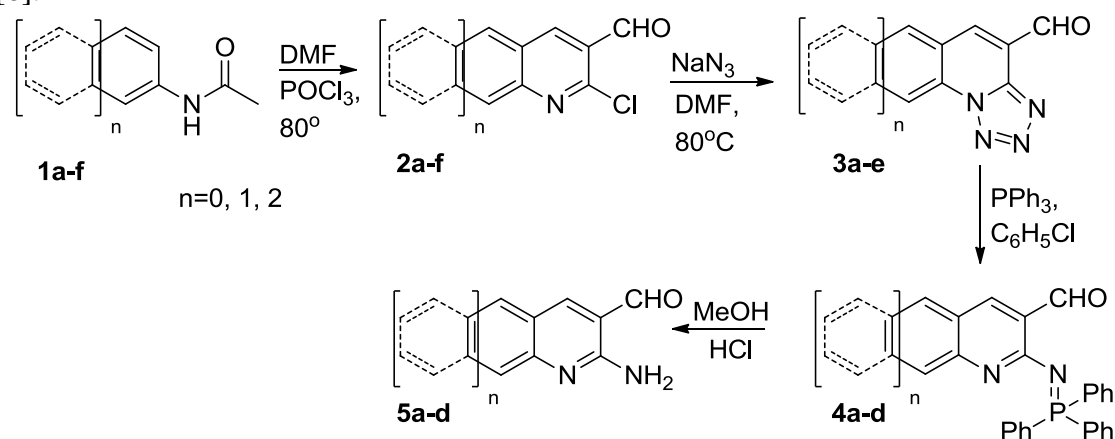
Small organic molecules with a conjugated π -electron system usually exhibit semiconducting behavior. Hence, they are potential materials for electronic and optoelectronic devices, such as organic field effect transistors (OFETs) [1,2], organic photovoltaic cells (OPVCs) [3] and organic light emitting diodes (OLEDs) [4]. Also, high degree of π -conjugation usually exposes unique fluorescent properties in a solution and solid state. A color of emission depends upon the size of the HOMO-LUMO energy gap, which for visible light (380-780 nm) corresponds to 1.5-3.2 eV [5]. However, synthesis of molecules obtaining eligible structure and photophysical properties required for these devices is challenging. Therefore, it is an obligation of chemists and physicists to unite for this highly meaningful research work.

Herein, we report a convenient synthesis and investigation of photophysical properties of benzo- and naphthoquinoline derivatives, which are valuable starting materials for a wide variety of N-heterocyclic compounds used in optoelectronic devices. Current results of the research lead to the conclusion that the examined materials are highly luminescent and could be perspective to use in the sphere of organic optoelectronics.

Discussion

Synthesis

Different investigated derivatives of quinoline were synthesized in the same manner (Scheme 1) [6].



Scheme 1. Synthesis of quinoline derivatives.

The primary aryl amines were taken as starting compounds and their acetylation occurred by the treatment with an acetic anhydride. The resulting aryl acetamides (**1a-f**) were further cyclized by the treatment with the Vilsmeier–Haack reagent (DMF+POCl₃). The next step of this method was replacing of chlorine group by sodium azide in DMF. The obtained tetrazole ring (**3a-e**) containing derivatives were treated with PPh₃ in chlorobenzene. The last step of

this useful method was acid hydrolysis of iminophosphoranes (**4a-d**) in HCl/MeOH solution. Derivatives of quinoline, benzoquinoline and naphthoquinoline (Table 1).

Table 1. Characteristics of photoluminescence and optical absorption.

Code	Scheme	PL _C HF	$\lambda_{\text{CHF}}^{\text{PL}*}$, nm (QY, %)	$\lambda_{\text{Layer}}^{\text{PL}*}$, nm	$\Delta\lambda_{\text{L}}$ nm	$\lambda_{\text{Layer}}^{\text{Abs}*}$, nm	$\Delta\lambda_{\text{Stokes}}$, nm
2d			487 (4)	545, 505	58	395	110
2c			485, 533 (11)	569	84	454	116
2b			480	477, 493	-3	408	69
2a			479, 546	479, 549	0, 3	378	101
2e			483	-	-	380	-
2f			481, 535	490, 542	9, 7	405	85
3d			536 (49)	596, 542	60	436	106
3b			485	555	70	391	164
3a			471	-	-	349	-
3e			476	-	-	325	-
4d			531 (15)	559	28	460	99
4c			532, 517 (12)	564	32	458	106
4b			515, 531 (16)	569	54	453	116
4a			534, 498 (8)	492, 562	-42	420	72
5d			493	561	68	412	149
5c			485 (17)	539, 505	54	438	67
5a			486, 528	556	70	402	154
5b			537, 503	563	26	424	139

* The first number in a column represents the highest intensity maximum.

** The value of the longest wavelength UV absorption peak, which corresponds to the shortest wavelength PL maximum (to be of the same electronic transition).

Measurements of values of the HOMO and the LUMO energy levels.

Measured values of HOMO and LUMO energy levels and optical band gap (E_{g_opt}) were evaluated to be in range of $E_{HOMO} = [-5,9; -5,5]$ eV, $E_{LUMO} = [-3,7; -3]$ eV, $E_{g_opt} = [1,9; 2,8]$ eV telling that essential parameters for device design as HOMO, LUMO and E_{g_opt} can be varied in relatively easy chemical way (Figure 1).

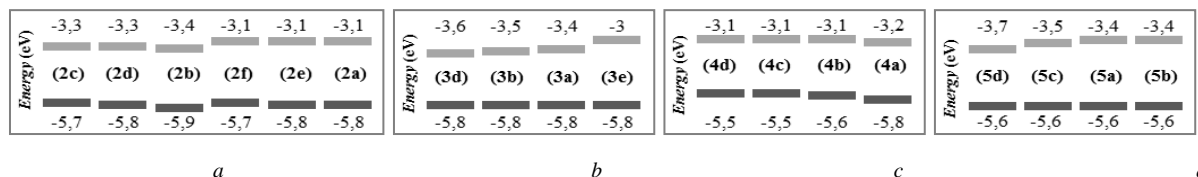


Figure 1. The energy diagram (values of the HOMO and the LUMO energy levels) of materials with chlorine - a. amino - b. iminophosphorane - c and tetrazole - d substituent group.

Investigation of photoluminescence and optical absorption

Continuing the material investigation, photoluminescence spectra of materials as thin films and as low concentration solutions were captured. Quantum yield (QY) of PL in solution was measured under 380 nm wavelength illumination for selected materials with the highest fluorescence intensity. PL spectra of thermally evaporated thin layers were compared to 10^{-6} mol/ml concentration chloroform solutions. Images of group (2, 3, 4, 5) materials solution photoemission and maxima points of solution and thin film PL spectra are presented in Table 1. Comparing to PL in solution, in most cases PL of thin film had a bathochromic shift (given in Table 1). Most of the examined materials showed high intensity fluorescence in solution as well as in the form of thin film reaching quantum yields of 49 %.

Conclusion

It is worth to emphasize that one single synthesis methodology was used for production of various quinoline derivatives. We also obtained important material characteristics: values of the HOMO ($E_{HOMO} = [-5,9; -5,5]$ eV), the LUMO ($E_{LUMO} = [-3,7; -3]$ eV) energy levels together with optical band gap ($E_{g_opt} = [1,9; 2,8]$ eV), Stokes' shift ($\Delta\lambda_{Stokes} = [64; 155]$ nm), differences between PL spectra in thin film and solution ($\Delta\lambda_{PL} = [-42, 84]$ nm) and solvatochromism (comparing PL in toluene, chloroform and 2-methoxyethanol). Material (3d) with condensed tetrazole moiety showed the highest value of PL quantum yield in chloroform solution (49 %), while others remained in interval QY = [4; 17] %.

With respect to these promising study results we continue investigation of the materials by incorporating them as an emissive layer into multi-layer OLED structures expecting high efficiency electroluminescence.

Acknowledgements

The study was funded by European Community's social foundation under Grant Agreement No. VP1-3.1-ŠMM-08-K-01-004/KS-120000-1756.

References

1. M. K. Leung, W. H. Yang, C. N. Chuang, J. H. Lee, C. F. Lin, M. K. Wei, Y. H. Liu, *Org. Lett.* **2012**, 14, 4986.
2. A. R. Murphy, J. M. J. Fréchet, *Chem. Rev.* **2007**, 107, 1066.
3. N. Koumura, Z. S. Wang, S. Mori, M. Miyashita, E. Suzuki, K. Hara, *J. Am. Chem. Soc.* **2006**, 128, 14256.
4. M. Mushrush, A. Facchetti, M. Lefenfeld, H. E. Katz, T. J. Marks, *J. Am. Chem. Soc.* **2003**, 125, 9414.
5. A. C. Grimsdale, Kh. L. Chan, R. E. Martin, P. G. Jokisz, A. B. Holmes, *Chem. Rev.*, **2009**, 109, 897.
6. D. P. Shelar, D. R. Birari, R. V. Rote, S. R. Patil, R. B. Toche, M. N. Jachak, *J. Phys. Org. Chem.*, 2011, 24, 203.

SYNTHESIS AND ANTIMICROBIAL ACTIVITY OF NOVEL ARYLPYRIMIDINYLUREAS, HYDRAZONES AND SEMICARBAZONES

J. Zurba¹, P. Kavaliauskas², V. Jakubkienė¹

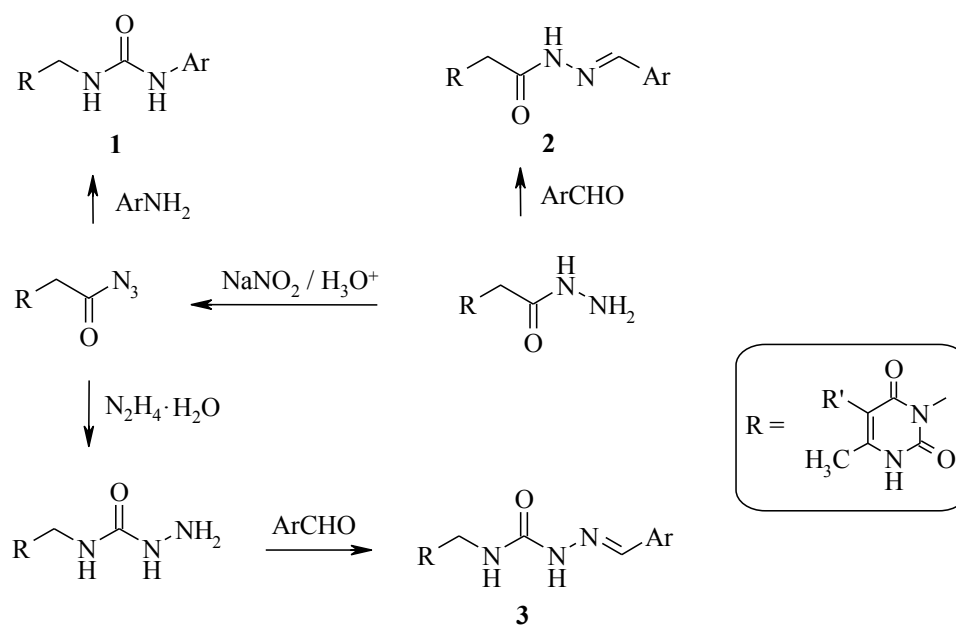
¹*Department of Organic Chemistry, Faculty of Chemistry, Vilnius University, Naugarduko 24, LT-03225, Vilnius, Lithuania*

²*Department of Biochemistry and Molecular Biology, Faculty of Natural Sciences, Vilnius University, Čiurlionio 21/27, LT-03101, Vilnius, Lithuania*

E-mail: virginija.jakubkiene@chf.vu.lt

In recent years naturally and synthetic heterocyclic compounds are of interest in pharmaceutical and pesticide research. Pyrimidines, in particular, cover the considerable position among compounds exhibiting diverse biological activities [1, 2]. On the other hand, compounds with the moiety of arylurea, hydrazone and semicarbazone are cited to show cytotoxic, antimicrobial, anti-inflammatory and analgesic activity [3-5].

Continuing our interest in the synthesis and investigation of pyrimidine-based compounds with potential biological activity [6], herein we present the synthesis and antimicrobial activity of several new arylpyrimidinylureas **1**, hydrazones **2** and semicarbazones **3**:



References

1. J. Delaney, E. Clarke, D. Hughes, M. Rice, *Drug Discov. Today*, **2006**, *11*, 839.
2. M. S. Novikov, O. N. Ivanova, A. V. Ivanov, A. A. Ozerov et al., *Bioorg. Med. Chem.*, **2011**, *19*, 5794.
3. T. Saurat, F. Buron, N. Rodriques, M. L. de Tauria et al., *J. Med. Chem.*, **2014**, *57*, 613.
4. A. P. Keche, G. D. Hatnapure, R. H. Tale, A. H. Rodge et al., *Bioorg. Med. Chem. Letters*, **2012**, *22*, 3445.
5. E. A. Voight, A. R. Gomtsyan, J. F. Daaneu, R. J. Perner et al., *J. Med. Chem.*, **2014**, *57*, 7414.
6. N. E. Cabrera-Benitez, E. Perez-Roth, M. Casula, A. Ramos-Nuez, C. Rios-Luci, C. Rodriguez-Gallego, I. Sologuren, V. Jakubkiene, A. S. Slutsky, J. M. Padron, J. Villar, *PLOS ONE*, **2012**, *7*, e48468.



Vilnius University, Faculty of Chemistry,
Naugarduko 24, Vilnius, Lithuania
January 23, 2015

Poster presentations

Environmental and Analytical Chemistry





DESIGN OF FIELD PORTABLE CAPILLARY ELECTROPHORESIS DEVICE WITH CONTACTLESS IMPEDANCE MEASURING DETECTOR

T. Drevinskas¹

*1 Vytautas Magnus University, Faculty of Natural Sciences, Dept. of Biology, Vileikos str. 8,
LT44404 Kaunas, Lithuania*

E-mail: tomas.drevinskas@gmail.com

Capillary electrophoresis is a becoming more and more popular. Numerous scientific groups are working on the field of miniaturization. However, miniaturized instruments lack user friendliness, automation, performance etc.

In this research work design of field portable capillary electrophoresis system coupled with contactless impedance measuring detector is discussed. Such detector can be operated from battery or cellphone charger. The system transmits data and operating instructions wirelessly via NRF24I01 module. Capacitance-to-digital converter integrated circuit [1] is used as a contactless impedance measuring detector. Stainless steel rods are used as electrodes. The prototype was originally developed with differential measurement capability, however, single-ended, or Wheatstone bridge detection configurations can be utilized as well [2].

Designed system is cube shaped. It contains miniature detector, vial lifting and holding mechanism, high voltage power source and control electronics. Preliminary tests show that system can be easily operated, however, additional upgrades are needed for user-friendliness. Additional results, benefits and issues will be presented/ discussed in the conference.

References

1. T. Drevinskas, M. Kaljurand, A. Maruška, *ELECTROPHORESIS*, **35** (2014) 2401-07.
2. T. Drevinskas, A. Maruška, V. Briedis, *ELECTROPHORESIS*, DOI: 10.1002/elps.201400320.

MENADIONE-MEDIATED AMPEROMETRY REVEALS DISTINCT MODES OF GALACTOSE ASSIMILATION BY YEAST *DEBARYOMYCES HANSENI* AND *PICHIA GUILLIERMONDII*

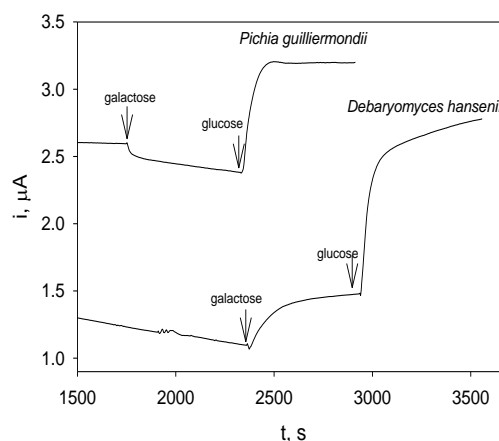
R. Garjonyte¹, A. Balynaite², V. Melvydas², A. Malinauskas¹

*1 Center for Physical Sciences and Technology, Gostauto 9, LT-01108, Vilnius, Lithuania
rasa.garjonyte@chi.lt*

2 Nature Research Center, Zaliuju ezeru 49, LT-08406, Vilnius, Lithuania

In most organisms, galactose is converted to glucose-6-phosphate (which thereafter enters classical glycolysis) by the action of several enzymes that constitute the Leloir pathway [1]. Two alternative pathways of galactose assimilation through production of galactonate (De Ley-Doudorof pathway) or through production of galactitol are identified as well [2]. Menadione-mediated amperometry at yeast-modified carbon paste electrodes is based on menadione reaction with NAD(P)H-dependent menadione-reducing enzymes. After subjection of yeast cells to glucose, the increases in anodic current responses are observed due to additional formation of NAD(P)H in glycolysis and pentose phosphate pathways [3]. Anodic responses to galactose and glucose obtained at electrodes containing *Debaryomyces hansenii* (as well as anodic responses to glucose at electrodes with *Pichia guilliermondii*) indicate that in these cases NAD(P)H is formed (Fig. 1), whereas cathodic current response to galactose at electrodes with *Pichia guilliermondii* indicate that NAD(P)H is consumed. Distinct responses to galactose suggest that the mechanisms of galactose assimilation are different. Anodic currents possibly correlate with the Leloir pathway. NAD(P)H is consumed during galactose conversion to galactitol [3]. This possibly can explain the cathodic currents.

Fig. 1 Menadione-mediated current responses at yeast-modified electrodes (as indicated) to additions of galactose and glucose (as indicated) in phosphate buffer at pH 6.5, menadione concentration 67 $\mu\text{mol/L}$, galactose and glucose concentrations 10 mmol/L, operating potential 0.1 V.



References

1. C. A. Sellick, R. N. Campbell, R. J. Reece, Int. Rev. Cell Mol. Biol. 269 (2008) 111.
2. K. Lai, M. I. Klapa, Metab. Eng. 6 (2004) 239.
3. R. Garjonyte, V. Melvydas, A. Paskevicius, V. Rasomavicius, A. Malinauskas, Centr. Eur. J. Biol. 9 (2014) 173.

ADSORPTION OF CYANIDES FROM AQUEOUS PHASE ONTO TWO MACROPOROUS ANION EXCHANGE RESINS

A. Gefenienė^{1,2}, J. Čerkauskaitė², D. Kaušpėdienė¹, R. Ragauskas¹, J. Vaičiūnienė¹

¹Center for physical sciences and technology, Institute of Chemistry,

A. Goštauto 9, LT-01108 Vilnius, Lithuania, E-mail: dana@ktl.mii.lt

²Lithuanian University of Educational Sciences, Studentų 39, LT-08106 Vilnius, Lithuania, E-mail: audrone.gefeniene@leu.lt

1. Introduction

Cyanides are used in some core industries, such as silver electroplating and mining, as it significantly enhances process efficiency and product quality. They are considered among the most dangerous compounds for the environment [1] and can be eliminated from effluent waters by adsorption onto anion exchange resins.

The adsorption properties of the ion exchanger depend on the nature of functional groups, the properties of the matrix of the initial inert polymer and its transformation during grafting the functional groups [2]. The macroporous polystyrenic polymers have permanent porosity due to phase separation arising during polymerization. The corresponding ion exchangers compared with the gel ones have the advantage to exchange larger ions and are more resistant to fouling by organic matter.

Two macroporous resins of polystyrene divinylbenzene matrix: DOC 2001 and D 201 (“Suqing”) were proofed as suitable adsorbents for the simultaneous removal of free cyanide and silver cyanide complex from plating effluents under batch conditions. The kinetic studies were conducted to reveal the relation between the macroporous matrix of strong base anion exchangers and their performance in the removal of cyanides.

2. Materials and Methods

2.1. Materials

Two macroporous strong base anion exchange resins with quaternary ammonium functional groups of polystyrene-divinylbenzene skeleton DOC 2001 and D 201 (Table 1) were used in this study.

Table 1. Salient properties of anion exchange resins

	DOC 2001	D 201
Weight Exchange Capacity mmol/g	≥ 3.8	≥ 3.7
Water Retention %	55-65	53-58
Particle Size %	(0.315-1.25 mm) ≥ 95	(0.315-1.25 mm) ≥ 95
BET surface area m ² /g	30-40	25

Macroporous resins have a double porosity: the small pores of the matrix itself and the large macropores created by the phase extender (Fig. 1). They are very stable, as the matrix is usually highly cross-linked.

2.2. Batch mode kinetic studies

Kinetic curves were recorded when the samples of sorbent 2.0 g were equilibrated with 100 mL of the mixture 101 mg/L free cyanide CN⁻ and 160 mg/L Ag(I) in the form of cyanide complex at 20°C during the predetermined time. Then the solutions were withdrawn and the residual concentrations of free cyanide and Ag(I) were measured.

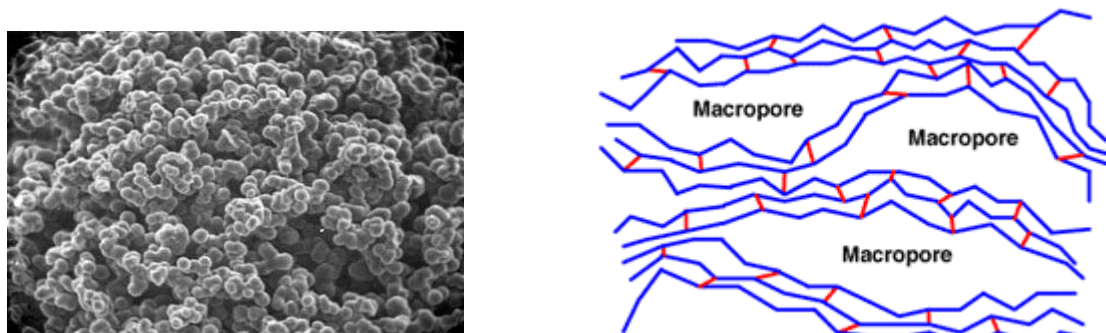


Fig. 1. SEM scans and structure of macroporous resins

2.3. Analysis

All the reagents used in the experimental work were of analytical grade (E. Merck)[®]. Argentometric titration was employed for free CN⁻ determination. The silver concentrations were measured using an ICP optical emission spectrometer (Optima 7000DV, Perkins Elmer).

The sorption capacities at equilibrium q_{eq} (mg/g) and q_t at time t (mg/g) were calculated by the following equation: $q_{e(t)} = (C_0 - C_{e(t)})V/W$ (1)

where C_0 , and C_e (or C_t) are the concentrations (mg/L) of the CN⁻ ions or Ag(I) in the solution before and after sorption, respectively, V is the volume of the solution (L) and W is the mass of the dry anion exchanger (g).

The sorption rate constant k_2 was obtained from the pseudo-second order rate model equation [3]: $t/q_t = 1/k_2 q_e^2 + t/q_e$ (2)

where k_2 (g/(mg min)) is the pseudo-second order rate constant; q_t (mg/g) and q_e (mg/g) the amount of sorbate adsorbed at time t and at equilibrium, respectively.

The rate constant of intraparticle diffusion was calculated after [4]:

$$q_t = k_i t^{0.5} + C \quad (3)$$

where q_t is the amount of sorbate on the surface of the sorbent at time t (mg/g), k_i is the intraparticle diffusion rate constant (mg/g min^{0.5}), t is the time (min) and C is the intercept (mg/g). To determine the initial adsorption behavior, the following equation [5] was used:

$R_i = 1 - \left(\frac{C}{q_{ref}} \right)$, where R_i is the initial adsorption factor of the IPD model, C (mg/g) and q_{ref} (mg/g) the initial and the final adsorption amount, respectively.

3. Results and discussion

3.1. Kinetic batch studies

Figure 2 shows sorption kinetics of free cyanide and silver cyanide complex from their mixture onto DOC 2001 and D 201 anion exchangers.

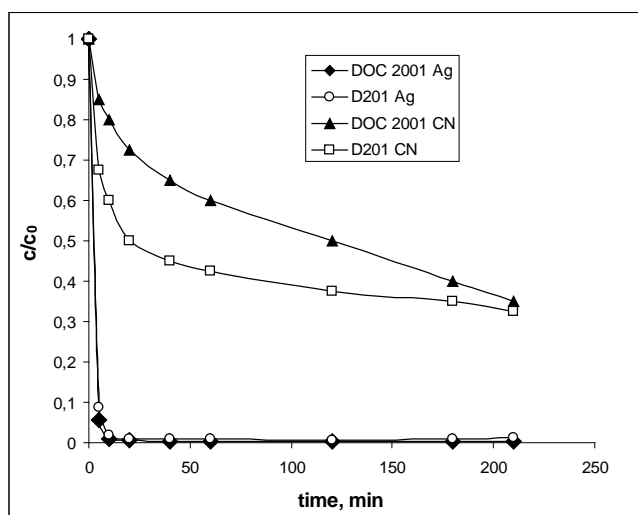


Fig. 2. Kinetics of free cyanide and silver cyanide complexes removal by anion exchange resins.

The rate of silver cyanide complex adsorption was extremely high within the first 5-10 min. The maximum amount of Ag(I) was adsorbed in the initial period of contact and the removal efficiency of more than 90 % was achieved. The kinetics of free cyanide initially was slower when compared to silver cyanide complex but the amount of adsorbed CN⁻ ions gradually increased with a further increasing in the mixing time, especially in the case of DOC 2001 anion exchanger (Fig. 2).

3.2. Sorption kinetics mechanism

Concerning the case of ion exchange, as several studies have demonstrated, is basically a diffusion-controlled process and although it differs from adsorption they share many common aspects, enough to accept the use of the same simplified kinetic equations [6]. Analysis of the experimental kinetic data with two theoretical models (pseudo-second order reaction and intraparticle diffusion) was used to describe the sorption kinetics.

The kinetic parameters determined using pseudo-second order model are listed in Table 2. The correlation coefficients (R^2) are high, in the range of 0.978-1, confirming a good agreement of kinetic model with experimental data. This confirmed that cyanide sorption rate limiting step may be chemical sorption or chemisorption involving valency forces through sharing or exchange of electrons between sorbent and sorbate. Further the experimental sorption capacities values agree very well with the calculated (Table 2).

Table 2. Pseudo-second-order rate constants and equilibrium sorption values.

Adsorbate	Anion exchanger	q_e experimental (mg/g)	q_e theoretical (mg/g)	k_2 (g/mg min)	R^2
CN ⁻	DOC 2001	3.79	3.58	$8.36 \cdot 10^{-3}$	0.978
	D 201	3.54	3.49	$3.10 \cdot 10^{-2}$	0.998
Ag(I)	DOC 2001	7.99	8.01	1.731	0.999
	D 201	7.95	7.96	4.788	1

As shown in Table 2, the pseudo-second order rate constants k_2 and the equilibrium adsorption capacities q_e calculated for silver cyanide complex sorption on both anion exchangers DOC 2001 and D 201 were greater than those for competing free cyanides.

Whereas the exchange capacity values of both macroporous anion exchangers are approximately equal (Table 1), it can be assumed that the type of the initial adsorption behavior depends on the properties of the polymeric matrix and the nature of solutes.

Table 3. Initial adsorption factors R_i and intraparticle diffusion rate constants k_{i1} and k_{i2} .

Adsorbate	Anion exchanger	Initial adsorption factor R_i	k_{i1} (mg/g min ^{0.5})	R^2	k_{i2} (mg/g min ^{0.5})	R^2
CN ⁻	DOC 2001	0.969	0.283	0.999	0.184	0.997
	D 201	0.784	0.395	0.999	0.082	0.981
Ag(I)	DOC 2001	0.167	0.413	1	0.019	0.924
	D 201	0.242	0.590	1	0.061	1

The R_i value was smaller for D 201 anion exchanger in respect of free cyanide sorption when compared to that for DOC 2001 anion exchanger. On the contrary, for the initial adsorption of silver cyanide complex anion exchanger DOC 2001 was more favorable (Table 3). After the rapid external surface adsorption, the intraparticle diffusion is rate-controlled. The experimental results suggest that intraparticle diffusion is a two-step process with different regimes. From Table 3, it can be seen that the diffusion rate of cyanides was higher in the first stage (k_{i1}) than in the second stage (k_{i2}) for both anion exchangers. In summary, both chemical and diffusional effects are important in the process of simultaneous uptake of silver cyanide complex and free cyanides.

4. Conclusions

1. The process of simultaneous uptake of free cyanide and Ag(I) cyanide complex by macroporous strong base anion exchange resins was studied through batch kinetic experiments. For this binary sorption system, both the selectivity and the rate of ion exchange are higher for Ag(I) cyanide complex than for free cyanide.
2. The uptake of Ag(I) cyanide complex begins with a period of fast external surface adsorption, whereas the initial adsorption of free cyanides can be characterized as weekly in the case of DOC 2001 anion exchanger, and as intermediately by using D 201 anion exchange resin.
3. The rate of intraparticle diffusion depends on both physicochemical characteristics of the anion exchangers and the nature of solutes.

References

1. Tool and Manufacturing Engineers Handbook. Volume III. Materials, Finishing and Coating. Dearborn, MI: Society for Manufacturing Engineers, SME, **1985**.
2. K. Dorfner (ed.), Ion Exchangers, Walter de Gruyter, Berlin, New York, **1991**.
3. I. S. Ho, *J. Hazard. Mater.*, **2006**, B136, 681.
4. W. J. Weber, J. C. Morris, *J. Sanit. Eng. Div. Am. Soc. Civ. Eng.*, **1963**, 89, 31.
5. F.-Ch. Wu, R. L. Tseng, R. S. Juang, *Chem. Eng. J.*, **2009**, 153, 1.
6. V. J. Inglezakis, A. A. Zorpas, *Desalin. Water Treat.*, **2012**, 39, 149.



Antimicrobial activity of Gold and Silver nanoparticles synthesized by chemical reduction method

Umme Thahira Khatoon^a, Arunas Ramanavicius^a, M.K.Mohan^b, G.V.S.Nageswara Rao^b

^a Faculty of Chemistry, Vilnius University, Vilnius, Lithuania.

^b Metallurgical and Materials Engineering Department, National Institute of Technology, Telangana, Warangal India.

Email Address: ummethahirakhatoon@gmail.com

Gold and silver nanoparticles have been used in nanotechnology and biotechnology due to their optical properties in the visible spectrum and high bio affinity. It is well known that the particles size influences the chemical and physical properties of gold nanoparticles [1]. Nanoparticles are great scientific interest as they are effectively a bridge between bulk materials and atomic or molecular structures. Nanoparticles have a very high surface area to volume ratio. This provides a tremendous driving force for diffusion, especially at elevated temperatures. [2-3]. The large surface area to volume ratio also reduces the incipient melting temperature of nanoparticles.. Gold and silver nanoparticles have many applications in biology, antimicrobial agents including deliver drugs or DNA into cells. They can also be used as sensors. The use of silver nanoparticles as antibacterial agent is relatively new. Because of their high reactivity due to the large surface to volume ratio, nanoparticles play a crucial role in inhibition bacterial growth in aqueous and solid media [4]. The antibacterial characteristics of gold and silver nanoparticles produced have been demonstrating by directly exposing microbe to colloid silver and gold particle solution.

In the present work, gold and silver nanoparticles are prepared and their antimicrobial activity is tested.

MATERIALS AND METHODS:

A) Material:

All chemicals were purchased without further purification, Sodium Borohydride (NaBH_4), Silver Nitrate (AgNO_3), Chloroauric acid (HAuCl_4), Tri Sodium Citrate ($\text{C}_6\text{H}_5\text{Na}_3\text{O}_7 \cdot 2\text{H}_2\text{O}$), Tannic Acid ($\text{C}_{76}\text{H}_{52}\text{O}_{46}$) were supplied by Merck & company. All chemicals were used as received. Double distilled water was also used for dilution of chemicals, Chloroauric acid, Silver nitrate is used as metal precursor, Sodium Borohydride & Tri sodium Citrate, tannic acid is used as reducing agent, distilled water is used through out the experiments.

B) Characterisation Techniques:

SPR of the sample was determined using UV-Visible spectroscopy. The spectrum of Ag Nps was recorded over a range of 408.22nm and 523 for Au Nps. The studies of size, morphology, of nanoparticles were determined by means of scanning electron microscopy (SEM). Samples for SEM studies were prepared by placing drop of Ag Nps and Au Nps on silicon plate. The average particle size analysis of Ag NPs and Au NPs were analysed by particle size analyser.

C) Preparation of Ag Np's

Prepare Sodium Borohydride, Tri Sodium Citrate, and Silver Nitrate solution with respective weights in distilled water. Mix NaBH_4 and $\text{Na}_3\text{C}_6\text{H}_5\text{O}_7$ in 100ml H_2O on magnetic stirrer. Add drop wise AgNO_3 through burette, notice the colour change. Initially the colour changes from colourless to yellow in first few drops. Change of colour from yellow to light brown to light algae green, final color of sample observed is yellow cum light algae green. The complete colloidal dispersed solution is seen.

D) Preparation of Au NPs

Prepare chloroauric acid, Tri sodium Citrate, tannic acid, solution with respective weights in distilled water. Prepare solution A (1% $\text{HAuCl}_4 \cdot 3\text{H}_2\text{O}$), and solution B (1% Tri sodium Citrate+ 1% Tannic acid). Prepare



solutions A and B in two different Erlenmeyer flasks with distilled water. Heat solutions A and B till some certain temperature add solution A to B while stirring. Colour change is observed, solution colour changes to red (final solution).

E) Test for antimicrobial activity of Ag and Au nanoparticles.

The antimicrobial susceptibility of synthesized gold and silver nanoparticles were investigated by Kirby-bauer diffusion method. It is also known as disc diffusion method. The antibiotics namely ampicillin, kanomycin, and neomycin are also studied to compare the activity with gold and silver nanoparticles.

KEYWORDS: Gold nanoparticles, silver nanoparticles, chemical reduction method, microbes, antibiotics.

ACKNOWLEDGEMENTS

This research has been supported by Faculty of physical chemistry and bio nanotechnas laboratory, Vilnius university, Lithuania. Umme is thankful to Faculty for synthesis of nanoparticles and laboratory for the antibacterial activities tests.

REFERENCES:

- 1) Sau TK, Murphy CJ, Seeded high yield synthesis of short Au nanorods in aqueous solution, *Langmuir*. 2004 Jul 20;20(15):6414-20.
- 2) Wilson M., Kannangara K., Smith G., Simmons M. *Nanotechnology, Basic Science and Emerging Technologies* (CRC, 2002) (ISBN 1584883391).
- 3) Daniel MC, Astruc D, Gold nanoparticles: assembly, supramolecular chemistry, quantum-size-related properties, and applications toward biology, catalysis, and nanotechnology, *Chem Rev*. 2004 Jan;104 (1):293-346.
- 4) Maribel G. Guzmán, Jean Dille, Stephan Godet, Synthesis of silver nanoparticles by chemical reduction method and their antibacterial activity, *International Journal of Chemical and Biomolecular Engineering*, 2:3 2009 104.

EFFECT OF SELECTED MICROMYCETES ON BIOINTERFACE OF STEEL

A. Lugauskas¹, E. Binkauskienė¹, I. Prosyčėvas², A. Selskienė¹,
V. Pakštas¹, D. Bučinskienė¹, A. Ručinskienė¹

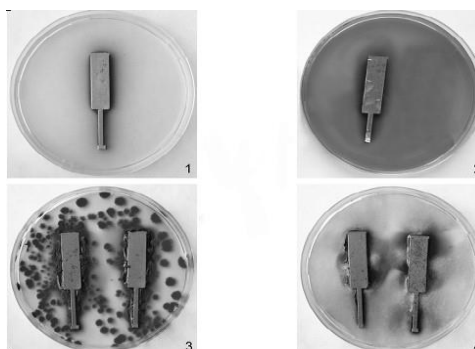
¹Institute of Chemistry, Center for Physical Sciences and Technology, A. Gostauto Str. 9, LT-01108 Vilnius, Lithuania

²Institute of Materials Science, Kaunas University of Technology, Savanoriu Ave. 271, LT-50131 Kaunas, Lithuania
E-mail: elenbink@ktl.mii.lt

The chemical and biodeterioration are the new sources of modification of microbiologically treated surface. The fungal biocorrosion products formed on steel surfaces under moisture influence play a major role in fungal physiology and induce health and safety issues [1-3]. The investigation of the steel surface corrosion is important due to iron importance in the industry and environment.

The aim of this study was to determine the influence of two selected strains of micromycetes *Penicillium palitans* strain 6 and *Arthrimum phaeospermum* strain 10 on the morphological and structural properties of carbon steel surfaces in the malt agar extract medium. Laboratory investigations were performed on low carbon steel plates placed in Petri dishes filled with a nutrient medium (Figure). Fungal growth was assessed by a light microscope. The morphology of surfaces was characterized by scanning electron microscopy, the structure – by the X-ray diffraction method, Fourier transformation infrared spectroscopy and X-ray fluorescence spectroscopy.

Figure. Fungal colonies: (1) exposed to air, 2) exposed to malt agar extract medium, (3) exposed to *P. palitans* 6, (4) exposed to *A. phaeospermum* 10, 30 days of exposure at 26 ± 2°C



A relation between the surface and interface fungal stimulated processes as well as the difference in consumption and production of microelements, which was caused by the growth of both strains, have been shown. More active physiological properties of *P. palitans* 6 fungus in comparison to those of *A. phaeospermum* 10 promoted a profound influence on the activity levels of biofilm organisms. The biotic oxidation of steel surface and formation of the mixed oxides on the biomodified steel surface have been observed [4].

References

1. A. Lugauskas, I. Prosyčėvas, R. Ramanauskas, A. Grigučėvičienė, A. Selskienė, V. Pakštas, Mater. Sci., 15 (2009) 224-235.
2. D. Xu, Y. Li, F. Song, T. Gu, Corros. Sci., 77 (2013) 385–390.
3. F. De Leo, G. Campanella, E. Proverbio, C. Urzì, Constr. Build. Mater., 49 (2013) 821-827.
4. E. Binkauskiene, A. Lugauskas, I. Prosyčėvas, V. Pakštas, A. Selskiene, D. Bučinskiene, A. Ručinskiene, Journal of Surface Engineered Materials and Advanced Technology, 4 (2014) 242-248.



**THE PRECIPITATE-SOLUTION EQUILIBRIA
IN THE PRESENCE OF EXCESS OF COMPLEXING AGENT**

Yu.P. Perelygin¹, M. Jaskula², I.V. Rashevskaya¹

1) Chair of Chemistry, Pensa State University, 40 Krasnaya Str., 440026 Pensa (Russia)

*2) Dept. of Physical Chemistry & Electrochemistry, Jagiellonian University, 3 Ingarden Str,
30-060 Cracow (Poland); Email: jaskula@chemia.uj.edu.pl*

The precipitation processes are widely used in hydrometallurgy, analytical chemistry, chemical separation and for the purification of waste waters, especially coming from the electroplating industry.

Some of commonly used anions, especially when the excessive concentration is used have the ability to create soluble complexes with obtained precipitates, what results in their dissolution. As a good example can serve hydroxyl OH^- ions as well as halide ions in the presence of silver cations.

The situation is much more complicated if a few various cations (especially of heavy metals) are simultaneously present in the solution and the hydroxyl ions OH^- , are used as the precipitating/complexing agent. It is a typical situation occurring during the purification of waste waters from the galvanic industry. The addition of OH^- ions changes the pH of the solution and influences on the precipitation (or redissolution) of deposit of another metal hydroxides. Therefore, the knowledge on the pH range where the precipitation of various hydroxides occurs is an important factor for experiment planning.

In our earlier papers the mathematical equations describing the content of solution, the concentrations (amounts) of various species (mole fraction of metal present in the deposit's form, or in complex etc.), the pH range where the precipitation occurs, as well as the pH value where the redissolution of the precipitate starts due to the creation of soluble complex were derived [1-4].

The paper present the most important results obtaining by use of those equations.

References

1. Y.P. Perelygin, M. Jaskula, Proc. Int. Sci-Appl. Conf. Modern Tendencies in Educ. & Sci., Tambov 2013, pp. 88-91.
2. Y.P. Perelygin, M. Jaskula, Vestn. Penz. Gosud. Univ., No 2 (2013), pp. 112-114.
3. Y.P. Perelygin, M. Jaskula, A.A. Fliagin, Proc. of 14. Int. Conf. on Ecological Security, Pensa 2014, pp. 59-62.
4. Y.P. Perelygin, M. Jaskula, I.V. Rashevskaya – in preparation.

INVESTIGATION LUBRICITY OF DIESEL WITH SECOND GENERATION OXYGENATES.

Ana Šarafutdinova^{a,*}, Lidija Kosychova^{a,b}

^aKlaipeda University, H.Manto 84, LT-91001 Klaipeda, Lithuania

^bVilnius University Institute of Biochemistry, Mokslininkų 12, LT-08662 Vilnius, Lithuania

E-mail: annsanko@yahoo.com

Constantly increasing fossil fuel prices and requirements reducing quantities of harmful emission led humanity to the search for alternative biofuel. The best approach to solve this problem is the use of oxygen-containing compounds as fuel additives and blending them with fuel. These blends usually enhance the combustion efficiency, burn rates, power output, and the ability to burn more fuel, but first of all, these blends offer the reduction of exhaust emissions. The importance of a sufficiently high lubricity of fuels became a topic of increased research after the introduction of low sulphur diesel fuels during the mid-nineties of the last century. Due to the hydro treatment used in the production of these fuels most of the fuel inherent lubricants were removed. This leads to increased friction and wears within the tribological contacts of the fuel-lubricating pumps and therefore drastically decreased the life expectancies of such systems. In the present time, more and more attention is paid to the new fuel blends, which increase lubricity. This investigation deals with the implementation of unblended diesel fuel in the standard test for fuel and lubricant (HFRR).

The Fig.1 shows the principal design of the HFRR as given in [1].

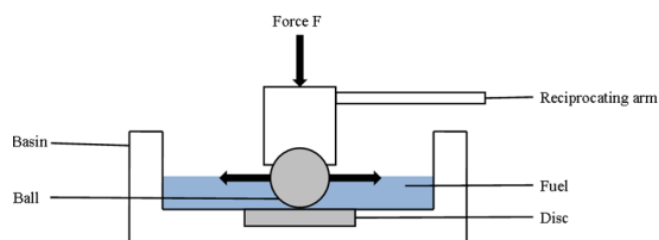


Fig.1. Test setup of the HFRR [1]

After each test the probes need to be evaluated with an optical microscope as shown in Fig.2.

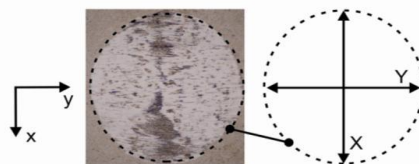


Fig.2. Determination of the wear scar diameter on the ball

The wear scar diameter (*WSD*) value of the specimen, ball alike, is determined by averaging the latitude of the scars in direction of the oscillation (*Y*) and vertical (*X*) to it as given in eq. 1 (Fig. 2). (1).

$$WSD = \frac{x+y}{2} \quad (1)$$

What is more it is a necessary to pay attention to the weather conditions before measurements (Fig. 3)

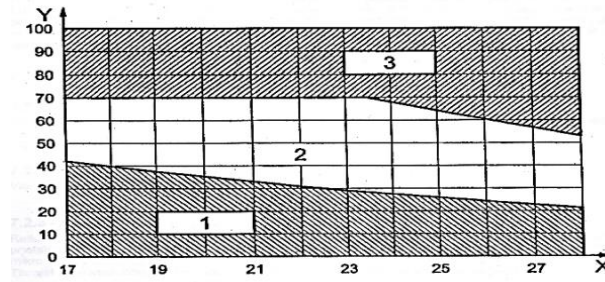


Fig. 3. Weather condition: X – air temperature, °C, Y – relative humidity, %, 1 – impossible conditions for the test (too dry) 2 – possible conditions for the test, 3 – impossible conditions for the test (too moist)

The weather conditions should be as in 2^d area .

The wear scar diameter (WSD) value can also calculate using formulas below:

$$1. \text{ The initial absolute vapor pressure: } AVP_1 = \frac{SD_1 \cdot 10^{V_1}}{750}, \text{ kPa} \quad (1.1.)$$

SD_1 – the relative humidity of the air at the beginning of the test,

$$V_1 = 8,017352 - \frac{1705,984}{231,864 + T_1}$$

T_1 – the air temperature at the beginning of the test, °C;

$$2. \text{ The final absolute vapor pressure: } AVP_2 = \frac{SD_2 \cdot 10^{V_2}}{750}, \text{ kPa} \quad (1.2.)$$

SD_2 – the relative humidity of the air at the end of the test,

$$V_2 = 8,017352 - \frac{1705,984}{231,864 + T_2}$$

T_2 – the air temperature at the end of the test, °C;

$$3. \text{ The average absolute vapor pressure: } AVP = \frac{AVP_1 + AVP_2}{2}, \text{ kPa} \quad (1.3.)$$

$$4. \text{ The approximate wear SCAR: } WDS = \frac{X+Y}{2} \quad (1.4.)$$

$$5. \text{ The corrected wear SCAR diameter: } WDPS = WDS + 60 \cdot (1,4 - AVP), \mu\text{m}. \quad (1.5.)$$

To gain a more detailed understanding of the properties influencing a fuels capability to reduce wear and friction in the HFRR several oxygenates were tested in Institute for Fluid Power Drives and Controls (IFAS)(Fig.3).

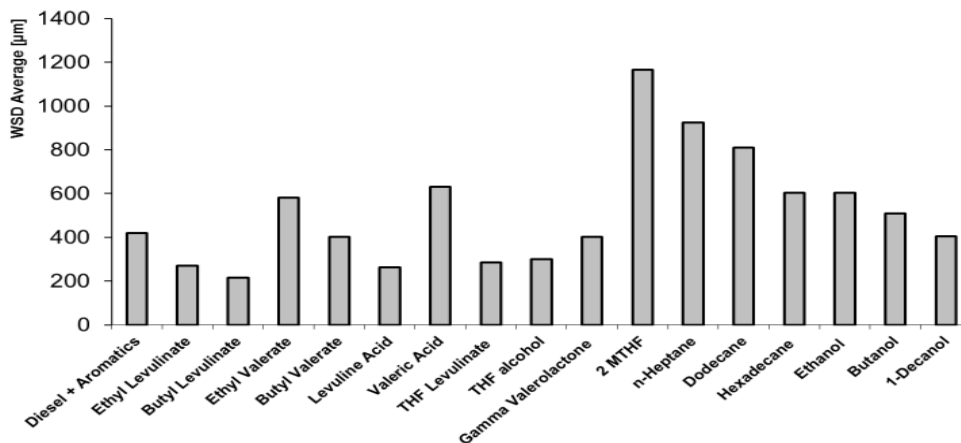


Fig.4. Wear scar diameters of the fluids previously investigated by Fatemimoughari [2]

According to the standard BS EN590:2014 which is applicable to commercial diesel car, the maximum permissible lubricity value of $460\mu\text{m}$. The research performed by A. Fatemimoughari showed that although quite different to conventional diesel fuel most biofuel candidates would pass the critical mark of $460\mu\text{m}$ or produce only slightly more severe wear scars [2]. A. Weinebeck and H. Murrenhoff determined the lubricity and found that the WSD average of anisole, cyclohexanone and cyclohexanol correspond to standard (Fig. 5) [3].

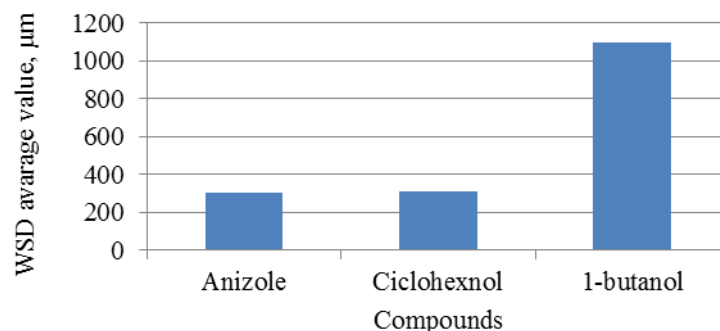


Fig.5. The lubricity of oxygenates used in the research

Taking into account that the so far proposed blends are taken from very different types of organic substances such as alcohols, ethers, ketones and furans, the understanding of their lubricating abilities by comparing their WSD values becomes a rather difficult task. To overcome this hindrance several second generation oxygenates (cyclohexanol, 1,4-dioxane, anisole and 1,4-dioxane) were included into our research. Their concentration was not larger than 13% (Table 1).

Table 1. Content of mixtures

Content of mixtures	Shortcut
Diesel	100D
1% 1,4- dioxane : 99% diesel	1Di:99D
2% 1,4- dioxane : 98% diesel	2Di:98D
3% 1,4- dioxane : 10% 1-butanol : 87% diesel	3Di:10B:87D
1% cyclohexanol : 99% diesel	1CiL:99D
2% cyclohexanol : 98% diesel	2CiL:98D
3% cyclohexanol : 97% diesel	3CiL:97D
3% anisole : 97% diesel	3A:97D

All mixtures were examined for the standard test for fuel and lubricant (HFRR). Wear scar diameters of diesel with cyclohexanol in the HFRR test shown in Fig. 6.

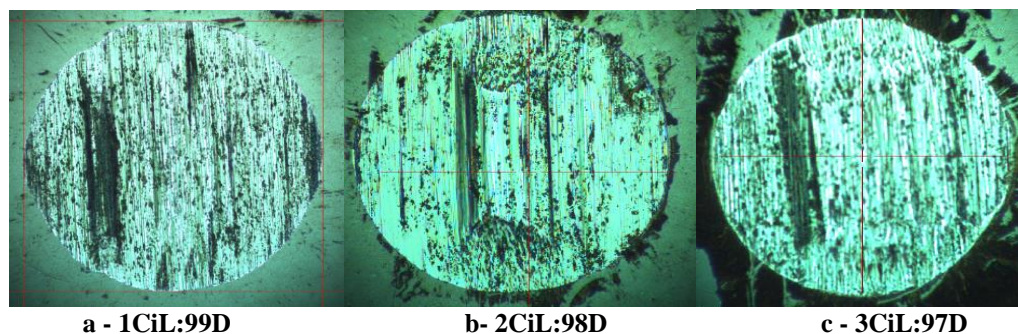


Fig.6. Wear scar diameters of diesel with cyclohexanol in the standard test for fuel and lubricant (HFRR)

Studies have shown that lubricity of unblended diesel fuel was high, $570\mu\text{m}$ and exceed the standard. All research second generation oxygenates mixtures with unblended diesel exceeds the standard too. The biggest lubricity was in the mixture unblended diesel with 3% cyclohexanol $627\mu\text{m}$. The mixtures lubricity WSD average is shown in Fig. 7. It was observed the increases of lubricity for mixtures unblended diesel with cyclohexanol and decreases with 1,4-dioxane.

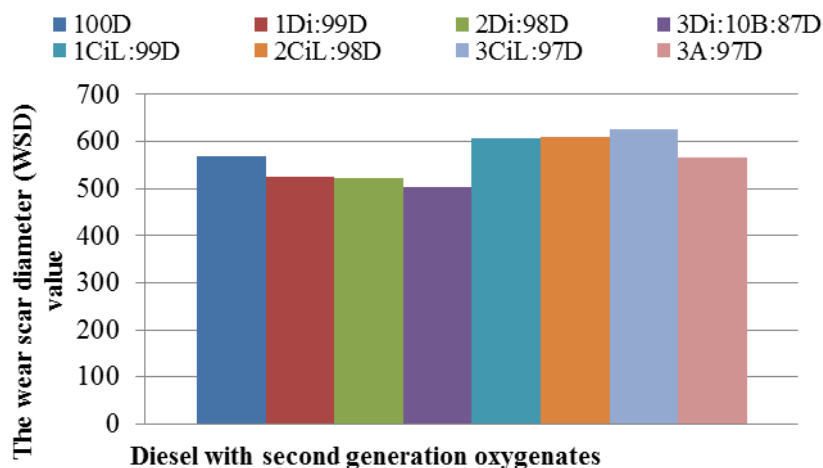


Fig.7.The lubricity of mixtures used in the research

The lubricity of marketable diesel was only $242\mu\text{m}$. The mixture of this marketable diesel with 3% cyclohexanol has lubricity of $355\mu\text{m}$ and it does not exceed the BS EN590:2014 standard as well.

The study of influence of cyclic oxygenates to properties of diesel fuel (density, kinematic viscosity, cold filter plugging point, heating value, thermal distillation, cetane number and cetane index of mixtures) shows that research oxygenates have the prospect of being used as additives for diesel fuels because of their physical and chemical properties. Moreover, these oxygenates are the by-products of various technological processes, therefore they can be used as secondary raw materials.

References

1. S. Heitzig, L. Leonhard, S. Drumm, H. Murrenhoff, J. Lang, G. Knoll, *Tribol.*, **2013**, 6, 17.
2. A. Fatemimoghari, Analysis of Tribological Properties for the Design of Synthetic Biofuels. *Shaker, Aachen*, **2012**, 129.
3. A. Weinebeck, H. Murrenhoff, *The 13th Scandinavian International Conference on Fluid Power, SICFP2013*, 3-5 June, Linköping, Sweden, **2013**, 345.



AMINO ACID IDENTIFICATION BY HILIC-MS/MS AND ENANTIOSELECTIVE DETERMINATION BY CHIRAL CHROMATOGRAPHY-MS/MS IN HYDROLYZED PROTEIN FERTILIZERS SAMPLES

L. Taujenis, V. Olšauskaitė, A. Padarauskas

*Department of Analytical and Environmental Chemistry, Vilnius University, Naugarduko 24,
LT-03225, Vilnius, Lithuania
E-mail: lukas.taujenis@chf.vu.lt*

Introduction

Increasing population demands effective and faster food production all over the world. Therefore macro and micronutrients, growth stimulants, inorganic, organic or amino acids based fertilizers are commonly used in agriculture. Amino acids are fundamental ingredients in protein biosynthesis and have strong influence in plants physiological activity. The use of amino acids during plant growth is a well-known method to increase crop yield and quality, beside that amino acids may form chelates with trace elements which can kill bacteria and insects and decrease amount of residual pesticides [1]. However, only L-amino acids can be effectively assimilated by plants and D-amino acids are not involved in enzymatic growth processes or might be even toxic in some cases [2].

Hydrolyzed protein fertilizers (HPF) are obtained by chemical or enzymatic hydrolysis of proteins from different origin and typically consists free amino acids, peptides and polypeptides [3]. The quality of HPF can be determined by total content of free and enantiomerically pure protein L-amino acids. Up to this date there were few articles that utilize determination of protein amino acids in HPF, but neither of them fully differentiates D/L-enantiomers [3, 4]. We suggest fast and reliable protein amino acids identification by hydrophilic interaction – tandem mass spectrometry (HILIC-MS/MS) and direct enantioselective separation followed by MS/MS determination methods for HPF analysis [5, 6].

Experimental

Chromatographic separations were performed using an Agilent 1290 Infinity LC system coupled with triple quadrupole 6410 tandem mass spectrometer equipped with an electrospray ionization (ESI) interface (Agilent Technologies, Santa Clara, CA). Three columns: 100 mm × 2.1 mm, i.d., 1.7 μm, Acquity BEH HILIC; 100 mm × 2.1 mm, i.d., 1.7 μm, Acquity BEH Amide; 100 mm × 2.1 mm, i.d., 3.0 μm, Atlantis HILIC were employed for HILIC

separations and 150 mm × 2.1 mm i.d., 5 μm, Astec CHIROBIOTIC T2 was used for enantioselective separation. Chromatographic and tandem MS conditions were set as described in [5, 6].

Results and discussions

HILIC separation

Three stationary phases were compared for amino acids separation in HILIC mode and BEH Amide column was selected for further optimization due to better resolution and lower peak tailing obtained with initial mobile phase. Next, various mobile phase additives were tested in terms of retention, resolution and MS signal response. Despite the fact that even under optimized conditions some acids (e.g., Asp and His) exhibits broad and tailing peaks, the obtained overall performance was adequate for identification purposes. In this study three acids (HCOOH, CH₃COOH and HCl) as additives to aqueous/acetonitrile 1:5 (v/v) extractant were briefly compared for the best extraction properties. Results showed that for the same samples acetic acid provided slightly higher peak areas for most of the analyzed amino acids. Developed method was applied to identify free protein amino acids in HPF samples. The results obtained are presented in Table 1.

Table 1. Analysis results of HPF samples. + is indicated if analyte was identified, N.D. – not detected.

Amino acid	Sample A	Sample B	Sample C	Sample B
Alanine	+	+	+	+
Arginine	+	+	+	+
Asparagine	+	N.D.	+	N.D.
Aspartic acid	+	+	N.D.	N.D.
Cysteine	N.D.	N.D.	N.D.	N.D.
Glycine	+	+	+	N.D.
Glutamine	+	N.D.	N.D.	N.D.
Glutamic acid	+	+	N.D.	N.D.
Histidine	+	+	+	+
Hydroxyproline	+	+	N.D.	N.D.
Isoleucine	+	+	+	+
Leucine	+	+	+	+
Lysine	+	+	+	+
Methionine	+	+	N.D.	N.D.
Phenylalanine	+	+	+	+
Proline	+	+	+	+
Serine	+	+	+	+
Threonine	+	+	+	+
Tyrosine	+	+	+	+
Tryptophan	+	+	+	+
Valine	+	+	+	+

Enantioselective separation

Several parameters such as nature and content of the organic modifier in the mobile phase, mobile phase pH and column temperature were tested in order to find the optimum conditions

allowing the highest enantiomeric resolution of the analytes. Three organic modifiers, namely acetonitrile, ethanol and methanol, were tested in current study. Methanol was chosen for further optimization due to its best performance. Ammonium acetate which exhibits adequate buffering capacity over the working pH range (3.8-6.8) of the stationary phase was employed for mobile phase pH adjustment. No significant effect on enantioselectivity within the pH range 4-6 was observed and only slightly better resolution was achieved at lower pH values.

Table 2. Determined Concentrations of the D- and L-Amino Acids in the Commercial HPF Samples (n = 3).

Analyte	Enantiomer	Determined amount, mg/g (\pm SD)				
		Sample A	Sample B	Sample C	Sample D	Sample E
Alanine	D-	N.D.	0.3 (0.1)	1.7 (0.2)	14.0 (0.3)	2.1 (0.3)
	L-	9.2 (0.2)	7.8 (0.7)	2.7 (0.3)	15.9 (0.4)	3.9 (0.3)
Arginine	D-	N.D.	N.D.	N.D.	N.D.	N.D.
	L-	7.1 (1.4)	9.5 (1.7)	0.82 (0.01)	1.1 (0.1)	1.2 (0.3)
Asparagine	D-	N.D.	N.D.	N.D.	N.D.	N.D.
	L-	1.9 (0.5)	1.8 (0.4)	0.07 (0.02)	N.D.	N.D.
Aspartic acid	D-/L-	10.9 (0.8)	14.9 (0.5)	0.25 (0.05)	12.5 (1.5)	N.D.
Cysteine	D-	N.D.	N.D.	N.D.	N.D.	N.D.
	L-	N.D.	N.D.	N.D.	N.D.	N.D.
Glutamic acid	D-/L-	151.6 (5.5)	34.4 (5.0)	0.50 (0.1)	11.5 (0.6)	31.9 (1.5)
Glutamine	D-	N.D.	N.D.	N.D.	N.D.	N.D.
	L-	0.6 (0.1)	2.8 (0.5)	0.05 (0.02)	N.D.	1.72 (0.5)
Glycine	-	18.8 (0.6)	38.0 (5.0)	5.3 (0.2)	68.2 (5.0)	11.2 (1.5)
Histidine	D-/L-	5.7 (0.3)	9.3 (2.0)	0.30 (0.05)	2.6 (0.1)	1.49 (0.2)
Leucine/Isoleucine	D-	N.D.	N.D.	N.D.	5.5 (0.5)	0.55 (0.1)
	L-	3.4 (0.7)	2.7 (0.2)	0.63 (0.04)	2.0 (0.1)	0.49 (0.05)
Lysine	D-	N.D.	N.D.	N.D.	5.8 (0.5)	N.D.
	L-	27.7 (0.9)	24.8 (1.3)	0.52 (0.01)	6.1 (1.0)	2.4 (0.4)
Methionine	D-	N.D.	N.D.	N.D.	0.62 (0.1)	N.D.
	L-	0.4 (0.1)	0.4 (0.1)	0.25 (0.1)	0.63 (0.1)	0.4 (0.2)
Phenylalanine	D-	N.D.	0.6 (0.1)	0.03 (0.01)	1.5 (0.1)	0.35 (0.1)
	L-	4.3 (0.4)	4.6 (0.1)	0.37 (0.1)	1.7 (0.1)	0.68 (0.2)
Proline	D-	1.0 (0.2)	2.1 (0.3)	0.18 (0.03)	10.8 (0.3)	1.6 (0.3)
	L-	5.9 (1.0)	6.6 (1.0)	0.18 (0.04)	11.4 (0.2)	1.9 (0.3)
Serine	D-	N.D.	N.D.	N.D.	1.5 (0.2)	N.D.
	L-	8.6 (0.1)	7.3 (1.6)	0.24 (0.1)	0.56 (0.05)	2.0 (0.2)
Threonine	D-	N.D.	N.D.	N.D.	N.D.	N.D.
	L-	7.7 (0.1)	7.9 (0.4)	0.8 (0.3)	N.D.	0.6 (0.1)
Tryptophan	D-	N.D.	N.D.	N.D.	N.D.	N.D.
	L-	1.4 (0.4)	1.4 (0.5)	0.07 (0.01)	ND	0.25 (0.03)
Tyrosine	D-	N.D.	N.D.	N.D.	0.80 (0.1)	N.D.
	L-	3.0 (0.4)	3.0 (0.4)	0.20 (0.03)	1.7 (0.1)	0.70 (0.1)
Valine	D-	N.D.	N.D.	0.02 (0.01)	1.1 (0.1)	0.03 (0.01)
	L-	2.0 (0.3)	7.7 (0.4)	0.61 (0.1)	1.6 (0.2)	0.42 (0.01)

From the temperature dependence obtained in gradient elution mode it was observed that for most amino acids at the lower temperature the resolution of the enantiomers increases. Such behavior can be attributed to steric interactions on teicoplanin CSP that plays important role in enantio-recognition mechanism. Complete enantioseparation of 15 D/L-amino acids enantiomer pairs was achieved in about 15 min. D/L-Glu and D/L-Asp pairs were partially resolved and only for D/L-His enantiomers no resolution was obtained. Proposed method was validated in terms of linearity, limits of detection (LOD) and limits of quantitation (LOQ), accuracy and precision. Five commercially available HPF samples were analyzed under optimized HPLC-MS/MS conditions.

Determined concentrations of the individual amino acid enantiomers are summarized in Table 2. The majority of the amino acids in sample C most likely exist in bonded form. Samples A and B had the highest enantiomeric purity, whereas in the sample D at least one fourth of the total amino acids amount was the D-enantiomer.

References

1. M. Jie, W. Raza, Y. C. Xu, *J. Plant Nutr.*, 31 (2008) 571-582.
2. H. Svennerstam, U. Ganeteg, C. Bellini, T. Näsholm, *Plant Physiol.*, 143 (2007) 1853-1860
3. L. Sanchez-Hernandez, N. S. Serra, A. L. Crego, *J. Agric. Food Chem.*, 61 (2013) 5022-5030.
4. M. I. Alarcón-Flores, R. Romero-González, A. G. Frenich, J. L. M. Vidal, R. C. Reyes, *Anal. Methods*, 2 (2010) 1745-1751.
5. L. Taujenis, V. Olšauskaitė, I. Valasnavičiūtė, A. Padarauskas, *Chemija*, 25 (2014) 101-106.
6. L. Taujenis, V. Olšauskaitė, A. Padarauskas, *J. Agric. Food Chem.*, 62 (2014) 11099-1108.



APPLICATION OF BIO- AND SYNTHETIC MATERIALS FOR ^{137}Cs SORPTION FROM AQUEOUS MEDIUM

Z. Žukauskaitė¹, B. Lukšienė¹, N. Tarasiuk¹, E. Maceika¹, S. Tautkus²

1 A State Research Institute Center for Physical Sciences and Technology, Savanorių ave. 231, LT-02300 Vilnius, Lithuania

2 Vilnius University, Faculty of Chemistry, Naugarduko st. 24, LT-03225 Vilnius, Lithuania

E-mail: zita9458@gmail.com

Artificial radioactive contaminants can spread in the environment as a result of nuclear weapon tests, nuclear accidents such as the Chernobyl nuclear power plant (NPP) accident in 1986, the Fukushima NPP accident in 2011 or unauthorized releases. ^{137}Cs is one of the main and common radionuclides, which is formed mainly as a nuclear fission product. ^{137}Cs with a half-life of 30.17 years undergoes radioactive decay with the emission of beta particles and relatively strong gamma radiation [1]. From the point of view of the radiological safety, cesium (^{137}Cs) is a major radioactive isotope because of its relatively long half-life, high solubility and transferability [2, 3]. Water systems are vulnerable to contamination accidents and bioterrorism attacks because they are relatively unprotected, accessible, and often isolated [4]. The sorption of radionuclides and heavy metals from aquatic systems has been studied, using both batch and column approaches. A wide range of materials have been evaluated for the sorption of heavy metals and radionuclides [4, 5]. Literature survey reveals that a wide spectrum of studies has been carried out for the removal of cesium (I) by using different methods such as precipitation, extraction, ion exchange, adsorption, bioaccumulation and electric-field-assisted techniques [4].

The main aim of this study was to investigate some kind of bio- and synthetic materials considering them as promising alternatives to commercial sorbents and to determine the uptake behavior of $^{137}\text{Cs}^+$ from aqueous solution similar to the radionuclide-bearing fresh water systems.

Laboratory-scale sorption experiments were conducted in the glass columns (i.d. 3 cm, length 40 cm). The influencing factors of $^{137}\text{Cs}^+$ sorption on different materials, including the contact time, an initial pH value, the initial $^{137}\text{Cs}^+$ concentration, the sorbent dosage and the flow rate, were studied.

Glass columns were filled with bio- and synthetic sorbents, such as moss, lichens, the filter material AFA-RMP-20 and the granular activated carbon. The lake water was spiked with ^{137}Cs to the concentration of $1\text{Bq}\cdot\text{L}^{-1}$, pH was kept at 6, and put into the column at a flow rate of $3.2\text{ mL}\cdot\text{min}^{-1}$. The sorption efficiencies were calculated from the amount of a radionuclide retained by the sorbent, which was determined by instrumental gamma-spectrometric analysis. The ^{137}Cs was most effectively accumulated by moss (27%) under applied conditions. The other studied sorbents can be ranked as follows: lichens (25%)<filter material (10%)<activated carbon (8%).

The sorption reversibility was tested by means of desorption experiments. Desorption experiments of the radiocesium sorbed onto moss and lichens by distilled water (solid:solution ratio 1: 4.5) were carried out. The flasks were agitated at a constant speed of 100 rpm for 20h. The supernatant was evaporated, the ^{137}Cs activity was measured and compared with that in



mosses where desorption was not done. Experimental results showed that the ^{137}Cs washed out from mosses and lichens amounted to 35.5 % and 18.7 %, respectively.

The process of desorption was also analyzed by installing two larger columns (i.d. 40 cm, length 70 cm) *in situ* on the shore of Lake Akmena. Columns were filled with dry moss (0.0952 kg), containing the ^{137}Cs activity concentration of 40.9 ± 1.6 Bq/kg. The lake water of 300 L volume was passed through the moss in one column within 100 min and in the another - within 200 min. After the 100 min the wash-out of ^{137}Cs (35.5%) was equal to that as in a case when the agitation of a sample was performed for 20 hours. A longer water-moss contact time during *in situ* experiments influenced a higher wash-out of ^{137}Cs (68.7%).

Sorption-desorption experimental results have shown that bio-sorbents and synthetic materials investigated in this study are not completely suitable sorbents for the radiocesium removal from aqueous media under studied conditions. Consequently, additional experiments, including sorbent modification, are foreseen.

This research was funded by a grant (No. MIP-041/2012) from the Research Council of Lithuania.

References

1. R. Yavari, Y.D. Huang, S.J. Ahmadi, J. Radioanal. Nucl. Chem., **287** (2010) 393-401.
2. Y. Chen, J. Wang, Nucl. Eng. Design., **242** (2012) 445– 451.
3. Y.J. Park, Y.C. Lee, W.S. Shin, S.J. Choi, Chem. Eng. J., **162** (2010) 685–695.
4. Li Ping, Yin Zhuoxin, Lin Jianfeng, Jin Qiang, Du Yaofang, Fan Qiaohui, Wu Wangsuo, Environ. Sci.: Proc. Imp., **16** (2014) 2278–2287.
5. F.E. Soetaredjo, A. Kurniawan, L.K. Ong, D.R. Widagdyo, S. Ismadji, RSC Adv., **4**, (2014) 52856–52870.



Vilnius University, Faculty of Chemistry,
Naugarduko 24, Vilnius, Lithuania
January 23, 2015

Poster presentations

Physical Chemistry



SYNTHESIS, CHARACTERIZATION AND PROPERTIES OF Pt-Ru-Co/Ti CATALYST

K. Antanavičiūtė, L. Tamašauskaitė-Tamašiūnaitė, E. Norkus

Center for Physical Sciences and Technology, A. Goštauto 9, LT-01108 Vilnius, Lithuania

E-mail: kornelija.antanaviciute@gmail.com

Introduction

Fuel cells are energy source, which generates electric power without any mechanical link. It is a great alternative for limited sources of fossil fuel. Fuel cells are very appealing because they are small and work in low temperatures. Also fuel cells are clean energy sources therefore during the energy making process only water and heat are produced. Sodium borohydride (NaBH_4) and small mass organic materials, such as methanol (CH_3OH), can be used as fuel. Since the sodium borohydride and methanol are used as fuel it is aimed to make active catalysts for sodium borohydride and methanol oxidation.

It is known that platinum (Pt) is a very efficient catalyst but its usage is limited by big price and lack of platinum. Platinum combination with other metals such as cobalt (Co) and ruthenium (Ru) is solution for minimizing the cost of catalyst. Bimetallic catalysts have better catalytic properties than pure metals. Also bimetallic catalysts are more stable and active than monometallic ones.

In the present study preparation of the Pt-Co, Ru-Co and Pt-Ru-Co catalysts, deposited onto the titanium surface (denoted as Pt-Co/Ti, Ru-Co/Ti and Pt-Ru-Co/Ti), using simple and cost-effective chemical methods: electroless Co deposition followed by a spontaneous Pt, Ru or Pt-Ru displacement from the platinum-, ruthenium- or platinum-ruthenium-containing solutions, respectively, is presented. The morphology, structure and composition of the prepared catalysts were examined by means of Field Emission Scanning Electron Microscopy (FESEM) and Inductively Coupled Plasma Optical Emission Spectroscopy (ICP-OES). Electrocatalytic activity of the Pt-Co/Ti, Ru-Co/Ti and Pt-Ru-Co/Ti catalysts towards the oxidation of methanol and sodium borohydride was investigated by means of cyclic voltammetry.

Experimental

Cobalt underlayer was deposited on the titanium foil (97% purity) using autocatalytic Co(II) ion reduction. Sodium hypophosphite ($\text{NaH}_2\text{PO}_2 \cdot \text{H}_2\text{O}$) was used as a reducing agent. At first, the Ti sheets (1 cm x 1 cm) were cleaned with acetone and distilled water and activated according to the following procedures: 1) the Ti sheets were immersed in 8.3 g l^{-1} SnCl_2 solution at 25°C for 1 min, 2) rinsed with distilled water, 3) then the Ti sheets were immersed in a 0.5 g l^{-1} PdCl_2 solution at 25°C for 1 min, 4) rinsed with distilled water. The activated Ti electrodes were immersed in the electroless cobalt plating solution at 80°C for 15 min. Composition of cobalt plating solution (M) is: $\text{CoSO}_4 - 0.1$; $\text{NH}_2\text{CH}_2\text{COOH} - 0.6$; $\text{NaH}_2\text{PO}_2 - 0.3$; $\text{C}_4\text{H}_6\text{O}_4 - 0.3$; $\text{pH}=9$.

The Pt-Ru-Co/Ti catalysts were prepared by immersion of the prepared Co/Ti electrodes in the 1 mM H_2PtCl_6 , 5 mM RuCl_3 and 0.1 M HCl solution at 25°C for 15 min. The Ru-Co/Ti catalysts were prepared by immersion of the Co/Ti electrodes in the 5 mM RuCl_3 and 0.1 M HCl solution at 25°C for 15 min, and the Pt-Co/Ti catalysts were prepared by immersion of Co/Ti in the 1 mM H_2PtCl_6 and 0.1 M HCl solution at 25°C for 15 min.

The morphology and composition of the fabricated catalysts were characterized using a SEM/FIB workstation Helios Nanolab 650 with an energy dispersive X-ray (EDX) spectrometer INCA Energy 350 X-Max 20.

Electrochemical measurements were made with a Zennium electrochemical workstation (ZAHNER-Elektrik GmbH & Co.KG). Pt-Ru-Co/Ti, Ru-Co/Ti and Pt-Co/Ti electrodes with a geometric area of 2 cm² were used as working electrode, Pt sheet was used as a counter electrode and Ag/AgCl/KCl electrode was used as reference electrode. Standard 80 ml three electrodes cell, which is adapted for deaeration, was used for electrochemical measurements.

Results and discussion

The Pt-Co, Ru-Co and Pt-Ru-Co catalysts were deposited onto the titanium surface using simple and cost-effective chemical methods: electroless Co deposition followed by a spontaneous Pt, Ru or Pt-Ru displacement from the platinum-, ruthenium- or platinum-ruthenium-containing solutions, respectively. Figure 1 shows FESEM images of the Co/Ti (a), Pt-Co/Ti (b), Ru-Co/Ti (c and e) and Pt-Ru-Co/Ti (d and f) catalysts. Table 1 presents data obtained from FESEM and ICP-OES analysis of the investigated catalysts.

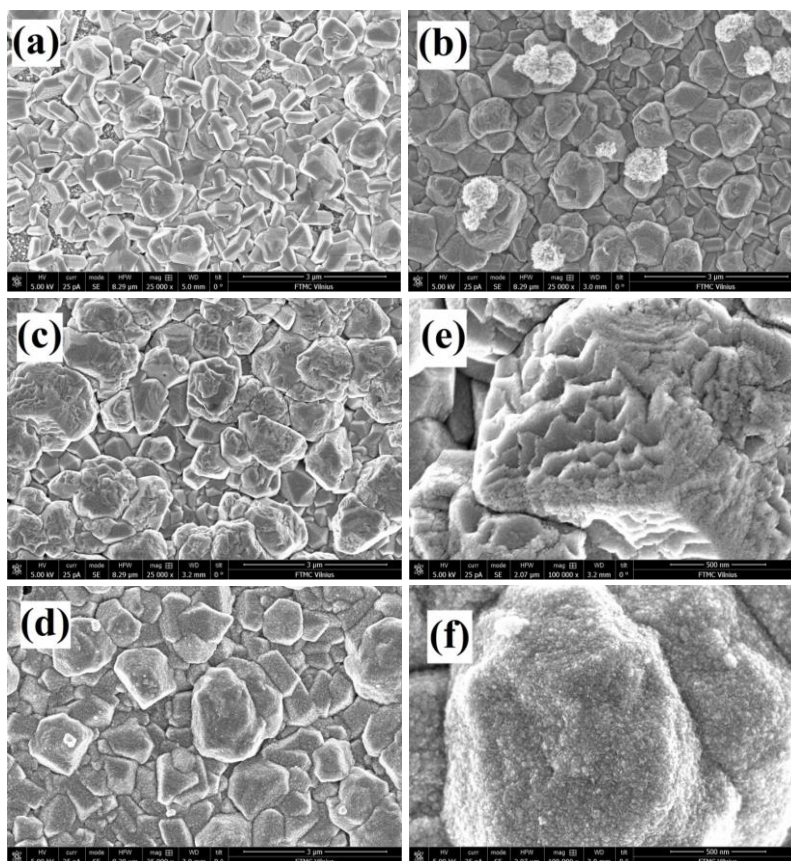


Fig. 1. FESEM images of the Co/Ti (a), Pt-Co/Ti (b), Ru-Co/Ti (c and e) and Pt-Ru-Co/Ti (d and f) catalysts surfaces.

As evident from Fig. 1a, electroless Co deposited onto the titanium surface produced a layer of polycrystalline Co with the average size of crystallites ca. 470-950 nm. The thickness of the electroless Co layer was ca. 1 μ m. Immersion of Co/Ti in the platinum-containing solution for 15 min results in the formation on the Co surface of Pt flowerlike structure. The

Pt nanoflowers are not spherical and consist of a large number of spearlike nanorods of size ca. 420-840 nm which are bonded to each other to form bigger secondary 3D flowerlike architectures. It was found that after immersion of Co/Ti in the ruthenium-containing solution for 15 min, Ru crystallites in size of 50-90 nm were deposited on the Co/Ti surface. Immersion of Co/Ti in the platinum-ruthenium-containing solution for 15 min results in deposition of Pt and Ru crystallites in size of 30-260 nm on the Co/Ti surface.

The Pt loadings of the as-prepared catalysts were analyzed by means of ICP-OES. It has been determined that the Pt loading was $92 \mu\text{g cm}^{-2}$ in the Pt-Co/Ti catalyst. The Pt and Ru loadings were 85 and $38 \mu\text{g cm}^{-2}$ in the Pt-Ru-Co/Ti catalyst. The Ru loading was $4 \mu\text{g cm}^{-2}$ in the Ru-Co/Ti catalyst.

The electrochemical behavior of the Pt-Ru-Co/Ti, Pt-Co/Ti and Ru-Co/Ti catalysts towards the oxidation of methanol (Fig. 2) and sodium borohydride (Fig. 3) was evaluated in alkaline medium using cyclic voltammetry. Figure 2 presents CVs of Pt-Ru-Co/Ti (a), Ru-Co/Ti (b) and Pt-Co/Ti (c) in a 1 M NaOH solution containing 1 M CH₃OH at 50 mV s^{-1} .

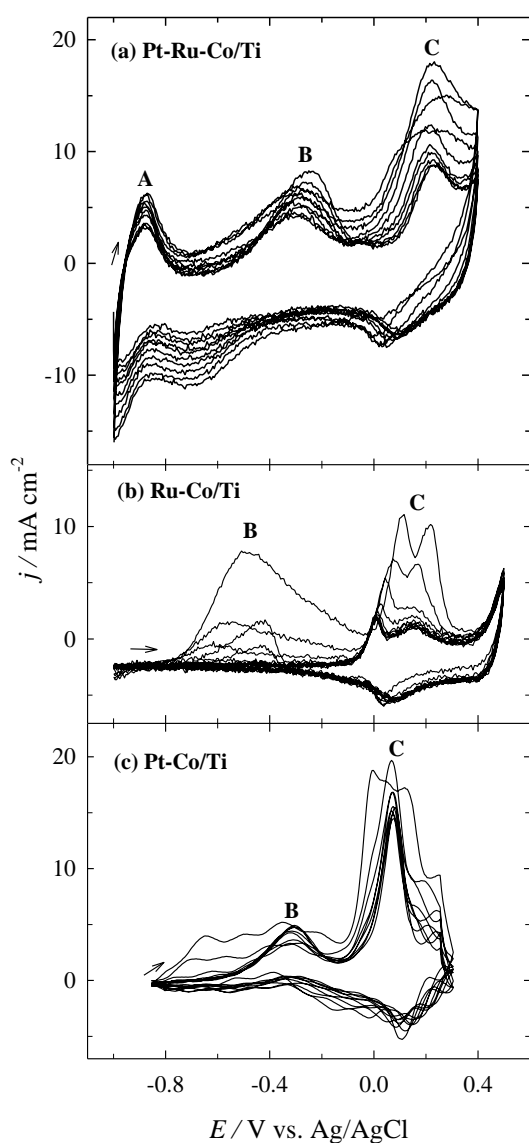


Fig. 2. CVs for Pt-Ru-Co/Ti, Ru-Co/Ti and Pt-Co/Ti catalysts recorded in 1 M NaOH + 1 M CH₃OH at a sweep rate of 50 mV s^{-1} .

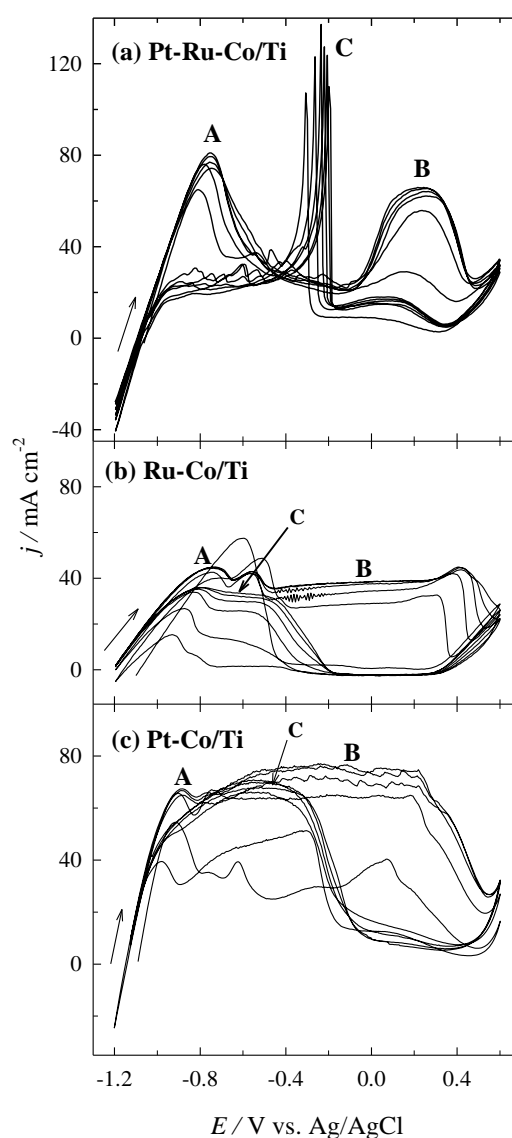


Fig. 3. CV for Pt-Ru-Co/Ti, Ru-Co/Ti and Pt-Co/Ti catalysts recorded in 1 M NaOH + 0.05 M NaBH₄ at a sweep rate of 10 mV s^{-1} .

As shown in Fig. 2, methanol oxidation on the investigated catalysts occurs differently. When Pt-Ru-Co/Ti catalyst is used (Fig. 2 a), three anodic peaks **A** at -0.860V, **B** at -0.250V and **C** at 0.220V are seen in the CVs plots. In the case of the Ru-Co/Ti catalyst (Fig. 2 b), two anodic peaks **B** at -0.1V and **C** at 0.1V are seen in the CVs plots. When Pt-Co/Ti catalyst is used (Fig. 2 c), two anodic peaks **B** at -0.3V and **C** at 0.1 are seen in the CVs plots. Anodic peaks were attributed to direct methanol oxidation on the investigated Pt-Ru-Co/Ti, Pt-Co/Ti and Ru-Co/Ti catalysts. During long-term cycling, the methanol oxidation current densities recorded on the Pt-Ru-Co/Ti and Pt-Co/Ti (Fig. 2a, c) stabilizes, while the methanol oxidation current densities recorded on the Ru-Co/Ti catalyst decreases. The Pt-Ru-Co and Pt-Co/Ti catalysts show higher activity and stability towards methanol oxidation as compared with those at the Ru-Co/Ti catalyst.

Figure 3 presents CVs of Pt-Ru-Co/Ti (a), Ru-Co/Ti (b) and Pt-Co/Ti (c) in 1 M NaOH solution containing 0.05 M NaBH₄ at 10 mV s⁻¹. As shown in Fig. 3, two anodic peaks **A** and **B** are seen in the CV plots recorded at Pt-Ru-Co/Ti, Ru-Co/Ti and Pt-Co/Ti. Anodic peak **A** is attributed to the oxidation of H₂ generated by catalytic hydrolysis of BH₄⁻ and peak **B** is related with direct oxidation of BH₄⁻ ions (Fig. 3). Borohydride oxidation current densities of peak **A** are ca. 1.2 and 1.8 times higher at Pt-Ru-Co/Ti than those at Pt-Co/Ti and Ru-Co/Ti, respectively. Current densities of peak **B** are ca. 1.2 and 1.9 times higher at Pt-Co/Ti as compared with those at Ru-Co/Ti and Pt-Ru-Co/Ti.

During long-term cycling borohydride oxidation current densities are stabilized, indicating high stability and efficiency of the investigated catalysts.

Conclusions

In this study a simple and cost-effective chemical methods: electroless Co deposition followed by a spontaneous Pt, Ru or Pt-Ru displacement from the platinum-, ruthenium- and platinum-ruthenium-containing solutions were used to prepare Pt-Co, Ru-Co and Pt-Ru-Co catalysts deposited onto Ti surface. It was found that immersion of Co/Ti in the platinum-containing solution for 15 min results in the formation on the Co surface of Pt flowerlike structure. The Pt nanoflowers are not spherical and consist of a large number of spearlike nanorods of size ca. 420-840 nm which are bonded to each other to form bigger secondary 3D flowerlike architectures. After immersion of Co/Ti in the ruthenium-containing solution for 15 min, Ru crystallites in size of 50-90 nm were deposited on the Co/Ti surface, while immersion of Co/Ti in the platinum-ruthenium-containing solution for 15 min results in deposition of Pt and Ru crystallites in size of 50-260 and 30 nm, respectively, on the Co/Ti surface.

It has been determined that the Pt-Ru-Co/Ti and Pt-Co/Ti catalysts exhibited an enhanced electrocatalytic activity towards methanol and sodium borohydride oxidation as compared to that of Ru-Co/Ti.

Acknowledgment

This research was funded by a grant (No. ATE-08/2012) from the Research Council of Lithuania.

BOROHYDRIDE OXIDATION ON GOLD-GRAPHENE MODIFIED TITANIA NANOTUBES

A. Balčiūnaitė, L. Tamašauskaitė-Tamašiūnaitė, E. Norkus

Center for Physical Sciences and Technology, A. Goštauto 9, LT-01108, Vilnius, Lithuania

E-mail: balciunaite.aldona@gmail.com

Introduction

Fuel cells are actively investigated as an attractive energy sources for cleaner power generation. One type of alkaline fuel cells - direct borohydride fuel cells (DBFC) are being developed for portable power supply. Since borohydride is used as fuel, the development of catalyst having reasonable costs and a high activity towards the oxidation of borohydride is industrially vital.

This work is focused on the fabrication of gold-graphene modified titania nanotube arrays as electrocatalysts for the oxidation of borohydride in an alkaline medium. The graphene modified titania nanotubes were obtained through in situ electrochemical reduction of a graphene oxide dispersion by cyclic voltammetry followed by electroplating of gold nanoparticles. The morphology, structure and composition of the prepared catalysts were examined by means of Field Emission Scanning Electron Microscopy and Inductively Coupled Plasma Optical Emission Spectroscopy. Evaluation of electrocatalytic activity of gold-graphene/titania nanotubes towards oxidation of borohydride was carried out by means of cyclic voltammetry and chronoamperometry.

Experimental

Self-ordered TiO₂ nanotube arrays in the present work were formed onto the Ti substrates by means of anodic oxidation. Briefly, prior to anodization, the 1 x 1 cm titanium sheets were degreased with ethanol, rinsed with deionized water and dried in an Ar stream. Titanium sheets were anodized in a 0.24 M H₂SO₄ solution containing 0.5 wt.% NH₄F at a constant potential of 20 V and room temperature for 1 h. The counter electrodes were two sheets of Pt. After anodization, the prepared TiO₂-NTs samples were rinsed thoroughly with deionized water and annealed at 500 °C for 3 h.

Deposition of a graphene film on the surface of TiO₂-NTs was carried out via in situ electrochemical reduction of graphene oxide (GO) dispersion (0.25 mg mL⁻¹, Graphene-Supermarket) by cyclic voltammetry. Au crystallites were electrodeposited on the TiO₂-NTs and GO/TiO₂-NTs electrodes in 1 mM HAuCl₄ + 0.1 M HCl (25 °C) at $j = 5 \text{ mA cm}^{-2}$, $t = 5 \text{ min}$.

The morphology and composition of the fabricated catalysts were characterized using a SEM/FIB workstation Helios Nanolab 650 with an energy dispersive X-ray (EDX) spectrometer INCA Energy 350 X-Max 20.

The Au metal loading was estimated from ICP-OES measurements. The ICP optical emission spectra were recorded using an ICP optical emission spectrometer Optima 7000DV (Perkin Elmer).

Results and discussion

TiO₂ nanotube arrays (Fig. 1a) in this study were prepared by anodic oxidation of Ti surface in an aqueous sulfuric acid solution containing some NH₄F and annealed at 500 °C for 3 h. The average tube diameter was ca. 100 nm and the thickness of titania layers was ca. 350 nm.

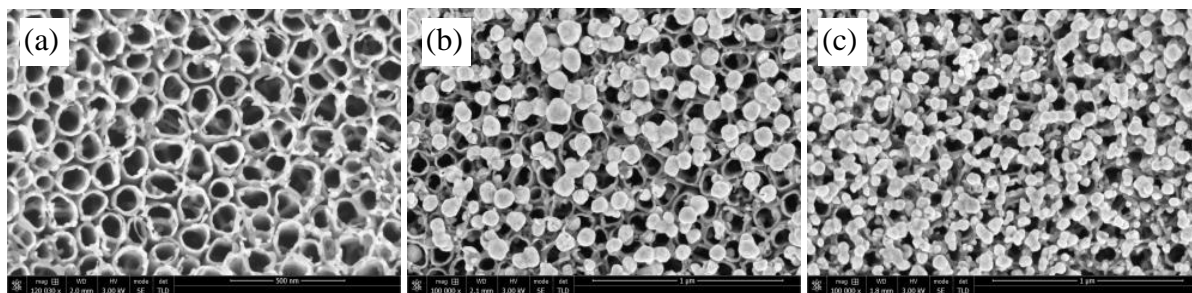


Fig. 1. FESEM images of: TiO₂-NTs (a), Au/TiO₂-NTs (b) and Au-GO/TiO₂-NTs (c). Au crystallites were electrodeposited on TiO₂-NTs and GO/TiO₂-NTs in the 1 mM HAuCl₄ solution (25 °C) at 5 mA cm⁻² for 5 min.

Deposition of a graphene film on the surface of TiO₂-NTs was carried out via in situ electrochemical reduction of graphene oxide dispersion by cyclic voltammetry and is presented in Fig. 2a.

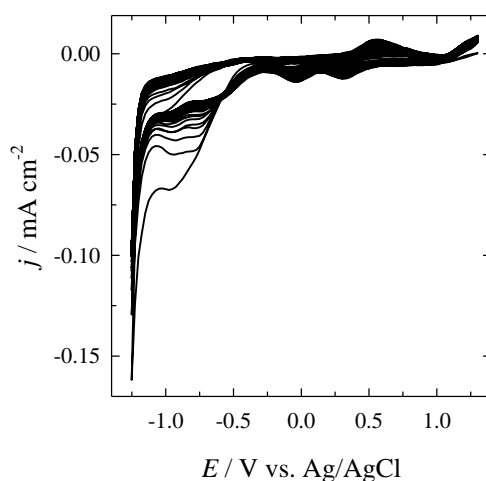


Fig. 2. Typical CVs of TiO₂-NTs recorded in the 0.25 mg mL⁻¹ GO in 0.1 M Na₂B₄O₇ (pH 9.18) solution at 50 mV s⁻¹.

Au crystallites were electrodeposited on the TiO₂-NTs and GO/TiO₂-NTs electrodes in 1 mM HAuCl₄ + 0.1 M HCl (25 °C) at $j = 5 \text{ mA cm}^{-2}$, $t = 5 \text{ min}$. Au crystallites in size of ca. 30-130 and 15-100 nm in size were electrodeposited on the TiO₂-NTs (Fig. 1b) and GO/TiO₂-NTs electrodes (Fig. 1c), respectively.

The Au loading in the fabricated catalysts was estimated using ICP-OES. It has been determined that the Au loadings were 73 $\mu\text{g Au cm}^{-2}$ Au/TiO₂-NTs and 65 $\mu\text{g Au cm}^{-2}$ for Au-GO/TiO₂-NTs.

The electrochemically active areas of Au surface created on the fabricated catalysts were determined from the cyclic voltammograms of the Au/TiO₂-NTs and Au-GO/TiO₂-NTs catalysts recorded in a deaerated 5 mM K₃Fe(CN)₆ + 1 M KCl solution at a scan rate of 50 mV s⁻¹ (Fig. 3). The calculated value of electrochemical surface area (ESA) was 0.15 cm² for Au/TiO₂-NTs and 0.81 cm² for Au-GO/TiO₂-NTs. It has been determined that ESA value of the Au-GO/TiO₂-NTs catalyst is 5.4 times higher than that of the Au/TiO₂-NTs catalyst.

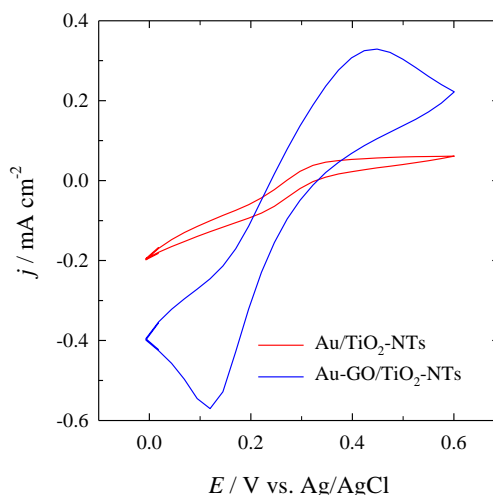


Fig. 3. Cyclic voltammograms for Au/TiO₂-NTs (red line) and Au-GO/TiO₂-NTs (blue line) recorded in a deaerated 5 mM K₃Fe(CN)₆ + 1 M KCl solution at 50 mV s⁻¹.

Figure 4a presents the oxidation of borohydride on the Au/TiO₂-NTs and Au-GO/TiO₂-NTs catalysts. It was found that Au-GO/TiO₂-NTs exhibited an enhanced electrocatalytic activity towards the anodic oxidation of BH₄⁻ comparing with unmodified TiO₂-NTs (Fig. 4a', the inset) and that modified with Au nanoparticles (Au/TiO₂-NTs). Borohydride oxidation current densities are ca. 5 times higher at the Au-GO/TiO₂-NTs catalyst as compared to those at Au/TiO₂-NTs.

Mass activity of borohydride oxidation is ca. 6 times higher at the Au-GO/TiO₂-NTs catalyst than that at Au/TiO₂-NTs (Fig. 4b).

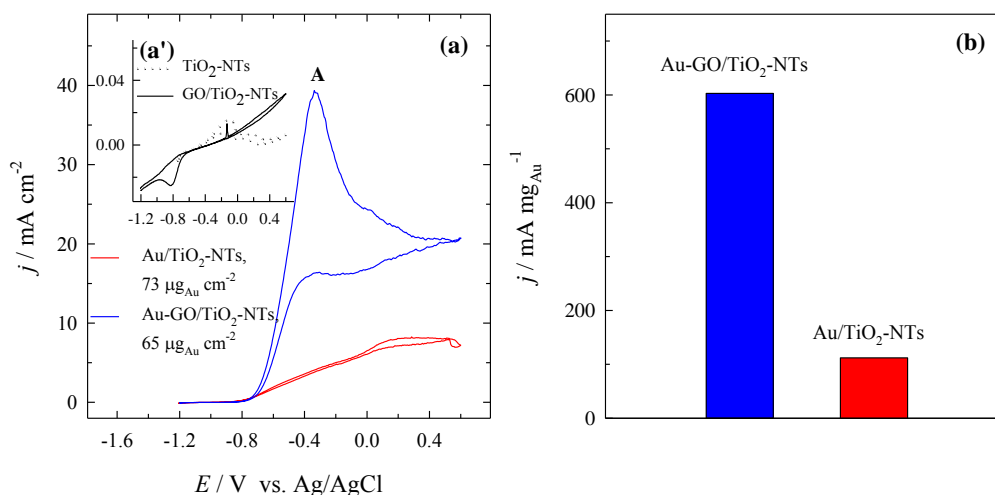


Fig. 4. Cyclic voltammograms for Au/TiO₂-NTs (red line) and Au-GO/TiO₂-NTs (blue line) (a); TiO₂-NTs (dotted line) and GO/TiO₂-NTs (solid line) (the inset, a') recorded in 0.05 M NaBH₄ + 1 M NaOH at 10 mV s⁻¹. (b) Current densities normalized by the Au loadings for the same catalysts.

The performance of different catalysts for the oxidation of BH₄⁻ ions can be further observed from chronoamperometric measurements. The chronoamperometric curves are shown in Fig. 5a. Current densities are ca. 3.8 times higher at the Au-GO/TiO₂-NTs catalyst as compared to those at Au/TiO₂-NTs. (Fig. 5a). Data in Fig. 5b presents the mass activity of investigated catalysts under chronoamperometric conditions. Mass activity is ca. 4.3 times higher at the Au-GO/TiO₂-NTs catalyst than that at Au/TiO₂-NTs (Fig. 5b).

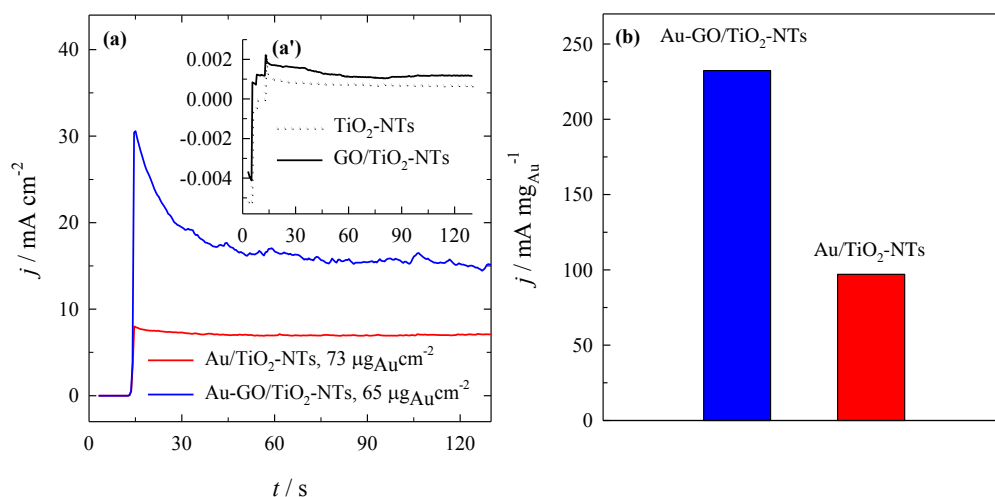


Fig. 5. Chronoamperometric curves for: Au/TiO₂-NTs (red line) and Au-GO/TiO₂-NTs (blue line) (a); TiO₂-NTs (dotted line) and GO/TiO₂-NTs (solid line) (the inset, a') catalysts recorded in 0.05 M NaBH₄ + 1 M NaOH. The potential was firstly held at open circuit for 10 s, then set to -0.1 V for 2 min. (b) Current densities normalized by the Au loadings for each catalyst.

Conclusions

Gold-graphene oxide modified TiO₂-NTs were prepared by a simple approach, e.g., anodization of Ti sheets in an aqueous sulfuric acid solution containing some NH₄F followed by annealing of prepared TiO₂-NTs at 500 °C for 3 h and deposition of a graphene oxide film on the surface of TiO₂-NTs via in situ electrochemical reduction of a graphene oxide dispersion by cyclic voltammetry and electrochemical deposition of Au crystallites on GO/TiO₂-NTs.

It was found that Au-GO/TiO₂-NTs exhibited an enhanced electrocatalytic activity towards the anodic oxidation of BH₄⁻ comparing with unmodified TiO₂-NTs and that modified with Au nanoparticles (Au/TiO₂-NTs). Borohydride oxidation current densities are ca. 5 times higher at the Au-GO/TiO₂-NTs catalyst as compared to Au/TiO₂-NTs. Mass activity of borohydride oxidation is ca. 6 times higher at the Au-GO/TiO₂-NTs catalyst than that at Au/TiO₂-NTs.

Gold-graphene modified titanium dioxide nanotube arrays seems to be a promising anode material for direct borohydride fuel cells.

Acknowledgment

This research was funded by a Grant (No. ATE-08/2012) from the Research Council of Lithuania.

INFLUENCE OF CHEMICAL ELEMENTS ON PROPERTIES OF RARE GARNETS MINERALS

I. Balčiūnaitė¹, A. Kleišmantas², E. Norkus¹

¹*Department of Catalysis, Institute of Chemistry, Center for Physical Sciences and
Technology, A. Goštauto 9, LT-01108 Vilnius, Lithuania,*

²*Department of Geology and Mineralogy, Faculty of Natural Sciences, Vilnius University,
M.K. Čiurlionio 21/27, LT-03101, Vilnius, Lithuania,
irenabalciunaite@yahoo.de*

INTRODUCTION

Garnets are a very broad group of minerals characterized by a variety of chemical elements and colours. Garnet has been a popular gemstone for thousands of years due to its many colours, its hardness, its commonality, and its luster.

Usual garnets are characterized by a warm and deep red colour. However, other colours of garnets are of increasing interest. The most highly valued are those of shiny green, attractive yellow, pink and colourless colours. The variety of colours depends on the chemical elements.

EXPERIMENTAL

Chemical analysis of the garnet group minerals was performed with the scanning electronic microscope “Quanta 250/450/650“, using an apparatus for coating the samples with metals “Emitech SC7620 Mini Sputter Coater” with CA7625 attachment for carbon coating.

RESULTS AND DISCUSSIONS

Rainbow garnet is called in this way because its surface glows like a rainbow. Having carried out the research of the amount of chemical elements it was found that in rainbow garnet aluminium oxide content varies from 1.71 to 3.64 %, silica oxide from 39.51 to 41.71 %, calcium oxide from 32.19 to 32.95 %, iron oxide from 23.49 to 24.91 %, manganese oxide from 0.24 to 0.32 %. These differences in the chemical composition determine difference in colour, and the multi – colourfulness of the rainbow garnet should depend on the surface reflectivity, i.e., irisation.

Demantoid is a variety of andradite. It is characterised by diamond luster, which gave it name in the nineteenth century. The colour varies from cold, very pale green to a mid or strong green, not as a rule a very livery colour and similar to certain shades of green in tourmaline, zircon, or olivine [1]. In demantoid the aluminium oxide from 0.99 to 1.38 %, silica oxide from 54.28 to 56.45 %, calcium oxide from 28.23 to 28.75 %, iron oxide from 13.93 to 15.99 %.

Tsavorite is a variety of grossularite, characterized by green colour. In dark green tsavorite the magnesium oxide content varies from 0.58 to 0.64 %, aluminium oxide from 21.89 to 21.92 %, silica oxide from 40.79 to 40.89 %, calcium oxide from 35.06 to 35.30 %, vanadium oxide from 0.40 to 0.57 %, manganese oxide from 0.76 to 0.81 %, titanium oxide about 0.39 %. In medium green tsavorite the magnesium oxide content varies from 0.40 to 0.73 %, aluminium oxide from 20.12 to 21.52 %, silica oxide from 39.62 to 43.90 %, calcium oxide from 31.91 to 37.59 %, vanadium oxide about 0.43 %, chrome oxide from 0.98 to 1.04 % manganese oxide from 0.42 to 0.72 %, titanium oxide from 0.35 to 0.37 %. Even though chromium (III) oxide (0.98 – 1.04 %) was found in medium green tsavorites, they are still lighter than tsavorites in which no chromium was found. Therefore, it might be asserted that the darker colour of a mineral, i.e., its colour tone is determined by manganese and titanium oxides. In darker tsavorites there was found higher content of manganese (II) oxide (0.76 – 0.81 %) and titanium (IV) oxide (0.39 %) compared to lighter tsavorites (respectively MnO 0.42 – 0.72 % and TiO₂ – 0.35 – 0.37 %) that might determine the darkness of the mineral.

In colourless grossularite the magnesium oxide content varies from 1.55 to 1.24 %, aluminium oxide from 27.14 to 30.14 %, silica from 52.95 to 55.75 %, calcium oxide from 12.56 to 18.42 %, the level of iron oxide is 0.25 %. In alexandrite effect having garnet the magnesium oxide content varies from 11.18 to 13.43 %, aluminium oxide from 22.03 to 25.29 %, silica oxide from 42.24 to 48.75 %, calcium oxide from 2.13 to 2.88 %, vanadium 0.46 to 0.61 %, manganese oxide from 8.63 to 17.37 %, iron oxide from 1.78 to 3.32 %, the level of chrome oxide is 0.37 %.

Hessonite is a variety of grossularite, which can vary from yellow to brown colour; sometimes this variety is referred to as essonite. Those are honey-yellow, yellow-brown garnets, tending to a reddish orange colour similar to that of spessartine. In hessonite the aluminium oxide content varies from 21.89 to 22.43 %, silica oxide from 45.34 to 47.51 %, calcium oxide from 27.52 to 29.51 %, manganese oxide from 0.26 to 0.41 %, iron oxide from 2.35 to 2.84 %. The colour of hessonite is determined by the content of manganese and iron oxides.

The blue colour-change garnet is the only one known example of the blue garnet. The interesting thing is that this garnet can change its colour in the same manner as alexandrite, therefore, the most correct name for this garnet would be the blue colour – change garnet [2]. In the garnet tested, the content of magnesium oxide varies from 11.18 to 13.43 %, manganese oxide – from 8.63 to 17.37 %, aluminium oxide – from 22.03 to 25.29 %, silicon oxide – from 42.24 to 48.75 %. In addition to these elements, the designated content of calcium oxide varies from 2.13 to 2.88 %, iron oxide – from 1.78 to 3.32 %, and colour determining chemical elements, i.e., vanadium oxide content varies from 0.46 to 0.61 %, chromium oxide – about 0.37 %.

CONCLUSIONS

After performed chemical analysis of garnet group minerals, the following might be stated:

- the rainbow garnet is a variety of andradite, as its chemical composition is predominantly of iron, calcium and silicon oxides, its multi-colourfulness depends on the surface reflectivity, i.e., irisation;
- demantoid colour is determined by the chromium oxide content;
- the colour of tsavorite is determined by the content of manganese and titanium oxides;
- in the colourless grossularite only small content of colour – determining chemical substances (MgO , Fe_2O_3) was found, thus, they may not affect the colour at all;
- the colour of hessonite is determined by the content of manganese and iron oxides.
- chemical composition of the blue colour – change garnet is the same as that of the pyrope and spessartine mixture, and its colour is determined by the content of vanadium and chromium oxides;

REFERENCES

1. C. Cipriani, A. Borelli, Gems and precious stone, Simon & Schuster's, New York, 1989.
2. http://www.secretsofthegemtrade.com/articles_8.htm

SELF-HEALING CERIUM CONVERSION COATINGS ON CARBON STEEL

O. Girčienė, L. Gudavičiūtė, A. Selskis, V. Jasulaitienė, A. Martušienė, R. Ramanauskas

Centre for Physical Sciences and Technology, Institute of Chemistry,

Goštauto 9, LT-01108, Vilnius, Lithuania

olgag@chi.lt

1. Introduction

Carbon steel is widely used in industry; however its susceptibility to corrosion in many environments limits its applications. For years, chromating has been applied to produce corrosion resistant conversion layers onto different substrates. Chromate conversion coatings have unrivaled self-healing abilities, which are believed to arise from the migration of a soluble Cr(VI) compound in the coating to a scratch or defect, where they are reduced to form a new protection layer. Self-healing is defined as the ability of material or surface to automatically heal or repair damages. Rare earth metal ions, such as cerium, lanthanum, and yttrium, have been recognized as an effective corrosion inhibitor for some aluminum alloys in a chloride-containing solution [1]. In series studies on the use of cerium ion in protective coatings, Hinton and Wilson reported that the cerium ion, which acts as an inhibitor in a solution, was as effective as the chromium ion [2]. The action of the cerium ion resembled that of the chromium ion, and CeO_2 acted as a barrier film. When a defect was generated, cerium ion in the film repaired it, due to dissolution from the film and oxidation on the defect site [3]. The study of cerium based conversion coatings on a galvanized steel have disclosed the influence of anions, such as Cl^- , NO_3^- , SO_4^{2-} , CH_3COO^- , in the coating deposition solution on their protective properties [4]. The presence of SO_4^{2-} in the solution brings into existence a complex between Ce^{3+} and SO_4^{2-} , which causes the incorporation of SO_4^{2-} into the cerium conversion coatings [5].

The aim of the present study was to evaluate the influence of SO_4^{2-} ions on the properties of chrome-free Ce conversion coatings on the carbon steel and to study self-healing capacities of it.

2. Experimental

2.1. Materials and samples preparation

Carbon steel specimens, 10×20 mm and 1 mm thick with an area of 4 cm² previously polished with emery paper up to grade 400, degreased with ethanol and rinsed with distilled water, were used as the working electrodes. The cerium conversion coatings FeCe1 and FeCe2 were formed by simple immersion of steel samples at 25°C for 24 h into solutions containing 0.05 M $\text{Ce}(\text{NO}_3)_3$ or 0.05 M $\text{Ce}(\text{NO}_3)_3$ + 0.025 M Na_2SO_4 , respectively.

2.2. Morphology and composition

The surface morphology and elemental composition of specimen were studied by a scanning electron microscope (SEM) Helios NanoLab dual beam workstation equipped with Oxford Instruments energy dispersive spectrometer (EDS) with X-Max 20 mm² detector.

The X-ray photoelectron spectroscopy (XPS) studies were performed with ESCALAB MK II spectrometer using X-radiation of MgK_α (1253.6 eV, pass energy of 20 eV). To obtain depth profiles, the samples were etched in the preparation chamber by ionised argon at a vacuum of 5×10^{-4} Pa. An accelerating voltage of ca. 1.0 kV and a beam current of 20 $\mu\text{A cm}^{-2}$ were used.

2.3. Electrochemical measurements

The corrosion behaviour of samples was investigated in an aerated stagnant 0.5 M NaCl solution. All electrochemical measurements were performed at ambient temperature with an

Autolab PGSTAT 302 potentiostat using a standard three-electrode system with a Pt counter electrode and a saturated Ag/AgCl reference electrode. All potentials are reported versus a saturated Ag/AgCl reference electrode.

The measurements of electrochemical impedance spectra (EIS) were performed at the open circuit potential with the FRA 2 module applying a signal of 10 mV amplitude in the frequency range of 20 kHz to 0.001 Hz. The data obtained were fitted and analysed using the EQUIVCRT program of Boukamp [6].

3. Results and discussion

3.1. Morphology and composition of cerium conversion coatings

SEM images of the surface morphology and cross sections of FeCe1 and FeCe2 conversion coatings formed on carbon steel are presented in Fig. 1.

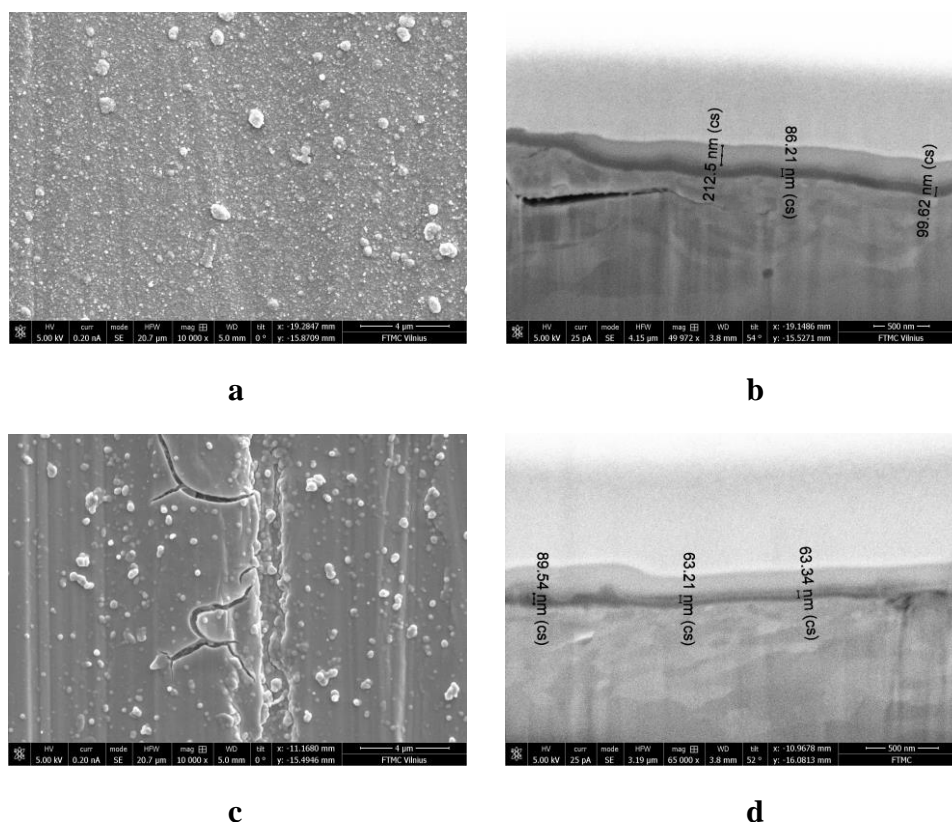


Fig. 1. SEM images of the carbon steel treated with (a, b) 0.05 M $\text{Ce}(\text{NO}_3)_3$ (FeCe1) and (c, d) 0.05 M $\text{Ce}(\text{NO}_3)_3$ + 0.025 M Na_2SO_4 (FeCe2) for 24 h.

Table 1. The elemental composition of the surface of samples

Sample	Elements, at. % (by EDS)							
	O	P	Mn	Fe	Mo	Ce	N	S
CS	7.5	0.09	0.33	91.96	0.1	-	-	-
FeCe1	30.38	-	0.26	68.76	-	0.60	-	-
FeCe2	24.56	-	0.28	74.10	0.33	0.33	-	0.72

It can be stated, that the presence of the sulphate ions in the conversion film deposition solution reduces the thickness and increases the number of structural defects, like cracks in the cerium conversion film (Fig. 1 a, c). The thickness of FeCe1 and FeCe2, according to

SEM measurements (Fig. 1 b, d) varies between 80 and 100 nm, and 60 and 80 nm, respectively.

EDS measurements enabled to determine the composition of the conversion films and the results obtained are listed in Table 1. The composition of both the films is rather similar, but the film formed in the solution containing sulphate additionally contained 0.5 at. % of S. This difference may be the reason of the increment in the internal stress of the film, which causes the appearance of cracks in these samples. The differences in Ce and Fe concentrations are related to variations in film thickness.

In order to determine the chemical composition and the oxidation state of Ce in the top layer of conversion films, XPS spectra after different surface sputtering times were obtained (Fig. 2) and analysed.

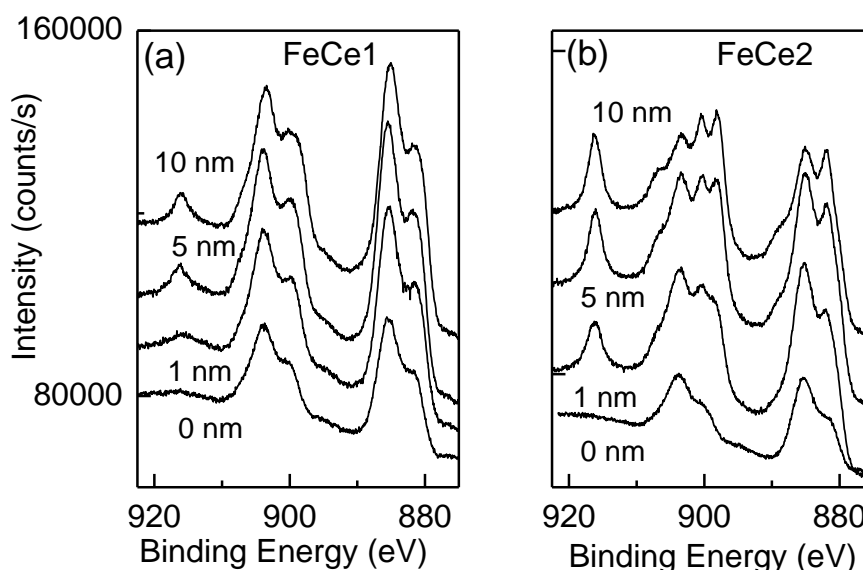
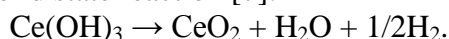


Fig. 2. XPS Ce3d spectra obtained on carbon steel treated with a solution containing: (a) 0.05 M $\text{Ce}(\text{NO}_3)_3$ and (b) 0.05 M $\text{Ce}(\text{NO}_3)_3$ + 0.025 M Na_2SO_4 for 24 h.

Paying attention to the elements, which may be responsible for the self-healing capability of conversion films, the oxidation states of Ce were analysed. The peak that appeared in the binding energy range from 916 to 917 eV is of crucial importance for determination of Ce oxidation state, because its presence is only associated with Ce^{4+} [7]. Meanwhile, Ce^{3+} and Ce^{4+} compounds were identified in the FeCe1 and FeCe2 films and the amount of Ce^{4+} was higher in the FeCe2 sample. It implies that the presence of SO_4^{2-} ions in the Ce conversion film solution enhances formation of Ce of a higher oxidation state. The presence of $\text{Ce}(\text{IV})$ can be due to a dismutation solid state reaction [7]:



3.2. Protective ability

EIS is widely used to characterize the corrosion behaviour of coating systems. EIS diagrams for investigated samples exposed to a 0.5 M NaCl solution are given in Fig. 3. To interpret the EIS data the $R_1(Q_1[R_2(R_3Q_2)])$ equivalent circuit model that is generally used to describe corrosion processes was applied. The calculated parameters of equivalent circuit are listed in Table 2.

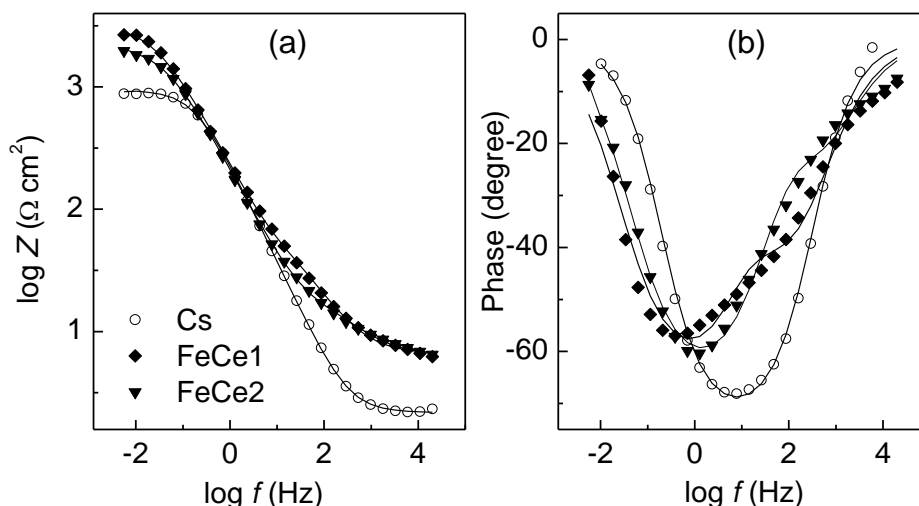


Fig. 3. Bode plots of EIS spectra after immersion of samples into a 0.5 M NaCl solution.

Table 2. EIS parameters obtained by fitting the Bode plots (Fig. 3) with the equivalent circuit $R_1(Q_1 [R_2(R_3Q_2)])$ measured after exposure of samples to a 0.5 M NaCl solution

Sample	R_1 , $\Omega \text{ cm}^2$	R_2 , $\Omega \text{ cm}^2$	$Y_0(Q_1) / 10^{-5}$ $\Omega^{-1} \text{ cm}^{-2} \text{ s}^n$	$n(Q_1)$	R_3 , $\Omega \text{ cm}^2$	$Y_0(Q_2) / 10^{-5}$ $\Omega^{-1} \text{ cm}^{-2} \text{ s}^n$	$n(Q_2)$	$R_1+R_2+R_3= R_p$, $\Omega \text{ cm}^2$
Cs	2				946	89.3	0.82	946
FeCe1	6	81	65.9	0.69	3230	47.4	0.79	3311
FeCe2	6	14	44.1	0.71	2176	75.1	0.76	2196

The results obtained (Table 2) show that the FeCe1 and FeCe2 samples possessed 3.5 fold and 2.3 fold higher R_p values, respectively, as compared to that of the Cs sample, which implies a higher protective ability of the FeCe1 film. The FeCe2 film was supposed to exhibit a higher protective ability with respect to the FeCe1 sample, because a higher amount of less soluble Ce (IV) compounds according to XPS measurements was detected for the FeCe2 film. However, a low conversion film thickness and the presence of cracks in the FeCe2 sample (Fig. 1 c) yielded a lower level of steel corrosion protection.

4. Conclusions

The cerium conversion films deposited in the solutions with and without SO_4^{2-} ions inhibited steel corrosion in chloride containing media. The presence of SO_4^{2-} in the cerium conversion film deposition solution increases the amount of Ce^{4+} compounds in the coatings, which supposedly should increase the protective ability of the film, however, a low film thickness and the presence of structural defects, like cracks, do not afford any tangible enhancement in corrosion protection.

ACKNOWLEDGMENTS

This research was supported by the Research Council of Lithuania under Grant Nr. MIP – 029-2013.

References

1. B.R.W. Hinton, D.R. Arnott, N.E. Ryan, *Metals Forum* 7 (1984) 211.
2. B.R.W. Hinton, L. Wilson, *Corros. Sci.* 29 (1989) 967.
3. R.G. Buchheit, S.B. Mamidipally, P. Schmutz, H. Guan, *Corrosion* 58 (2002) 3.
4. Y. Kobayashi, N. Yamashita, Y. Fujiwara, M. Yamashita, *J. Surf. Fin. Soc. Jpn.* 55 (2004) 276.
5. Y. Kobayashi, Y. Fujiwara, *Electrochim. Acta* 51 (2006) 4236.
6. B.A. Boukamp, *J. Electrochem. Soc.* 142 (1995) 1885.
7. M.A. Arenas, J.J. Damborenea, *Surf. Coat. Technol.* 187 (2004) 320.

STUDY OF MOLECULAR INTERACTIONS IN CHOLESTEROL-PHOSPHOLIPID MONOLAYER USING SUM FREQUENCY GENERATION SPECTROSCOPY

E. Golovinas¹, L. Abariūtė¹, G. Valinčius¹, G. Niaura²

1 Vilnius University, Universiteto 3, LT-01513 Vilnius, Lithuania

2 Center for Physical Sciences and Technology, A. Goštauto 9, LT-01108 Vilnius, Lithuania

E-mail: edvardasg2007@gmail.com

There is abundant evidence gathered in recent years suggesting that cell plasma membranes contain phase-separated domains of different lipid and protein composition. It is well-recognized that the organization of both lipids and proteins plays an important role in cellular membrane regulation and function [1]. Different techniques have been used to study model lipid membranes, including atomic force microscopy, vibrational spectroscopy and computer simulations [2–4]. In this work a combination of sum frequency generation (SFG) spectroscopy and surface pressure measurements was used to study conformational order in Langmuir monolayers prepared from pure lipids and their mixtures.

SFG spectroscopy is a second-order nonlinear optical process which can be used to obtain a vibrational spectrum of molecules at an interface, which provides information about orientation and conformation of the molecules. The high surface specificity arises from the nature of the process: even-ordered nonlinear optical processes vanish in centrosymmetric media under the electric-dipole approximation. Therefore, the sum frequency signal arises mainly from an interface where centrosymmetry is necessarily broken.

Lipid monolayers were prepared in a Langmuir trough (Nima 1002) by spreading aliquots of 0.1 mM lipid solutions (table 1) in HPLC grade chloroform on Milli-Q water surface at room temperature (20 °C), and compressing the monolayer in three steps: firstly, lipid solution was spread until a surface pressure of ~8 mN/m was achieved; secondly, the spreading was continued until the surface pressure reached ~26 mN/m; thirdly, the monolayer was compressed into the liquid-condensed (LC) phase until just before the collapse. The solvent was allowed to evaporate for a minimum of 20 min prior to measurements. Spectra were gathered after each step at 1000–1800, 2000–2300 and 2700–3600 cm⁻¹ in *ssp* (*s* - SF, *s* - 532 nm and *p* - IR beams, respectively) and *sps* polarization combinations. The lipids chosen were dioleoylphosphatidylcholine (DOPC), cholesterol-d7 (Chol-d7) and sphingomyelin (SM).

Table 1. Studied lipid mixture compositions

No.	Lipid mixture composition, DOPC:Chol-d7:SM, mol %
1	100:0:0
2	0:100:0
3	0:0:100
4	70:30:0
5	60:30:10
6	62:30:8
7	64:30:6
8	66:30:4
9	68:30:2

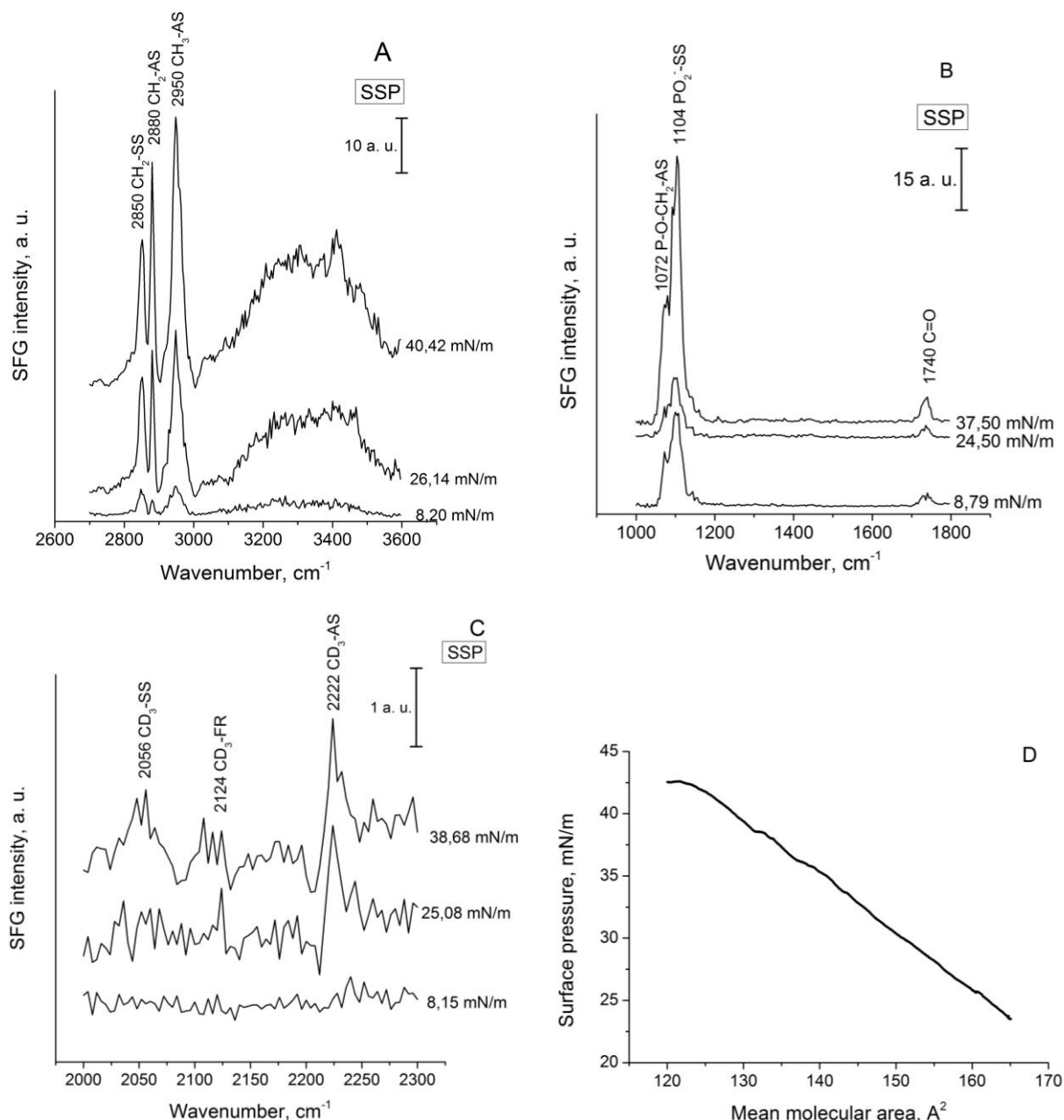


Figure 1. SFG spectra (A–C) and surface pressure isotherm (D) of mixture No. 8. Spectra shown were gathered in *ssp* polarization combination and normalized to IR beam intensity.

All three spectra in Figure 1 show the influence of compression to relative intensity of vibrational bands and, therefore, monolayer order. Fig. 1 A shows the C–H stretch spectral region. The peak at 2850 cm^{-1} corresponds to CH_2 symmetric stretch (SS), while the peak at 2950 cm^{-1} is due to terminal CH_3 antisymmetric stretch (AS). It is common in literature to assign the peak at 2880 cm^{-1} to CH_2 antisymmetric stretch [5–7] but assigning the peak to CH_3 -SS may show greater monolayer order and fewer *gauche* conformations in the lipid chains with increasing surface pressure [8]. Presence of intense CH_2 -SS and CH_2 -AS resonances in SFG spectra suggest disordering of alkyl chains due to existence of *gauche* defects. Increasing relative intensity of CH_3 -AS, comparing to CH_2 -SS with compression of surface layer shows increase in ordering of the monolayer. Peaks in spectrum B can be easily identified. The resonances at 1072, 1104 and 1740 cm^{-1} belong to asymmetric stretching vibration of P–O group (PO-AS), symmetric stretching vibration of PO_2 group (PO_2 -SS), and

stretching vibration of C=O group, respectively. These resonances are associated with phospholipids in the mixture [5, 7]. Interestingly, the intensity dependence of these bands on surface pressure is non-monotonic; in the first stage the intensity decreases as pressure increases from 8.79 to 24.50 mN/m, indicating decrease in order of phospholipids head group. However, considerable growth in intensity is visible as the surface pressure increases further to 37.50 mN/m. Such behavior points on the reorganization of the head groups of the phospholipids in the mixture at the interface with increasing the compression of the monolayer. Spectrum C shows the C–D stretch region with peaks at 2056, 2124 and 2222 cm^{-1} assigned to $\text{CD}_3\text{-SS}$, $\text{CD}_3\text{-Fermi resonance (FR)}$ and $\text{CD}_3\text{-AS}$ respectively, of Chol-d7 [9, 10]. Observation of these resonances indicates that cholesterol molecules are co-adsorbed at interface. Importantly, at low surface pressure (8.15 mN/m) no alignment of deuterated groups is visible. However, as surface pressure reaches the 25.08 mN/m value the resonance at 2222 cm^{-1} considerably increases, indicating formation of ordered cholesterol structures at interface. In conclusion, by using sum frequency generation technique we have monitored ordering of particular molecular groups of mixed monolayer at air/water interface with increasing surface pressure.

References

1. K. Simons, M. J. Gerl, Nat. Rev. Mol. Cell Biol., 11 (2010) 688-699.
2. R. K. Gupta, K. A. Suresh, Eur. Phys. J., 14 (2004) 35-42.
3. C.-Y. Chung, J. Boik, E. O. Potma, Annu. Rev. Phys. Chem., 64 (2013) 77-99.
4. S. A. Pandit., E. Jakobsson, H. L. Scott, Biophys. J., 87 (2004) 3312-3322.
5. K. Czamara *et al.*, J. Raman Spectrosc., (2014).
6. R. Lu, W. Gan, B.-H. Wu, H. Chen, H.-F. Wang, J. Phys. Chem. B, 108 (2004) 7297-7306.
7. A. D. Meade, F. M. Lyng, P. Knief, H. J. Byrne, Anal. Bioanal. Chem., 387 (2007) 1717-1728.
8. C. Weeraman *et al.*, Langmuir, 28 (2012) 12999-13007.
9. G. Ma, H. C. Allen, Langmuir, 22 (2006) 5341-5349.
10. M. H. Wood *et al.*, Langmuir, 29 (2013) 13735-13742.

EVALUATION OF Pt-Co NANOCATALYSTS ACTIVITY TOWARDS METHANOL OXIDATION IN ACIDIC MEDIUM

J. Jablonskienė, A. Matusevičiūtė, R. Kondrotas, R. Juškėnas, L. Tamašauskaitė-Tamašiūnaitė

*Center for Physical Sciences and Technology, A. Gostauto 9, Vilnius LT-0110, Lithuania
E-mail: jol.jab@gmail.com*

Introduction

Among the different types of fuel cell technologies, direct methanol fuel cells (DMFCs) are the most suitable for mobile and portable electronic applications because of their high volumetric energy density, relatively low operating temperature and the convenience of a liquid fuel [1]. Graphene as a catalyst support has incurred an intense interest in fuel cell applications due to its unique, outstanding physicochemical properties, such as an extremely high specific surface area ($2600 \text{ m}^2 \text{ g}^{-1}$), a superior electronic conductivity, a high surface to volume ratio and a high stability. Graphene can act as an ideal substrate for growing and anchoring various nanocrystalline Pt and Pt-based alloys for high-performance electrocatalytic devices. The combination of metal nanoparticles and graphene opens up new possibilities for design of the next generation catalysts.

In our previous works [2, 3] it has been shown that the graphene supported platinum-cobalt catalysts prepared by means of microwave synthesis enhance electrocatalytic activity towards the oxidation of borohydride and ethanol in an alkaline medium and are promising anode materials for direct borohydride fuel cells (DBFCs) and ethanol fuel cells (DEFCs). In the present study the activity of the graphene supported platinum-cobalt nanoparticles towards the electro-oxidation of other fuel, i.e. methanol, in an acidic medium was investigated. The composition of prepared catalysts was examined by Inductively Coupled Plasma Optical Emission Spectroscopy (ICP-OES). The shape and size of catalyst particles were determined by Transmission Electron Microscopy (TEM).

Experimental

The graphene supported platinum-cobalt nanoparticles (denoted as PtCo/GR catalyst) with the different Pt:Co molar ratios were prepared by microwave heating of ethylene glycol (EG) solutions of Pt(IV) and Co(II) salts as was described in [2, 3]. The reduction of Pt and Co nanoparticles was carried out in the microwave reactor Monowave 300 at a temperature of 170°C for 30 min. For comparison, the graphene supported platinum nanoparticles (denoted as Pt/GR catalyst) was prepared at 170°C for 30 s. The synthesized catalysts were washed with acetone, ultra-pure water, then filtered and dried in a vacuum oven at 80°C for 2 h.

A shape and size of catalyst particles were examined using a transmission electron microscope Tecnai G2 F20 X-TWIN equipped with an EDAX spectrometer with r-TEM detector. For microscopic examinations, 10 mg of sample was first sonicated in 1 ml of ethanol for 1 h and then deposited on the Cu grid covered with a continuous carbon film. The Pt and Co metal loadings were estimated from ICP-OES measurements. The ICP optical emission spectra were recorded using an ICP optical emission spectrometer Optima 7000DV (Perkin Elmer).

A three-electrode electrochemical cell was used for electrochemical measurements. Pt/GR and PtCo/GR catalysts were employed as a working electrode, a Pt sheet was used as a counter electrode and an Ag/AgCl/KCl electrode was used as reference. The catalyst layer was obtained according to the following steps: at first 10 mg of the PtCo/GR or Pt/GR

catalysts were dispersed ultrasonically for 1 hour in a solution containing 0.25 μl of 5 wt. % Nafion and 0.75 μl deionized H_2O . Then 5 μl of the prepared suspension mixture was pipetted onto the polished surface of a glassy carbon electrode with a geometric area of 0.07 cm^2 and dried in air for 12 h.

All electrochemical measurements were performed with a Zennium electrochemical workstation. Steady state linear sweep voltammograms were recorded in a 1 M CH_3OH + 0.5 M H_2SO_4 solution at a linear potential sweep rate of 50 mV s^{-1} from 0 to 1.5 V at a temperature of $25\text{ }^\circ\text{C}$. The electrode potential is quoted versus the standard hydrogen electrode (SHE). The presented current densities are normalized with respect to the geometric area of catalysts. All solutions were deaerated by argon for 15 min prior to measurements.

Results and discussions

In the study a rapid microwave heating method was used to prepare the graphene supported platinum-cobalt nanoparticles with the different Pt:Co molar ratios. Figure 1 shows HRTEM images and corresponded EDX spectra of the graphene supported Pt nanoparticles (a, d) and graphene supported PtCo nanoparticles with the Pt:Co molar ratios equal to 1:6 (b, e) and 1:48 (c, f).

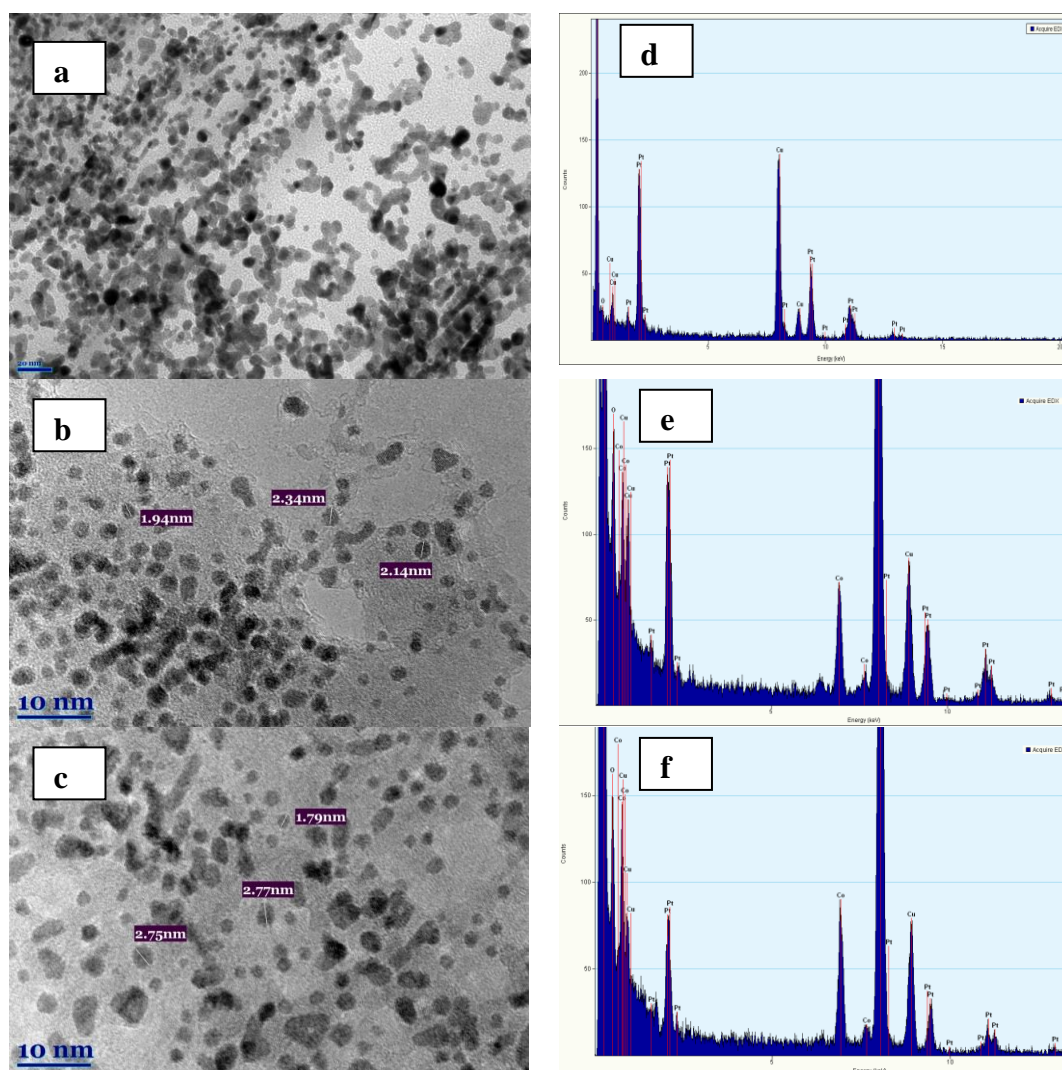


Fig.1. HRTEM images and corresponded EDX spectra of Pt/GR (a, d), PtCo(1:6)/GR (b, e) and PtCo(1:48)/GR (c, f).

According to the data of TEM analysis, Pt nanoparticles in size of 5-6 nm were deposited on the surface of graphene (Fig. 1a). In the case of graphene supported PtCo catalysts, the Pt nanoparticles of ca. 1-3 nm in size were deposited on the surface of graphene (Fig. 1b, c). In all cases Pt nanoparticles were uniform and well dispersed on the surface of graphene. The EDX spectra confirm the presence of Pt and PtCo nanoparticles in the investigated Pt/GR, PtCo(1:6)/GR and PtCo(1:48)/GR catalysts (Fig. 1d, e, f).

The Pt loadings in the synthesized catalysts were analysed and confirmed by ICP optical emission spectrometry measurements. It has been determined that the Pt loadings were $125 \mu\text{g Pt cm}^{-2}$ in the Pt/GR and 114, 100 and $138 \mu\text{g Pt cm}^{-2}$ in the PtCo/GR catalysts with the Pt:Co molar ratios equal to 1:3, 1:6 and 1:48, respectively.

The electroactive surface area (ESA) of platinum in the synthesized catalysts were determined from the cyclic voltammograms of Pt/GR, PtCo/GR (1:3), PtCo/GR (1:6) and PtCo/GR (1:48) recorded in 0.5 M H_2SO_4 solution at a sweep rate of 50 mV s^{-1} by calculating the charge associated with hydrogen adsorption.

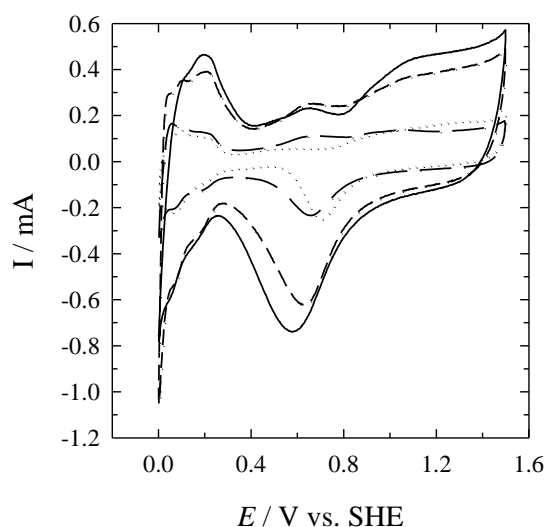


Fig.2. CVs of the PtCo(1:3)/GR (solid line), PtCo(1:6)/GR (long dashed line), PtCo(1:48)/GR (short dashed line) and Pt/GR (dotted line) catalysts recorded in 0.5 M H_2SO_4 at a sweep rate 50 mV s^{-1} ; 25°C .

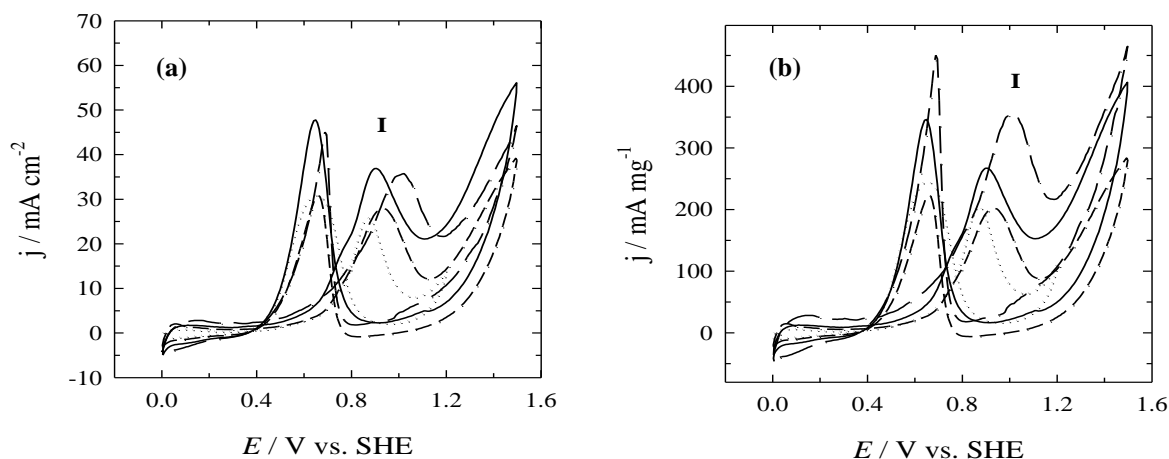


Fig.3. (a) CVs of the PtCo(1:3)/GR (solid line), PtCo(1:6)/GR (long dashed line), PtCo(1:48)/GR (short dashed line) and Pt/GR (dotted line) catalysts recorded in 1 M $\text{CH}_3\text{OH} + 0.5 \text{ M H}_2\text{SO}_4$ at a sweep rate 50 mV s^{-1} ; 25°C . (b) The same data normalized by the Pt loadings for each catalyst.

The determined ESA values are 1.8 cm^2 for Pt/GR, 5.3, 4.5 and 2.8 cm^2 for PtCo/GR (1:3), PtCo/GR (1:6) and PtCo/GR (1:48) catalysts, respectively. These results show that the ESA values of the investigated PtCo/GR catalysts are 1.6-2.9 times higher than those of the Pt/GR catalyst.

The electrocatalytic properties of the Pt/GR and PtCo/GR catalysts were investigated towards methanol oxidation reaction in acidic medium by means of cyclic voltammetry. As shown in Fig. 3a, the peak **I** in the forward scan corresponds to the oxidation of methanol. Methanol oxidation current densities values (peak **I**) ca. 1.1-1.4 times higher at the PtCo(1:48)/GR, PtCo(1:3)/GR and PtCo(1:6)/GR catalysts than those at the Pt/GR catalyst. Highest electrocatalytic activity towards the electro-oxidation of methanol shows the graphene supported PtCo catalyst with a Pt:Co molar ratio equal to 1:3 as compared with those at the graphene supported PtCo catalyst with the Pt:Co molar ratio equal to 1:6 and 1:48 and the Pt/GR catalyst (Fig. 3a). The highest Pt-mass activity shows the PtCo/GR catalysts with the Pt:Co molar ratio equal to 1:6 (Fig. 3b).

Conclusions

The graphene supported platinum-cobalt catalysts with the Pt:Co molar ratios equal to 1:3, 1:6 and 1:48 and with the Pt nanoparticles of ca. 1-3 nm in size, were prepared by microwave synthesis. Highest electrocatalytic activity towards the electro-oxidation of methanol shows the graphene supported PtCo catalyst with a Pt:Co molar ratio equal to 1:3 as compared with those at the graphene supported PtCo catalyst with the Pt:Co molar ratio equal to 1:6 and 1:48 and the Pt/GR catalyst. The highest Pt-mass activity shows the PtCo/GR catalysts with the Pt:Co molar ratio equal to 1:6.

The graphene supported PtCo catalysts synthesized by means of rapid microwave synthesis seem to be a promising anode material for direct methanol fuel cells.

Acknowledgement

This research was funded by a Grant (No. ATE-08/2012) from the Research Council of Lithuania.

References

1. J. Zeng, J. Y. Lee, *J. Power Sources*, **140** (2004) 268-273.
2. L. Tamašauskaitė-Tamašiūnaitė, A. Radomskis, K. Antanavičiūtė, J. Jablonskienė, A. Balčiūnaitė, A. Žielienė, et al., *Int. J. Hydrogen Energy*, **39** (2014) 4282-4290.
3. V. Kepenienė, J. Jablonskienė, J. Vaičiūnienė, R. Kondrotas, R. Juškėnas and L. Tamašauskaitė-Tamašiūnaitė, *ECS Transactions*, **59** (1) (2014) 217-228.

In_xGa_{1-x}N PERFORMANCE AS A BAND-GAP-TUNABLE PHOTO-ELECTRODE FOR PHOTOELECTROCHEMICAL GENERATION OF HYDROGEN

J. Juodkazytė¹, B. Šebeka¹, I. Savickaja¹, A. Kadys², E. Jelmakas², T. Grinys², S. Juodkazis^{2,3}, T. Malinauskas²

1 Centre for Physical Sciences and Technology, A. Goštauto 9, LT-01108 Vilnius, Lithuania

2 Institute of Applied Research, Vilnius University, LT-10222 Vilnius, Lithuania

3 Centre for Micro-Photonics, Swinburne University of Technology, Hawthorn, VIC 3122, Australia

E-mail: jurga.juodkazyte@ftmc.lt

Possibility to tune the band gap energy, E_g , of a semiconductor by doping is an attractive method for solar energy harvesting. The E_g of GaN is ~ 3.4 eV and can be reduced by adding indium [1]. The In_xGa_{1-x}N is chemically stable semiconductor with the band gap ranging from 0.7 to 3.4 eV depending on indium content.

Samples of In_xGa_{1-x}N were grown on a ~ 3.5 μm thick GaN. Thickness of indium gallium nitride layers was 70 – 100 nm. A thin 2–3 nm InGa_{1-x}N layer with constantly changing In concentration from 1–2% to 10% was used as a buffer. The buffer is required to relax lattice mismatch induced stress. Samples were grown on 2-in (001) sapphire substrates in a close-coupled 3 \times 2-in flip-top showerhead MOCVD reactor (Aixtron Ltd). Photoelectrochemical measurements were performed in the photoelectrochemical cell (PEC) shown in Fig. 1a.

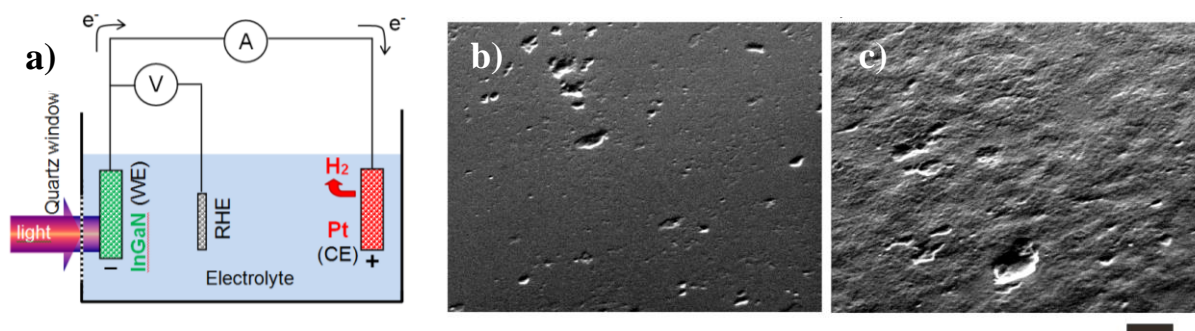


Fig. 1. Schematic representation of PEC used for experiments (a): WE - working electrode, CE - counter electrode, RHE is reversible hydrogen electrode used as reference; intensity of simulated solar illumination was ~ 100 mW/cm^2 ; SEM images of GaN electrode before (b) and after (c) exploitation in PEC, scale bar: 1 μm .

The study of photoelectrochemical performance of n-In_xGa_{1-x}N electrodes with x ranging between 0 and 1 revealed that pure n-GaN is the most efficient from the view point of photoelectrochemical generation of hydrogen under simulated 1 Sun illumination and zero external bias [2]. Higher photocurrents were observed in the alkaline medium, which can be attributed to the higher rate of anodic reaction in alkaline solutions compared to the acidic ones. It has been shown that photocurrent density increases with electron concentration and mobility of electrons in the GaN layers, whereas introduction of In to n-GaN, even at x as low as 0.1, leads to decreased rates of the anodic process and, consequently, lower photocurrent density. This has been attributed to passivation of GaN by InN and lower crystalline quality of In_{0.1}Ga_{0.9}N material. Higher photocurrent, however, results in faster photo-corrosion of the semiconductor surface (Fig. 1b, c).

References

1. J. Li, J. Y. Lin, H. X. Jiang, Appl. Phys. Lett., 93 (2008) 162107-1–162107-3.
2. J. Juodkazytė, B. Šebeka, I. Savickaja, A. Kadys, E. Jelmakas, T. Grinys, S. Juodkazis, K. Juodkazis, T. Malinauskas, Sol. Energ. Mat. Sol. Cells, 130 (2014) 36–41.



METAL OXIDES SUPPORTED PLATINUM NANOPARTICLES AS ELECTROCATALYSTS FOR ETHANOL OXIDATION

V. Kepenienė, L. Tamašauskaitė-Tamašiūnaitė, J. Vaičiūnienė, R. Kondrotas, V. Pakštas, E. Norkus,

Center for Physical Sciences and Technology, A. Goštauto 9, LT-01108 Vilnius, Lithuania

E-mail: virginalisk@gmail.com

Introduction

The aim of this study was to investigate the activity of CeO₂/C and Nb₂O₅/C supported platinum nanoparticles composites (denoted as Pt-CeO₂/C and Pt-Nb₂O₅/C), prepared by the rapid microwave synthesis method, towards the oxidation of ethanol in an alkaline medium. The electrocatalytic activity of the Pt-CeO₂/C and Pt-Nb₂O₅/C catalysts with respect to ethanol oxidation was investigated by means of cyclic voltammetry. The electrochemical behaviour of the fabricated catalysts towards the oxidation of ethanol was compared with that of carbon supported bare Pt catalyst (denoted as Pt/C). The transmission electron microscopy (TEM) was used to determine the shape and the size of catalyst particles. Inductively coupled plasma optical emission spectroscopy (ICP-OES) was employed to determine the composition of the synthesized catalysts.

It has been found that the CeO₂/C and Nb₂O₅/C catalysts supported Pt nanoparticles enhance the ethanol oxidation current densities up to ca. 6 times, the mass activities for ethanol oxidation up to ca. 8 times and the specific activities for ethanol oxidation up to ca. 3 times as compared to those of graphite supported bare Pt catalyst.

Experimental

In this work, the primary CeO₂/C and Nb₂O₅/C composites were prepared according to the following procedures: at first, dry CeO₂ or Nb₂O₅ powders were mixed with carbon (mass ratio being 1:1) in a 2-propanol solution by ultrasonication for 30 min. with further desiccation of the mixture. Further CeO₂/C and Nb₂O₅/C composites were heated at 500°C for 2 h. Then Pt nanoparticles were dispersed over CeO₂/C and Nb₂O₅/C composites by the rapid microwave heating method. Typical preparation consists of the following steps: at first, the solution containing 1.9 mM of H₂PtCl₆ and 1 M of glycerol was prepared. pH of the solution was adjusted to 11.65 by adding dropwise a 0.4 M NaOH solution. Then 100 mg of CeO₂/C or Nb₂O₅/C were added to the reaction mixture and sonicated for 20 min. For the microwave irradiation, the reaction mixture was put into a microwave reactor Monowave 300 (Anton Paar). The reduction of Pt nanoparticles was carried out at a temperature of 170°C for 30 s. For comparison, the carbon supported Pt catalyst was also prepared at 170 °C for 30 s. After preparation, the synthesized catalysts were washed with acetone, ultra-pure water with the resistivity of 18.2 MΩ cm⁻¹, then filtered and dried in a vacuum oven at 80°C for 2 h.

Characterization of catalysts

A shape and size of catalyst particles were examined using a transmission electron microscope Tecnai G2 F20 X-TWIN equipped with EDAX spectrometer with r-TEM detector. For microscopic examinations, 10 mg of sample was first sonicated in 1 ml of ethanol for 1 h and then deposited on the Cu grid covered with a continuous carbon film.

The Pt metal loadings were estimated from ICP-OES measurements. The ICP optical emission spectra were recorded using an ICP optical emission spectrometer Optima 7000DV (Perkin Elmer).

Electrochemical measurements

The catalyst layer was obtained according to the following steps: at first, the 10 mg of the Pt-CeO₂/C, Pt-Nb₂O₅/C or Pt/C catalysts were dispersed ultrasonically for 1 h in a solution containing 0.25 μl of 5 wt.% Nafion and 0.75 μl deionized H₂O to produce a homogeneous slurry. Then 5 μl of the prepared suspension mixture was pipetted onto the polished surface of a glassy carbon electrode with a geometric area of 0.07 cm² and dried in air for 12 h.

All electrochemical measurements were performed with a Zennium electrochemical workstation (ZAHNER-Elektrik GmbH & Co.KG). Steady state linear sweep voltammograms were recorded in a 1 M C₂H₅OH + 0.5 M NaOH solution at a linear potential sweep rate of 50 mV s⁻¹ from -0.5 to 0.5 V at a temperature of 25 °C. The electrode potential is quoted *versus* the standard hydrogen electrode (SHE). The presented current densities are normalized with respect to the geometric area of catalysts. All solutions were deaerated by argon for 15 min prior to measurements.

Results and discussions

The Pt/C, Pt-CeO₂/C and Pt-Nb₂O₅/C catalysts were synthesized by rapid microwave synthesis method. The metal oxides powder was mixed with carbon and heated at 500°C for 2h and then Pt nanoparticles were dispersed on the obtained CeO₂/C and Nb₂O₅/C composites as described in the experimental part.

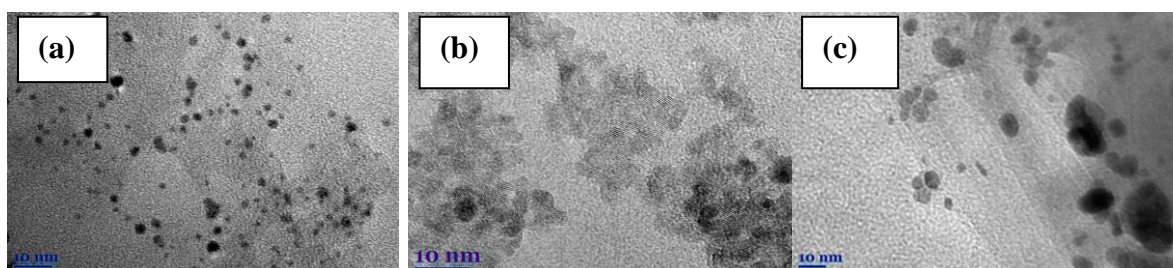


Fig. 1. TEM images of the Pt/C (a), Pt-CeO₂/C (b) and Pt-Nb₂O₅/C (c) catalysts.

Figure 1 shows TEM images of the Pt/C (a), Pt-CeO₂/C (b) and Pt-Nb₂O₅/C (c) catalysts. The Pt nanoparticles of ca. 4-7 nm in size were deposited on the surface of carbon supported CeO₂ and Nb₂O₅ (Fig. 1, b,c). For comparison, the Pt/C catalyst was synthesized with Pt nanoparticles of ca. 3-5 nm in size as depicted from Fig. 1a. In all cases the Pt nanoparticles were uniform and well dispersed on the surface of carbon.

The Pt loading of the synthesized catalysts was determined by ICP-OES. It was found that the Pt loadings were 0.128, 0.157 and 0.114 mg Pt cm⁻² in the Pt/C, Pt-CeO₂/C and Pt-Nb₂O₅/C catalysts, respectively.

The electrochemically active surface areas (ESAs) of Pt in the synthesized catalysts were determined from the cyclic voltammograms of the Pt-CeO₂/C, Pt-Nb₂O₅/C and Pt/C catalysts recorded in a deaerated 0.5 M H₂SO₄ solution at a sweep rate of 50 mV s⁻¹ by calculating the charge associated with hydrogen adsorption (220 $\mu\text{C cm}^{-2}$) [1] (Fig. 2). It has been determined that the values of ESA are 1.8 cm² for Pt/C and 2.7 and 3.5 cm² for the Pt-CeO₂/C and Pt-Nb₂O₅/C catalysts, respectively. The specific activity has been determined to be 20 m² g⁻¹ Pt for Pt/C, 24 m² g⁻¹ Pt for Pt-CeO₂/C and 44 m² g⁻¹ Pt for Pt-Nb₂O₅/C.

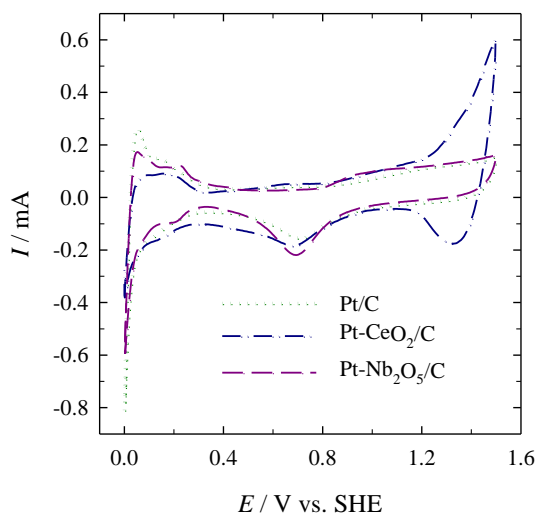


Fig. 2. Cyclic voltammograms of the Pt-CeO₂/C (*dash-dotted line*), Pt-Nb₂O₅/C (*dashed line*) and Pt/C (*dotted line*) catalysts recorded in 0.5 M H₂SO₄ at a sweep rate of 50 mV s⁻¹.

The electrocatalytic activity of the Pt-CeO₂/C, Pt-Nb₂O₅/C and Pt/C catalysts with respect to the oxidation of ethanol was investigated by cyclic voltammetry. Figure 3 presents positive potential-going scans of investigated catalysts recorded in 1 M C₂H₅OH + 0.5 M NaOH at a sweep rate of 50 mVs⁻¹. In the forward sweep, anodic peaks are observed at -0.03 V for Pt/C, 0.04 V for Pt- CeO₂/C and 0 V for Pt-Nb₂O₅/C catalysts (Fig. 3). This peak is related with the direct oxidation of ethanol in an alkaline medium [2].

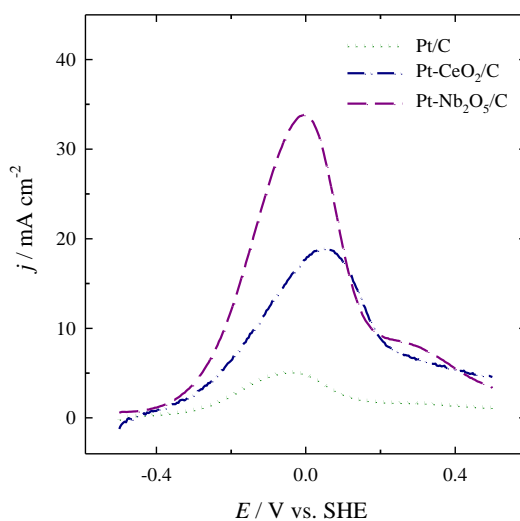


Fig. 3. Stabilized positive-potential going scans (10th cycles) of the Pt-CeO₂/C (*dash-dotted line*), Pt-Nb₂O₅/C (*dashed line*) and Pt/C (*dotted line*) catalysts recorded in 1 M C₂H₅OH + 0.5 M NaOH at a sweep rate of 50 mV s⁻¹.

Noteworthy, oxidation peaks on the Pt-CeO₂/C (*dash-dotted line*) and Pt-Nb₂O₅/C (*dashed line*) catalysts are much higher than those on Pt/C (*dotted line*). Ethanol oxidation current densities on the Pt-CeO₂/C and Pt-Nb₂O₅/C catalysts are ca. 4.0 and 6.0, respectively, times higher as compared to that of the bare Pt/C catalyst (Fig. 3).

To evaluate the electrocatalytic activity of investigated catalysts, ethanol oxidation current densities were normalized by the electrochemically active surface areas and Pt loadings to represent the specific and mass activity of catalysts. Figure 4 shows comparison of current

densities (a), specific (b) and mass activities (c) towards the oxidation of ethanol for the prepared catalysts. Assuming ca. 2.0 times higher ESAs value of the Pt-CeO₂/C and Pt-Nb₂O₅/C catalysts as compared with that of Pt/C, the surface area normalized ethanol oxidation current densities are ca. 2.5 and 3.4 times higher on the Pt-CeO₂/C and Pt-Nb₂O₅/C catalysts, respectively (Fig. 4, b).

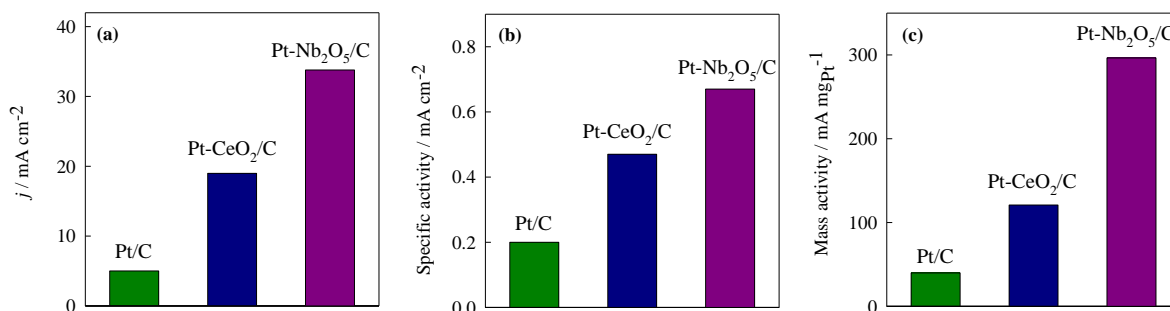


Fig. 4. Comparison of current densities (a), specific (b) and mass activities (c) towards the oxidation of ethanol at 0 V vs. SHE for Pt/C, Pt-CeO₂/C and Pt-Nb₂O₅/C recorded in 1 M C₂H₅OH + 0.5 M NaOH at 50 mV s⁻¹.

The mass activities for ethanol oxidation are ca. 3 and 7 times higher at the Pt-CeO₂/C and Pt-Nb₂O₅/C catalysts, respectively, as compared to those at the Pt/C catalyst (Fig. 4, c).

It has been found that cerium(IV) oxide/C or niobium(V) oxide/carbon supported Pt nanoparticles catalysts show an enhanced electrocatalytic activity towards the oxidation of ethanol in an alkaline medium as compared with that of the carbon supported bare Pt catalyst.

Conclusions

A rapid microwave heating method was used to prepare the CeO₂/C and Nb₂O₅/C supported platinum nanoparticles as electrocatalysts towards the oxidation of ethanol. The both investigated Pt-CeO₂/C and Pt-Nb₂O₅/C catalysts show a higher activity towards the oxidation of ethanol when compared with that of Pt/C catalyst.

Acknowledgment

Postdoctoral fellowship is being funded by European Union Structural Funds project "Postdoctoral Fellowship Implementation in Lithuania".

References

1. H. Angerstein-Kozłowska, B. E. Conway and W. B. A. Sharp, *J. Electroanal. Chem.*, **43**, 9 (1973).
2. R. Manohara and J. B. Goodenough, *J. Mater. Chem.*, **2**, 875 (1992).

MICROWAVE-ASSISTED SYNTHESIS OF PLATINUM SUPPORTED CERIUM OXIDE-GRAPHENE FOR METHANOL OXIDATION

V. Kepenienė, M. Vagner, A. Balčiūnaitė, A. Matusėvičiūtė, L. Tamašauskaitė-Tamašiūnaitė, E. Norkus

Center for Physical Sciences and Technology, A. Goštauto 9, LT-01108 Vilnius, Lithuania
E-mail: lortam@ktl.mii.lt

Introduction

Direct methanol fuel cells (DMFCs) are being developed especially for portable power supply. Since methanol is used as fuel, the development of electrocatalysts having reasonable costs and a high electroactivity and stability for the oxidation of methanol is industrially vital. It was found that addition of metal oxides (e.g. MnO_2 , TiO_2 , CeO_2 , WO_3 , Fe_2O_3) to noble metal based catalysts enhance their performance. In the present study fabrication of the platinum supported cerium oxide-graphene (denoted as Pt-CeO₂/GR) by means of microwave-assisted synthesis is presented. The Pt-CeO₂/GR catalysts with the Pt:Ce molar ratios equal to 2:1, 1:1 and 1:10 (denoted as Pt-CeO₂/GR-1, Pt-CeO₂/GR-2 and Pt-CeO₂/GR-3) were synthesized. The electrocatalytic activity of prepared catalysts was investigated towards the electro-oxidation of methanol by cyclic voltammetry.

Experimental

The platinum supported CeO₂-graphene catalysts were prepared by microwave synthesis. Typical preparation consisted of the following steps: 0.26 ml of 0.0974 M H₂PtCl₆ aqueous solution, 0.94, 9.4 or 85.4 mg CeCl₃, 0.2 ml of 10 mM sodium dodecylsulfate (SDS) and 0.2 ml of 10 M NaOH were mixed with 17 ml of ethylene glycol (EG). Then, 0.3 g of graphene was added to the mixture and sonicated for 30 min. The reaction mixture was put into a microwave reactor Monowave 300 (Anton Paar) at a temperature of 150°C for 5 min. After preparation, the synthesized catalysts were washed with acetone, ultra-pure water with the resistivity of 18.2 MΩ cm⁻¹, then filtered and dried in a vacuum oven at 80°C for 2 h.

The Pt and Ce metal loadings were estimated from Inductively Coupled Plasma Optical Emission Spectroscopy (ICP-OES) measurements. The ICP optical emission spectra were recorded using an ICP optical emission spectrometer Optima 7000DV (Perkin Elmer).

A conventional three-electrode electrochemical cell was used for electrochemical measurements. The working electrode was a thin layer of Nafion-impregnated catalyst cast on a glassy carbon electrode. The catalyst layer was obtained as follows: at first the required amount of Pt-CeO₂/GR or Pt/GR catalysts was suspended by sonication for 2 h in 0.25 μl of 5wt.% Nafion (D521, 1100 EW, Ion Power Inc.) and 0.75 μl of deionized water solution, producing a homogeneous slurry. Then 5 μL of the prepared suspension mixture was pipetted onto the polished surface of a glassy carbon electrode with a geometric area of 0.07 cm² and dried in air for 12 h. The Pt-CeO₂/GR catalysts were employed as working electrodes, a Pt sheet was used as a counter electrode and an Ag/AgCl/KCl electrode was used as reference.

All electrochemical measurements were performed with a Zennium electrochemical workstation (ZAHNER-Elektrik GmbH & Co.KG). Steady state linear sweep voltammograms were recorded in a 1 M CH₃OH + 0.5 M NaOH solution at a scan rate of 50 mV s⁻¹ at a temperature of 25 °C. The presented current densities are normalized with respect to the geometric area of catalysts. All solutions were deaerated by argon for 15 min prior to measurements.

Results and discussion

The platinum supported CeO_2 -graphene catalysts with the Pt:Ce molar ratios equal to 2:1, 1:1 and 1:10 were prepared by means of microwave synthesis. It has been determined that the Pt and Ce loadings were: 42 and $14 \mu\text{g cm}^{-2}$ for Pt- CeO_2 /GR with the Pt:Ce molar ratio equal to 2:1, 54 and $42 \mu\text{g cm}^{-2}$ for Pt- CeO_2 /GR with the Pt:Ce molar ratio equal to 1:1 and 90 and $664 \mu\text{g cm}^{-2}$ for Pt- CeO_2 /GR with the Pt:Ce molar ratio equal to 1:10. For comparison, the carbon supported platinum catalyst (denoted as Pt/C) with the Pt loading of $385 \mu\text{g cm}^{-2}$ was used.

The electrochemically active surface areas (ESAs) of Pt in the synthesized catalysts were determined from the cyclic voltammograms of Pt- CeO_2 /GR with the different Pt:Ce molar ratios recorded in a deaerated 0.5 M H_2SO_4 solution at a sweep rate of 50 mV s^{-1} by calculating the charge associated with hydrogen adsorption ($220 \mu\text{C cm}^{-2}$) (Fig. 1). It has been determined that the values of ESA are 1.0, 1.4 and 1.6 cm^2 for the Pt- CeO_2 /GR-1, Pt- CeO_2 /GR-2 and Pt- CeO_2 /GR-3 catalysts with the Pt loadings of 42, 54 and $90 \mu\text{g cm}^{-2}$, respectively. The ESA value for the Pt/C catalyst is 0.9 cm^2 .

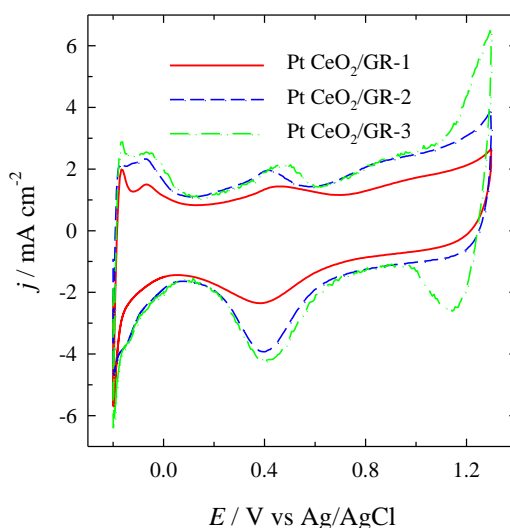


Fig. 1. CVs of the Pt- CeO_2 /GR-1 (solid line), Pt- CeO_2 /GR-2 (dashed line) and Pt- CeO_2 /GR-3 (dash-dotted line) catalysts recorded in 0.5 M H_2SO_4 at 50 mV s^{-1} ; 25°C .

Activity of the Pt- CeO_2 /GR catalysts with the Pt:Ce molar ratios equal to 2:1, 1:1 and 1:10 was evaluated towards the electro-oxidation of methanol in an alkaline medium by cyclic voltammetry. Figure 2 shows CVs for the Pt/GR (a), Pt- CeO_2 /GR-1 (b), Pt- CeO_2 /GR-1 (c) and Pt- CeO_2 /GR-1 (d) catalysts recorded in 1 M $\text{CH}_3\text{OH} + 0.5 \text{ M NaOH}$ at a scan rate of 50 mV s^{-1} . As evident from Fig. 2, in the forward sweep, anodic peaks **A** are seen in the CVs plots at ca. -0.2, -0.15, -0.05 and -0.15 V for the investigated Pt/C (a), Pt- CeO_2 /GR-1 (b), Pt- CeO_2 /GR-2 (c) and Pt- CeO_2 /GR-3 (d) catalysts, respectively, and are related to the direct oxidation of methanol in an alkaline medium. In the reverse sweep, anodic peaks **B** attributed to the removal of the incompletely oxidized carbonaceous species formed in the forward sweep were detected at ca. -0.3 V for the all investigated catalysts. In all cases the reverse anodic peaks **B** recorded on the investigated catalysts are lower as compared to direct methanol oxidation peaks **A** (Fig. 2). During long-term cycling the methanol electro-oxidation current density values (anodic peak **A**) recorded at the all investigated catalysts are slightly decreased and then are stabilized, indicating a high efficiency of the investigated Pt- CeO_2 /GR catalysts and the absence of any significant catalyst losses.

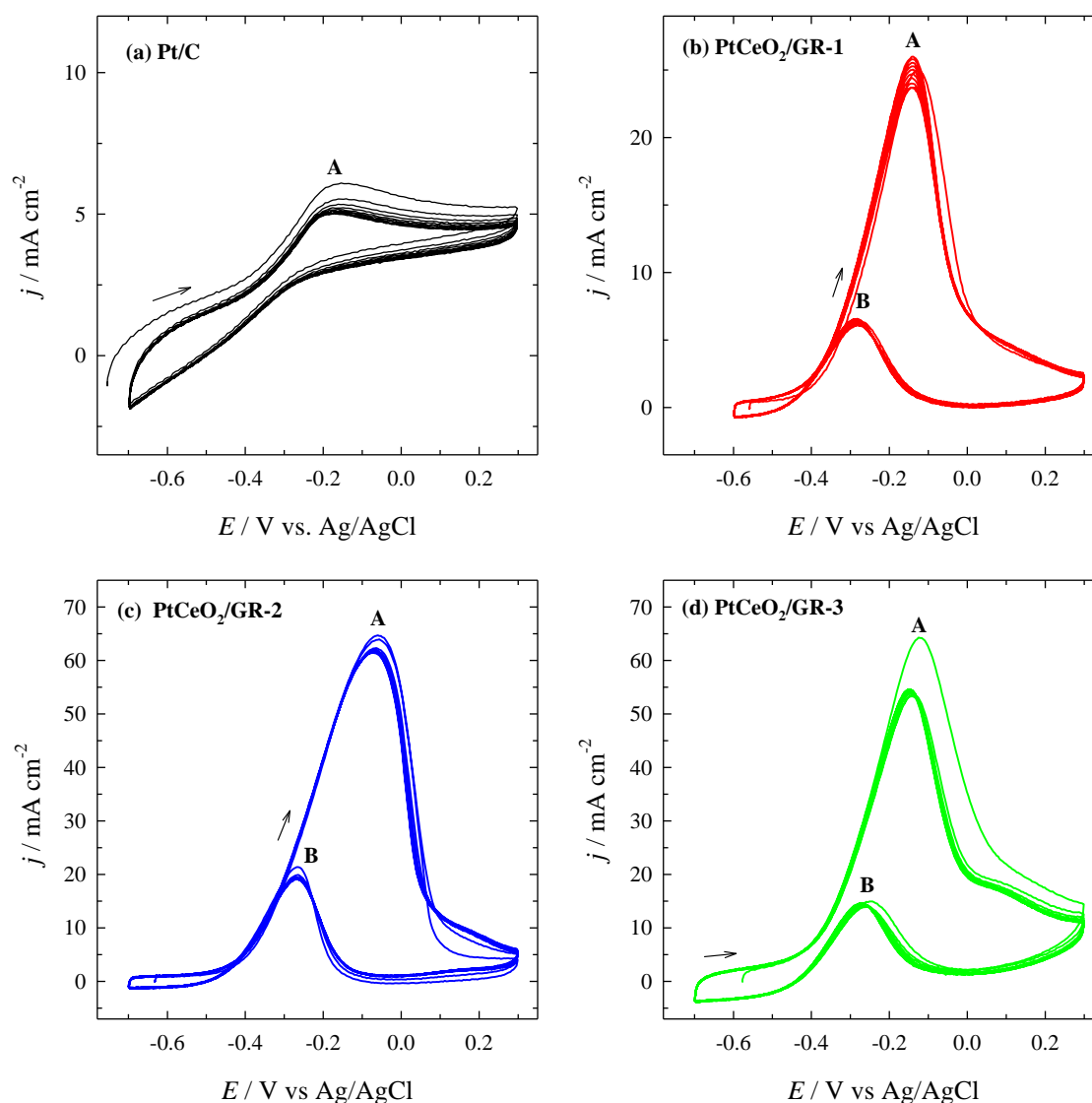


Fig. 2. CVs of Pt/GR (a), Pt-CeO₂/GR-1 (b), Pt-CeO₂/GR-2 (c) and Pt-CeO₂/GR-3 (d) recorded in 1 M CH₃OH + 0.5 M NaOH at 50 mV s⁻¹; 25 °C.

Figure 3a shows positive-potential going stabilized scans (10th cycles) of the electro-oxidation of methanol recorded on the bare Pt/C (*dotted line*), Pt-CeO₂/GR-1 (*solid line*), Pt-CeO₂/GR-2 (*dashed line*) and Pt-CeO₂/GR-3 (*dash-dotted line*) catalysts. As clearly seen from the data in Fig. 3a, the obtained stabilized methanol oxidation current densities are greater at the Pt-CeO₂/GR-1, Pt-CeO₂/GR-2 and Pt-CeO₂/GR-3 catalysts as compared to those at the Pt/C catalyst. Furthermore, methanol oxidation current densities are ca. 5.2, 12.1 and 10.8 times higher at the Pt-CeO₂/GR-1, Pt-CeO₂/GR-2 and Pt-CeO₂/GR-3 catalysts than those at the bare Pt/C catalyst. The Pt-CeO₂/GR catalyst with the Pt:Ce molar ratio equal to 1:1 shows highest activity towards the electro-oxidation of methanol. Ca. 1.1 and 2.4 times greater methanol oxidation current densities are obtained at the latter catalyst as compared to those at the Pt-CeO₂/GR catalysts with the Pt:Ce molar ratios equal to 1:10 and 2:1, respectively.

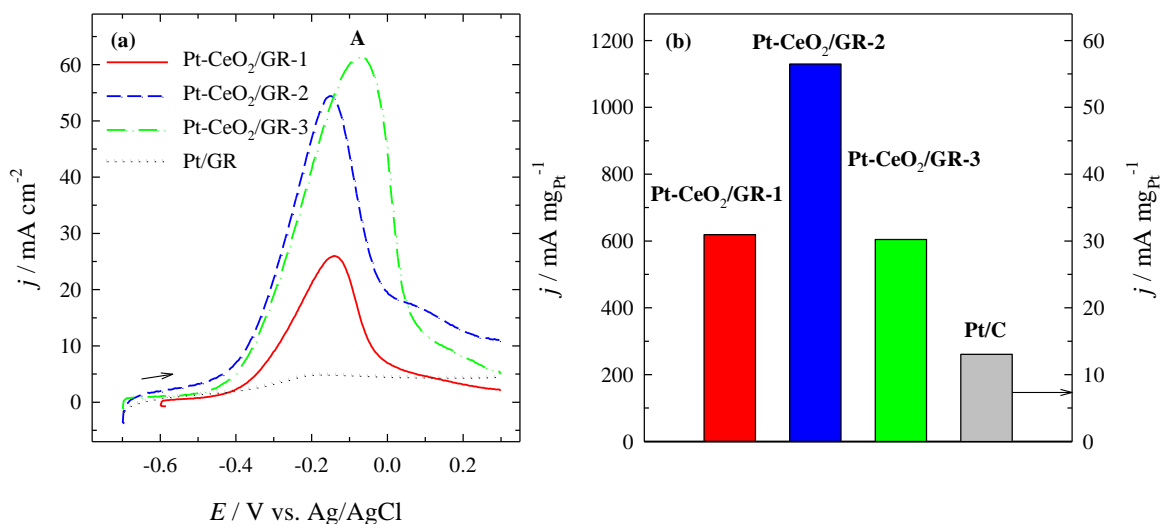


Fig. 3. (a) Positive-potential going scans for Pt/C (*dotted line*), Pt-CeO₂/GR-1 (*solid line*), Pt-CeO₂/GR-2 (*dashed line*) and Pt-CeO₂/GR-3 (*dash-dotted line*) recorded in 1 M CH₃OH + 0.5 M NaOH at 50 mVs⁻¹; 25 °C. (b) The same data are normalized by the Pt loadings for each catalyst.

To represent the mass activity of the investigated catalysts, methanol oxidation current densities were normalized by the Pt loadings for each catalyst. Figure 3b shows bar columns of methanol oxidation Pt-mass activities for the investigated catalysts at a the potential value of peak **A**. Methanol oxidation current densities normalized by the Pt loadings are ca. 47, 87 and 46 times greater at the Pt-CeO₂/GR-1, Pt-CeO₂/GR-2 and Pt-CeO₂/GR-3 catalysts as compared to those at Pt/C (Fig. 3b). The highest Pt-mass activity for methanol oxidation (1129.6 mA mg_{Pt}⁻¹) has Pt-CeO₂/GR with the Pt:Ce molar ratio equal to 1:1. The Pt-mass activity is ca. 1.8 and 1.9 times higher at Pt-CeO₂/GR-2 (Pt:Ce equal to 1:1) than that at Pt-CeO₂/GR-1 (Pt:Ce equal to 2:1) and Pt-CeO₂/GR-3 (Pt:Ce equal to 1:10), respectively.

Conclusions

In this study the platinum supported cerium oxide-graphene catalysts with the Pt:Ce molar ratios equal to 2:1, 1:1 and 1:10 were prepared by means of microwave synthesis.

It has been determined that the prepared Pt-CeO₂/GR catalysts with the Pt:Ce molar ratios equal to 2:1, 1:1 and 1:10 show enhanced electrocatalytic activity towards the electro-oxidation of methanol comparing with the carbon supported bare Pt catalyst. The Pt-CeO₂/GR catalyst with the Pt:Ce molar ratio equal to 1:1 exhibits the highest activity for the electro-oxidation of methanol as compared with that of Pt-CeO₂/GR catalysts with the Pt:Ce molar ratios equal to 2:1 and 1:10 and bare Pt/C catalyst.

The synthesized platinum supported cerium oxide-graphene catalysts seems to be a promising anodic material in production of direct methanol fuel cells.

Acknowledgment

V. Kepenienė acknowledges Postdoctoral fellowship is being funded by European Union Structural Funds project "Postdoctoral Fellowship Implementation in Lithuania".

THE EFFECT OF ELECTROLYTE BATH COMPOSITION ON THE Zn CONTENT IN AgZn NANOWIRES GROWN INSIDE AAO TEMPLATES

E. Kurowska-Tabor¹, K. Gawlak¹, G.D. Sulka¹, M. Jaskuła¹

¹ Faculty of Chemistry at Jagiellonian University in Krakow, ul. Ingardena 3,
30-060 Krakow, Poland

E-mail: kurowska@chemia.uj.edu.pl

During the recent years, there has been a rapid growth of interest in fabrication and characterization of all kinds of nanostructured materials because of their unique properties such as electronic, magnetic and optoelectronic [1]. Periodic structures, for example nanopores, nanotubes or nanowires have gained a lot of excitement because of the high order and high surface area that can significantly improve their properties. An example of such kind of material is nanoporous silver which offers many potential applications, such as: molecular adsorption, ion exchangers, medical materials or heterogeneous catalysts [2]. Moreover, nanostructured silver is recently extensively studied as a promising material for sensing applications (e.g. for amperometric detection of H₂O₂) [3]

Nanoporous Ag nanowires were obtained by two-step procedure. During the first step anodic aluminum oxide (AAO) was used as a template for electrodeposition of AgZn nanowires. Three different electrolytes were used for electrodeposition: 1) cyanide bath where the molar ratio of Ag to Zn was 1:3, 2) cyanide bath where the molar ratio of Ag to Zn was 1:10, 3) an alkaline cyanide bath where the molar ratio of Ag to Zn ratio was 1:10, 4) nitrate bath with thiourea. During the second step a selective etching of Zn was performed in 5% sulfuric acid solution. The morphology of as obtained nanostructures and their composition were characterized using a Scanning Electron Microscope and EDS microanalysis, respectively.

As obtained nanoporous Ag nanowires will be used for detection and determination of hydrogen peroxide. It is strongly believed that such electrodes exhibit a low limit of determination, quick current response, high sensitivity, selectivity and stability.

References

1. G.D. Sulka; in: *Nanostructured Materials in Electrochemistry*, Ali Eftekhari (Ed.), **2008** Wiley-VCH, pp 1-116.
2. C. Zhang, J. Sun, J. Xu, X. Wang, H. Ji, C. Zhao, Z. Zhang, *Electrochim. Acta* **63** (2012) 302-311.
3. E. Kurowska, A. Brzózka, M. Jarosz, G.D. Sulka, M. Jaskuła, *Electrochim. Acta* **104** (2013) 439-447.

Acknowledgements

The project was funded by the National Science Centre granted under decision no. DEC-2012/07/N/ST5/00155.



STUDY OF ARTIFICIAL LIGHT HARVESTING ANTENNAE BY QUANTUM CHEMICAL METHODS

Svetlana Malickaja¹, Mindaugas Macernis^{1,2} and Juozas Sulskus¹, Leonas Valkunas^{1,2}

1 Department of Theoretical Physics, Faculty of Physics, Vilnius University, Vilnius, Lithuania

2 Center for Physical Sciences and Technology, Vilnius, Lithuania

E-mail: svetlana.malickja@ff.vu.lt

Carotenoids play a crucial role in the energy dissipation process by quenching chlorophyll singlet excited states in photosynthetic antennae. Additionally, they are also involved in the photoprotection process in green plants as quenchers of chlorophyll triplets and, thus, responsible for protection of the system from the singlet oxygen generation [1]. Artificial light-harvesting antennae are used for better understanding the details of carotenoids involved in light harvesting, energy transfer, electron transfer, and photoprotective processes [1,2]. These artificial structures are capable of performing the specific functions carried out by their natural counterparts. The experimental and theoretical investigation allows one to determine photophysical and photochemical mechanisms underlying the behaviour of the natural systems [2].

Here we present our quantum chemical study of phthalocyanine-carotenoid dyads in which a phenylamino group links phthalocyanine to carotenoids having 8–11 backbone double bonds. We analysed the structures in the ground and excited electronic state, the dependence of electronic excitation characteristics of dyads on the conjugation length of carotenoids. The geometry optimizations were performed using DFT (in the ground electronic state) and TD-DFT (in the excited electronic state) with the CAM-B3LYP long-distance corrected exchange-correlation functional and the 6-31G(d,p) basis set.

References

1. R. Berera, C. Herrero, I. H. M. van Stokkum, M. Vengris, G. Kodis, R. E. Palacios, H. van Amerongen, R. van Grondelle, D. Gust, T. A. Moore, A. L. Moore, J. T. M. Kennis, *PNAS* **103** (2006) 5343–5348.
2. M. Kloz, S. Pillai, G. Kodis, D. Gust, T. A. Moore, A. L. Moore, R. van Grondelle, J. T. M. Kennis, *J. Am. Chem. Soc.* **133** (2011) 7007–7015.

SERS STUDY OF 4-IMIDAZOLEMETHANOL INTERACTION WITH COPPER ELECTRODE

I. Matulaitienė¹, E. Pociūtė², Z. Kuodis¹, O. Eicher-Lorka¹, G. Niaura¹

1 Center for Physical Sciences and Technology, A. Goštauto 9, LT-01108 Vilnius, Lithuania

2 Faculty of Chemistry, Vilnius University, Naugarduko 24, LT-03225 Vilnius, Lithuania

E-mail: ieva.matulaitiene@ftmc.lt

Biological molecules containing imidazole (Im) ring such as histamine and histidine are involved in various processes of mammals. Im ring plays important role in coordination of metal ions in proteins and peptides [1, 2]. Surface enhanced Raman spectroscopy (SERS) is able to provide the better understanding on interaction between biological molecules containing Im ring and the metal surface. In this work the simplest imidazole derivative, 4-Imidazolemethanol (ImMeOH), was chosen. It does not contain surface active or bulky functional groups, thus facilitates direct interaction of Im group with the metal surface. Copper electrode was chosen for its biological properties; histamine interacts with its receptor through copper ions, also copper plays role in some enzyme-substrate interactions.

In neutral aqueous solutions ImMeOH can exist in two tautomeric forms (Figure 1) depending on which nitrogen atom of Im ring is protonated (N1 or N3). They can be distinguished by Raman spectroscopy based on their specific vibrations [3–5]. It was found that Tautomer-I dominates in aqueous solutions of ImMeOH.

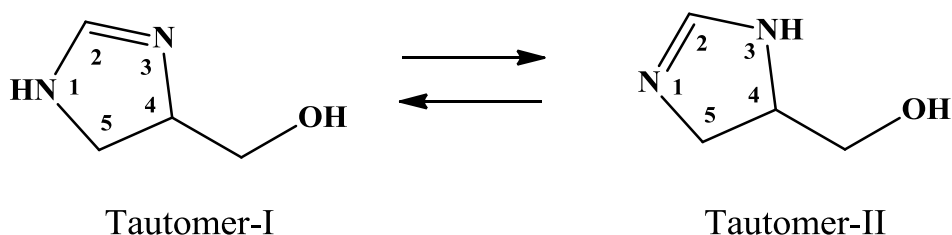


Figure 1. Structures of 4-Imidazolemethanol (ImMeOH) tautomers.

To understand which tautomeric form interacts with copper surface, SERS measurements were performed. Figure 2 compares SERS spectra of ImMeOH at broad selected Cu electrode potentials (from -0.5 V to -1.1 V). The intensive band visible near $937\text{--}952\text{ cm}^{-1}$ belongs to adsorbed phosphate anion. The strong bands near $1279\text{--}1280\text{ cm}^{-1}$ and $1579\text{--}1589\text{ cm}^{-1}$ belong to imidazole functional group vibrations of adsorbed ImMeOH. It shows that ImMeOH chemisorbs with phosphate anions on Cu electrode surface. Positions of two bands near 1579 and 1491 cm^{-1} ($E = -1.1$ V) are very sensitive to electrode potential. The $\nu(\text{C4}=\text{C5})$ vibrational mode near 1579 cm^{-1} is sensitive to Im ring bonding with metal surface. Observed decrease in peak frequency at more negative electrode potential could be associated with decreased interaction strength with metal either changes in tautomeric forms for adsorbed ImMeOH.

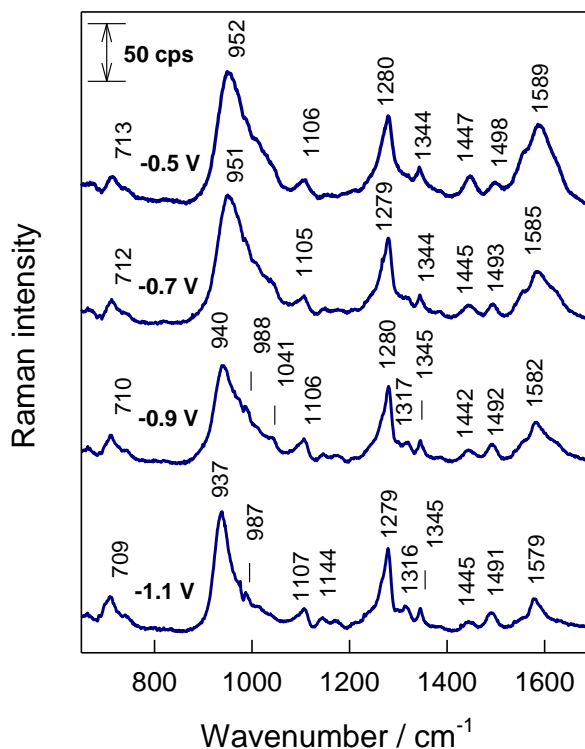


Figure 2. SERS spectra of ImMeOH adsorbed on Cu electrode at broad electrode potentials range (from -0.5 V to -1.1 V), in the fingerprint spectral region. Measurement conditions: 0.1 M Na_2SO_4 solution containing 0.01 M phosphate buffer (pH 7.0) and 10^{-4} M of ImMeOH; excitation wavelength, 785 nm; laser power at the sample, 30 mW; integration time, 300 s.

To ensure accurate assignments of the bands isotopic substitution was performed. Labile hydrogen atoms at Im ring and OH group were substituted by deuterium atoms. Figure 3 shows SERS spectra of ImMeOH in solutions prepared with H_2O and D_2O at -1.1 V electrode potential.

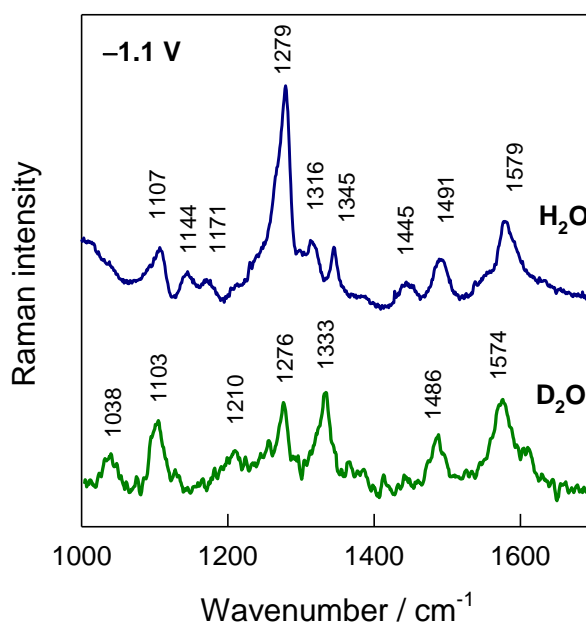


Figure 3. SERS spectra of ImMeOH adsorbed on Cu electrode at -1.1 V potential in solutions prepared from H_2O and D_2O . Measurement conditions: 0.1 M Na_2SO_4 solution containing 0.01 M phosphate buffer (pH 7.0) and 10^{-4} M of ImMeOH; excitation wavelength, 785 nm; laser power at the sample, 30 mW; integration time, 300 s.

Well-defined bands at 1579 and 1491 cm^{-1} clearly shift in D_2O solution to 1574 and 1486 cm^{-1} , respectively. Based on earlier observations and quantum chemical calculations these two bands were assigned to $\nu(\text{C4}=\text{C5})$ and mixed $\nu(\text{C2}-\text{N3})+\beta(\text{C2H})$ vibrational modes, respectively. Downshift in frequencies confirms that in adsorbed state one of the imidazole ring nitrogen atom is protonated. The peak at 1279 cm^{-1} shifts slightly, it was assigned to Im ring breathing mode coupled with C2H in-plane bending vibration. Position of this band is useful to discriminate tautomeric forms of imidazole ring appearing near 1282 and 1260 cm^{-1} for Tautomer-I and Tautomer-II, respectively [4]. Thus, SERS data provide evidence that in the adsorbed state of ImMeOH the Tautomer-I dominates. Therefore, the interaction with surface must take place through the N3 atom of Im ring (Fig. 1). The intensification of the band near 1328 cm^{-1} was clearly observed earlier in D_2O solution Raman spectrum. Thus, observation the similar band in the SERS spectrum (1333 cm^{-1}) of copper electrode immersed in D_2O solution confirms the domination of Tautomer-I in adsorbed state of Im MeOH. The intense peak in D_2O SERS spectrum near 1103 cm^{-1} corresponding to mixed $\nu(\text{N1}-\text{C2})+\beta(\text{N1H})+\beta(\text{C2H})$ mode is shifted by 5 cm^{-1} comparing with solution D_2O Raman spectrum. This frequency shift indicates that in the adsorbed state the N1H group of Im ring is involved in the hydrogen bonding interaction of different strength comparing with the solution case. In conclusion, we have demonstrated that Im ring of ImMeOH interacts with copper electrode surface through the N3 atom. Potential-dependent studies revealed decrease in frequency of $\nu(\text{C4}=\text{C5})$ vibrational mode at more negative electrode potentials indicating decrease in interaction strength with the metal surface.

References

1. H. Takeuchi, *Biopolymers*, **72** (2003) 305–317.
2. V. Feyer, O. Plekan, N. Tsud, V. Cháb, V. Matolín, K.C. Prince, *Langmuir*, **26** (2010) 8606–8613.
3. F.J. Ramfrez, I. Tunon, J.A. Collado, E. Silla, *J. Am. Chem. Soc.*, **125** (2003) 2328–2340.
4. A. Toyama, K. Ono, S. Hashimoto, H. Takeuchi, *J. Phys. Chem. A*, **106** (2002) 3403–3412.
5. J.G. Mesu, T. Visser, F. Soulimani, B.M. Weckhuysen, *Vibr. Spectrosc.*, **39** (2005) 114–125.

MICROWAVE-ASSISTED SYNTHESIS OF GRAPHENE SUPPORTED SILVER AND PLATINUM-SILVER NANOPARTICLES FOR FORMALDEHYDE OXIDATION

A. Matusėvičiūtė, A. Balčiūnaitė, R. Kondrotas, L. Tamašauskaitė-Tamašiūnaitė, E. Norkus

*Center for Physical Sciences and Technology, A. Goštauto 9, LT-01108 Vilnius, Lithuania
E-mail: agnemat29@gmail.com*

Introduction

Recently, graphene as catalyst support has incurred intense interest in fuel cell applications due to its unique, outstanding physicochemical properties, such as extremely high specific surface area ($2600 \text{ m}^2 \text{ g}^{-1}$) [1]. Carbon nanostructural materials have received a great deal of attentions for their possible electrochemical and catalytic applications in a wide variety of technical areas, thanks to their unique structural features, electronic properties, thermal conductivity and electrochemical stability. Graphene, as a new two-dimension carbon nanomaterial, has attracted significant attention recently, because of its unique properties and potential applications including its antimicrobial characteristic. The ideal monolayer graphene has extended honeycomb structure lattice of sp^2 hybridized carbon and is only one atom thick [2, 3].

It has been known that antimicrobial materials are widely used in the daily life to protect the public health. Ag NPs is the high efficient antimicrobial agent. However, Ag NPs is easy to agglomerate in the process of preparation.

This work is focused on the preparation of the graphene supported silver, platinum and platinum-silver catalysts via rapid microwave heating as electrocatalysts for the oxidation of formaldehyde in an alkaline medium.

Experimental

Fabrication of catalysts by microwave synthesis

The graphene supported Pt-Ag catalyst (denoted as Ag/GR and Pt-Ag/GR) was prepared by microwave synthesis. Typical preparation consisted of the following steps: 1.8 ml of 0.0974 M H_2PtCl_6 aqueous solution and 0.02 g AgNO_3 and 0.2 ml of 10 M NaOH were mixed with 18 ml of ethylene glycol (EG). Then, 0.3 g of graphene was added to the mixture and sonicated for 30 min. For the microwave irradiation, the reaction mixture was put into a microwave reactor Monowave 300 (Anton Paar). The reduction of Pt-Ag nanoparticles was carried out at a temperature of 150°C for 30 s. For comparison, the graphene supported silver (denoted as Ag/GR) and platinum (denoted as Pt/GR) catalysts were prepared under the same conditions. After preparation, the synthesized catalysts were washed with acetone, ultra-pure water with the resistivity of $18.2 \text{ M}\Omega \text{ cm}^{-1}$, then filtered and dried in a vacuum oven at 80°C for 2 h.

Characterization of catalysts

The shape and size of catalyst particles were examined using a transmission electron microscope Tecnai G2 F20 X-TWIN equipped with an EDAX spectrometer with an r-TEM detector. For microscopic examinations, 0.010 g of sample were first sonicated in 1 ml of ethanol for 1 h and then deposited on Cu grid covered with a continuous carbon film.

The Ag and Pt metal loadings were estimated from Inductively Coupled Plasma Optical Emission Spectroscopy (ICP-OES) measurements. The ICP optical emission spectra were recorded using an ICP optical emission spectrometer Optima 7000DV (Perkin Elmer).

Electrochemical measurements

A conventional three-electrode electrochemical cell was used for electrochemical measurements. The working electrode was a thin layer of Nafion-impregnated catalyst cast on a glassy carbon electrode. The catalyst layer was obtained as follows: at first the required amount of Ag/GR, Pt/GR or PtAg/GR catalysts was suspended by sonication for 2 h in 0.25 μl of 5wt.% Nafion (D521, 1100 EW, Ion Power Inc.) and 0.75 μl of deionized water solution, producing a homogeneous slurry. Then 5 μL of the prepared suspension mixture was pipetted onto the polished surface of a glassy carbon electrode with a geometric area of 0.2 cm^2 and dried in air for 12 h. The Pt/GR, Ag/GR and PtAg/GR catalysts were employed as working electrodes, a Pt sheet was used as a counter electrode and an Ag/AgCl/KCl electrode was used as reference.

All electrochemical measurements were performed with a Zennium electrochemical workstation (ZAHNER-Elektrik GmbH & Co.KG). Steady state linear sweep voltammograms were recorded in a 0.05 M HCHO + 1 M NaOH solution at a linear potential sweep rate of 10 mV s^{-1} at a temperature of 25 $^{\circ}\text{C}$. The presented current densities are normalized with respect to the geometric area of catalysts. All solutions were deaerated by argon for 15 min prior to measurements.

Results and discussion

The graphene supported silver, platinum and platinum-silver catalysts were prepared by means of microwave synthesis. Figure 1 shows TEM views of the Ag/GR (a), Pt/GR (b) and PtAg/GR (c) catalysts. It was found that Ag nanoparticles in size of 6-30 nm were deposited on the surface of graphene in the Ag/GR catalyst (Fig. 1a). Pt nanoparticles of 1-4 nm in size were deposited on the surface of graphene in the Pt/GR and Pt-Ag/GR catalysts (Fig. 1b,c).

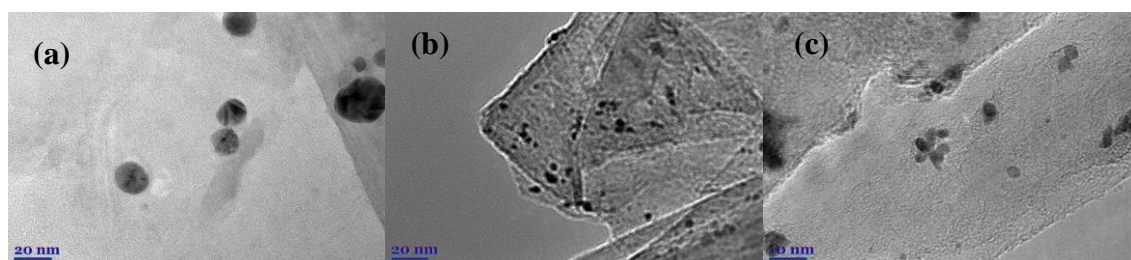


Fig.1. TEM views of the Ag/GR (a), Pt/GR (b) and PtAg/GR (c) catalysts prepared by microwave synthesis.

The Pt loadings in the synthesized catalysts were determined by ICP optical emission spectrometry measurements. It has been determined that the Pt loading was 52 $\mu\text{g Pt cm}^{-2}$ in the Pt/GR catalyst. The Ag loading was 44 $\mu\text{g Ag cm}^{-2}$ in the Ag/GR catalyst. The Pt and Ag loadings were 48 and 43 $\mu\text{g cm}^{-2}$, respectively, in the Pt-Ag/GR catalyst.

Activity of the Ag/GR, Pt/GR and Pt-Ag/GR catalysts was evaluated towards formaldehyde oxidation in an alkaline medium by cyclic voltammetry. Figure 2 shows CVs for the Ag/GR (a), Pt/GR (b) and Pt-Ag/GR (c) catalysts recorded in 0.05 M HCHO + 1 M NaOH at a scan rate of 10 mV s^{-1} . In the case of Ag/GR catalyst (Fig. 1a), two anodic peaks **A0** and **A** are seen in the CVs plots. Peak **A** is attributed to formaldehyde oxidation. Peak **A1** may be attributed to the formation of silver oxides, while the cathodic peak **C1** observed in

the reverse scan at ca. 0 V is related with a reduction of the silver oxides and consequent reactivation of the electrode surface.

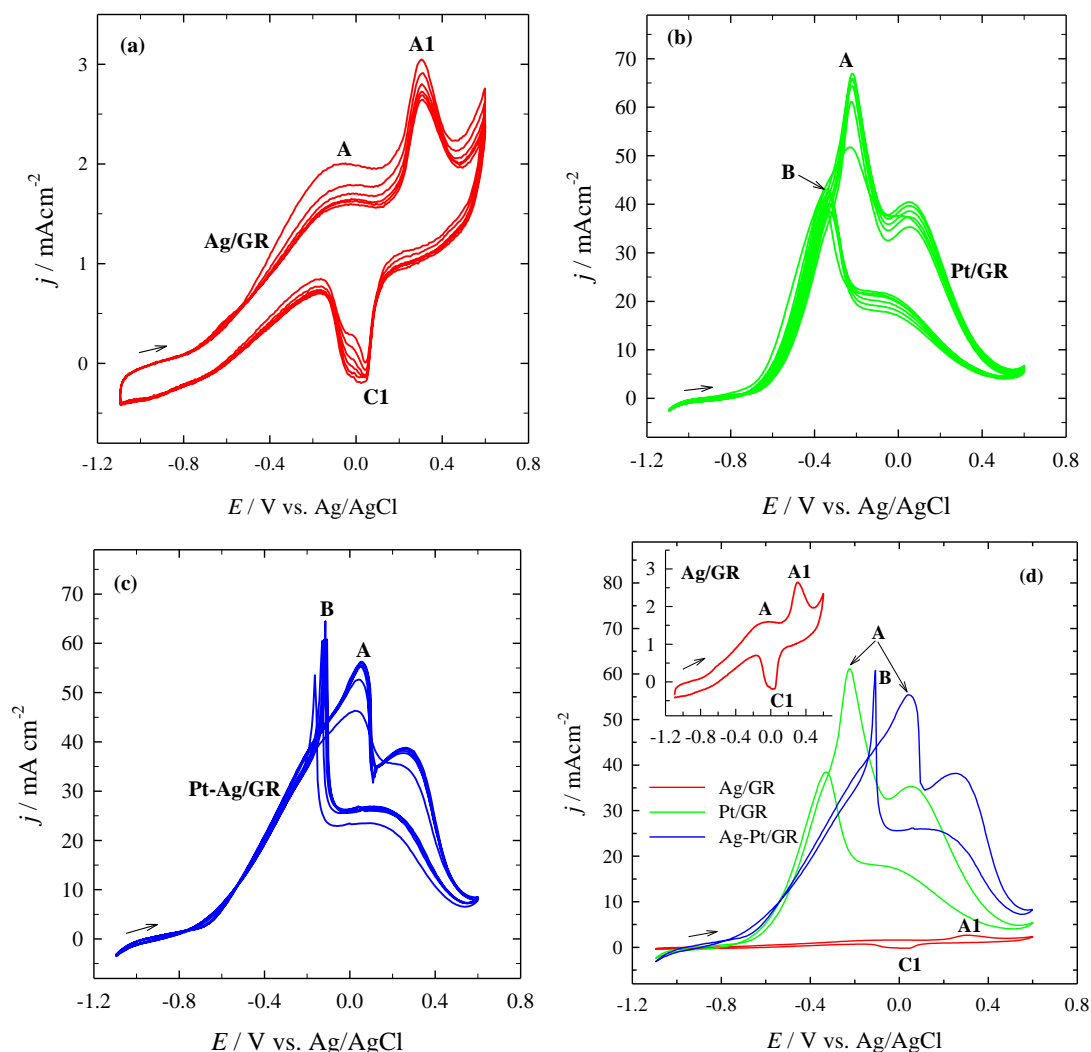


Fig. 2. CVs of Ag/GR (a), Pt/GR (b) and Pt-Ag/GR (c) recorded in 0.05 M HCHO + 1 M NaOH at 10 mV s⁻¹; 25 °C. (d) Stabilized CVs (5th cycles) for the same catalysts.

In the case of the Pt/GR and Pt-Ag/GR catalysts, wide double anodic peaks **A** are seen in the CVs plots (Fig. 2b,c). Notably, formaldehyde oxidation current densities are significantly higher at Pt/GR and Pt-Ag/GR as compared with those at Ag/GR.

During long-term cycling, formaldehyde oxidation current densities are stabilized and remain constant, indicating a high efficiency of the investigated catalysts and the absence of any significant catalyst losses.

Conclusions

In this study the graphene supported silver, platinum and platinum-silver nanoparticles catalysts were prepared by means of microwave synthesis. It was found that Pt nanoparticles in size of 1-4 nm were deposited on the surface of graphene in the Pt/GR and Pt-Ag/GR catalysts, while Ag particles of 6-30 nm in size were deposited on the surface of graphene in the Ag/GR catalyst.



It has been determined that the Pt/GR and Pt-Ag/GR catalysts exhibited enhanced activity towards the oxidation of formaldehyde as compared with that of the Ag/GR catalyst.

Acknowledgment

This research was funded by a Grant (No. ATE-08/2012) from the Research Council of Lithuania.

References

1. R. England, LabPlus International-April / May, (2003) 1-3.
2. Z. Gan, X. Zheng, D. Wei and others, , Superlattices and Microstructures, **47** (2010) 705-709.
3. Z. Wang, M. Shoji, H. Ogata, Applied Surface Science, **259** (2012) 219-224.

INFLUENCE OF Co-P LAYER ON THE STRUCTURE AND ELECTROCHEMICAL PROPERTIES OF Se-WO₃ THIN FILMS

S. Ostachavičiūtė, E. Valatka

*Department of Physical and Inorganic Chemistry, Kaunas University of Technology,
Radvilėnų pl. 19, LT-50254 Kaunas, Lithuania
E-mail: simona.ostachaviciute@ktu.lt*

Se-WO₃, Co-P and Se-WO₃/Co-P films were formed on the FTO glass substrate in order to evaluate their structure and the influence of Co-P layer on the electrochemical properties of Se-WO₃ thin films. It was established that cobalt based oxygen evolving catalyst has a positive effect on the electrocatalytic activity of Se-WO₃ thin films. When Se-WO₃/Co-P catalyst is used the onset potential of oxygen evolution reaction is at approximately 0.8 V.

Keywords: tungsten oxide, OER, Co-P

Introduction

It is well established that the oxygen evolution reaction (OER) is a rate-limiting step of the water photosplitting process. A rutile-type RuO₂ and IrO₂ have been identified to exhibit the lowest overpotential toward the OER. However, their practical use as electrocatalytic materials is hindered by the limited availability of ruthenium and iridium compounds in the Earth's crust. For these reasons, the efforts have been made in the search of OER catalyst based on earth-abundant elements. In 2008, Nocera and Kanan reported for the first time that the electrolysis of Co²⁺ salts in neutral phosphate electrolyte using ITO electrodes leads to the formation of highly active water oxidation catalyst [1-3]. The as-deposited cobalt phosphate compound (termed Co-P) has been proved to be very active in neutral pH solutions. It has been demonstrated that the cobalt phosphate compound, when coupled with semiconductors, can enhance the efficiency of photoelectrochemical water splitting.

The aim of this work was to synthesize Se-WO₃ catalysts modified with Co-P layer and to investigate the structure and electrochemical properties of such composites.

Materials and Methods

Se-WO₃ thin films on FTO (TEC15) glass substrate were prepared by electrochemical deposition using a standard three electrode cell. Both selenious acid (H₂SeO₃, 99.8 % purity) and sodium tungstate (Na₂WO₄·2H₂O, purity 99.7 %) were obtained from Reachim (Russia) and used as received. The electrolyte itself was prepared according to the following procedure. Firstly, sodium tungstate solution was mixed with hydrogen peroxide (H₂O₂, 30%, Lach-Ner, Czech Republic). Afterwards, selenious and nitric acids (HNO₃, 65%, Penta, Czech Republic) were added to the solution containing tungsten(VI)-peroxo complex. All measurements were carried out at an ambient temperature. The as-deposited samples were thermally treated under air atmosphere at 400 °C for 1 h. Optimal conditions for the electrodeposition were -0.6 V and 20 min.

The layer of Co-P oxygen evolving catalyst was formed using electrochemical route: it was formed at 1.1 V from 0.1 M phosphate buffer + 0.5 mM Co(NO₃)₂ solution. The duration of synthesis for bare Co-P layer on TEC15 glass substrate was 60 minutes and 10 minutes if the layer was formed on the Se-WO₃ thin film.

0.1 M phosphate buffer of pH 7 was prepared using following procedure: 61.5 ml of K₂HPO₄ (> 98 %, Reachim, Russia) and 38.5 ml KH₂PO₄ (> 98 %, Reachim, Russia) of 1 M stock solutions were combined and then diluted to 1 litre with distilled water.

All scanning electron microscopy (SEM) images were acquired using *Helios Nanolab 650* (FEI, Netherlands) scanning electron microscopes operating at 2 kV accelerating voltage. Integrated *EDX detector* (Oxford Instruments plc, United Kingdom) was used for Energy-dispersive X-ray spectroscopy (EDX).

The electrocatalytic activity of prepared catalyst was investigated using voltammetric methods. The electrochemical measurements were performed by computer-controlled *Autolab PGSTAT12* (Ecochemie, The Netherlands) potentiostat/galvanostat. A photoelectrochemical quartz cell was employed. The electrolyte volume was 100 mL. Throughout the paper all potentials are referred to Ag, AgCl | KCl_(sat) reference electrode. A platinum wire was used as a counter electrode. 0.1 M phosphate buffer (pH 7) was used as a supporting electrolyte.

Results and discussion

Figure 1 demonstrates SEM images of FTO/Se-WO₃ (a), FTO/Co-P (b) and FTO/Se-WO₃/Co-P (c, d) electrodes. Porous structure of Se-WO₃ can be easily distinguished under the islands of Co-P catalyst. The thickness of Se-WO₃ films is ~300 nm and that of Co-P is ~450 nm. The results of EDX analysis of Se-WO₃/Co-P are provided in Table 1.

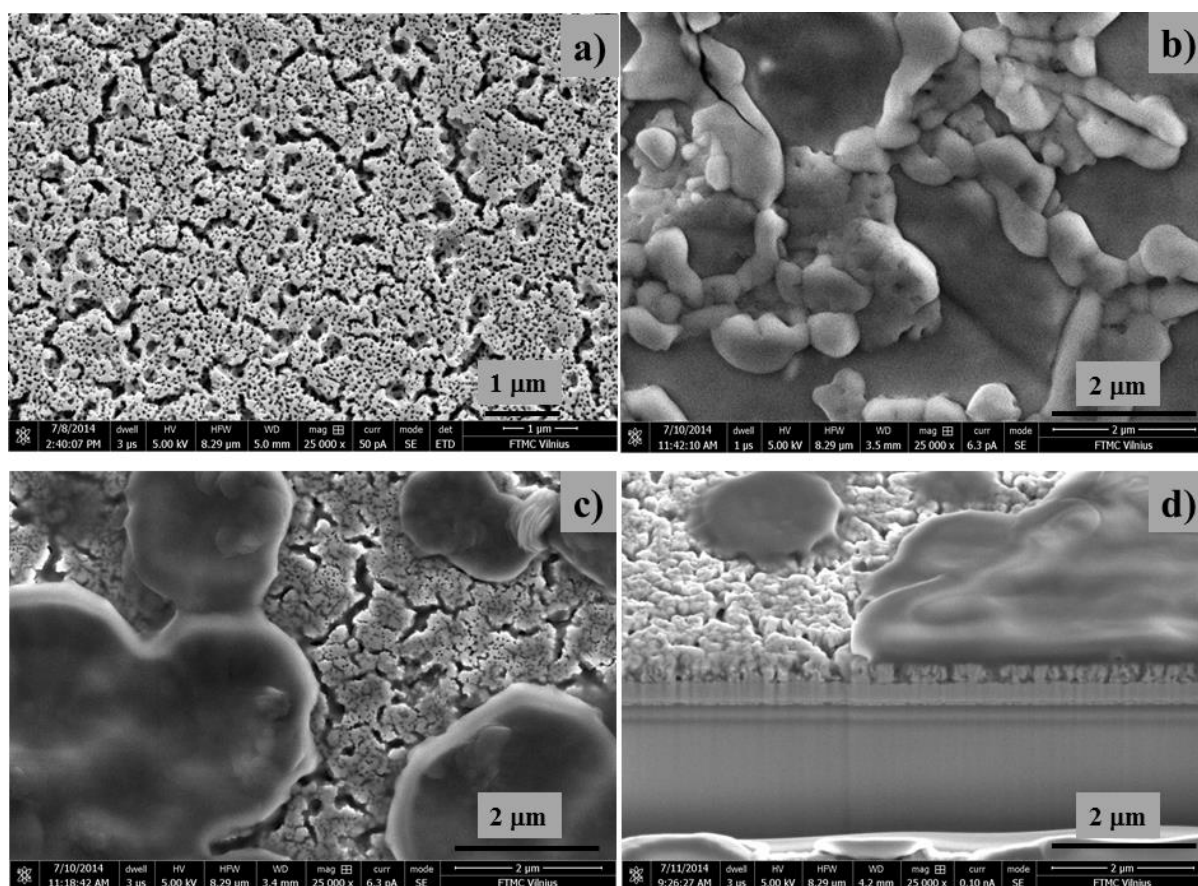


Fig. 1. SEM images of FTO/Se-WO₃ (a), FTO/Co-P (b) and FTO/Se-WO₃/Co-P (c, d) electrodes

Table 1. Atomic composition of Se-WO₃/Co-P film on FTO glass substrate

Atomic composition (%)						
O	Na	P	K	Co	Se	W
62.40	0.67	7.69	14.31	8.14	0.24	6.55

Voltammograms of prepared Se-WO₃, Co-P and Se-WO₃/Co-P anodes (Figure 2) in the dark demonstrate that the presence of oxygen evolving catalyst shifts the onset potential for this reaction: for Se-WO₃/Co-P catalyst it starts at approximately 0.8 V.

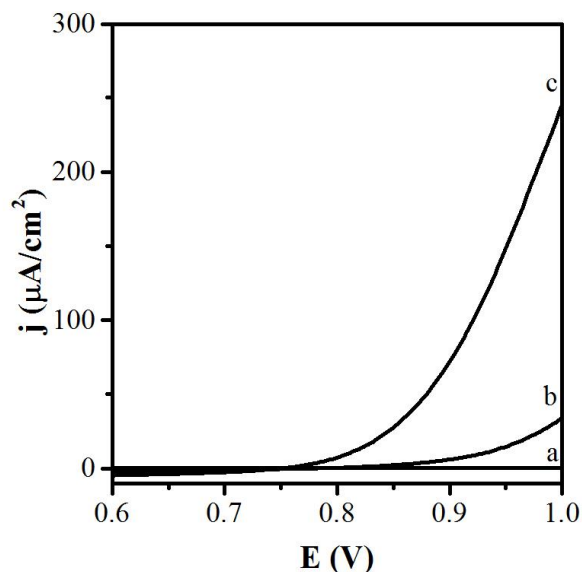


Fig. 2. Characteristic voltammograms in the dark of Se-WO₃ (a), Co-P (b) and Se-WO₃/Co-P (c) films on FTO glass in 0.1 M phosphate buffer. Potential scan rate $v = 10 \text{ mV}\cdot\text{s}^{-1}$

In order to evaluate electrocatalytic activity of prepared Se-WO₃/Co-P catalyst, the Tafel slopes b were calculated (Figure 3). Data used for Tafel plots was obtained via chronoamperometry: multiple current profiles were recorded at constant potential varying from 0.8 to 1.0 V at 0.02 V step, time of each experimental run being 5 min.

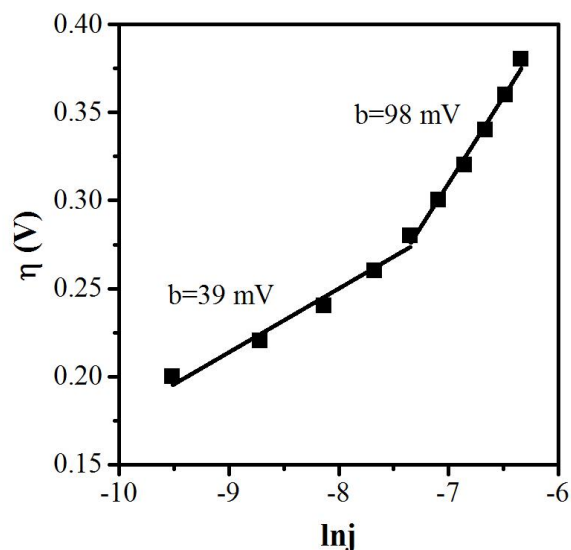


Fig. 3. Tafel plot for FTO/Se-WO₃/Co-P electrode. Supporting electrolyte: 0.1 M phosphate buffer (pH 7)

It is generally accepted that oxygen evolution reaction on oxide electrodes proceeds in a following mechanism [4, 5]:



where Δ – surface active site.

The analysis of reaction mechanism is mostly based on the value of the Tafel slope. In Figure 3 two different Tafel slope values can be observed as a function of overpotential, a lower slope (39 mV) at low overpotentials and a higher one (98 mV) at high overpotentials, which is quite common for the oxide electrodes. This transition can be attributed to change in rate determining step of the same mechanism or change in mechanism. According to the proposed mechanism, step (1) is the rate determining step (Tafel slope close to 120 mV) if oxygenated intermediates are weakly binded to the surface of a catalyst. If oxygenated intermediates are adsorbed strongly, step (1) is very fast and then step (2) (Tafel slope close to 40 mV) or (3) (Tafel slope close to 60 mV) become rate determining. The latter is preferable and observed in the materials which are more active in electrocatalysis.

Conclusions

Se-WO₃, Co-P and Se-WO₃/Co-P films were deposited by electrochemical methods and their structure and electrochemical properties were examined. SEM and EDX analyses revealed that porous surface of Se-WO₃ is covered with islands of Co-P oxygen evolving catalyst in the composite Se-WO₃/Co-P thin films. Voltammetric data of prepared electrocatalysts showed that Co-P layer on the Se-WO₃ thin films shifts onset potential for the oxygen evolution reaction: this reaction starts at approximately 0.8 V. Calculated Tafel slope b for FTO/Se-WO₃/Co-P electrode is 39 mV at the range of low overpotentials and 98 mV at higher overpotentials. This data shows that Se-WO₃/Co-P catalyst is promising in search of highly effective electrocatalyst for anodic water oxidation.

Acknowledgements

The authors wish to express their gratitude to Arnas Naujokaitis (Center for Physical Sciences and Technology, Vilnius) for the SEM images and EDX analysis.

References

1. M. W. Kanan, D. G. Nocera, *Science*, **2008**, 321 (5892), 1072.
2. M. W. Kanan, Y. Surendranath, D. G. Nocera, *Chem. Soc. Rev.*, **2009**, 38(1), 109.
3. D. K. Bediako, C. Costentin, E.C. Jones, D. G. Nocera, J. M. Saveant, *J. Am. Chem. Soc.*, **2013**, 135(28), 10492.
4. E. Guerrini, S. Trassatti, *Russ. J. Electrochem.*, **2006**, 42 (10), 1017.
5. H. Dau, C. Limberg, T. Reier, M. Risch, S. Roggan, P. Strasser, *Chemcatchem*, **2010**, 2 (7), 724.



EFFECT OF THE MODIFICATION OF NANOPOROUS TITANIUM DIOXIDE LAYERS ON DRUG DELIVERY PROFILES

A. Pawlik¹, M. Jarosz¹, G. D. Sulka¹

1 Department of Physical Chemistry & Electrochemistry, Faculty of Chemistry, Jagiellonian University in Krakow, Ingardena 3, 30060 Krakow, Poland

E-mail: anna9.pawlik@uj.edu.pl

Titanium and its alloys are widely used as implantable materials. They have disability to bond to the surrounding bones what can lead to post-operative infections or implant failure. Advances in nanotechnology have led to the improvement in cytocompatibility properties of implantable materials. Anodization of titanium results in formation of a bioactive and nanoporous titanium dioxide layer. These layers are not only more biocompatible compared to unanodized titanium, but also can be used as efficient drug delivery systems (DDS). Drugs, such as analgetics, can be effectively loaded inside the formed nanopores of anodic TiO₂ [1].

Nanoporous TiO₂ layers were prepared via a three-step anodization process in an ethylene glycol electrolyte which contains fluoride ions, at the constant anodizing potential of 40 V. The first and second step of anodization last 3 h, while the duration of the third one was 10min. Ibuprofen as a representative of anti-inflammatory drugs was used for drug delivery studies. It was loaded by pipetting 1 ml of the drug solution (10 wt.%) onto the nanoporous TiO₂ surface and this step was repeated after evaporation of the solvent. The loaded samples were then immersed in a phosphate buffer solution (PBS, pH = 7.2) at 37 °C. The whole volume of solution was collected at appropriate time intervals and replaced with the fresh PBS. The drug content was determined by spectrophotometry. Drug release profiles were compiled based on calculated concentrations of the medicine. The proposed function, being a combination of desorption and diffusion processes, was fitted to the resulting profiles. The modification of the crystalline structure by heat-treatment by simple immersion in a sodium hydroxide solution were examined. The modified and non-modified nanoporous titanium dioxide layers were characterized by Scanning Electron Microscopy. The contact angle tests were performed as well.

References

1. Ch. Yao, T.J. Webster, Journal of Biomedical Materials Research. Part B, Applied Biomaterials, **91** (2009) 587 – 595.

Acknowledgements:

The research was partly funded from the project Interdisciplinary PhD Studies “Molecular sciences for medicine” (co-financed by the European Social Fund within the Human Capital Operational Programme).

Anna Pawlik acknowledges the financial support from the The Marian Smoluchowski Kraków Scientific Consortium "Matter – Energy – Future"



EFFECT OF HYDRODYNAMIC CONDITIONS ON GROWTH OF ANODIC TITANIUM DIOXIDE (ATO) LAYERS

Karolina Syrek, Joanna Kapusta-Kołodziej, Magdalena Jarosz, Grzegorz D. Sulka

*Department of Physical Chemistry & Electrochemistry, Faculty of Chemistry, Jagiellonian University in Krakow, Ingardena 3, Krakow 30060, Poland
E-mail: syrek@chemia.uj.edu.pl*

Anodic titanium dioxide is very popular material among scientists around the world because of its physicochemical properties. Self-ordered TiO₂ was synthesized for the first time in 1999 by Zwillling et al.[1] in a process of anodization of titanium in electrolyte containing fluoride anions. Since then, investigations are aimed at understanding a mechanisms of formation and morphology of ATO layers synthesized under different operating conditions. The structure of nanoporous anodic titanium dioxide is affected by the following parameters such as: type and composition of electrolyte (e.g. water content and presence of fluoride anions), pH, previous usage of electrolyte, voltage, time of anodization, temperature [2], and hydrodynamic conditions.

Nanoporous anodic titanium dioxide layers were synthesized at 20 °C by a three-step anodization carried out at the constant voltages of 30 V in the electrolyte based on an ethylene glycol containing fluoride ions [3]. The effect of stirring speed on the growth of anodic TiO₂ layers was investigated in the range of 0 – 500 rpm. It was found that the thickness of grown oxide layers, and consequently, the rate of oxide formation depend directly on the stirring speed. The morphological characterizations and photoelectrochemical properties of received anodic oxide layers were studied in detail.

References

1. V. Zwillling, D. David, M. Perrin, Y. Aucouturier, *637* (1999), 629–637.
3. M. Jarosz, A. Pawlik, J. Kapusta-Kołodziej, M. Jaskuła, G.D. Sulka, *Electrochim. Acta* (2014), *136*, 412–421
6. G.D. Sulka, J. Kapusta-Kołodziej, A. Brzózka, M. Jaskuła, *Electrochim. Acta*, 2010, *59*, 4359–4367

Acknowledgments

This research was supported by the National Science Centre, Poland (Grant No. N N204 213340).



GRAPHENE AND NIOBIUM(V) OXIDE/GRAPHENE SUPPORTED PLATINUM-COBALT CATALYSTS AS CATHODE MATERIAL FOR FUEL CELLS

R. Stagniūnaitė, V. Kepenienė, E. Norkus, L. Tamašauskaitė-Tamašiūnaitė

Center for Physical Sciences and Technology, A. Goštauto 9, LT-01108 Vilnius, Lithuania

E-mail: norkus@ktl.mii.lt

Introduction

Fuel cells have received increasing attention over the last decade for their potential to be a key component of a future green energy system. Proton exchange membrane fuel cells (PEMFCs) have drawn a great deal of attention in recent years as energy conversion devices, due to their high efficiency and low/zero emissions. The fuel cell can produce electrical energy continuously and directly due to the electrochemical reactions - fuel oxidation and oxygen reduction.

Platinum supported high surface area carbon (e.g., black carbon, Vulcan X-72) is one of the most active catalysts used as a cathode in low temperature fuel cells. However, the degradation and corrosion of carbon support, at the cathode working conditions in PEMFC, is a major cause to lose of the cell performance during PEMFC operation [1]. The search of catalysts having high stability and activity is industrially vital.

It was found that adding of transition metals or metal oxides to the Pt-based catalysts enhances electrocatalytic properties of catalysts as compared to bare Pt catalysts and allows reducing the Pt amount in the catalyst. In our previous works the Co/graphene and Nb₂O₅/graphene supported Pt catalysts (denoted as PtCo/GR and PtCoNb₂O₅/GR), prepared by microwave synthesis, were investigated as anodic materials for ethanol and methanol oxidation [2, 3]. The PtCo/GR and PtCoNb₂O₅/GR catalysts show an enhanced activity towards ethanol and methanol oxidation reaction as compared with those at the bare Pt/C catalyst and are promising anodic materials for alcohols fuel cells [2-4]. So, the aim of this work is to investigate activity of our prepared PtCo/GR, PtCoNb₂O₅/GR and Pt/C catalysts towards oxygen reduction reaction (ORR).

Experimental

Preparation of catalysts

The PtCo/GR catalyst was prepared by microwave heating of ethylene glycol (EG) solutions of Pt(IV) and Co(II) salts as was described in [2]. Typical preparation consists of the following steps: 0.25 ml of 0.096 M H₂PtCl₆ and 0.6 ml of calculated concentration of CoCl₂ solution were mixed with 18 ml of EG. Then, pH of the solution was adjusted to 11.7 by adding dropwise a 1 M NaOH solution. 100 mg of graphene was added to the mixture and sonicated for 30 min. For the microwave irradiation, the reaction mixture was put into a microwave reactor Monowave 300 (Anton Paar). The reduction of Pt nanoparticles was carried out at a temperature of 170°C for 30 min.

The PtCoNb₂O₅/GR catalyst was prepared in the same manner, only base support was 100 mg dry niobium oxide powder mixed with graphene, with the mass ratio of 1 : 1 [3].

For comparison, the carbon supported Pt catalyst was also prepared by microwave heating of 1 M glycerol (Gl) solutions of Pt(IV) salt at 170 °C for 30 s. The duration of Pt/GR preparation was shortened to 30 s with the aim to compare the obtained PtCo/GR, PtCoNb₂O₅/GR and Pt/C catalysts having approximately the similar size of Pt particles in the

created catalysts. After preparation, the synthesized catalysts were washed with acetone, ultra-pure water with the resistivity of $18.2 \text{ M}\Omega \text{ cm}^{-1}$, then filtered and dried in a vacuum oven at 80°C for 2 h.

Characterization of catalysts

A shape and size of catalyst particles were examined using a transmission electron microscope Tecnai G2 F20 X-TWIN equipped with an EDAX spectrometer with r-TEM detector. For microscopic examinations, 10 mg of sample was first sonicated in 1 ml of ethanol for 1 h and then deposited on the Cu grid covered with a continuous carbon film.

X-ray diffraction patterns were recorded using a D8 diffractometer (Bruker AXS, Germany, 2003) with Cu $K\alpha$ radiation using a Ni/graphite monochromator. A step-scan mode were used in the 2-theta range from 20° to 90° with a step length of 0.02° and a counting time of 5 s per step.

The Pt and Co metal loadings were estimated from ICP-OES measurements. The ICP optical emission spectra were recorded using an ICP optical emission spectrometer Optima 7000DV (Perkin Elmer).

Electrochemical measurements

The working electrode was a thin layer of Nafion-impregnated catalyst cast on a glassy carbon electrode. The catalyst layer was obtained according to the following steps: at first, the required amounts of the PtCo/GR, PtCoNb₂O₅/GR or Pt/C catalysts were dispersed ultrasonically for 1 hour in a solution containing $0.25 \mu\text{l}$ of 5 wt.% Nafion (D521, 1100 EW, Ion Power Inc.) and $0.75 \mu\text{l}$ deionized H₂O to produce a homogeneous slurry. Then $5 \mu\text{l}$ of the prepared suspension mixture was pipetted onto the polished surface of a glassy carbon electrode with a geometric area of 0.07 cm^2 and dried in air for 12 h.

All electrochemical measurements were performed with a Zennium (ZAHNER-Elektrik GmbH & Co.KG) and AUTOLAB electrochemical workstations. The electrochemically active surface areas (ESAs) of the prepared catalysts were determined from the cyclic voltammograms of the PtCo/GR, PtCoNb₂O₅/GR and Pt/C catalysts recorded in a deaerated $0.5 \text{ M H}_2\text{SO}_4$ solution at a sweep rate of 50 mV s^{-1} [5]. The ESAs for the catalysts was estimated from the integrated charge of the hydrogen adsorption region (Q_H) in the cyclic voltammograms and calculated according to Eq. (1) [5]:

$$\text{ESA} (\text{cm}^2) = Q_H (\mu\text{C}) / 220 (\mu\text{C cm}^{-2}) \quad (1)$$

where $220 \mu\text{C cm}^{-2}$ is the charge required to oxidize a monolayer hydrogen adsorbed on Pt. ESA values ($\text{m}^2 \text{ g}^{-1}$) were calculated according to Eq. (2):

$$\text{ESA} (\text{m}^2 \text{ g}^{-1}) = Q_H / \text{Pt loading} \times 220 \quad (2)$$

For the ORR measurements the working electrode was pretreated electrochemically over a potential range of 0-1.5 V with a scan rate 50 mV s^{-1} for 30 min before each measurement. The $0.5 \text{ M H}_2\text{SO}_4$ solution was saturated with O₂ by purging solution with 99.999% O₂ for 15 min. The ORR measurements were performed by linear scan voltammetry from 0.8 V to 0.5 V vs. SHE in the cathodic direction at 5 mV s^{-1} in the $0.5 \text{ M H}_2\text{SO}_4$ solution saturated with O₂ at a temperature of 25°C . The electrode potential is quoted *versus* the standard hydrogen electrode (SHE). The presented current densities are normalized with respect to the geometric area of catalysts.

Results and discussions

The Co/GR and Nb₂O₅/GR supported Pt catalysts were prepared by microwave synthesis as described in experimental part. According to the data of TEM analysis, Pt nanoparticles in size of 2 and 1.3 nm were deposited in the PtCo/GR and PtCoNb₂O₅/GR catalysts, respectively [2, 3]. In the case of the PtCo/GR catalyst, the formation of platinum solid solution in cobalt was detected by XRD [2]. It has been determined that the orthorhombic and monoclinic niobium(V) oxides were predominant in the PtCoNb₂O₅/GR catalyst [3].

The Pt loadings, determined by ICP-OES, were 0.143 mg Pt cm⁻² in the Pt/GR and 0.165 and 0.285 mg Pt cm⁻² in the synthesized PtCo/GR and PtCoNb₂O₅/GR catalysts, respectively.

The electrochemically active surface areas (ESAs) of Pt in the synthesized catalysts were determined from the cyclic voltammograms of the Pt/GR, PtCoNb₂O₅/GR and PtCo/GR catalysts recorded in a deaerated 0.5 M H₂SO₄ solution at a sweep rate of 50 mV s⁻¹ by calculating the charge associated with hydrogen adsorption (220 μC cm⁻²) (Fig. 1) [5]. It has been determined that the values of ESA are 4.8 cm² for Pt/GR and 4.8 and 4.3 cm² for the PtCo/GR and PtCoNb₂O₅/GR catalysts, respectively. The specific activity has been determined to be 48 m² g⁻¹ Pt for Pt/GR, 42 m² g⁻¹ Pt for PtCo/GR and 21 m² g⁻¹ Pt for PtCoNb₂O₅/GR.

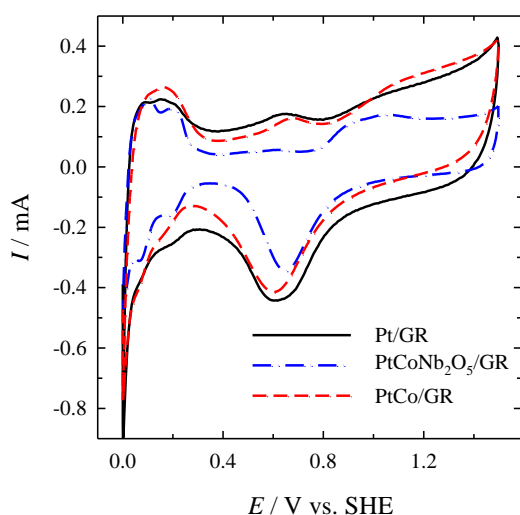


Fig. 1. Cyclic voltammograms of Pt/GR (black line), PtCoNb₂O₅/GR (dash-dotted line) and PtCo/GR (dashed line) catalysts recorded in 0.5 M H₂SO₄ at a sweep rate of 50 mV s⁻¹.

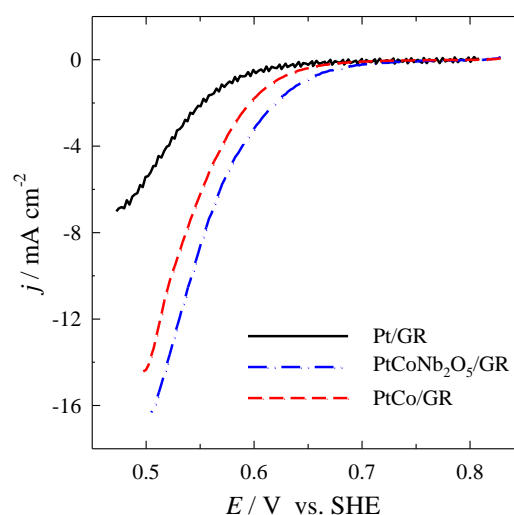


Fig. 2. Linear sweep voltammetry scans for the Pt/GR (black line), PtCoNb₂O₅/GR (dash-dotted line) and PtCo/GR (dashed line) catalysts recorded in the O₂ – saturated 0.5 M H₂SO₄ solution at 5 mV s⁻¹.

The reduction of oxygen was investigated at the PtCo/GR, PtCoNb₂O₅/GR and Pt/GR catalysts electrochemically pretreated in 0.5 M H₂SO₄ at 50 mV s⁻¹ for 30 min. The potential was scanned from ca. 0.8 V in the cathodic direction to 0.5 V vs. SHE at a scan rate of 5 mV s⁻¹. The experimental results are shown in Fig. 2. As seen from the data obtained, the Pt/C catalyst performed low ORR activity with the onset potential of 0.65 V, while the PtCo/GR and PtCoNb₂O₅/GR catalysts show higher onset potentials of 0.68 and 0.7 V, respectively, as well as higher ORR current densities (Fig. 2).

To represent the mass and specific activities of the investigated catalysts towards ORR, the current densities at 0.6 and 0.55 V were normalized by the Pt loadings and electrochemically active surface areas for each catalyst. Figure 3 presents comparison of mass (a) and specific (b) activities of Pt/GR, PtCo/GR and PtCoNb₂O₅/GR at 0.6 and 0.55 V.

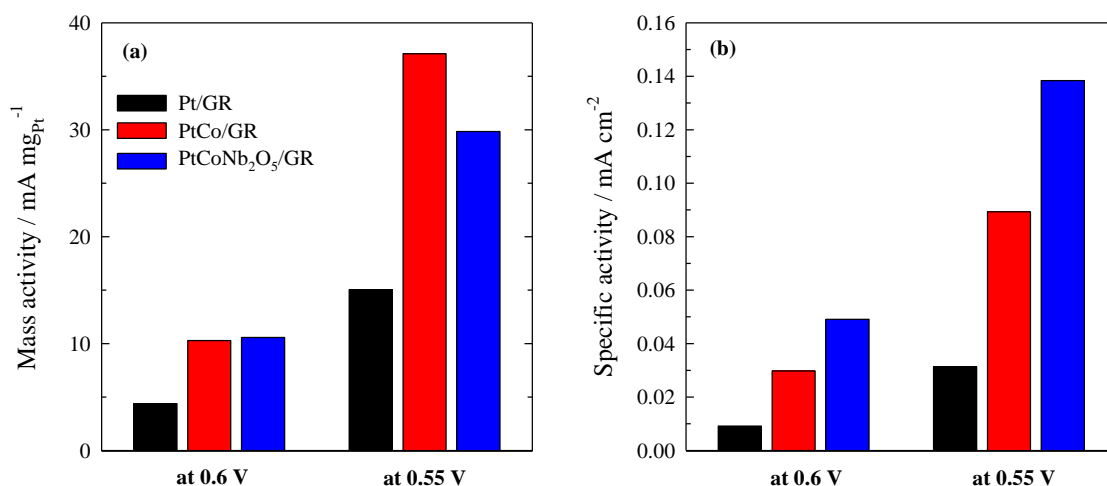


Fig. 3. Comparison of mass (a) and specific (b) activities for Pt/GR, PtCo/GR and PtCoNb₂O₅/GR at 0.6 and 0.55 V.

As evident, the Pt-mass activity is ca. 2.3 and 2.4 times higher at PtCo/GR and PtCoNb₂O₅/GR at 0.6 V vs. SHE than that at Pt/GR. At 0.55 V, the Pt-mass activity is ca. 2.0 and 2.5 times greater at PtCoNb₂O₅/GR and PtCo/GR as compared with that at Pt/GR (Fig. 1a). Oxygen reduction current densities normalized by the electrochemically active surface areas are ca. 2.7 and 5.4 times at 0.6 V and 2.9 and 4.4 times at 0.55 V higher at PtCo/GR and PtCoNb₂O₅/GR than those at Pt/GR.

Conclusions

The PtCo/GR and PtCoNb₂O₅/GR catalysts prepared by means of microwave synthesis show enhanced activity towards oxygen reduction as compared with that at bare Pt/GR catalyst. The PtCo/GR and PtCoNb₂O₅/GR catalysts show higher onset potentials, as well as higher current densities towards oxygen reduction reaction as compared with those at the bare Pt/GR catalyst.

Acknowledgment

R. Stagniūnaitė acknowledges support by project "Promotion of Student Scientific Activities" (VP1-3.1-ŠMM-01-V-02-003) from the Research Council of Lithuania. This project is funded by the Republic of Lithuania and European Social Fund under the 2007-2013 Human Resources Development Operational Programme's priority 3.

References

1. M. Yaldagard, N. Seghatoleslami, and M. Jahanshahi, *Appl. Surf. Science* **315** (2014) 222-234.
2. V. Kepeniene, L. Tamašauskaite-Tamašiūnaite, J. Jablonskiene, J. Vaičiūniene, R. Kondrotas, R. Juškenas, and E. Norkus, *J. Electrochem. Soc.* **161** (14) (2014) F1354-F1359.
3. V. Kepeniene, J. Vaičiūniene, R. Kondrotas, V. Pakštas, L. Tamašauskaitė-Tamašiūnaitė, and E. Norkus, *ECS Transactions*, **64** (3) (2014) 1147-1159.
4. V. Kepeniene, L. Tamašauskaitė-Tamašiūnaitė, J. Jablonskienė, M. Semaško, J. Vaičiūniene, R. Kondrotas, E. Norkus. *Proceedings of the International Congress on Green and Renewable Energy [IC 2014]*, (2014), Bangkok, Thailand p. 84-89.
5. H. Angerstein-Kozłowska, B. E. Conway and W. B. A. Sharp, *J. Electroanal. Chem.*, **43**, 9 (1973).

THIN FILM Mg-Nb ALLOYS: STRUCTURE AND CORROSION IN CHLORIDE MEDIUM

L. Staišiūnas, R. Kondrotas, A. Griguzevičienė, K. Leinartas, P. Miečinskas, E. Juzeliūnas

Center for Physical Sciences and Technology, A. Goštauto st. 9, LT-01108 Vilnius, Lithuania
E-mail: asta@chi.lt

Magnesium has great potential for applications in fields of portable electronics, computers, aircraft or automotive industry. An issue is an intrinsically high susceptibility of this metal to corrosion. However, in biomedical applications, a high corrosion activity of magnesium is regarded as a valuable property, which enables dissolution of implants in-vivo, so that there is no need for secondary surgery to remove temporary implants [1-4].

Mg-Nb alloy films have been formed by the magnetron sputtering technique (Univex 350, Leybold). The interaction (corrosion behaviour) of thin Mg-Nb layers with high chloride-contained balanced Hank's solution was studied by Fei Tecnai F20 electron transmission microscope equipped with a field emission electron gun. The cross sections of 50 nm thick of pristine Mg-9Nb layer on glass substrate and that of after immersion for 10 min in Hank's were cut using the FEI Helios Nanolab Dual Beam workstation equipped with Ga ion gun. Ga³⁺ ions with the energy of 30 kV were used to cut the foils. A Pt layer was *in situ* deposited prior to the cutting to protect the samples surface. STEM images were acquired with a high angle annular dark field detector (HAADF) from Fischione instr. Local elemental profiles were measured using EDX (an energy dispersive X-ray spectrometer) detector. A step size of 5 nm was used for profile spectra acquisition.

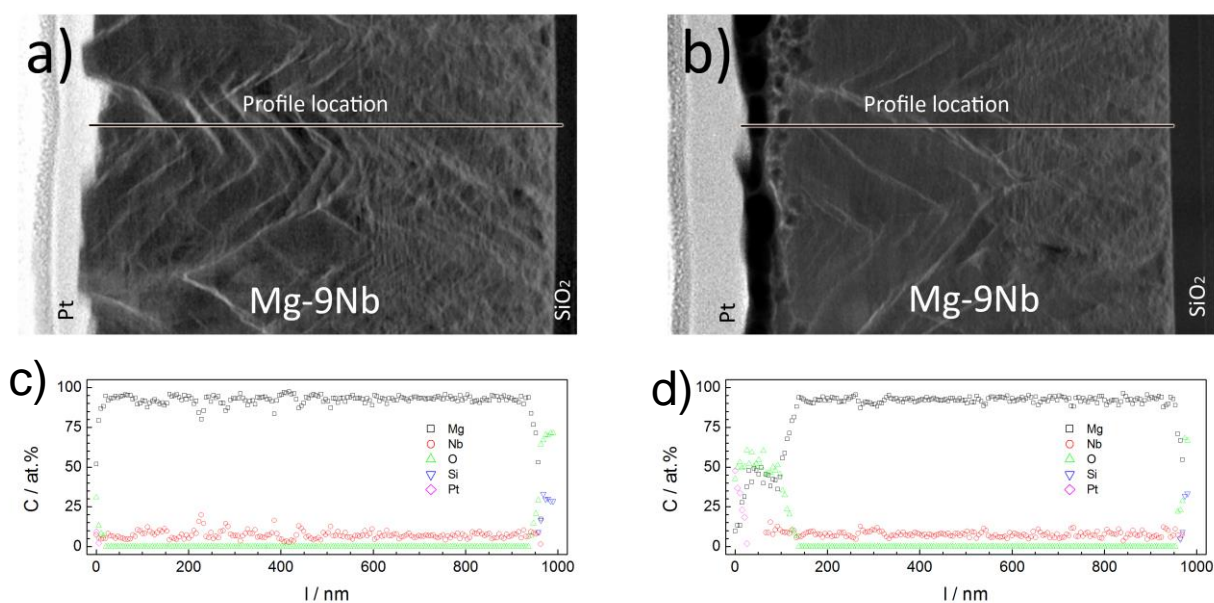


Fig. 1. HAADF images and EDX elemental profiles of as deposited (a, c) and corroded (b, d) Mg-9Nb samples.

Cross sections of pristine and solution affected samples of thin Mg-9Nb alloys are shown in Fig. 1. The thickness of formed Mg-9Nb layer was ~1000 nm. As deposited sample shows

non uniform “pyramid”-like structure of layer bulk and little oxidation of the surface (Fig. 1 a, c). HAADF images show niobium enriched locations in layer bulk (brighter zones in Fig 1 a, b). After 5 min immersion in Hanks solution a corroded layer of ~150 nm formed on the sample surface (Fig. 1 b). According to the EDX profile of corrosion products two layers were distinguished: the top one is magnesium and oxygen with approximate ratio 1:1 (possibly MgO) or 1:2 (possibly Mg(OH)₂), and a deeper one consisting of partly oxidized niobium and magnesium (Fig. 1 d).

Mg-9Nb alloy films have been formed using the magnetron sputtering technique. The structure of as deposited layer and one affected by Hank’s solution was studied by STEM HAADF imaging. Distribution of alloy elements in corrosion layer was evaluated.

Acknowledgement. This research was funded by a grant (No. MIP-119/2012) from the Research Council of Lithuania

References

1. F. Witte, V. Kaese, H. Haferkamp, E. Switzer, A.M. Linderberg, C.J. Wirth, H. Windhagen, *Biomaterials*, **2005**, *26*, 3557.
2. M. P. Staiger, A. M. Pietak, J. Huadmai, G. Dias, *Biomaterials*, **2006**, *27*, 1728.
3. F. Witte, *Acta Biomater.*, **2010**, *6*, 1680.
4. M. Alvarez-Lopez, M.D. Pereda, J.A. del Valle, M. Fernandez-Lorenzo, M.C. Garcia-Alonso, O.A. Ruano, M.L. Escudero, *Acta Biomater.*, **2010**, *6*, 1763.

STRUCTURE OF PHENYL-TERMINATED SELF-ASSEMBLED MONOLAYERS WITH AMIDE GROUP REVEALED BY SERS

M. Špandyreva, I. Ignatjev, Z. Kuodis, O. Eicher-Lorka, G. Niaura

Center for Physical Sciences and Technology, A. Goštauto str. 9, LT-01108 Vilnius, Lithuania

E-mail: marija.spandyreva@gmail.com

The interaction of organothiol compounds with metal substrates (usually gold and silver), as well as the interaction between the adsorbates, controls the formation of densely packed and ordered structures called self-assembled monolayers (SAMs), which provide the possibility of changing interfacial properties in a controllable manner and have been found to be extremely useful in many applications including studies of distant electron transfer phenomena, electrocatalysis, in the field of biotechnology [1–3]. In order to gain insight into the forces responsible for the structural organization of the monolayer, especially in the initial formation stage, techniques which are extremely sensitive to minor changes in molecular bond length and geometry must be applied [3, 4]. The adsorption of 1-alkanethiols at Au surfaces has been studied with many analytical methods. In general, the conclusions from these studies are that highly ordered, defect-free monolayer films are spontaneously formed at Au surfaces. Raman scattering in the $\nu(\text{C-S})$, $\nu(\text{C-C})$, $\nu(\text{S-H})$, and $\nu(\text{C-H})$ regions can be used to directly characterize the number of location of *gauche* conformations in a series of 1-alkanethiol films at Ag [2].

Surface-enhanced Raman spectroscopy (SERS) is a powerful analytical tool providing molecular-structural information on species adsorbed on nanostructured metals (primarily Au, Ag and Cu) [1–4]. Surface Raman scattering is used to study self-assembled monolayers formed from 1-alkanethiols at both electrochemically roughened and mechanically polished polycrystalline Ag electrodes [2, 3]. The aim of the present work comprises the identification of the different spectral features of self-assembled monolayer (SAM) with amide group formed on electrochemically roughened Au, Ag and Cu electrodes immersed in (N-(2-phenylethyl)-8-sulphanyloctanamide (MOPHE) ethanolic 1mM solution (Fig. 1).

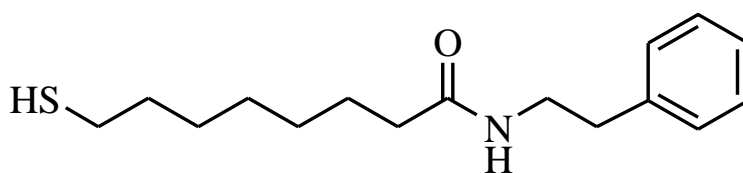


Fig. 1. Structure of (N-(2-phenylethyl)-8-sulphanyloctanamide (MOPHE). The compound was synthesized in our laboratory.

The Echelle type spectrometer RamanFlex 400 (PerkinElmer, Inc.) equipped with thermoelectrically cooled (-50°C) CCD camera and fiber-optic cable for excitation and collection of the Raman spectra and the 785 nm beam of the diode laser was used as the excitation source. The laser power at the sample was restricted to 20 mW. Spectra were collected with an integration time of 10 s. Each spectrum was recorded with accumulation of 30 scans, yielding total acquisition time of 300 s. The monolayers were prepared by immersion of the electrode in ethanolic solution containing 0.1 mM of MOPHE.

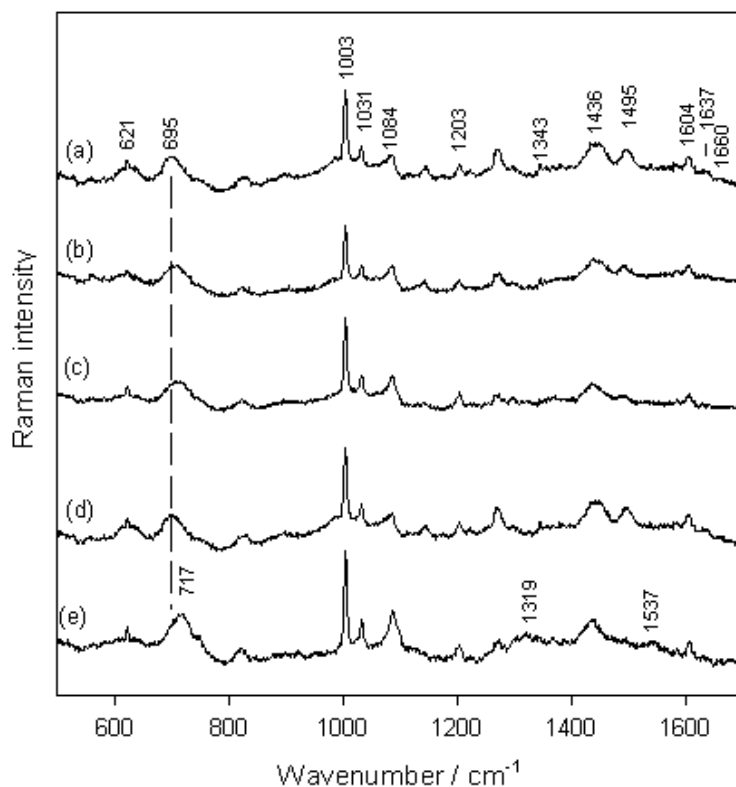


Fig. 2. SERS spectra of monolayers on rough silver from 1 mM MOPHE ethanolic solution. The monolayers were prepared by immersion of silver electrode in solution containing 1 mM MOPHE for (a) 5s, (b) 30s, (c) 30min, (d) 1h, (e) 21h. Spectra were normalized to the intensity of the most intense band at 1003 cm^{-1} . Excitation wavelength is 785 nm .

Figure 2 shows SERS spectra of MOPHE at Ag electrode obtained at different immersion time in adsorption solution. Only fingerprint spectral region will be analyzed in this work. Alkanethiol monolayers have been extensively studied by the SERS technique and important spectral marker bands have been established [1]. Thus, the most intense band in the spectra of the SAM at 1003 cm^{-1} belongs to phenylalanine ring trigonal breathing mode F12. Other Phe ring vibrational modes are visible at 621 cm^{-1} (sharp low intensity peak, F6b), 1031 cm^{-1} (F18a), 1203 cm^{-1} (F7a), and 1604 cm^{-1} (F8a). Conformation of adsorbed alkanethiols in the vicinity of the metal surface may be analyzed from the characteristic C–S stretching modes appearing at 695 and 620 cm^{-1} for *trans* and *gauche* conformers of C–C–S fragment, respectively. These bands provide information about the interaction strength of S atom with the metal surface, assuming that stronger interaction corresponds to lower frequency [2, 3, 5]. Interestingly, the frequency of the band associated with *trans* conformer, $\nu(\text{C–S})_{\text{T}}$, clearly increases from 695 to 717 cm^{-1} with increasing the adsorption time. Thus, bonding with silver surface is stronger at the initial adsorption stage. This might be associated with interaction of S atom with the most reactive surface sites at short adsorption times. The other important finding is growth in intensity of the band near 1084 cm^{-1} with increasing adsorption time. Quantum chemical analysis of the MOPHE molecule and adsorption complex has revealed that this mode belongs to C–C stretching vibration of hydrocarbon chain of MOPHE in all-*trans* conformation. This mode was designed as $\nu(\text{C–C})_{\text{T}}$. Increase in intensity of $\nu(\text{C–C})_{\text{T}}$ mode is consistent with increased ordering in the monolayer at higher surface coverages.

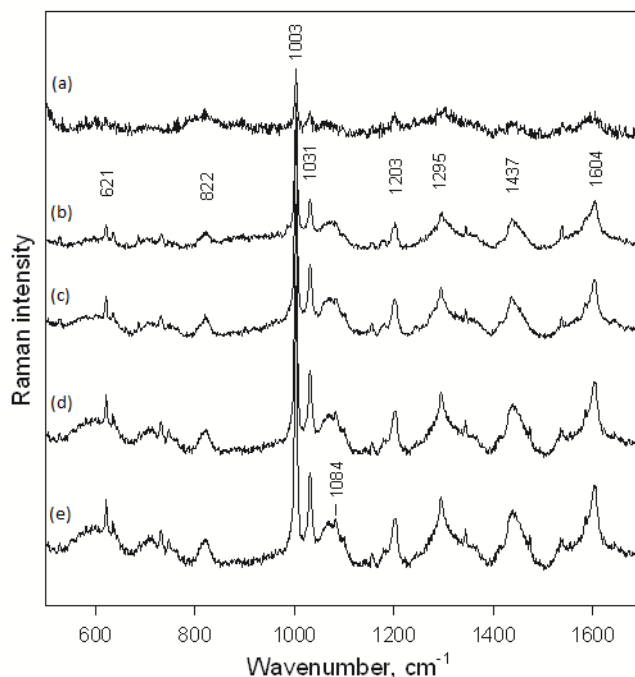


Fig. 3. SERS spectra of monolayers formed on rough gold from 1 mM MOPHE ethanolic solution. The monolayers were prepared by immersion of gold electrode in solution containing 1 mM MOPHE for (a) 5s, (b) 30s, (c) 30min, (d) 1h, (e) 24h. Excitation wavelength is 785 nm.

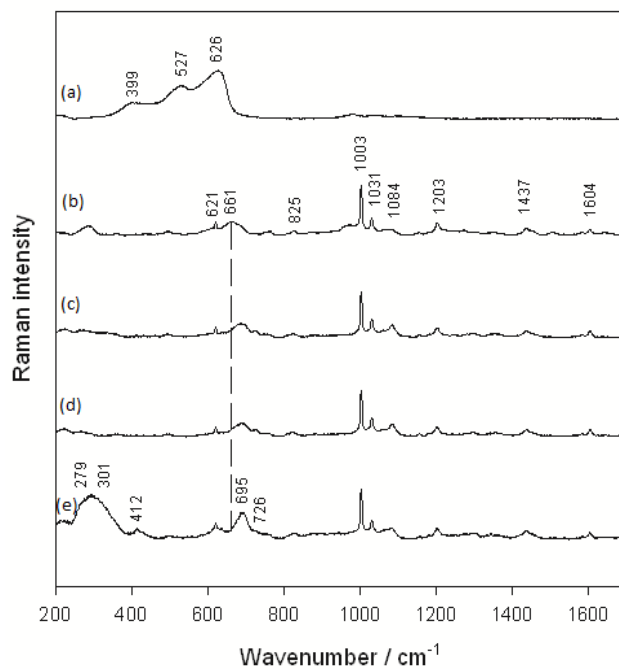


Fig. 4. SERS spectra of monolayers formed on rough copper from 1mM MOPHE ethanolic solution. The monolayers were prepared by immersion of copper electrode in solution (pH=2) containing 1 mM MOPHE (a) 5s, (b) 30s, (c) 30min, (d) 1h, (e) 45h. Spectra were normalized to the intensity of the most intense band at 1003 cm^{-1} . Excitation wavelength is 785 nm.

Figures 3 and 4 show SERS spectra of MOPHE obtained at different immersion times for Au and Cu electrodes, respectively. In the case of Au electrode the enhancement of the relative intensity of F8a mode near 1604 cm^{-1} is clearly visible (Fig. 3). This indicates different alignment of Phe ring with respect to the Au surface as compared with Ag electrode. Analysis of C–S stretching range shows considerable decrease in intensity, especially at the initial adsorption stage. According to the surface selection rules such decrease in intensity is associated with more parallel alignment of C–S bond with respect to the electrode surface [5]. SERS analysis of Cu electrode shows presence of broad surface oxide bands near 626 , 527 , and 399 cm^{-1} for spectrum obtained at 5 s adsorption time (Fig. 4) [6]. Longer adsorption times result in complete disappearance of surface oxide film and appearance of characteristic bands due to adsorbed MOPHE. The relative intensity and alignment of Phe ring with respect to the electrode surface is similar as in the case of Ag electrode. Importantly, the frequency of $\nu(\text{C–S})_{\text{T}}$ mode observed after 30 s adsorption time appears at lower wavenumber comparing with Ag electrode, indicating stronger interaction of S atom with Cu. Increase in adsorption time results in considerable upshift of $\nu(\text{C–S})_{\text{T}}$ frequency. Based on analysis of relative intensities of $661\text{--}695\text{ cm}^{-1}$, $\nu(\text{C–S})_{\text{T}}$, and lower frequency broad band due to $\nu(\text{C–S})_{\text{G}}$ vibration suggest that the *trans* conformer of MOPHE dominates in the case of Cu electrode.

In conclusion, surface-enhanced Raman spectroscopy (SERS) was used to detect adsorption time induced different spectral features and structural changes of phenyl-terminated self-assembled monolayers on Ag, Au, and Cu electrodes. The SERS band near 1084 cm^{-1} was assigned to C–C stretching vibration of alkyl chains of adsorbed MOPHE in all-*trans* configuration. Intensity of this band was found to increase in the case of Ag electrode indicating ordering of the monolayer. For Au electrode, the more parallel with respect to surface alignment of Phe ring and C–S bond comparing with Ag and Cu electrodes was suggested. Upshift in the $\nu(\text{C–S})_{\text{T}}$ frequency with increasing adsorption time was detected for Ag and Cu electrodes indicating weakening of the surface-ligand interaction strength.

References

1. V. Voiciuk, G. Valinčius, R. Budvytytė, A. Matijoška, I. Matulaitienė, G. Niaura, *Spectrochim. Acta A*, 95 (2012) 526–532.
2. M.A. Bryant, J. E. Pemberton. *J. Am. Chem. Soc.*, 113 (1991) 3629–3637.
3. M.A. Bryant, J.E. Pemberton, *J. Am. Chem. Soc.*, 113 (1991) 8284–8293.
4. I. Razmūtė-Razmūtė, Z. Kuodis, O. Eicher-Lorka, G. Niaura, *Phys. Chem. Chem. Phys.*, 12 (2010) 4564–4568.
5. I. Matulaitienė, Z. Kuodis, O. Eicher-Lorka, G. Niaura, *J. Electroanal. Chem.*, 700 (2013) 77–85.
6. G. Niaura, *Electrochim. Acta*, 45 (2000) 3507–3519.

INVESTIGATION OF HYDRAZINE OXIDATION ON ZnCo MODIFIED WITH GOLD NANOPARTICLES

A. Zabielaite, A. Balčiūnaitė, S. Lichušina, D. Šimkūnaitė, L. Tamašauskaitė-Tamašiūnaitė, E. Norkus

Center for Physical Sciences and Technology, A. Goštauto 9, LT-01108, Lithuania

E-mail: a.zabielaite@gmail.com

Introduction

Since fuel cell systems are progressively entering the market one more critical issue in their commercialization such as a relatively high cost of catalyst arises; therefore, cheaper substitutes are of increasing interest. The necessity for cost-effective catalysts has initiated the development of precious-metal – non-precious-metal bimetallic or even multi-metallic systems resulting in reduced content of the expensive material. Recent electrochemical studies suggest that the Pt- or Au-based binary electrocatalysts denoted as PtM or AuM (M=Co, Ni, Cu, Fe, Zn) not only permit to control the content of the catalyst, but they definitely perform the apparently improved activity and stability as compared to monometallic one and therefore are highly preferred.

In our previous work it has been shown that the AuZnCo/Ti catalysts with the Au loadings of 31, 63 and 306 $\mu\text{g cm}^{-2}$ show enhanced catalytic activity towards the electro-oxidation of BH_4^- ions as compared to that of the ZnCo/Ti, Co/Ti or Zn/Ti catalysts [2]. Herein, the activity of the AuZnCo/Ti catalysts with different Au loadings towards hydrazine oxidation in an alkaline medium was investigated by means of cyclic voltammetry.

Experimental

Titanium foil (99.7% purity, 0.127 mm thick), N_2H_4 , HAuCl_4 , CoSO_4 and ZnO were purchased from Sigma-Aldrich Supply. H_2SO_4 (96%) and NaOH (99%) were purchased from Chempur Company. All chemicals were of analytical grade. Deionized water with the resistivity of $18.2 \text{ M}\Omega \text{ cm}^{-1}$ was used to prepare all the solutions.

The ZnCo alloy coatings with the thickness of $\sim 5 \mu\text{m}$ were deposited on the titanium surface (1 x1 cm) via electrodeposition from the electrolyte described in Ref. [1]. Prior to ZnCo alloy deposition, the titanium plates were degreased with acetone and then pretreated in diluted H_2SO_4 (1:1 vol) at 90°C for 10 s.

Au crystallites were deposited on the ZnCo/Ti surface via the galvanic displacement technique. The ZnCo/Ti catalysts were immersed into the 1 mM HAuCl_4 + 0.1 M HCl solution at 25°C for 0.5, 1 and 5 min, respectively. The surface-to-volume ratio was $1.3 \text{ dm}^2 \text{ l}^{-1}$. After plating, the samples were taken out, thoroughly rinsed with deionized water and air dried at room temperature. Then, the prepared catalysts were used for measurements of hydrogen generation from the sodium borohydride solution without any further treatment.

A conventional three-electrode electrochemical cell was used for electrochemical measurements. AuZnCo/Ti and ZnCo/Ti catalysts were employed as a working electrode, a Pt sheet was used as a counter electrode and an Ag/AgCl/KCl electrode was used as reference.

All electrochemical measurements were performed with a Metrohm Autolab potentiostat (PGSTAT100) using Electrochemical Software (Nova 1.6.013). Steady state linear sweep voltammograms were recorded in a 0.05 M N_2H_4 + 1 M MaOH solution at a linear potential sweep rate of 10 mV s^{-1} at a temperature of 25°C . The presented current densities are

normalized with respect to the geometric area of catalysts. All solutions were deaerated by argon for 30 min prior to measurements.

Results and discussion

The ZnCo alloy was electrodeposited on the titanium surface followed by its modification with Au nanoparticles by the galvanic displacement technique. It was found that immersion of the ZnCo/Ti electrodes into the gold-containing solution for 0.5 and 1 min results in the formation of Au crystallites of ca. 16 to 50 nm in size on the ZnCo/Ti surface, while immersion of the ZnCo/Ti electrode into the gold-containing solution for 5 min results in the deposition of larger Au crystallites ca. 50-200 nm in size on the ZnCo surface [2].

The electrochemical behavior of the ZnCo/Ti and AuZnCo/Ti catalysts with different Au loadings towards the oxidation of hydrazine was evaluated in an alkaline medium using cyclic voltammetry. Figure 3 presents CVs of the ZnCo/Ti and AuZnCo/Ti catalysts with the Au loadings of 31, 63 and 306 $\mu\text{g cm}^{-2}$ in the 0.05 M N_2H_4 + 1 M NaOH solution at 10 mV s^{-1} . The solid line represents the CV cycle of the ZnCo/Ti catalyst recorded in the 1 M NaOH solution. During the anodic scan two well-expressed anodic peaks: peak **A0** at lower potential values and peak **A** at more positive potential values are seen in the CVs plots for the ZnCo/Ti and AuZnCo/Ti electrodes. Peak **A** is related to the direct hydrazine oxidation. As seen from the data in Fig. 1, ca. 2 times higher current densities under peak **A** are obtained at the AuZnCo/Ti catalysts with the Au loadings of 31, 63 and 306 $\mu\text{g cm}^{-2}$ as compared to those at ZnCo/Ti.

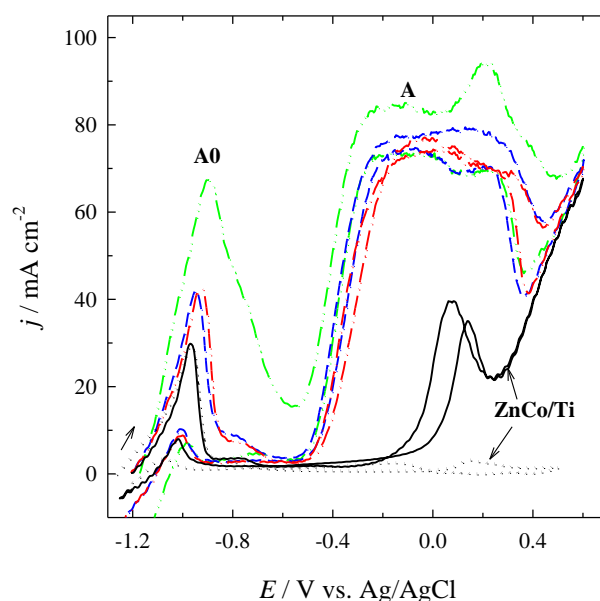


Figure 1. CVs for ZnCo/Ti (solid line) and AuZnCo/Ti with the Au loadings of 31 (dash-dotted line), 63 (dash line) and 306 (dash-dot-dotted line) $\mu\text{g cm}^{-2}$ recorded in 0.05 M N_2H_4 + 1 M NaOH at 10 mVs^{-1} . The dotted line represents the CV of ZnCo/Ti in 1 M NaOH.

To compare the activity of the investigated AuZnCo/Ti catalysts hydrazine oxidation current densities were normalized by the Au loadings to represent the mass activity of catalysts. The obtained data are shown in Fig. 2. As evident from Fig. 2, the highest Au-mass activity shows the AuZnCo/Ti catalyst with the lower Au loading of 31 $\mu\text{g cm}^{-2}$ as compared with that at the AuZnCo/Ti catalyst with the higher Au loadings of 63 and 306 $\mu\text{g cm}^{-2}$.

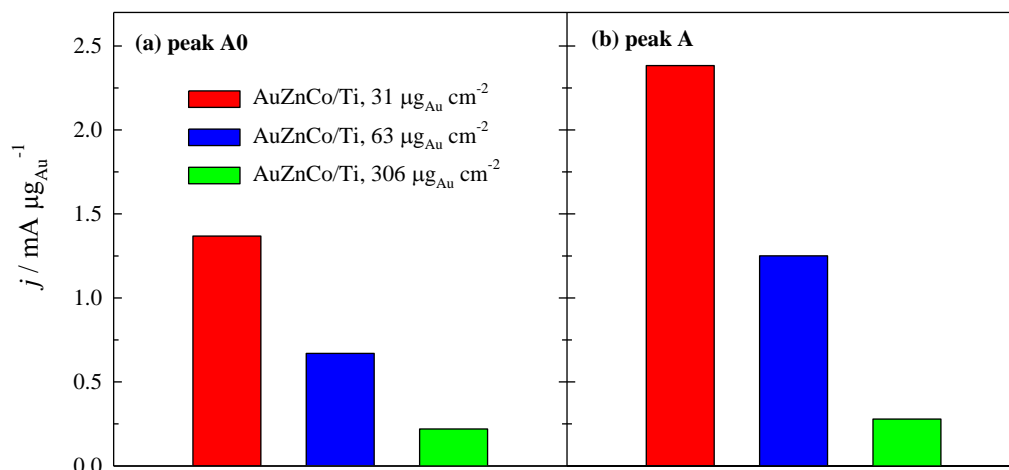


Figure 2. Bar columns of current densities at peak A for the AuZnCo/Ti catalysts with the Au loadings of 31, 63 and $306 \mu\text{g cm}^{-2}$ in $0.05 \text{ M N}_2\text{H}_4 + 1 \text{ M NaOH}$ at 10 mV s^{-1} .

Conclusions

It has been determined that the AuZnCo/Ti catalysts with the Au loadings of 31, 63 and $306 \mu\text{g cm}^{-2}$ show enhanced catalytic activity towards electro-oxidation of hydrazine ions as compared to that of ZnCo/Ti catalysts.

References

1. E. Juzeliunas, S. Lichusina. Patent of the Republic of Lithuania No. 5481 26.03.2008.
2. A. Balčiūnaitė, S. Lichušina, D. Šimkūnaitė, A. Zabielaitytė, A. Selskis, L. Tamašauskaitė-Tamašiūnaitė, E. Norkus, ECS Transactions, **64(3)** (2014) 1103-1112.



NANOGOLD ELECTRODES FABRICATION AND THEIR APPLICATION FOR SENSING OF ADRENALINE

E. Wierzbicka, G. D. Sulka

*Jagiellonian University in Krakow, Department of Physical Chemistry and Electrochemistry, Ingardena 3, 30060 Krakow, Poland
E-mail: wierzbicka@chemia.uj.edu.pl*

Growing interest in development of methods for fabrication of nanomaterials is caused by the fact that new properties of well-known materials can be discovered. Typically, it is associated with a highly ordered internal structure of these materials.

Among other methods used for fabrication of nanostructured materials with unique and desirable properties for sensor applications, electrochemistry offers a direct methods to obtain and test nanostructured sensors in a fast and low-cost way. Electrochemical sensors based on nanostructured materials are characterized by high selectivity, sensitivity and large surface to volume ratio.

Adrenaline (AD) is a very important hormone and neurotransmitter which controls mammalian nervous systems. The concentration of AD in body fluids is strongly correlated with many physiological phenomena such as acceleration of the heartbeat, increased blood pressure, bronchodilation, mydriasis, etc. Disturbances in AD levels in the human body is associated with serious health consequences including Parkinson's disease. In addition, AD as a drug is widely used for the treatment of cardiac arrest, anaphylaxis, hypertension and many others. Therefore, determination of concentration of adrenaline is important for developing new drugs and diagnosis of neurological disorders.

Among various nanomaterials, nanoporous gold can be used as an electrochemical adrenaline sensor for a highly sensitive indication of its content in the blood. Two different types of electrodes were studied here. The first type of nanoporous electrode was obtained by a simultaneous deposition of Ag and Au on platinum followed by selective etching of silver in concentrated nitric acid. The second electrode was prepared by sputtering and electrodeposition of Au on a nanoporous anodic aluminum oxide (AAO) template. Scanning electron microscopy (SEM) was used to characterize the morphology of fabricated Au electrodes. The electrochemical response of adrenaline sensors was studied by cyclic voltammetry in a phosphate buffer solution. The cyclic voltammetry (CV) and linear sweep voltammetry (LSV) were used to record the current response to different concentrations of AD.



Chemistry and Chemical Technology 2015

Vilnius University, Faculty of Chemistry,
Naugarduko 24, Vilnius, Lithuania
January 23, 2015

Poster presentations

Polymer Chemistry and Technology



PREPARATION AND INVESTIGATION OF Se THIN LAYERS ON HOME MADE POLYIMIDE FILMS COMPOSITE

I. Berulis¹, S. Žalėnėnė¹, L. Pečiulytė¹, V. Krylova¹

1 Kaunas University of Technology, Radvilėnų str. 19, zip code, Kaunas, Lithuania

E-mail: irmantas.berulis@ktu.edu

Over the past two decades, scientists have shown significant scientific and technological interest in polymer-inorganic nanocomposites. The incorporation of inorganic nanoparticles into polymer matrices can result in novel high-performance materials that find applications in many industrial fields.

Polyimide (PI) is one of the fastest growing classes of thermoplastics and can serve as a model of the polymer-inorganic nanocomposite. Polyimides were found to have the combination of thermal stability (>500 °C), mechanical robustness, high ductility, low coefficient of thermal expansion, and chemical resistivity to many corrosives and solvents.

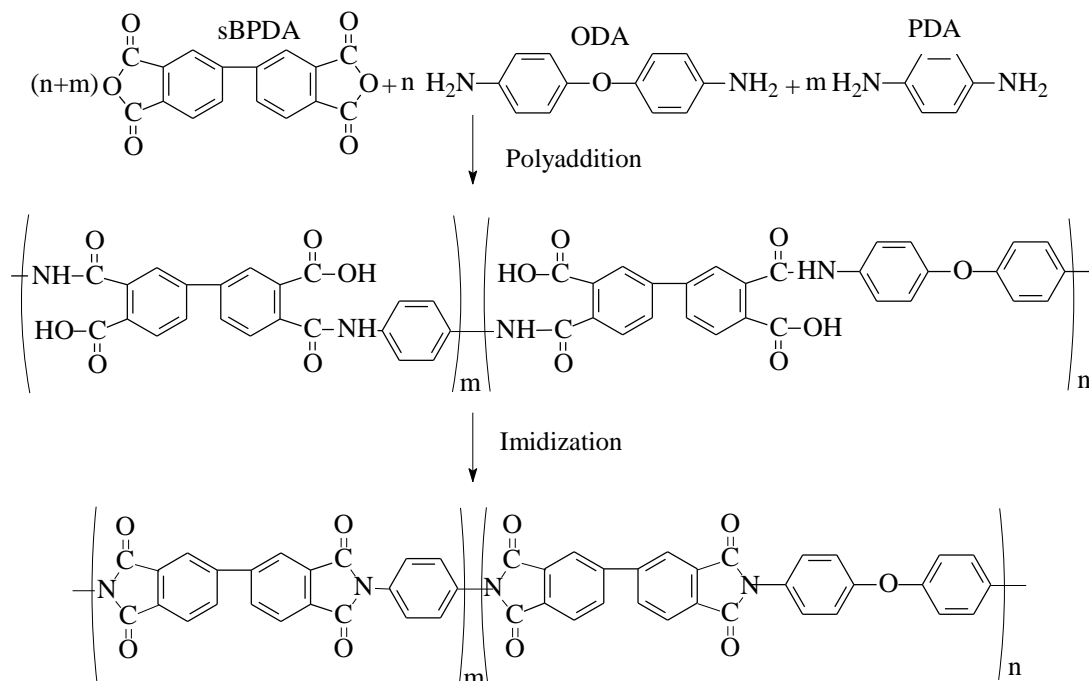
Polyimide starts as an imide-containing polymer molecule. There are two general structure types of polyimides: linear structure polyimides in which the imide group is part of a polymer chain, and heterocyclic structures, which are polymer molecules in which the imide group is part of a cyclic unit in the chain [1]. However, in its intrinsic state, PI does not possess the surface properties required for preparation of polymer-inorganic nanocomposite. In a usage PI films as the substrates for depositing semiconducting films, a serious drawback of PI material is its hydrophobicity and low free surface energy [2]. It results in a weak molecular interaction between the composite components. The free energy of PI surface can be increased by creating new functional chemical groups on the material surface layer, which greatly affect the surface polarity and the adhesion properties of the polymer towards the inorganic composite material [3]. In general all surface modification techniques share the common goal of controlling the nature and number of chemical functional groups on the polymer surface. The chemical method can be easily conducted as it does not require specialized equipment and hence can be easily adopted in any small-scale laboratory.

Selenium (Se) exists in a number of allotropic forms. One allotrope of Se is a red amorphous (a-Se). The a-Se is of interest for different technological applications. It is believed to be an inorganic polymer consisting of covalently bonded chains. Resistivity of a-Se is exceedingly high (about 10^{16} Ω cm) making the material a very good insulator. However, it is a photoconductor and if an electric field is present to separate the photogenerated electrons and holes, it can generate significant currents [4]. Se has a high reactivity toward a variety of chemicals, which can be explored to transform Se element into many other important functional materials [4, 5].

Our aim was to synthesise PI thin films, improve its adhesion by chemical etching, deposited Se thin layers by chemical bath deposition method and characterize these layers by XRD technique.

The main materials used were 4,4'-oxydianiline (ODA), *p*-phenylenediamine (PDA), 3,3',4,4'-biphenyltetracarboxylic dianhydride (sBPDA), *N*-methylpyrrolidone (NMP). Processable, film-forming PAAs were obtained by adding solid powder sBPDA to a stirred ODA/PDA solution in NMP at 10-15°C. The solids content of the materials was 15 wt%. The reaction mixture was stirred in the air atmosphere for ca. 6-12 h until the dynamic viscosity of the preparation reached 150-250 Pa·s. The intrinsic viscosity of 0.5 g/dL PAA solution in NMP was found to be on average 3 dL/g at 25°C. The dynamic viscosity of PAAs was measured with a rotational viscosimeter REOTEST-2, gradually increasing shear strain at 14°C. Intrinsic viscosity of polymer solutions in NMP at 25°C was measured using dilution type Ubbelohde viscosimeter. The polymer films were prepared from NMP solutions of PAAs

at solids content of 15%. PAA films were converted into PI films during thermal imidization. The films formed on fixed cylindrical base and then imidized. The castings were dried and cured by the heating in three stages: at 100-120, 130-160 and 250-270°C. PI synthesis is shown as follows:

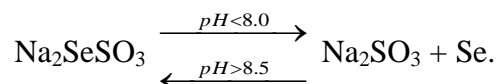


15 mm × 70 mm size samples of PI film of 60 μm thicknesses were used for the experiments. For depositing Se layer the PI sample requires an initial surface treatment process in order to facilitate its hydrophilicity. Polymer surface etching parameters exhibited in Table.

Table. Parameters used for API etching

Sample Nr.	Etching solution		Treatment parameters	
	Composition	Concentration, mol/L	Temperature, °C	Time
1	–	–	–	–
2	H ₂ SO ₄ H ₃ PO ₄ CrO ₃	7.2 6.6 0.36	20±1	12 h
3	H ₂ SO ₄ H ₃ PO ₄ CrO ₃	7.2 6.6 0.36	90±1	20 min
4	KOH	4.25	90±1	20 min

As Se source we introduce simple synthetic route and an environmentally benign precursor, Na₂SeSO₃. Na₂SeSO₃ solution (0.1 mol/L), was prepared by refluxing 5 mmol selenium powder and 7 mmol Na₂SO₃ in 50 mL deionized water for 2 h at 90°C temperature. Na₂SeSO₃ is sensitive to the acidity of the solution. It synthesized in an alkaline aqueous solution, while the dismutation phenomenon (which can separate out elemental selenium) will occur when it is in a neutral or acidic solution at room temperature. The transformation of the Na₂SeSO₃ is shown as follows:



All solutions were prepared using distilled water and analytical grade reagents. Only freshly prepared solutions were used for measurements and were not de-aerated during the experiments. Thus obtained samples were removed from the reaction solution, rinsed with distilled water, and dried at room temperature.

The prepared composite films were also characterized by XRD using X-ray diffraction (Bragg-Brentano circuit on a diffractometer). Figure 1a shows the XRD patterns of the PI (curve 1) and PI/Se composite films (curve 2-4), deposited on polymer samples etched with various solution, prepared according to processing conditions devoted in Table. Figure 1b shows the XRD pattern of prepared Se particles in the same conditions but in the absence of PI. The results of X-ray analysis showed (Figure 1a, curve 1) that the PI films are semicrystalline containing high amount of amorphous phase. The crystallinity index of PI is 13.7%. This peak was also depicted in the all diffractograms of PI/Se composite films (curve 2-4). In all these diffractograms appear new peak at $2\theta = 26.8^\circ$, suggesting the formation of Se particles in PI matrix.

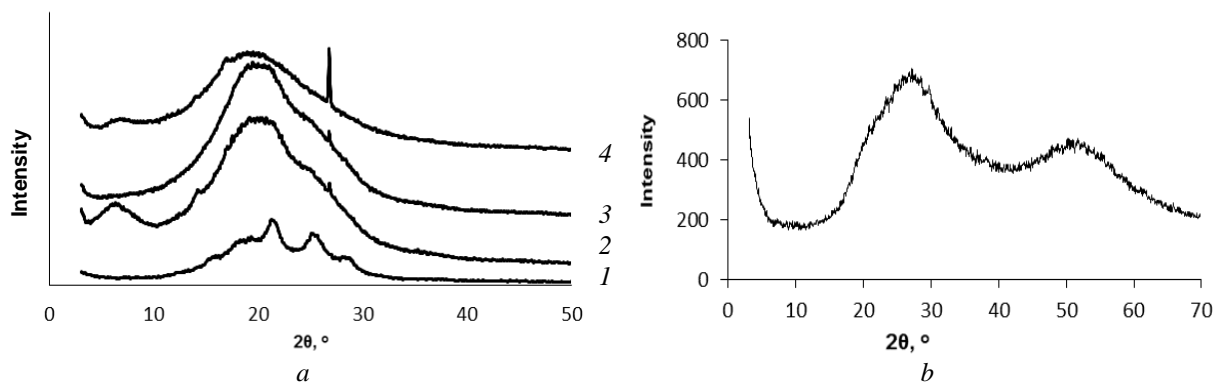


Figure 1. XRD patterns of (a) PI/Se composite films, and (b) Se particles.

The obtained results are important knowledge for the optimization of PI-Se composite deposition conditions.

References

1. J. Cardoso, O. GomezDaza, L. Ixtlilco, M.T.S. Nair, P.K. Nair, *Semicond. Sci. Technol.*, **2001**, 16, 123.
2. L. Pečiulytė. *Summary of Doctoral Dissertation*, 2009, 29.
3. K. Bindu, M. Lakshmi, S. Bini, C. Sudha Kartha, K.P. Vijayakumar, T. Abe, Y. Kashiwaba, *Semicond. Sci. Technol.*, **2002**, 17, 270.
4. Y.C. Li, H.Z. Zhong, R. Li, Y. Zhou, C.H. Yang, Y.F. Li., *Adv. Funct. Mater.*, **2006**, 16, 1705.
5. E.S. Smotkin, C. Lee, A.J. Bard, A. Campion, M.A. Fox, T.E. Mallouk, S.E. Webber, J.M. White., *Chem. Phys. Lett.*, **1988**, 152, 265.

SYNTHESIS AND PROPERTIES OF 1,3,6,8-CARBAZOLE-BASED COMPOUND LINKED VIA ETHYNYL-CONTAINING LINKAGES

M. Bistrickas, D. Gudeika, J.V. Grazulevicius

Department of Polymer Chemistry and Technology, Kaunas University of Technology, Radvilenu pl. 19, LT-05424 Kaunas, Lithuania

Abstract. 1,3,6,8-Carbazole-substituted derivative is described. This molecule consist of four 2-ethynyl-6-methoxynaphthalenyl moieties covalently linked to a carbazole core. Thermal, optical and electrochemical properties were determined. Carbazole derivative demonstrated relatively high thermal stability with 5% weight at 412 °C.

Keywords: carbazole, moiety, thermal.

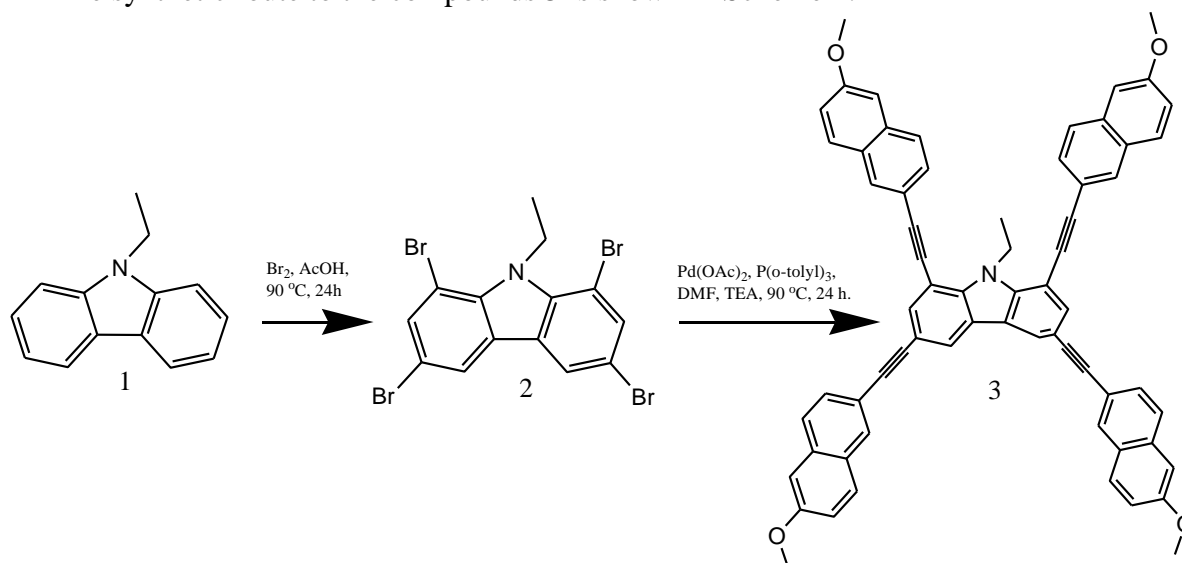
Introduction

Carbazoles are prevalent as structural motifs in various synthetic materials. As is well known, the properties of carbazole derivatives are closely related to their molecular structures. In the previous papers, the derivatives of carbazole unit as central core were commonly prepared by functionalizing at its 3,6- [2], 2,7- [3] or 9- [4] positions. The as-prepared compounds with thermally and morphologically stable properties can expand the application of carbazole in organic light-emitting devices (OLEDs). Due to their thermal stability, good film-forming properties and high luminescence, the starburst molecules have attracted much more attention to the application in OLEDs, photovoltaics and field effect transistors.

In this study, we report a carbazole derivative by using carbazole as the central core and functionalizing at its 1,3,6,8-positions with 2-ethynyl-6-methoxynaphthalenyl moieties and investigation of their thermal, optical, photophysical and electrochemical properties.

Results and Discussion

The synthetic route to the compounds **3** is shown in Scheme 1.



Scheme 1. Synthetic route to the compound **3**.

The intermediate compound 1,3,6,8-tetrabromo-9-ethyl-9H-carbazole (**2**) was synthesized by bromination of commercially available 9-ethyl-9H-carbazole (**1**): to a solution of 9-ethyl-

9*H*-carbazole in glacial acetic acid, a solution of bromine in glacial acetic acid was added. The structures of the intermediates (**1**, **2**) and compound **3** were confirmed by ¹H, ¹³CNMR and mass spectrometry methods. Compound **3** are soluble in organic solvents, such as acetone, ethylacetate. The target compound **3** was synthesized by a Sonogashira cross-coupling reaction of bromo derivative **2** and 2-ethynyl-6-methoxynaphthalene.

Target compound **3** demonstrate thermal stability with 5% weight at 412 °C, as confirmed by thermogravimetric analysis (Fig.1).

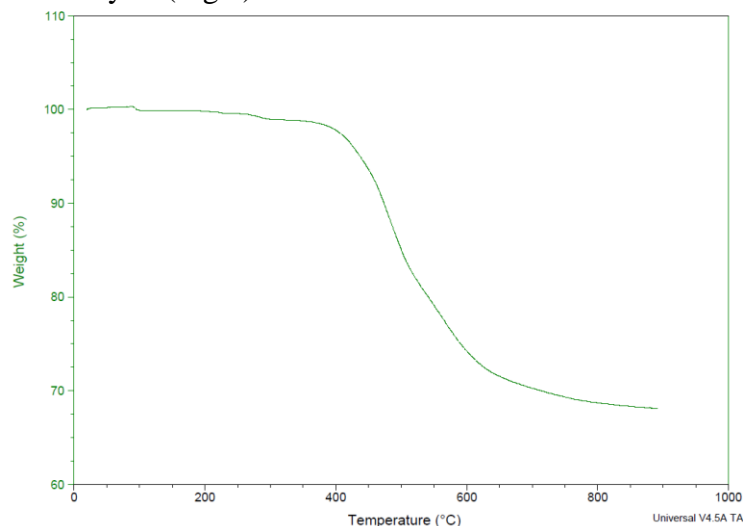


Fig. 1. TGA curve of compound **3** at the heating rate of 20 °C/min in N₂ atmosphere.

The behaviour under heating of **3** was studied by differential scanning calorimetry (DSC) under a nitrogen atmosphere. It was found that compound **3** can exist only in crystalline state. The DSC curve for **3** at first heating reveals only melting at 235 °C, and no crystallization takes place during cooling or second heating scans, and glass transition was not registered during the second heating.

The optical (UV-vis) and fluorescence (FL) properties of compound **3** were estimated by UV-vis absorption and FL spectroscopy. The absorption spectra of compound **3** in dilute THF solutions are shown in Fig. 2. The lowest energy absorption maximum (λ_{abs}) of compound **3** is located at 369 nm and the FL maxima (λ_{em}) is at 403 nm.

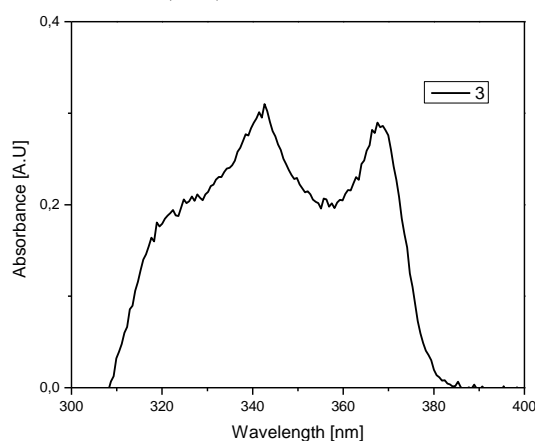


Fig. 2. UV-vis absorption spectra of the dilute THF solutions (10⁻⁵ M) of compound **3**.

Oxidation potential of compound **3** was measured by cyclic voltammetry (CV) in dichloromethane using tetrabutylammonium hexafluorophosphate as the supporting salt and are referenced to the internal standard ferrocene/ferrocenium (Fc/Fc⁺).

The CV revealed a chemically quasi-reversible oxidation (p-doping) procedure. An oxidation potential was observed. To elucidate the energetic conditions for energy and electron transfer in dilute DCM solutions, the ionization potential (IP_{CV}), electron affinity (EA_{CV}) values were estimated. The IP_{CV} value of the synthesized compound **3** was found to be 5.29. The EA_{CV} value for compound **3** was -2.39 eV.

Conclusions

We synthesized a 1,3,6,8-carbazole-substituted derivative containing of four 2-ethynyl-6-methoxynaphthalenyl moieties covalently attached to an extended carbazole system. The synthesized compound exhibit thermal stability with 5% weight loss temperature exceeding 412 °C. The ionization potential, electron affinity values were estimated by cyclic voltammetry. The ionization potential and electron affinity values of the final compound were found to be 5.29 eV and -2.39 eV, respectively.

References

- [1] W. Jiang, Z. J. Ge, P. Y. Cai, B. Huang, Y. Q. Dai, Y. M. Sun, J. Qiao, L. D. Wang, L. Duan, Y. Qiu, *J. Mater. Chem.*, **2012**, 22, 12016.
- [2] W. Y. Hung, L. C. Chi, W. J. Chen, Y. M. Chen, S. H. Chou, K. T. Wong, *J. Mater. Chem.*, **2010**, 20, 10113.
- [3] J. Y. Shen, X. L. Yang, T. H. Huang, J. T. Lin, T. H. Ke, L. Y. Chen, C. C. Wu, M. C. P. Yeh, *Adv. Funct. Mater.*, **2007**, 17, 983.
- [4] K. E. Linton, A. L. Fisher, C. Pearson, M. A. Fox, L. O. Palsson, M. R. Bryce, M. C. Petty, *J. Mater. Chem.*, **2012**, 22, 11816.

SYNTHESIS AND PROPERTIES OF 1,3,6,8-SUBSTITUTED CARBAZOLE DERIVATIVES

M. Bistrickas, D. Gudeika, L. Peculyte, J.V. Grazulevicius

Department of Polymer Chemistry and Technology, Kaunas University of Technology, Radvilenu pl. 19, LT-05424 Kaunas, Lithuania

Abstract. A series of carbazole derivatives, with ethenylaryl groups attached to C-1,3,6,8 positions of a 9-ethyl-9*H*-carbazole core were synthesized and their thermal, optical, photophysical and electrochemical properties were investigated. All the compounds were found to be capable of glass formation with glass transition temperatures up to 59 °C. Their 5% weight loss temperatures ranged from 289 to 415 °C.

Keywords: carbazole, thermal stability, glass transition.

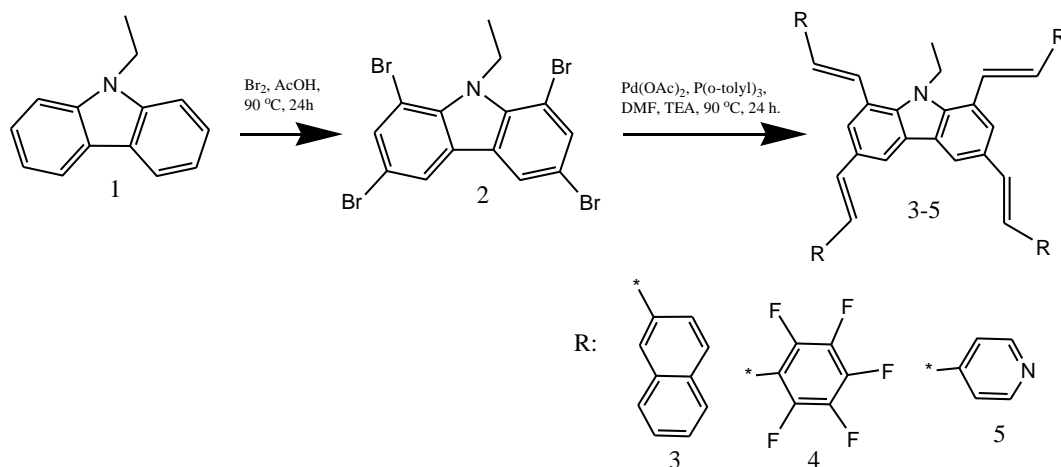
Introduction

Carbazole derivatives represent a distinguished class of nitrogen-containing aromatic heterocyclic compounds owing to their desirable electronic and charge-transporting properties. They are widely used in optoelectronic devices [1]. The properties of carbazole derivatives are closely related to their molecular structures. In the previous works, the derivatives of carbazole were commonly prepared by functionalizing at its C-3,6 [2], C-2,7 [3] or N-9 [4] positions. A series of carbazole derivatives functionalized by a Suzuki cross coupling reaction at C-1,3,6,8 positions with various aryl moieties was described [5]. The optical, electrochemical, thermal and electroluminescent properties of the prepared carbazole derivatives were also investigated. However, to the best of our knowledge, the tetrasubstituted derivatives of carbazole with various ethenylaryl arms have not yet been described.

In this study, we report on the synthesis of a series of carbazole derivatives containing carbazole as the central core functionalized at its C-1,3,6,8 positions with various ethenylaryl moieties and on the thermal, optical, photophysical and electrochemical properties of the synthesized compounds.

Results and Discussion

The synthetic route to compounds **3-5** is shown in Scheme 1.



Scheme 1. Synthetic route to compounds **3-5**.

The intermediate compound 1,3,6,8-tetrabromo-9-ethyl-9*H*-carbazole (**2**) was synthesized by bromination of 9-ethyl-9*H*-carbazole (**1**) by bromination with bromine in glacial acetic acid. The target compounds **3-5** were synthesized by Heck reactions of bromo derivative **2** with 2-ethylnaphthalene, 1-ethenyl-2,3,4,5,6-pentafluorobenzene or 4-ethenylpyridine, respectively. Compounds **3-5** were obtained in 45-63% yields and were characterized by ^1H and ^{13}C NMR, mass spectrometries. They were found to soluble in organic solvents, such as dichloromethane, dimethylformamide, tetrahydrofuran.

The thermal properties of compounds **3-5** were investigated by differential scanning calorimetry (DSC) and thermogravimetric analysis (TGA). The results are summarized in Table 1.

Table 1. Thermal characteristics of compounds **3-5**.

Compound	$T_g / ^\circ\text{C}$ (2 nd heating)	$T_m / ^\circ\text{C}$	$T_{cr} / ^\circ\text{C}$	$T_{ID-5\%} / ^\circ\text{C}$
3	134	291	-	415
4	66	178	-	376
5	59	163, 163 ^a	73	289

^a 2nd heating scan, T_g – glass transition temperature, T_m – melting temperature, T_{cr} – crystallization temperature; $T_{ID-5\%}$ – 5% weight loss temperature.

Compounds **3-5** exhibited relatively high thermal stabilities with 5% weight loss temperatures ($T_{ID-5\%}$) of 415 °C, 376 °C, and 289 °C, respectively. Compound **3** with 2-ethylnaphthalenyl substituents exhibited higher thermal stability than compounds **4** and **5** with 1-ethenyl-2,3,4,5,6-pentafluorophenyl and 4-ethenylpyridinyl moieties, respectively.

After the synthesis compounds **3-5** were obtained as crystalline substances. In the first heating scan of the DSC experiment the samples of **3** and **4** showed endothermic melting signals (T_m) with the maximum at 291 and 178 °C. The samples were cooled down and in the second heating scans only glass transitions at 134 and 66 °C were registered. The crystalline sample of compound **5** demonstrated the different behavior: the sample of **5** melted at 163 °C on the first heating scan. When the melt sample was cooled down and heated again, the glass transition was observed at 59 °C, followed by exothermic crystallization signal at 73 °C and melting signal at 163 °C.

The optical and photophysical properties of compounds **3-5** were estimated by UV-vis absorption and fluorescence spectrometries. The dilute solutions in THF of compounds **3-5** exhibited absorption maxima in the range of 355-380 nm and fluorescence intensity maxima in the region from 400 nm to 470 nm.

The electrochemical behavior of the derivatives **3-5** was probed by cyclic voltammetry (CV) in anhydrous dichloromethane at room temperature. The results are summarized in Table 2.

Table 2. Electrochemical characteristics of compounds **3-5**.

Compound	E_{onset}^{ox} vs Fc/V ^{a)}	IP_{CV} , eV ^{b)}	EA_{CV} , eV ^{c)}	E_g^{opt} , eV ^{d)}
3	0.47	5.27	-2.41	2.86
4	0.78	5.58	-2.72	2.86
5	0.67	5.47	-2.25	3.22

^{a)} E_{onset}^{ox} is measured vs. ferrocene/ferrocenium. ^{b)} Ionization potentials estimated according to $IP_{CV} = (E_{onset}^{ox} + 4.8)$ [eV], ^{c)} $E_{LUMO} = -(|E_{HOMO}| - E_g^{opt})$, ^{d)} E_g^{opt} - estimated from the edges of electronic absorption spectra).

The ionization potential (IP_{CV}) values of compounds were calculated by using oxidation onset potentials vs. ferrocene/ferrocenium (Table 2). The electron affinity (EA_{CV}) values were deduced from the difference between the IP_{CV} values and the band-gaps (E_g^{opt}) obtained

from the absorption spectra. IP_{CV} varied from 5.27 to 5.58 eV and EA_{CV} values were in the range from -2.72 to -2.25 eV for the three derivatives. IP_{CV} values of compounds **4** and **5** was higher than that of **3** because of the electron-accepting ability of the 1-ethenyl-2,3,4,5,6-pentafluorophenyl and 4-ethenylpyridinyl moieties. The values of IP_{CV} and EA_{CV} of these compounds were found to be higher compared to those of the similar starburst 1,3,6,8-tetraaryl-substituted carbazole derivatives in which the chromophores are linked *via* the single bonds [5].

Conclusions

Tetra-substituted carbazole derivatives, with ethenylaryl groups attached to C-1,3,6,8 positions of a 9-ethyl-9*H*-carbazole core have been synthesized and studied by thermogravimetric analysis, differential scanning calorimetry, UV, fluorescence spectrometries, cyclic voltametry. The analysis revealed that compound with 2-ethenyl-naphthalenyl substituents exhibited higher thermal stability than compounds with 1-ethenyl-2,3,4,5,6-pentafluorophenyl and 4-ethenylpyridinyl moieties. The synthesized compounds form glasses with glass transition temperatures of 59-134 °C. The dilute solutions of the synthesized derivatives exhibit absorption maxima in the range of 355-380 nm, and fluorescence intensity maxima in the range of 400-470 nm. The ionization potential values of the synthesized materials range from 5.27 to 5.58 eV.

Acknowledgement

This research was funded by the **European Social Fund** under the **Global Grant** measure.

References

- [1] W. Jiang, Z. J. Ge, P. Y. Cai, B. Huang, Y. Q. Dai, Y. M. Sun, J. Qiao, L. D. Wang, L. Duan, Y. Qiu, *J. Mater. Chem.*, **2012**, 22, 12016.
- [2] J. Ostrauskaite, V. Voska, G. Buika, V. Gaidelis, V. Jankauskas, H. Janeczek, J.D. Sidaravicius, J. V. Grazulevicius, *Synth. Met.*, **2007**, 138, 457.
- [3] A. Tomkeviciene, J.V. Grazulevicius, K. Kazlauskas, A. Gruodis, S. Jursenas, T.H. Ke, C.C. Wu, *J. Phys. Chem. C*. **2011**, 115, 4887.
- [4] N. Seidler, S. Reineke, K. Walzer, B. Lussem, A. Tomkeviciene, J.V. Grazulevicius, K. Leo, *Appl. Phys. Lett.* **2010**, 96, article No. 093304.
- [5] F. Niu, H. Niu, Y. Liu, J. Lian, P. Zeng, *RSC Adv.*, **2011**, 1, 415.



APPLICATION OF STABLE ISOTOPE RATIO MASS SPECTROMETRY FOR THE STOICHIOMETRY DETERMINATION IN THE BIOCOMPOSITE

A. Garbaras^{1,2}, Eivydas Andriukonis¹, V. Remeikis², L. Mikoliunaite³, A. Popov⁴, A. Ramanavicius^{1,3}

1 Laboratory of NanoBioTechnology, Institute of Semiconductor Physics, State Research Institute Centre for Physical and Technological Sciences, A. Gostauto g. 11, LT-01108 Vilnius, Lithuania.

2 Laboratory of Mass Spectrometry, Institute of Physics, State Research Institute Centre for Physical and Technological Sciences, Savanoriu av. 231, LT – 02300 Vilnius, Lithuania

3 Department of Physical Chemistry, Faculty of Chemistry, Vilnius University, Naugarduko st. 24, LT – 03225, Vilnius, Lithuania.

*4 NanoTechnas – Center of Nanotechnology and Materials Science, Faculty of Chemistry, Vilnius University, Naugarduko 24, LT – 03225 Vilnius, Lithuania
E-mail: garbaras@ar.fi.lt*

The stable isotope ratio mass spectrometry is a conventional method used in archaeology, medical, environmental (Ceburnis et al. 2011) and paleoenvironmental reconstruction studies (Zernitskaya et al. 2014). However new insights and applicability of the equipment often opens new research areas and improves our understanding of the ongoing processes. Recent work by Garbaras et al. (2015) demonstrated the applicability of stable isotope ratio mass spectrometry method for the determination of stoichiometry between compounds forming polypyrrole and glucose oxidase composite.

Therefore the stable isotope ratio mass spectrometry method was applied for the stoichiometry determination of the complex biocomposites. Yeast cells *Saccharomyces cerevisiae* and conducting polymer polypyrrole is reported to form a composite. Natural abundance and isotopically labelled pyrrole (¹⁵N-Py) was used in the experiment. Nitrogen and carbon isotope ratios in the biocomposites were measured using an elemental analyzer (EA) (Flash EA1112) coupled to IRMS (Thermo delta plus advantage) via ConFlo III interface. The isotope mixing model was applied for the evaluation of the constitution of the biocomposite. In this work we demonstrate first results on stoichiometry determination in biocomposite using isotopically labelled pyrrole. We expect that this novel work will widen the research opportunities of the stable isotope ratio mass spectrometry research field.

References

1. D. Ceburnis, A. Garbaras, S. Szidat, M. Rinaldi, S. Fahrni, N. Perron, L. Wacker, S. Leinert, V. Remeikis, M. C. Facchini, A. S. H. Prevot, S. G. Jennings, and C. D. O'Dowd, *Atmos. Chem. Phys.* **11** (2011) 2749-2772.
2. V. Zernitskaya, M. Stancikaite, B. Vlasov, V. Seiriene, D. Kiseliene, G. Gryguc and R. Skipityte, *Quatern. Int.*, (2014) (**In Press**).
3. A. Garbaras, L. Mikoliunaite, A. Popov, A. Ramanaviciene, V. Remeikis, A. Ramanavicius. *Phys. Chem. Chem. Phys.* (2015) (**In press**). DOI: 10.1039/C4CP04885G

SYNTHESIS OF ANIONIC MOLECULAR BRUSHES BY „RAFT GRAFTING FROM“ APPROACH

J. Jonikaitė-Švėgždienė, V. Merkytė, T. Krivorotova, R. Makuška

Department of Polymer Chemistry, Vilnius University, Naugarduko 24, LT-03225 Vilnius, Lithuania, juratejonikaite@gmail.com

Polymerization by RAFT of styrenic copolymers bearing anionic side chains is reported. RAFT polymerization directed to block copolymers was mediated by three different RAFT chain transfer agents (CTA), two of them demonstrated excellent control of styrene polymerization. Block copolymers pSt-b-pCMS with M_w/M_n 1.2 to 1.7 were synthesized and modified to polyCTA. Acrylic acid (AA) side chains were attached to the polystyrene-based backbone via "grafting from" approach.

Keywords: RAFT polymerization, 4-chloromethylstyrene, acrylic acid, anionic brushes

Introduction

Molecular brushes are type of one-dimensional macromolecules with short densely grafted side chains attached to a linear backbone [1, 2]. Varying the length and density of these side chains, the length of the backbone, monomers, that are used, the stiffness, size and morphology of the resulting cylindrical objects can be controlled [3]. Stimuli-responsive polymer materials are playing an increasingly important part in a diverse range of applications, such as drug delivery, diagnostics, tissue engineering and „smart“ optical systems [4-6]. One of the most attractive methods to synthesize molecular brushes bearing anionic side chains is reversible addition-fragmentation chain transfer polymerization (RAFT). Because of the possibility of direct polymerization of negatively charged vinyl monomers under mild condition, RAFT process allows facile synthesis of molecular brushes with negatively charged side chains [7-9].

In the present study we demonstrate synthesis of anionic molecular brushes containing polystyrene-based backbone and poly(acrylic acid) side chains. Synthesis pathway is shown in Fig. 1. RAFT polymerization of styrene (St) and 4-chloromethylstyrene (CMS) resulting in block copolymers was performed using 3 different trithiocarbonate-based chain transfer agents (CTA). 4-Chloromethylstyrene units were modified by attaching butylthiocarbothioylthio moieties, and RAFT polymerization of acrylic acid (AA) via "grafting from" approach was realized.

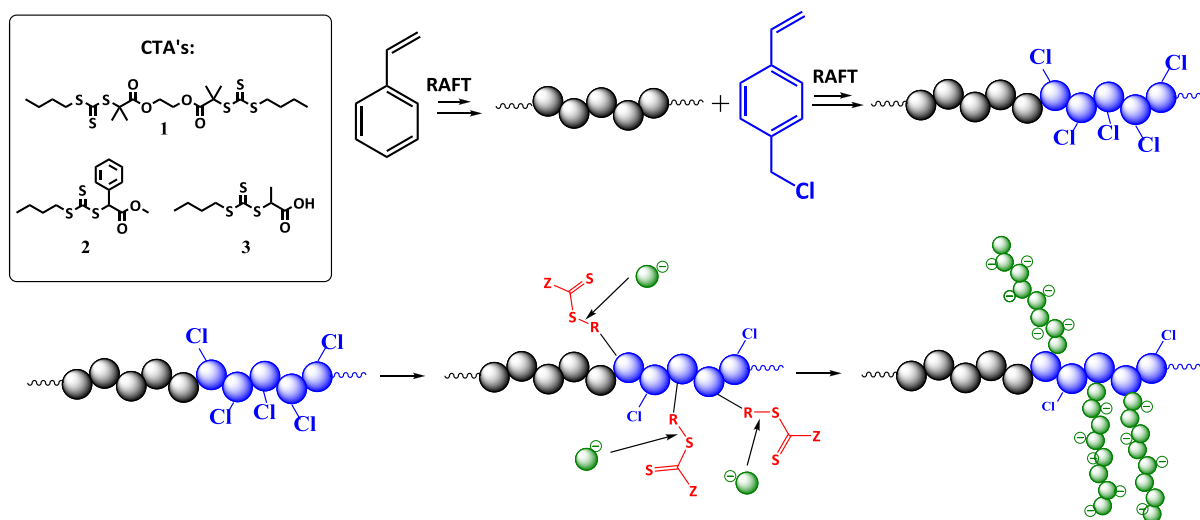


Fig.1. Synthetic route to anionic molecular brushes from densely functionalized polyCTA

Results and Discussion

RAFT polymerization of styrene was initiated by 4,4'-azobisisobutyronitrile (AIBN) and carried out in the presence of various CTA (Fig. 1.). Synthesis of bifunctional bis(trithiocarbonate) (CTA1) and S-methoxycarbonylphenylmethyl butyl trithiocarbonate (CTA2) were developed in our laboratory, and 2-propanoic acid butyl trithiocarbonate (CTA3) was synthesized by known method [10]. Polymerization conditions and results are presented in Table 1. Molecular weight, MWD and dispersity (M_w/M_n) of the polymers were determined by SEC with triple detection. M_n of the polymers varied from 2 000 to 14 000, M_w/M_n being as low as 1. Calculated values of M_n based on the ratio of the monomer to CTA and the monomer conversion, were in good agreement with those determined from SEC.

Table 1. RAFT polymerization of St at 80 °C in toluene (CTA1 and CTA2) and DMF (CTA3). $[St]_0 = 1.7$ M

Entry	CTA	$[St]_0/[CTA]_0/[AIBN]_0$	τ , hrs	q, %	$M_n \cdot 10^{-3}$	DP	M_w/M_n
1	1	400/2/1	2	9.3	2.8	22	1.17
2			8	11.7	3.2	26	1.27
3			12	12.0	3.5	29	1.30
4	2	400/2/1	16	59.7 ^{c=8.7 M}	10.8	100	1.31
5			8	14.4	6.3	57	1.10
6			8	7.2	5.1	46	1.07
7	3	100/2/1	20	34.0	2.4	21	1.15
8			8	17.1	4.3	39	1.07
9			8	20.5	13.5	127	1.10

Using polystyrene (pSt) with trithiocarbonate end groups as macro-CTA, RAFT polymerization of CMS was carried out in toluene at various initial concentrations of CMS, pSt and the initiator. Copolymerization conditions and results are presented in Table 2. M_n of the diblock copolymers pSt-*b*-pCMS was 6 000 to 18 000, and M_w/M_n 1.2 to 1.7. Block copolymers pSt-*b*-pCMS were analyzed by FT-IR, RAMAN and ¹H NMR spectroscopy, SEC, DLS and DSC. It was determined that the length of the both blocks was similar, the degree of polymerization in pSt and pCMS blocks being 30 to 40. Hydrodynamic radius (R_h) of the diblock copolymers depended on M_n and was in the range 2 to 4 nm. The copolymers demonstrated typical properties of amorphous polymers. Glass transition temperature (T_g) of pSt-*b*-pCMS was rather low, 53 °C to 65 °C, which was predetermined by rather low molecular weight of the diblock copolymers.

Table 2. Results of RAFT polymerization of CMS (in toluene at 80 °C, $\tau = 20$ hrs, $[CMS] = 0.5-0.7$ M), and parameters of diblock copolymers pSt-*b*-pCMS.

Entry	pSt	$[CMS]_0/[pSt]_0/[AIBN]_0$	q, %	$M_n \cdot 10^{-3}$	DP[(St):(CMS)]	M_w/M_n	T_g , °C	R_h , nm (SEC)	R_h , nm (DLS)
1	1	400/1.5/1	17.1	8.2	22:36	1.23	62.7	2.71	3.21
2	2	380/1.7/1	19.3	8.0	26:32	1.26	65.2	2.47	2.88
3	3	350/1.5/1	14.4	10.3	29:44	1.17	62.2	2.79	2.88
4	4	400/5/1	29.6	18.3	100:50	1.41	53.2	3.87	3.90
5	-	430/2/1	10.8	7.6	29:28	1.27	61.9	2.73	2.81
6	-	370/2.8/1	18.4	6.3	23:23	1.30	64.9	2.01	2.18
7	7	150/2/1	8.1	7.1	21:31	1.67	-	1.99	2.24
8	-	800/2/1	24.0	15.9	87:43	1.30	60.0	3.36	3.93

Modification of 4-chloromethylstyrene units in diblock copolymers pSt-*b*-pCMS was done by known method [11]. The ratio of the integral of the signal at 3.37 ppm (methylene protons of butyl group adjacent to thiocarbonyl group) to that at 4.54 ppm (methylene protons of benzyl group) confirmed that the degree of substitution of 4-chloromethyl groups to butylthiocarbonothioylthio moieties was 95–98%. ¹H NMR spectra are shown in Fig. 2.

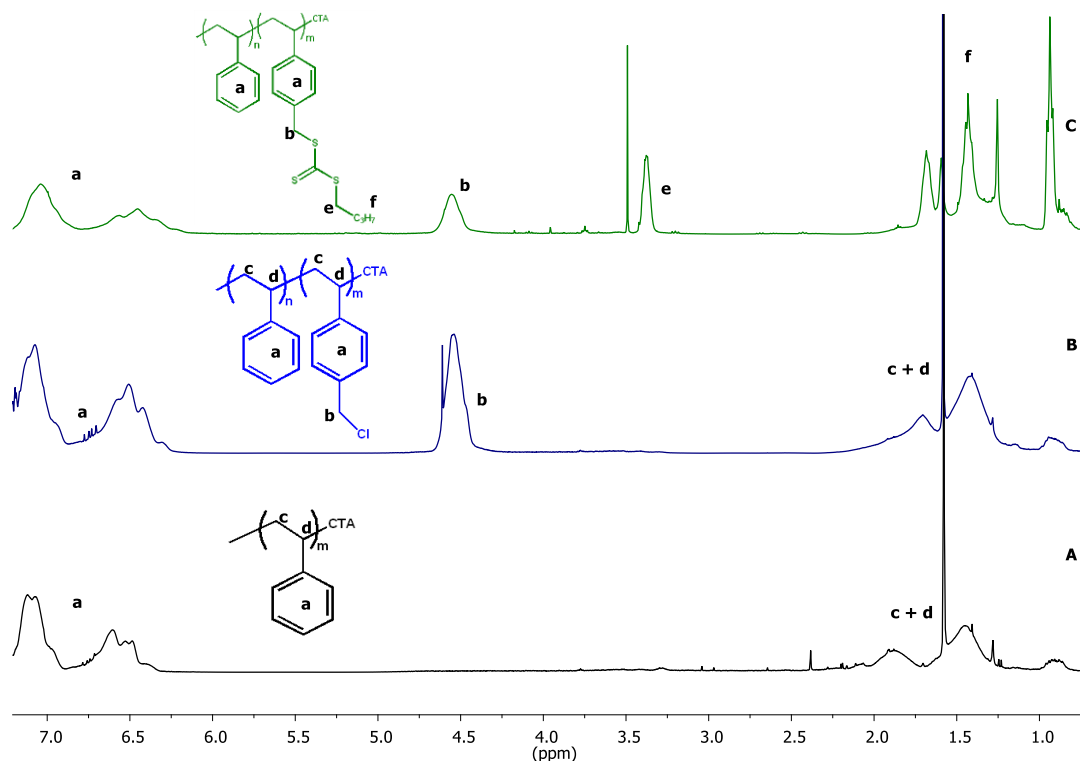


Fig.2. ^1H NMR spectra of pSt (A), pSt-*b*-pCMS (B) and polyCTA (C)

PolyCTA were used for the synthesis of anionic molecular brush. RAFT polymerization of AA was carried out in 1,4-dioxane (DO) by the method described in our previous work [7]. The obtained anionic molecular brushes are under study.

Conclusions

Excellent control of RAFT polymerization of styrene with M_w/M_n as low as 1.1 was realized using monofunctional RAFT CTA's. Worse control (M_w/M_n higher than 1.3) of RAFT polymerization using CTA1 can be attributed to bifunctionality of CTA. RAFT polymerization was successfully used for the synthesis of diblock copolymers pSt-*b*-pCMS. 4-Chloromethylstyrene units in well-defined polystyrene-based backbone were modified by attaching butylthiocarbonothioylthio moieties which gave polyCTA. RAFT polymerization of acrylic acid (AA) in the presence of polyCTA resulted in anionic molecular brushes.

Acknowledgements. Financial support from the Research Council of Lithuania under the project MIP-51/2012 is gratefully acknowledged.

References

1. A. Bhattacharya, B. N. Misra. *Prog. Polym. Sci.* 2004, 29, 767–814.
2. W. Dongxia, S. Xiaohui, T. Tao, et al. *J. of Polym. Science: Part A: Polym. Chem.* 2010, 48, 443–453.
3. L. Zhou, Z. Ke, Ch. Chong, et al. *J. of Polym. Science: Part A: Polym. Chem.* 2009, 47, 5557–5563.
4. E. Crownover, C. L. Duvall, A. Convertine, et al. *Journal of Controlled Release* 2011, 155, 167–174.
5. M. A. C. Stuart, W. T. S. Huck, J. Genzer, et al. *Nature Materials* 2010, 9, 101–113.
6. M. A. Hickner, H. Ghassemi, Y. S. Kim, et al. *Chem. Rev.* 104, 2004, 4587–4612.
7. T. Krivorotova, J. J.-Svezdiene, P. Radzevicius, R. Makuska. *Reactive & Funct. Polym.* 2014, 76, 32–40.
8. D. Hua, J. Tang, J. Cheng, et al. *Carbohydrate Polymers* 2008, 73, 98–104.
9. K. Zhang, Z. Wang, Y. Li, et al. *Carbohydrate Polymers* 2013, 92, 662–667.
10. Ch. Ferguson, R. J. Hughes, D. Nguyen, et al. *Macromolecules* 2005, 38, 2191–2204.
11. Z. Zheng, J. Ling, A. H. E. Müller. *Macromol. Rapid Commun.* 2014, 35, 234–241.

GLYCEROL-BASED POLYMERIC COMPOSITES REINFORCED WITH PRODUCTION WASTES

S. Kašėtaite^{1*}, J. Ostrauskaitė¹, V. Gražulevičienė²

¹*Department of Polymer Chemistry and Technology, Kaunas University of Technology, Radvilenu pl. 19, LT-50254 Kaunas, Lithuania.*

E-mail: sigita.kasetaitė@ktu.edu

²*Institute of Environment and Ecology, Aleksandras Stulginskis University, Studentu g. 11, LT-53361 Akademija, Kaunas region*

Composites consisting of glycerol-based thermoset reinforced with rapeseed cake, phosphogypsum, and horn meal have been obtained by photocross-linking using a mixture of triarylsulfonium hexafluoroantimonates as photoinitiator. The effect of the origin and amount of the different production wastes used as fillers on the kinetics of photopolymerization of glycerol diglycidyl ether and on the mechanical, thermal, and rheological properties of the resulted polymeric composites was investigated.

Keywords: composites, photocross-linking, thermoset

Introduction

The replacement of petroleum-derived plastics and composites by bio-based materials obtained from inexpensive, renewable, natural resources has the potential to greatly impact the industries of plastics, coatings, and composites [1]. Glycerol, the by-product of biodiesel refining is a promising candidate which can be used as monomer in the synthesis of polymers as it is or after chemical modification. New opportunities for the conversion of glycerol into value-added chemicals have emerged in recent years as a result of its unique structure, properties, bioavailability, and renewability [2]. Cationic photopolymerization of glycerol diglycidyl ether was chosen for the production of the glycerol-based polymeric composites because of its important advantages such as the absence of inhibition by oxygen, low shrinkage, good adhesion, and good mechanical properties of the UV-cured materials [3].

The aim of the present work was focused on the investigation of the effect of the varying origin and amount of the different production wastes used as the fillers on the kinetics of photopolymerization of the glycerol diglycidyl ether batches and on the mechanical, thermal, and rheological properties of the resulted polymeric composites.

Results and discussion

The composites were obtained by photopolymerization of glycerol diglycidyl ether with the different production wastes used as fillers, i.e rapeseed cake, phosphogypsum, and horn meal. The mixture of triarylsulfonium hexafluoroantimonates was used as photoinitiator. The (20-50) % concentration of the fillers was used in the batches.

The kinetics of photopolymerization was qualitatively evaluated by the measurements of storage modulus G' , loss modulus G'' , loss factor $\tan \delta$, and complex viscosity η^* which were recorded as a function of irradiation time. The typical dependencies of G' , G'' , $\tan \delta$, and η^* on the irradiation time for the photocross-linking of the batch of glycerol diglycidyl ether with 50 % of phosphogypsum are presented in Fig. 1. When the irradiation of the batch starts, G' , G'' , $\tan \delta$, and η^* increase very fast indicating propagation and the network formation in the initial stage of photopolymerization. G' increases faster and exceeds G'' while $\tan \delta$ starts to decrease in the intermediate stage which occurs in the first several minutes of the reaction. The increase in the magnitude of G' can be explained by the formation and consolidation of a

three-dimensional network which is characterized by the transformation of a Newtonian viscous fluid to an elastic solid. During the late stage, G' and G'' continues to increase with time due to the gel aging. The smaller values of G'' compared to those of G' , show the dominant elasticity of the system and indicate the existence of a permanent three-dimensional network formed by the interconnection of polymeric chains. All the studied batches showed the similar features. The main effect of the decrease of the concentration of the filler in the batch was the reduction of the induction period and thus, of the gel time estimated by the crossover point of the G' and G'' curves and the higher values of G' , G'' , and η^* .

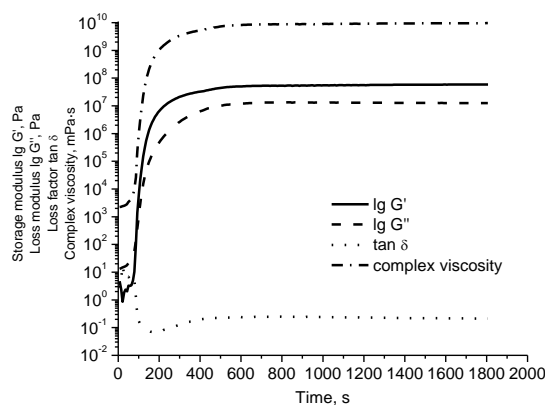


Figure 1. Dependence of storage modulus, loss modulus, loss factor, and complex viscosity of the batch of glycerol diglycidyl ether with 50 % of phosphogypsum on the irradiation time

The chemical structure of the photocross-linked products was confirmed by IR spectroscopy. The yield of the insoluble fraction of the polymeric composites obtained after Soxhlet extraction in chloroform for 72 h was in the range of (50-90) %. The density of cross-links calculated according to the theory of rubber elasticity ranged from $2.4 \cdot 10^{-5} \text{ mol/m}^3$ to $8.1 \cdot 10^{-5} \text{ mol/m}^3$.

It was established by thermogravimetric analysis that the thermal degradation temperatures at the weight loss of 10 % of the polymeric composites were in the range of (175-292) °C. The differential scanning calorimetry measurements revealed that all the photocross-linked polymeric composites were the amorphous materials with the glass transition temperatures being in the range from 22 °C to 38 °C. The hardness of the polymeric composite films measured with a Hepler consistometer ranged from 4 MPa to 26 MPa. The tensile strength ranged from 1.1 MPa to 21.4 MPa. The elongation at break was found to be in the range of (3.1-10.8) %. The Young modulus ranged from 17.1 MPa to 748.5 MPa.

Conclusions

Composites consisting of glycerol-based thermoset reinforced with rapeseed cake, phosphogypsum, and horn meal have been obtained by photocross-linking. The increase of the concentration of the glycerol diglycidyl ether in the batch resulted in the increase of the overall reaction rate and in the formation of the more rigid network. The highest values of the hardness, tensile strength, and the Young modulus was shown by polymeric composites reinforced with phosphogypsum.

References

1. Quirino, R.L.; Garrisonb, T.F.; Kesslerb M.R. *Green Chem.*, 2014, 16, 1700–1715.
2. Fertier, L.; Koleilat, H.; Stemmelen, M.; Giani, O.; Joly-Duhamel, C.; Lapinte, V.; Robin, J.J. *Prog. Polym. Sci.*, 2013, 38, 932-962.
3. Sangermano, M. *Pure App. Chem.*, 2012, 84, 2089-2101.

ELECTROACTIVE POLYMERS CONTAINING ELECTRONICALLY ISOLATED NAPHTHYL-SUBSTITUTED CARBAZOLE RINGS

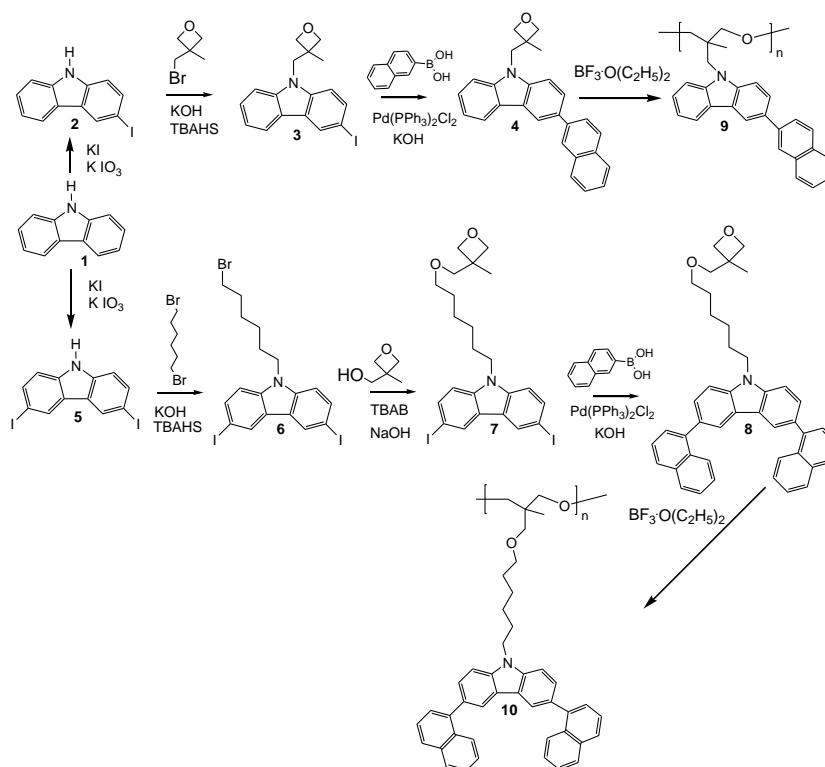
G. Krucaite, D. Tavgeniene, D. Sipaviciute, B. Stulpinaite

Department of Polymer Chemistry and Technology, Kaunas University of Technology, Radvilenu plentas 19, LT50254, Kaunas, Lithuania

Polymers containing electro-active fragments are known for various applications such as organic light emitting diodes (OLEDs), electrographic photoreceptors, photovoltaic cells or thin film transistors. Thin layers of polymers can be fabricated by using simple techniques, i.e. casting or spin-coating from solutions and are suitable for application in large area devices. Derivatives containing aryl substituted carbazole rings have been widely studied as electro-active layers in devices and described in literature [1, 2, 3, 4, 5, 6, 7, 8, 9]. Recently it was also observed that derivatives containing electronically isolated carbazole rings are very promising host materials for electro-phosphorescent OLEDs [10, 11]. We present here new polymers containing naphthyl (di)substituted carbazole rings and their application in electroluminescent OLEDs.

The synthetic route demonstrating preparation of the polyethers (**9-10**) containing electroactive 3-naphthylcarbazolyl or 3,6-dinaphthylcarbazolyl chromophores is shown in Scheme 1. 3-Iodo-9H-carbazole (**2**) and 3,6-diiodo-9H-carbazole (**5**) were synthesized from commercially available 9H-carbazole (**1**) by Tucker iodination procedure [12]. The iodo-derivative **2** was converted to oxetanyl-functionalized key derivative **3** by reaction with large excess of 3-bromomethyl-3-methyloxetane under basic conditions in the presence of a phase transfer catalyst. The monomers **4** was obtained from 3-iodo-9-(3-methyloxetan-3-ylmethyl)carbazole by Suzuki reaction with 1-naphthalene boronic acid.

The diiodo-derivative **5** was alkylated with 1,6-dibromohexane under basic conditions to give 3,6-diiodo-9-(6-bromohexyl)carbazole (**6**). Compound **6** was then treated with 3-hydroxymethyl-3-methyloxetane in two-phase system of aqueous 50 % NaOH and toluene to give the oxetane-based monomer **7**. The oxetanyl functionalized diiodo-derivative was converted to monomer **8** via the Suzuki coupling reaction by using an excess of 1-naphthalene boronic acid. Polymers **9-10** were prepared by cationic polymerization of the corresponding monomers (**4** or **8**) in 1,2-dichloroethane solutions using $\text{BF}_3 \cdot \text{O}(\text{C}_2\text{H}_5)_2$ as an initiator. Low-molecular-weight fractions of the products of polymerizations were removed by Soxhlet extraction of the raw polymers with methanol.



Scheme 1.

Molecular weights and polydispersity indices (PDI) of the synthesized polymeric materials were estimated by GPC. The number-average molecular weights (M_n), weight-average molecular weights (M_w) and PDI of these polymers are presented in the Table 1. The molecular weights of the polymers only slightly depend on the nature of electroactive moieties attached to the polymerizable oxetane ring. The monomer containing 3-naphthylcarbazol-9-yl units yielded oligomers with higher molecular weight. The lower molecular weight of polymer **10** could probably be explained by low solubility of the formed polymeric material in dichloroethane. It should be mentioned that molecular weights of the polymers **9-10** are very close to those of the similar polyethers containing unsubstituted carbazolyle rings [13].

Table 1. Molecular weights and PDI of polymers **9-10**

Polymer	M_n	M_w	PDI
9	1800	7100	3.9
10	1530	3520	2.3

Hole transporting properties of the synthesized polymers **9** and **10** were tested in electroluminescent devices. The two layers OLEDs were prepared using Alq_3 for the electroluminescent/electron transporting layer. Aluminium was used as a cathode with a thin electron injection layer of LiF. When a positive voltage was applied to the devices a bright green electroluminescence of Alq_3 was observed with an emission maximum at around 520

nm. This demonstrated that hole injection and charge mobility in the hole transporting layers of polymers **9-10** was fully sufficient for an effective charge carrier recombination occurring within the Alq₃ layer. The highest efficiency of 3.3 cd/A was obtained in the device containing charge-transporting layer of polymer **9** with electro-active 3-naphthylcarbazole units.

Acknowledgements

This research was funded by a grant No. MIP-024/2013 from the Research Council of Lithuania.

Dr. B. Zhang (Changchun Institute of Applied Chemistry, China) is thanked for measurements of the OLED's characteristics.

References

- [1] S. Beaupre, P.-L.T. Boudreault, M. Leclerc. *Advanced Materials* 2010, 22, 6–27.
- [2] S. Grigalevicius. *Synthetic Metals* 2006, 156, 1–12.
- [3] S. Grigalevicius, J.V. Grazulevicius, V. Gaidelis, V. Jankauskas. *Polymer* 2002, 43, 2603–2608.
- [4] V. Vaitkeviciene, A. Kruzinauskiene, S. Grigalevicius, J.V. Grazulevicius, R. Rutkaite, V. Jankauskas. *Synthetic Metals* 2008, 158, 383–390.
- [5] R. Karpicz, S. Puzinas, S. Krotkus, K. Kazlauskas, S. Jursenas, J.V. Grazulevicius, S. Grigalevičius, V. Gulbinas. *Journal of Chemical Physics* 2011, 134, Article Number: 204508.
- [6] S. Grigalevicius, G. Blazys, J. Ostrauskaite, J.V. Grazulevicius, V. Gaidelis, V. Jankauskas, E. Montrimas. *Synthetic Metals* 2002, 128, 127–131.
- [7] G. Blazys, S. Grigalevicius, J.V. Grazulevicius, V. Gaidelis, V. Jankauskas, V. Kampars, *Journal of Photochemistry and Photobiology A-Chemistry* 174 (2005) 1.
- [8] A. Balionyte, S. Grigalevicius, V. Jankauskas, G. Garsva, J. V. Grazulevicius. *J. Photochem. Photobiol. A: Chem.* 216 (2004) 249.
- [9] M. Kirkus, J. V. Grazulevicius, S. Grigalevicius, R. Gu, W. Dehaen, V. Jankauskas. *European Polymer Journal* 2009;45:410–17.
- [10] K.S. Yook, J. Y. Lee. *Advanced Materials* 2012, 24, 3169–3190.
- [11] J.H. Jou, W.B. Wang, S.M. Shen, S. Kumar, I.M. Lai, J.J. Shyue, S. Lengvinaite, R. Zostautiene, J.V. Grazulevicius, S. Grigalevicius, S.Z. Chen, C.C. Wu. *Journal of Materials Chemistry* 2011, 21, 9546-9552.
- [12] Tucker, S. H., *J. Chem. Soc.* 1 (1926) 548.
- [13] R. Stanionyte, G. Buika, J.V. Grazulevicius, S. Grigalevicius, *Polymer International*, 57 (2008) 1036.

DERIVATIVES OF INDOLE WITH REACTIVE FUNCTIONAL GROUPS AS ELECTROACTIVE MATERIALS

R. Laurinavičiūtė¹, L. Pečiulytė¹, D. Volyniuk¹, J.V. Gražulevičius¹

¹*Department of Polymer Chemistry and Technology,
Faculty of Chemical Technology,
Kaunas University of Technology
Radvilėnų pl. 19, Kaunas, Lithuania
e-mail: rasa.laurinaviciute@ktu.edu*

We synthesized new derivatives of indole and carbazole as well as indole twin compounds with reactive vinylbenzyl groups and studied their photopolymerization by IR spectroscopy. The properties of the monomers were studied by the different experimental tools.

Keywords: indole, carbazole, radical polymerization, ionization potential.

Introduction

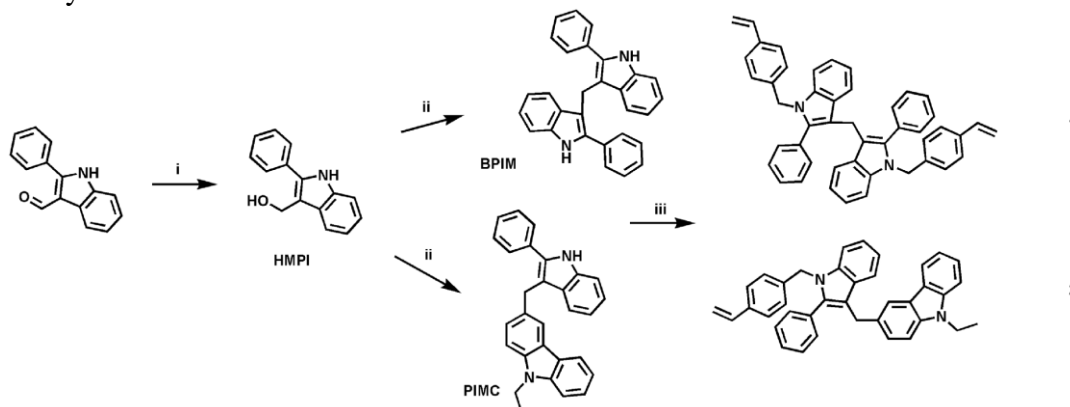
Organic charge-transporting materials which are also known as organic semiconductors are used in optoelectronic devices such as electrophotographic photoreceptors, light emitting diodes, solar cells. Charge-transporting polymers have some important advantages with respect to their low-molar-mass counterparts and molecularly doped polymers. They usually possess good mechanical properties and high morphological stability. In addition, no diffusion between layers is observed in the multilayer devices when polymers are used for the preparation of charge-transporting layers [1, 2].

Various indole derivatives were synthesized, and their properties were investigated [3, 4]. One common characteristic for the indole derivatives are large Stokes shift values, which leads to suitable luminescence assays, for example developing of sensors [5] or optoelectronic devices [6].

In this work indole twin compound and the derivative of indole and carbazole with polymerizable vinylbenzyl- groups were synthesized and investigated in order to identify correlations between the molecular structures of the compounds and their optical, electrochemical and photophysical properties. We also investigated the possibility of the preparation of insoluble polymeric layers by photocross-linking of the twin derivative of indole containing vinylbenzyl groups.

Results and Discussion

The synthesis of the new indole-based monomers is described in the Scheme 1.



Scheme 1. Synthesis of the derivatives of indole. (i) NaBH₄, methanol, 0-5 °C, 2 h; (ii) BF₃ triethyl etherate, dichloromethane, 3 h; (iii) 4-vinylbenzylchloride, K-tBuO, BTMAC, DMSO, r. t., 48h.

Thermal properties of the monomers were investigated by thermogravimetric analysis (TGA) and differential scanning calorimetry (DSC). The thermal characteristics of compounds **1** and **2** are collected in Table 1. The temperatures of the onset of the thermal degradation of indole twin compound **1** was found to be 215 °C, while that of compound **2** containing carbazole moiety was much higher (327 °C). Compound **1** was isolated after the synthesis as the crystalline substance. Its melting point was found to be 120 °C. We did not manage to transform it to the glassy state. Compound **2** was found to be capable of the formation of molecular glass. Its glass transition temperature was found to be 85 °C. The glass transition temperature (T_g) is one of the most important parameters for the organic materials to be applied in optoelectronics.

UV and fluorescence spectra of the dilute solutions and thin films of **1** and **2** are shown in Figure 1.

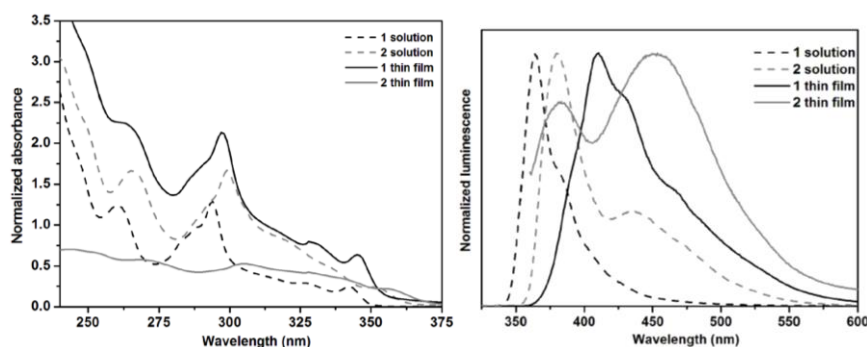


Figure 1. UV and fluorescence ($\lambda_{ex} = 350$ nm) spectra of the solutions and thin films of **1** and **2**.

The wavelengths of the absorption and emission maxima are collected in Table 1. The UV spectra were found to be similar. They absorb UV radiation in the range from 200 to 375 nm. The absorption bands in the region of 275–330 nm can be ascribed to a localized aromatic π - π^* transition of 2-phenyl indole moiety. The wavelengths of fluorescence intensity maxima were found to be in the range from 325 to 500 nm for both compounds. The fluorescence spectra of the thin films of the monomer **1** showed a significant red-shift (up to 100 nm) with respect of that of the solution indicating enhanced intermolecular interactions in the solid state. As for the monomer **2**, the second emission band appears at 451 nm in the emission spectra of the thin film, likely due to the formation of an intermolecular excimer. The triplet energy levels established for neat films of the monomers from their phosphorescence spectra reach 2.63 eV for **1** and 2.59 eV for **2**.

The solid-state ionization potentials of the monomers were measured by the method of electron photoemission spectrometry and by cyclic voltammetry (Table 1). The values of ionization potentials recorded by the two methods were found to be comparable. 2-Phenyl indole based compound **1** showed higher ionization potential than compound **2** containing both 2-phenyl indole and carbazole moieties.

Table 1. Thermal, photophysical and electrochemical characteristics of the monomers **1** and **2**.

	Compound	1	2
	T_m^a , °C	120	- ^b
	T_g^c , °C	-	85
	T_{ID}^d , °C	215	327
Solution	λ_{Abs}^e , nm	342	300
	λ_{PL}^f , nm	364	381
	Stokes shift ^g , nm	22	81
Neat film	λ_{Abs} , nm	345	355
	λ_{PL} , nm	410	451
	λ_{PH}^h , nm	472	478
	Stokes shift, nm	65	96
	E_T^i , eV	2.63	2.59
	$E_{ox\ onset\ vs.\ Fc}^j$, V	0.71	0.40
	IP^k , eV	5.79	5.41
	IP_{CV}^l , eV	5.81	5.50
	$E_g^{opt\ m}$, eV	3.36	3.29
	EA_{CV}^n , eV	2.45	2.21

^a – melting point observed at the first heating scan of the DSC measurement; ^b – not detected; ^c – glass transition from DSC curves; ^d – initial weight loss temperature obtained from TGA curves; ^e – wavelengths of absorption maxima; ^f – wavelengths of emission maxima; ^g – $\lambda_{FI} - \lambda_{Abs}$; ^h – wavelengths of phosphorescence maxima; ⁱ – triplet energy calculated from $1240/\lambda_{PH}$; ^j – onset oxidation potential of the sample vs. onset oxidation potential of ferrocene; ^k – ionization potential estimated by electron photoemission in air method; ^l – ionization potential, $IP_{CV} = E_{onset\ ox\ vs.\ Fc} + 5.1\ eV$ [7, 8]; ^m – optical band gap calculated from $1240/\lambda_{Abs\ onset}$ (onset absorption); ⁿ – electron affinity, $EA_{CV} = IP_{CV} - E_g^{opt}$.

Photocross-linking of monomer **1** was studied using ATR-FTIR spectrometry. For the measurements the solution of monomer **1** containing 3 mol % of photoinitiator cyclopentadienyl(fluorene)iron(II)hexafluorophosphate was drop-casted on the surface of ATR-FTIR analysis crystal and the observation of the decrease of the intensity of absorption band of vinyl group under exposure of UV radiation source was performed.

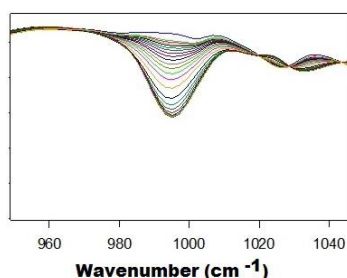


Figure 2. Fragments of the FTIR spectra of the compound **1** recorded during the photocuring.

Fig. 2 shows the fragments of FTIR spectra of the film of compound **1** at the different stages of photocuring. They illustrate the decrease of the intensity of absorption bands of vinyl groups at $997\ cm^{-1}$ with the increase of the time of photocuring. The conversion of vinyl groups of compound **1** reached ca 90 % after 15 min.

Acknowledgements

This research was funded by the **European Social Fund** under the **Global Grant** measure.



References

1. R. Lygaitis, V. Getautis, J.V. Grazulevicius, *Chem. Soc. Rev.* **2008** 37 770–788.
2. V. Getautis, M. Daškevičienė, T. Malinauskas, V. Gaidelis, V. Jankauskas, Z. Tokarski, *Synthetic Met.* **2005** 155 599–605.
3. M.G. Balemans, F. C. van de Veerdonk, *Experientia* **1967** 23 906–907.
4. G.E. Philbrook, J.B.Ayers, J.F.Garst, J.R. Totter, *Photochem. Photobiol* **1965** 4 869–876.
5. O. Shimomura, *Bioluminescence: Chemical Principles and Methods* **2006**.
6. C.W. Chiu, T.J. Chow, C.H. Chuen, H.M. Lin., Y.T. Tao, *Chem. Mater* **2003** 15 4527–4532.
7. C. Cardona, W. M. Li, A. Kaifer, D. Stockdale and C.G. Bazan, *Adv. Mater.* **2011** 23 2367–2371.
8. R. Rybakiewicz, P. Gawrys, D. Tsikritzis, K. Emmanouil, S. Kennou, M. Zagorska, A. Pron, *Electrochim. Acta* **2013** 96 13–17.

ENZYMATIC DEGRADATION OF STARCH AND ITS CATIONIC DERIVATIVES

E. Lekniute-Kyzike, J. Bendoraitiene

*Department of Polymer Chemistry and Technology, Faculty of Chemical Technology, Kaunas University of Technology, Radvilenu pl. 19, Kaunas, Lithuania
E-mail: edita.lekniute@ktu.edu*

Introduction

Starch is natural, renewable and biodegradable low-cost raw material. It is used in many food and industrial products [1]. Starch is a relatively simple polymer composed of glucose molecules that are linked together in two different forms. Amylose, which makes up to 20-30% of normal starch, is an essentially linear molecule in which the glucose units are joined end-to-end by α -1,4 linkages. Amylopectin is the major component of starch (comprising 70-80%) and is a much larger branched molecule in which about 5% of the glucose units are joined by α -1,6 linkages [2].

Chemical modification of starch is carried out to enhance the positive attributes and eliminate the shortcomings of native starch. However, such modification can decrease the degradability of polysaccharides. Enzymatic degradation of starch and its derivatives with α -amylase is one of the methods to investigate the biodegradability. α -Amylase is able to cleave α -1,4 glycosidic bonds present in the inner part (endo-) of the amylose or amylopectin chain (Fig. 1). The end products of α -amylase action are oligosaccharides with varying length with α -configuration, α -limit dextrins, which constitute branched oligosaccharides, glucose and maltose [3-5].

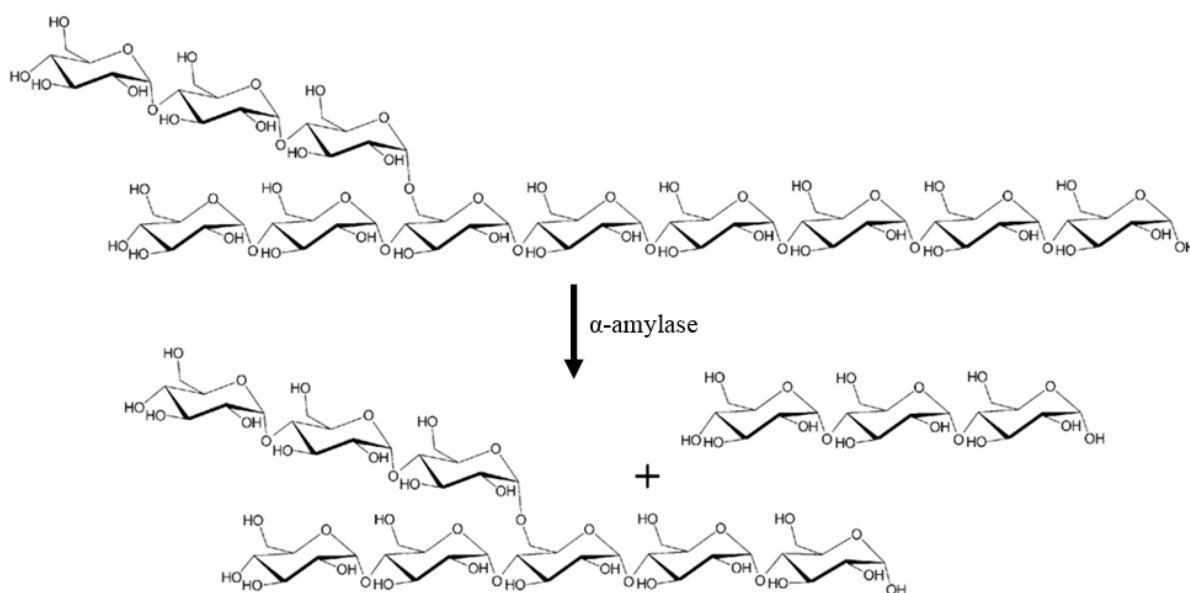


Fig.1. Schematic representation of the reactions catalyzed hydrolases acting on starch [3]

Results and Discussions

Cationic starch (CS) derivatives with quaternary ammonium groups were obtained by etherification of potato starch with glycidyltrimethylammonium chloride in the presence of a base. CSs with different degree of substitution (DS=0.06, 0.10, 0.20, 0.30 and 0.54) were obtained.

Degradation level of starch and CSs was estimated by Fourier transform infrared spectroscopy (FTIR), by measuring the amount of reducing sugars (RS) [6] and viscosity of their solutions in water.

The enzymatic degradation of native and modified starches was performed using α -amylase preparation (Liquozyme® Supra (800 KNU/g), Novozymes A/S). Water dispersions (3%) of starch or cationic starch derivative was mixed with various amounts of α -amylase (0.2, 2.0 and 20 mg per g of polysaccharide), and then was investigated using Brabender Micro Visco-Amylo-Graph®.

The maximum (η_{max}) and the final (η_{final}) viscosities are shown in Table 1. Dispersions of native and cationic starches in water gelatinized differently: η_{final} of gelatinized starch was low because of limited swelling of granules – 238 BU, however even at low degree of cationic substitution (0.06) the viscosity noticeably increased – 353 BU. By further increasing the DS of CS the η_{final} remained similar – about 400 BU. The highest maximum viscosity was obtained for CSs with DS 0.06-0.20, it shows that the granules of cationic starches were maximally swollen. When α -amylase was added to the dispersions, the maximum and final viscosities decreased in all cases. It has been noticed that the biggest decrease of η_{max} was for native starch, also the changes of viscosity for CS with DS 0.06-0.30 were similar, but when DS was higher (0.54) the viscosity reduced minimally. The same tendency was observed and for intrinsic viscosity (η_{intr}) data (Table 1). It can be concluded that cationic groups is limiting factor to enzymatic hydrolysis and reduce the degradability, especially when degree of substitution is 0.54, apparently due to pure availability of α -1,4 glycosidic bonds.

Table 1. Results of Brabender viscoamylograms and intrinsic viscosity

DS	Amount of α -amylase, mg/g								
	0		0.20			2.0		20	
	η_{max}^* , BU	η_{final}^* , BU	η_{max}^* , BU	η_{final}^* , BU	η_{intr}^{**} , ml/g	η_{max}^* , BU	η_{final}^* , BU	η_{max}^* , BU	η_{final}^* , BU
0	170	238	41	9	11.65	7	6	5	4
0.06	909	353	846	13	17.46	452	9	31	6
0.10	912	418	920	13	19.41	530	10	92	7
0.20	1050	375	1112	14	27.69	484	12	8	8
0.30	649	467	451	15	57.45	235	11	25	9
0.54	591	462	484	27	347.31	401	17	149	12

* 5% tolerance limit; ** at 25 (± 0.1) °C

The determined amount of reducing sugars in the samples also confirm such observation. The dependence of RS on DS of starches at different amounts of α -amylase is shown in Fig.2. As one can see, when the amount of enzyme is 0.2 mg/g the degradation level is not high, for

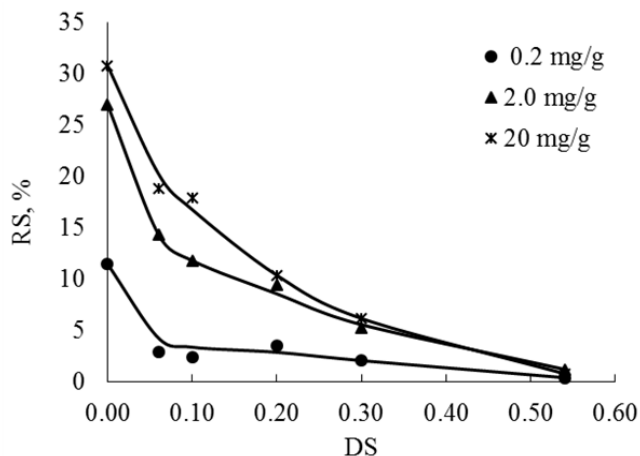


Fig. 2. The dependence of the amount of reducing sugars (%) on DS of starches after degradation by α -amylase

native starch RS is about 10% and for CSs is about 2-3%. The amount of reducing sugars also increase with the increasing amount of enzyme up to 2.0 mg/g, especially in the case of native starch, where RS content increases almost 3 times. But when the amount of α -amylase was increased up to 20 mg/g, no significant changes were observed in RS content. Fig. 2 shows, that RS of cationic starches depended on the degree of substitution. CS with higher DS is less degradable, and the amount

RS is much lower.

The chemical changes resulting from the enzymatic degradation of the granules were detected by FTIR (Fig. 3). The bands at 1149 cm^{-1} (peak C) and 1076 cm^{-1} (peak B) are associated to the ordered structures of starch, whereas, the band at 1015 cm^{-1} (peak A) is associated to the amorphous structures of starch [7]. Enzymatic degradation of starch with α -amylase resulted in the decreased in the intensity of peaks B and C, meanwhile the intensity of the band A was increased. The same changes were noticed for cationic starches with DS 0.06-0.30, except for the CS with DS 0.54, where no remarkable changes were observed. These results suggest that the ordered structure of investigated starches was disrupted as a result of enzymatic degradation.

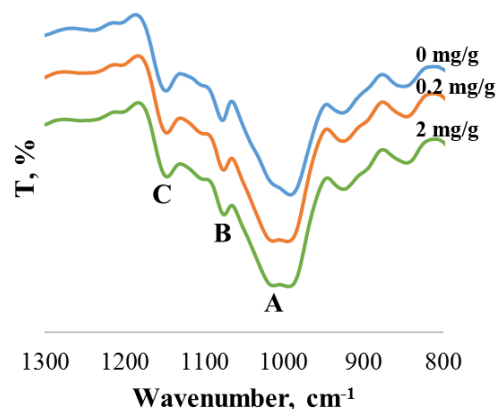


Fig. 3. FTIR spectra of potato starch - without and with α -amylase

Conclusions

Cationic starch is less susceptible to enzymatic degradation than native starch. The degradability of polysaccharides decreases with increasing the degree of substitution, especially in case when DS is 0.54.

Acknowledgments

The authors are grateful to the Research Council of Lithuania for a financial support of the MIP034/14 project.

References

1. R. P. Ellis, M. P. Cochrane, M. F. B. Dale, C. M. Dupus, A. Lynn, I. M. Morrison, R. D. M. Prentice, J. S. Swanston, S. A. Tiller, *Journal Sci Food Agric*, **1998**, 77, p. 289-311.
2. S. C. Zeeman, J. Kossmann, A. M. Smith, *Annual Review of Plant Biology*, **2010**, p. 61
3. M. J.E.C. van der Maarel, H. Leemhuis, *Carbohydrate Polymers*, **2013**, 93, 1, p. 116-121.
4. A. Ayoub, S. Gruyer, C. Bliard, *Int. Journal of Biological Macromolecules*, **2003**, 32, p. 209-216.
5. Z. Zhu, Y. Lei, *Journal of Adhesion Science and Technology*, **2015**, 29, 2, p. 116-132.
6. Food Chemicals Codex, Fourth Edition. *First Supplement*, National Academic Press, **1996**, p. 18.
7. N. Dupuy, C. Wojciechowski, C.D. Ta, J.P. Huvenne, P. Legrand *Journal of Molecular Structure*, **1997**, 410-411, p. 551-554.



PREPARATION OF POLY(URETHANE-UREA) MICROCAPSULES USING POLY(VINYL ALCOHOL) AS THE POLYOL

S. Mačiulytė, T. Kochanė, S. Budrienė

Department of Polymer Chemistry, Vilnius University, Naugarduko 24, LT-03225 Vilnius, Lithuania

e-mail: maciulyte.sandra@gmail.com

Abstract

Poly(urethane-urea) microcapsules (PUUMC) were synthesized from polyol poly(vinyl alcohol) (PVA) and hexamethylene diisocyanate (HMDI) by inverse emulsion method via polyaddition reaction. The PUUMC were characterized by chemical analytical methods FT-IR spectra, thermal analysis, surface area, pore volume and size analysis. Also, by carefully analysing the influencing factors including: catalyst, surfactant and their concentrations, the initial molar ratio of PVA and HMDI and stirring rate the optimum synthesis conditions were found out. Depending on reaction stirring rate, the range of PUUMC size distribution was from 425 to 30 μm . These PUUMC have potential application in biotechnology for enzyme encapsulation.

Introduction

Polyurethanes and polyurea polymers are emerging as useful biomaterials for biomedical applications because of their synthetic versatility, excellent mechanical and physical properties and good biocompatibility and biodegradability [1]. Their potential uses have been discussed for a variety of pharmaceutical, medical and cosmetic applications such as drug or other bioactive materials encapsulation and controlled release [2]. Microencapsulation is described as a process of enclosing micron-sized particles of solids or droplets of liquids or gasses in an inert shell, which in turn isolates and protects them from the external environment. The products obtained by this process are called microparticles, microcapsules and microspheres which differentiate in morphology and internal structure [3]. According to the literature data, the shell of poly(urethane-urea) microcapsules was synthesized from low or medium molecular weight diols and diisocyanates. The aim of present study is to investigate synthesis and properties of poly(urethane-urea) microcapsules (PUUMC) from high molecular weight polyol poly(vinyl alcohol) (PVA) and hexamethylene diisocyanate (HMDI) via interfacial polyaddition reaction in W/O emulsion system.

Experimental

Materials. 1,6-hexamethylene diisocyanate (HMDI), poly(vinyl alcohol) 100000 (PVA, degree of hydrolysis 86-89 mol %) and Span 85 were purchased from Fluka, Switzerland. Toluene was purchased from Rechem, Slovakia, dibutyltin dilaurate (DBTDL) was purchased from Merck, Germany, diethyl ether was purchased from Lachner, Czech Republic. **Synthesis and characterization of poly(urethane-urea) microcapsules.** PUUMC from PVA and HMDI were synthesized by the interfacial polyaddition in W/O emulsion. Aqueous phase was 0.2 M PVA solution in water and the oil phase was 1.15 % of Span 85 and 0.05 - 1.00 % of DBTDL solution in toluene. PVA solution was emulsified in organic phase. After emulsification, HMDI was added to the reaction mixture. The initial molar ratio of PVA and

HMDI was varied from 1:1 to 1:9. The mixture was stirred continuously using a blade stirrer at 70 °C for 2 hours to complete the formation of the poly(urethane-urea) (PUU) shell. The stirring rate was varied from 400 to 1500 rpm. The PUUMC were separated by filtration using filter paper and washed with diethyl ether and distilled water, and then were lyophilized by using lyophiliser Labconco Corporation FreeZone Plus. It was assumed that the yield of shell is the same as yield of dried PUUMC. The chemical structure of PUUMC was characterized by using the Perkin Elmer FRONTIER FT-IR spectrometer and chemical analytical methods [4].

Results and Discussion

Synthesis of PUU microcapsules (PUUMC) was carried out by interfacial polyaddition reaction of HMDI and PVA in W/O emulsion. The microencapsulation process can be divided in two consecutive steps: the first emulsification step governs the size and the size distribution of the PUUMC, in the second step shells of the PUUMC are formed by interfacial polyaddition reaction of HMDI in the external toluene phase and PVA in the dispersed phase. The properties of PUUMC depend on many factors, including used surfactant and its concentration, the initial molar ratio of PVA and HMDI, and stirring rate.

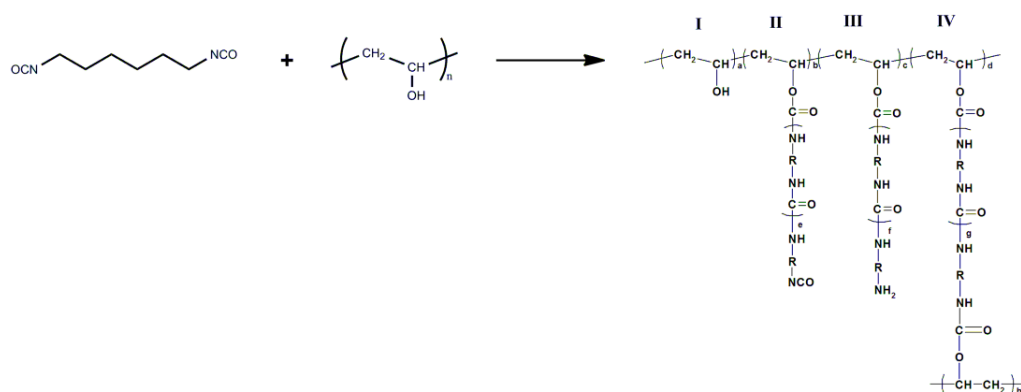


Fig. 1. Structure of shell of PUUMC

The structure of shell of PUUMC has been proven by FTIR spectra and by chemical analytical methods, which were used to determine quantity of hydroxyl and isocyanate groups in dried PUUMC. The PUUMC shell formation by polyaddition reaction is illustrated in Fig. 1. Immediately after synthesis, PUUMC shell consists of macromolecules with four types of constitutional units: unreacted hydroxyethylene constitutional unit of PVA (type I), constitutional unit with one urethane group which was formed by reaction between hydroxyl group of PVA and one isocyanate group of HMDI and free isocyanate group at the end of the branch (type II) and/or free amino group at the end of the branch (type III), which could be formed by reaction between free isocyanate group at the end of the branch and water, and constitutional unit with two urethane groups after crosslinking reaction of two isocyanate groups and two hydroxyl groups of PVA chains (type IV). The poly(urea) segments could present in constitutional units of type II – IV. The formation of poly(urea) segments was caused by the hydrolysis of the diisocyanate to yield the corresponding primary diamine. The (di)amine formed reacts very fast with the (di)isocyanate forming a urea linkages. It is known, that the microcapsules size can be controlled by the stirring rate [5]. The size distribution of PUUMC was investigated by using the optical microscope Olympus BX51. Changing the

stirring rate of mixture from 400 to 1500 rpm resulted in decreasing the mean diameter of PUUMC from 425 to 30 μm (Fig. 2a).

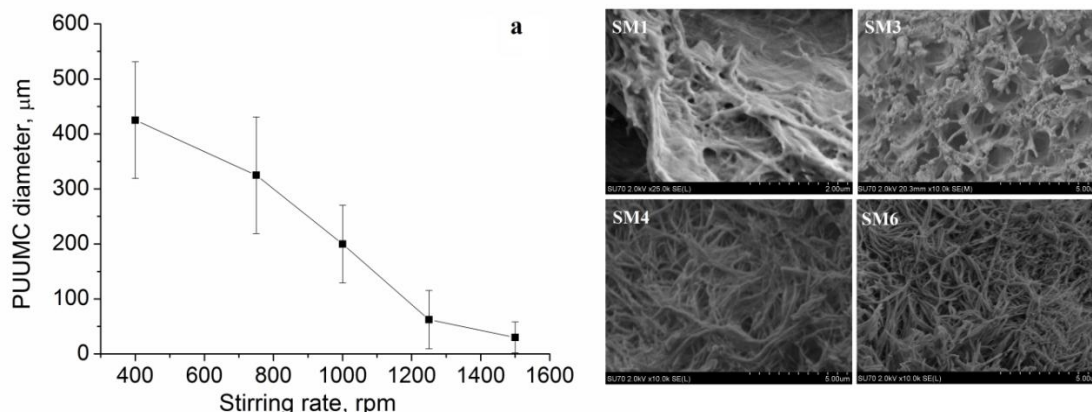


Fig. 2. PUUMC mean diameter as a function of stirring rate (a) and SEM photos of PUUMC: SM1 ([PVA]:[HMDI]=1:3, uncatalyzed reaction), SM3 ([PVA]:[HMDI]=1:9, uncatalyzed reaction), SM4 ([PVA]:[HMDI]=1:9, 0.2 % DBTDL), SM6 ([PVA]:[HMDI]=1:9, 0.6 % DBTDL)

Changing the initial molar ratio of PVA and HMDI from 1:1 to 1:9 resulted in increasing yield of dried PUUMC from 52 to 66 % (Fig. 3a) and decreasing quantity of hydroxyl groups from 10 to 5 %, because of the possibility of crosslinking between hydroxyl groups of PVA and isocyanate groups of HMDI is increased. DBTDL has specific catalyst effect on the reaction of isocyanate group with hydroxyl group and no measurable effect on the reaction of isocyanate group with amino group [6]. Increasing the concentration of catalyst DBTDL from 0 to 1% resulted in increasing yield of PUUMC (Fig. 3b) and decreasing quantity of hydroxyl groups from 5.0 to 2.4 % in the shell of PUUMC.

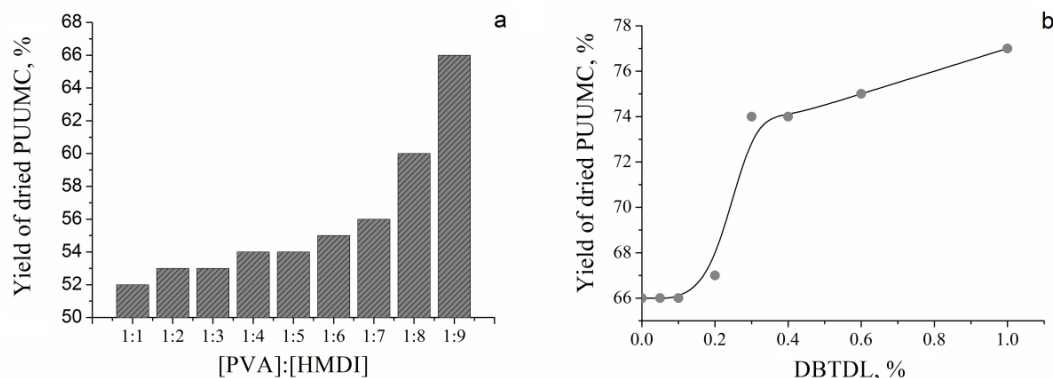


Fig. 3. Yield of dried PUUMC as a function of initial molar ratio of PVA and HMDI (a) and DBTDL concentration (b)

Surface area and porosity are important physical properties and contribute to understanding the formation, structure and potential application of microcapsules. These parameters were measured by using the instrument Tristar II, which used the Brunauer-Emmett-Teller (BET) equation to describe the surface area and Barrett-Joyner-Halenda (BJH) equation to describe the pore size and volume. The nitrogen adsorption and desorption isotherms were determined at $-196\text{ }^{\circ}\text{C}$. Profile of nitrogen adsorption/ desorption isotherms of all PUUMC samples is assigned to type IV of gas sorption isotherms, as categorized according to the IUPAC classification with the H3 hysteresis loops, which provided distribution of slit-shaped pores

width [7]. The information about the surface area, the total pore volume and the average pore size is summarized in Table 1. Changing the initial molar ratio of PVA and HMDI from 1:1 to 1:9 in the synthesis of PUUMC resulted in increasing urea segments and cross-links (units II-IV in the Fig.1) and increasing the surface area from 3.6 to 20.1 m²g⁻¹. Influence of catalyst DBTDL on the porous properties and surface area of PUUMC was more significant. The surface area was increased from 20.1 to 58.0 m²g⁻¹ and total pore volume was increased from 0.03 to 0.26 cm³g⁻¹, when catalyst DBTDL was unused and used for microcapsules synthesis, respectively. These parameters were less influenced by concentration of DBTDL.

Table 1

Porous properties and surface area of lyophilized microcapsules					
Sample code	Initial conditions of PUUMC synthesis		Surface area (m ² g ⁻¹)	Total pore volume (cm ³ g ⁻¹)	Pore size (nm)
	Molar ratio of PVA and HMDI	DBTDL (%)			
SM1	1:3	-	3.6	0.01	11.55
SM2	1:6	-	12.3	0.04	13.23
SM3	1:9	-	20.1	0.03	12.32
SM4	1:9	0.2	58.0	0.23	16.11
SM5	1:9	0.4	56.9	0.26	18.55
SM6	1:9	0.6	57.0	0.25	17.76

The morphology of PUUMC was investigated by using SEM (Fig. 2 b). The SEM photos confirmed porosity analysis results which showed that increasing the concentration of HMDI in reaction mixture resulted in increasing pore size and pore volume of shell of PUUMC. The surface area, pore size and pore volume of shell of PUUMC were bigger, when DBTDL was used for microcapsules synthesis

Conclusion

Novel microcapsules from poly(vinyl alcohol) and hexamethylene diisocyanate (HMDI), were synthesized via an interfacial polyaddition reaction in W/O emulsion system. Physical and chemical properties of PUUMC can be controlled by varying synthesis conditions including: catalyst DBTDL and surfactant Span 85 and their concentrations, the initial molar ratio of PVA and HMDI and stirring rate. The size of PUUMC could be controlled by stirring rate of emulsion. The largest surface area and slit-shaped form pore volume of PUUMC were obtained when DBTDL was used for PUUMC synthesis.

Acknowledgements

This work was funded by the European Social Fund under National Integrated Programme Biotechnology & Biopharmacy, grant VP1-3.1-SMM-08-K01-005.

References

1. G. Morral-Ruiz, P. Melgar-Lesmes, M.L. García, C. Solans, M.J. García-Celma, *Polym.*, **2012**, 53, 6072-6080.
2. E. P. Cipolattia, A. Valérioa, G. Nicolettia, E. Theilackera, P. H. H. Araújoa; C. Sayera, J. L. Ninowa, D. Oliveira, *J. Mol. Catal. B: Enzym.*, **2014**, 109, 116–121.
3. Venkata N., Jyothi N., Prasanna M., Prabha S., Seetha Ramaiah P., Srawan G., Sakarkar S. N, *J. Microencapsulation*, **2010**; 27(3), 187–197.
4. Makuska R. (Ed.) et al. *Synthesis and Characterization of Polymers (In Lithuanian)*. University Press, Vilnius, Lithuania, 2006.
5. T. Nesterova, K.D. Johansen, L.T. Pedersen, S. Kiil, *Prog. Org. Coat.*, **2012**, 75, 309–318.
6. Z. Li, J. Li, W. Yuan, B. Sun, F. Zhang, Z. Wang, *Front. Mater. Sci. China.*, **2008**, 2 (1), 99–104.
7. K. S. W. Sing, *Pure&Appl Chem.*, **1982**, 54, 2201-2218.

SYNTHESIS AND INVESTIGATION OF GOLD NANOPARTICLES-POLYPYRROLE AND GLUCOSE OXIDASE-POLYPYRROLE NANOCOMPOSITES

A. Popov¹, L. Mikoliunaite^{2,3}, A. Ramanavicius^{2,3}, A. Ramanaviciene¹

1 NanoTechnas – Center of Nanotechnology and Materials Science, Faculty of Chemistry, Vilnius University, Naugarduko 24, LT-03225 Vilnius, Lithuania

2 Laboratory of NanoBioTechnology, Institute of Semiconductor Physics, State Research Institute Centre for Physical and Technological Sciences, A. Gostauto g. 11, LT-01108 Vilnius, Lithuania

3 Department of Physical Chemistry, Faculty of Chemistry, Vilnius University, Naugarduko 24, LT-03225, Vilnius, Lithuania

E-mail: anton.popov87@gmail.com

Conducting polymers are widely used due to their unique properties: light-weight, mechanical strength, processing advantages as well as their excellent electronic properties with conductivity covering the whole range from insulator to metal [1]. Exclusive characteristics such as biocompatibility, capability to transduce energy, arising from interaction of analyte with a biorecognition layer into electrical signals that are easily monitored, and possibility to use it on the surface of almost any type of electrode allow conducting polymers to be used in biosensors. Among all the polymers polypyrrole (Ppy) is one of the most extensively used conducting polymer in design of bioanalytical sensors [2]. Biomolecules or inorganic nanoparticles of different nature and size in combination with Ppy can be used to improve physicochemical properties of the nanocomposites and widen their potential application fields [3,4].

In this work the synthesis of gold nanoparticle and polypyrrole (AuNP/Ppy), as well as glucose oxidase and polypyrrole (GOx/Ppy) nanocomposites was investigated. Synthesis of polypyrrole nanocomposites was carried out using two techniques at various concentration of monomer. Chemical synthesis of AuNP/Ppy nanocomposites was performed in-situ using a tetrachloroauric acid as a gold source for the enlargement of AuNP and as an oxidant for polymerization of Ppy in solution with AuNP. During the enzymatic synthesis of GOx/Ppy nanocomposites glucose oxidase from *Aspergillus niger* and the substrate glucose were used to obtain the initiator of the polymerization - hydrogen peroxide. During this process GOx molecules are encapsulated in Ppy layer [5]. UV-VIS spectrophotometry was used for the observation of the polymerization reaction. An interval between 400 and 700 nm was registered. The growth of the nanocomposites was evaluated using dynamic light scattering.

References

1. L. Mikoliunaite, R. Kubiliute, A. Popov, J. Voronovic, S. Sakirzanovas, A. Ramanaviciene, A. Ramanavicius, *Chemija*, **25(2)** (2014) 63-69.
2. S. Chen, W. Chen, G. Xue, *Macromolecular Bioscience*, **8(6)** (2008) 478-483.
3. R. Gangopadhyay and A. De, *Chem. Mater.*, **12** (2000) 608 – 622.
4. A. Ramanavicius, A. Ramanaviciene, A. Malinauskas, *Electrochimica Acta* **51** (2006) 6025–6037.
5. A. Ramanavicius, A. Kausaite, A. Ramanaviciene, *Sensors and Actuators B: Chemical*, **111** (2005) 532–539

STABILIZATION OF CONDUCTING POLYMERS COMPOSED FROM NATURAL MONOMERS ON ELECTRODE SURFACE

A. Radzevič, R. Celiešiūtė, T. Rakickas, Š. Vaitekoniš, R. Pauliukaitė

*Department of Nanoengineering, Center for Physical Sciences and Technology, Savanoriu Ave 231, 02300 Vilnius, Lithuania
E-mail: aneta.radzevic@gmail.com*

Folic acid (FA) or vitamin B₉, and riboflavin (Rf) or vitamin B₂ are essential for DNA synthesis as well as for FAD synthesis and enzyme activity in organisms. These natural compounds can be polymerized electrochemically and form conducting polymers [1-4].

Both vitamins were polymerized electrochemically on glassy carbon or pyrolytic graphite electrodes separately from different polymerization solutions applying cyclic voltammetry. Electropolymerization conditions such like potential window, solution pH, and number of potential cycles were optimized empirically [1,2]. The polymerization of polyfolate (PFA) and polyriboflavin (PRf) under optimized conditions are presented in Fig. 1.

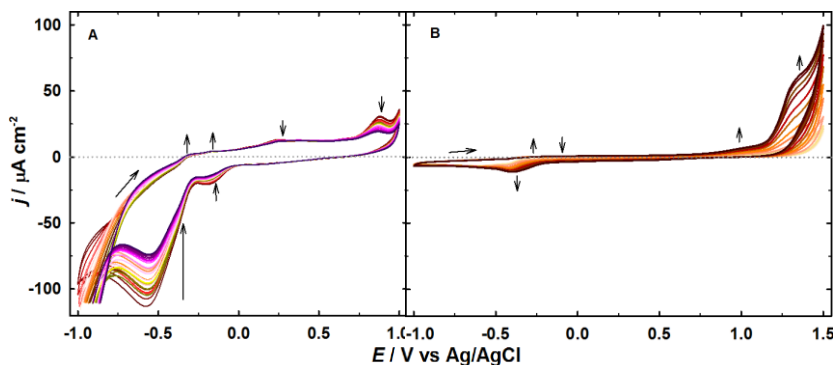


Fig. 1. Polymerization of FA [1] (A) and Rf (B) on glassy carbon electrode. Polymerization conditions were: 0.1 M KCl/HCl pH 2.0, 0.1 mM FA, 32 cycles (A); 0.1 M phosphate buffered saline solution pH 7, 1.0 mM Rf, 35 cycles (B); potential scan rate was 50 mV/s.

The morphology of these polymer films was studied using atomic force microscopy (AFM). Both PFA and PRf were formed from nanoparticles but their size was different being smaller in PFA case. Both polymers were relatively soft and sticking to an AFM probe.

Detailed electrochemical investigation showed stability differences of the polymers at the electrode surface: PFA was washed from the surface quite fast but PRf was stable enough. In order to stabilize PFA, the layer of graphene modified chitosan composite was placed on the top and this procedure increased stability of the polymer ~3 times [1]. Another approach to stabilize PFA is co-polymerization with PRf. Such conducting polymers show good electron transfer properties and can be employed as redox polymers for mediation in sensors and biosensors [2].

References

1. R. Celiešiūtė, T. Venckus, Š. Vaitekoniš, R. Pauliukaite, *Electrochim. Acta*, **138** (2014) 62-68.
2. T. Venckus, R. Celiešiūtė, A. Radzevič, T. Rakickas, Š. Vaitekoniš, Ž. Ruželė, R. Pauliukaite, *Electroanalysis*, **26** (2014) 2273-2282.
3. M. He, X. Zheng, *J. Mol. Liq.*, **173** (2012) 29-34.
4. Y.N. Ivanova, A.A. Karyakin, *Electrochem. Commun.*, **6** (2004) 120-125.

Acknowledgement

This research is funded by the European Social Fund under the Global Grant measure, Project No. VP1-3.1-ŠMM-07-K-01-124.

DIPHILIC PROPERTIES OF PROPYLENE OXIDE AND OCTENYL SUCCINIC ANHYDRIDE MODIFIED STARCHES AND THEIR COATINGS

R. Rutkaitė, M. Babelytė, P.P. Danilovas, V. Navikaitė

Kaunas University of Technology, Department of Polymer Chemistry and Technology,

Radvilenu plentas 19, LT- 50254, Kaunas, Lithuania

E-mail: ramune.rutkaite@ktu.lt

Abstract: Starch was dually chemically modified with propylene oxide and octenyl succinic anhydride for developing food contact materials and their diphilic properties were compared to those of single modified starches, and native starch. The aggregation behavior of enzymatically hydrolyzed starch derivatives was studied in aqueous solution by employing the fluorescence probe and dynamic light scattering techniques, and the water contact angle measurements were carried out on modified starches based coatings.

Introduction

Starch is a bulk energy storage substance in plants, and is widely available as a source of various products for industry. Native granular starch generally has limited solubility in water; it does not contain lipophilic groups and therefore does not form emulsions. When modified with octenyl succinic anhydride (OSA), the normally hydrophilic starch gains a hydrophobic element resulting in whole molecules with amphiphilic character. Meanwhile, hydroxypropylation of starch imparts improved shelf life, cold water swelling and reconstituting properties to a formulated product. A unique application of such specialty starches is in preparation of oil-in-water emulsions, which can be used for encapsulation of sensitive food-grade ingredients and bioactive substances.

The aim of this work was synthesis of propylene oxide and OSA modified potato starches, and study of their diphilic characteristics in water as well as surface character of their coatings.

Results and Discussion

Hydroxypropylated potato starch (PS-HP) with DS_{HP} of 0.2 was obtained by the etherification of native potato starch with propylene oxide (12% of the dry weight of starch) in the presence of alkaline catalyst [1]. OSA starches (PS-OSA) and OSA hydroxypropylated starches (PS-HP-OSA) with DS_{OSA} varying from 0.007 to 0.02 were obtained from the esterification reaction between OSA (1, 2 and 3% of the dry weight of starch) and hydroxyl groups of starch or hydroxypropylated starch, respectively [2]. The characteristics of prepared single and dually modified starch samples are given in Table 1.

Table 1. Composition of prepared starch derivatives

Sample	HP content, %	DS_{HP}	OSA content, %	DS_{OSA}	Reaction yield, %
P-native	-	-	-	-	-
P-OSA _{0.0076}	-	-	0.97	0.0076	97.2
P-OSA _{0.0123}	-	-	1.56	0.0123	78.2
P-OSA _{0.0200}	-	-	2.52	0.0200	84.2
P-HP _{0.2}	6.69	0.2	-	-	55.8
P-HP _{0.2} -OSA _{0.007}	6.69	0.2	0.91	0.007	91.0
P-HP _{0.2} -OSA _{0.015}	6.69	0.2	1.89	0.015	94.5
P-HP _{0.2} -OSA _{0.020}	6.69	0.2	2.66	0.020	88.7

The P-native and modified starch derivatives were subjected to enzymatic liquefaction to ensure that the starch derivatives thus produced are substantially free of residual starch granules. The hydrolyzates obtained from different starch derivatives were isolated from the solution and dextrose equivalent (DE) was determined. The DE values of hydrolyzed P-native, P-OSA_{0.0076}, P-OSA_{0.0123} and P-OSA_{0.0200} samples were 15.11±0.51, 13.18±0.26, 12.14±0.57 and 10.28±0.14, respectively. Meanwhile, hydrolyzed P-HP_{0.2}, P-HP_{0.2}-OSA_{0.007}, P-HP_{0.2}-OSA_{0.015} and P-HP_{0.2}-OSA_{0.0200} had DE values of 7.43±0.28, 5.97±0.15, 4.51±0.23 and 5.48±0.51, respectively.

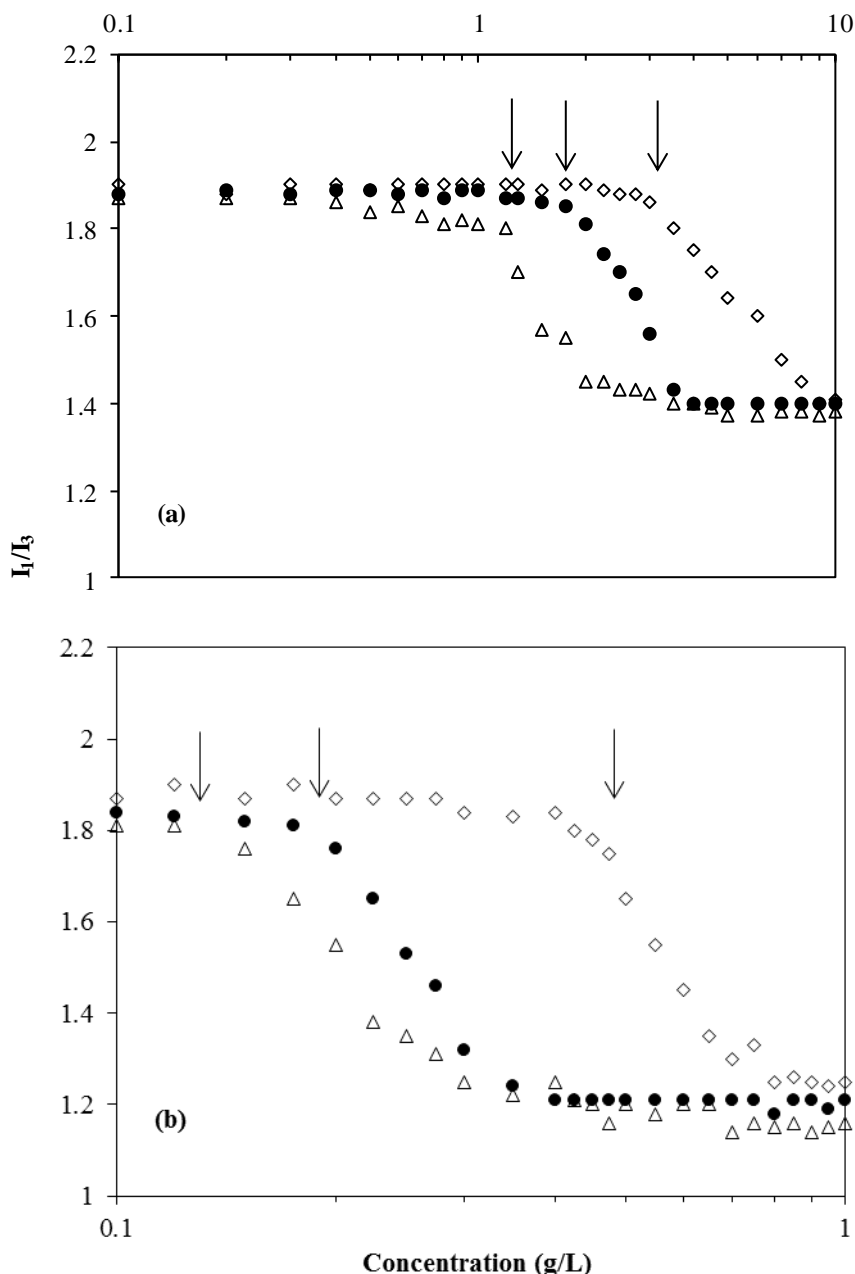


Fig. 1. I_1/I_3 ratio of the vibronic band intensities of pyrene (10^{-5} M) as a function of hydrolyzed P-OSA (a) and P-HP-OSA (b) concentration in water: P-OSA_{0.0076} and P-HP_{0.2}-OSA_{0.007} (\diamond), P-OSA_{0.0123} and P-HP_{0.2}-OSA_{0.015} (\bullet), P-OSA_{0.020} and B-HP_{0.2}-OSA_{0.020} (Δ), respectively. Estimated CACs indicated with the arrows.

Information about association behavior of enzymatically hydrolyzed modified starches in water was obtained from fluorescence measurements using pyrene as a probe. The ratio of intensities (I_1/I_3) of the pyrene fluorescence emission spectrum reports the micropolarity and

hydrophobicity of the region in which is solubilized. The I_1/I_3 intensity ratio was measured as a function of concentration hydrolyzed modified starches in water (Fig. 1).

P-native is a hydrophilic system and the ratio I_1/I_3 of the emission spectrum of remains about 1.9 (aqueous environment for pyrene) in wide concentration range. For the hydrolyzed P-OSA and P-HP-OSA samples the ratio I_1/I_3 will depend on the degree of OSA substitution and chemical structure of the sample. Both samples present the same behavior, i.e. initially the I_1/I_3 decreases slightly as the concentration is increased and an inflection point can be identified when the polymer concentration reaches a value which is dependent on the DS_{OSA} . CAC values were determined from curves of I_1/I_3 versus polymer concentration, as indicated with the arrows in Fig. 1. The CAC was defined as the intercept of the tangents to the curve before and after the point of inflection.

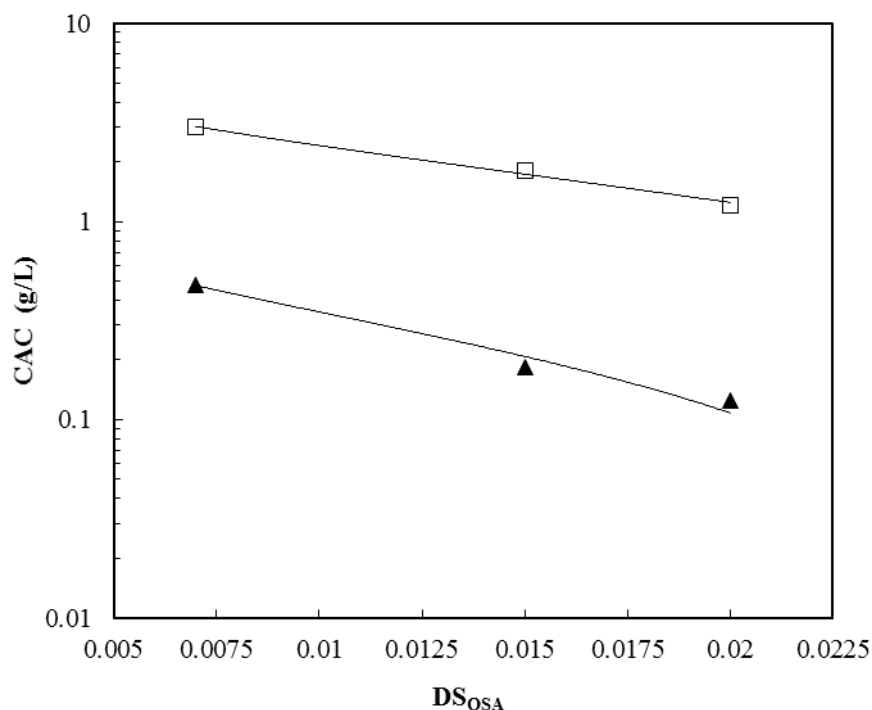


Fig. 2. CACs determined by pyrene I_1/I_3 ratios as a function of degree of OSA substitution for P-OSA (□) and P-HP-OSA (▲).

Fig. 2 shows that the CAC decreases with increasing DS_{OSA} and the same behavior was exhibited for single and dually modified starches. In general hydroxypropylation decreased the CAC by a magnitude of 10. We should not forget that the DE values achieved by the enzymatic hydrolysis of P-HP-OSA samples were 2-2.5 times lower i.e. the chain length of macromolecules remained longer. Thus the higher molecular weight led to the formation of hydrophobic microenvironments that occur at lower polymer concentrations. The solution behavior observed here by OSA and dually modified starches might be explained by postulating the existence of intermolecular interactions, since the content of hydrophobic OSA groups is not sufficient to promote intramolecular interactions. As can be seen from Fig. 2 linear relationships can be obtained for the logarithm of CAC as a function of DS_{OSA} . This type of relationship is normally found for the critical micelle concentration of nonionic surfactants. Therefore it is believed that the macromolecules tend to undergo intermolecular hydrophobic association and the observed behavior is similar to that of common surfactants. Finally it could be concluded that investigated hydrolyzates of modified starch derivatives can associate in water and form aggregates suitable for solubilization of hydrophobes. The highest solubilization capabilities possess modified starches containing highest OSA content.

The surface characteristics of modified starches (non-hydrolyzed) based coatings were assessed by performing water contact angle measurements at 65% relative humidity. Surface water contact angle is a parameter that provides a quantitative characterization of material surface energy. An increase in water contact angle indicates an enhancement of hydrophobic character of surface.

Table 2. Water contact angle of modified starches based coatings

P-native and OSA modified starches		P-HP and OSA modified hydroxypropylated starches	
Sample	Water contact angle, °	Sample	Water contact angle, °
P-native	52.36±0.55	P-HP _{0.2}	65.81±0.90
P-OSA _{0.0076}	57.23±0.72	P-HP _{0.2} -OSA _{0.007}	60.55±0.78
P-OSA _{0.0123}	60.55±1.37	P-HP _{0.2} -OSA _{0.015}	62.50±0.84
P-OSA _{0.0200}	63.25±1.03	P-HP _{0.2} -OSA _{0.020}	68.86±1.48
P-native/Premo®Star OPV FDA	79.16±1.51	P-HP _{0.2} /Premo®Star OPV FDA	-
P-OSA _{0.0076} /Premo®Star OPV FDA	79.34±0.56	P-HP _{0.2} -OSA _{0.007} /Premo®Star OPV FDA	86.90±0.27
P-OSA _{0.0123} /Premo®Star OPV FDA	82.91±0.32	P-HP _{0.2} -OSA _{0.015} /Premo®Star OPV FDA	86.75±0.16
P-OSA _{0.0200} /Premo®Star OPV FDA	78.55±0.66	P-HP _{0.2} -OSA _{0.020} /Premo®Star OPV FDA	87.27±0.17

Table 2 lists the water contact angle data of the coatings prepared from modified starches and composite coatings from modified starches (4.76 wt%), and commercial lacquer Premo®Star OPV FDA (95.24 wt%). Compared to water contact angle of P-native sample, which is 52.36°±0.55°, the modification with OSA significantly increased the water contact angle of the P-OSA coatings from 57.23°±0.72° to 63.25°±1.03°, which indicated the hydrophobic character of coatings was enhanced. Furthermore, by addition of propylene oxide moieties even higher water contact angle values in the range from 60.55°±0.78° to 68.86°±1.48° were obtained. For P-native and P-OSA composite coatings much higher water contact angle values similar to that of Premo®Star OPV FDA lacquer (82.91°±0.32°) were obtained. By addition of P-HP-OSA to the composite coatings also higher water contact angle values were recorded. The higher values of water contact angle obtained in both cases P-HP-OSAs were used, might be explained by the increase in microroughness of the coatings surface. It is well known that the surface morphology affects the water contact angle and an increase in microroughness is accompanied by hydrophobic properties [3]. Equally, it could be noted that modified starches based coatings might be characterized as moderately hydrophobic.

Acknowledgements

The authors are grateful to the Research Council of Lithuania and National Paying Agency under the Ministry of Agriculture for financial support of the project MT 1131.

References

1. H.L. Lee, B. Yoo, *LWT – Food Science and Technology*, **2011**, *44*, 765.
2. J.A. Han, J.N. BeMiller, *Carbohydrate Polymers*, **2007**, *67*, 366.
3. A. Gandini, *Macromolecules*, **2008**, *41*, 9491.



STUDY OF INFLUENCE OF OLIGOBUTADIENES' MOLECULAR PARAMETERS ON THEIR RHEOLOGICAL PROPERTIES

S. Saitarly¹, Yu. Pushkarev², V. Plavan¹

¹*Kiev National University of Technologies & Design,*

2, Nemirovich-Danchenko str., 01011 Kiev, Ukraine,

E-mail: zvetov4ek1990@mail.ru

²*Odessa National Polytechnic University*

1, Shevchenko avenue, 65044 Odessa, Ukraine

Abstract

The article deals with determination of dependencies between molecular parameters and rheological properties of new types of oligobutadienes, which is aimed at their usage as a base for sealing materials and protective coverings. It has been found out that the value of molecular mass has impact upon oligobutadienes' viscosity, though, it does not determine their deformation behavior.

Introduction

Liquid oligomers are more and more often coming into use as a base for polymer composites. In order to calculate the procedure of their preparing, the information on dependencies associating oligomers' stress and strain rate with their different molecular mass at processing temperatures is needed [1]. The works [2-4] have shown that most oligobutadienes (OB) with molecular mass of about 2000 g/mol, containing no functional groups demonstrate the properties close to Newtonian fluids. Viscosity abnormality is only peculiar to OB with molecular mass of more than 6000 g/mol which predominantly contain linear 1,4-components (84%), mostly including components of 1,4-cis structure (64%). The work is aimed at determination of dependencies between molecular parameters and rheological properties of new types of oligobutadienes, with the purpose of their usage as a base for sealing materials and protective coverings.

Object and methods of investigation

The object of the research is new types of OB predominantly containing vinyl components KRASOL-LB, containing no functional groups and KRASOL-LBH with terminated hydroxyl (Czech Republic) [5] as well as hydrogenated oligobutadienediols (HOBD) NISSO-GI (Japan) with residual content of non-saturated 1,2-components <7% [6].

The research was carried out on rotational rheometer «RHEOTEST-2» with the system of coaxial cylinders with ratio of their radii 1,02 within the range of shear rate 1,5÷656 c⁻¹.

Results and Discussion

The study of rheological properties of OB predominantly containing (≥60%) 1,2-components (LB-2000) when the values of their molecular mass are relatively equal ($\overline{M}_n = 1962$ g/mol and $\overline{M}_n = 2194$ g/mol correspondingly) has shown the viscosity growth of

bifunctional oligobutadiene LBH compared to LB with no change in the character of these oligomers' deformation behavior (fig. 1).

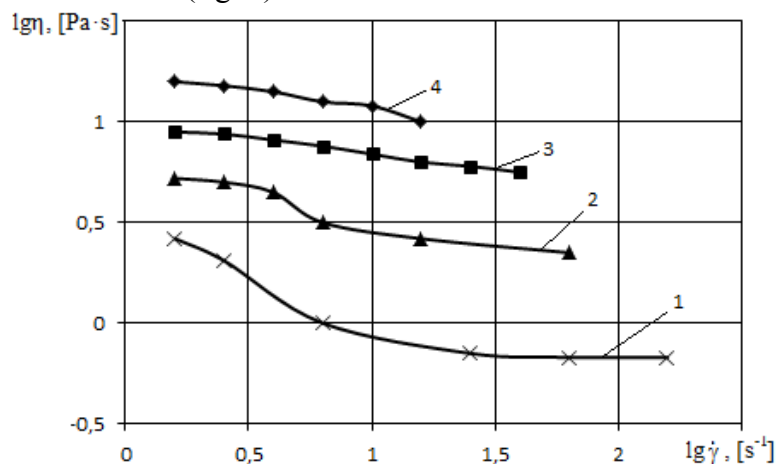


Fig.1 Rheological dependencies of OB with no functional groups (1,2) and with OH-groups (3,4) at temperatures of 20°C (2,4) and 40°C (1,3)

The microstructure of components in the OB's molecular chain has also very slight influence over its rheological properties (table1, fig.2).

Table 1

Characteristics of OB obtained by means of free-radical (a) and anionic (b) polymerization

Indicators	Sample A	Sample B
1. Molecular mass, g/mol	3500	2194
2. Hydroxyl content (including terminal)	1,8%	~1,5%
3. Hydroxyl value, mg KOH/g	-	50.22
4. Microstructure of components, % 1,4-cis	32	15
	59	25
	9	60

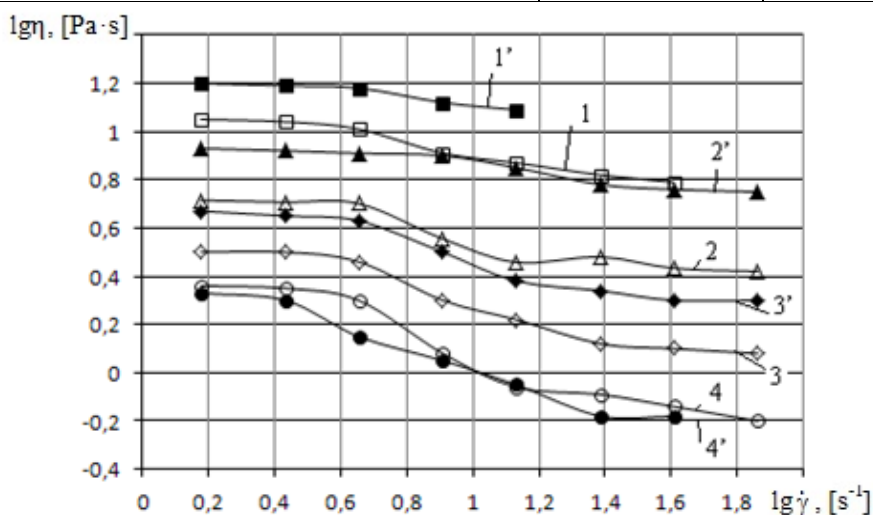


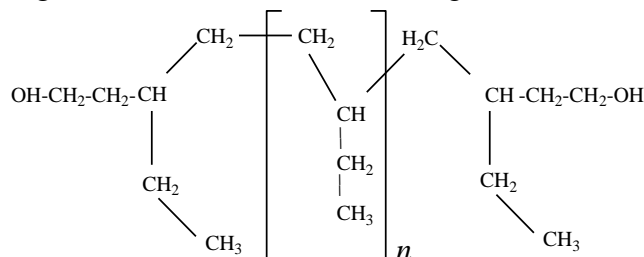
Fig.2 Viscosity dependence (η) on shear rate (γ) of oligobutadienes, sample A (1-4) and sample B (1'-4') at temperatures (°C) of 1,1'-20; 2,2'-40; 3,3'-60; 4,4'-80.

Initial viscosity of oligobutadienediols (OBD) predominantly containing vinyl components (sample A) is somewhat higher than that of linear oligobutadienediols' viscosity. With temperature rise this difference decreases and disappears at 80°C.

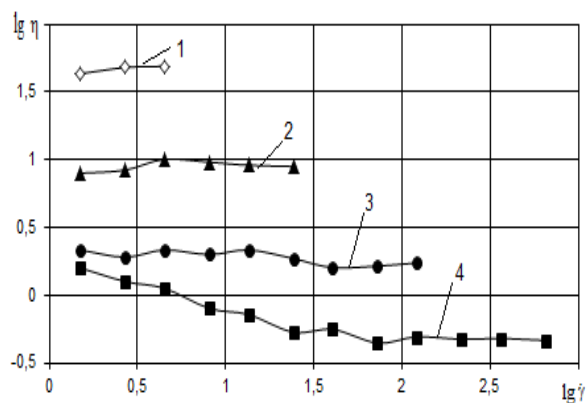
At low shear rates the oligomer's structure is characterized by the highest Newtonian viscosity and corresponds to its initial state, not changed by deforming. Restructuring in oligomer caused by shear at the initial stage is balanced out by the influence of temperature motion which reproduces the original structure.

With the increase in shear rate, especially temperature rise, the viscosity reduction is observed. Every point on structural branches corresponds to the state of dynamic balance between destruction and reconstruction processes of the structure conditioned by intermolecular forces between oligomer's macromolecules. At sufficiently high shear rates the oligomer's fluctuation networks collapse and viscosity values approach to the value of the lowest Newtonian viscosity[7].

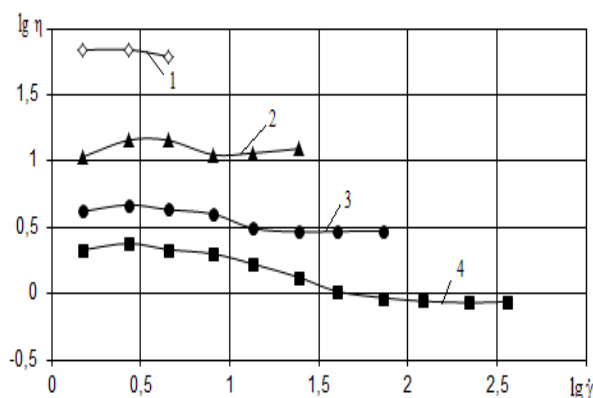
Hydrogenated 1,2-oligobutadienediols(1,2-OBD) of general formula



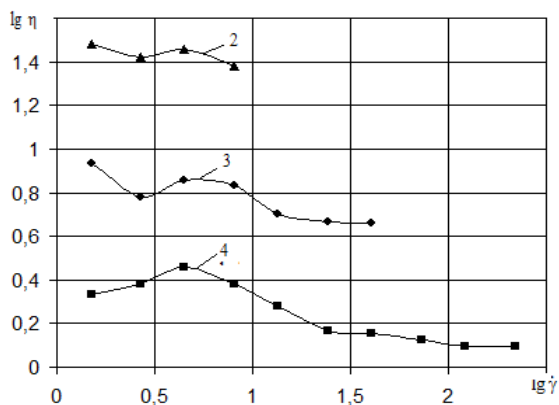
with residual content of 1,2-vinyl components <7% and molecular mass of $\overline{M}_n = 1500$ g/mol, $\overline{M}_n = 2000$ g/mol, $\overline{M}_n = 3100$ g/mol are characterized by higher viscosity values in case the values of \overline{M}_n compared to oligobutadienediols and oligobutadienes with no functional groups are relatively equal (fig. 3).



a



b



c

Fig. 3. Dependence of viscosity η on shear rate $\dot{\gamma}$

1,2-OBD:

a— $\overline{M}_n = 1500$ g/mol,

b— $\overline{M}_n = 2000$ g/mol,

c— $\overline{M}_n = 3100$ g/mol

at temperatures of 20(1);
40 (2); 60 (3); 80 (4) °C

Rheological properties of 1,2-HOB are similar to viscosity dependence on shear rate for non-hydrogenated OBD and OB with no functional groups.

The values of activation energy of the researched oligobutadienes' viscous flow (E_{act}) calculated on the basis of experimental data are represented in Table 2.

Table 2

The values of activation energy of the researched oligobutadienes' viscous flow

Oligobutadiene	\overline{M}_n	Components content	E_{act} , kJ/mol
1,4-OB	2130	1,4-cis 75% 1,4-trans 23%	14,9
1,4-OBD	3500	1,4- cis 31,7% 1,4- trans 59,2%	10,4
1,2-OB	1962 3058 5050	1,2-components >60%	17,6 17,7 19,5
1,2-OBD	2194	1,2- components >60%	12,5
1,2-HOBD	1500 2000 3100	1,2- components <7%	27,6 23,4 22,9

As can be seen from the data obtained, as molecular mass increases, the viscosity of OB grows up and the value of activation energy of viscous flow decreases.

Conclusions

1. The researched oligobutadienes are weakly structured liquids, fluctuation networks of which are destroyed under the influence of homogeneous shear and temperature.
2. Molecular mass value has impact on OB's viscosity but it does not determine their deformation behavior.
3. As molecular mass increases, the viscosity of OB grows up and the value of activation energy of viscous flow decreases.
4. OB predominantly containing vinyl 1,2-components, especially hydrogenated OBD, are characterized by higher values of activation energy of viscous flow compared to similar linear OB.

References

1. Edvard T. Severs. *Rheology of Polymers*/ Translated form English. Edited by A. Ya. Malkin. – Moscow: Chemistry, **1966**.
2. Yu. N. Pushkarev *Rheological properties of butadiene oligomers* // STAC «Chemical industry» - Cherkasy : Cherkasy State Research Institute for Technical and Economic Information in Chemical Industry, **1993**.- Issue 2 - P. 27-29.
3. Yu. N. Pushkarev *Oligobutadienes-based ebonite compositions and coverings*. – Kharkiv :BurunKniga, **2012**. – 172 p.
4. Ye.A. Bondareva, Yu.N. Pushkarev, B.V. Kunshenko *Rheological properties of oligobutadienes predominantly containing 1.2-components* // Works of Odesa Polytechnic University, **2011**. – Issue 2(36). – P.264-268.
5. *Liquid Polybutadienes KRASOL* / KapalnePolybutadieny – Kaučuka.s.-Kralypu nad Vltavou, **2002**.
6. *NISSO-PB / GI-series* – Nippon Soda Co., LTD, **2011**.
7. S. V. Saitarly, Yu. N. Pushkarev, B. V. Kunshenko *Rheological properties of hydrogenated 1.2-oligobutadienes with hydroxyl groups* // Works of Odesa Polytechnic University, **2011**. –Issue 2(36). – P. 270-273.

THE INFLUENCE OF MICROPOROUS PU FILM ON THE ANTIMICROBIAL PROPERTIES OF SILVER NANOPARTICLES TREATED TEXTILE

**A. Sankauskaitė¹, P. Bekampienė¹, I. Prosyčevas², V. Urbelis², S. Varnaitė-Žuravliova¹,
D. M. Tumėnienė¹, S. Stygienė¹**

*1 State research institute Center for Physical Sciences and Technology, Savanorių ave. 231,
LT-02300, Vilnius, Lithuania*

*2 Kaunas University of Technology, K. Donelaičio st. 73, LT-44249, Kaunas, Lithuania
E-mail: sankauskaite@lti.lt*

Abstract

This research aims to increase the absorption of silver nanoparticles on surface of textile material and thereby improve antimicrobial activity and its durability to laundering. For this purpose the surface pre-activation with low-pressure plasma as well as microporous polyurethane (PU) coating was applied. The scanning electron microscopy (SEM) and Fourier transform infrared spectroscopy (FTIR) were used to determine morphological and chemical changes after surface pre-activation. The silver nanoparticles treated samples were tested for their antimicrobial activity using the agar diffusion test. The results showed the improved resistance of microporous film coated textile materials with incorporated Ag nanoparticles to microorganisms *E.coli*, *K. pneumoniae* and *S. aureus* colonies growing after repeated washing cycles.

Introduction

Antimicrobial textile is one of the rapidly growing areas of functional textiles for medical and protective purposes. Antimicrobial properties of textile materials may be provided by either treatment with an organic (biguanide, isothiazolinone, ammonium organosilicon derivatives, etc.), inorganic (Cu, Ag, Zn metal ions, zeolites, ceramic substrate with metallic ions, etc.) and natural origin (chitosan, molluscs, polysaccharides, seaweed and plant extracts) products [1, 2]. The application of nano-scale size silver (Ag) particles in antimicrobial finishing is favourable due to their stability and high surface area to volume ratio [3-6]. However, the most important challenge is to develop low-cost fabric loaded with Ag nanoparticles which can be laundered and still retain their antimicrobial barrier properties. Therefore the aim of this research was to increase the absorption of silver nanoparticles on surface of textile material and thereby improve antimicrobial activity and its durability to laundering. For this purpose the surface pre activation with low-pressure plasma as well as microporous polyurethane (PU) coating was applied. Fibre surface pre-activation by plasma treatment in comparison with water based chemical treatments is environmentally friendly and efficient technique which offers great potential for significant improvements in fibre surface properties, based on changes in physical and chemical properties. Whereas, the microporous coating creates an open cell barrier which can accumulate higher amount of finishing agents and thereby improve barrier properties of textile material to pathogenic action of microorganisms.

Experimental

The flame retardant antistatic fabric *Nomex III Antistatic* (composition – 93% meta-aramid *Nomex*, 5% para-aramid *Kevlar*, 2% carbon fiber *P140*; mass per unit area – 286 g/m²) intended for applications in protective clothing was used for further antimicrobial functionalization with silver (Ag) nanoparticles (NPs). The aqueous solution of Ag nanoparticles was prepared according to a chemical reduction method described elsewhere [7]. The size of the nanoparticles was determined by dynamic light scattering using *Zetasizer Nano ZS* instrument (Malvern Instruments, UK). The average size of Ag NPs was 47.4±3.0 nm.

The surface pre-activation was performed using low-pressure oxygen (O₂) gas plasma at following treatment conditions: base pressure – 0.4 mbar, gas flow – 10 cm³min⁻¹, power –

100 W and treatment time – 120 s. The low-pressure plasma was created by radiofrequency electric field of 13.56 MHz generated in *Junior Plasma System SN 004/123* equipment (Europlasma, Belgium).

The microporous polyurethane (PU) coating was produced according to the crushed foam method. 100 g of a polyurethane compound *Tubicoat MP* and 5 g (5%) of a melamine resin cross-linking agent *Tubicoat HT* (from CHT-Bezema, Germany) were mixed and foamed in undiluted conditions by means of a *Heidolph RZR-50* laboratory mixer until a weight of foam 210 g/l was achieved. The foam was applied on the outer layer of textile using a knife coater, dried at 100 °C in the laboratory oven *TFO/SIM 350 9* and crushed at 4.7 bar in the laboratory padder *EVP-350*. After this, the coated samples were impregnated with Ag nanoparticles solution (180 mg/l) on the padder, dried and curried at 170° C in the oven and cold-calendered at 20 bar on a *Universal Calender 350*.

The changes in fabric morphology and chemical structure were investigated by means of differential scanning calorimetry (DSC), Fourier transform infrared spectroscopy (FTIR) and scanning electron microscopy (SEM) analysis. The thermal analysis of the fibre samples were carried out using a *Q100 TA DSC* series thermal analyzer. The fibres between 3.5-4.5 mg were taken for analysis and heated up at 10°C·min⁻¹ rate from 10 to 375°C. FTIR analysis at the attenuated total reflectance (ATR) mode was carried out using a *Nicolet 5070* spectrometer. The spectra were recorded at the wave numbers from 4000 to 400 cm⁻¹ with the 4 cm⁻¹ resolution. The scanning electron microscope model *Hitachi S-3400N* was used to investigate the surface morphology. The surface wettability of the samples was measured with a drop of distilled water on the surface. Antibacterial activity was determined using the Agar diffusion plate test according to the requirements of standard ISO 20645:2004.

Results

Textile material pre-activation with low-pressure plasma revealed that the different surface changes were obtained. Despite the inherent hydrophilicity of this material after the plasma treatment the surface wetting was improved; the wetting angle was reduced from 30° to 0. This can be explained by the removal of finishing agents (such as sizing, softening and etc.) and increase of surface roughness. The surface micrographs are presented in Figure 1.

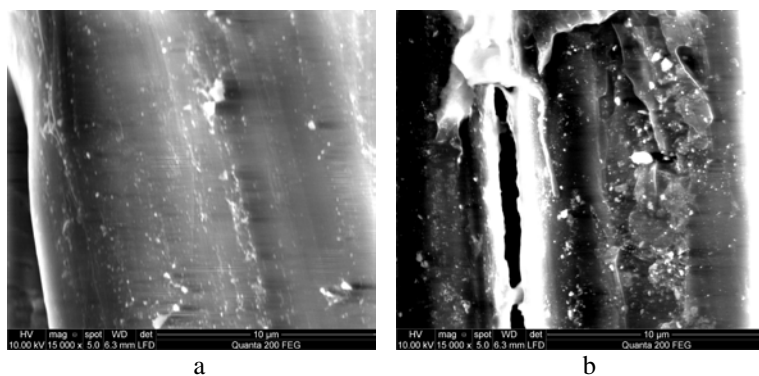


Figure 1. SEM images of (a) untreated and (b) plasma treated samples

It can be seen that after plasma treatment textile surface appears to be grainy. The remains of finishing agents can be distinguished as well as the increase of surface roughness due to slight etching. Such changes increase material surface area and improve physisorption ability. It is also important to note that plasma treatment affects only the fibre surface without changing the bulk properties of the material. The FTIR spectra alterations indicated the attachment of functional groups as well as presence of newly formed bonds. The newly formed peaks revealed COOH, –CH₃, –CH₂ functional groups grafted on the surface of fibres as well as

newly formed C–O, C=O, C–H, O–H chemical bonds. The increase of spectra intensity in the range 2400–2300 cm^{-1} after plasma treatment can be mainly related to stretches of amines. While, the changes in the range 600-500 cm^{-1} can be related with stretching vibrations of hydrogen containing C–H and O–H functional groups. These results confirm that after successful pre-activation the sample can be further subjected for functionalization.

The results of antimicrobial activity are shown in Table 1. It can be seen that after plasma pre-activation the proper antibacterial properties of Ag NPs treated textiles were obtained. However, after laundering, samples showed poor antibacterial activity. These results can be supported by SEM observations presented in figure 2.

Table 1. Antibacterial activity of Ag NPs treated samples

Treatment	Bacteria		
	<i>E. coli</i>	<i>K.pneumoniae</i>	<i>S. aureus</i>
Untreated	good	poor	poor
O ₂ plasma	good	good	good
O ₂ plasma; laundering	poor	poor	poor
O ₂ plasma; PU coating; laundering	good	good	good

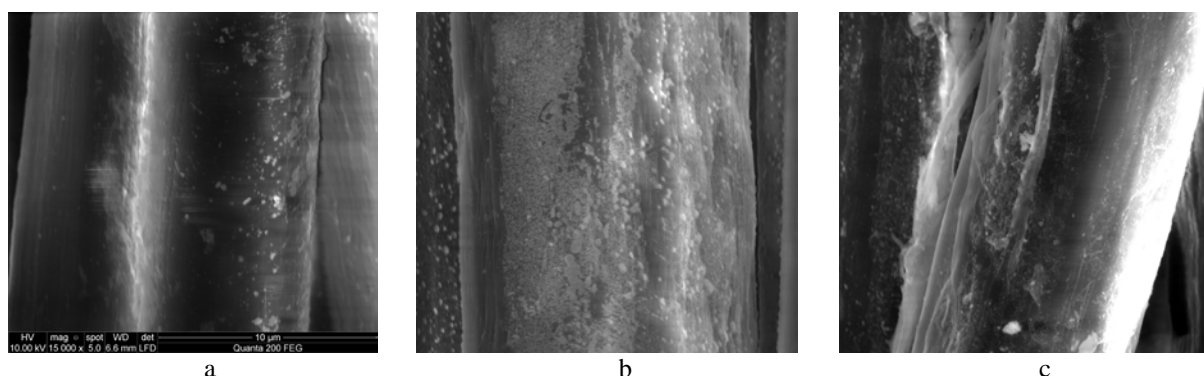


Figure 1. SEM images of Ag NPs treated samples (a) without and (b) with plasma pre-activation and (c) plasma pre-activated sample after laundering procedure

In order to obtain permanent antimicrobial properties the fabric was coated with microporous coating which possesses higher surface area in comparison with textile. The results have shown that sample adsorbs higher quantities of Ag NPs on textile surface. The results showed the improved resistance of microporous film coated textile materials with incorporated Ag nanoparticles to microorganisms *E.coli*, *K. pneumoniae* and *S. aureus* colonies growing after repeated washing cycles.

Acknowledgments. The work was carried out in the frame of the Eureka project E! 5799 BATAN Barrier Textiles and Nanomaterials.

References

1. Y. Gao, R. Cranston. *Text Res J*, **2008**; 78, 60, pp. 60–72
2. M. Joshi, A.S. Wazed, R. Purwar, S. Rajendran. *Indian J Fibre Text*, **2009**, 34, pp. 295–304.
3. M. Radetic, V. Ilic, V. Vodnik, S. Dimitrijevic, P. Jovančić, Z. Šaponjic, J.M. Nedeljkovic. *Polym Adv Technol*, **2008**, 19, p.1816–1821.
4. H.J. Lee, S.Y. Yeo, S.H. Jeong. *J Mater Sci*, **2003**, 38, 10, pp. 2199–2204.
5. Y. Gao, R. Cranston. *Text Res J*, **2008**, 78, pp. 60–72.
6. C.H. Xuea, J. Chen, W. Yin, S.T. Jia, J.Z. Ma. *Appl Surf Sci*, **2012**, 258, pp. 2468–2472.
7. A. Šileikaitė, J. Puišo, I. Prosyčevass, S. Tamulevičius. *Materials Science*, **2009**, 15, 1, pp. 21–27.

ENVIRONMENTALLY FRIENDLY CHEMICAL SYNTHESIS OF POLYPYRROLE PARTICLES

R. Simanaityte¹, D. Gabrielaitis¹, A. Kausaite-Minkstimiene¹

*1 Department of Analytical and Environmental Chemistry, Faculty of Chemistry, Vilnius University, Naugarduko st. 24, LT-03225 Vilnius, Lithuania
E-mail: rezerfordis@gmail.com*

Conjugated or electrically conducting polymers (CPs) are an exciting new class of organic polymers with conjugated double bonds combining properties of metals and polymers. The modern development of these polymers began in 1977 as A. J. Heeger, A. G. MacDiarmid and H. Shirakawa developed special polymers with metal-like properties [1,2]. These unconventional properties of an organic material encourage worldwide interest and numerous other CPs with properties similar to those of polyacetylene were synthesized, such as polyaniline, polypyrrole (PPy) and thiophene. Nowadays, CPs have numerous practical applications such as battery electrodes [3], sensors [4] and biosensors [5], various biomedical devices [6], e-Textiles [7], artificial muscles [8] and enzyme immobilization matrices [9]. Among the conjugated polymers, PPy is one of the most extensively studied because of its high electrical conductivity [10] and biocompatibility [11], good environmental and thermal stability [12], interesting technological applications and facile synthesis.

In this study, we synthesized PPy particles dispersed in aqueous solution using chemical oxidative polymerization technique and H_2O_2 as an oxidant. The progress of the polymerization reaction was monitored by UV-vis molecular absorption spectroscopy. The aim of the current study was to investigate in detail the influence of H_2O_2 and pyrrole concentration, temperature and pH of media on the PPy formation rate. The morphology and spectral properties of formed PPy particles were analyzed.

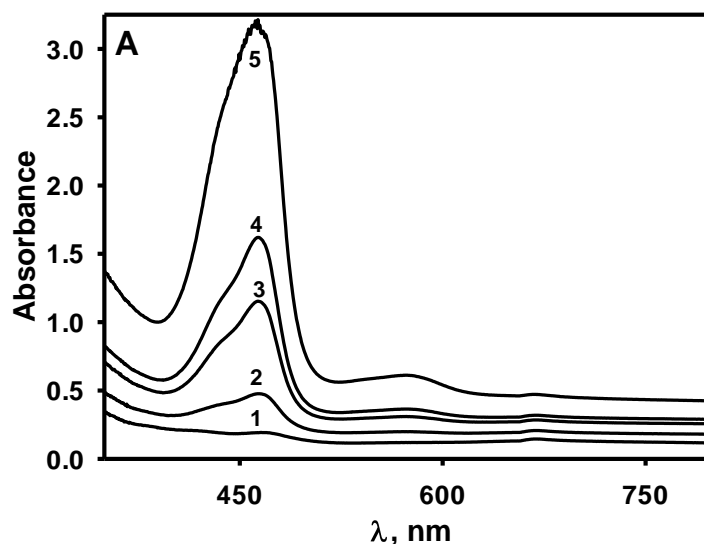


Fig. 1. Absorption spectra of pyrrole oligomers in A-PBS pH 3.0 containing 200 mM pyrrole and 300 mM H_2O_2 (1 – 23, 2 – 96, 3 – 173, 4 – 217, 5 – 408 h from the start of the polymerization).

In order to evaluate the effect of pH on the PPy formation rate the absorption spectra of buffer solutions composed of 0.05 M CH_3COONa , 0.05 M Na_2HPO_4 and 0.05 M KH_2PO_4 (A-PBS) and containing 300 mM H_2O_2 and 200 mM pyrrole at pH ranging from 1.0 to 7.0 were recorded. The absorption of samples was registered during 408 h after the start of polymerization. The main evidence of polymerization process was the origin and increase of

absorption peak at 460 nm (Fig. 1) indicating the presence of PPy oligomers [13]. The absorption peak at 460 nm is assigned to electronic transitions associated with the presence of polarons and/or bipolarons in the material. Indistinctly expressed absorption peaks at 570 and 669 nm are related to $n \rightarrow \pi^*$ transition and polaron, respectively [14]. Results presented in Fig. 2 show relationship between absorbance of pyrrole oligomers and the pH value of polymerization solution. It clearly seen that the best medium for PPy formation was strongly acidic medium and the highest absorbance value and the highest PPy formation rate was observed at pH 1.0. An increase in the pH value resulted in a decrease of the PPy formation rate, and polymer formation was almost undetectable when pH of polymerization solution exceeded pH 7.0.

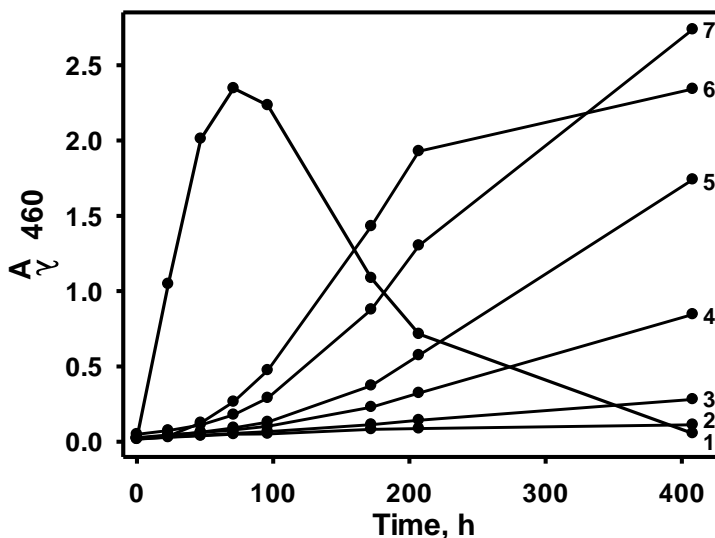


Fig. 2. Absorbance at $\lambda = 460$ nm vs duration of polymerization (1 – pH 1.0, 2 – pH 7.0, 3 – pH 6.0, 4 – pH 5.0, 5 – pH 4.0, 6 – pH 2.0, 7 – pH 3.0). Conditions: A-PBS, 200 mM pyrrole, 300 mM H_2O_2 .

It was observed that pyrrole undergoes polymerization in the absence of an oxidant. Autopolymerization of pyrrole was much faster in the acidic solutions and almost undetectable when pH of this mixture exceeded pH 6.0. But autopolymerization of pyrrole was significantly slower if compared with oxidative pyrrole polymerization.

The effect of oxidant concentration on the PPy formation rate was also investigated. For this purpose polymerization solutions containing 200 mM of pyrrole and different concentrations of H_2O_2 (50, 150 and 300 mM) were examined. The highest rate of polymer formation was observed at 300 mM concentration of H_2O_2 . At this concentration the oxidant-to-monomer molar ratio value was 1.5. Similar effect using ammonium peroxydisulfate as an oxidant has been reported by Blinova et al [15].

In order to determine the effect of monomer concentration on the rate of polymer formation the concentration of H_2O_2 was kept constant at 300 mM. The PPy synthesis was performed at monomer concentrations of 50, 100 and 200 mM. The highest rate of polymer formation was observed at highest concentration of pyrrole.

The effect of polymerization temperature on the rate of PPy formation was investigated. For this reason, the PPy synthesis was performed at constant temperature of 18, 40 or 60°C. The concentrations of pyrrole and H_2O_2 were 200 and 300 mM, respectively. It was detected that the PPy formation rate increases with increasing polymerization temperature. At higher temperatures polymerization occurs faster and resulting in a greater percentage of insoluble polymer precipitate in solution. The similar effect has been reported by Kaynak et al [16].

The morphology of PPy particles was characterized by scanning electron microscopy (SEM). SEM image presented in Fig. 3 revealed that the morphology of formed layer of PPy

particles was identical to that, which is commonly observed for PPy obtained by the chemical oxidative polymerization. As can be seen, the PPy particles were of about 50–100 nm in diameter and tends to aggregate into a larger structures of 600–1000 nm in diameter with irregular granular morphology. This morphology is commonly produced by the formation of solid-state nuclei, followed by the adsorption of precipitated oligomers. Similar morphology of PPy particles synthesized by chemical oxidative polymerization technique has been reported by other authors [17].

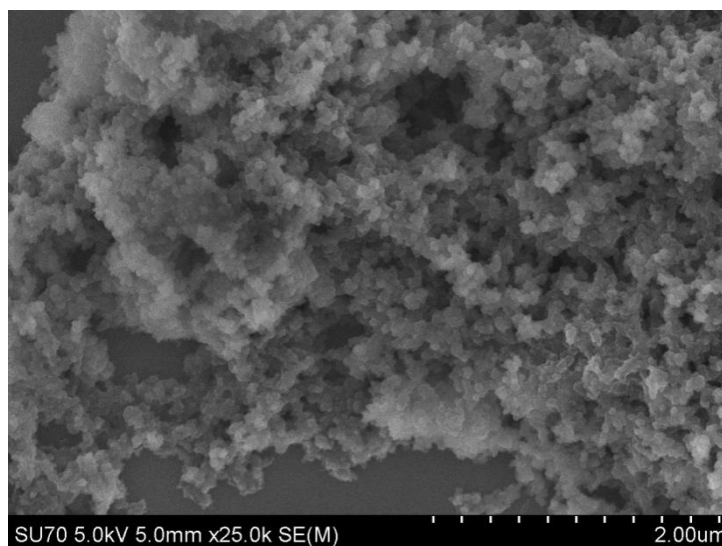


Fig. 3. SEM image of PPy particles synthesised in A-PBS, pH 2.0, containing 50 mM H₂O₂ and 200 mM pyrrole at 18°C temperature within 24 h.

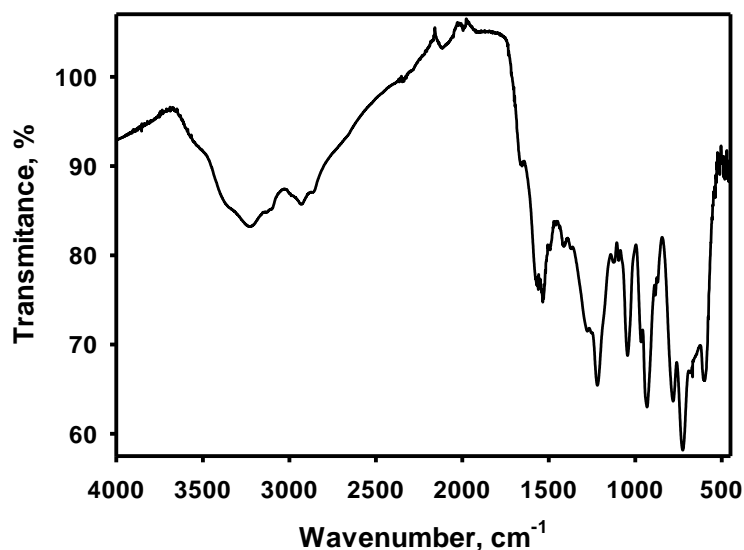


Fig 4. FTIR spectrum of PPy particles synthesised in A-PBS, pH 2.0, containing 50 mM H₂O₂ and 200 mM pyrrole at 18°C temperature within 24 h.

At this study, the Fourier-transform infrared spectroscopy (FTIR) analysis has been performed in order to identify specific absorption peaks of our synthesized PPy. FTIR spectrum presented in Fig. 4 shows very similar peaks to those described in other studies. A broad infrared absorption band in the range of 2000–3700 cm⁻¹, with maximums at about 3234 and 2928 cm⁻¹ wave number can be assigned to the conducting form of PPy [18]. The peak at 1534 cm⁻¹ can be assigned to C=C stretching vibration [19]. An indefinite peak at

1281 cm^{-1} indicates the C–H or C–N in-plane deformation [20]. A peak at 1219 cm^{-1} can be attributed to the breathing vibration of the pyrrole ring [20] or C–N stretching vibration [21]. A sharp peak at 1044 cm^{-1} corresponds to C–H and N–H in-plane deformation [22]. A sharp peak at 933 cm^{-1} can be assigned to C–H out-of-plane deformation [20] or C=C in-plane bending of pyrrole ring [19], whereas the peaks at 781, 733 and 601 cm^{-1} are induced by C–H out-of-plane ring deformation [23]. The results indicate that the molecular structure of the PPy particles is identical to that of the PPy synthesized by other researchers using conventional methods.

PPy-based nano- and micro-particles have attracted much attention because of its broad range of applications. The facile preparation of PPy particles in aqueous media and its surface modification by various functional groups makes these particles particularly suitable for the covalent attachment of proteins and other biologically active materials. Modified PPy particles can be used for biosensor design [24]. It should also be added that in this research investigated synthesis of PPy particles could be recognized as ‘environmentally friendly’ because single hazardous material H_2O_2 , which was used, isn’t stable and its excess is rapidly converted into water and oxygen. Because of this and good biocompatibility these particles are attractive for biomedical applications in-vivo as drug carriers. In such carriers the drug can be embedded into the particle or covalently bound to its surface what allows to achieve targeted and precisely controlled drug delivery [25].

References

1. H. Shirakawa, E.J. Louis, A.G. MacDiarmid, C.K. Chiang, A.J. Heeger, *J. Chem. Soc. Chem. Commun.*, **474** (1977) 578–580.
2. C.K. Chiang, Y.W. Park, A.J. Heeger, H. Shirakawa, E.J. Louis, A.G. MacDiarmid, *Phys. Rev. Lett.*, **39** (1977) 1098–1101.
3. J.H. Kim, A.K. Sharma, Y.S. Lee, *Mater Lett.*, **60** (2006) 1697–1701.
4. S. Radhakrishnan, S. Paul, *Sens. Actuat. B*, **125** (2007) 60–65.
5. A. Kausaite-Minkstimiene, V. Mazeiko, A. Ramanaviciene, A. Ramanavicius, *Sens. Actuat. B*, **158** (2011) 278–285.
6. D.D. Ateh, H.A. Navsaria, P. Vadgama, *J. R. Soc. Interface*, **3** (2006) 741–752.
7. E. Hakansson, A. Kaynak, T. Lin, S. Nahavandi, T. Jones, E. Hu, *Synth. Met.*, **144** (2004) 21–28.
8. Sh.-Ch. Luo, *Polym. Rev.*, **53** (2013) 303–310.
9. A. Sassolas, L.J. Blum, B.D. Leca-Bouvier, *Biotechnol. Adv.*, **30** (2012) 489–511.
10. S. Machida, S. Miyata, A. Techagumpuch, *Synth. Met.*, **31** (1989) 311–318.
11. A. Vaitkuviene, V. Kaseta, J. Voronovic, G. Ramanauskaite, G. Biziuleviciene, A. Ramanaviciene, A. Ramanavicius, *Haz. Mat.*, **167** (2013) 250–251.
12. R. Ansari, *E-J. Chem.*, **3** (2006) 186–201.
13. W. Zheng, J.M. Razal, G.M. Spinks, V.T. Truong, P.G. Whitten, G.G. Wallace, *Langmuir*, **28** (2012) 10891–10897.
14. X.G. Li, L.X. Wang, M.R. Huang, Y.Q. Lu, M.F. Zhu, A. Menner, *J. Springer, Polymer*, **42** (2001) 6095–6103.
15. N.V. Blinova, J. Stejskal, M. Trchova, J. Prokes, M. Omastova, *Eur. Polym. J.*, **43** (2007) 2331–2341.
16. A. Kaynak, R. Beltran, *Polym. Int.*, **52** (2003) 1021–1026.
17. J. Mansouri, R.P. Burford, *J. Membrane Sci.*, **87** (1994) 23–34.
18. H.V.R. Dias, M. Fianchini, R.M.G. Rajapakse, *Polymer*, **47** (2006) 7349–7354.
19. D.P. Dubal, S.V. Patil, A.D. Jagdale, C.D. Lokhande, *J. Alloy. Compd.*, **509** (2011) 8183–8188.
20. R. Cruz-Silva, E. Amaro, A. Escamilla, M.E. Nicho, S. Sepulveda-Guzman, L. Arizmendi, J. Romero-Garcia, F.F. Castillon-Barraza, M.H. Farias, *J. Colloid Interf. Sci.*, **328** (2008) 263–269.
21. C. He, C. Yang, Y. Li, *Synthetic Met.*, **139** (2003) 539–545.
22. S. Geetha, D.C. Trivedi, *Mater. Chem. Phys.*, **88** (2004) 388–397.
23. S. Faghihnasiri, M.S. Baei, M. Ardjmand, *Middle East J. Sci. Res.*, **15** (2013) 1345–1352.
24. A. Ramanavicius, Y. Oztekin, Z. Balevicius, A. Kausaite-Minkstimiene, V. Krikstolaityte, I. Baleviciute, V. Ratautaite, A. Ramanaviciene, *Proc. Eng.*, **47** (2012) 825–828.
25. C. Chauvierre, C. Vauthier, D. Labarre, P. Couvreur, M.C. Marden, L. Leclerc, *Cell Mol. Biol.*, **50** (2004) 233–239.



Adsorption of methyl orange on cationic cross-linked starches with tertiary amino groups

Deimante Simanaviciute, Ramūnas Vinciūnas, Rima Klimaviciute

Kaunas University of Technology, Radvilenu pl. 19, LT-50254, Kaunas, Lithuania

E-mail: deimante.simanaviciute@ktu.edu

Abstract. The equilibrium adsorption of methyl orange (MO) on cross-linked cationic starch derivatives containing different amount of tertiary amino groups, expressed as nitrogen content (1.4 % (CSTE-1.4) and 2.9 % (CSTE-2.9), respectively), was investigated at temperatures of 22 °C, 30 °C, 60 °C. The Langmuir, Freundlich and Dubinin–Radushkevich adsorption models were applied to describe the adsorption isotherms of MO. The thermodynamic parameters of the adsorption were calculated.

Introduction

Starch derivatives with quaternary ammonium groups, including cross-linked derivatives, can adsorb various anions from aqueous media: acid [1] and disperse [2] dyes, hexavalent chromium [3] or anionic iodine derivatives [4]. In all cases, the adsorption occurred due to electrostatic interaction between the positively charged groups of the adsorbent and anions of the adsorbates.

In alkaline conditions starch could interact with 2-chloroethyl-diethylamine hydrochloride (DEAE) and form the derivatives containing the tertiary amino groups. Such starch derivatives could be used for immobilization of phenolic acids as antioxidants to improve their stability. For the best understanding of interactions between weak carboxylic acids and weak cations of modified starch, first of all, interaction with compounds having strong sulfo groups should be investigated.

The aim of present work was to investigate the equilibrium adsorption of methyl orange as model compound with strong sulfo group on the cross-linked starches with tertiary amino groups.

Materials and methods

Cross-linked starches with tertiary amino groups (CSTE) were obtained by two step reaction. In first stage potato starch was cross-linked with 0.05 mol/GPU (glucopyranose unit) of epichlorhidrin and when cationized with 2-chloroethyl-diethylamine hydrochloride (DEAE) at temperature of 20 °C. Composition of cationization reaction mixture (in moles) was GPU:DEAE:NaOH:H₂O = 1:(0.47 or 0.94):3.24:72.

For equilibrium adsorption 0.1 g of dry CSTE was placed into Erlenmeyer flask and 100 ml of methyl orange (MO) solution with different concentration was added. The flask was stoppered, placed into a water bath with temperature control ± 1 °C and shaken for 60 min at temperatures of 22, 30 or 60 °C. After adsorption the mixture was filtered through a filter paper and residual concentration of MO in filtrate was estimated by measuring the light absorption at 435 nm.

Result and discussion

The adsorption isotherms of MO on two CSTE samples with different amount of introduced nitrogen (1.4 % (CSTE-1.4) and 2.9 % (CSTE-2.9) are shown in Fig. 1.

The Langmuir, Freundlich and Dubinin–Radushkevich adsorption models were used to describe obtained adsorption isotherms. The calculated values of the main parameters of

adsorption models are given in Table 1 along with the values of the linear correlation coefficient (R^2). The Langmuir adsorption model describes the adsorption of MO on both CSTE with the great approximation ($R^2 > 0.99$), except the adsorption of MO on CSTE-1.4 at temperature of 22 °C, and confirmed that MO is adsorbed onto CSTE due to the electrostatic interactions. The Freundlich and Dubinin-Radushkevich models fitted to the experimental data with lower values of R^2 . With the increase of adsorption temperature the values of the Langmuir sorption capacity Q_L and equilibrium constant K_L , Freundlich constant n_F and Dubinin-Radushkevich adsorption energy E_{DR} increased for both adsorbents. The calculated values of E_{DR} confirmed that MO was adsorbed by ion exchange mechanism and values of the Freundlich constant n_F showed that conditions for MO adsorption onto both CSTE are favourable.

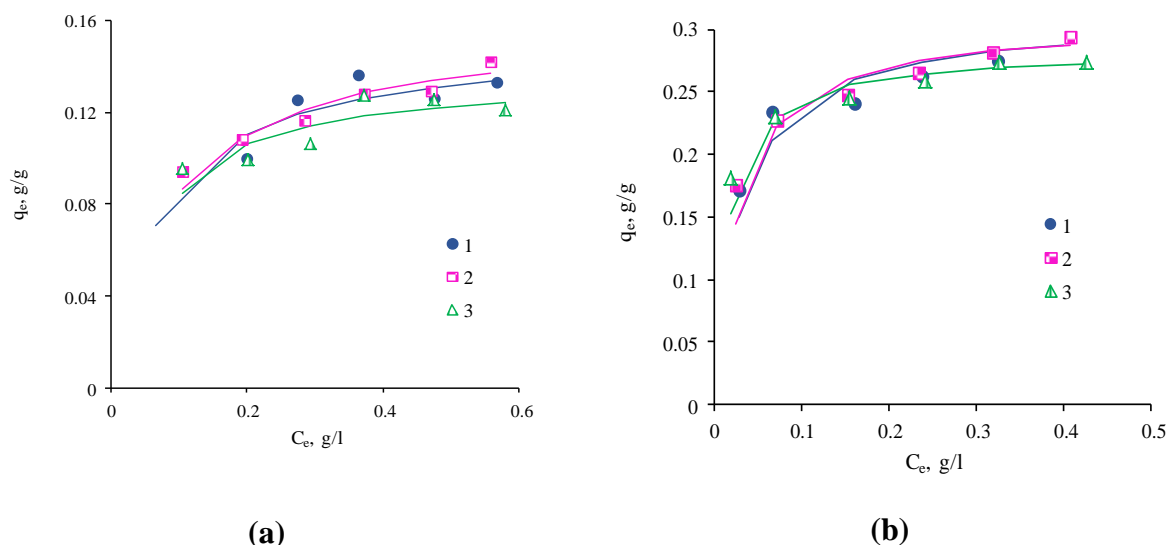


Fig.1. Adsorption isotherms of MO on CSTE-1.4 (a) and CSTE-2.9 (b) at temperature: 1 – 22 °C; 2 – 30 °C; 3 – 60 °C. Symbols represent experimental data and lines represent fitted curves of the Langmuir model.

It should be noted that CSTE-2.9 having twice a higher amount of introduced nitrogen (higher amount of tertiary amino groups) adsorbed twice a higher amount of MO in comparison to MO adsorption on CSTE-1.4 (Table 1).

Table 1. Influence of temperature on parameters of adsorption models for adsorption of MO on CSTE-1.4 and CSTE-2.9

Adsorption temperature, °C	Langmuir model			Freundlich model		Dubinin–Radushkevich model	
	Q_L , g/g	K_L , l/g	R^2	n_F	R^2	E_{DR} , kJ/mol	R^2
CSTE-1.4							
22	0.152	13.0	0.9690	3.63	0.9691	12.3	0.9683
30	0.159	11.4	0.9907	4.24	0.9810	13.9	0.9773
60	0.131	18.6	0.9956	7.18	0.9330	20.0	0.9130
CSTE-2.9							
22	0.310	32.2	0.9912	4.84	0.9944	15.4	0.9895
30	0.306	37.4	0.9968	5.75	0.9858	17.2	0.9911
60	0.283	59.1	0.9987	7.41	0.9728	21.5	0.9841

Data presented in Fig. 1 were used to calculate the thermodynamic parameters of MO adsorption on CSTE-1.4 and CSTE-2.9. The obtained values of changes of the Gibbs free energy (ΔG^0), enthalpy (ΔH^0) and entropy (ΔS^0) are presented in Table 2. The low negative

values of ΔG° evidenced the low affinity of MO to both investigated CSTE. However, the values ΔG° calculated from data of MO adsorption on CSTE-2.9 were higher in comparison to ΔG° values calculated for MO adsorption on CSTE-1.4.

The positive values of changes of enthalpy and entropy suggested that adsorption of MO on both CSTEs was the endothermic process and the order of the system decreased during adsorption.

Table 2. Influence of temperature on thermodynamic parameters for adsorption of MO on CSTE-1.4 and CSTE-2.9

Adsorption temperature, °C	$\ln K_C$	K_C	R^2	ΔG° , kJ/mol	ΔH° , kJ/mol	ΔS° , J/mol K	R^2
CSTE-1.4							
22	1.57	5	0.9255	-3.7			
30	2.35	11	0.9514	-5.9	134	465	0.9463
60	4.67	107	0.8958	-12.2			
CSTE-2.9							
22	4.55	95	0.9741	-11.2			
30	5.64	283	0.9881	-14.2	119	440	0.9943
60	7.33	1527	0.9765	-19.1			

Conclusion

1. The equilibrium adsorption of methyl orange (MO) on cross-linked cationic starch derivatives containing different amount of tertiary amino groups, expressed as nitrogen content (1.4 % (CSTE-1.4) and 2.9 % (CSTE-2.9), respectively) was investigated at temperatures of 22 °C, 30 °C, 60 °C. The Langmuir, Freundlich and Dubinin–Radushkevich adsorption models have been used to describe the obtained adsorption isotherms. The calculated values of adsorption models confirmed that MO adsorption proceeded due to electrostatic interaction between tertiary amino groups of starch derivative and sulfo group of MO dye.

2. Thermodynamic parameters of adsorption of MO on CSTE-1.4 and CSTE-2.9 were calculated. The positive values of changes of enthalpy and entropy suggested that adsorption of MO on both CSTE was the endothermic process and the order of the system decreased during the adsorption.

References

1. R. Klimavičiūtė, A. Riauka, A. Žemaitaitis, J. Polym. Res., 2007, 14, 67.
2. R. Klimaviciute, J. Bendoraitiene, R. Rutkaite, A. Žemaitaitis, Int. J. Chem. Eng, 2008, 1, 161.
3. R. Klimaviciute, J. Bendoraitiene, R. Rutkaite, A. Žemaitaitis, J. Hazard. Mater, 2010, 181, 624.
4. R. Klimaviciute, J. Bendoraitiene, R. Rutkaite, J. Šiugždaitė, A. Žemaitaitis, Int. J. Biol. Macromol, 2012, 51, 800.
5. O. Hamdaoui, E. Naffrechoux, J. Hazard. Mater, 2007, 147, 381.

Study of polyolefin grafting reactions

A. Slietsov¹, B. Savchenko¹, N. Sova¹, V. Paharenko¹

Kiev National University of Technology and Design

Nemirovich-Danchenko 2, 01011, Kiev, Ukraine

Abstract— Polyethylene was functionalized with maleic anhydride (MA) in the presence of dicumyl peroxide (DCP) via different methods such as reactive extrusion and in solid state phase. Also was used petroleum, which increased the degree of grafting MA. It was found that using petroleum has positive effect on all methods of functionalization PE.

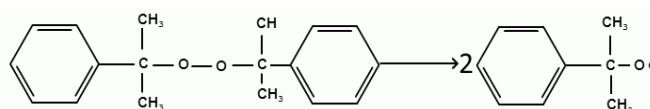
Keywords: petroleum, grafting, maleic anhydride, dicumyl peroxide

Introduction

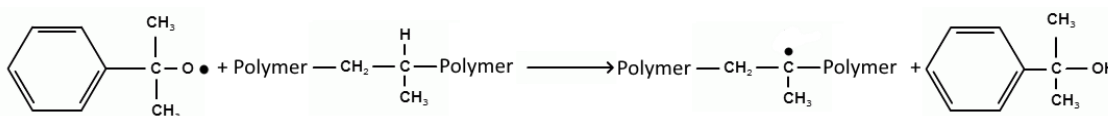
Polyolefin's are one of the most important thermoplastics in the world today. It has gained an important position among other polymers due to its versatile and broad range of applications [1]. Polymers like polyethylene (PE) and polypropylene (PP) is widely used in different applications such as packaging, films, threads, parts of automobile industry, etc. Functionalization of polyolefin's is an effective way of increasing their polarity and so its affinity with other polar materials. The introduction of polar groups in their backbones improve the physicochemical properties of the parent polymers and promote adhesion with other materials. MA is one of the widely used monomers for grafting. Polyolefin's grafted with MA are useful as a compatibilizers for blends or composites [2].

Mechanism of grafting consists of 5 main stages:

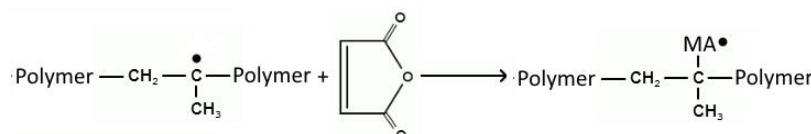
1. Peroxide decomposition.



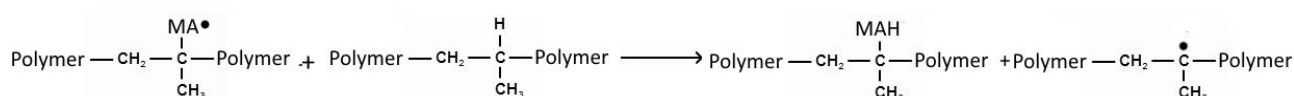
2. Initiation



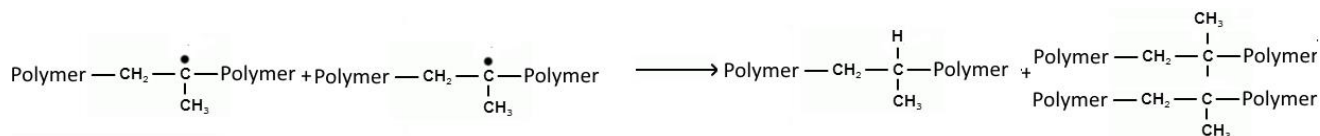
3. Propagation.



4. Chain transfer



5. Termination



Polyolefin's can be functionalized by different methods such as grafting in solution, reactive extrusion systems, grafting in solid state. The traditional method is grafting in polymer solution. This method consists in solution polyolefin in the xylene or decaline. Then peroxide (DCP) is added as initiator and MA. Reaction take place at moderate temperature range from 80 to 100°C with intensive steering. For removing unreacted MA, selective dissolution or vacuum drying can be used. [3].

Another method of Functionalization of polyolefin's is the reactive extrusion. Method consists of two steps: polyolefin mixed with the DPC and MA in a proportion and fed into the single-screw or two-screw extruder heated to a temperature 160-190°C. Then the product obtained from the extrusion is cooled and granulated. The second step is evacuation of unreacted MA from granular polymer. Advantage of this method is flexible possibility of controlling extruder pressure, temperature, residence time in the reaction zone. However, a single screw extruder can't give qualitative mixing and as result is a product with a low degree of grafting. Twin-screw extruders are open systems when much part of the MA is evaporates which reduces the degree of grafting and generate ecological issue.

The most modern way of grafting of functional groups is solid state phase grafting (SPG), where graft copolymerization was carried out by using peroxide, pure oxygen, ozone as an initiator and interfacial agent as solvent or swelling agent. Grafting process takes place at considerably lower temperatures than in other methods, above melting point of the target polymer.

Experimental

Functionalization was carried out by standard and modified techniques. Peroxide initiator was added as solution in swelling agent which allows increasing initiator/polymer contact area. Experimentally was found good solubility of DCP in paraffin oil under moderate temperature up to 100 to 100 weight pars at 50 – 70°C.

Grafted polyethylene was prepared using reactive extrusion method with a single screw extruder (D = 25, L / D = 25). The premix was prepared in a in a high speed mixer. First step of preparing the premix is dissolving DCP in paraffin oil (the ratio is 1:5). This solution 0.6% was then added to the mixer wherein the polyethylene powder (MFI=6) is heated to 90°C. After 5 minutes of mixing the initiator with polyethylene at a speed of 1500 rpm is added 2,5% MA. To determine the degree of grafting is first necessary to remove unreacted MA. The obtained product is washed in acetone, and then it is filtered and dried in a vacuum at 100°C. The evaluation of grafting degree was determined by titrating the acid groups [5]. The acid number (AN) and grafted MAH content were determined as following:

$$AN = \frac{mL\ KOH * N\ KOH * 56.1}{m(\text{polymer})} : \quad MA(\%) = \frac{AN * 98}{112.2}$$

Melt flow index (MFI) measurement was carried out with accordance to ISO 1133.

To determine the role of paraffin oil in this system control experiment was carried out a wherein the initiator added without dissolution step. Also, a similar experiment was conducted in a twin screw extruder with separate dosing and side-feeder loaded with MA. The enlarged twin-screw side-feeder unit gives increased throughput of solid materials. A first dispensing zone loaded by polyethylene mixed with initiator dissolved in paraffin oil with same proportions.

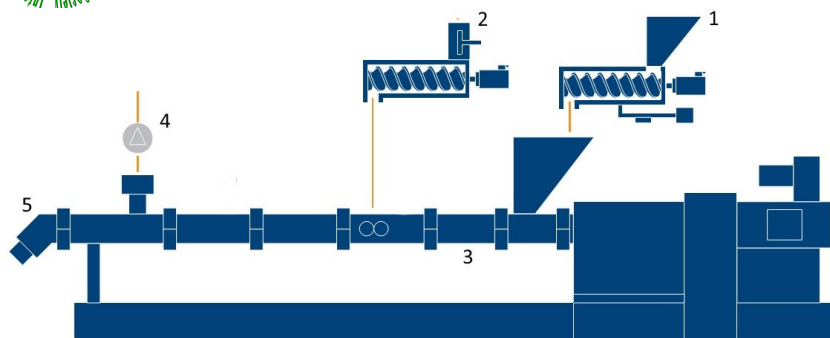


Fig.1. Reactive extrusion in twin-screw extruder: 1 – straw feeder, 2 – side-feeder, 3 – twin-screw extruder, 4 – vacuum degassing, 5 – die.

Co-rotating twin-screw extruders provide helical material transport and continuous material transfer between the screws. In conjunction with the shear energy input, this operating principle guarantees optimum compounding results in terms of distribution. Optimal screw elements for grafting are presented in the figure below.

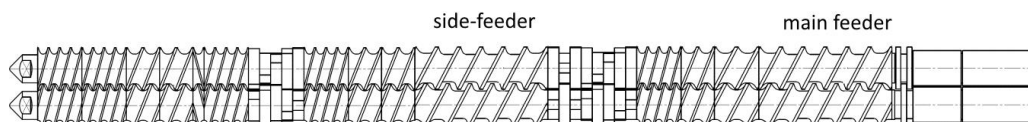


Fig.2. Screw elements for reactive extrusion.

Experiment with paraffin oil was also tested in SPG method of grafting. Twin-rotor open mixer was loaded with polyethylene powder and in paraffin oil initiator solution. This mixture was mixed for 15 minutes and then MA was added, the reaction temperature 90-100°C.

Result and Discussion

Titration infrared spectroscopy (IRS) methods was used on acetone washed and dried products to determine the ratio of grafted anhydride. Results are summarized in Table 1.

Table 1

Degree of MA grafting, % m.

Method of grafting	Processing in single-screw extruder	Processing in two-screw extruder	Processing by SPG
Without paraffin oil	1,06	1,21	1,51
With paraffin oil	1,32	1,71	2,10
MFI, g\10 min (2.16 kg, 190°C)			
Without paraffin oil	2,1	3,2	3,8
With paraffin oil	3,3	3,9	4,3

Table shows that the degree of grafting increasing with adding of paraffin oil with different methods of processing, in the same time MFI values is higher which can be explained as lubrication effect and as more effective peroxide mixing and reduction of DCP induced cross linking. Probably, paraffin oil acting as swelling agent for polyolefin and simultaneously as transport agent for DCP allowing more effective radical initiation.

Conclusion

Polyethylene was functionalized with MA and DCP in optimum processing conditions by solid state grafting. Anhydride grafting degree can be increased by using paraffin oil as DCP carrier. The properties of functionalized PE were characterized by titration and IRS. The whole process showing promising result and should be more studied.



References

1. K. Mehta, S. Kumar, G. S. Chauhan, and. B. N. Mishra, Grafting onto isotactic polypropylene. III. Gamma rays induced graft copolymerization of water soluble vinyl monomers, *J. Appl. Polym. Sci.*, vol. 41, pp. 1171 -1175, March **2003**.
2. Boen NK1, Hillmyer MA Post-polymerization functionalization of polyolefins, *Chem Soc Rev.* **2005** Mar; 34(3):267-75.
3. R. M. Ho, A. C. Su, C. H. Wu, S. Chen, Functionalization of polypropylene via melt mixing, *Polymer* 34 **1993** 3264-3269
4. John M. O'Leary, Jr., Wilmington, Del, C. Polypropylene plasticized with petrolatum *US* 3,281,390, October 25, **1966**.
5. Mousa Ghaemy*, Solaiman Roohina, Grafting of Maleic Anhydride on Polyethylene in a Homogeneous Medium in the Presence of Radical Initiators, *Iranian Polymer Journal*, 12 (1), **2003**, 21-29



Chemical recycling of polyester waste

I. Sliptsova¹, B. Savchenko¹, N. Sova¹, V. Paharenko¹

*Kiev National University of Technology and Design
Nemirovich-Danchenko Street, 2, 01011, Kiev, Ukraine*

Abstract

In this work the problem of disposal of polyethyleneterephthalate heavy wastes (PET) was investigated and the chemical decomposition of PET and his copolymer polyethylene glycol (PET-G). Reasoned features of the glycolysis and glycolysis PET and PET-G, identified differences of end products of depolymerization. Were found advantages and disadvantages of chemical degradation in extrusion equipment and chemical reactor.

Introduction

The mechanical, and chemical methods are the main methods of processing of waste (PET). For recycling of highly contaminated or mixed waste most promising is the chemical method, which is based on depolymerization to oligomers or monomers, which then can be used for production of alkyds, adhesives, unsaturated polyester resins and polyurethane compositions.

PET is a complex aromatic polyester, which is one of the most common polymers in the manufacture of bottles, containers, films and synthetic fibers. Waste PET are mixed blend different grades of PET contaminated waste. Some amount of resin is very dirty or contaminated and can not be recyclable by classical methods, due to low viscosity, a large amount of impurities and color.

The main application of virgin PET is bottle production, and for the last decades classical PET homopolymer was replaced by modern and versatile PET-copolymers which is dominated now on the resin market. From the different grades of PET copolymers most growing application and market sharing belong to high level PET copolymers known as glycol modified PET or PET-G. Compared to classical PET, PET-G is amorphous and cannot be crystallized during melt cooling, it known buy outstanding clarity, impact behavior and process ability. Chemical recycling of classical PET and PET copolymers is well studied in literature, but very little attention is given to PET-G as main recycling target.

Traditionally, PET depolymerization process is carried out in chemical reactors. The idea of using extrusion equipment for such reactions are more promising, due to the process control simplicity and possibility of caring reactor in one step and equipment unit in continuous way. For this purpose single or double screw extruders can be used. Single crew extruders have an advantage over two screws by their lover cost, and double screw extruders having better mixing efficiency [1-3].

Depolymerization can be accomplished by various methods solvolysis. This is methods such as glycolysis, glycerolysis, aminolysis, methanolysis. The reaction of glycolysis is the molecular degradation of PET by glycol, in the presence of catalysts, mainly metal acetates. Typically, the reaction of glycolysis taking from 3 to 8 hours, depending on the selected glycol, at $180 \div 250$ °C. Depolymerization of PET waste by glycolysis produces oligomeric diols and polyols, or monomeric units of BHET (bis-hydroxyethylterephthalate) or dimethylterephthalate (DMT) [4]. Glycerolysis is the reaction of PET with glycerol or monoglycerides, which is gaving intermediate oligomeric products for alkyd resins designed for coatings.

Experimental

Waste PET and PET-G, propylene glycol (PG) and glycerol (GI) was used as a feedstock for chemical recycling in the classical chemical reactor and in the extruder setup. The chemical depolymerization method of glycolysis was conducted on a laboratory extrusion setup based on 25mm extruder (fig.1), with three zones of heating. The screw was cooled in feed area for preventing boiling of glycol. The passage duration of the reaction mixture in the extruder ranged from 2 to 20 min, depending on the rotation speed of the extruder screw and straw feeder productivity which was independently adjusted.

The stability of process was controlled by die pressure and temperature measurement. The depolymerization product was filtered by mesh filter which was located in the die head 6, then recyclate was casted on the conveyer belt 9, which was made from heat and stick resistant material. The recyclate was cooled by air steam on the conveyer belt.

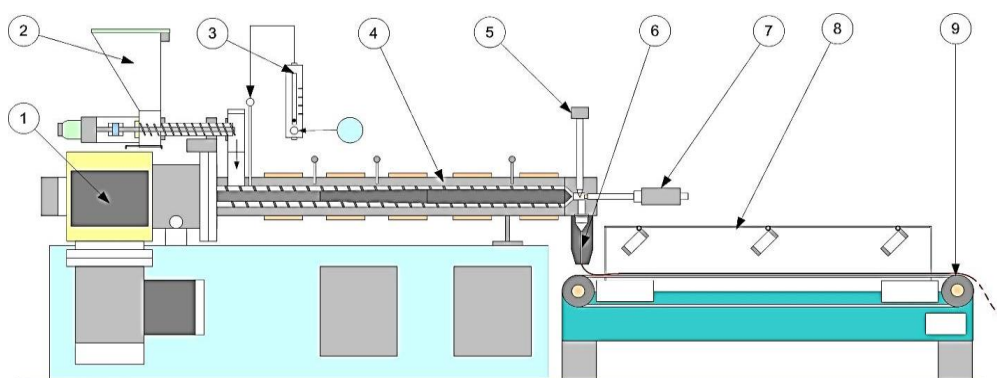


Fig. 1. Depolymerization setup: 1 – drive system 2 – straw feeder, 3 - peristaltic dosing pump, 4 – single screw extruder, 5 - melt temperature sensor, 6 – cast die head, 7 - melt pressure sensor, 8 – cooling fans 9 - feed conveyor.

Process parameters for depolymerization of PET and PET-G (tab. 1) in the extruder.

Table 1

Depolymerization conditions for PET and PETG by singles crew extrusion

№	The material	Temperature zones, °C			Screw speed, rpm
		I	II	III	
1	PET	150	265	180	10-12
2	PET-G	100	200	150	10-12

The discontinuous glycolysis process of PET and PETG was conducted in the classical reactor for duration time 5 hours at $180 \div 220$ °C the following raw material weight ratios was used: PET / PG as 1/1, 1 / 2, 1 / 3, 1 / 4 2/1; glycerolysis was conducted under the same conditions with PET ratios (and PETG) / GI as 1/1, 1/3, 3/1. The classical reactor, equipped with stirrer and control and regulation system with data recording on the PC. Determination of the temperature of the reaction mixture was carried out using thermocouple sensor. The depolymerization process was carried out in a vacuum, with nitrogen substitution or in the nitrogen flow controlled by flow meter.

During reaction flow temperature changes versus time was recorded (fig.2) which allows to control the depolymerization process stability and to determinate heat effect of the reaction.

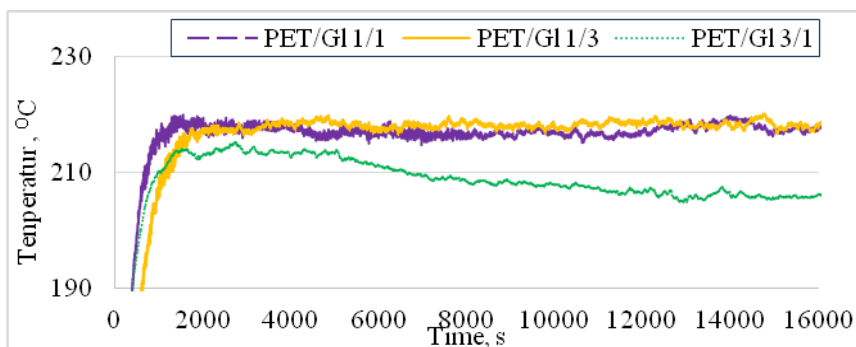


Fig.2. The temperature changes over time during depolymerization of PET.

In cases where the PET is in excess, the process of depolymerization occurs at a lower temperature which can be explained by the formation of products different in composition than other relationships.

The determination of acid and hydroxyl number and molecular weight depolymerization products was performed by the standard method. The content of BHET and oligomers were determined by selective dissolution techniques.

Result and discussion

The recyclate has a high percentage of BHET, when PG is used in large excess and surplus in PET - a mixture of lower oligomers. Percentage of oligomers in recyclate depends on the type and content chosen glycol. Molecular mass (MM) oligomers depends on the content of glycol, the glycol content with a smaller MM is the lower (tab.2).

Table 2

The composition and properties of recyclate

Material	Equipment	Ratio	Acid number mgNaOH/g	Hydroxyl number mgNaOH/g	Molecular weight	Content of oligomers, %	Content of BHET, %	Content of solubles, %
PET / PG (wt.r)	Reactor	2/1	13,0	16,0	3080	64	28	8
		1/1	8,0	20,0	2860	41	52	9
PET / PG (wt.r))		1/2	5,0	37,0	1900	28	61	11
		1/3	4,5	50,0	1470	15	75	10
PET / Gl (wt.r))		1/4	3,0	72,0	1070	8	82	10
		3/1	12,5	18,0	2620	82	6	12
		1/1	11,0	38,00	1630	72	12	16
PETG /Gl (wt.r))		1/3	8,5	70,0	1020	58	31	9
		3/1	7,5	27,0	2320	83	8	9
	1/1	6,0	54,0	1330	75	10	15	
PETG / Gl (wt.r))	Extruder	1/3	4,0	80,0	950	68	11	21
		3/1	12,0	20	2500	78	10	12
		1/1	10,0	42	1540	71	13	16
		1/3	9,0	58	1190	66	14	20

The hydrolysis products were subjected to IR spectroscopy with different content of PG (wt. r.): PET / PG: 1/1; PET / PG: 1/2; PET / PG: 1/3; PET / PG: 1/4; PET / PG: 2/1.

After depolymerization the change of intensity of peaks at the frequencies of C = O groups (1721 cm^{-1}), a benzene ring ($1576, 1524\text{ cm}^{-1}$), methylene groups ($2940, 2891, 1452$



cm⁻¹), ether groups -C-O- C, complex ether groups (1271, 1124, 1020 cm⁻¹); methylene groups connected by oxygen bridge (733 cm⁻¹), hydroxyl groups OH (3400 cm⁻¹) was recorder and interpreted. Peak intensity of 3400 cm⁻¹, corresponding to the OH groups increases with the content of glycol. The kinetics of depolymerization in the extruder is similar in chemical reactor, but reaction intensity is much higher. The recyclate of PETG obtained in single screw extruder has more content BHET due to more intensive depolymerization process.

Conclusion

The recyclates of PET and PETG are different which is revealed by their MM, which is estimated by the acid and hydroxyl. The content of oligomeric products are larger, and MM is higher and the content of BHET is more, when MM of recyclate is lower. The type of glycol is a factor that affects the composition of recyclate: using GI content of oligomers is higher, and conversely using PG becomes more content of BHET.

IR spectra showing change in the intensity peaks at a frequency of 730 cm⁻¹, 1020 cm⁻¹, 1274 cm⁻¹, 1720 cm⁻¹, 2800-3000 cm⁻¹ and 3400 cm⁻¹, indicating a change in the chemical polyester structure.

PET-G depolymerization products are different from traditional PET copolymer products by higher content of oligomer products rather than monomer products which is preferable for some application stream like UPR. Depolymerization temperature is lower than for classical PET.

The several advantages were found by conducting depolymerization reaction in extrusion equipment compared to the chemical reactor, which include possibility of strict temperature and reaction intensity control, energy efficiency and continuous production process.

References

1. J. Scheirs, E. Timothy Long Modern Polyesters: *Chemistry and Technology of Polyesters and Copolyesters*. Wiley, **2003**.
2. F. Awaja, D. Pavel. Recycling of PET, *European Polymer Journal*, **2005**, 41, 465-1467.
3. N. Pingale, V. Palekar, S. Shukla, Glycolysis of postconsumer poly(ethyleneterephthalate) waste, *Journal of Applied Polymer Science*, **2010**, 115, 249-254.
4. I. Pogrebnyak, B. Savchenko, N. Sova, V. Paharenko, Wood-filled composition based on recycled PET. Preparation and properties, *Journal of Plastics*, **2013**, 6, 41-43 (in russ.)
5. G. Macijauskas, V. Jankauskaitė, Epoxy resin and polyurethane compositions from glycolized poly(ethyleneterephthalate) wastes, *Materials science*, **2013**, 3, 1320-1392.

IN SITU MODIFICATION OF BACTERIAL CELLULOSE BY ADDING ESSENTIAL OIL DURING FERMENTATION

J. Širvaitytė¹, P. Bekampienė², J. Domskienė¹, I. Jonuškienė¹, V. Valeika¹

¹ Kaunas University of Technology, K. Donelaičio st. 73, LT-44249, Kaunas, Lithuania

² State Research Institute Center for Physical Sciences and Technology, Savanorių ave. 231, LT-02300, Vilnius, Lithuania

E-mail: bekampiene@lti.lt

Introduction

Bacterial cellulose (BC) differently from plant cellulose (PC) does not require remedial processing to remove unwanted biopolymers and retains a higher degree of polymerization, crystallization and water holding capacity [1]. These properties make BC attractive for a wide range of applications, e.g. in chemical, paper, food, medicine and other fields of industry [2]. In medicine, a gelatinous BC sheets can be used as an artificial skin to temporarily cover the wounds [1]. It has inherent permeability to liquids and gases and does not irritate skin. Therefore, during the wound healing process serves as breathable physical barrier against microorganisms [3]. Active wound dressings are impregnated with antimicrobials (topical antibiotic and antifungal products). Silver sulfadiazine, methylene blue, crystal violet, honey, polyhexamethylene biguanide and cadexomer iodine are commonly used as antimicrobials, to prevent local infection, especially in the case of chronic wounds [4]. Inorganic and organic antiseptic agents have shown a certain degree of success for various medical applications, however, the use of all-natural medicinal extracts such as essential oils has a great potential in pharmaceutical applications and *in vivo* patient care. It is well known that essential oils (EOs) that contain substituted phenols (eugenol, thymol, carvacrol, and guaiacol) exhibit strong antibacterial and antioxidant effects. Among them, lavender oil has been used for centuries as healing agent for burns and natural antiseptic [5]. Therefore, the aim of the study was to provide antibacterial properties for BC by its *in situ* modification using *Lavandulae officinalis* essential oil in BC fermentation process.

Methods and materials

BC preparation. The BC was produced using Kombucha strains primary referred to the gram-negative bacteria species *Gluconacetobacter xylinus* (formerly *Acetobacter xylinum*) which are easily and efficiently synthesized [6]. The strain was cultivated in freshly prepared liquid medium. Black tea (2 g) was added to 1 L water and allowed to boil for 5 min. The obtained tea solution was cooled to room temperature and filtered. Then, 10 g of sucrose and 100 ml of 6% yeast extract were added. The prepared solution was incubated with Kombucha strain and fermentation was carried out at 20±1°C temperature and 65±5% relative air humidity for 7 days in a static cultivation conditions. The received membrane was washed with water, dried on horizontal surface and subjected to analysis. The group of samples was prepared with 5% of *Lavandulae officinalis* essential oil (LO) purchased from company “Mėta” (Lithuania).

Antimicrobial susceptibility. The gram negative rod-like lactose fermenting bacteria, belonging to family Enterobacteriaceae *Escherichia coli* (ATCC 8739), was used for the investigation of antimicrobial activity of BC. The selected bacteria were cultivated on Luria-Bertani (LB) media (composition: NaCl – 10.0 g/L; Tripton – 10.0 g/L; yeasts extract – 5.0 g/L). Bacterial suspensions of 0.25 ml were inoculated on plates with LB. The BC and BC/LO samples having diameter 10 mm were placed in Petri plates. The test paper (diameter 10 mm) was well impregnated by LO and placed in Petri plate as a control sample. Inoculated Petri

plates were incubated at 35-37°C temperature, for 24 hours. Resistance to essential oil and BC, BC/LO was evaluated calculating (mm) inhibition zones.

Thermal and spectroscopic characterisation. FTIR spectra were recorded using Perkin–Elmer Spectrum BX II FTIR System spectrophotometer. The spectra were recorded at the wave numbers from 4000 to 400 cm^{-1} with the 4 cm^{-1} resolution. DSC analyses were carried out using Universal V4.1D TA Instruments calorimeter. The samples were examined at a heating rate of 10 $^{\circ}\text{C}\cdot\text{min}^{-1}$ under nitrogen atmosphere.

Results

Preliminary investigation had shown that LO, as it was expected, formed the film on the surface of liquid medium and slowed down the formation of BC membrane due to lack of oxygen [7]. EOs does not mix or dissolve in water, but due to their small size of molecules easily penetrates through cell walls and affects various biochemical processes. The established thickness of BC samples after 7 days of cultivation was 0.85 mm for BC and 0.11 mm for BC/LO, respectively. It shows that in the case of BC/LO the fermentation process was significantly slower. Also, it can be assumed that *Lavandulae officinalis* essential oil affects the growing process of bacteria which produces BC because of its antibacterial activity.

The next step of this investigation was to determine *Lavandulae officinalis* essential oil diffusion into BC matrix during cultivation process that ensures the antibacterial properties for BC. The biological activity of essential oils depends on their chemical composition. The chemical composition of the essential oil was analysed using GS/MS and 30 constituents of *Lavandulae officinalis* essential oil and was specified in previous study [8]. The analysis of these samples showed that the main components are linalool (32.22%) and linalyl acetate (42.14%). To evaluate BC and LO interactions the DSC and FTIR spectroscopy was carried-out.

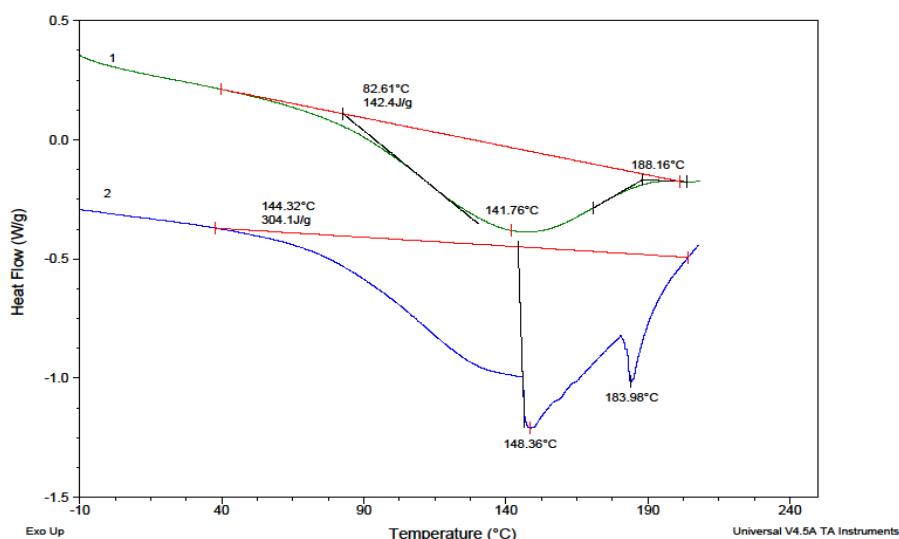


Fig. 1. DSC thermograms of BC (1) and BC/LO (2)

The thermal behaviour of BC and BC/LO obtained by the DSC is presented in Figure 1. According to literature, at temperatures of 80-140°C, there is known to be an occurrence of transformation related to the melting of the crystalline phase of cellulose [9]. It can be seen that introduction of LO lead to the endothermic peak temperature shift from 142 $^{\circ}\text{C}$ to 148 $^{\circ}\text{C}$ and increase in specific heat of fusion from 142 Jg^{-1} to 304 Jg^{-1} which indicates higher amount of crystalline regions present in BC/LO sample. Whereas, the second peak at 183°C in curve 2 (Fig. 1) can be attributed to LO evaporation process and confirms LO diffusion into BC

matrix. These results can be supported by the other research works; the DSC curves of Orange, Lemongrass, and Basil oils have shown endothermic peaks at 179°C, 230°C, and 220°C, respectively, related to the oil evaporation [10].

The recorded IR spectra for pure BC and BC/LO are presented in Fig. 2 (B). The IR spectra of Linalool will be analysed for comparison as it is one of the main components of LO. The bands at 3340, 2823, 1648, 1424 and 1030 cm^{-1} (Fig. 2 (B)) are typical to native BC [11, 12]. However, no obvious peaks, which could be attributed to Linalool, were attained in IR spectra of tested samples. The differences between BC and BC/LO spectra's were also alike.

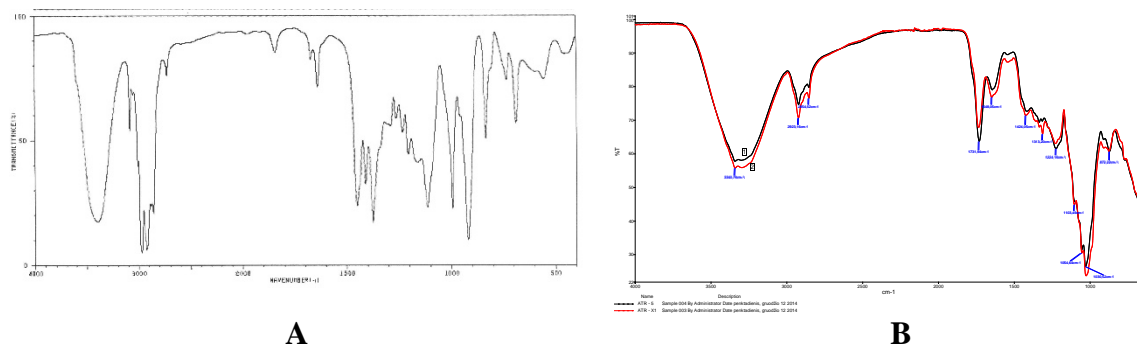


Fig. 2. FTIR spectra's of pure Linalool (A) and investigated samples (B): 1 – BC; 2 – BC/LO

BC, by itself, has no ability to prevent infection. However, the lavender essential oil has the potential to reverse bacterial resistance to *Escherichia coli* [13] which is one of the leading causes of infection in wounds [14]. Therefore, the next step of investigation was to determine antibacterial properties of BC and BC/LO to *E.coli*. The received results are presented in Figure 3.

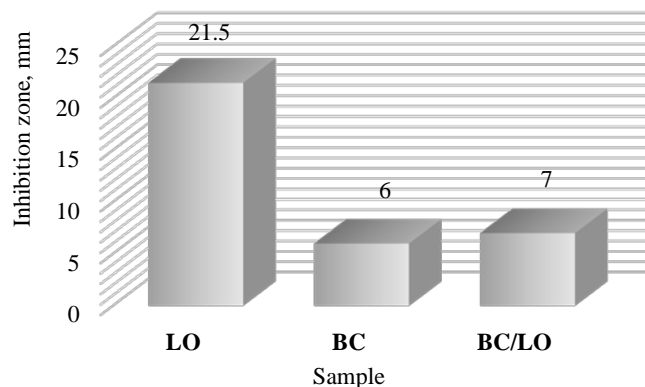


Figure 3. The zone of inhibition (mm) of investigated samples

It can be seen that *E.coli* is sensitive to LO. BC samples have inhibited *E.coli* action but, probably, it occurs because of its low pH (2.74). BC/LO samples have shown only slightly higher results than BC.

Discussion

The preliminary results of the investigation have shown that *in situ* modification of BC with *Lavandulae officinalis* essential oil during fermentation decreases the productivity of cultivation process. It should be studied the influence of variation of essential oil concentration and of its addition method on the fermentation process to obtain required antibacterial properties of BC.



References

1. P. Chen, S.Y. Cho, H.J. Jin. *Macromolecular Research*, 2010, 18, 4, pp. 309-320.
2. P.M. Visakh, A.P. Mathew, S. Thomas. *Advances in Natural Polymers*. Springer, Berlin-Heidelberg, **2013**.
3. G.D. Mogoşanu, A.M. Grumezescu. *International Journal of Pharmaceutics*, **2014**, 463, 2, pp. 127-36.
4. M. Zilberman, J.J. Elsner. *Journal of Controlled Release*, **2008**, 130, 3, pp. 202-215.
5. A. Kunicka-Styczynska, M. Sikora, D. Kalemba. *Journal of Applied Microbiology*, **2009**, 107, pp. 1903-1911.
6. C. Zhu, F. Li, X. Zhou, L. Lin, T. Zhang. *J Biomed Mater Res A*, **2014** 102, 5, pp. 1548-1557.
7. D. Raghunathan. *International Journal of Current Microbiology and Applied Science*, **2013**, 2, 12, pp 275-290.
8. J. Širvaityte et al. *Revista de chimie*, **2011**, 62, 9, pp. 884-893.
9. G. Johnsy et al. *International Journal of Biological Macromolecules*, **2005**, 37, pp. 189-194.
10. P. Martins. *10th International Conference on Chemical and Process Engineering*, pp. 463.
11. W. Hu, S. Chen, Z. Yang, L. Liu, H. Wang. *Journal of Physical Chemistry B*, **2011**, 115, pp. 8453–8457.
12. W. Hu, S. Liu, S. Chen, H. Wang. *Cellulose*, **2011**, 18, pp. 655–661.
13. P. S. X. Yap et al. *Journal of Applied Microbiology*, **2014**, 116, 5, pp. 1119-1128.
14. M.A. Saeed et al. *The Journal of Antibiotics*, **2009**, 62, 6, pp. 319-23.

THE INFLUENCE OF ZEOLITE CATALYST ON POLYPROPYLENE WASTE THERMAL DECOMPOSITION KINETICS AND THERMODYNAMICS

E. Valančienė^{1,2}, L. Miknius², N. Pedišius¹

¹Lithuanian Energy Institute, Breslaujos str. 3, LT-44403 Kaunas, Lithuania
e-mail: egle.andrikaityte@gmail.com

²Kaunas University of Technology, Radvilėnų pl. 19, LT-50254 Kaunas, Lithuania

Abstract

The aim of this research is to analyse the influence of regenerated FCC catalyst amount to kinetic and thermodynamic parameters of PP waste thermolysis. The activation energies, pre-exponential factors were determined by the requirements of standard ASTM E 1641 procedure. Thermodynamic parameters were calculated using transition state theory. The activation energies, logarithmic values of pre-exponential factors, the changes of entropy and enthalpy show tendency to decrease with increasing FCCC amount in the mixture. Only the changes of free Gibb's energies are similar for all mixtures analysed and they are in the range of 196.94-219.95 kJ/mol. These results are important for applying a new catalyst in the thermal decomposition of plastics because it requires detailed research of this catalyst influence on the decomposition reaction and determined reaction kinetic and thermodynamic parameters. These parameters are very important to the reactor design as well as development of polymer recycling in the industrial scale and for modelling of catalytic thermolysis of plastic wastes.

Introduction

Nowadays polyolefins are widely used as industrial and household thermoplastics which also are the main components of plastic wastes. The environmental problems of plastic waste disposal in landfill, or its incineration, have led to increasing interest in their recycling by thermal or catalytic degradation to obtain fuels (diesel and gasoline) and/or valuable chemicals [1]. The most commonly used catalysts in the catalytic degradation of polymers are acidic zeolite catalysts: silica-alumina, β -zeolite, Y-zeolite, mordenite, HZSM-5, MCM-41, etc., which are of similar pore size and structure or acidity [2]. Applying a new catalyst in the thermal decomposition of plastics requires detailed research of this catalyst influence on the decomposition reaction and determined reaction kinetic and thermodynamic parameters which are very important to the reactor design as well as development of polymer recycling in the industrial scale and for modelling of catalytic thermolysis of plastic wastes.

Materials and Methods

Polypropylene was collected from the household. Zeolite regenerated NaceR™ FCC ("Grace", USA) catalyst was received from PC "ORLEN Lietuva" refinery. The catalyst amounts in the mixtures with PP were 0, 1, 3, 5, 10, 25, 50 percent.

Thermogravimetry experiments were carried out with Perkin Elmer TGA 4000 (USA) at inert atmosphere at a temperature range of 303-823 K. Nitrogen gas flow rate was set to 20 ml/min. The amount of PP used in the single experiment was 3±1 mg. The PP samples were ground and mixed with appropriate amount of catalyst mechanically before each experiment. Samples were loaded without pressing into an open ceramic crucible.

Calculation of activation energy. Activation energies were calculated by standard method ASTM E 1641 [3] using the following equation:

$$E = -\left(\frac{R}{b}\right) \cdot \Delta(\log \beta) / \Delta\left(\frac{1}{T}\right) \quad (1)$$

where b – approximation derivative which is equal to 0.457 K on the first iteration. Then calculating E_{i-1}/RT values, a new b estimation was chosen. Resubmitting this value of b to the previous equation the value of E_i was estimated. The procedure was repeated while the activation energy change was less than 1 %. The calculation performed by this procedure is named ASTM in this paper.

Calculation of pre-exponential factor A. According to ASTM E 1641 standard, the pre-exponential factor is estimated by the following equation [3]:

$$A = -\left(\frac{\beta}{E}\right) \cdot R \cdot \ln(1 - \alpha) \cdot 10^a \quad (2)$$

where a is approximation integral.

Thermodynamic parameters (such as enthalpies (ΔH^\ddagger), Gibbs free energies (ΔG^\ddagger), and entropies (ΔS^\ddagger)) of activated complex formation were calculated using transition state theory by Eqs. (3)-(5) [4]:

$$\Delta H^\ddagger = E_a - RT \quad (3)$$

$$\Delta G^\ddagger = E_a - RT_m \ln\left(\frac{k_B T_m}{hA}\right) \quad (4)$$

$$\Delta S^\ddagger = \frac{\Delta H^\ddagger - \Delta G^\ddagger}{T_m} \quad (5)$$

where k_B is the Boltzmann constant, h is the Plank constant, T_m is a maximum temperature, ΔS^\ddagger and ΔH^\ddagger are the changes of entropy and enthalpy, respectively, for the formation of the activated complex from the reagent.

Results and Discussion

PP waste pyrolysis is the single step reaction as it is proved by TG curves. Sample plots for variations of PP conversions (α) at different heating rates (fig. 1) and for all PP and FCC catalyst mixtures at 2.5 K/min heating rate (fig. 2) are shown below. When heating rate is slower, then the same PP conversion value is reached at lower temperatures (fig. 1). PP degradation reaction also occurs at the lower temperatures when FCC catalyst is added to the reaction mixture. When more catalyst amount is added, the lower temperature is needed to complete the reaction (when $\alpha = 1$). The mixtures containing FCC catalyst of 0 % and 50 % reach final conversions at temperatures of 720 K and 653 K, respectively (fig. 2). The pyrolysis of polypropylene occurs by a radical mechanism and the initiating radicals are formed by cleavage of C-C bonds under elevated temperature. In this case the instability of macromolecules is often due to the presence of anomalous weak bonds in the polymer [5]. Thermocatalytic thermolysis generally proceeds through carbenium ions.

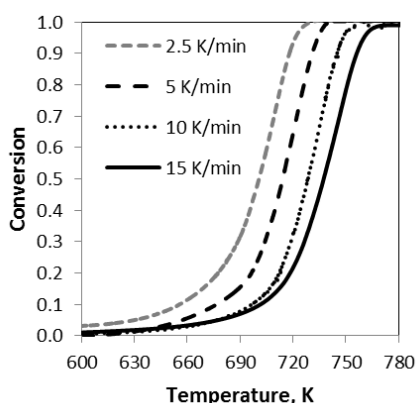


Fig. 1. Variations of PP conversions with temperature at different heating rates

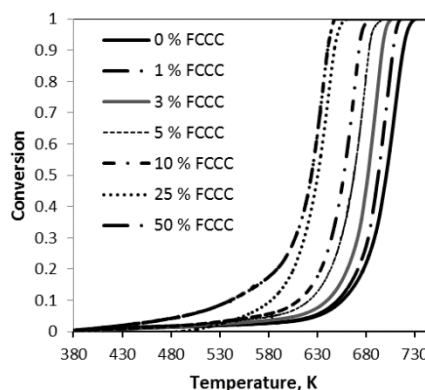


Fig. 2. Variations of PP conversions with temperature for different PP and FCC catalyst (FCCC) mixtures ($\beta = 2.5$ K/min)

The values of kinetic and thermodynamic parameters of decomposition reaction of polypropylene waste and FCCC mixtures are presented in the table 1. The activation energies, logarithmic values of pre-exponential factors, the changes of entropy and enthalpy show tendency to decrease with increasing FCCC amount in the mixture. Only the change of free Gibb's energy is similar for all mixtures analysed and it is in the range of 196.94-219.95 kJ/mol.

Table 1. The values of kinetic and thermodynamic parameters for different mixtures

Parameter	FCC catalyst amount, %						
	0	1	3	5	10	25	50
E_a , kJ/mol	125.37	120.66	113.16	93.66	91.33	72.44	58.23
$\ln A$, [A]=min ⁻¹	18.396	17.350	16.325	13.219	13.521	10.128	8.078
T_m , K *	710.15	701.15	691.15	679.15	668.15	641.15	636.15
ΔS^\ddagger , J·mol ⁻¹ ·K ⁻¹ *	-141.49	-150.08	-158.49	-175.05	-181.52	-209.38	-226.36
ΔH^\ddagger , kJ·mol ⁻¹ *	119.47	114.83	107.41	88.60	85.77	67.11	52.94
ΔG^\ddagger , kJ·mol ⁻¹ *	219.95	220.06	216.95	207.48	207.05	201.35	196.94

* - Heating rate 2.5 K/min.

Conclusions

The thermal conversion characteristics of polypropylene waste mixed with various amounts of regenerated fluid catalytic cracking catalyst (FCCC) were quantitatively identified and the dependences of these parameters on the FCCC amount used were determined. The activation energies, pre-exponential factors were determined by standard ASTM E 1641 procedure requirements. Thermodynamic parameters were calculated using transition state theory. The activation energies, logarithmic values of pre-exponential factors, the changes of entropy and enthalpy shows tendency to decrease with increasing FCCC amount in the mixture. Only the changes of free Gibb's energy are similar for all mixtures analysed and they are in the range of 196.94-219.95 kJ/mol.

References

1. A. De Stefanis, P. Cafarelli, F. Gallese, E. Borsella, A. Nana, G. Perez. *J. Anal. Appl. Pyrolysis* 104 (2013) 479–484.
2. N. Miskolczi, L. Bartha, G. Deak. *Polym. Degrad. Stab.* 91 (2006) 517-526.
3. ASTM E 1641-99. Standard Test Method for Decomposition Kinetics by Thermogravimetry.
4. Y. Xu, B. Chen. *Bioresour. Technol.* 146 (2013) 485–493.
5. S. Kumara, A. K. Panda, R. K. Singh. *J. Resour. Conserv. Recy.* 55 (2011) 893– 910.

SYNTHESIS AND PROPERTIES OF MONOMER AND POLYMER BASED ON INDANDIONE MOIETY

V. Zilinskaite, M. Bistrickas, D. Gudeika, J.V. Grazulevicius

Department of Polymer Chemistry and Technology, Kaunas University of Technology, Radvilenu pl. 19, LT-05424 Kaunas, Lithuania

Abstract. Monomer and polymer based on indandione were synthesized and characterized. It was found that the polymer exhibited lower electrochemical ionization potential value (5.58 eV) compared to the monomer (5.64 eV).

Keywords: indandione, monomer, polymer, ionization potential.

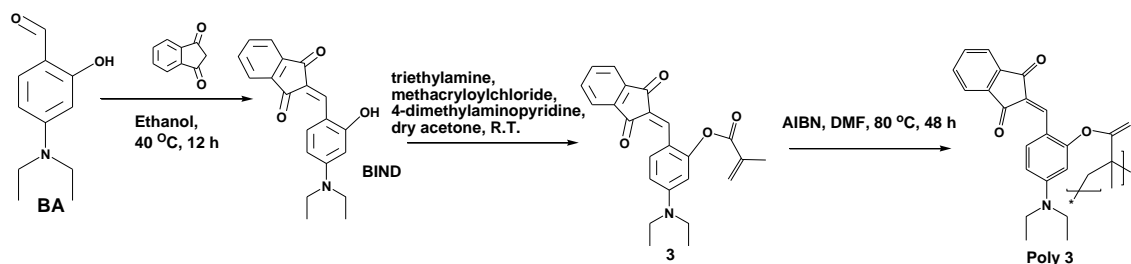
Introduction

Electroactive glass-forming low-molar-mass compounds and polymers are known for various applications such as organic field-effect transistors, solar cells and etc. [1-3]. Amorphous electro-active layers of the polymers can be fabricated by using simple techniques, such as casting or spin-coating from solutions. Such processable materials are advantageous for the application in large area devices. To our knowledge, polymers containing 1,3-indandione moieties as electroactive pendants have not yet been studied and described in the literature in detail.

The aim of this work was the synthesis and investigation of indandione-based methacryloyl monomer, and investigation of the possibility of its free radical polymerization using 2,2'-azobis(2-methylpropionitrile) (AIBN) as an initiator.

Results and Discussion

The synthetic route to indandione-based compounds is shown in Scheme 1.



Scheme 1. Synthesis of monomers **BIND**, **3** and polymer (**poly 3**).

The monomer **3** containing methacryloyl group was synthesized by two step procedure. In the first step, an intermediate compound **BIND** was produced by the reaction of commercially available 2-hydroxy-4-diethylaminobenzaldehyde (**BA**) and 1,3-indandione. In the second step, monomer **3** was prepared by reaction of **BIND** with methacryloyl chloride at the room temperature in dry acetone. Finally, free radical polymerization of **3** using AIBN as the initiator was performed in septum capped scintillation vials under nitrogen at 80 °C in dimethylformamide (DMF) for 48 h. The resulting viscous solutions were diluted with DMF and the polymer precipitated in excess ethyl acetate, giving the polymer **poly 3** in good yield (74 %).

Low-molar-mass fractions were removed from the polymer by Soxhlet extraction of the product of polymerization with methanol. The synthesized low-molar-mass derivatives were

identified by mass spectrometry and ^1H NMR spectroscopy. The compounds were soluble in common organic solvents (THF, chloroform, acetone). Polymerization of the monomer **3** confirmed by IR spectroscopy. The main evidence of the polymer formation is certainly the disappearance of some characteristic signals of the double bond in the spectrum. Thus the absorption bands at 992 cm^{-1} and 881 cm^{-1} assigned respectively to the C-H bending and C-H rocking mode of vinyl group and the stretching vibration band of C=C at 1635 cm^{-1} disappeared in the IR spectrum of **poly 3**.

The number average (M_n) and weight average (M_w) molecular weights and polydispersity index (PI) of the **poly 3** were determined by GPC using polystyrene standards are summarized in Table 1. The number average (M_n) and weight average (M_w) molecular weights of the **poly 3** was determined by GPC using polystyrene standards.

Table 1. Molecular weights and polydispersity index of polymer **poly 3**.

Polymer	poly 3
M_n	4594
M_w	6055
M_w/M_n	1.32

The behavior under heating of compounds **3** and **poly 3** was studied by DSC and TGA. All the synthesized compounds (**3** and **poly 3**) demonstrate rather high thermal stability. The 5% weight loss temperatures were $190\text{ }^\circ\text{C}$ (for **3**) and $225\text{ }^\circ\text{C}$ (for **poly 3**), as confirmed by TGA with a heating rate of $20\text{ }^\circ\text{C}/\text{min}$. The DSC thermograms of **3** are shown in Fig. 1.

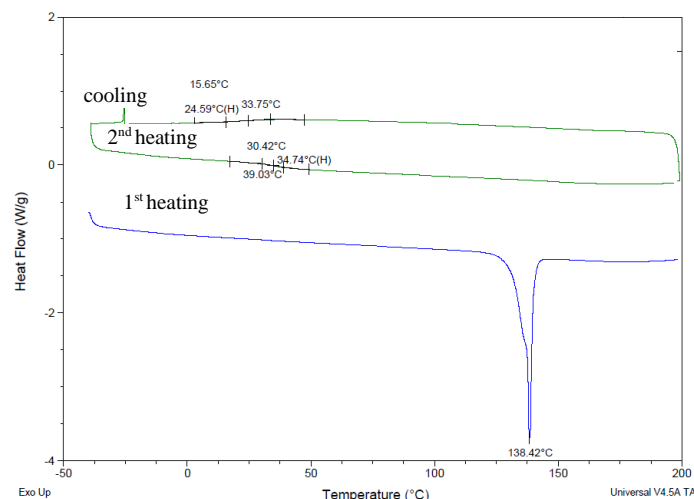


Fig. 1. DSC curves of compound **3** at the heating/cooling rate of $10\text{ }^\circ\text{C}/\text{min}$ in N_2 atmosphere.

Monomer **3** after the synthesis was obtained as crystalline material. When the crystalline sample of **3** was heated, the endothermic peak due to melting was observed at $138\text{ }^\circ\text{C}$. When the melt sample was cooled down and heated again, the glass transition was observed at $39\text{ }^\circ\text{C}$ and on further heating no peaks due to crystallization and melting appeared. **Poly 3** was obtained as amorphous substance as it was confirmed by DSC analysis. Polymer **poly 3** demonstrates higher glass-transition ($T_g = 71\text{ }^\circ\text{C}$) than that of monomer **3**.

UV-vis absorption and fluorescence (FL) spectra of the dilute THF solution of monomer **3** and polymer **poly 3** is shown in Fig. 2. The comparison of UV-vis absorption spectra of the monomer **3** with the spectrum of their polymer **poly 3** are red shifted in comparison with that of **3** ($\Delta\lambda_{\text{max}} = 2\text{ nm}$). The comparison of FL spectra of monomers **3** with that of the polymer **poly 3** revealed bathochromic shifts of the spectra of polymer with respect to that of the corresponding monomer **3** ($\Delta\lambda_{\text{max}} = 2\text{ nm}$).

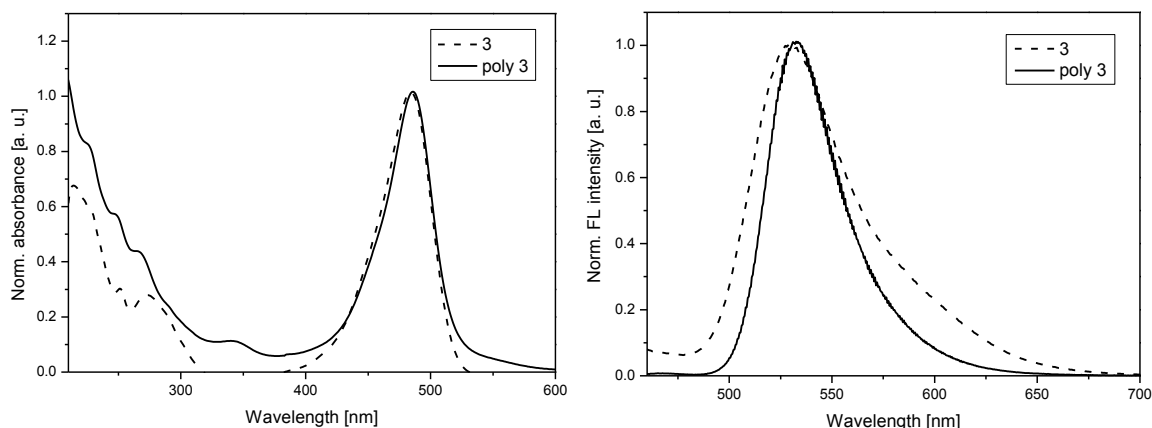


Fig. 2. UV-vis absorption and fluorescence spectra of the dilute THF solutions (10^{-5} M) of compounds **3** and **poly 3**. Absorption maximum wavelength was used as excitation wavelength.

The ionization potential (IP_{CV}), electron affinity (EA_{CV}) values of monomer **3** and polymer (**poly 3**) were estimated by cyclic voltammetry (CV). It was found that the IP_{CV} and EA_{CV} values of monomer **3** were 5.64 eV and -2.83 eV, respectively. **Poly 3** showed slightly lower IP_{CV} (5.58 eV) than the monomer **3**.

Conclusions

Indandione-based monomer and the corresponding polymer were synthesized and characterized. Their thermal, electrochemical, optical and photophysical properties were studied. The monomer and polymer can form molecular glass with glass transition temperatures of 39 and 71 °C, respectively. The polymer had number average molecular weight of 6055 and with polydispersity index of 1.32.

References

- [1] A. Hagfeldt, G. Boschloo, L. Kloo, H. Pettersson, *Chem. Rev.*, **2010**, *110*, 6595.
- [2] M. Liangw, J. Chen, *Chem. Soc. Rev.*, **2013**, *42*, 3453.
- [3] J. Baldenebro-López, J. Castorena-González, N. Flores-Holguín, J. Almaral-Sánchez, D. Glossman-Mitnik, *Int. J. Mol. Sci.*, **2012**, *13*, 4418.